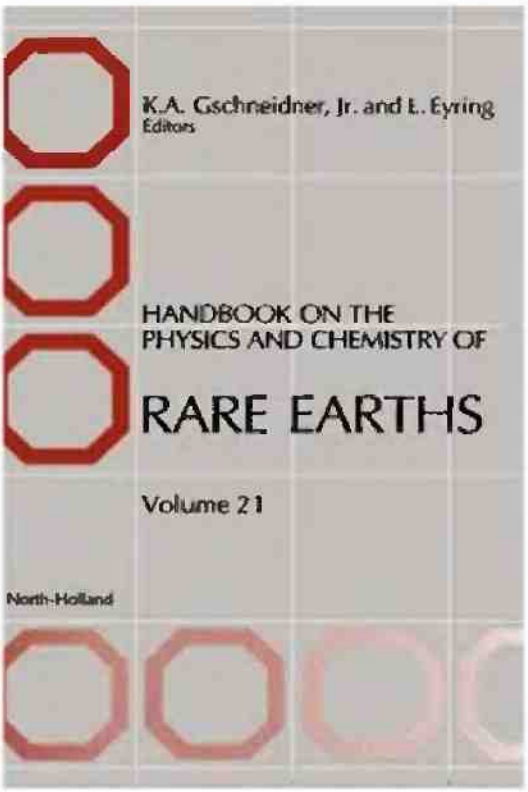

Handbook on the Physics and Chemistry of Rare Earths, volume 21

Elsevier, 1995

Edited by: Karl A. Gschneidner, Jr. and LeRoy Eyring
ISBN: 978-0-444-82178-2

Handbook on the Physics and Chemistry of Rare Earths
Vol. 21
edited by K.A. Gschneidner, Jr. and L. Eyring

PREFACE

Karl A. GSCHNEIDNER, Jr., and LeRoy EYRING

These elements perplex us in our rearches [sic], *baffle us in our speculations, and haunt us in our very dreams. They stretch like an unknown sea before us – mocking, mystifying, and murmuring strange revelations and possibilities.*

Sir William Crookes (February 16, 1887)

The contributions to this volume focus on selected chemical aspects of rare-earth materials. The topics covered range from a basic treatment of crystalline electric-field effects and chemical interactions in organic solvents, to separation processes, electrochemical behaviors which impact corrosion, oxidation resistance, chemical energy storage and sensor technology, and to analytical procedures.

Underlying the most subtle chemical and optical properties of these elements and their compounds in the condensed state are the crystal field effects. Garcia and Faucher discuss this phenomenon in non-metallic compounds in Chapter 144.

Bautista begins the volume by reviewing important new solvent extraction procedures as well as emerging alternative separation processes such as photochemical separation, precipitation stripping, and supercritical extraction, in Chapter 139. Scientific and industrial procedures are illustrated.

In order to satisfy the most demanding needs for rare earths either for direct use or as components in advanced materials and devices it is necessary to obtain accurate trace analysis. Bhagavathy, Prasada Rao and Damodaran (Chapter 146) examine eight major analytical techniques and tabulate and assess the most effective procedures of each.

Environmental corrosion and degradation of metals and alloys impose enormous losses in modern industrial societies. In Chapter 140 Hinton considers a wide variety of methods using rare-earth solutions and salts to modify advantageously the costly deterioration of metals and alloys. This topic is expanded by Ryan in Chapter 141, giving particular attention to protection against high-temperature oxidation, sulfidization and hot-salt corrosion.

The versatility of the rare earths in addressing current technical problems is reviewed in Chapters 142 and 143. In the former the use of rare-earth intermetallics, principally $LaNi_5$-based materials to provide the skyrocketing need for environmentally friendly, usually portable, battery power is discussed by Sakai, Matsuoka and Iwakura. Adachi and

Imanaka present, in the latter chapter, an account of the use of the rare earths to satisfy the growing demand for chemical sensors for a wide variety of substances found in our environment that require monitoring. These include oxygen, fluorine, sulfur dioxide, carbon dioxide, moisture, alcohol, and nitric oxide.

Finally, in Chapter 145 Bünzli and Milicic-Tang review the solvation, interaction and coordination of rare-earth salts in a variety of organic solvents including dimethylacetamide, dimethylsulfoxide, various alcohols, acetonitrile, and propylenecarbonate under strict anhydrous conditions. They also contrast these interactions with those in which water is present with organic solvents.

CONTENTS

CONTENTS OF VOLUMES 1–20

VOLUME 4: Non-metallic compounds – II

1979, 1st repr. 1984; ISBN 0-444-85216-6

VOLUME 5

1982, 1st repr. 1984; ISBN 0-444-86375-3

VOLUME 6

1984; ISBN 0-444-86592-6

VOLUME 7

1984; ISBN 0-444-86851-8

VOLUME 8

1986; ISBN 0-444-86971-9

VOLUME 9

1987; ISBN 0-444-87045-8

VOLUME 10: High energy spectroscopy

1988; ISBN 0-444-87063-6

VOLUME 11: Two-hundred-year impact of rare earths on science

1988; ISBN 0-444-87080-6

VOLUME 12

1989; ISBN 0-444-87105-5

VOLUME 13

1990; ISBN 0-444-88547-1

VOLUME 14

1991; ISBN 0-444-88743-1

VOLUME 15

1991; ISBN 0-444-88966-3

MASTER INDEX, Vols. 1–15
1993; ISBN 0-444-89965-0

VOLUME 16
1993; ISBN 0-444-89782-8

VOLUME 17: Lanthanides/Actinides: Physics – I
1993; ISBN 0-444-81502-3

VOLUME 18: Lanthanides/Actinides: Chemistry
1994; ISBN 0-444-81724-7

VOLUME 19: Lanthanides/Actinides: Physics – II

1994; ISBN 0-444-82015-9

VOLUME 20

1995; ISBN 0-444-82014-0

Handbook on the Physics and Chemistry of Rare Earths
Vol. 21
edited by K.A. Gschneidner, Jr. and L. Eyring

Chapter 139

SEPARATION CHEMISTRY

Renato G. BAUTISTA
Department of Chemical and Metallurgical Engineering, University of Nevada, Reno, NV 89557-0136, USA

Contents

List of symbols

Alamine 336	mixture of 8- and 10-carbon straight chain tertiary amine
Aliquat 336	tricapryl monomethyl ammonium chloride
Calixarenes	(1, *n*)-cyclophanes
DACDA	macrocyclic 1, 10-diaza-4, 7, 13, 16-tetraoxacyclooctadecane-N, N′-diacetic acid
DAPDA	macrocyclic 1, 7-diaza-4, 10, 13-trioxacyclopentadecane-N, N′-diacetic acid
DBTPA	dibutylmonothiophosphoric acid
DDTPA	didodecylmonothiophosphoric acid
DTPA	diethylenetriaminepentaacetic acid
EDTA	ethylenediamine tetraacetic acid
HDEHP	di-2-ethylhexyl phosphoric acid
HTTA	thenoyltrifluoroacetone
K22DD	an aza-crown ether: 4, 13-didecyl-1, 7, 10, 16-tetraoxa-4, 13-diazacyclooctadecane
L1	calixarene *p*-tert-butylcalix/6/arene hexacarboxylic acid
L2	calixarene *p*-tert-butylcalix/4/arene tetracarboxylic acid
L3	calixarene [3, 1, 3, 1]-cyclophane
LIX 63	anti isomer of 5, 8-diethyl-7-hydroxy-6-dodecanone oxime
LIX 70	2-hydroxy-3-chloro-5-nonyl-benzophenone oxime
PC-88A	2-ethylhexyl phosphonic acid mono-2-ethylhexyl ester
PHEN	1, 10-phenanthroline
RCOOH	napthenic acids
SME 529	2-hydroxy-5-nonyl-acetophenone oxime, anti-isomer
Socal 355L	diluent
TBP	tri-*n*-butyl phosphate
Versatic 10	2-ethyl-2-methylheptanoic acid

1. Introduction

The separation chemistry and technology of rare earths have developed to a sufficiently high degree of sophistication that very high purity products can generally be produced when required. The mineralogy (Haskin and Paster 1979), beneficiation (Bautista and Wong 1989, Gupta and Krisnamurthy 1992), and extraction (Bautista and Wong 1989, Bautista 1992, Bautista and Jackson 1992, Gupta and Krisnamurthy 1992) of the rare earths from resources such as monazite, bastnasite, xenotime, euxenite and as by-products of other metal resources processing are equally well developed and efficient. The rare earths present in these ores and other resources are readily leached into solution as a nitrate, sulfate or chloride (Bril 1964, Bautista 1990, Gupta and Krisnamurthy 1992).

The primary separation technique used in the first half of this century involved mainly fractional precipitation to obtain satisfactory intermediate grade concentrates (Krumholz et al. 1958, Ryabchikov 1959, Healy and Kremers 1961, Topp 1965, Callow 1966, 1967).

The first successful ion-exchange separation of rare earths using 5% citric acid–ammonium citrate eluant at low pH carried out on either H^+-state or NH_4^+-state resin beds was reported in a collection of nine scientific papers in 1947 (Tompkins et al. 1947, Spedding et al. 1947a–c, Marinsky et al. 1947, Harris and Tompkins 1947, Ketelle and Boyd 1947, Boyd et al. 1947, Tompkins and Mayer 1947). This technique, however, was uneconomical for moderate- or large-scale rare earth separation.

Spedding et al. (1954a,b) reported the use of Fe^{3+} and Cu^{2+} as the retaining ions to form soluble ethylenediaminetetraacetic acid (EDTA) complexes, thus allowing redeposition of the rare earths on the resin bed and the transport of the chelating agent off the column in soluble form. The pilot plant for the ion-exchange separation of rare earths using EDTA is described by Powell and Spedding (1959a,b). Powell (1979) reviewed the separation chemistry of rare earths with primary emphasis on the ion-exchange process.

The chemistry of the rare earths is characterized by the similarity in the properties of the trivalent ions and their compounds. Krumholz (1964) reviewed the structure, properties, solubilities and coordination chemistry of rare earth ions in solution. Moeller (1961) reviewed the electronic configurations, size relationships and various oxidation states of rare earths. Carnall (1979) reviewed the literature on the absorption and fluorescence spectra of rare earth ions in solution. The complexes formed by rare earth ions have been reviewed by Thompson (1979).

The analytical chemistry of rare earths has been reviewed by Banks and Klingman (1961), Loriers (1964), Ryabchikov (1959), and Ryabchikov and Ryabukhin (1964). Fassel (1961) reviewed the analytical spectroscopy of rare earth elements. In volume 4 of this Handbook chapters can be found on the chemical spectrophotometric and polarographic methods (O'Laughlin 1979), spark source mass spectrometry (Conzemius 1979, Taylor 1979), optical atomic emission and absorption (DeKalb and Fassel 1979), X-ray excited optical luminescence (D'Silva and Fassel 1979), neutron activation (Boynton 1979), mass spectrometric stable isotope dilution analysis (Schuhmann and Philpotts 1979), and shift reagents and NMR (Reuben and Elgavish 1979).

Table 1
The rare earths: chronology, atomic number and ionic radii

Year	Element	Symbol	Atomic number	Ionic radius [R^{3+} ion, CN = 6] (Å)	Discoverer
1794	Yttrium	Y	39	0.900	Gadolin
1814	Cerium	Ce	58	1.010	Berzelius
1839	Lanthanum	La	57	1.045	Mosander
1843	Erbium	Er	68	0.890	Mosander
1878	Terbium	Tb	65	0.923	Mosander
1878	Ytterbium	Yb	70	0.868	Marignac
1879	Samarium	Sm	62	0.958	de Boisbaudran
1879	Scandium	Sc	21	0.745	Nilson
1879	Holmium	Ho	67	0.901	Cleve
1879	Thulium	Tm	69	0.88	Cleve
1880	Gadolinium	Gd	64	0.938	Marignac
1885	Praseodymium	Pr	59	0.997	Auer von Welsbach
1885	Neodymium	Nd	60	0.983	Auer von Welsbach
1886	Dysprosium	Dy	66	0.912	de Boisbaudran
1896	Europium	Eu	63	0.947	Demarçay
1907	Lutetium	Lu	71	0.861	Urbain
1945	Promethium	Pm	61	0.97	Glendenin/Marinsky

Rare earths have been known for over two hundred years since the discovery of yttrium in 1794 by Gadolin (Weeks 1956, Szabadvary 1980). Table 1 lists the chronology of their discovery (Habashi 1990), their atomic number and ionic radii (Gschneidner 1993).

2. Solvent extraction

The earlier work on the solvent extraction of rare earths has been reviewed by Peppard (1961, 1964) and Weaver (1964, 1968, 1974).

The conventional separation scheme is to leach the primary ore or concentrates and use the resulting solution containing the rare earth mixtures as the feedstock to the solvent extraction plant. Solvent extraction of the rare earth mixture in the leached solution separates them into bulk concentrates of light (La, Ce, Pr, Nd, etc.), middle (Sm, Eu, Gd, etc.) and heavy (Tb, Dy, Ho, Er, Tm, Yb, Lu, Y) rare earths. A typical solvent extraction of rare earths in a HCl medium is with di-2-ethylhexyl phosphoric acid, HDEHP, in a kerosene diluent. The individual rare earth is separated from the bulk light, middle, and heavy rare earth solution mixtures by additional individual rare earth solvent extraction streams. The number of stages for solvent extraction cascades or batteries increases with the increase in purity of each individual rare earth produced. Further purification

of individual rare earths into the high ninety-nines purity are usually carried out by ion exchange and/or chromatographic techniques. The concentrated, stripped rare earth solution from the extraction is precipitated as an oxalate from which the rare earth oxide is produced after calcination.

The primary industrial extractants in use for the separation of rare earths by solvent extraction are di-2-ethylhexyl phosphoric acid (HDEHP), tributyl phosphate (TBP), carboxylic acids, and amines. Many other extractants have been examined and reported in the literature in the search for improving the extraction and separation of individual rare earths. This chapter discusses several of these extractants for their interesting chemistry and potential future development, in addition to the available industrial extractants now in use and proposed for the separation of rare earths.

The solvent extraction reaction chemistry in specific medium, extractants, pH, diluents, and in synergistic systems are discussed in relation to the transfer of the rare earth extractable complex from the aqueous phase to the organic phase.

2.1. *Carboxylic acids*

Carboxylic acids are commercially available and are relatively inexpensive. Naphthenic acids have the general formula RCOOH, where R is a radical derived predominantly from cyclopentane or a homolog of cyclopentane.

Bauer and Lindström (1964) reported moderate success in the use of naphthenic acid as an extractant for rare earth sulfates with diethylether or *n*-hexanol as a diluent. The extraction required 6 mols of naphthenic acid to 1 mol of rare earth oxide at pH $\approx$ 7.6. Rare earth extraction was dependent on pH, naphthenic acid concentration, and the mol ratio of naphthenic acid to rare earth.

Addition of an aqueous phase chelating reagent such as EDTA enhanced the separation factors to 2.2 for adjacent yttrium group elements. Addition of DTPA enhanced the separation factor to 3.5 for adjacent cerium group elements.

Preston (1985) described the solvent extraction behavior of a large number of metal cations including rare earth nitrates in solutions of Versatic 10 (2-ethyl-2-methylheptanoic acid), naphthenic, 2-bromodecanoic and 3, 5-diisopropylsalicylic acids in xylene. The last two acids extract metal cations under more acidic conditions, pH $\approx$ 1–2. For Versatic 10 the order of extraction of yttrium and lanthanides is La < Ce < Nd < Gd < Y < Ho < Yb and for naphthenic acids it is La < Ce < Y < Nd < Gd $\approx$ Ho $\approx$ Yb. The lanthanides tend to form complexes of predominantly ionic nature. In the case of Versatic 10, the stability of the complexes increases uniformly with atomic number due to the increase in electrostatic energy as a result of the decrease in ionic radius. The primary branched naphthenic acid allows the formation of complexes with high coordination number, nine for La to Nd, eight and eventually six as the metal ionic radius decreases. In general, the extraction of a metal ion M^{n+} by a carboxylic acid H_2A_2 can be represented by the reaction

$$\left[M^{n+}\right]_{AQ} + \left[\tfrac{1}{2}m2H_2A_2\right]_{ORG} \rightleftarrows [MA_n(HA)_{m-n}]_{ORG} + \left[nH^+\right]_{AQ}.$$

A fundamental study of the extraction of trivalent lanthanides and yttrium nitrates by carboxylic acids in xylene diluent was reported by duPreez and Preston (1992). The steric parameter E_s' of the substituent alkyl group, representing the steric bulk of the carboxylic acid molecule, shows a definite relationship to the extractabilities of the lanthanides defined by their atomic numbers. The extraction reaction of a trivalent lanthanide Ln^{3+} by a carboxylic acid dimer is

$$\left[jLn^{3+}\right]_{AQ} + [xj(H_2A_2)]_{ORG} \rightleftarrows \left[(LnA_3(HA)_{(2x-3)})_j\right]_{ORG} + \left[3jH^+\right]_{AQ},$$

where j is the degree of oligomerization of the extracted complex and x is the number of carboxylic ligands per metal ion extracted.

The extraction of trivalent rare earths by sterically hindered carboxylic acids, $-E_s' > 2$, such as 2-ethylhexanoic, 1-methyl-cyclohexanecarboxylic, 2, 2 ,3-trimethylbutanoic, Versatic 10 and 2-butyl-2-ethylhexanoic can be represented by the reaction

$$\left[Ln^{3+}\right]_{AQ} + [3H_2A_2]_{ORG} \rightleftarrows [LnA_3(HA)_3]_{ORG} + \left[3H^+\right]_{AQ}.$$

The pH values at which 50% extraction occurs, $pH_{0.5}$, decrease from lanthanum through to lutetium, in the same order as the decrease in ionic radii with increase in atomic number. Yttrium behaves more like the middle lanthanides, such as gadolinium or terbium.

With the straight-chain and less sterically hindered carboxylic acids, $-E_s' < 1$, such as *n*-hexanoic, *n*-octanoic, 3-cyclohexylpropanoic, iso-nonanoic and cyclohexanecarboxylic acids, the $pH_{0.5}$ values go from lanthanum through a minimum to the middle rare earths and then gradually increase through to lutetium. The yttrium behavior in this case is more similar to the lighter lanthanides such as cerium and praseodymium.

The extraction of the light and middle rare earths by the straight-chain and less sterically hindered carboxylic acid, $-E_s' < 1$, may be represented by the reaction

$$\left[2Ln^{3+}\right]_{AQ} + [6H_2A_2]_{ORG} \rightleftarrows [(LnA_3(HA)_3)_2]_{ORG} + \left[6H^+\right]_{AQ}.$$

For the heaviest rare earths, the extraction reaction may be represented by

$$\left[2Ln^{3+}\right]_{AQ} + [5H_2A_2]_{ORG} \rightleftarrows [(LnA_3(HA)_2)_2]_{ORG} + \left[6H^+\right]_{AQ}.$$

2.2. *Tri-n-butyl phosphate*

Warf (1949) was the first to report the use of tributyl phosphate (TBP) as an extractant for the preferential extraction of Ce(IV) with respect to La(III) in 8–10 F HNO_3. The extractability of rare earths from an aqueous HCl phase and from an aqueous phase 8 to 15.6 M HNO_3 by diluted and pure TBP was studied by Peppard et al. (1953, 1957) and was shown to increase with increasing atomic number.

Hesford et al. (1959) determined the dependence of the distribution ratio K for nine different trivalent lanthanides in 15.6 M HNO_3 vs. TBP diluted with 1–5% kerosene. On

the basis of the slope of log K vs. log % TBP, the extractable species was determined to be $M(NO_3)_3(TBP)$. The TBP concentration vs. log K was found to be independent of the acidity. The mechanism of extraction of a trivalent rare earth was represented by the extraction reaction

$$\left[M^{3+}\right]_{AQ} + \left[3NO_3^-\right]_{AQ} + [3TBP]_{ORG} \rightleftarrows [M(NO_3)_3(TBP)_3]_{ORG}.$$

Yoshida (1964) investigated the solvent extraction behavior of lanthanides in the system M^{3+}–$HClO_4$–TBP and reported the distribution ratio of the lanthanides to be third-power dependent upon the concentration of perchlorate ions in the aqueous phase and sixth-power dependent upon the concentration of TBP in the organic phase. The lanthanide extraction reaction can be represented by

$$\left[M^{3+}\right]_{AQ} + 3\left[ClO_4^-\right]_{AQ} + 6[TBP]_{ORG} \rightleftarrows [M(ClO_4)_3(TBP)_6]_{ORG}.$$

The lanthanide distribution ratio was observed to increase with atomic number.

The nature of the solvent–solute complex formation in $NdNO_3$–TBP–H_2O was reported by Bostian and Smutz (1964) using infrared spectra of the organic phase data composition and weight measurements made from equilibrium extraction experiments. It was determined that the complexing takes place at the P=O bond on the solvent molecules. The dependence of the extraction on the solvent structure variation suggests that the complex is formed by weak intermolecular attractions depending on dipole effects. The complex formation reaction over the entire concentration range can be represented by

$$[Nd(NO_3)_3]_{AQ} + [3TBP \cdot H_2O]_{ORG} \rightleftarrows [Nd(NO_3)_3 \cdot 3TBP]_{ORG} + [3H_2O]_{AQ}.$$

The temperature effect on the extraction of lanthanides in the TBP–HNO_3 system was measured by Fidelis (1970) at 10, 17, 25 and 40°C. The separation factors for adjacent lanthanides and their enthalpy, relative free energy, and entropy associated with the extraction process, were calculated.

The extraction of mineral acids such as HCl, HNO_3, H_2SO_4, $HClO_4$ and HF from aqueous solutions by concentrated and diluted TBP has been reported by Hesford and McKay (1960). $HClO_4$ was found to be a strong electrolyte in TBP. The first ionization constants of HCl, HNO_3 and H_2SO_4 were all determined to be equal to about 9×10^{-5}. The monosolvates HCl·TBP, HNO_3·TBP, H_2SO_4·TBP, and $HClO_4$·TBP were formed with $HClO_4$ also yielding higher solvates. With the exception of HNO_3, the water content of the TBP phase increased with acid concentration.

A critical examination of the large amount of data on the extraction of mineral acids from aqueous solutions by TBP has been made by Davis et al. (1966) and Hardy (1970). The activities of TBP in equilibrium with water, with aqueous nitric acid and with hydrochloric acid have been calculated by means of the Gibbs–Duhem equation and compared to the distribution data for the TBP–HNO_3–H_2O and TBP–H_2O systems and the TBP–HCl–H_2O and TBP–H_2O systems. The activity of TBP decreases more sharply

at high HNO_3 concentration than at high HCl concentration in the equilibrated TBP phase. This is due to HNO_3 being more strongly extracted by TBP and displacing water from the TBP phase (strong bond between TBP and HNO_3), whereas HCl and H_2O are co-extracted by TBP (TBP weakly bonded to hydrated HCl).

Hoh and Wang (1980) reported the rate of extraction of nitrate (denitration) by a solution of 75% tributyl phosphate diluted with kerosene and the rate of stripping of nitrate (acid recovery) from nitrate-loaded TBP with water. The experiments carried out in a mixing vessel indicate an optimum rpm for extraction. Their experimental observations can be explained by the results of Sheka and Kriss (1959) where $HNO_3 \cdot$TBP predominates at nitric acid concentration up to 4 M and $3HNO_3 \cdot$TBP is the dominant species up to 9 M nitric acid concentration. The first extraction period is the rate controlling step.

2.3. *Di-2-ethylhexyl phosphoric acid*

2.3.1. *Chloride medium*

Peppard et al. (1958) proposed the extraction mechanism for lanthanides by HDEHP based on tracer concentration studies as

$$\left[M^{3+}\right]_{AQ} + \left[3(HG)_2\right]_{ORG} \rightleftarrows \left[M(HG_2)_3\right]_{ORG} + \left[3H^{+}\right]_{AQ},$$

where $(HG)_2$ is the dimeric form of the HDEHP in the organic phase and M^{3+} is the trivalent lanthanide ion. This reaction indicates that the extraction is strongly pH dependent.

Lenz and Smutz (1966) confirmed that three H^+ ions are liberated to the aqueous phase for every rare earth ion extracted into the organic phase for concentrated lanthanide solutions. Dimerized HDEHP is a more efficient extractant than monomerized HDEHP up to 1 M $SmCl_3$.

Harada et al. (1971) defined the conditions under which rare earth polymers of HDEHP are formed to be a function of the initial HDEHP concentration, final acidity, and final aqueous concentration of the metal. When the initial HDEHP concentration is less than 1.5 M, the polymers form at a ratio of HDEHP to metal concentration of less than 6.5. The minimum HDEHP concentration for polymer formation is different for each lanthanide at aqueous lanthanide concentrations of more than 0.2 M. The degree of polymerization n for Y, Ho, etc. is 4000, 600 for La and Yb, and 3 for Fe(III). The polymer is soluble in a mixture of benzene and cyclohexane, but decomposes in concentrated HCl, HNO_3, and H_2SO_4 at room temperature and in 2 M HCl at its boiling point.

Sato (1989) investigated the extraction of all the rare earths by HDEHP in kerosene. The extraction efficiency increases with increase in atomic number in the order of $La < Ce < Pr < Nd < Sm < Eu < Gd < Tb < Dy\ (\approx Y) < Ho < Er < Tm < Yb < Lu$. The distribution coefficients of rare earths decrease with increasing temperature, with the effect greater for the heavy rare earths than for the light rare earths. The separation factors of rare earths in 0.1 mol dm^{-3} HCl with 0.05 mol dm^{-3} HDEHP in kerosene are listed in table 2. The HDEHP selectivity is best for the separation of light from heavy rare earths.

Table 2
Separation factor[a] of rare-earth elements in the extraction systems Ln(III)–HCl–HDEHP

Ln_1	Ln_2												
	Ce	Pr	Nd	Sm	Eu	Gd	Tb	Dy	Ho	Er	Tm	Yb	Lu
La	2.14	2.28	2.43	11.8	26.3	44.6	71.1	101	125	212	319	414	425
Ce		1.07	1.14	5.2	12.3	20.9	33.3	47.2	58.4	99.1	149	193	199
Pr			1.06	5.16	11.5	19.5	31.1	41.1	54.7	92.7	139	181	186
Nd				4.86	10.8	18.3	29.2	41.5	51.3	87.1	131	170	175
Sm					2.23	3.75	6.02	8.55	10.6	17.9	27.0	35.1	36.0
Eu						1.69	2.70	3.83	4.74	8.04	12.0	15.7	16.2
Gd							1.60	2.26	2.80	4.75	7.15	9.30	9.55
Tb								1.42	1.76	2.98	4.48	5.83	5.90
Dy									1.24	2.10	3.16	4.11	4.22
Ho										1.70	2.55	3.31	3.41
Er											1.50	1.90	2.01
Tm												1.30	1.34
Yb													1.03

[a] $\alpha = E_a^0(Ln_1)/E_a^0(Ln_2)$; $E_a^0(Ln_1)$ and $E_a^0(Ln_2)$ represent the distribution coefficients of Ln_1 and Ln_2, respectively, in the extraction from 0.1 mol dm^{-3} hydrochloric acid solution with 0.2 mol dm^{-3} DEHPA in kerosene.

2.3.2. *Nitrate medium*

The complex formations and reaction stoichiometry of the equilibrium extraction of lanthanum nitrate by purified-water equilibrated HDEHP was reported by Kosinski and Bostian (1969). The transfer of water molecules from the lanthanum-enriched organic phase to the aqueous phase was verified, indicating that it should be included in the extraction mechanism. The three predominant extraction mechanisms involving pure lanthanum ions and partially nitrated lanthanum ions are

$$\left[La^{3+}\right]_{AQ} + \left[3\left[(HDEHP)_2 \cdot H_2O\right]\right]_{ORG} \rightleftarrows \left[La\left[H(HDEHP)_2\right]_3\right]_{ORG} + \left[3H_2O\right]_{AQ} + \left[3H^+\right]_{AQ},$$

$$\left[LaNO_3^{2+}\right]_{AQ} + \left[2\left[(HDEHP)_2H_2O\right]\right]_{ORG} \rightleftarrows \left[La(NO_3)\left[H(HDEHP)_2\right]_2\right]_{ORG} + \left[2H_2O\right]_{AQ} + \left[2H^+\right]_{AQ},$$

$$\left[La(NO_3)_2^{+}\right]_{AQ} + \left[(HDEHP)_2H_2O\right]_{ORG} \rightleftarrows \left[La(NO_3)_2H(HDEHP)_2\right]_{ORG} + \left[H_2O\right]_{AQ} + \left[H^+\right]_{AQ}.$$

The lanthanum ion replaces the hydrogen ions and interacts with the P=O structure of the solvent. The dimer structure is maintained throughout the extraction since only one hydrogen molecule and one water molecule are displaced per dimer consumed.

Fidelis (1971) measured the distribution coefficients and separation factors of selected lanthanides in the HDEHP–HNO_3 system over the temperature range 10–50°C. The distribution coefficients decreased with increase in temperature.

2.3.3. *Sulfate medium*

The extraction of Ce(IV) from sulfuric acid solution by HDEHP dissolved in kerosene as a function of sulfate and HDEHP concentration and pH was determined by Tedesco et al. (1967). The first extraction reaction represents tracer concentration and the second represents saturation concentration:

$$\left[Ce^{4+}\right]_{AQ} + [4(HX)_2]_{ORG} \rightleftarrows [CeH_4X_8]_{ORG} + \left[4H^+\right]_{AQ},$$

$$\left[nCe^{4+}\right]_{AQ} + [2n(HX)_2]_{ORG} \rightleftarrows [(CeX_4)_n]_{ORG} + \left[4nH^+\right]_{AQ}.$$

The above two reactions represent the mechanism of extraction of Ce(IV) at pH $\approx$ 1.0 or lower. At higher pH, the reactions are

$$\left[(CeO)^{2+}\right]_{AQ} + [2(HX)_2]_{ORG} \rightleftarrows [CeOH_2X_4]_{ORG} + \left[2H^+\right]_{AQ},$$

$$\left[n(CeO)^{2+}\right]_{AQ} + [n(HX)_2]_{ORG} \rightleftarrows [(CeOX_2)_n]_{ORG} + \left[2nH^+\right]_{AQ}.$$

The above reactions are dominant at pH $\approx$ 1.7 or higher.

The presence of sulfate and bisulfate ions in the extraction of europium by HDEHP results in the formation of complexes of europium in the aqueous phase. Cassidy and Burkin (1971) quantitatively analyzed the extraction of Eu(III) from sulfate–perchlorate solutions by correcting for the value of $[Eu^{3+}]_{AQ}$, or of its activity in the equilibrium constant.

2.4. *Amines*

Amines extract rare earths in reversed order compared to organophosphates. Aliphatic amines form salts with acids in aqueous solution and precipitate the hydroxides of metals. The solubility of amines in water decreases with increase in molecular weight. Primary amines extract from sulfate solutions while the tertiary amines extract from nitrate solutions. The lighter rare earths are preferentially extracted by amines and when used with aqueous soluble aminocarboxylic acid, chelating reagents preferentially extract the heavy rare earths.

Coleman (1963) reviewed the application of amines as an extractant in the separation of metals, with particular attention to amine extraction mechanism, separation and recovery. Amines extract metals by an anion exchange mechanism, given by the reaction

$$\left[mR_3NH^+X^-\right]_{ORG} + \left[MX^{-m}_{(m+n)}\right]_{AQ} \rightleftarrows \left[(R_3NH)_mMX_{(m+n)}\right]_{ORG} + [mX^-]_{AQ},$$

or by adduct formation:

$$\left[mR_3NH^+X^-\right]_{ORG} + [MX_n]_{AQ} \rightleftarrows \left[(R_3NH)_mMX_{(m+n)}\right]_{ORG},$$

where R is an alkyl group, M is a lanthanide ion and X is an inorganic anion.

The separation of light rare earths (cerium group) sulfates obtained from bastnasite by primary amine with or without an aqueous phase chelating reagent was studied by Bauer et al. (1968). Kerosene was used as the diluent. The pH of the lanthanide–amine system affects the molecular species present in both the aqueous and organic phases. The extraction of rare earths at high acid concentrations is inhibited due to the formation of stable amine bisulfate

$$[(RNH_3)_2SO_4]_{ORG} + [H_2SO_4]_{AQ} \rightleftarrows [2RNH_3HSO_4]_{ORG}.$$

The lanthanides at high pH values form nonextractable hydrolysis products with amine salt reverting to free-base form

$$[(RNH_3)_2SO_4]_{ORG} + [2OH^-]_{AQ} \rightleftarrows [2RNH_2]_{ORG} + \left[SO_4^{=}\right]_{AQ} + [2H_2O]_{AQ}.$$

The lanthanides are extracted in the intermediate pH range by formation of an extractable neutral salt

$$[(RNH_3)_2SO_4]_{ORG} + [M_2(SO_4)_3]_{AQ} \rightleftarrows [2RNH_3M(SO_4)_2]_{ORG},$$

where R is an alkyl group and M is the lanthanide ion. A pH value greater than 2 was required for the aqueous phase in the presence of aminocarboxylic acid chelating reagents. Diethylenetriaminepentaacetic acid (DTPA) enhanced the separation factors to values greater than 2. Ethylenediaminetetraacetic acid (EDTA) was not as effective.

Gruzensky and Engel (1959) reported the separation of yttrium and rare earth nitrates with a tertiary amine, 10% by volume of tri-*n*-butylamine diluted in a ketone, 3-methyl-2-butanone. The maximum extraction was obtained when sufficient amine was present to neutralize the aqueous phase to the point of precipitation. Extraction increased with metal concentration and the separation factors were found to be affected by the concentration of amine.

Bauer (1966) studied the extraction of lanthanides in tertiary amines with the addition of aqueous-phase chelating reagents. EDTA and DTPA were used as the chelating reagents. Certain aqueous-phase chelate compounds solubility-limited the range of the lanthanide concentrations to between 15 and 45 gm/l. The salting out effect for lanthanide nitrate was enhanced with the addition of lithium nitrate. Alamine 336, a mixture of 8- and 10- carbon straight chain tertiary amines, was dissolved in an inert organic diluent. Nitric acid was equilibrated with the organic phase to minimize pH changes during extraction. Rapid phase disengagement was obtained with 33% amine concentration at pH between 3 and 4. Stripping of the lanthanides from the organic phase was carried out with 1.2 M ammonium chloride solution.

The quaternary ammonium compounds which have amine-type structure in the presence of a chelating reagent were successfully used by Bauer and Lindström (1968, 1971) to separate La–Pr, Pr–Nd, and Nd–Sm. Aliquat 336, tricaprylyl monomethyl ammonium chloride diluted with Socal 355L and containing the chelating reagent DTPA,

was found to effectively separate the light rare earth group. Optimum separation was obtained by closely controlling pH, nitrate ion concentration and extractant concentration.

With all the rare earths chelated with DTPA, a rare earth displacement method for releasing one rare earth from the DTPA was used. Copper, which is not extractable by the quaternary ammonium compound and which has a high stability constant with DTPA relative to the light rare earth–DTPA stability constants, was used as the displacement metal.

High purity separation of Pr and Nd (99.9%) was carried out by Hsu et al. (1980) using quaternary alkylammonium nitrate $R_3CH_3N^+NO_3^-$ (0.65 M) in xylene as diluent. The extraction reaction was determined to be

$$\left[M^{3+}\right]_{AQ} + \left[3L^-\right]_{AQ} + \left[\tfrac{3}{2}(R_4N^+L^-)_2\right]_{ORG} \rightleftarrows \left[ML \cdot 3R_4N^+L^-\right]_{ORG},$$

where M^{3+} represents the trivalent rare earth ions, L^- the nitrate ion, $(R_4N^+L^-)_2$ the quaternary ammonium nitrate, and $ML{\cdot}3R_4N^+L^-$ the extractable species.

Efficient extraction of light rare earths by tertiary amines and quaternary amine compounds can be carried out only at high inorganic nitrate concentration. The practical supporting electrolyte used is ammonium nitrate, which is less efficient than lithium nitrate. Formation of undissociated lanthanide nitrates which can form extractable complexes requires the presence of a high concentration of NO_3^- ions. Cerna et al. (1992) reported the enhanced extraction of light rare earths by Aliquat 336 in aromatic and aliphatic diluents by increasing the NH_4NO_3 concentration to 4 or 8 M.

The observed decrease in separation factor with increased extractant loading was attributed to three different extraction reaction mechanisms as a result of the presence of three extractable complexes in the organic phase.

At small lanthanide concentrations, the equilibrium extraction reaction between the quaternary ammonium salt and $Ln(NO_3)_3$ is

$$[nR_3CH_3NNO_3]_{ORG} + [Ln(NO_3)_3]_{AQ} \rightleftarrows [R_3CH_3NNO_3)_n \cdot Ln(NO_3)_3]_{ORG}.$$

The stoichiometric coefficient n was found to decrease with extractant loading, and complexes with a low amine to metal ratio were formed in the region of high lanthanide concentrations.

The formation of the anionic species $Ln(NO_3)_4^-$ is given by the reaction

$$Ln^{3+} + 4NO_3^- \rightleftarrows Ln(NO_3)_4^-.$$

The cation of the dissociated amine nitrate in the aqueous phase reacts with $Ln(NO_3)_4^-$. The resulting complex is transferred into the organic phase according to the extraction reaction

$$\left[R_3CH_3N^+NO_3^-\right]_{ORG} + \left[Ln(NO_3)_4^-\right]_{AQ} \rightleftarrows \left[R_3CH_3N^+Ln(NO_3)_4^-\right]_{ORG} + \left[NO_3^-\right]_{AQ}.$$

Further reaction of this 1:1 complex formed by the above anion exchange reaction with another molecule of $Ln(NO_3)_3$ results in the formation of the 1:2 amine to metal complex:

$$\left[R_3CH_3N^+Ln(NO_3)_4^-\right]_{ORG} + [Ln(NO_3)_3]_{AQ} \rightleftarrows \left[R_3CH_3N^+Ln(NO_3)_4^-Ln(NO_3)_3\right]_{ORG}.$$

The $Ln(NO_3)_3$ in the above reactions is in equilibrium with Ln^{3+} and NO_3^- ions:

$$Ln^{3+} + NO_3^- \rightleftarrows Ln(NO_3)_3.$$

The supporting electrolyte, NH_4NO_3, increases the NO_3^- concentration by the equilibrium reaction

$$NH_4^+ + NO_3^- \rightleftarrows NH_4NO_3,$$

and shifts all the equilibrium reactions to the right.

2.5. *Hydroxyoximes*

The equilibrium extraction of Ce(III) and La(III) from sodium chloride solutions by the commercial extractant SME 529, 2-hydroxy-5-nonyl-acetophenone oxime, in *n*-heptane diluent was found by Urbanski et al. (1992) to be highly dependent on the pH and extractant concentration. SME 529 contains mainly the *anti*-form (> 99%) which is a much better extractant than the *syn*-isomer. The equilibration time was around 2 minutes and the disengagement time was found to depend on the extractant concentration and pH. Phase disengagement is very slow and lanthanum hydroxide precipitate appears at the interface at pH values where extraction and precipitation occur simultaneously. Precipitation generally occurs above pH ≈ 6.5. The extraction of cerium is more efficient below pH ≈ 6.5 compared to lanthanum and thus less cerium is precipitated.

The cerium extraction reaction into SME 529 solution in *n*-heptane is

$$\left[Ce^{3+}\right]_{AQ} + [3HR]_{ORG} \rightleftarrows [CeR_3]_{ORG} + \left[3H^+\right]_{AQ}.$$

Hydrolyzed lanthanum species is extracted according to the reaction

$$\left[La^{3+}\right]_{AQ} + [2HR]_{ORG} + [H_2O]_{AQ} \rightleftarrows [LaR_2OH]_{ORG} + \left[3H^+\right]_{AQ}.$$

The extraction of La(III) and Ce(III) from aqueous NaCl solutions with LIX 70 in kerosene or *n*-heptane diluent have been reported by Abbruzzese et al. (1992). LIX 70 is 2-hydroxy-3-chloro-5-nonylbenzophenone oxime with an *anti*- to *syn*-isomer ratio of about 7.3 and contains about 40% of a hydrocarbon diluent and about 1% v/v of LIX 63.

The equilibration time is about 2 minutes and no lanthanum hydroxide precipitates are formed at pH above 6.5. Both Ce and La can be extracted quantitatively with LIX 70,

with Ce more extractable at lower pH. The extraction of both metals depends on pH and extractant concentration. Ce and La complexes with LIX 70 in the organic phase are formed according to the extraction reaction

$$\left[Ln^{3+}\right]_{AQ} + [3HR]_{ORG} \rightleftarrows [LnR_3]_{ORG} + \left[3H^+\right]_{AQ},$$

with the extractant HR as a monomeric species.

2.6. *Synergic extractants*

Cox and Davis (1973) studied the extraction of Dy, Ho, Tm and Cm with thenoyltrifluoroacetone (HTTA)/TBP/dilute HNO_3/kerosene. One molecule of TBP was found to associate with one molecule of $HTTA{\cdot}H_2O$ to form a metal complex, $M^{3+}(TTA)_2(NO_3)(TBP)_2$. Their experimental data indicate only two HTTA molecules are valence bonded to the metal ion, since one ion of H^+ is released to the aqueous phase from each HTTA molecule thus bonded. This also indicates that one NO_3^- group is present in the complex to balance the charge on the trivalent metal ion. Additional work by Hayden et al. (1974) on Dy indicates that dysprosium is present as $Dy(NO_3)_2^+$ in the aqueous phase, further supporting the conclusion that the extractable complex in the organic phase is of the form $Dy(NO_3)(TTA)_2(TBP)_2$.

Synergistic extraction of Sm and Gd using a mixture of tributyl phosphate and Aliquat 336 and the influence of diluents, salting out agents and acidity was studied by Huang and Bautista (1983). This is one of the best systems for the separation of Sm and Gd, with a separation factor greater than 3. NH_4NO_3 was extracted by pure TBP or pure Aliquat 336, but was not extracted by a mixture of TBP and Aliquat 336.

The synergistic extraction of Am(III), Cm(III), Eu(III), Ce(III), and Pm(III) from an aqueous acetate buffer system at $pH \approx 4.8$ into thenoyltrifluoroacetone (HTTA)/4, 13-didecyl-1, 7, 10, 16-tetraoxa-4, 13-diazacyclooctadecane (K22DD)/chloroform phase was reported by Ensor et al. (1988). The extraction reaction for trivalent metal ions by HTTA alone is

$$\left[M^{3+}\right]_{AQ} + [3HTTA]_{ORG} \rightleftarrows [M(TTA)_3]_{ORG} + \left[3H^+\right]_{AQ}.$$

In the presence of a synergistic agent, the overall extraction reaction is

$$\left[M^{3+}\right]_{AQ} + [3HTTA]_{ORG} + [K22DD]_{ORG} \rightleftarrows [M(TTA)_3K22DD]_{ORG} + \left[3H^+\right]_{AQ}.$$

The synergism between HTTA and K22DD significantly increased the distribution coefficients of these metal ions by factors of 10^4–10^5, compared to no extraction using HTTA alone. The extraction increased rapidly with increasing K22DD concentration before it levels off at the highest concentration used. Comparison of the organic phase stability constants with other macrocyclic agents showed the importance of the nitrogen donor groups in the synergistic activity. There was no significant effect of the cavity size on the extractability.

The synergistic extraction of europium from acetate media with didodecylmonothiophosphoric acid (DDTPA) and 1, 10-phenanthroline (PHEN) in a toluene diluent was compared to that of dibutylmonothiophosphoric acid (DBTPA) and PHEN by Kondo et al. (1992). The extraction reaction of ionic Eu by DDTPA (HR) and PHEN can be represented by

$$\left[Eu^{3+}\right]_{AQ} + [3HR]_{ORG} + [PHEN]_{ORG} \rightleftarrows [EuR_3 \cdot PHEN]_{ORG} + \left[3H^+\right]_{AQ}.$$

The synergistic effect of the DBTPA system was found to be superior to that of the DDTPA system.

An extensive study of the synergistic enhancement by TBP of the extraction of lanthanides by trioctylmethylammonium nitrate (Aliquat 336) was reported by Majdan and Kolarik (1993). The assessment of the separation potential of this synergistic system was carried out with the extraction of nine Ln(III) and Y(III). Extraction of adjacent Ln(III), effect of diluents, a wider range of extractant concentrations, compositions of the extracted complexes, absence or presence of TBP and the effect on the separation factors were among the variables taken into account in the experimental work.

The synergistic effect was found to be dependent on the diluent. It is pronounced with a mixed dodecane/xylene diluent, and is weak with mixed heptane/xylene, hexane/xylene, and pure xylene diluents. The organic phase was found to contain simultaneously two or three synergistic complexes, with the compositions $(A^+)(Ln(NO_3)_4 \cdot 2B^-)$, $(A^+)(Ln(NO_3)_4 \cdot 3B^-)$, and $(A^+)_2(ln(NO_3)_5 \cdot B^{2-})$, where Ln is a lanthanide (III), A^+ is a trioctylmethylammonium cation and B is a tributyl phosphate molecule. The synergistic complex stability was found to decrease with increase in atomic number. Increasing the tributyl phosphate concentration gradually suppressed the separation factors for Pr–Nd and Eu–Gd pairs.

Kubota et al. (1993) compared the extraction equilibria and extraction mechanism of the lanthanides with 2-ethylhexyl phosphonic acid mono-2-ethylhexyl ester (PC-88A) in *n*-heptane diluent and HDEHP and in the presence of diethylenetriamine-pentaacetic acid (DTPA). The extraction equilibrium of PC-88A in *n*-heptane can be expressed as

$$\left[M^{3+}\right]_{AQ} + [3(HR)_2]_{ORG} \rightleftarrows [MR_3 \cdot 3HR]_{ORG} + \left[3H^+\right]_{AQ},$$

where HR is PC-88A. The separation factors for adjacent lanthanides were the same for PC-88A and HDEHP. The presence of DTPA in the aqueous phase at high pH ($pH > 1.5$) decreases the distribution coefficient of each lanthanide. The separation factors between Y and Ho and Er are increased by the addition of DTPA.

2.7. *Macrocyclic extractants*

The results of using a crown ether carboxylic acid (sym-dibenzo-16-crown-5-oxyacetic acid) as the extractant in the solvent extraction of lanthanides was reported by Tang and Wai (1986). High extraction efficiencies and significant selectivities were observed.

Crown ether carboxylic acid was dissolved in a 80:20 chloroform–heptanol mixture and was contacted with the aqueous solution of the lanthanides. The solubility of sym-dibenzo-16-crown-5-oxyacetic acid in water at different pH was measured by its ultraviolet absorption.

The solvent extraction of $^{177}Lu^{3+}$ in the pH range 6–7 is quantitative. Only several minutes of shaking is required to obtain 98% extraction without addition of a counterion. $^{177}Lu^{3+}$ can be back extracted into water at pH below 3 after a few minutes of shaking. The presence of chloride, nitrate, sulfate and acetate (1×10^{-2} M) did not decrease extraction efficiency. The extraction of 1×10^{-5} M lanthanides (La^{3+}, Pr^{3+}, Sm^{3+}, Eu^{3+}, Tb^{3+}, Er^{3+}, and Yb^{3+}) with an excess of the chelating agent (3×10^{-3} M) are also nearly quantitative (> 98%) around pH ≈ 6.5. The stoichiometry of the extracted lanthanide–sym-dibenzo-16-crown-5-oxyacetate complex is 1:2 with a net charge of +1. The lanthanide cations are found to fit the cavity of the crown ether carboxylate without any problem.

The nature of the extractable species in the solvent extraction of aqueous complexes of La(III), Eu(III) and Lu(III) with macrocyclic ligands 1, 7-diaza-4, 10, 13-trioxacyclopentadecane-N, N′-diacetic acid (DAPDA) and 1, 10-diaza-4, 7, 13, 16-tetraoxacyclooctadecane-N, N′-diacetic acid (DACDA) using thenoyltrifluoroacetone (HTTA) as the extractant in chloroform, nitrobenzene and benzene, has been compared by Manchanda et al. (1988). The extraction reaction is

$$\left[Ln^{3+}\right]_{AQ} + [3HA]_{ORG} \rightleftarrows [LnA_3]_{ORG} + \left[3H^{+}\right]_{AQ},$$

where HA is protonated HTTA and $[HA]_{ORG}$ is the concentration of HTTA in the organic phase at equilibrium. The highest extraction equilibrium constant is obtained with nitrobenzene and the extraction for both ligands is in the order of nitrobenzene > benzene > chloroform. The favored extractable complexes in the high dielectric constant diluent nitrobenzene are ternary species ion pairs of the type $[Lu(DAPDA)^{+}TTA^{-}]$ which are not readily formed in nonpolar benzene.

The solvent extraction of trivalent lanthanides (La, Nd, Eu, Er, and Yb) in three calixarene-type cyclophanes was described by Ludwig et al. (1993). Calixarenes are (1, *n*)-cyclophanes with a cavity formed by bridged phenyl units and various derivatives are formed with the introduction of substituents onto the skeleton. The three calixarenes studied are *p*-tert-butylcalix/6/arene hexacarboxylic acid (L1), *p*-tert-butylcalix/4/arene tetracarboxylic acid (L2) and [3, 1, 3, 1]-cyclophane (L3). L1, L2 and L3 have different cavity sizes and contain carboxylic acid groups at the "lower" rim to achieve a high coordination number for Ln^{3+} and to prevent the phase transfer of counter anions.

The extractability of the lanthanides from the aqueous phase at pH ≈ 2–3.5 with L1 into chloroform is Nd, Eu > La > Er > Yb. A cation exchange mechanism with a 1:2 metal:ligand complex is indicated. With an excess of Na^{+} in the aqueous phase, the extractability of the lanthanides decreases and the lanthanides are extracted as 1:1 complexes at low extractant concentration.

The smaller cavity in L2 dissolved in chloroform or toluene resulted in lower distribution coefficients compared to L1. The order of extraction of the 1:2 metal:extractant

complexes for the water–toluene system is Eu > Nd > Yb > Er > La. Extractability and selectivity increased with addition of excess Na^+.

Heavy lanthanides were better extracted than the light and medium ones by the third cyclophane, L3, with a cavity size similar to L1 containing four carboxylic acid groups. The order of extractability is Yb > Er, Eu > Nd > La at pH ≈ 3.0.

2.8. *Other extractants*

Freiser (1988) summarized the results of a systematic investigation of the equilibrium extraction behavior of selected trivalent lanthanides with various chelating reagent families. For a monomeric weak acid extractant, HL, the formation of both simple ($a = 0$) and self adduct ($a > 0$) chelates are given by the reaction

$$\left[Ln^{3+}\right]_{AQ} + [(3 + a)HL]_{ORG} \rightleftarrows [LnL_3 \cdot aHL]_{ORG} + \left[3H^+\right]_{AQ}.$$

The following reaction applies in the presence of a neutral auxiliary ligand, or adductant, B:

$$\left[Ln^{3+}\right]_{AQ} + [(3 + a)HL]_{ORG} + [bB]_{ORG} \rightleftarrows [LnL_3 \cdot aHL \cdot bB]_{ORG} + \left[3H^+\right]_{AQ}.$$

The reaction system involving ion pair extraction of anionic chelates is given by

$$\left[Ln^{3+}\right]_{AQ} + [(4 + a)HL]_{ORG} + \left[Q^+, X^-\right]_{AQ} \rightleftarrows \left[Q^+LnL_4 \cdot aHL)^-\right]_{ORG} + \left[4H^+\right]_{AQ} + [X^-]_{AQ}.$$

where Q^+, X^- is the ion pair.

The formation of a cationic intermediate chelate, either coordinated or ion paired with thiocyanate is represented by

$$\left[Ln^{3+}\right]_{AQ} + [2HL]_{ORG} + [CNS^-]_{AQ} \rightleftarrows [LnL_2 \cdot CNS]_{ORG} + \left[2H^+\right]_{AQ}.$$

The extraction reaction for the acidic phosphorus ligands which exist predominantly as dimers in the organic phase is

$$\left[Ln^{3+}\right]_{AQ} + [3(HL)_2]_{ORG} \rightleftarrows [Ln(HL_2)_3]_{ORG} + \left[3H^+\right]_{AQ}.$$

In the presence of an adductant this becomes

$$\left[Ln^{3+}\right]_{AQ} + [2(HL)_2]_{ORG} + [B]_{ORG} \rightleftarrows [Ln(HL_2)L_2 \cdot B]_{ORG} + \left[3H^+\right]_{AQ}.$$

The extraction of the lanthanide chlorides by 2-ethylhexyl-2-ethylhexylphosphonic acid (EHEHPA) in kerosene has been reported by Sato (1989). The extraction efficiency in EHEHPA also increases with atomic number, but lower in comparison with HDEHP

Table 3
Separation factor[a] of rare-earth elements in the extraction systems Ln(III)–HCl–EHEHPA

Ln_1	Ln_2												
	Ce	Pr	Nd	Sm	Eu	Gd	Tb	Dy	Ho	Er	Tm	Yb	Lu
La	1.30	1.42	1.67	3.33	6.52	9.52	22.5	36.4	93.9	117	156	175	199
Ce		1.09	1.28	2.57	5.02	7.36	17.3	28.0	72.3	90.5	120	135	152
Pr			1.17	2.35	4.59	6.72	15.8	64.2	66.0	82.7	110	123	140
Nd				2.00	3.94	5.74	13.5	21.8	56.3	70.5	93.7	105	119
Sm					1.96	2.87	6.74	10.9	28.2	35.3	46.8	52.6	59.5
Eu						1.46	3.45	6.39	14.4	18.0	24.0	26.9	30.4
Gd							2.35	3.81	9.82	12.3	16.3	18.3	20.7
Tb								1.62	4.18	5.23	6.95	7.81	8.83
Dy									2.58	3.23	4.29	4.82	5.45
Ho										1.25	1.66	1.87	2.11
Er											1.33	1.49	1.69
Tm												1.12	1.26
Yb													1.13

[a] $\alpha = E_a^0(Ln_1)/E_a^0(Ln_2)$; $E_a^0(Ln_1)$ and $E_a^0(Ln_2)$ represent the distribution coefficients of Ln_1 and Ln_2, respectively, in the extraction from 0.1 mol dm^{-3} hydrochloric acid solution with 0.2 mol dm^{-3} EHEHPA in kerosene.

under the same conditions. The separation factors for the extraction of rare earths from 0.1 mol/dm^3 hydrochloric acid solution with 0.2 mol/dm^3 EHEHPA in the Ln(III)–HCl–EHEHPA–kerosene system are given in table 3. EHEHPA is more selective for the separation of heavy rare earths from light rare earths in this system.

The extraction mechanisms of $Nd(SCN)_3$, $Nd(ClO_4)_3$ and $Nd(NO_3)_3$ with di(1-methylheptyl) methyl phosphonate (P-350) in kerosene or hexane have been characterized by Huang et al. (1989). The extraction reactions for the salting out agents can be represented by

$$[Nd^{3+}]_{AQ} + [3A^-]_{AQ} + [n(RO)_2CH_3PO]_{ORG} \rightleftarrows [NdA_3 \cdot n(RO)_2CH_3PO]_{ORG}.$$

where A^- represents SCN^-, ClO_4^- or NO_3^-. In this extraction system, the M^{3+} and the anion A^- are extracted simultaneously into the organic phase to form the extracted complex such as MA_3nL, where L is the extractant. In the aqueous phase, hydration water of the metal ion, M^{3+}, or anion, A^-, is removed.

The extraction equilibrium of Ce(III) and La(III) in NaCl solutions with 7-(4-ethyl-1-methyloctyl)-8-hydroxyquinoline (KELEX 100) in *n*-heptane with the addition of 10% v/v *n*-decanol has been reported by Urbanski et al. (1990) to be dependent on the pH as well as on the extractant, metal and chloride concentrations. The lanthanide–KELEX complex, LnR, is formed in the organic phase by the cation exchange reaction

$$[Ln^{3+}]_{AQ} + [3HR]_{ORG} \rightleftarrows [LnR_3]_{ORG} + [3H^+]_{AQ},$$

where HR is the extractant KELEX 100. The possibility also exists that the hydrolyzed species $LaOH^{2+}$ is extracted according to the reaction

$$[LaOH^{2+}]_{AQ} + [3HR]_{ORG} \rightleftarrows [LaR_3]_{ORG} + [2H^+]_{AQ} + H_2\cdot$$

3. Photochemical separation

Donohue (1977) described the photochemical separation of Eu from other rare earths using a low pressure mercury lamp with no filter at 185 nm and with a Vycor filter at 254 nm, and an ArF excimer laser operating at 193 nm. Equimolar mixtures (0.01 M) of binary or ternary lanthanide perchlorates and 0.05 M K_2SO_4 in 10% isopropanol were used in the experiments. The separation factors for the binary mixture Eu/Ln varied from 1 for Eu/Pr to >200 for Eu/Tm.

The irradiation of Eu^{3+} in its charge transfer band is

$$Eu^{3+}(H_2O) \xrightarrow{190\text{ nm}} Eu^{2+} + H^+ + \cdot OH.$$

The isopropanol scavenged the radicals formed in the above primary process

$$(CH_3)_2CHOH + \cdot OH \rightarrow H_2O + (CH_3)_2\cdot COH.$$

The Eu^{2+} are precipitated with sulfate, forming the insoluble $EuSO_4$. The presence of the sulfate ions makes possible the shift of the charge-transfer band to the longer wavelength light at 240 nm. The precipitate is formed homogeneously during the photolysis. Further reduction of Eu^{3+} by organic radicals is by the reaction

$$(CH_3)_2\cdot COH + Eu^{3+} \rightarrow Eu^{2+} + H^+ + (CH_3)_2C{=}O.$$

Separation of Eu from a solution mixture of $SmCl_3$, $EuCl_3$, and $GdCl_3$ in a rare earth saturated ethanol–isopropanol system by photoreduction of Eu with a high pressure mercury lamp has been carried out by Qiu et al. (1991). The yield of Eu(II) was 95% and the purity of the precipitated Eu was 92%. $EuCl_2$ was produced by photoreduction and precipitated from the alcohol mixture. The photochemical separation process is as follows:

Step 1: dissolution and complexation.

$$(Sm, Eu, Gd)Cl_3 \cdot nH_2O + 3EtOH \rightarrow (Sm, Eu, Gd)Cl_3 \cdot 3EtOH + nH_2O,$$

$$(Sm, Eu, Gd)Cl_3 \cdot nH_2O + 3(\text{isopropanol}) \rightarrow (Sm, Eu, Gd)Cl_3 \cdot 3(\text{isopropanol}) + nH_2O.$$

Step 2: photoexcitation.

$$(Sm, Eu, Gd)Cl_3 \cdot 3EtOH \xrightarrow{h\nu} (Sm, Eu, Gd)^{\bullet}Cl_3 \cdot 3EtOH,$$

$$(Sm, Eu, Gd)Cl_3 \cdot 3(isopropanol) \xrightarrow{h\nu} (Sm, Eu, Gd)^{\bullet}Cl_3 \cdot 3(isopropanol).$$

Step 3: electron transition.

$$Eu^{\bullet}Cl_3 \cdot 3EtOH \rightarrow EuCl_2 + 2EtOH + \text{organic oxidation products},$$

$$Eu^{\bullet}Cl_3 \cdot 3(isopropanol) \rightarrow EuCl_2 + 2(isopropanol) + \text{organic oxidation products}.$$

The reduction potential of Sm(III) and Gd(III) is more negative than that of Eu(III)/Eu(II). This only makes the reduction of Eu(III)–Eu(II) possible, although Sm(III) and Gd(III) are also excited during the photoreduction.

Step 4: precipitation.

$EuCl_2$ was precipitated and separated from the other rare earths since the solubility of $EuCl_2$ in an EtOH-isopropanol mixture is low. The water content of the alcohol mixture must be kept low in order to precipitate $EuCl_2$.

4. Precipitation stripping

Recovery of rare earths from very dilute leach solutions by conventional solvent extraction technique can be a problem due to the high acid concentration that is required for the stripping of low rare earth concentrations. The stripped solution containing very low rare earth concentrations needs to be neutralized prior to the precipitation of the rare earths as an oxalate. The very high consumption of the neutralizing reagent can create technical, environmental and/or economic problems.

The rare earths form slightly soluble double sulfates with ammonium and alkali metal sulfates. Addition of an appropriate salt to the stripping solution can facilitate the removal of the very low concentration rare earth ions from the aqueous phase without neutralization. When sulfuric acid is used as the acidic reagent in the stripping solution, the precipitation step can be combined with stripping in the same stage. Success of this procedure depends on the stripping behavior of the lanthanide ions and on the nature of the precipitated solid.

Zielinski et al. (1991) reported the precipitation stripping of lanthanum and neodymium from an equimolar mixture of monomeric and dimeric di-2-ethylhexyl phosphoric acid in a kerosene diluent. The sulfuric acid strip solution contained potassium sulfate, sodium sulfate or ammonium sulfate as the precipitating reagent. The precipitation efficiency for lanthanum and neodymium reached up to 98% with the addition of potassium or sodium sulfate, compared to 80% for lanthanum, and 70% for neodymium with the addition of ammonium sulfate.

Both lanthanum and neodymium double sulfates are precipitated. The general formula of the double sulfates is $xMe_2SO_4 yLn_2(SO_4)_3 nH_2O$. The co-precipitated salts are potassium hydrogen sulfate, sodium sulfate or lanthanum/neodymium sulfate, depending on the composition of the strip solution. Precipitation occurs only in the aqueous phase.

Additional results on the single-stage selective stripping of Nd–Eu, representing the light rare earths, Nd–Dy, and Dy–Er representing the heavy rare earths, from HDEHP with sulfuric acid solutions containing Na_2SO_4 have been reported by Zielinski and Szczepanik (1993). Light lanthanides are readily stripped and precipitated compared to the heavy lanthanides. As a result, the concentration of heavy lanthanides in the solution after stripping of the light lanthanides is higher than their concentration in the original solution.

5. Ion-exchange

Separation and purification of microquantities of scandium (III) from macroquantities of rare earths on selective ion-exchangers has been described by Hubicki (1990). The chelating and ion-exchangers examined include phosphonic gel and macroporous, aminophosphonic, various carboxylic, amino-acids with different matrix compositions, polyphenol, amphoteric (snake in cage polymers), cellulose phosphate, zirconium phosphate, and copolymer of polystyrene with divinylbenzene. The phosphonic, aminophosphonic and cellulose-phosphate were the most effective.

The great stability of the scandium complexes with phosphonic and aminophosphonic acids enhances the selective separation of microquantities of Sc(III) from Y(III), La(III) and Ln(III). The concentration of the rare earth solution was up to 500 g/l and the acidity of the rare earth solutions purified from scandium reached 6 M HCl. Phosphonic ion-exchangers are not only useful in the selective separation but also in the purification of Sc(III) since 6 M HCl solution does not elute Sc(III) by gradient elution with 0.5–6 M acid.

With the exception of the isoporous ion-exchangers with the functional group EDTA, the other amino-acid types examined can be used in the purification of rare earth element salts from Sc(III). The most effective carboxylic ion-exchanger is the polymethacrylic type for purifying La(III) from Sc(III).

Preparation of 99.99% Sc_2O_3 from feedstock of around 70% Sc_2O_3 by extraction chromatography at room temperature with greater than 90% recovery has been reported by Gongyi and Yuli (1989, 1990). Purification was carried out on two chromatographic columns containing tributyl phosphate as the stationary phase supported by hydrophobic silica gel or polystyrene–divinylbenzene copolymer. The feed solution containing 2–4 g/l Sc_2O_3 and a small amount of citric acid was passed through column 1 to remove impurities in the stock solution with very little loss of scandium. The effluent from column 1, adjusted to 3–4 M perchloric acid, passed through column 2 for further purification of scandium. Scandium was eluted with 1 M HCl from column 2 and precipitated with oxalic acid followed by calcination to scandium oxide.

6. Supercritical extraction

Synthesis of the normal carbonates of La^{3+}, Nd^{3+}, Sm^{3+}, Eu^{3+}, Gd^{3+}, Dy^{3+}, and Ho^{3+} by the reaction of an aqueous suspension of the lanthanide oxide with CO_2 at or over the critical temperature of 31°C and critical pressure of 72.9 atm has been reported by Yanagihara et al. (1991). The carbonates of Pr^{3+}, Tb^{3+}, Er^{3+}, and Yb^{3+} either did not form or gave very low yields under the experimental conditions studied.

In a patent based on the above results, Fernando et al. (1991) separated the trivalent lanthanide oxides or hydroxides from the tetravalent lanthanides which do not react with carbon dioxide under supercritical conditions. The rare earth carbonates from the trivalent oxides or hydroxides of La, Nd, Sm, Eu, Gd, Dy, Ho, Pm, Tm, and Lu can readily be formed after one hour at 40°C and 100 atm with yields of up to 95% of the normal carbonates, instead of the hydroxy carbonates. The oxides or hydroxides of Pr, Tb, Er, Yb, and Ce do not form carbonates under these conditions.

The solid precipitates formed after supercritical reaction consist of rare earth carbonates and unreacted rare earth oxides and/or hydroxides. Addition of 0.5 M HCl to the solids at ambient temperature and pressure solubilizes the rare earth carbonates. The unreacted rare earth oxides and/or hydroxides are left in the solid phase. The solution containing the rare earths can then be further separated into individual rare earths by conventional solvent extraction or ion exchange. Separation of rare earth carbonates is carried out in dilute acid. ThO_2, ZrO_2 and CeO_2 either did not react or gave very low yields under the experimental conditions.

7. Industrial producers

Production of rare earth compounds from bastnasite, a fluo-carbonate mineral containing mostly cerium, lanthanum, neodymium and praseodymium and small quantities of samarium, gadolinium and europium at Molycorp was described by Harrah (1967). High purity yttrium and europium oxides are produced, together with a concentrate of lanthanum, praseodymium/neodymium and samarium/gadolinium. The europium solvent extraction circuit organic phase consists of 10% di-2-ethyl hexyl phosphoric acid in a kerosene diluent. The europium strip solution is 4N hydrochloric acid. Samarium and gadolinium is precipitated with Na_2CO_3 from the solution after europium is removed.

An outline of the Rhône-Poulenc separation flowsheet to produce high purity rare earth oxides from various ores such as monazite, bastnasite and euxenite was published by Agpar and Poirier (1976). After the leaching step, non-rare earth elements and radioactive products are removed. The first solvent extraction stream in a chloride medium produces non-separated rare earth compounds, such as dehydrated rare earth chlorides used as the feedstock for the electrolysis to produce mischmetal.

A second solvent extraction stream in a nitrate medium is used to produce separated rare earth oxides. Individual rare earths in solution are separated from each other in a series of solvent extraction streams. Lanthanum (99.995% La_2O_3) which remains in

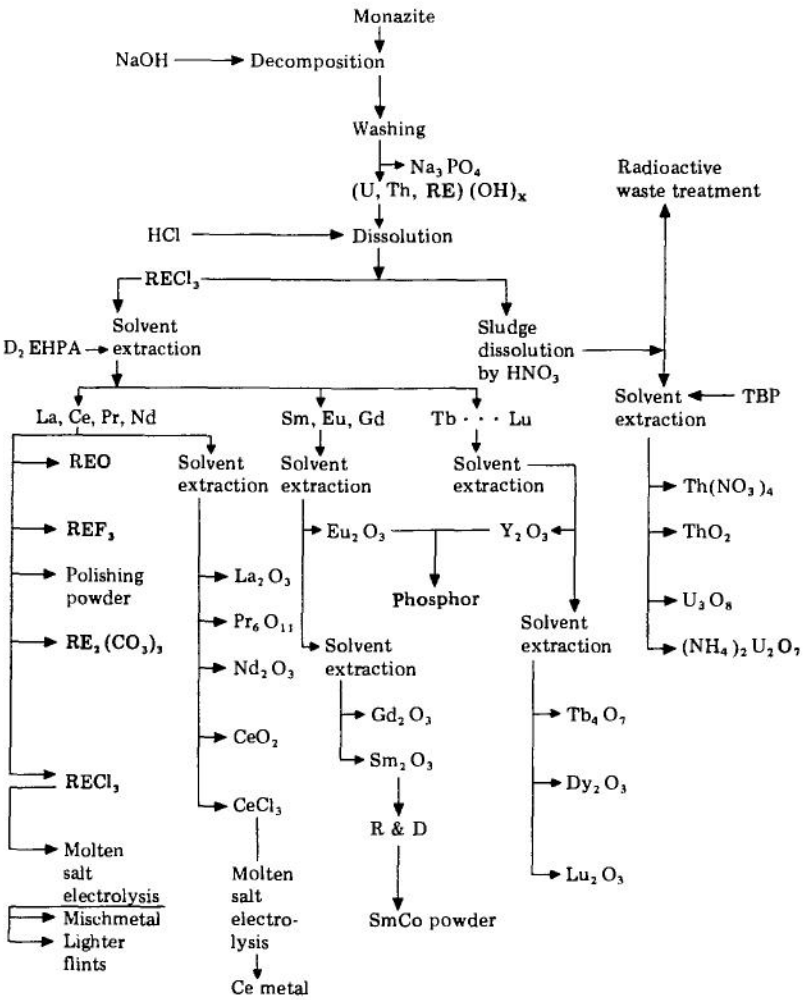

Fig. 1. Simplified flowsheet of the Yao Lung Chemical plant.

the aqueous phase is separated from the Ce, Pr, Nd, Sm, Eu, Gd, Tb, Y, etc. mixtures that go into the organic phase. CeO_2 (99.5%) is separated at the Nd–Sm stream. Didymium chloride (after primary Ce removal) is produced from which the following rare earth oxides are recovered in sequence: Pr_6O_{11}, 96%; Nd_2O_3, 95%; Sm_2O_3, 96%; Eu_2O_3, 99.99%; Gd_2O_3, 99.99%; Tb_4O_7, 99.9%; and Y_2O_3, 99.99%.

Separation of each element by solvent extraction is carried out in multistage batteries of mixer–settlers for each rare earth element. A minimum of 50 mixer–settler stages per stream is required to obtain a product with a purity of 4 or 5 nines. For economic and technical reasons the ion-exchange method is only used for laboratory and pilot scale production to produce small tonnage of rare earths.

The extractants used in the solvent extraction processing include organo–phosphorus compounds, amines and carboxylic acids. The Rhône-Poulenc solvent extraction separation flowsheet has become the standard for all industrial producers.

Zhang et al. (1982) summarized the rare earth industry in China. The Peoples Republic of China has the largest proven reserve of rare earth oxides in the world. Their production is mainly from the bastnasite–monazite concentrate from the Baotu iron ore deposit in Inner Mongolia (Northern China), monazite ore deposits in Southern China and the adsorbed rare earth oxides on clay found in Jiangxi province. The Yao Lung Chemical plant in Shanghai was the first of their rare earth processing plants, which went on stream in 1964. The Yao Lung Chemical Co. flowsheet for the separation and extraction of rare earth oxides from monazite is reproduced in fig. 1.

8. Summary and conclusions

The major industrial producers of rare earths recover individual rare earths from monazite, bastnasite, euxenite, and other rare earth containing raw material, through a series of unit operations. These unit operations include leaching with an appropriate lixiviant, separation and concentration by solvent extraction and/or ion exchange, precipitation as an oxalate and calcination to produce the individual oxide. Solvent extraction technology is the most efficient and economical separation method presently available.

The development of new extractants with enhanced selectivity for each individual rare earth will have a major impact on their separation, concentration, and purification. Completely new separation technologies that can compete with the efficient and economical multistage solvent extraction operation may yet be developed from any of the emerging separation processes discussed in this chapter. However, the new technology must be a "quantum" development to be adopted by the industry.

References

Abbruzzese, C., P. Fornari, R. Massidda and T.S. Urbanski, 1992, Hydrometallurgy **28**, 179–190.

Agpar, H., and P. Poirier, 1976, Preprint, 12th Rare Earth Research Conference, Vail, CO, 1976, 12 pp.

Banks, C.V., and D.W. Klingman, 1961, Analytical chemistry of the rare earths, in: The Rare Earths, eds F.H. Spedding and A.H. Daane, reprinted 1971 (R.E. Krieger Publishing Co., Huntington, NY) pp. 570–593.

Bauer, D.J., 1966, Extraction and Separation of Selected Lanthanides with a Tertiary Amine, RI 6809 (US Bureau of Mines) 13 pp.

Bauer, D.J., and R.E. Lindström, 1964, Naphthenic Acid Solvent Extraction of Rare Earth Sulfates, RI 6396 (US Bureau of Mines) 19 pp.

Bauer, D.J., and R.E. Lindström, 1968, Differential extraction of rare earth elements in quaternary ammonium salt–chelating agent systems, in: Proc. 7th Rare Earth Research Conf. (CONF-681020) pp. 413–423.

Bauer, D.J., and R.E. Lindström, 1971, Differential Extraction of Rare Earth Elements in Quaternary Ammonium Compound–Chelating Agent Systems, RI 7524 (US Bureau of Mines) 16 pp.

Bauer, D.J., R.E. Lindström and K.B. Higbie, 1968, Extraction Behavior of Cerium Group Lanthanides in a Primary Amine–Chelating Agent System, RI 7100 (US Bureau of Mines) 12 pp.

Bautista, R.G., 1990, Industrial extraction and purification techniques for rare earths, in: Rare Earths in Alaska, Proc. Symp., Aug. 17–18, 1988, Fairbanks (Alaska Science and Engineering Advisory Commission) pp. 47–58.

Bautista, R.G., 1992, Mineral Proc. Extractive Met. Rev. **8**, 175–182.

Bautista, R.G., and N. Jackson, 1992, Rare Earths, Resources, Science, Technology and Applications (TMS, Warrendale, PA).

Bautista, R.G., and M.M. Wong, 1989, Rare Earths, Extraction, Preparation and Applications (TMS, Warrendale, PA).

Bostian, H., and M. Smutz, 1964, J. Inorg. Nucl. Chem. **26**, 825–836.

Boyd, G.E., J. Schubert and A. Adamson, 1947, J. Am. Chem. Soc. **69**, 2818–2829.

Boynton, W.V., 1979, Neutron activation analysis, in: Handbook on the Physics and Chemistry of Rare Earths, Vol. 4, eds K.A. Gschneidner Jr and L. Eyring (North-Holland, Amsterdam) pp. 457–470.

Bril, K.J., 1964, Mass extraction and separation, in: Progress in the Science and Technology of the Rare Earths, Vol. 1, ed. L. Eyring (Pergamon Press, Oxford) pp. 30–61.

Callow, R.J., 1966, The Rare Earth Industry (Pergamon Press, London).

Callow, R.J., 1967, The Industrial Chemistry of the Lanthanons, Yttrium, Thorium, and Uranium, 1st Ed. (Pergamon Press, London).

Carnall, W.T., 1979, The absorption and fluorescence spectra of rare earth ions in solution, in: Handbook on the Physics and Chemistry of Rare Earths, Vol. 3, eds K.A. Gschneidner Jr and L. Eyring (North-Holland, Amsterdam) pp. 171–208.

Cassidy, P.W., and A.R. Burkin, 1971, Extraction of europium from sulfate-perchlorate solutions by di-2-ethylhexyl phosphoric acid, in: Proc. Int. Solvent Extraction Conf. 1971, Vol. I, eds J.G. Gregory, B. Evans and P.C. Weston (Society of Chemical Industry, London) pp. 476–482.

Cerna, M., E. Volaufova and V. Rod, 1992, Hydrometallurgy **28**, 339–352.

Coleman, C.F., 1963, Nucl. Sci. & Eng. **17**, 274–286.

Conzemius, R.J., 1979, Analysis of rare earth matrices by spark source massed spectrometry, in: Handbook on the Physics and Chemistry of Rare Earths, Vol. 4, eds K.A. Gschneidner Jr and L. Eyring (North-Holland, Amsterdam) pp. 377–404.

Cox Jr, E.C., and M.W. Davis Jr, 1973, Sep. Sci. **8**(2), 205–243.

Davis Jr, M.W., J. Mrochek and C.J. Hardy, 1966, J. Inorg. Nucl. Chem. **28**, 2001–2014.

DeKalb, E.L., and V.A. Fassel, 1979, Optical atomic emission and absorption methods, in: Handbook on the Physics and Chemistry of Rare Earths, Vol. 4, eds K.A. Gschneidner Jr and L. Eyring (North-Holland, Amsterdam) pp. 405–440.

Donohue, T., 1977, J. Chem. Phys. **67**(11), 5402–5404.

D'Silva, A.P., and V.A. Fassel, 1979, X-ray excited optical luminescence of the rare earths, in: Handbook on the Physics and Chemistry of Rare Earths, Vol. 4, eds K.A. Gschneidner Jr and L. Eyring (North-Holland, Amsterdam) pp. 441–456.

duPreez, A.C., and J.S. Preston, 1992, Solv. Extr. Ion Exch. **10**(2), 207–230.

Ensor, D.D., M. Nicks and D.J. Pruett, 1988, Sep. Sci. Technol. **23**(12–13), 1345–1353.

Fassel, V.A., 1961, Analytical spectroscopy of the rare earth elements, in: The Rare Earths, eds F.H. Spedding and A.H. Daane (R.E. Krieger Publishing Co., Huntington, NY) pp. 594–613.

Fernando, Q., N. Yanagihara, J.T. Dyke and K. Vemulapalli, 1991, Formation of Rare Earth Carbonates Using Supercritical Carbon Dioxide, US Patent 5 045 289, Sept. 3, 1991.

Fidelis, I., 1970, J. Inorg. Nucl. Chem. **32**, 997–1003.

Fidelis, I., 1971, Influence of temperature on the extraction of lanthanides in the HDEHP–HNO_3 system, in: Proc. Int. Solvent Extraction Conf. 1971, Vol. II, eds J.G. Gregory, B. Evans and P.C. Weston (Society of Chemical Industry, London) pp. 1004–1007.

Freiser, H., 1988, Solv. Extr. Ion Exch. **6**(6), 1093–1108.

Gongyi, G., and C. Yuli, 1989, Preparation of high purity scandium oxide by extraction chromatography, in: Rare Earths, Extraction, Preparation and Applications, eds R.G. Bautista and M.M. Wong (TMS, Warrendale, PA) pp. 163–170.

Gongyi, G., and C. Yuli, 1990, Hydrometallurgy **23**, 333–340.

Gruzensky, W.G., and G.T. Engel, 1959, Trans. Metall. Soc. AIME **215**, 738–742.

Gschneidner Jr, K.A., 1993, Physical properties of the rare earths, in: Handbook on the Physics and Chemistry of Rare Earths, Cumulative Index Volumes 1–15, eds K.A. Gschneidner Jr and

L. Eyring (North-Holland, Amsterdam) pp. 509–521.

Gupta, C.K., and N. Krisnamurthy, 1992, Int. Mater. Rev. **37**(5), 197–248.

Habashi, F., 1990, The rare metals and their position in the periodic table, in: Rare Metals '90, Proc. Int. Symp. on Processing of Rare Metals (Osaka University, Japan) pp. 47–52.

Harada, T., M. Smutz and R.G. Bautista, 1971, Polymers of iron and rare earths and di-2-ethylhexyl phosphoric acid, in: Proc. Int. Solvent Extraction Conf. 1971, Vol. II, eds J.G. Gregory, B. Evans and P.C. Weston (Society of Chemical Industry, London) pp. 950–956.

Hardy, C.J., 1970, J. Inorg. Nucl. Chem. **32**, 619–625.

Harrah, H.W., 1967, Rare earth concentration at molybdenum corporation of America, Part 2, Solvent extraction plant, Deco Trefoil **31**(5, November–December) 9–16. (Denver Equipment Co., Denver, CO.).

Harris, D.H., and E.R. Tompkins, 1947, J. Am. Chem. Soc. **69**, 2792–2800.

Haskin, L.A., and T.P. Paster, 1979, Geochemistry and mineralogy of the rare earths, in: Handbook on the Physics and Chemistry of Rare Earths, Vol. 3, eds K.A. Gschneidner Jr and L. Eyring (North-Holland, Amsterdam, 1979) pp. 1–80.

Hayden, J.G., I.H. Gerow and M.W. Davis Jr, 1974, Sep. Sci. **9**(4), 337–350.

Healy, R.M., and H.E. Kremers, 1961, Separation of rare earths by fractional crystallization, in: The Rare Earths, eds F.H. Spedding and A.H. Daane, reprinted 1971 (R.E. Krieger Publishing Co., Huntington, NY) pp. 29–37.

Hesford, E., and H.A.C. McKay, 1960, J. Inorg. Nucl. Chem. **13**, 156–164.

Hesford, E., E.E. Jackson and H.A.C. McKay, 1959, J. Inorg. Nucl. Chem. **9**, 279–289.

Hoh, Y.H., and W.K. Wang, 1980, Ind. Eng. Chem., Proc. Des. Dev. **19**, 64–67.

Hsu, K.H., C.H. Huang, T.C. King and P.K. Li, 1980, in: Proc. Int. Solvent Extraction Conf., Vol. 2 (Université de Liège, Liège, Belgium) paper 80–82.

Huang, C.H., and R.G. Bautista, 1983, Sep. Sci. & Technol. **18**, 1667–1683.

Huang, C.H., R.F. Hu and G.X. Xu, 1989, Solv. Extr. Ion Exch. **7**(3), 489–497.

Hubicki, Z., 1990, Hydrometallurgy **23**, 319–331.

Ketelle, B.H., and G.E. Boyd, 1947, J. Am. Chem. Soc. **69**, 2800–2812.

Kondo, K., F. Nakashio and H. Ohtsubo, 1992, Solv. Extr. Ion Exch. **10**(4), 655–662.

Kosinski, F.E., and H. Bostian, 1969, J. Inorg. Nucl. Chem. **31**, 3623–3631.

Krumholz, P., 1964, Solution chemistry, in: Progress in the Science and Technology of the Rare Earths, Vol. 1, ed. L. Eyring (Pergamon Press, New York) pp. 110–138.

Krumholz, P., K. Bril, S. Bril, J. Behmoiras, F. Gottdenker and F.W. Lima, 1958, in: Proc. 2nd U.N. Int. Conf. on Peaceful Uses of Atomic Energy, A/Conf. 15/P/2491 (Brazil) pp. 184–195.

Kubota, F., M. Goto and F. Nakashio, 1993, Solv. Extr. Ion Exch. **11**(3), 437–453.

Lenz, T.G., and M. Smutz, 1966, J. Inorg. Nucl. Chem. **28**, 1119–1120.

Loriers, J., 1964, La chimie analytique des terres rares, in: Progress in the Science and Technology of the Rare Earths, Vol. 1, ed. L. Eyring (Pergamon Press, New York) pp. 351–398.

Ludwig, R., K. Inoue and T. Yamato, 1993, Solv. Extr. Ion Exch. **11**(2), 311–330.

Majdan, M., and Z. Kolarik, 1993, Solv. Extr. Ion Exch. **11**(2), 331–348.

Manchanda, V.K., C.A. Chang and J. Peng, 1988, Solv. Extr. Ion Exch. **6**(5), 835–857.

Marinsky, J.A., L.E. Glendenin and C.D. Coryell, 1947, J. Am. Chem. Soc. **69**, 2781–2785.

Moeller, T., 1961, The chemistry of the rare earths, in: The Rare Earths, eds F.H. Spedding and A.H. Daane, reprinted 1971 (R.E. Krieger Publishing Co., Huntington, NY) pp. 9–28.

O'Laughlin, J.W., 1979, Chemical spectrophotometric and polarographic methods, in: Handbook on the Physics and Chemistry of Rare Earths, Vol. 4, eds K.A. Gschneidner Jr and L. Eyring (North-Holland, Amsterdam) pp. 341–358.

Peppard, D.F., 1961, Separation of rare earths by liquid–liquid extraction, in: The Rare Earths, eds F.H. Spedding and A.H. Daane, reprinted 1971 (R.E. Krieger Publishing Co., Huntington, NY) pp. 38–54.

Peppard, D.F., 1964, Fractionation of rare earths by liquid–liquid extracion using phosphorus-based extractants, in: Progress in the Science and Technology of the Rare Earths, Vol. 1, ed. L. Eyring (Pergamon Press, New York, 1964) pp. 89–109.

Peppard, D.F., J.P. Faris, P.R. Gray and G.W. Mason, 1953, J. Phys. Chem. **57**, 294–301.

Peppard, D.F., W.J. Driscoll, R.J. Sironen and S. McCarthy, 1957, J. Inorg. Nucl. Chem. **4**, 326.

Peppard, D.F., G.M. Mason, W.J. Driscoll and R.J. Sironen, 1958, J. Inorg. Nucl. Chem. **7**, 276–285.

Powell, J.E., 1979, Separation chemistry, in: Handbook on the Physics and Chemistry of Rare Earths, Vol. 3, eds K.A. Gschneidner Jr and L. Eyring (North-Holland, Amsterdam) pp. 81–109.

Powell, J.E., and F.H. Spedding, 1959a, Trans. Metall. Soc. AIME **215**, 457–463.

Powell, J.E., and F.H. Spedding, 1959b, Basic principles involved in the macroseparation of adjacent rare earths from each other by means of ion exchange, in: Adsorption, Ion Exchange, and Dialysis, Chemical Engineering Progress Symposium Series, Vol. 55, no. 24 (American Institute of Chemical Engineers, New York) pp. 101–113.

Preston, J.S., 1985, Hydrometallurgy **14**, 171–188.

Qiu, L.F., X.H. Kang and T.S. Wang, 1991, Sep. Sci. & Technol. **26**(2), 199–221.

Reuben, J., and G.A. Elgavish, 1979, Shift reagents and NMR of paramagnetic lanthanide complexes, in: Handbook on the Physics and Chemistry of Rare Earths, Vol. 4, eds K.A. Gschneidner Jr and L. Eyring (North-Holland, Amsterdam) pp. 483–514.

Ryabchikov, D.I., 1959, Engl. Trans., 1960, Rare Earth Elements, Extraction, Analysis, Applications (Academy of Sciences, USSR, Moscow).

Ryabchikov, D.I., and V.A. Ryabukhin, 1964, Soviet research on analytical chemistry of the rare earths, in: Progress in the Science and Technology of the Rare Earths, Vol. 1, ed. L. Eyring (Pergamon Press, London) pp. 399–415.

Sato, T., 1989, Hydrometallurgy **22**, 121–140.

Schuhmann, S., and J.A. Philpotts, 1979, Mass spectrometric stable-isotope dilution analysis for lanthanides in geochemical materials, in: Handbook on the Physics and Chemistry of Rare Earths, Vol. 4, eds K.A. Gschneidner Jr and L. Eyring (North-Holland, Amsterdam) pp. 471–482.

Sheka, Z.A., and E.G. Kriss, 1959, Russ. J. Inorg. Chem. **4**, 1153–1156.

Spedding, F.H., A.F. Voigt, E.M. Gladrow and N.R. Sleight, 1947a, J. Am. Chem. Soc. **69**, 2777–2781.

Spedding, F.H., A.F. Voigt, E.M. Gladrow, N.R. Sleight, J.E. Powell, J.M. Wright, T.A. Butler and P. Figard, 1947b, J. Am. Chem. Soc. **69**, 2786–2792.

Spedding, F.H., E.I. Fulmer, T.A. Butler, E.M. Gladrow, M. Gobush, P.E. Porter, J.E. Powell and J.M. Wright, 1947c, J. Am. Chem. Soc. **69**, 2812–2818.

Spedding, F.H., J.E. Powell and E.J. Wheelright, 1954a, J. Amer. Chem. Soc. **76**, 612–613.

Spedding, F.H., J.E. Powell and E.J. Wheelright, 1954b, J. Amer. Chem. Soc. **76**, 2557–2560.

Szabadvary, F., 1980, in: Handbook on the Physics and Chemistry of Rare Earths, Vol. 2, eds K.A. Gschneidner Jr and and L. Eyring (North-Holland, Amsterdam) pp. 33–80.

Tang, J., and C.M. Wai, 1986, Anal. Chem. **58**, 3233–3235.

Taylor, S.R., 1979, Trace element analysis of rare earth elements by spark source mass spectrometry, in: Handbook on the Physics and Chemistry of Rare Earths, Vol. 4, eds K.A. Gschneidner Jr and L. Eyring (North-Holland, Amsterdam) pp. 359–376.

Tedesco, P.H., V.B. de Rumi and J.A. Gonzalez Quintana, 1967, J. Inorg. Nucl. Chem. **29**, 2813–2817.

Thompson, L.C., 1979, Complexes, in: Handbook on the Physics and Chemistry of Rare Earths, Vol. 3, eds K.A. Gschneidner Jr and L. Eyring (North-Holland, Amsterdam) pp. 209–297.

Tompkins, E.R., and S.W. Mayer, 1947, J. Am. Chem. Soc. **69**, 2859–2865.

Tompkins, E.R., J.X. Khym and W.E. Cohn, 1947, J. Am. Chem. Soc. **69**, 2769–2777.

Topp, N.E., 1965, The Chemistry of the Rare-Earth Elements (Elsevier, London).

Urbanski, T.S., A. Abbruzzese, P. Fornari and R. Massidda, 1990, Hydrometallurgy **25**, 185–195.

Urbanski, T.S., C. Abbruzzese, P. Fornari and R. Massidda, 1992, Hydrometallurgy **28**, 1–12.

Warf, J.C., 1949, J. Am. Chem. Soc. **71**, 3257–3258.

Weaver, B., 1964, Liquid–liquid extraction of the rare earths, in: Progress in the Science and Technology of the Rare Earths, Vol. 1, ed. L. Eyring (Pergamon Press, New York) pp. 85–88.

Weaver, B., 1968, Liquid–liquid extraction of the rare earths, in: Progress in the Science and Technology of the Rare Earths, Vol. 3, ed. L. Eyring (Pergamon Press, New York) pp. 129–148.

Weaver, B., 1974, Solvent extraction in the separation of rare earths and trivalent actinides, in: Ion Exchange and Solvent Extraction, Vol. 6, eds J.A. Marinsky and Y. Marcus (Marcel Dekker, New York) pp. 189–277.

Weeks, M.E., 1956, in: Discovery of the Elements, 6th Ed. (American Chemical Society, Easton, PA) pp. 695–727.

Yanagihara, N., K. Vemulapalli, Q. Fernando and J.T. Dyke, 1991, J. Less-Common Met. **167**, 223–232.
Yoshida, H., 1964, J. Inorg. Nucl. Chem. **26**, 619–625.
Zhang, B.Z., K.Y. Lu, K.C. King, W.C. Wei and W.C. Wang, 1982, Hydrometallurgy **9**, 205–210.
Zielinski, S., and A. Szczepanik, 1993, Hydrometallurgy **33**, 219–226.
Zielinski, S., M. Buca and A. Szczepanik, 1991, Hydrometallurgy **26**, 243–254.

Handbook on the Physics and Chemistry of Rare Earths
Vol. 21
edited by K.A. Gschneidner, Jr. and L. Eyring
Elsevier Science B.V.

Chapter 140

CORROSION PREVENTION AND CONTROL

Bruce R.W. HINTON
DSTO – Aeronautical and Maritime Research Laboratory,
Ship Structures and Materials Division, Melbourne, Australia

Contents

List of symbols and abbreviations

CCC	chromate conversion coating	RH	relative humidity
CF	corrosion fatigue	RSP	rapid solidification processing
CFC	corrosion fatigue cracking	SCC	stress corrosion cracking
E_{corr}	corrosion potential	SCE	saturated calomel electrode
E_{pit}	pitting potential	SEM	scanning electron microscopy
EC	environmental cracking	TEM	transmission electron microscopy
I_{corr}	corrosion current	TTF	time to failure
I_{pass}	passive current	σ_y	yield stress
K	stress intensity		
K_{ISCC}	stress intensity threshold for stress corrosion cracking		

1. Introduction

1.1. *Cost of corrosion*

Throughout our daily lives, we constantly see the effects of environmental degradation on metal and alloys. Common examples are rusted car panels and structural steel components, powdered and stained architectural aluminium, pitted aluminium kitchen utensils, powdered galvanized coatings on steel, tarnished silver, and the green patina on brass or copper. Examples not commonly seen include pitting of stainless steel in chemical plants, rusting of steel in cooling towers and the exfoliation or layered degradation of aluminium alloy aircraft components. These are all examples of metallic corrosion. Much of this would seldom be considered as life threatening. As a consequence, it rarely attracts much attention. However, the economic costs of corrosion to the community are only now being realized. These costs are certainly not trivial.

A study by Hoar (1971) on behalf of the Department of Trade and Industry in the United Kingdom, found that the annual cost of corrosion in the UK was 1365 million pounds. A similar study in the USA in 1981 estimated the annual cost of corrosion to be 70 billion US$ (Bennett and Kruger 1981). Even areas of new and advancing technology such as the aircraft industry cannot escape the ravages of corrosion. In 1990 the US Air Force calculated that maintenance costs associated with corrosion amounted to 718 million US$ per year (Cooke et al. 1990). These cost penalties include not only the costs of corrosion protection and prevention, but also the costs of replacement and loss of production time as a result of corrosion. Of course, some of these costs cannot be avoided

completely. Nevertheless, the numbers cited above do indicate the order of magnitude of the economic cost of corrosion to the community, and the need for effective corrosion prevention and control programs.

Just as the community is becoming aware of the costs of corrosion, it is also becoming aware of the problems associated with many of the standard methods of corrosion prevention and control. Some of the developing areas of research to be described in the following chapter are the results of attempts to achieve effective corrosion prevention and control, and at the same time comply with the ever increasing demands of environmental health and safety legislation.

1.2. *The corrosion process*

Corrosion, its control and prevention is an enormous section of the science of metals. It is served by many disciplines including metallurgy, electrochemistry, physics, and chemical engineering. It would be unproductive to attempt to provide a comprehensive review of the subject here. For such a reference the reader is directed to the excellent volumes edited by Shreir (1976) and the book by Evans (1961). The following sections summarize background required for the concepts referred to throughout the chapter.

Metallic corrosion in aqueous environments is an electrochemical process generally consisting of two or more partial reactions, which occur at or near microstructural features on the metal or alloy surface. These features include grain boundaries, intermetallic phases and particles or flaws in naturally occurring protective oxide films. A simple schematic of the process is shown in fig. 1. At anodic sites on the surface, e.g. intermetallic particles or the adjacent matrix, or at the base of flaws in oxide films, metal dissolution occurs i.e. $M \rightarrow M^{n+} + ne^{-}$. At cathodic areas, which may be surfaces of intermetallic particles or the mouths of flaws in oxide films, cathodic reactions occur, such as the reduction of oxygen

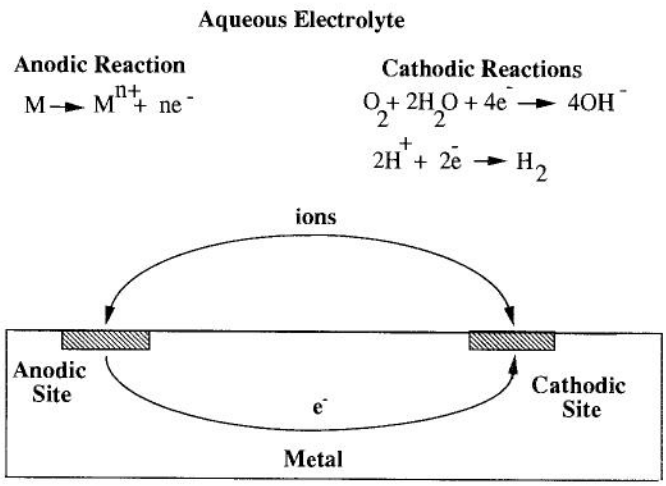

Fig. 1. A schematic representation of the corrosion process on a metal surface in an aqueous environment.

$O_2 + 2H_2O + 4e^- \rightarrow 4OH^-$ and the evolution of hydrogen $2H^+ + e^- \rightarrow H_2$. Electrons move from the anodic site through the metal to the cathodic site where they take part in the cathodic reactions. Movement of ionic charge occurs through the aqueous phase between the two sites, thereby completing the electrochemical circuit.

1.3. *Corrosion tests*

The corrosion rates of metals and alloys may be measured by a number of techniques, which have been comprehensively described by Ailor (1971). During the course of this chapter, two of these techniques will be frequently mentioned. The simplest procedure for determining the corrosion rate is to measure the weight of a metal coupon before and after exposure to a given environment, calculate the loss in weight and divide by the exposure time and the coupon surface area. In the literature, corrosion rates are quoted in a range of units e.g. mg dm^{-2} day^{-1}, $\mu g\, m^{-2}\, s^{-1}$, or mpy (mils per year). The latter is a measure of penetration rate. The ASTM have published standard procedures for conducting weight-loss tests, within ASTM G-31 "Standard Recommended Practice for Laboratory Immersion Corrosion Testing of Metals" and ASTM G-1 "Preparing, Cleaning and Evaluating Corrosion Test Specimens". After exposure to the corrosive environment, any corrosion product is removed by the appropriate treatment before the final weight is measured. When corrosion inhibitors are being assessed, the effectiveness of the inhibitor is often described in terms of inhibitor efficiency as a percentage. This is simply the weight loss $\times 100$ divided by the original weight. The most common aqueous environments chosen for corrosion testing are generally solutions of NaCl. The test specimens may be continuously immersed in the environment, or withdrawn for drying periods before re-immersion. Corrosion tests are also frequently carried out in a chamber of salt fog or spray, with the spray being a solution of 5% NaCl. This test procedure is outlined by ASTM B-117 "Salt Spray Fog Testing".

Rates of corrosion can also be measured using an electrochemical technique known as potentiodynamic polarization. The potential of the test metal electrode relative to a reference electrode (commonly the saturated calomel electrode SCE) is varied at a controlled rate using a potentiostat. The resultant current density which flows in the cell via an auxiliary electrode, typically platinum, is recorded as a function of potential. The schematic curve in fig. 2 is typical of data obtained from such a test. These data can provide various parameters in addition to corrosion rate, all of which are suitable for describing corrosion resistance. The corrosion potential E_{corr} is nominally the open circuit or rest potential of the metal in solution. At this potential, the anodic and cathodic processes occurring on the surface are in equilibrium. When the sample is polarized to potentials more positive than E_{corr} the anodic processes, such as metal dissolution, dominate (Anodic Polarization Curve). With polarization to potentials more negative than E_{corr} the cathodic processes involved in the corrosion reaction such as oxygen reduction and hydrogen evolution dominate (Cathodic Polarization Curve). These separate halves of the total polarization curve may provide information about the rates of anodic and cathodic processes. The current density at any particular potential is a measure of the

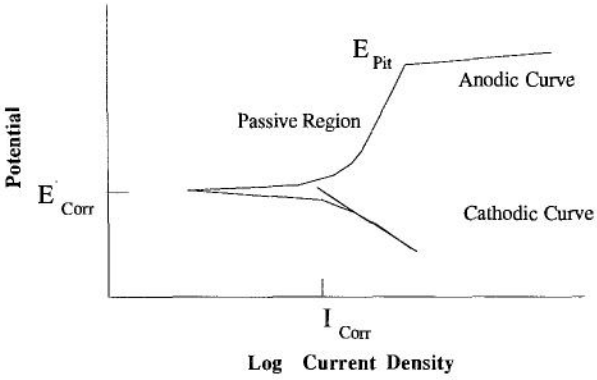

Fig. 2. Typical data obtained from a potentiodynamic polarization test.

rate of the anodic or cathodic process at that potential. The corrosion current I_{corr} can be determined by an extrapolation to E_{corr} (Tafel Extrapolation) of the anodic or cathodic curves in the vicinity of E_{corr}, as shown in fig. 2. The corrosion rate (current density) so determined may be related to a weight-loss rate using Faraday's Law.

As the potential of a sample is increased from E_{corr}, the data may indicate a region in which the current I changes very little (I_{pass}). This behaviour (Passive Region) is generally associated with the formation, growth and presence of a passive surface film which may be e.g. an oxide or hydroxide. At a given potential the current increases by orders of magnitude for small increases in potential. This potential is known as the pitting potential E_{pit}. E_{pit}, I_{pass} and $E_{pit} - E_{corr}$ (ΔE) may all represent a measure of resistance to corrosion: the higher E_{pit}, the smaller I_{pass} and the larger ΔE, the higher the corrosion resistance.

1.4. *Corrosion prevention and control*

1.4.1. *Exclusion of moisture*

An obvious method for preventing corrosion is to exclude an aqueous environment from the metal surface, particularly if it contains potentially harmful ions such as chloride, sulphate and nitrate. Paint coatings and oil based films such as water displacing fluids are commonly used for this purpose. Most of the polymeric binders in commercial paints are permeable to water. However, paints contain additives which may slow the rate of diffusing moisture and/or inhibit corrosion of the underlying substrate. For example, particles of iron oxide included in the paint, trap water at their interface with the polymeric binder and thereby slow the rate of permeation. Pigments such as zinc chromate slowly leach CrO_4 ions into water diffusing to the metal substrate. The CrO_4 ions may inhibit corrosion of the metal substrate.

1.4.2. *Alloying*

The corrosion resistance of the metal surface may be improved by alloying additions. The best known example of this is stainless steel. The addition of Cr to the steel in sufficient

quantities allows a Cr rich oxide to form on the steel surface. The Cr oxide is very resistant to attack in most aqueous environments and therefore protects against corrosion.

1.4.3. *Surface modification*

Other techniques for corrosion control involve modification of the existing metal surface. For example, the composition of the metal surface may be altered to a more corrosion resistant alloy using techniques such as ion implantation, thermal diffusion and laser melting. Metals may be deposited onto the corrosion susceptible substrate by electroplating, hot dipping or vapour deposition. The deposited metals chosen are those that will corrode preferentially to the substrate in the event of damage to the deposited metal coating (galvanic protection). Zinc galvanizing and cadmium on steel are good examples of sacrificial metallic coatings. Alternatively, the deposited metal such as chromium or nickel may protect the substrate, e.g. steel, by having a very high corrosion resistance.

Naturally occurring oxide films on most metals do not usually provide optimum corrosion protection, and this may be modified or replaced to provide a further means of corrosion control. Common examples are the anodizing of aluminium alloys or the chromating of aluminium, zinc, cadmium or magnesium. With anodizing, the natural oxide film on the aluminium is thickened electrolytically by up to 5 μm. Chromating, described in detail later in the chapter, replaces the existing metal oxide film with a mixed chromium/metal oxide film of better corrosion resistance.

1.4.4. *Modification of the environment*

A further technique for corrosion prevention or control involves modification of the corrosive environment. This may be achieved by adding solutions of corrosion inhibitors to the environment. These chemicals protect the metal surface by either (i) thickening or modifying the existing oxide film, thereby slowing the rate of dissolution at anodic sites (see fig. 1), e.g. nitrates and chromates, (ii) causing compounds such as hydroxides to precipitate at anodic or cathodic sites, thereby retarding the partial reactions and breaking or increasing the resistance in the electrochemical circuit (fig. 1); zinc, lead and magnesium salts have been used for these applications, or (iii) producing an adsorbed film on the metal surface creating a physical barrier to oxygen, water or chloride ions, all of which are important in the corrosion process. The choice of corrosion inhibitor depends on the metal alloy and the environmental conditions. Often a mixture of corrosion inhibitors is used to synergistically achieve a better level of corrosion control.

Rare-earth metal (R) compounds have been used in the protection of metals from oxidation at high temperatures for many years. This subject is the topic for another review by Dr. Neil Ryan in this volume (see ch. 141). In the last 10 years, soluble R salts have also been considered for application in corrosion prevention and control at low temperatures i.e. below 100°C. It is the purpose of this chapter to review published research, which demonstrates how these salts may be used to control and prevent corrosion

by the approaches outlined above. (Throughout this chapter where an R salt is quoted as having been used, it is as the hydrated form.)

2. Modification of the environment

For almost 100 years chromate compounds (Cr^{6+}) have been used as effective and inexpensive corrosion inhibitors for many alloy systems, including Al, Zn and steel, in a wide range of aqueous environments. However, chromates are now recognized as both highly toxic and carcinogenic (US Public Health Service 1989), and therefore municipal and government regulations concerning the disposal of chromate solutions are becoming more stringent (Blaser 1976) and expensive to comply with. These factors have lead to extensive worldwide research to develop effective alternative inhibitors. Most attention has been focussed on the use of other non-toxic oxyanions such as molybdates. Organic compounds such as thioglycollates, phosphonates, or mixtures of inorganics such as phosphates, borates, silicates and surfactants such as sulphonates have also attracted a great deal of attention as alternatives.

The use of metal cations as inhibitors of corrosion in aqueous solution has not been widely addressed, nevertheless, it has a long history (Evans 1924, Borgmann 1937, Thornhill 1945). Zn has been the only commercially significant cation used. It is used in recirculating water systems and as a pigment in paints. This early work on metal cation inhibitors, and the search for non-toxic alternatives to chromates motivated a systematic investigation of the effectiveness of R salts as corrosion inhibitors at the Aeronautical Research Laboratory (ARL) Melbourne, in 1984. These salts were seen as attractive alternatives to chromates because they were non-toxic and the commercial grade salts were relatively cheap. The ARL work showed that these salts effectively inhibited the corrosion of Al alloys (Hinton et al. 1984, 1985, Arnott et al. 1987), mild steel (Hinton et al. 1988) and Zn (Hinton and Wilson 1989). Also, Goldie and McCarroll (1984) published a patent which claimed that solutions of R salts inhibited the corrosion of steel, Al and Cu in salt solution.

In the following section, the results of several studies which have demonstrated the effectiveness of R salts as inhibitors of various types of corrosion are reviewed and the mechanisms of inhibition discussed.

2.1. *Corrosion inhibition of Al alloys*

Al alloys are widely used structural alloys on land, sea and in the air. In these environments corrosion is a recurring problem mainly because the integrity of the naturally protective Al oxide film is reduced by the presence of alloying elements.

Various studies (Hinton et al. 1985, Hinton 1989) have shown that the rates of corrosion of high strength Al alloys 2024 and 7075 (see table 1 for compositions), as determined by weight-loss tests, in quiescent 0.1 M NaCl solution, after 21 days immersion were reduced by the presence (in solution) of small concentrations of various R chlorides (figs. 3, 4).

Table 1
Composition of aluminium alloys

A.A.[a]	Composition limits (weight %)							
	Si	Fe	Cu	Mn	Mg	Cr	Zn	Ti
2014	0.50–1.2	1.0	3.9–5.0	0.4–1.2	0.2–0.8	0.10	0.25	0.15
2024	0.50	0.50	3.8–4.9	0.3–0.9	1.2–1.8	0.10	–	–
6061	0.4–0.8	0.70	0.15–0.40	0.15	0.8–1.2	0.15–0.35	0.25	0.15
7075	0.5	0.7	1.2–2.0	0.30	2.1–2.9	0.18–0.40	5.1–6.1	0.20

[a] Aluminium Association designation.

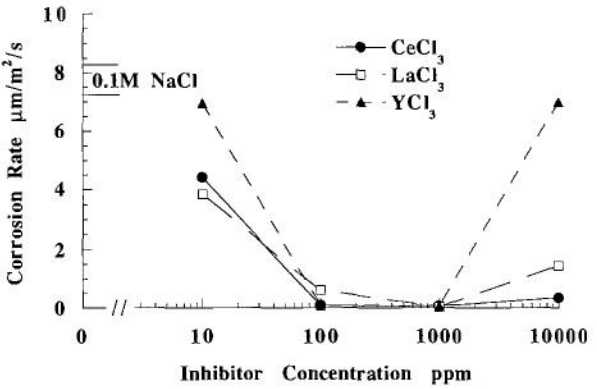

Fig. 3. Variation in corrosion rate of 2024 Al alloy in 0.1 M NaCl with R chloride concentration.

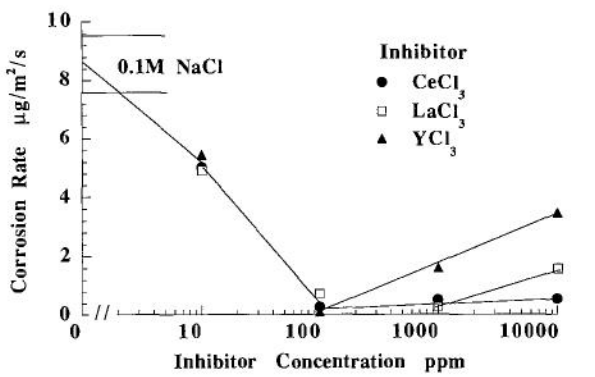

Fig. 4. Variation in corrosion rate of 7075 Al alloy in 0.1 M NaCl with R chloride concentration.

These data indicate that maximum inhibition occurred at concentration levels around 100 and 1000 ppm. The lowest corrosion rates observed were at least an order of magnitude less than the rates in 0.1 M NaCl without inhibitor. In similar tests using the common inhibitor Na_2CrO_4 at 100 ppm, the corrosion rate of 7075 Al alloy was 0.017 $\mu gm^{-2}\ s^{-1}$, which is lower than, but comparable with the lowest rates shown in figs. 3, 4.

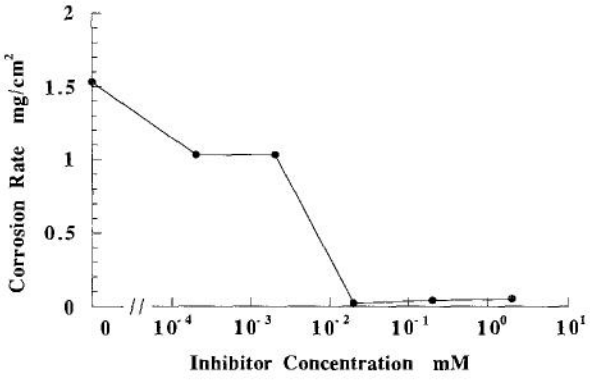

Fig. 5. Variation in corrosion rate of 2014 Al alloy in 0.6 M NaCl with $Ce_2(SO_4)_3$ concentration (after Baldwin et al. 1987).

After 21 days immersion in a solution containing $\geqslant$ 100 ppm R salt, the Al alloy was covered with a lightly coloured transparent film which was shown to contain R oxides (Hinton and Arnott 1989). The corrosion inhibition observed was related to the presence of this film on the surface. The colour of the film depended on the R cation used. Films formed in the presence of cerous cations were typically yellow (Hinton et al. 1984, 1985). The surfaces appeared uncorroded, apart from isolated areas of light surface etching. By comparison, when immersed in NaCl solution without any R salt, the alloy quickly blackened, became deeply pitted and was covered with white deposits of Al corrosion product. Similar studies by Baldwin et al. (1987), using alloy 2014, have also shown that $Ce_2(SO_4)_3$ is capable of reducing the corrosion rate in 0.6 M NaCl solution by up to 50 times (fig. 5).

At higher concentrations, e.g. 1000–10 000 ppm, the inhibition efficiency with alloys 2024 and 7075 is reduced and the inhibited corrosion rate appears to be dependent on the type of R cation. These results have not been completely explained (Hinton et al. 1984, 1985), but may be related to (a) the nature of the protective film or (b) the observation that the observed R oxide films are thicker and more defective when formed in solutions containing > 1000 ppm R cation. Also, the La and Ce films tended to be powdery and have poor adhesion. Defective films would not be expected to provide good corrosion inhibition.

The level of inhibition provided by the R salt in corrosive aqueous environments depends on the type of both anion and cation. Two separate studies by the author and Baldwin et al. (1987) have shown that many of the R chloride salts are good inhibitors i.e. inhibitor efficiencies > 75%, though some are better than others (table 2). The reasons for these differences have not been explained. Hinton and Arnott (1989) and Arnott et al. (1989) have shown that the films which form on the surfaces and which are believed to be associated with the inhibition have very different morphologies and compositions (see sect. 2.5 below). The differences in corrosion inhibition performance may well be associated with these different compositions, structures and the nature of any defects in these films.

Table 2
Corrosion rates for aluminium alloys 7075 and 2014 (Baldwin et al. 1987) in NaCl solution with and without various R chloride inhibitors

Rare earth chloride	Corrosion rate ($\mu g\,m^{-2}\,s^{-1}$)	
	7075: 0.1 M NaCl; [RCl] = 100 ppm	2014: 0.6 M NaCl; [RCl] = 2 mM
None	7.600–9.600	9.09
Y	0.063–0.109	–
La	0.076–1.360	1.26
Ce	0.105–0.412	0.22
Pr	0.542	0.83
Nd	0.175–1.120	1.05
Tb	–	1.10
Yb	–	2.36

Table 3
Corrosion rates for aluminium alloys 7075 (Hinton 1992) and 2014 (Baldwin et al. 1987) in NaCl solution with and without various cerium salt inhibitors

Cerium salt	Corrosion rate ($\mu g\,m^{-2}\,s^{-1}$)	
	7075: 0.1 M NaCl; [Ce salt] = 1000 ppm	2014: 0.6 M NaCl; [Ce salt] = 2 mM
None	7.6–9.6	9.09
Chloride	0.41–0.58	0.22
Nitrate	–	1.70
Sulphate	0.45–0.48	0.11
Perchlorate	0.16	1.37
Oxalate	–	1.82
Acetate	0.06	–

Table 3 lists the corrosion rates obtained from weight-loss tests for 7075 and 2014 Al alloys immersed in NaCl solutions with additions of various Ce salts (Hinton 1992, Baldwin et al. 1987). The level of inhibition observed is strongly dependent on the anionic component of the inhibitor salt. (A dependence also detected by Hinton et al. (1985) using electrochemical corrosion tests with the same alloy). For 7075 Al alloy in particular, the corrosion rates shown for cerous perchlorate and cerous acetate are significantly lower than those for the other Ce salts. Chloride ions are the most corrosive of anions (Evans 1961). They are known to contribute to the breakdown of the protective natural oxide film and to accelerate the onset of pitting corrosion, particularly with Al alloys (Shreir 1976). If the level of inhibition is seen as a balance between the corrosion-inducing tendencies of the anion and the corrosion-inhibiting properties of the cation, then the lower corrosion rates observed with $Ce(ClO_4)_3$ and $Ce(CH_3COO)_3$ may be related to the lower total chloride concentration in the test solution. Surprisingly, for the tests with 2014 this reasoning is not applicable, because the inhibited corrosion rate

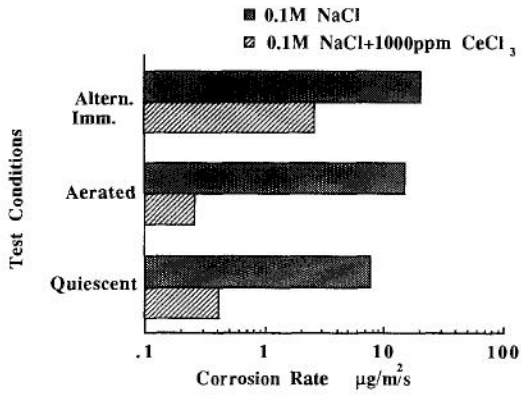

Fig. 6. Effects of test conditions on the corrosion rate of 7075 Al alloy in 0.1 M NaCl and in 0.1 M NaCl with 1000 ppm $CeCl_3$.

in the presence of $CeCl_3$ is less than that for $Ce(ClO_4)_3$. The results in table 3 further illustrate the strong inhibiting properties of the Ce cation.

Most inhibitors are required to function in aqueous environments in various states of aeration. Furthermore, there may be a requirement for them to be added to an environment to help prevent the further development of corrosion. The data referred to above were obtained in quiescent NaCl solutions open to air. The performance of R salt inhibitors under various conditions of aeration, i.e. alternate immersion, constant immersion in a quiescent test solution and constant immersion in an aerated test solution, has been studied by Hinton (1989). The weight-loss data obtained for tests with 7075 Al alloy in 0.1 M NaCl containing 1000 ppm $CeCl_3$ are shown in fig. 6. The R salts are effective inhibitors even under the most severe corrosion conditions, some of which are typical of service conditions. For example, the inhibition efficiency is greatest in a continuously aerated solution. This is consistent with a mechanism of inhibition based on the formation of the R oxide on the metal surface (see sects. 2.6 and 2.8). Continuous aeration will favour the reduction of oxygen with the formation of hydroxyl ions, and consequently promotes the precipitation of the R oxide and its coverage of the metal surface.

Inhibitors are used not only to prevent corrosion but to retard further development once corrosion has started. An atomic absorption technique has been used to assess the ability of R salts to reduce further corrosion of the 7075 alloy (Hinton et al. 1985). This technique involves monitoring the Zn concentration in the test solution, from which the weight loss of the specimen can be estimated. Figure 7 shows the weight loss determined by this technique for specimens constantly immersed in quiescent 0.1 M NaCl solution. These data indicate that the addition of R chlorides to the solution (at 1000 ppm), at the times indicated in the figure by the arrows, significantly reduced the corrosion rate. With additions of $CeCl_3$ and $LaCl_3$ the rate is reduced by a factor of 10, whereas YCl_3 reduces the rate by only a factor of 5.

The R salts are clearly effective inhibitors of Al alloy corrosion in short term tests; however, no data have been published which would indicate their effectiveness in any

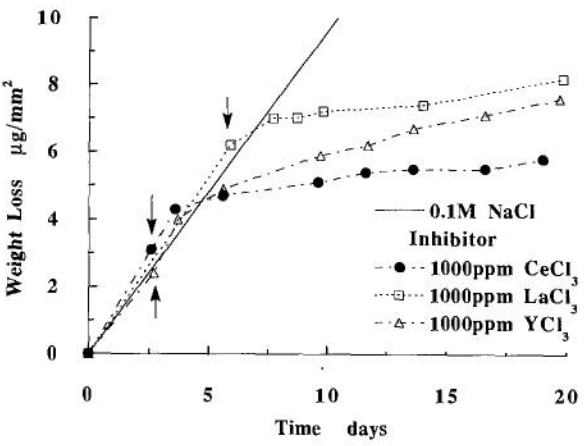

Fig. 7. Weight loss as a function of time for 7075 Al alloy in 0.1 M NaCl, before and after the addition (arrow) of various R chlorides.

long term situation. The long term efficacy of inhibitors is important, because it is a necessary consideration in the economics of inhibitor level maintenance.

2.1.1. *Galvanic, crevice and differential aeration corrosion*

Corrosion control in recirculating water systems is always complicated by the presence of dissimilar metals in contact, crevices, and areas where an oxygen deficiency exists (differential aeration), e.g. welds and joints. Unfortunately, protective paint schemes almost always break down in these areas and localized corrosion follows.

2.1.1.1. *Galvanic corrosion.* Extensive laboratory tests at ARL have shown that R salts are effective inhibitors of galvanic corrosion of Al alloys when associated with a variety of dissimilar metals, and exposed to a range of environments (Hinton 1989). The galvanic test specimen used consisted of a cathode, e.g. copper rod, mounted concentrically within a hole in a block of 7075 Al alloy anode material. The entire assembly, including electrical connections, was potted in epoxy resin, and its base abraded on a silicon carbide grinding paper to expose a planar section through the anode and cathode. The current flowing after immersion of the couple in a corrosive medium was monitored using a zero resistance ammeter. This current indicates the rate of galvanic corrosion of the anode.

Typical anodic current density versus time data, obtained with a Cu/7075 couple (area ratio Cu/Al = 0.0039), immersed in a quiescent 0.1 M NaCl solution, are presented in fig. 8 (Hinton 1989). The anodic current density, after an initial rapid decrease, changed very little with immersion time in NaCl solution. With 1000 ppm $CeCl_3$ in solution, the current falls rapidly to an equilibrium value much less than the current in the uninhibited NaCl solution. The presence in solution of other R salts, e.g. La, Nd, and Pr chlorides, have been found to similarly reduce the equilibrium galvanic current. In fig. 8 it is seen that the addition of $CeCl_3$ to a solution in which a galvanic couple has been active for some time also reduces the current density to a value approaching that observed for the test in which

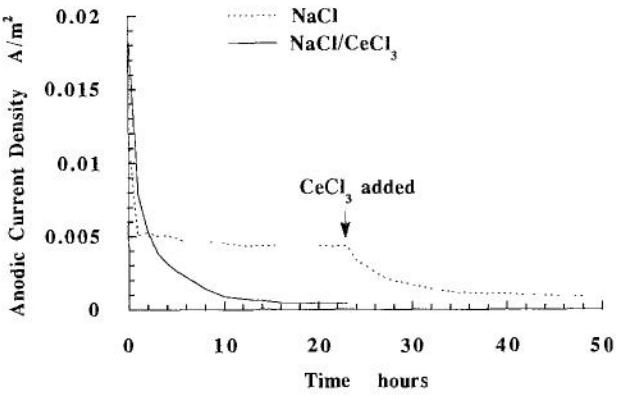

Fig. 8. Variation in galvanic current density with time for an Al–Cu couple in 0.1 M NaCl, and in 0.1 M NaCl with 1000 ppm $CeCl_3$.

$CeCl_3$ was present from time zero. These data indicate the particular ability of R salts to retard established galvanic corrosion. After testing in aqueous solution containing R salts it was noted that the Cu cathodes were covered with a thick film of R oxide with a morphology similar to that observed on Al alloy weight-loss corrosion specimens tested in similar solutions (to be fully described in sect. 2.5). The insulating epoxy resin between the cathode and the anode and some of the anode itself was also covered with the film. However, the extent of coverage and thickness of the film decreased with distance from the cathode. The formation of this film is consistent with the proposal that the R oxide forms as a result of the oxygen reduction reaction on the cathode (Hinton et al. 1984). It would appear that the inhibition of galvanic corrosion is a consequence of the polarization of the reactions occurring on the cathode, by the formation on the cathode of the R oxide film.

The ability of $CeCl_3$ to inhibit galvanic corrosion between other dissimilar metal couples has also been investigated (Hinton 1989). The efficiency of inhibition (fig. 9)

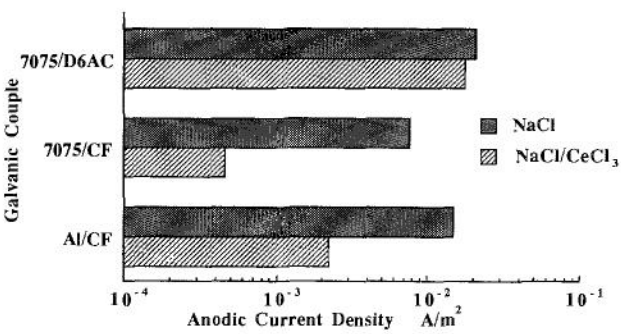

Fig. 9. Equilibrium galvanic current density for the couples (i) 7075Al/D6AC steel, (ii) 7075Al/carbon fibre epoxy composite (CF), (iii) pure Al/carbon epoxy composite, in 0.1 M NaCl with/without 1000 ppm $CeCl_3$ (cathode area to anode area ratio = 0.025).

depends on the type of galvanic couple. This result is to be expected, since the rate at which the particular cathode is covered by the Ce oxide, and the extent of coverage, will depend on the equilibrium current density for the dominant reaction, oxygen reduction in an aerated solution (at the particular cathode), and (possibly) on the driving force in terms of the potential difference between the electrodes.

2.1.1.2. *Crevice corrosion.* Hinton et al. (1985) have studied the inhibition of corrosion associated with crevices formed by a rubber "O" ring stretched over a cylinder of alloy 7075. These assemblies were immersed in 0.1 M NaCl solutions containing different concentrations of $CeCl_3$ and the corrosion rates determined from the weight losses from the cylindrical specimens. Specimens immersed in NaCl alone for 21 days sustained heavy localized attack (crevice corrosion) beneath the "O" ring, while the areas away from the "O" ring became blackened but not obviously corroded. Values of pH = 2.5–3.5 were measured within the region of localized attack with narrow band pH papers. The acidification of this region and the intensity of corrosion indicates that true crevice corrosion conditions (Shreir 1976) develop on this specimen, with the anodic and cathodic reactions spatially separated. The presence of $CeCl_3$ in solution significantly reduced (a) the localized attack to a light etching and staining, and (b) the corrosion rate by at least a factor of 10 (fig. 10). It was noted (Hinton et al. 1985) that the area of the specimen away from the "O" ring, where the cathodic reactions such as reduction of oxygen would be dominant, was covered with a yellow film when the inhibitor was present.

Metal-matrix composites are thought to corrode by a crevice corrosion mechanism with the crevice forming at the fibre/matrix interface (Cosgrave and Hinton 1991). They have studied the corrosion behaviour of an Al alloy 6061/boron metal-matrix composite in 0.1 M NaCl solution. As shown in fig. 11, the presence of 1000 ppm $CeCl_3$ in the test solution, significantly reduced the corrosion rate of the composite, particularly at long immersion times. After testing with $CeCl_3$ present, a thick opaque yellow film of hydrated Ce oxide was observed on the surface of the composite. Cosgrave and Hinton concluded that the presence of this film was responsible for the corrosion protection, and that the

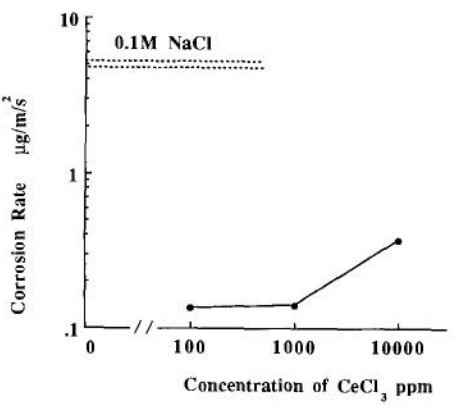

Fig. 10. Variation in corrosion rate of 7075 Al alloy crevice in 0.1 M NaCl with $CeCl_3$ concentration.

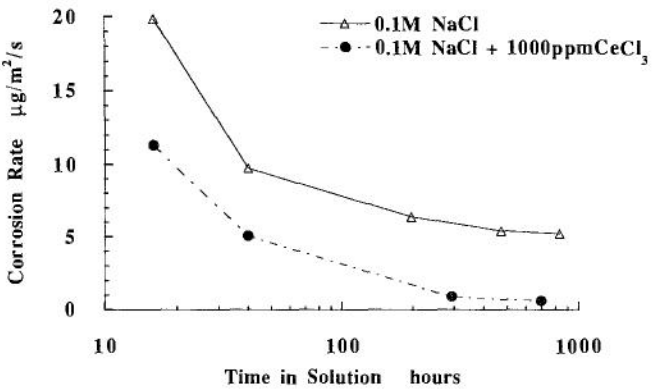

Fig. 11. Variation in corrosion rate with time for Boron/6061 Al alloy metal matrix composite in 0.1 M NaCl, and in 0.1 M NaCl with 1000 ppm $CeCl_3$.

formation of this film was associated with cathodic processes initially occurring around actively corroding crevices at the fibre/matrix interfaces.

With a situation involving a crevice or other regions of oxygen deficiency, cathodic reactions such as the reduction of oxygen occur away from the crevice. These reactions are balanced by anodic reactions, e.g. dissolution of metal, which occur within the crevice or beneath any deposit which may restrict the access of oxygen to the metal surface. An electrochemical circuit is established similar to that shown schematically in fig. 1, with movement of electrons through the metal from the site of localized dissolution to the cathodic sites and a movement of negative charge via OH^- and Cl^-, through the solution. Inhibition of corrosion can be achieved if the rates of either the anodic or cathodic reactions can be reduced or the electrochemical circuit broken. The inhibition of the crevice corrosion would again appear to be due to the formation of R oxides at cathodic areas, where they stifle the oxygen reduction reaction, and effectively break the electrochemical corrosion circuit.

2.1.2. *Environmental cracking*

Generally, corrosive attack takes considerable time to develop, and while corrosion can ultimately render a component or structure unserviceable, it is unlikely to happen at a rate rapid enough to lead to catastrophic failure. One form of corrosion which is insidious and which may lead to catastrophic failure is environmental cracking (EC), i.e. stress-corrosion cracking (SCC) and corrosion-fatigue cracking (CFC). SCC is the result of the conjoint action of a constant stress, either residual or operating, and a corrosive environment. CFC is the result of a fluctuating stress acting in conjunction with a corrosive environment. Unfortunately, EC occurs in many alloy systems and environments common to a wide variety of industries, including the power, chemical and transport industries. Furthermore, EC is not always associated with extensive corrosion damage and cracking may initiate from a small isolated pit. This situation frequently occurs in

aircraft structures, particularly in those components made from high-strength Al alloys, which may be susceptible to SCC.

In order for EC to develop, a favourable combination of metallurgical, mechanical and environmental variables must exist. Often, in a given situation, it is difficult to alter the metallurgical and mechanical variables contributing to EC. Hence, it may be more convenient to modify the environment and thereby reduce the likelihood of EC occurring.

2.1.2.1. *Stress-corrosion cracking.* Hinton et al. (1985) have studied the effects of several R chlorides on the SCC behaviour of 7075 Al alloy in NaCl solution. Figure 12 shows the time to failure (TTF) of "Tuning Fork" specimens loaded to either of two stress levels, 0.5 or 0.75% of the yield stress $\sigma_y \approx 450$ MPa for 7075, and subjected to alternate immersion in 0.1 M NaCl solutions containing various R chlorides at 1000 ppm. The presence of the R chlorides significantly increases the TTF at both stress levels. The longer TTF at the lower stress is expected, as the mechanical driving force for SCC is reduced. Specimens immersed in a solution containing $CeCl_3$ had the longest TTF. At $0.5\sigma_y$, the specimen life was 70 times greater when $CeCl_3$ was added to the NaCl solution. It is generally accepted that TTF data are dominated by the time to initiate SCC. Figure 12 indicates that the addition of R salts to the test environment delays the initiation of cracking. Hinton et al. (1985) have also shown that these R salts reduce the rate of SCC propagation. In fig. 13 crack length is plotted as a function of time for tests in 0.1 M NaCl and 0.1 M NaCl with 1000 ppm $CeCl_3$. These tests were conducted on edge-notched specimens, fatigue pre-cracked to the same stress level (below K_{Iscc}) and loaded in cantilever bending. The initial stress intensity levels were almost identical. These data show that the cracking rate in the presence of $CeCl_3$ is much lower than in the absence of $CeCl_3$. However, as final failure is approached and crack growth is dominated more by mechanical factors than by environmental factors, rates of growth remain unaffected when $CeCl_3$ is present.

In an electrochemical sense, SCC is similar to crevice corrosion and differential aeration corrosion, in that anodic and cathodic areas are spatially separated. With SCC, the anodic processes occur at the crack tip while cathodic processes occur on the crack flanks and near the crack mouth. Hinton et al. (1985) have proposed that the inhibition

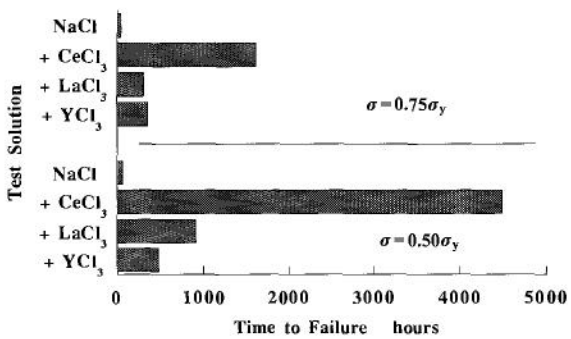

Fig. 12. Effects of the presence of 1000 ppm R chloride on the time to failure of 7075 Al alloy stress corrosion specimens in 0.1 M NaCl at two stress levels expressed as a fraction of the yield stress.

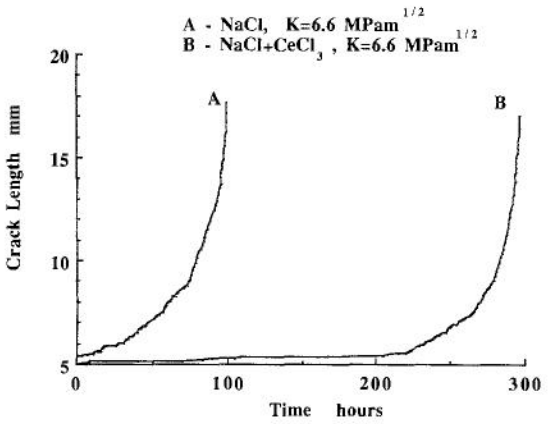

Fig. 13. Variation in stress corrosion crack length with time for 7075 Al alloy specimens tested at two initial stress intensity (K) levels in 0.1 M NaCl with and without 1000 ppm $CeCl_3$.

of SCC is due to the formation of R oxide at cathodic sites. The presence of this oxide causes a reduction in the rate of the cathodic reaction, which, in turn, reduces the rate of the anodic reaction at a crack initation site or at a crack tip. Thus, the rate of SCC is reduced and TTF is prolonged.

2.1.2.2. *Corrosion fatigue.* Hinton et al. (1985) have shown that the presence of R salts in the test solution significantly changes the sensitivity of the 7075 alloy to corrosion fatigue in NaCl solution. Their results, obtained with cantilever bend specimens tested at two stress levels and at a frequency of 50 Hz, are summarized in fig. 14. There is very little influence of the environment on the cycles to failure at the higher stress level, where metallurgical and surface variables have a much stronger influence on crack initiation than does corrosion damage. The influence of the environment at the low stress level is quite significant. In laboratory air, the specimen remained unbroken after 400×10^5 cycles. The addition of $CeCl_3$ to the NaCl solution increased the fatigue life by almost a factor of 6. With this type of CF test, up to 95% of the cycles to failure are generally related to

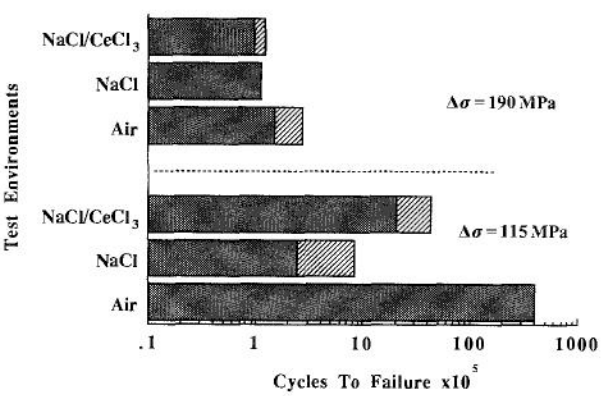

Fig. 14. Effects of test environments air, 0.1 M NaCl, and 0.1 M NaCl with 1000 ppm $CeCl_3$, on the cycles to failure of 7075 Al alloy fatigue test specimens, at two alternating stress levels. The hatched regions indicate scatter bands.

the initation of the fatigue crack. Data in fig. 14 show that $CeCl_3$ in solution with NaCl strongly inhibits the early initation of fatigue cracking in this corrosive environment.

The observation that R cations inhibit the initation of SCC (fig. 12) and CFC (fig. 14) on plain surfaces is clearly related to the ability of the inhibitor to prevent corrosion pits from developing and growing into significant stress raisers. With R cations present, some superficial surface attack does develop, but at a slow rate and with a low-risk profile. Thus, a long period of time or a large number of cycles is required before the stress localization, necessary to initiate cracking, develops. Hence, resistance to SCC is increased and CFC failure is delayed.

2.2. *Corrosion inhibition of steel*

Mild steel is a widely used material in recirculating water systems, where it is protected from corrosion by the presence of inhibitors. Traditionally, chromates and Zn salts have been the most commonly used inhibitors in these systems. However, because of government restrictions on the discharge of heavy metals (Lake 1988) and the toxicity of chromates (US Public Health Service 1989), alternative inhibitors which are environmentally acceptable, are receiving increased attention.

The effectiveness of R salts as inhibitors of the corrosion of mild steel, was first demonstrated in a patent by Goldie and McCarroll (1984). They found, using weight-loss immersion tests (1 week), that 0.001 M of eleven R nitrates and Y nitrate produced corrosion-inhibition efficiencies of 82 to 100%, respectively, in aerated 3.5% NaCl solution. Hinton et al. (1988), also using weight-loss tests, have shown that $CeCl_3$ is an effective corrosion inhibitor for AS 1020 mild steel in quiescent soft tap water open to air (fig. 15). At pH = 5.5, $CeCl_3$ concentrations of only 50 ppm are required to produce significant reductions in corrosion rate. Concentrations greater than this have very little added effect. During immersion in solutions containing $\geqslant$ 50 ppm $CeCl_3$, a blue-

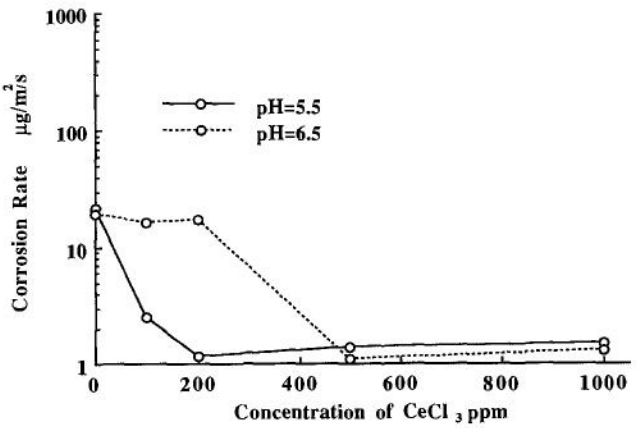

Fig. 15. Variation in corrosion rate with $CeCl_3$ concentration for mild steel in tap water at two pH levels.

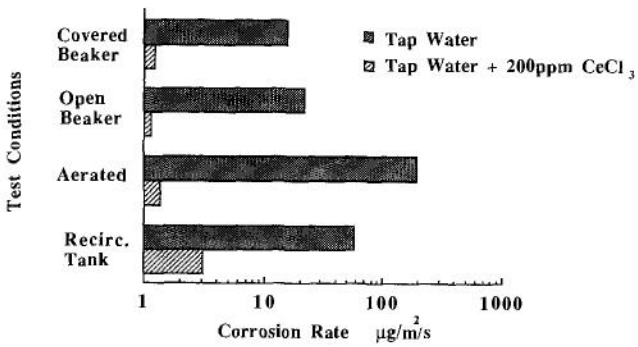

Fig. 16. Effects of various states of aeration on the corrosion rates of mild steel in untreated tap water and in water with 200 ppm $CeCl_3$.

coloured interference film formed over a lightly etched steel substrate. With increasing immersion time, this film, which provides the corrosion protection, developed a yellow colour. During immersion in untreated tap water, the same steel quickly became heavily corroded beneath a layer of brown rust. In water at pH = 6.5, $CeCl_3$ was only an effective inhibitor at concentrations > 200 ppm. It has been suggested (Hinton et al. 1988) that the poor inhibition at < 200 ppm is related to the tendency for Ce^{3+} ions to precipitate from solution at pH 6.5–7. Higher concentrations of $CeCl_3$ are required to enable the protective film to form before bulk precipitation of the cation can occur.

$CeCl_3$ has been found to also effectively inhibit the corrosion of mild steel in hard water and in hard water with a high chloride content (Hinton 1989).

As with Al alloys, the efficiency of inhibition with R salts depends on the degree of aeration of the test solution (fig. 16). Hinton et al. (1988) obtained weight-loss data from tests in: (a) quiescent tap water with restricted access of air, (b) quiescent tap water with unrestricted access of air, (c) continuously aerated tap water, and (d) tap water continuously recirculated using a pump and overhead spray. It was found that the $CeCl_3$ inhibitor was most efficient (99.2%) in the continuously aerated water. Long term tests indicate that $CeCl_3$ continues to inhibit the corrosion of mild steel over a period of several months in a recirculating water system (Hinton 1989), and that the rate of corrosion changes very little over this period of exposure.

2.2.1. *Galvanic and differential aeration corrosion*

Hinton et al. (1988) have immersed a copper–mild steel galvanic couple in tap water containing 200 ppm $CeCl_3$ for 20 hours until the Ce oxide film was observed on the copper cathode. The couple was then removed, washed and immersed into tap water without any $CeCl_3$. In this instance the galvanic current remained virtually unchanged from the equilibrium value which was observed before the switch in test solutions. This indicates that the R oxide films, which form on cathodic areas, continue to inhibit galvanic corrosion even after the removal of the inhibiting cations from solution.

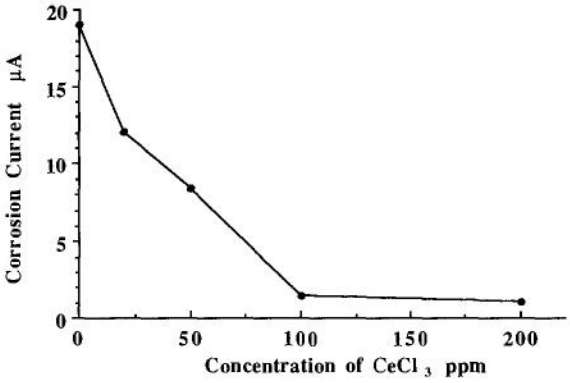

Fig. 17. Effect of $CeCl_3$ concentration on the equilibrium current flowing in a differential aeration cell on mild steel in tap water.

Differential aeration corrosion commonly occurs in recirculating water systems where debris or sludge gathers and prevents access of oxygen to the metal surface. Hinton et al. (1988) have assessed the ability of $CeCl_3$ to inhibit differential aeration corrosion on mild steel with a cell designed to restrict access of oxygen to one electrode (Hatch 1952). This cell consisted of two 25×25 mm mild steel electrodes located 25 mm apart, with a single thickness of filter paper clamped on to one electrode to restrict the access of oxygen to the surface. The reverse side of this electrode was masked with lacquer. Both electrodes were immersed in continuously aerated test solution (pH = 5.5), and the current, which is related to the corrosion rate of the anode beneath the filter paper, was monitored with a zero resistance ammeter. The influence of various concentrations of $CeCl_3$ on the equilibrium current flowing in the differential aeration cell after 20 hours is illustrated in fig. 17. Concentrations of 100–200 ppm $CeCl_3$ reduced the equilibrium current by approximately a factor of 10. After tests in uninhibited tap water at pH 5.5, the steel beneath the filter paper on the anode surface was extensively pitted and covered with rust. The cathode surface was only slightly stained. However, after tests in water containing 200 ppm $CeCl_3$ (pH 5.5), the anode was only slightly stained and the cathode was covered with a yellow film (Hinton et al. 1988).

2.2.2. *Inhibition in acid solution*

The effectiveness of the R salts as inhibitors of corrosion of steel in aqueous acidic environments has also been noted. I. Singh and M. Singh (1987) have studied the corrosion of mild steel in 2N H_2SO_4 using weight-loss tests. They observed that up to 120 ppm $Ce_2(SO_4)_3$ effectively inhibited the corrosion of the steel during exposure for 3 hours. The maximum inhibition occurred at a concentration of 25 ppm. They also noted a 50% increase in inhibition efficiency when either of the organic compounds thiourea or allylthiourea was also present. A vacuum extraction method was used to measure the hydrogen absorbed during the corrosion tests. The amount of hydrogen absorbed decreased with increasing concentration of the Ce^{4+} ions alone or in the presence of the organic compounds. Singh and Singh concluded that the Ce^{4+} ions adsorbed on the surface

of the steel in preference to the hydrogen ions thereby suppressing the hydrogen evolution reaction. This reaction is the cathodic half of the corrosion process. A suppression of this reaction would retard the corrosion rate of the steel in the acid solution. However, the reduction of the Ce^{4+} ions cannot be ruled out as an alternative cathodic reaction, and the possibility of this being associated with a lower corrosion rate.

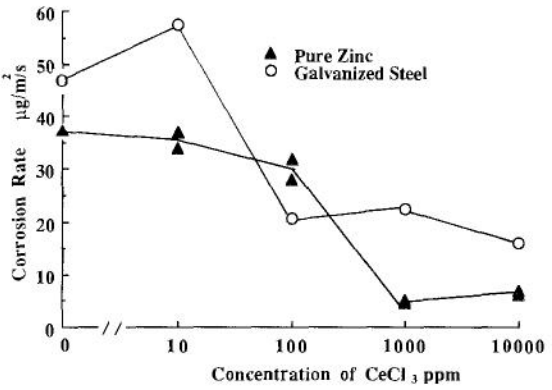

Fig. 18. Effect of $CeCl_3$ concentration on the corrosion rate of Zn and galvanized steel in 0.1 M NaCl.

2.3. *Corrosion inhibition of zinc*

Hinton and Wilson (1989) have investigated the effectiveness of $CeCl_3$ as a corrosion inhibitor for pure Zn and galvanized steel in 0.1 M NaCl. Their results (fig. 18), based on weight-loss tests, show that the corrosion rates of both pure Zn and galvanized steel are reduced when 100 ppm or more of $CeCl_3$ is present. A concentration of 1000 ppm reduces the rate for Zn by almost a factor of 10, and the rate for galvanized steel to around one-half of the rate in 0.1 M NaCl. After the corrosion tests, the surfaces of the Zn and galvanized steel were covered with a thin transparent yellow film. The only evidence of corrosion beneath the film was isolated shallow pits and areas of light etching. In contrast, surfaces exposed to 0.1 M NaCl solution appeared deeply pitted and covered with a thick layer of white/grey corrosion product. The corrosion rates for galvanized steel were generally higher than those for Zn. This is probably related to the effect of the steel substrate on the corrosion process and to the lead content of the Zn coating (Hinton and Wilson 1989).

It was also shown by Hinton and Wilson that $CeCl_3$ inhibited the corrosion in soft tap water of pure Zn and of steel electroplated with Zn.

2.4. *Corrosion inhibition of copper*

No evidence of R salts having been used as corrosion inhibitors for Cu or Cu alloys could be found in the open literature. However, Goldie and McCarroll (1984) claim in their patent that the corrosion of copper when immersed in a 3.5% NaCl solution containing 0.001 M $Y(NO_3)_3$ was significantly reduced. They quoted a corrosion efficiency of 87%.

This is an area worthy of further research, as Cu alloys are widely used in recirculating cooling water systems to which corrosion inhibitors are added.

2.5. *Characteristics of the corrosion inhibiting films*

As described in the preceding sections, the surfaces of Al alloys, Zn and steel, when exposed to aqueous solutions containing sufficient levels of R salts to inhibit corrosion, with the exception of steel in acid solution (I. Singh and M. Singh 1987), become covered with a film of R hydroxide or hydrated oxide. The presence of these films is associated with significantly reduced rates of corrosion. It is clear therefore that these films inhibit corrosion. Detailed scanning electron microscopy (SEM) studies have indicated that the topography and structure of these films are complex, and that while the structure and composition of the film may differ with each specific substrate, the films possess many common features (Hinton and Arnott 1989).

The films formed on the different metal substrates in the presence of R salts consist of an apparently featureless background layer together with crystalline particles of varying size, shape and arrangement (figs. 19–24). These particles were observed to be an integral part of the background layer (Hinton and Arnott 1989). The background layer begins to form soon after immersion and gradually covers the metal surface. With time, a fine particulate structure can be resolved in the SEM. This structure coarsens and the films gradually thicken to between 100–500 nm with increasing immersion time, as the concentration of R oxide in the film increases (Hinton and Arnott 1989). Auger electron spectroscopy (AES) studies (Hinton et al. 1988, Hinton and Wilson 1989, Hinton and Arnott 1989) have shown that for steel and Zn exposed to solutions containing 1000 ppm $CeCl_3$, the films consist of mixed oxides of Ce and the substrate metal (e.g. figs. 25, 26). In the case of 7075 Al alloy exposed to a solution containing 1000 ppm $CeCl_3$, the film consisted almost entirely of Ce oxide (fig. 27) (Hinton et al. 1984, 1985, Arnott et al. 1987) with virtually no Al oxide. X-ray photoelectron spectroscopy (XPS) studies have indicated that Ce oxide in these films is hydrated (Arnott et al. 1985). From the relative concentrations of Ce and O in the film, it was inferred that cerium is present in both the trivalent and tetravalent states (Arnott et al. 1985, 1989). Davenport et al. (1991a) have used X-ray adsorption techniques to study the valency of Ce in oxide films formed on Al substrates and then exposed to a NaCl solution containing soluble Ce salt. They observed that after 5 days immersion the film contained only Ce in the 3 valence state, whereas after 7 days the film contained Ce in the 4 valence state.

The larger crystalline particles seen in the films (figs. 19–24) with lateral dimensions up to 300 μm, either develop as isolated single crystals with lenticular, dendritic, acicular (needle-like) or spheroidal shapes, or grow into various crystalline formations. The shape and size of the particles are determined by the substrate and the specific R cation used (figs. 19–24). Energy dispersive X-ray analysis studies have indicated that these particles are rich in the particular R cation present in the test solution (Hinton and Arnott 1989). X-ray diffraction studies have indicated a crystalline structure which could not readily be identified (Hinton and Arnott 1989). Using the SEM, some microscopic evidence

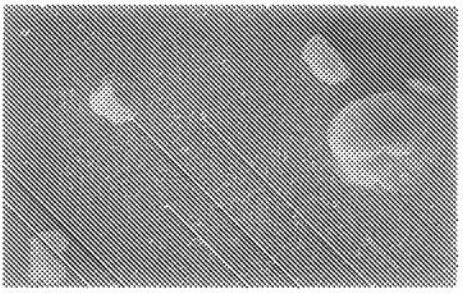

Fig. 19. 7075 Al alloy surface after 14 days in $NaCl/CeCl_3$ solution. ×1150. Note crystalline particles and cracks in film. (From Hinton 1992.)

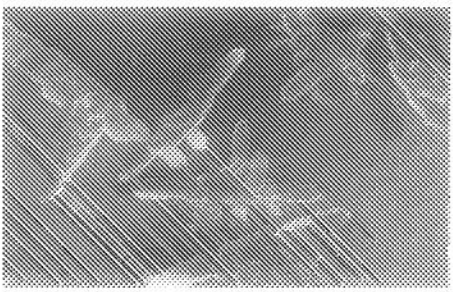

Fig. 20. 7075 Al alloy surface after 48 hours in $NaCl/LaCl_3$ solution. ×150. (From Hinton 1992).

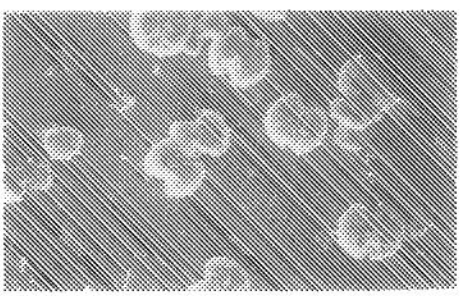

Fig. 21. 7075 Al alloy surface after 21 days in $NaCl/PrCl_3$ solution. ×440. (From Hinton 1992.)

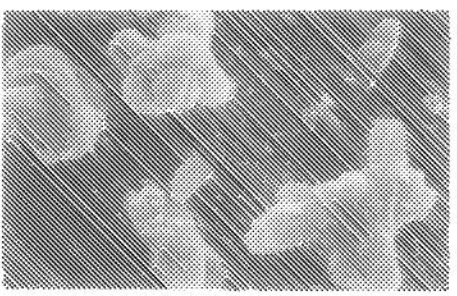

Fig. 22. Clusters of plate-like particles on 7075 Al alloy after 14 days in $NaCl/NdCl_3$ solution. ×3500. (From Hinton 1992.)

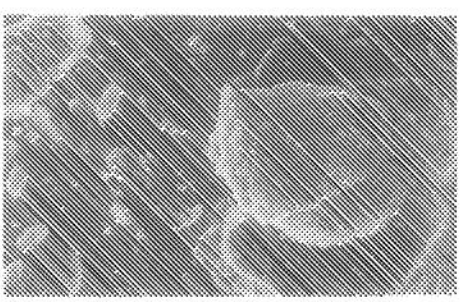

Fig. 23. Crystalline particles on a Zn surface after 21 days in $NaCl/CeCl_3$ solution. ×900. Note cracked background film. (From Hinton 1992.)

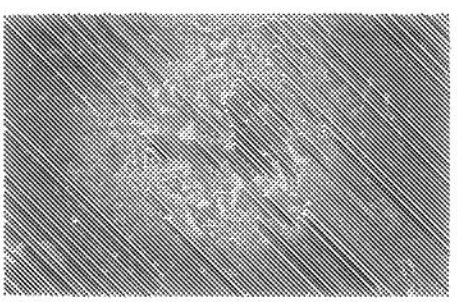

Fig. 24. Crystalline particles on a steel surface after 7 days in tap water containing $CeCl_3$. ×45. Note spalling of background film caused by too high beam current in SEM. (From Hinton 1992.)

of limited corrosion, associated with microstructural features, has been detected on the substrate metal, after lifting these films.

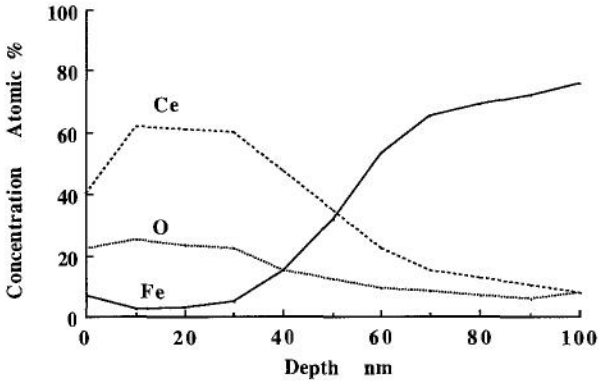

Fig. 25. Auger profiles of atomic concentration as function of sputter depth for mild steel after immersion for 7 days in tap water containing $CeCl_3$.

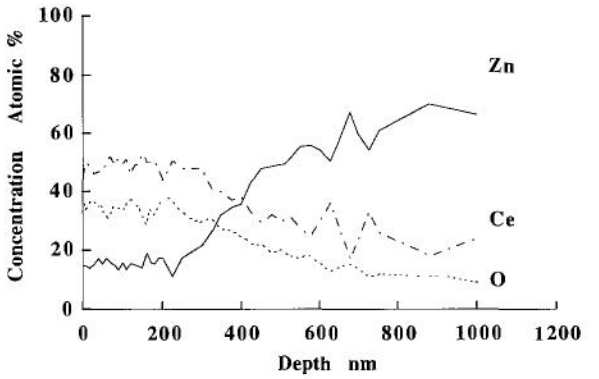

Fig. 26. Auger profiles of atomic concentration as function of sputter depth for Zn after immersion for 21 days 0.1 M NaCl containing 1000 ppm $CeCl_3$.

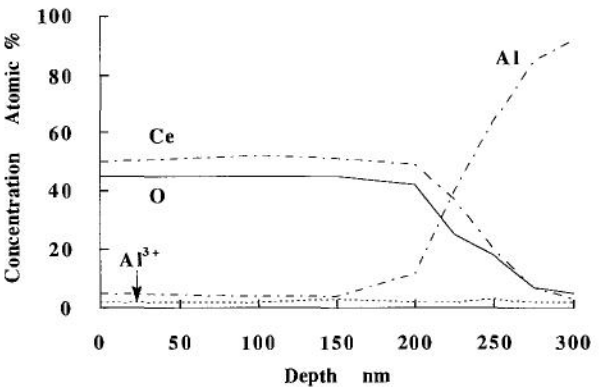

Fig. 27. Auger profiles of atomic concentration as function of sputter depth for 7075 Al alloy after immersion for 21 days in 0.1 M NaCl containing 1000 ppm $CeCl_3$.

The hydrated oxide films, which provide corrosion inhibition, adhere so strongly to the metal substrates that, in most cases, they can only be removed by chemical dissolution or by abrasion (Hinton et al. 1984). The strong adhesion of these films could be associated

with the structural relationships between the R oxides, the substrate oxides and the substrate metal, which are yet to be defined.

2.6. *Film formation and growth*

It has been proposed (Hinton et al. 1984, 1985, Arnott et al. 1987) that a cathodic mechanism is responsible for the formation of the R oxide on the metal surface. This mechanism requires the activation across the metal surface of many electrochemical cells associated with microscopic features such as grain boundaries, precipitates, constituent phases and inclusions, or with submicroscopic features such as flaws in existing naturally occurring oxide films. At these sites, anodic reactions (metal dissolution) and cathodic reactions (oxygen reduction and hydrogen evolution) occur. The cathodic processes generate alkaline conditions close to the metal surface. These conditions lead to localized precipitation of an hydrated R oxide or hydroxide and the formation of the film. Strong evidence for film formation on cathodic surfaces has been obtained in different experiments, described later in this paper. As described earlier (sect. 2.5) for the case of Ce salts as the corrosion inhibitor, the valency of the Ce in the film may vary depending on the time of exposure in the corrosive environment. Davenport et al. (1991a,b) have pointed out that it is thermodynamically possible for Ce^{4+} to exist in the alkaline regions that develop near the metal surface with oxygen as the oxidizing agent, although Mansfeld et al. (1990a) believe that Ce^{4+} cannot form in solution under these conditions due to the absence of a strong oxidizing agent. However, Hinton and Wilson (1989) have argued that the strong oxidizing conditions could arise where H_2O_2, a powerful oxidizing agent, may form as an intermediate species during the cathodic reduction of oxygen. Churchill (1937) has detected the formation of H_2O_2 when freshly abraded Al was exposed to oxygenated water. He also found that H_2O_2 could be produced by cathodically polarizing Al surfaces. Mayne and Burkhill (1980) have shown that H_2O_2 was associated with the cathodic polarization of mild steel in solutions of neutral and high pH. Also, H_2O_2 has been detected during the corrosion of Zn in oxygenated water (Thorne and Roberts 1954). It is therefore highly likely that Ce will exist in both valency states at or near the metal surface. Under the conditions of high pH which develop in these regions, the hydroxides of both valence states may precipitate (Pourbaix 1966). However, once the pH falls, the $Ce(OH)_3$ may redissolve as it is the least stable of the Ce hydroxides at the lower pH levels (Mansfeld et al. 1990a). This could account for the gradual enrichment of the film in Ce^{4+} as observed by Davenport et al. (1991a).

For film formation and growth to occur, there must be some corrosion and evidence of this has been noted (Hinton and Arnott 1989). However, the extent of corrosion as indicated by corrosion tests, is clearly very small (Hinton 1989, Hinton et al. 1984, 1985, 1988), probably because the rate of corrosion is controlled by the impedance to the cathodic reactions imposed by the presence of the surface film.

AES studies have indicated that the metal surface is gradually covered with the R oxide film during immersion in solutions containing R cations (Hinton et al. 1984, 1985, 1988, Hinton 1989, Hinton and Arnott 1989, Hinton and Wilson 1989). This process is

consistent with the deposition and growth of islands of R oxide (Arnott et al. 1987, 1989). These islands are thought to be associated with the more active anodic and cathodic sites located within the metal microstructure. The formation and growth of the oxide in this way is believed to produce the background layer observed in the SEM.

Hinton and Arnott (1989) consider that the development of the much larger particles (needles and plates) and crystalline formations is an indication that, even though complete coverage occurs, anodic and cathodic processes must continue through sub-microscopic defects in the film. The size of some particles suggests that quite localized high levels of pH must exist and extend into the solution, to sustain the growth of these particles and formations. The high localized levels of alkalinity necessary for the growth of these particles could be associated with cathodic processes occurring on the background film, in association with anodic processes occurring through flaws in the background layer (sub-microscopic corrosion). These flaws would arise as islands of oxide coalesce to create the R oxide film.

The particles and formations contained within these protective R oxide films differ in a spectacular way depending on the R cation and the substrate (figs. 19–24). The reasons for these differences are not clear at this time. However, they may be associated with the influence of the substrate and the R oxide film on the cathodic reactions and, subsequently, on the level and profile of alkalinity produced by these reactions across the surface. Explanations for the various film morphologies may well be found in the research findings of those who study the formation and growth of R oxide films by roasting R salts (e.g. Kang and Eyring 1992). Electrochemical studies (see sect. 2.7) have shown that the type of R cation and substrate can have a strong influence on the oxygen reduction reaction. Thus, variations in film composition, concentration of R oxide, the film structure and, the number of sub-microscopic flaws present, probably account for the different levels of corrosion inhibition observed with different R cations (figs. 3, 4 and table 2).

2.7. *Electrochemical polarization data*

Electrochemical techniques, in particular potentiodynamic polarization, are useful for studying the mechanism of corrosion inhibition. The polarization behaviour of Al alloys, Zn, and mild steel in aqueous environments containing various R salts has been extensively studied (Hinton et al. 1984, 1985, 1988, Arnott et al. 1987, Hinton 1989, Hinton and Arnott 1989, Hinton and Wilson 1989).

2.7.1. *Aluminium alloys*

The polarization curves for 7075 Al alloy, tested in a quiescent air-saturated 0.1 M NaCl solution, with and without separate additions of $CeCl_3$, $PrCl_3$ and YCl_3 at concentrations of 1000 ppm, are shown in fig. 28 (Arnott et al. 1989). On the anodic arm of the polarization data (i.e. at potentials more positive than E_{corr}), the current increased rapidly with small changes in potential. This behaviour is typical of a corroding surface where the corrosion potential (E_{corr}) and the pitting potential (E_{pit}) are almost identical, in this case at around −0.72 V SCE. On the cathodic arm of the curve, the current density changes

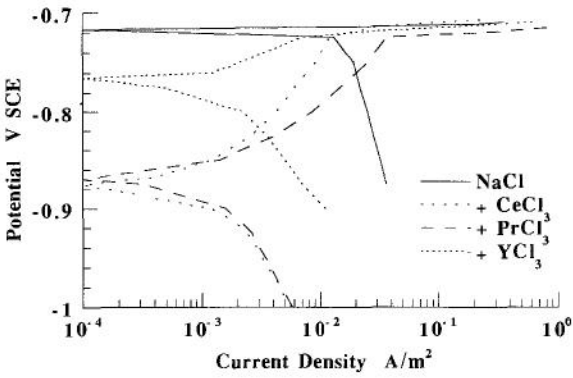

Fig. 28. Polarization data for 7075 Al alloy in 0.1 M NaCl and 0.1 M NaCl with 1000 ppm of various R chlorides.

very little as the potential varies from −0.72 V to −0.86 V, indicating that oxygen reduction is the principal cathodic reaction. With the addition of R salts the cathodic arm was shifted toward more negative potentials and lower current densities, indicating a reduction in the rate of the oxygen reaction. The effect of the R salt on the cathodic reaction leads to a shift of E_{corr} in the negative direction away from E_{pit} and into a region where the alloy is passive. This shift was some 160 mV more negative than E_{pit} for $CeCl_3$ and $PrCl_3$, and 50 mV more negative for YCl_3. With Al alloys, a widening of the gap between E_{corr} and E_{pit} is associated with increased resistance to corrosion, particularly corrosion pitting (Hinton et al. 1984). These data further illustrate the powerful corrosion-inhibiting properties of the R salts. It is interesting to note that Lichtenberger-Bajza and Boczor (1977) observed a widening of the gap between E_{corr} and E_{pit} during polarization tests in NaCl solution with an Al–Zn–Mg alloy containing 0.2% Ce compared with the same alloy without Ce. This observation suggests that a precipitate of Ce oxide may have formed on the alloy surface, as a result of Ce going into solution, or that Ce oxide may be present in the natural Al oxide film on the alloy, and that the Ce oxide film may be responsible for the increased resistance to pitting.

Baldwin et al. (1987) have also observed effects on the cathodic kinetics of 2014 when tested in aerated 0.6 M NaCl containing 2 mM of Ce salts (fig. 29). The type of anion has a strong effect on E_{corr} and the current densities near E_{corr}. However, the kinetics of the cathodic reaction at higher current densities is largely unaltered by the type of anion. The effects of aeration and pH on the polarization behaviour in the presence of R salts have been studied by Baldwin et al. (1987). The corrosion current data determined from Tafel extrapolation are shown in table 4. These data show that the effects of R salts in de-aerated solutions are not as clear as in aerated solutions. In acidic solutions the R salts provide no corrosion inhibition.

All of the polarization data obtained with Al alloys clearly indicate that the R salts when providing inhibition act as cathodic inhibitors.

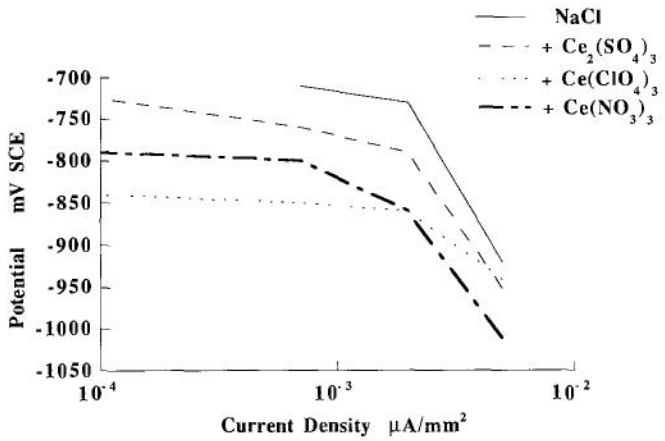

Fig. 29. Cathodic polarization data for 2014 Al alloy in 0.6 M NaCl and 0.6 M NaCl with 2 mM of various Ce salts (after Baldwin et al. 1987).

Table 4
Effect of aeration and pH on corrosion current density of aluminium alloy 2014 tested in 0.6 M NaCl solution with and without various cerium salts (after Baldwin et al. 1987)

Inhibitor	Corrosion current density ($\mu A\,cm^{-2}$)		
	Aerated	Deaerated	Aerated pH = 3
None	11.2	0.251	17.7
$Ce_2(SO_4)_3$	0.140	0.079	12.5
$Ce(NO_3)_3$	0.126	7.90	10.0
$Ce(ClO_4)_3$	0.141	0.282	13.3

2.7.2. *Steel*

Hinton et al. (1988) have shown that the anodic polarization behaviour of mild steel in soft tap water at pH 5.5 was unaffected by the presence in solution of $CeCl_3$. However, the presence of $CeCl_3$ had a significant effect on the cathodic polarization behaviour as shown in fig. 30. With no inhibitor present, the cathodic current density became almost independent of potential as the potential was scanned in the negative direction. This indicated that oxygen reduction was the principal cathodic reaction occurring in the potential region studied. With the addition of 100 ppm $CeCl_3$, at potentials more negative than E_{corr}, current densities were reduced by up to an order of magnitude indicating that the presence in solution of $CeCl_3$ reduced the rate of the oxygen reduction reaction. The presence of $CeCl_3$ also shifted E_{corr} some 230 mV more negative to approximately −0.53 V, where the steel is passive, and rapid corrosion rates would not be expected. After a potentiodynamic scan in the negative direction the steel electrode was covered with a pale yellow film.

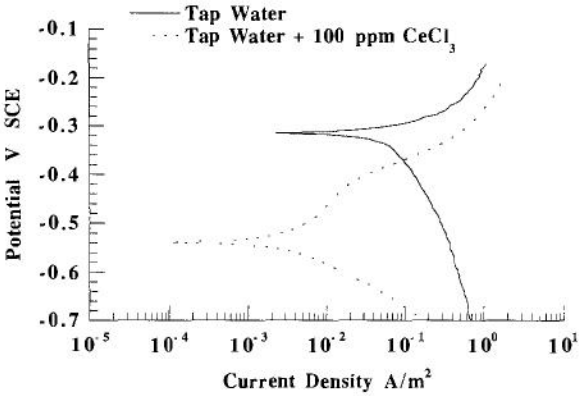

Fig. 30. Polarization data for mild steel in tap water and tap water with 100 ppm of $CeCl_3$.

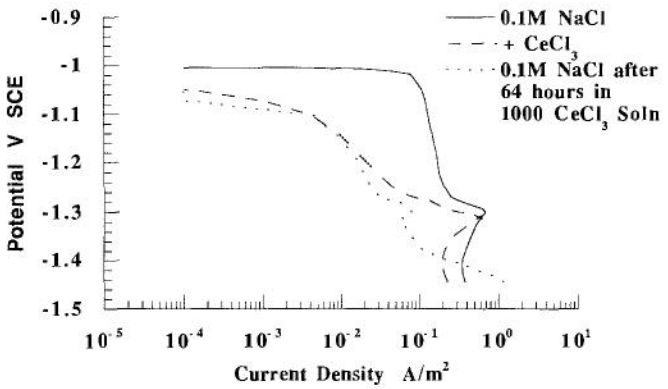

Fig. 31. Cathodic polarization data for Zn in 0.1 M NaCl and 0.1 M NaCl with 1000 ppm $CeCl_3$. (After Hinton and Wilson 1989.)

2.7.3. *Zinc*

Cathodic polarization data (fig. 31) have been obtained by Hinton and Wilson (1989) for Zn tested in quiescent air-saturated 0.1 M NaCl solution. These data show that oxygen reduction is again the principal cathodic reaction occurring during the corrosion of Zn. At potentials just negative of E_{corr}, the rate of the cathodic reaction is reduced when $CeCl_3$ is present. A Zn specimen was held in a solution containing 1000 ppm $CeCl_3$ for 64 hours, during which time the surface became covered with a yellow film. A polarization scan was then carried out in 0.1 M NaCl with no $CeCl_3$ present. Figure 31 shows that after immersion in $CeCl_3$, the polarization curve is also shifted to lower current densities. This evidence strongly suggests that the presence of the yellow Ce oxide film on the Zn surface is responsible for a reduction in the cathodic reaction occurring during the corrosion of Zn.

2.8. *Mechanisms of corrosion inhibition*

The general conclusions from the polarization tests described above are that the presence of R salts in solution have very little effect on the kinetics of the anodic half of the corrosion reaction. However, they do have a most significant effect on the rate of the cathodic half of the reaction. In particular, the R cations reduce the rate of the oxygen reduction reaction. Clearly the R cations act as cathodic inhibitors. For corrosion tests with all three metal systems, yellow or bluish films with a yellow tinge were observed. These films were similar to those formed in cathodic polarization corrosion experiments when R cations were present in aqueous solution. Further evidence, as described earlier (sects. 2.1.1, 2.2.1), that these films are associated with the inhibition is the formation of Ce oxide/hydroxide on the cathode when a galvanic couple was immersed in solution containing $CeCl_3$, and the accompanying decrease in galvanic current.

From these important observations, the following mechanism of corrosion inhibition can be proposed (Hinton 1992), as schematically shown in fig. 32. This mechanism requires (as described in sect. 2.6 above) the activation across the metal surface of many electrochemical cells each associated with microscopic features such as grain boundaries, precipitates, constituent phases, inclusions, or sub-microscopic features, such as flaws in existing oxide films. At these sites, anodic reactions (metal dissolution) and cathodic reactions (oxygen reduction) occur. The cathodic processes generate alkaline conditions close to the metal surface, leading to localized precipitation of hydrated R oxides or hydroxides, and the formation of the film. The presence of the R oxide film at cathodic sites on the metal surface, creates a barrier to the supply of oxygen, or of electrons to the oxygen reduction reaction. Davenport et al. (1991a) have argued in support of

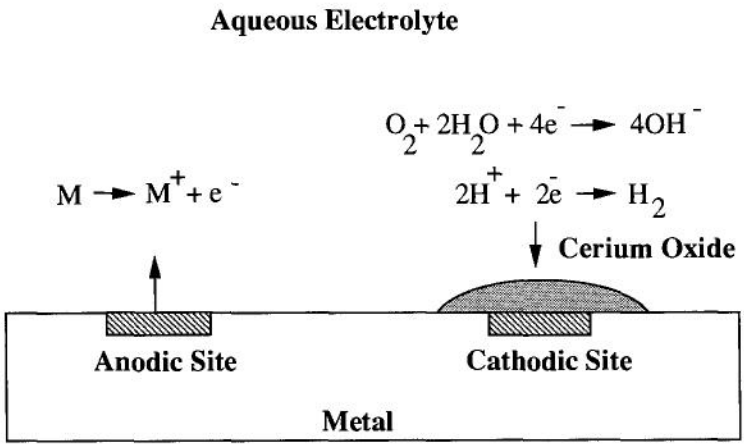

Fig. 32. Schematic model of the formation of an hydrated Ce oxide film on a metal surface exposed to an aqueous environment containing a Ce salt.

the proposition that the R oxide film is electronically insulating. They observed that in an oxide film prepared on Al, the Ce^{3+} converted to Ce^{4+} with exposure time in NaCl solution. As the Pourbaix diagram for the Ce–H_2O system indicates, the oxidation of Ce^{3+} to Ce^{4+} is only possible at potentials of around +0.4 V SCE (Pourbaix 1966). However, they measured the corrosion potential of Al in the NaCl solution at −0.8 V SCE. They concluded that the conversion of Ce from the 3 to 4 valence state could only take place if the oxide film was electronically insulating. Hence, if the rate of the cathodic reaction is reduced or stopped, the electrochemical circuit is broken and, since this reaction is rate-controlling in the corrosion process under aerated conditions (see fig. 32), dissolution of the metal (i.e. corrosion) will cease and inhibition is achieved.

Recent results published by Isaacs et al. (1991) suggest that R salts may not always act as cathodic inhibitors. In an elegant experiment using a vibrating probe electrode they were able to show that for mild steel corroding in 0.01 M NaCl solution, the addition of 0.005 M $CeCl_3$ caused a large existing anodic current density to disappear and E_{corr} to increase. Under these test conditions, they deduced that Ce ions were acting as anodic inhibitors.

3. Corrosion prevention by alloying

3.1. *Magnesium alloys*

3.1.1. *Introduction*

Aircraft designers are constantly seeking to achieve lower fuel consumption and increased performance through higher power to weight ratios. Hence there is a continuing interest in the fabrication of structural components from lighter metals and alloys. Mg alloys are especially attractive in this regard, because of their low density, high specific strength and stiffness. Good corrosion resistance in aqueous environments is an important property required of most aircraft structural alloys. While pure Mg has good corrosion resistance in these environments, Mg alloys can be very susceptible to corrosion (Uhlig 1963). This poor corrosion performance is associated mainly with impurity metals such as Fe, Ni, and Cu and the microstructural phases which they form (Uhlig 1963). In electrochemical terms these phases are more noble than the surrounding matrix. They may act as local cathodes which efficiently sustain cathodic reactions such as the reduction of oxygen. This in turn drives the rapid dissolution (corrosion) of the adjacent matrix. To improve corrosion resistance, alloys have been produced with low impurity levels (King 1990), and with alloying elements such as Al which may promote the formation of a more protective surface oxide film (Bray 1990).

For many years, R elements have also been a common addition to both cast and wrought Mg alloys to reduce porosity, and to increase high temperature strength and creep resistance (Bray 1990). However, in recent years, greater attention has been directed towards the role which R elements play in the improved corrosion resistance of the newly developed alloys. The following section examines the effects of R additions to Mg alloys

produced by conventional ingot casting and rapid solidification processes (RSP), and the mechanisms by which improved corrosion performance is achieved.

3.1.2. *Cast alloys*

Unsworth (1989) in a recent review of the role of R elements in the development of Mg alloys has listed the corrosion rates (table 5) of various experimental and commercially developed alloys when immersed in saltwater solutions. Some alloys contained specific R elements while others contained R additions which were a mix of elements with atomic numbers from 57–71. All of the alloys had been heat treated by solution annealing followed by age hardening. For comparative purposes, some corrosion rate data from other sources (Uhlig 1963) for pure Mg and commercially pure Mg (99.8%) (Braun 1979) are included. The solid solubility at room temperature of most R's in Mg is very small. Thus, at the levels of R shown, most of them would be present as Mg–R intermetallic phases.

There are several noteworthy trends in these data. (i) The addition of 0.5% R to Mg has reduced the corrosion rate by an order of magnitude. (ii) A further increase in the R content by a factor of 10 plus the addition of Zr reduced the corrosion rate by another order of magnitude (Zr is known to refine the grain size which is an important requirement for high-temperature strength, Unsworth 1989). (iii) Alloy WE54, which has deliberate additions of Y (75% Y balance Gd, Tb, Dy and Er) and Nd (80% Nd, 20% Pr) was found to corrode at a rate of only 5–15 mpy. (iv) A comparison of the results for EK31A with EK33A and ZE41 strongly suggests that the addition of Zn to Mg in the presence of R elements is most detrimental. However, surprisingly, by increasing the Zn content for a lower R level and replacing the Zr with Mn, a rate of only 50 mpy was recorded. This latter observation is difficult to explain. Zn is significantly more noble than Mg, and increasing its concentration in the alloy should be detrimental to the corrosion resistance.

Table 5
Corrosion rates in NaCl solution for cast and heat treated Mg alloys (after Unsworth 1989)

Alloy designation	Composition (weight %)						Corrosion rate (mpy)
	Zn	Zr	Mn	Nd	Y	R	
Pure Mg[a]	–	–	–	–	–	–	10
99.98% Mg[b]	–	–	–	–	–	–	1000–5000
Mg	–	–	–	–	–	0.5	300–400
EK31A	–	0.40	–	–	–	3.5–4.0	20–40
WE54	0.3–5	0.4–1	–	1.5–2	5–5.5	–	5–15
EK33A	2–3	0.4–1	–	–	–	2.4–4	200–300
ZE41	3.5–5	0.4–1	–	–	–	0.75–1.75	350–500
Mg	6	–	0.5	–	–	0.75	50

[a] Uhlig (1963). [b] Braun (1979).

Because these alloys have been commercially developed, the full compositional, heat treatment and corrosion testing details are not available. It is difficult to identify the particular effects of R additions on the corrosion resistance of these alloys from the data shown, because of the absence of a systematic variation in the particular R addition or concentration. There is however, sufficient evidence in table 5 to suggest that R additions play a role in improving the corrosion resistance of Mg casting alloys, but it is difficult to draw conclusions regarding the nature of that role. As with other alloys, the corrosion resistance of Mg alloys is generally associated with the stability, solubility and defect structure of the naturally occurring oxide film, and the tendency for the various phases in the microstructure to act as local anodes and cathodes. Unfortunately there is no evidence in the literature to indicate whether or not R additions modify the properties of the surface oxide film on the cast Mg alloys or alter the electrochemical balance of the microstructure.

3.1.3. *Alloys processed by rapid solidification (RSP)*

Many of the alloying elements used with Mg, e.g. Al, Zn, and R's, have limited solid solubility in Mg at room temperature. As a result, the microstructure may contain coarse intermetallic particles in addition to the Mg-alloying element solid solution. Such a microstructure is not conducive to good corrosion resistance because intermetallic particles are quite often preferential sites for corrosion initiation.

RSP has provided a means for preventing the formation of these undesirable microstructures, and for producing extended solid solubility, a finer grain size (Hehmann et al. 1988), a finer distribution and greater volume fraction of hardening particles (Bray 1988) and therefore, an improved chemical homogeneity (Chang et al. 1989). All of these microstructural modifications, in particular the elimination of coarse intermetallic particles, contribute to both the increased strength and corrosion resistance of these alloys (Hehmann et al. 1988).

RSP involves rapidly cooling the metal from the molten state at rates approaching 10^5 K s^{-1}. Various techniques (Lewis et al. 1986) are employed to achieve these rates:

(i) atomization of molten metal by spraying to form powder or flake particulates,
(ii) continuous chill casting of ribbon or thin strip by impinging a stream of molten metal on to a rotating cooled block or drum (melt spinning)
(iii) rapid in-situ melting and re-solidification through intimate contact with a chilled surface.

Following solidification, the rapidly cooled samples are then ground to fine powders. Alloys are then further processed by standard powder metallurgy processing routes (Chang et al. 1989).

With the focus on RSP for production of Mg alloy components, a greater interest has been shown in the role of all alloying elements and their effects on mechanical properties and corrosion resistance. The discovery that R additions to the RSP Mg alloy AZ91 dramatically increased the corrosion resistance (Chang et al. 1986), have stimulated a number of further investigations into the effects of R additions on the corrosion resistance of Mg alloys (Hehmann et al. 1988).

Table 6
Effect of R addition on the corrosion rates of cast and RSP alloys in 0.01 M NaCl (after Krishnamurthy et al. 1986, 1988a–c)

Alloy	Corrosion rate (mpy)	
	Cast	RSP
Pure Mg[a]	10	–
99.98% Mg[b]	1000	–
Mg–2%Ce	51	40
Mg–5%Ce	18	–
Mg–21%Ce	23	20
Mg–10%Nd	5.39	5
Mg–20%Nd	8	4
Mg–15%Y	–	50
Mg–20%Y	–	80
Mg–26%Y	–	20

[a] Uhlig (1963). [b] Braun (1979).

3.1.3.1. *Binary Mg alloys.* Krishnamurthy et al. (1986, 1988a–c) have extensively studied the corrosion behaviour of binary alloys with Ce, Nd and Y produced by conventional casting techniques and RSP, such as melt spinning and splat quenching. They have used polarization techniques to measure corrosion rates in 0.01 M NaCl solutions. A summary of their results is presented in table 6. The data for the Ce alloys are as published. However, the data for the Nd and Y alloys have been calculated using Tafel extrapolation and standard formulae (Shreir 1976) from the published polarization plots.

The addition of R's to both the cast and RSP alloys reduced the corrosion rate compared with the commercially pure Mg, the higher concentrations of Ce and Y producing the greatest effect. Comparing one group with the other, the microstructures of the cast alloys and the RSP alloys were quite different. The microstructure of the cast alloys correspond with the equilibrium phase diagrams. That is, primary dendrites of Mg–R solid solution with a coarse eutectic phase containing, for example, the intermetallic phase $Mg_{12}R$ (Krishnamurthy et al. 1986, 1988a–c). With increasing R content the proportion of eutectic phase increases. The cooling rates used during RSP are not sufficiently rapid to completely eliminate all second phases from the microstructure. Thus, the microstructures consisted of the Mg–R solid solution containing a fine dispersion of intermetallic phases, e.g. $Mg_{12}Nd$ in the Mg–Nd alloys (Krishnamurthy et al. 1986, 1988a–c).

In general, the RSP microstructures were much finer and more homogeneous than those of the cast alloys. Because of these microstructural differences, different corrosion behaviour could be expected. However, the corrosion rate data for alloys produced by both processing routes were similar. Hence, the beneficial effects observed may not entirely be attributed to the refined microstructure.

A clearer picture of the effect of R additions on the corrosion behaviour of these binary Mg alloys (Krishnamurthy et al. 1986, 1988b,c) emerges from the polarization

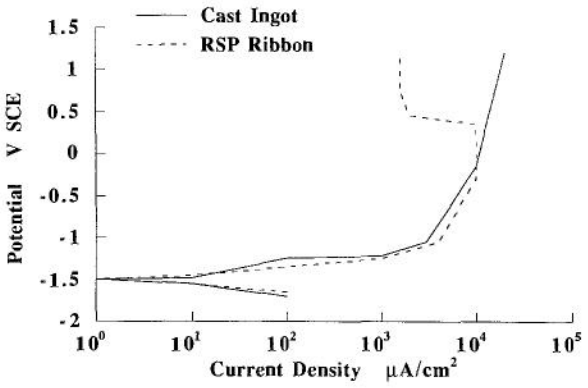

Fig. 33. Polarization data for both a cast and a RSP Mg20%Nd in 0.01 M NaCl (after Krishnamurthy et al. 1988b).

curves, examples of which are shown in fig. 33. The data for the cast ingot Mg–Nd alloy are typical of most Mg alloys tested in NaCl solutions. At potentials more positive than the corrosion potential, the current density, as a measure of the corrosion rate, increased rapidly with increasing potential once pitting had occurred. However, the specimen gradually became covered with a corrosion product film consisting mostly of $Mg(OH)_2$ (Krishnamurthy et al. 1988b). As observed, this film effectively limits the current density to a constant value. This value represents the rate at which corrosion occurs, at the applied potential (driving force for corrosion), in the presence of the corrosion product. At a potential of around +0.4 V SCE, for the melt spun ribbon and the splat quenched specimens, the current density decreased by a factor of around 10. Krishnamurthy et al. have called this effect pseudopassivation. A greater reduction in current density in this pseudopassivation region was observed for the splat quenched alloy compared with the ribbon alloy. Heat treatment of the ribbon by ageing resulted in further current density reduction. The finer the dispersion of the second phase particles (i.e. with a more homogeneous microstructure), the more pronounced is the pseudopassivation effect.

At higher Nd concentrations, the pseudopassivation effect occurred at lower potentials. Furthermore, similar pseudopassivation effects are observed with the Mg–Y melt spun alloys. However, relative to the Mg–Nd alloys, these effects occurred at higher potentials with increasing Y concentration. Krishnamurthy et al. (1988b) also observed a pseudopassivation effect with Ce, Nd and Y additions to a RSP alloy Mg–6Zn–0.5Zr.

The surface of the Mg–20% Nd alloy was examined using the scanning electron microscope and energy dispersive X-ray analysis, before and after the onset of pseudopassivation, as the potential was scanned in the positive direction (Krishnamurthy et al. 1988b). Before pseudopassivation, the surface was typical of corroded Mg, i.e. covered with a corrosion product film, with the appearance of cracked mud. This film (table 7) contained both Mg and Nd in approximately the same ratio as in the alloy. After anodically polarizing into the pseudopassivation region, the film has a significantly greater concentration of Nd and a reduced chloride ion concentration. Moreover, another secondary film is observed using SEM, inside the cracks in the corrosion product.

Table 7
EDAX analyses of Mg–Nd surface polarized in 0.01 M NaCl (after Krishnamurthy et al. 1988b)

Voltage range	Region	Composition (weight %)		
		Mg	Nd	Cl
Passive	Corrosion product	66.4	17.7	15.9
	Cracks in corrosion product	73.1	21	5.9
Pseudopassive	Corrosion product	76.6	22.2	1.02
		80.6	18.6	0.87
	Cracks in corrosion product	52.3	35.8	0.70

Table 8
Effect of R addition on corrosion rates of cast and RSP binary alloys in 0.001 M NaCl and distilled water (after Hehmann et al. 1988)

Alloy addition	Type of RSP	Test solution	Corrosion rate (mpy)
2.2% La	Splat quenched	NaCl	0.04–0.06
6.7% La	Melt spun	NaCl	23
2.2% Ce	Splat quenched	NaCl	0.05
7.3% Ce	Melt spun	NaCl	59
7.7% Y	Melt spun	Water	10–20
17.7% Y	Melt spun and heat treated	Water	0.3–0.6

Furthermore, as table 7 shows, this film has an even higher concentration of Nd. The observations of Krishnamurthy et al. (1988b) suggest that the corrosion resistance of these RSP binary alloys is associated with the formation of a R rich film.

Hehmann et al. (1988) have investigated the corrosion behaviour of Mg–La and Mg–Ce binary alloys produced either by splat quenching or melt spinning. The corrosion rates in 0.001 M NaCl and distilled water were calculated from polarization data. A selection of the data is shown in table 8. Unfortunately, insufficient experiments have been carried out to enable a complete comparison of both melt spun and splat quenched samples for each alloy composition. However, the data in table 8 show some significant trends. The La and Ce alloys when splat quenched corrode at rates almost 3 orders of magnitude less than the melt spun alloys. The splat quenched alloys have a more homogeneous microstructure than the alloys produced by melt spinning (Hehmann et al. 1988) with an almost complete absence of intermetallic second phase particles, possibly because the cooling rate with splat quenching is much faster. Unfortunately, the effect of splat quenching was not investigated for the Mg–Y alloy. The corrosion rate for a melt spun Mg–Y alloy, when tested in distilled water was 10–20 mpy. Ageing at 360°C for 2 hours resulted in the precipitation of finely dispersed $Mg_{25}Y_4$ particles throughout the Mg solid solution. After this heat treatment, the rate of corrosion was far less than in the initial melt spun condition (Hehmann et al. 1988).

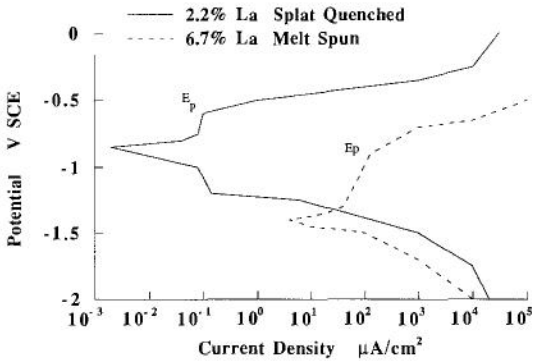

Fig. 34. Polarization data for both a splat quenched Mg–2.2%La alloy and a melt spun Mg–6.7%La alloy in 0.001 M NaCl (after Hehmann et al. 1988).

Polarization data obtained by Hehmann et al. (1988) for a Mg–La alloy are replotted in fig. 34. While it is difficult to compare the two sets of data because the method of RSP and the level of La concentration are different, some differences are worth noting. E_{pit} for the splat quenched Mg–2.2%La alloy is 300 mV higher than that for the melt spun alloy. Also, the current density in the passive region E_{pass} is at least two orders of magnitude lower for the splat quenched alloy. Both of these observations provide very strong indications of the good corrosion resistance of the structurally more homogeneous splat quenched alloy (Hehmann et al. 1988).

3.1.3.2. *Ternary alloys.* Ahmed et al. (1990) have studied the corrosion behaviour of several splat quenched Mg–Zn and Mg–Al alloys containing Ce and Nd additions. They used weight-loss techniques and a test solution of 3% NaCl buffered with $Mg(OH)_2$. Their results are shown in table 9.

These results provide no clear indication of any significant effects of R addition on the corrosion rates of these alloys, although some reductions in corrosion rate were observed depending on the composition of the Mg solid solution. Additions to the Mg–Zn alloys generally increased the corrosion rate, whereas additions of Ce and Nd to the Mg–Al alloys reduced the corrosion rates. It is difficult to assess how significant these effects are because they are quite small and no indications of variability for the experiments were given. Possibly, the test solution of 3% NaCl was too severe and any effects of R additions were too subtle to be detected. All the corrosion rates seem to be very high. This may be related to the testing time of only 17 hours.

3.1.3.3. *Quaternary alloys.* Chang et al. (1986) have studied the corrosion behaviour of Mg–5%Al–2%Zn alloys with various R additions, prepared by either planar flow casting or melt spinning, and consolidation into extruded bars. All of the alloys possessed a fine homogeneous microstructure, with grain sizes around 1 μm or less and Mg–R intermetallic particle sizes of 0.04–0.07 μm. The corrosion rates were calculated from weight-loss measurements after immersion in 3% NaCl solution for 4 days. The results are shown in table 10 (Chang et al. 1986). These data indicate that the corrosion rates

Table 9
Effect of R addition on corrosion of Mg–Zn and Mg–Al alloys in 3% NaCl (after Ahmed et al. 1990)

Alloy	R addition	Corrosion rate (mpy × 10^3)
Mg–5%Al	–	0.55
	0.5% Ce	0.45
	2.3% Ce	0.38
	0.6% Nd	0.28
	1.6% Nd	0.42
Mg–10%Al	–	0.78
	0.3% Ce	0.35
	2.7% Ce	0.40
	0.6% Nd	0.39
	2.4% Nd	0.45
Mg–4%Zn	–	0.45
	0.5% Ce	0.50
	1.5% Ce	0.75
	1.8% Nd	0.50
	3.9% Nd	0.40
Mg–8%Zn	–	0.87
	0.5% Ce	0.90
	1.5% Ce	0.92
	2.3% Nd	0.85
	4.7% Nd	1.18

with Ce additions present were very high, whereas Pr, Nd and Y additions in excess of 1% were beneficial to the corrosion performance.

Table 10
Effect of R addition to a Mg–5%Al–2%Zn alloy on the corrosion rate in 3% NaCl (after Chang et al. 1986)

Rare earth addition	Corrosion rate (mpy)
0.5% Ce	545
1.0% Ce	766
0.5% Pr	315
1.0% Pr	29
1.0% Pr–0.55% Si	14
1.0% Y	12
2.0% Y	8
1.0% Nd	11
1.0% Nd–0.5% Mn	22

3.1.3.4. *Summary of RSP data.* Published data relating to R additions indicate both positive or negative effects on corrosion resistance. Therefore, it is difficult to draw conclusions as to what conditions produce these effects simply because many of the studies have lacked a systematic approach to the variation of important variables such as type and concentration of R addition. Furthermore, in most studies control data for pure or commercially pure Mg were never determined. In some cases commercial alloys with no R content were used for comparison, but these alloys were usually complex ternary or quaternary alloys with very different basic concentrations and methods of production. It is therefore difficult to know what constitutes a low or base corrosion rate.

The following examples illustrate some of the conflicting results to be found in the literature. (i) For binary alloys, concentrations of Ce (5%), Nd (20%) and Y (26%) have been found to produce low corrosion rates (Krishnamurthy et al. 1988a–c). In contrast, however, other studies have shown that concentrations of La and Ce (~7%) were not as beneficial at concentrations of 2%; additions of Nd had no effect, and the corrosion rate for a Mg–17.7%Y alloy was only low when tested in distilled water, and then only in the heat treated condition (Hehmann et al. 1988). These latter results were further complicated by the different RSP methods used. (ii) Low corrosion rates have been found for a commercial Mg–R–Zr cast alloy (EK31A), whereas a Mg–Zn–R cast alloy (EK33A) shows poor corrosion resistance (Unsworth 1989). (iii) Similar results have been found with complex RSP alloys. Additions of Ce and Nd lowered the corrosion rates for Mg–Al alloys, while additions of Ce and Nd to Mg–Zn alloys increased the rate or had no effect (Ahmed et al. 1990). These results suggest that the combination of R and Zn is detrimental to corrosion resistance. However, Krishnamurthy et al. (1988c) obtained low corrosion rates when Y and Ce were added to a RSP Mg–Zn–Zr alloy. Additions of Nd did not affect corrosion rates calculated from their polarization data, although with Nd present a pseudopassivation effect was observed (Krishnamurthy et al. 1988b). (iv) In contrast, the extensive studies of Chang et al. (1986) have shown that additions of Pr, Nd or Y to a RSP Mg–Al–Zn alloy all lower the corrosion rate significantly, whereas the addition of Ce has virtually no effect.

These conflicting published results could be due to a number of factors:

The microstructure of the test alloy. This clearly plays an important role in the corrosion process, in particular, the structural and chemical homogeneity as indicated by the type, size, distribution and presence of any intermetallic phases. These phases may change in composition and distribution from binary to the more complex alloys. The presence and distribution of these phases also change with method of alloy preparation, e.g. cast, RSP, type of RSP and the subsequent heat treatment.

Technique for measuring corrosion rate. The studies described have generally used either of two techniques i.e. weight-loss or electrochemical polarization. It could be argued that long term (e.g. days) weight-loss tests give a more accurate picture of corrosion performance because pits have time to develop, while corrosion rates determined from Tafel extrapolation of polarization data typically take only a few minutes to obtain after a short immersion time. This may not give a complete picture of the corrosion process. In general, pitting does not develop as the potential is scanned around E_{corr}.

This requires anodic polarization to beyond E_{pit}. A more complete characterization of corrosion behaviour involves a determination of both the corrosion rate (I_{corr}) and E_{pit}. It is difficult to compare corrosion performance when different parameters are used as the basis for comparison.

Test environment. A range of test solutions has been used to assess corrosion resistance including distilled water, 0.001 M, 0.01 M, 0.1 M and 3% NaCl. Corrosion rates for a control sample could easily vary, over this range of chloride concentrations, by an order of magnitude or more. Some test environments may well have been too severe for the effects being studied, e.g. type of R addition and concentration, making subtle changes too difficult to detect.

The most likely reason for conflicting evidence for any beneficial influence of R additions on corrosion of Mg alloys is that most research programs primarily aim to optimize mechanical properties; thus corrosion behaviour is a secondary consideration.

3.1.4. *Mechanisms of corrosion resistance*

The only systematic studies of the effects of R additions on corrosion resistance are those involving RSP alloys. Any discussion of the mechanisms for the R effects should therefore be based on these studies.

The good corrosion resistance of RSP alloys is considered to result mainly from the more homogeneous microstructure with a fine dispersion of second phase intermetallic particles (Chang et al. 1989). Such a microstructure minimizes the large areas of intermetallic phase particles which would otherwise act as efficient cathodes. Makar et al. (1988) have noted with corroded RSP alloys, that pits are much more evenly distributed across the metal surface compared with cast alloys in which they appear to be more localized.

In the literature, discussion of possible corrosion mechanisms has centered around two concepts: (a) the role of the second phase R rich particles such as $Mg_{12}Nd$, and (b) the formation of a protective film. Various authors (Krishnamurthy et al. 1988c, Bray 1990, Hehmann et al. 1988) have suggested that R rich phases are preferentially attacked as a result of their being electrochemically less noble than the adjacent Mg matrix. That is, a galvanic couple is established in which the R rich phase cathodically protects the matrix. Table 11 shows the standard electrode potentials for various alloying elements and Mg. It is clear that La, Ce, Pr, and Nd are more active than Mg, while Y has the same electrode potential. Chang et al. (1989) have argued that these differences are negligible, even though a difference of 100 mV can be sufficient to drive a galvanic couple.

It must be remembered that electrochemical potential is a thermodynamic quantity and as such, in corrosion terms, is really only an indication of what might take place. It is difficult to see that this potential difference alone is responsible for the improved corrosion resistance. For example in the studies cited, alloys containing Ce additions where the potential difference between Mg and Ce is 110 mV according to table 11, did not always corrode at a low rate, whereas Y additions improved the corrosion resistance significantly, although there is no potential difference between Mg and Y. It should be

Table 11
Standard electrode potentials for various alloying additions to Mg (Vanysek 1990–91)

Element	Standard potential (Volts)
Zn	−0.76
Al	−1.66
Y	−2.37
Mg	−2.37
Nd	−2.44
Pr	−2.46
Ce	−2.48
La	−2.52

remembered, when assessing arguments based on potential data, that values of standard electrode potentials appear to vary widely depending on the source of the data.

Chang et al. (1989) have used this electrode potential argument differently. They believe that because the potential differences between the R rich phases and the Mg matrix are negligible, the driving force for galvanic interaction between the two is very low and therefore these alloys are less susceptible to corrosion. However, neither argument carries much weight without any knowledge of the actual electrode potentials of R rich intermetallic phases. Clearly, these will not be the same as the R elements listed in table 11.

On the evidence available, the most plausible reason for the improved corrosion resistance associated with R additions to Mg alloys is the formation of a protective film on the surface. The polarization data of Krishnamurthy et al. (1986, 1988b,c) for Mg–Nd, Mg–Y and Mg–Zn–R alloys, which show the presence of a pseudopassivation region at high anodic potentials, together with SEM and EDAX evidence indicate that during corrosion a R oxide film develops on the surface of the alloy. This strongly suggests that this film could be responsible for the reduction in corrosion rates observed. This view is supported by several authors (Hehmann et al. 1988, Chang et al. 1986). Protective films formed on Mg–Nd and M–Y alloys, observed by Krishnamurthy et al. (1988b), consisted of an outer layer of $Mg(OH)_2$, beneath which was another film, rich in both Mg and the R element. A similar observation has been made by Makar et al. (1988) who studied a corroded RSP Mg–Al alloy. Using surface analyses, they found an outer layer of MgO covering a mixed film of Mg and Al oxide.

There has been some speculation in the literature as to how this protective film forms. Hehmann et al. (1989) have studied the corrosion behaviour of RSP spun ribbon Mg–Al alloy in 0.001 M NaCl solution; increasing the Al concentration to 23% decreased the corrosion rate by two orders of magnitude. By analyzing the composition of the test solution with respect to time, they found that early in the test Mg dissolved, but this ceased after a few minutes. However, with the same Mg–Al alloy, prepared by a non RSP technique, Mg continued to dissolve. Hehmann et al. (1989) conclude that the improved

corrosion resistance of the Mg–Al alloy was due to the formation of an Al enriched surface layer with better corrosion resistance than Mg. They have extended this theory to the case of the R containing alloys (Hehmann et al. 1988), suggesting that the less noble R rich second phase particles are dissolved from the surface, upon exposure to the environment, leaving a surface depleted in R which is more resistant to corrosion. They have also suggested that the dissolution of the R rich phases may be followed by deposition of a R oxide film which inhibits further corrosion; a corrosion protection mechanism similar to that proposed for the inhibition of aluminium alloys in solutions containing R salts (Hinton et al. 1984).

The SEM/EDAX results of Krishnamurthy et al. (1988b) may well be consistent with such a mechanism. However, a more complete study using surface analysis techniques such as Auger or X-ray photoelectron spectroscopy and progressive sputtering through the film is needed to confirm these ideas. Observations by Krishnamurthy et al. (1988b) of a R rich layer closer to the substrate alloy could also be consistent with a gradual attack of R rich phases in the microstructure, followed by precipitation of the R oxide on a sufficient scale to eventually reduce the corrosion rate (corresponding to the onset of pseudopassivation). The observation that pseudopassivation was not observed with alloys produced by conventional ingot metallurgical processes may be due to the inhomogeneous distribution of large R rich phases producing insufficient coverage of the protective film on a microstructural scale. Such an explanation is also consistent with the observation that the heat treatment of Mg–Nd alloys (Krishnamurthy et al. 1988b) produced a greater pseudopassivation effect when compared with the non-heat-treated alloys. Heat treatment produces a fine dispersion of R rich particles.

Krishnamurthy et al. (1988b) observed, that R element type and concentration both affect the potential at which pseudopassivation occurs, and also the value of the current density in the pseudopassivation region. The magnitude of both these parameters will be determined by the nature of the R oxide formed, its ionic or electronic conductivity and the solubility product of the oxide which will govern the kinetics of precipitation.

The R additions appear to have a beneficial effect on the corrosion resistance of Mg alloys. However, at present it is not entirely clear how these additions are involved in producing these effects. Further systematic studies, particularly involving surface analysis techniques, are required.

3.2. *Aluminium alloys*

3.2.1. *Introduction*

The demands by the aerospace industry for light-weight materials with better high-temperature strength, creep resistance and stiffness has renewed interest in the further development of aluminium alloys. High-temperature strength and stability are typically associated with microstructures consisting of a fine dispersion of stable, incoherent intermetallic particles in the ductile Al matrix (Frazier et al. 1989). These dispersions inhibit grain growth at high temperatures and impede the movement of dislocations. Microstructures have been developed by using alloying elements which have low solid

state solubility and diffusivity in Al and a low liquidus temperature (Towner 1985). The most suitable alloying elements are the transition metals and the R metals (Mondolfo 1979). Low solubility and diffusivity ensures the precipitation of a large volume fraction of relatively small intermetallic particles when rapidly cooled, and a low liquidus temperature allows easier processing. However, the slow cooling rates associated with conventional ingot casting techniques produce macrosegregation with coarse primary intermetallic phases, resulting in microstructures which have poor strengths both at low and high temperatures. Rapid solidification processing (RSP), powder metallurgical (PM) techniques and mechanical alloying are now used to produce the more desirable microstructures (Jha et al. 1989). Not only must these light-weight alloys have good high-temperature properties but also good corrosion resistance. As with Mg alloys, the improved corrosion resistance of Al alloys has yet to be investigated in any systematic manner.

3.2.2. *Aluminium–iron–rare earth alloys*

Khobaib and Kirchoff (1985) have studied the corrosion behaviour of a commercially produced Al–8.4 to 8.9%Fe alloy with Ce additions in NaCl solutions. These alloys produced by the Alcoa Company using RSP and PM techniques were fabricated by extrusion (Angers et al. 1987). They had microstructures containing small intermetallic particles of Al_6Fe, $Al_{13}Fe_4$ and $Al_{10}Fe_2Ce$ finely dispersed in a solid solution matrix (Angers et al. 1987, Frazier et al. 1989). Khobaib and Kirchoff used a polarization technique to study the effects of Ce concentration on I_{corr}. The data in fig. 35 indicate that by increasing the Ce concentration up to 7%, the I_{corr} is reduced by a factor of 5. Values of E_{pit} taken from the published polarization curves are also plotted in fig. 35. With increasing Ce concentration, a corresponding increase in E_{pit} is noted. This is consistent with the increase in corrosion resistance as indicated by a decrease in corrosion current. Unfortunately, no data are available for the Al–Fe alloy without Ce. However, an extrapolation of data to zero Ce concentration indicates an E_{pit} of around −800 mV SCE. When this value is compared with an E_{pit} of −720 mV SCE for cast 99.99% Al determined

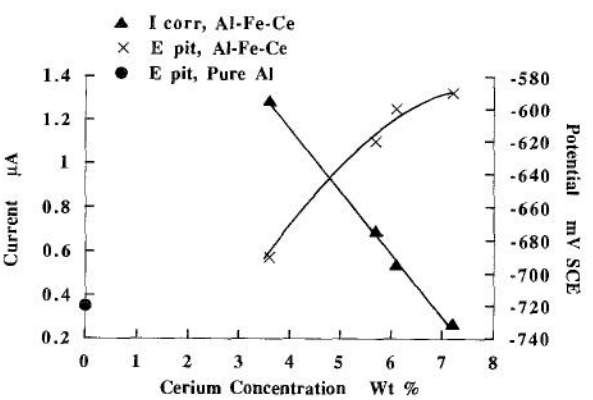

Fig. 35. The effect of Ce concentration on the corrosion current and pitting potential of an Al–Fe–Ce alloy in NaCl (after Khobaib and Kirchoff 1985).

in 0.1 M NaCl (Khobaib and Kirchoff 1985), it would appear that the binary Fe rich dispersoids may serve to reduce the pitting potential and therefore, pitting resistance, while additions of Ce improve it.

Langenbeck et al. (1986) have tested the same Al–Fe–Ce alloys in aerated and de-aerated 3.5% NaCl solution for 16 days, and observed somewhat different trends. The corrosion rates were very low and the results mixed. Tests in the aerated solution with increasing Ce concentration (from 3.7 to 6.9%) increased the corrosion rates from 0.25 to 0.6 mpy, while in the de-aerated solution the corrosion rate decreased from 0.5 to 0.4 mpy. From the available data it is difficult to assess the reasons for these differences. Data obtained by Khobaib and Kirchoff would have been collected over a short test period, perhaps minutes, whereas Langenbeck et al. exposed the same alloys to 0.1 M NaCl for 16 days. Quite possibly, any beneficial effects of the Ce additions may only be short lived.

Fass et al. (1987, 1988a) and Fass and Eliezer (1989) have used polarization tests to study the corrosion behaviour of a melt spun ribbon of Al–8%Fe alloy with and without additions of 4%Er, in 3.5% NaCl solution. They found that the presence of Er lowers E_{pit}, increases I_{pass} in the passive range, and reduces ΔE (the difference between E_{corr} and E_{pit}), when compared to the Al–8%Fe alloy. These results indicate that Er additions reduce the corrosion resistance of the Al–Fe alloy.

From the three sets of data cited above, it would seem that the effects of R additions on the corrosion behaviour of an Al–Fe alloy are far from clear. The very low corrosion rates (Khobaib and Kirchoff 1985, Langenbeck et al. 1986) for the Al–Fe alloys relative to other structural aluminium alloys such as 7075 and 2024 make it difficult to identify any significant effects of R additions.

3.2.3. *Aluminium–rare earth alloys*

Using polarization techniques, Fass et al. (1987, 1988a,b), Eliezer et al. (1988) and Fass and Eliezer (1989) have investigated the effects of Er additions to Al at various concentration levels, the influence of the RSP cooling rate and the subsequent heat treatment temperature on the corrosion behaviour in 3.5% NaCl solution. Figure 36 shows replotted polarization data for an as cast (slow cooling rate) and a melt spun RSP (fast cooling rate) Al–11%Er alloy (Fass et al. 1988a). Also plotted are data obtained by Hinton et al. (1986) for 99.99% pure as cast Al tested in 0.1 M NaCl solution. These data indicate that, in the as-cast condition, the addition of 11% Er has a detrimental effect on the corrosion resistance of Al. The presence of Er reduced E_{pit} and increased I_{pass}. However, for the RSP alloy, E_{pit} was increased by 150 mV, thus indicating an improvement in corrosion resistance. Fass and Eliezer (1989) also found that different R additions at a concentration of 11% had a small but significant effect on the pitting potential. E_{pit} for additions of Ce, Sm, Gd, and Er were −630, −590, −575 and −570 mV SCE, respectively. They also found that any beneficial effects of Er were unchanged by increasing Er concentration between 1 and 11%. However, heat treatment of the RSP Al–11%Er alloy for 2 hours at 500°C, reduced E_{pit}, decreased ΔE and increased I_{corr} (Fass and Eliezer 1989); all indications of reduced corrosion resistance.

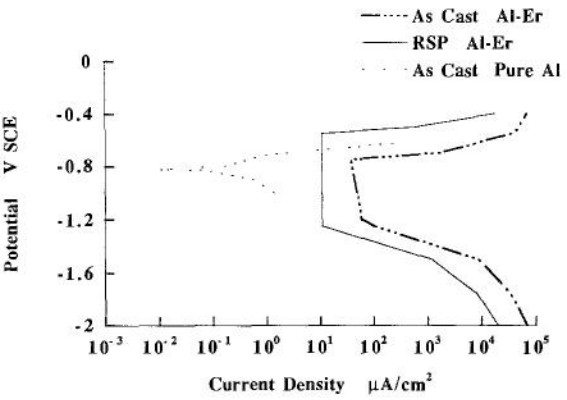

Fig. 36. Polarization data for a cast and a RSP Al–11%Er alloy in 3.5% NaCl (after Fass et al. 1987) and for cast pure Al in 0.1 M NaCl (after Hinton et al. 1986).

RSP Al–Er alloys possess an almost featureless microstructure consisting of a very fine distribution of Al_3Er intermetallic particles in aluminium solid solution matrix (Savage et al. 1986). In contrast, the as-cast alloy has a dendritic network of intermetallic phases throughout the solid solution (Fass et al. 1987, 1988a,b, Fass and Eliezer 1989). Heat treatment (500°C) of the RSP samples, results in a coarse non-uniform dispersion of intermetallic particles throughout the solid solution matrix (Fass and Eliezer 1989). These differences in microstructure were reflected in the different forms of corrosion attack after polarization in the NaCl solution. Pitting was light and only slightly localized on the RSP alloy, whereas on the as-cast, and heat treated (500°C) samples, the attack was deeper and more localized. This suggests that the increased corrosion resistance of the RSP Al–Er alloys is associated with the more homogeneous microstructure.

Auger electron spectroscopy carried out on the surfaces of the Al–Er samples before and after the polarization testing (Eliezer et al. 1988, Fass and Eliezer 1989) revealed that before testing, the surface of the Al–11%Er alloy was almost entirely covered with Al_2O_3 to a depth of about 4 nm. After corrosion testing, the thickness of the oxide layer was around 30 nm and it was a mixed oxide of Al and Er, with Er concentrated near the oxide–metal interface. This observation is similar to that described earlier for Mg–Nd RSP alloy after polarization tests in chloride solution (Krishnamurthy et al. 1986, 1988b,c).

3.2.4. *Mechanisms of corrosion resistance*

There are many similarities between the corrosion behaviour of the RSP R containing Al alloys and Mg alloys. From the evidence available it is difficult to determine if the addition of Ce to the Al–Fe alloys improves corrosion resistance. Limited data for Al–R alloys suggest that R additions, in particular Er, can produce a small increase in corrosion resistance.

If the improvement in the corrosion performance of the RSP Al–Er alloy is due solely to Er, a dissolution and deposition mechanism may be responsible. During anodic polarization, the intermetallic phases would very likely be selectively attacked, as suggested by an examination of the standard electrode potentials for Er (–2.296 V)

and Al (−1.66 V). Hence, the small improvement in corrosion resistance, for the RSP Al–Er alloy, as shown by an increase in E_{pit}, may be the result of an Er rich film (as observed by Eliezer et al. 1988 and Fass and Eliezer 1989) forming on the surface during the early stages of polarization.

If a mechanism described by Hinton et al. (1984), analogous to that which provides protection for 7075 Al alloy immersed in a solution containing R metal salts applies, as the Er rich dispersoids dissolve, and the pH level near the surface increases, an hydrated Er oxide will precipitate onto the metal surface. The observations that the respective corrosion resistances of the as-cast and the RSP heat treated Al–Er alloys were less than that for the RSP alloy could be related to the non-uniform coverage of the surface by a passive film of hydrated Er oxide, a situation attributed to the non-homogeneous distribution of the coarse intermetallic Er rich phases. A finer, more chemically homogeneous microstructure in the RSP alloy would be expected to give a higher density of initial sites for localized corrosion of the intermetallic particles, and thus a more uniform coverage by the passive film.

3.3. *Zinc alloy coatings*

Zinc based metallic coatings (e.g. galvanizing) have been used for some time to provide corrosion protection for steel substrates. The basis of this protection is due firstly to the sacrificial protection afforded by the zinc coating to the steel substrate, and secondly to the slower rate of zinc corrosion compared to that of the steel.

While these coatings may provide adequate protection in most environments, they do not always perform well in very aggressive marine and industrial environments or at high temperatures (Zoccola et al. 1978). Some of these deficiencies have been overcome by alloying the Zn with Al.

The Bethlehem Steel Co. have developed a commercial hot dip coating called Galvalume which consists of Al–43.4Zn–1.6Si (Zoccola et al. 1978). This coating has been found to provide 2 to 5 times the level of protection provided by galvanized coatings in a range of atmospheric environments (Zoccola et al. 1978). Further research with these alloyed coatings has seen the development of a coating containing Zn–5%Al (Hubrecht et al. 1985). This coating is attractive especially for production because it has a melting point 200°C lower than Galvalume, and better fluidity in the coating bath (Hubrecht et al. 1985). Additions of R elements such as La and Ce to the Zn–5%Al have been found to provide better wetting of the steel substrate during dipping, and hence, a more uniform coating thickness (Weinberg et al. 1990). The commercial coating (known as Galfan) contains Zn–5%Al–0.001%La–0.001%Ce and its corrosion protection performance is far superior to both galvanized and Galvalume coatings in both laboratory salt spray and outdoor marine environments (Hubrecht et al. 1985).

There have been no systematic studies to determine the role, if any, of the R additions for improving the corrosion performance of Galfan. The data collected from several sources and presented in table 12 show some interesting trends. The times for red rust to appear on steel panels coated with the Zn–5%Al and the Zn–5%Al–R alloys after

Table 12
Time to rust in the ASTM B 117 salt spray test for Zn–Al coatings on steel substrates

Coating	Time to rust (hours)	
	Coating thickness 25 μm	Coating thickness 35 μm
Zn–5%Al[a]	750–1000	1033–1377
Zn–5%Al + R[b]	900–1190	1220–1520

[a] Zoccola et al. (1978)
[b] Hubrecht et al. (1985)

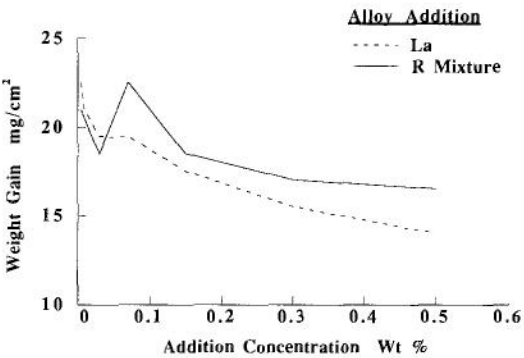

Fig. 37. Weight gain of a Zn–27%Al as a function of both La and mixed R additions in water at 95–100°C (after Rongzhang et al. 1987).

testing in a salt spray to ASTM B-117, suggest that even allowing for the scatter, the presence of a small amount of R improves the corrosion performance at both coating thicknesses. These results are consistent with data reported by Rongzhang et al. (1987), who investigated the corrosion behaviour in water at 95–110°C of a Zn–27%Al alloy with additions of La or unspecified R's (10 days exposure). The data shown in fig. 37 indicate a small but well defined reduction in corrosion rate as the concentration of the R addition was increased.

Weinberg et al. (1990) have studied the segregation of elements in the Galfan coating using Secondary Ion Mass Spectrometry. They found a continuous layer of aluminium oxide at the surface of the Galfan coating. While the R elements were distributed throughout the metallic coating, there was a higher concentration in the aluminium oxide layer. Further work is required on specimens exposed to corroding environments to determine the role, if any, of the R elements in the improved corrosion performance of the Galfan coating.

3.4. *Steels*

Small concentrations of R elements, in particular Ce, may be added to steels to modify the size and shape of nonmetallic inclusions, particularly manganese sulphides, and thus improve the mechanical properties (Poole and Franklin 1978). However, only a few studies have examined the effects of these additions on the corrosion behaviour.

Various publications have concluded that the presence of the R's contribute to an improvement in corrosion resistance. Zhenyuan et al. (1987) have found that 0.055% unspecified R added to a carbon steel improved the resistance to atmospheric corrosion. They concluded that the R stabilized the magnetite scale in the presence of moisture. Popov (1981) observed that the addition of 0.07% Ce to a 26% Cr steel reduced its rate of corrosion by a factor of 2 when exposed to a range of severe industrial environments for 5000 hours. The improvement in corrosion resistance with Ce addition was associated with refinement and spheroidization of the carbides and nitrides in the microstructure. Vyazovikina et al. (1990) have studied the corrosion behaviour in 0.5 M H_2SO_4 of a ferritic Fe–Cr–Al alloy with and without the addition of 0.5% La. The La was present in the microstructure as La_2O_3 particles and La-containing carbides in the grain boundaries. In Fe–Cr alloys, the Cr produces a passive Cr oxide film on the steel surface. Vyazovikina et al. showed, using polarization tests, that the La addition improved the level of passivation due to the Cr and thereby improved the corrosion resistance. They concluded, from surface analysis, that during exposure to the H_2SO_4 solution, the La preferentially dissolved from the grain boundaries and that this facilitated the transport of Cr into the Cr oxide passive surface layer, thereby increasing the corrosion resistance.

Unfortunately, in some of the studies cited, the elemental analysis of the steels containing the R additions were different from those of the control steels with no R addition. In many instances these differences in composition may well have had a greater influence on corrosion behaviour than the R addition. It is difficult to determine whether or not the changes in corrosion behaviour are associated solely with the presence of the R's. Fundamental and systematic studies of the effects of R additions on the corrosion behaviour of Fe based alloys, combining surface analyses before and after corrosion testing, would be beneficial if only to indicate whether or not the formation of a R oxide film on the surface was playing a role in improving corrosion resistance.

3.5. *Copper alloys*

Copper and copper alloys are extensively used in a wide range of environments because of their good natural corrosion resistance. The aluminium bronzes (Cu–5 to 12%Al) combine excellent strength with good overall corrosion resistance. Recently, the addition of R elements such as Ce, La, and Nd have been found to improve the machinability of these alloys (Kumar and Sharan 1979).

Extensive studies of the corrosion behaviour of a Cu–9%Al alloy containing various additions of R's have recently been carried out by Singh et al. (1989) and Verma et al. (1990). The corrosion rate data obtained by Singh et al. with tests in 1% HNO_3 solution are shown in fig. 38. These data indicate that after immersion for 48 hours in 1% HNO_3, small concentrations (~0.05%) of R elements in Cu–9%Al promote a reduced rate of corrosion. However, at R concentrations significantly $> 0.05\%$, the corrosion rates approach those obtained in alloys without any R additions. Verma

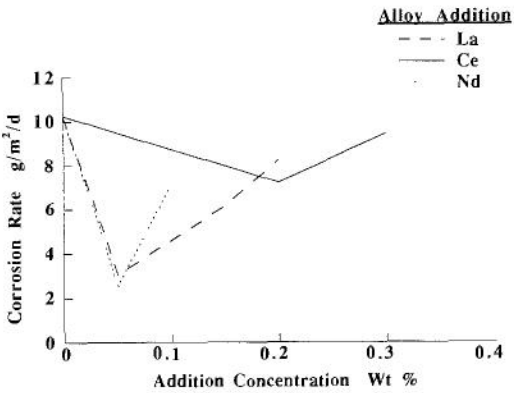

Fig. 38. Corrosion rates for a Cu–9%Al in 1% HNO_3 as a function of R alloying additions (after Singh et al. 1989).

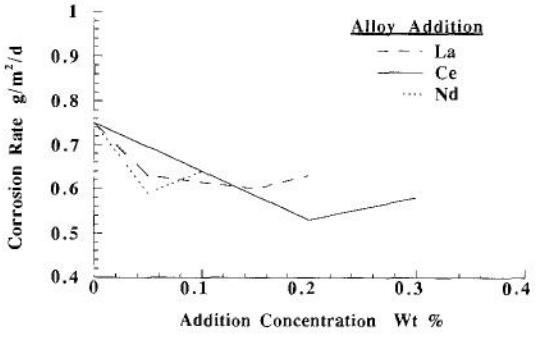

Fig. 39. Corrosion rates for a Cu–9%Al in 1.7% H_2SO_4 as a function of R alloying additions (after Verma et al. 1990).

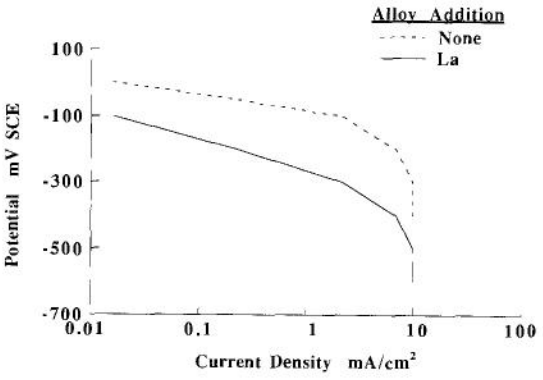

Fig. 40. Cathodic polarization data for a Cu–9%Al alloy with and without 0.05%La in 1% HNO_3 (after Singh et al. 1989).

et al. (1990) tested the same alloy in 1.7% H_2SO_4. Their results, shown in fig. 39, again indicate that small additions of R elements effectively reduce rates of corrosion. However, the reductions in corrosion rate in H_2SO_4 solution are not as large as those in 1% HNO_3 solution.

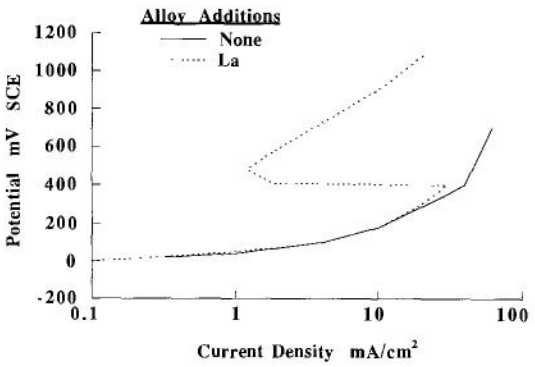

Fig. 41. Anodic polarization data for a Cu–9%Al alloy with and without 0.05%La in 1% HNO_3 (after Singh et al. 1989).

Cathodic polarization data, obtained after a stabilizing period at the corrosion potential, indicated that small concentrations (0.05%) of the R's decreased the rate of the cathodic reaction by up to two orders of magnitude. Figure 40 is a typical example of data obtained with tests in both acid solutions. At low cathodic polarization potentials i.e. < -300 mV, the data are coincident as oxygen reduction becomes the dominant cathodic reaction. At potentials more positive than -300 mV, the presence of La decreases the rate of the cathodic reaction. Anodic polarization data (see fig. 41 as a typical example for both acid solutions), obtained with alloys containing low concentrations of R's, showed similar trends to the data obtained for Mg–Nd alloys (Krishnamurthy et al. 1988a–c). At high anodic polarization ~400 mV SCE, the test surface becomes passivated and the current density reduced by an order of magnitude.

The similarities between the Cu alloy data and those obtained with the Mg–R binary alloy, encourages speculation about possible mechanisms of inhibition. The Cu–Al alloy, produced as described by Singh et al. (1989), would have a duplex microstructure consisting of $\alpha+\gamma$ eutectoid phase distributed in a solid solution α matrix (Polin 1987). This eutectoid is normally very susceptible to corrosion (Polin 1987). Because the solubility of the R's in copper is generally quite limited (Hawkins and Hultgren 1973), during solidification the R elements would be expected to segregate in and around the eutectoid phase. Over the 48 hour period of immersion before cathodic polarization, a dissolution and precipitation process may have occurred such that a R rich oxide or hydroxide is formed on the electrode surface. During subsequent polarization, the presence of the oxide or hydroxide could have the effect of reducing the rates of cathodic reactions. Likewise, during anodic polarization, these segregated R rich regions of the microstructure would commence corroding. By a dissolution and precipitation mechanism, a R rich oxide film may tend to form on the surface and eventually cause the electrode to passivate with a two orders of magnitude reduction in current density. Of course, any R oxide would need to be insoluble at the pH of the test solution. The effects observed in both papers (Singh et al. 1989, Verma et al. 1990) warrant further investigation.

4. Corrosion control by surface modification

4.1. *Conversion coatings*

4.1.1. *Aluminium alloy substrates*

The ability for chromates to be reduced to chromium oxide and to thus form a protective film on metal surfaces is the basis for the conventional chromate conversion coating process (CCC). The use of a chromium oxide based film, as a protective coating or conversion coating (chromating), can be traced to the 1920's, when a process for zinc was developed (see Biestek and Weber 1976) for the metal finishing industry. Chromate conversion coatings are the standard pretreatment prior to painting for aluminium alloys, zinc, cadmium and magnesium. This conversion coating technology not only provides corrosion protection but also improves the adhesion of subsequent paint coatings.

Conversion coating processes produce a thin film of predominantly chromium oxide on metal surfaces. The colour of this film depends on the substrate metal, and may vary in colour, from pale-yellow to gold to dark-brown or black. Today, the most commonly used CCC process for aluminium, zinc and cadmium (Biestek and Weber 1976) is an acid treatment (pH 1–2), based on a two-part solution containing a source of hexavalent chromium ion, e.g. chromate, dichromate or chromic acid. The solution for treating aluminium alloys, generally contains fluoride ion, which assists in the dissolution of the original oxide film, and an accelerator, e.g. ferricyanide, to facilitate the formation of the chromium oxide (Biestek and Weber 1976).

One of the benefits of chromating is that the mixed (chromium/substrate metal) oxide coating provides better corrosion resistance than the natural substrate metal oxide alone. Additional corrosion protection is provided by chromate ions entrapped in the coating. These ions are readily leached from the coating and act as corrosion inhibitors. The ability of any CCC to improve the adhesion of paint coatings may be related to its cellular microstructure (Biestek and Weber 1976), which provides a base with more attachment points.

It has been recognized over the past 15 years that the continued use of chromate chemicals is undesirable because of their toxicity and carcinogenicity (US Public Health Service 1989). The obvious protective properties of the R oxides suggest that, once applied to a metal surface, they too should be able to act as a protective coating, in a manner similar to a chromate conversion coating.

4.1.1.1. *Immersion treatments.* Hinton et al. (1984, 1986) first investigated the application of this particular concept to the protection of Al alloy substrates. They immersed 7075 aluminium alloy specimens in a quiescent (open to air) 1000 ppm $CeCl_3$ solution for various times up to 161 hours. After immersion, the specimens were removed and washed in distilled water and polarization tests were carried out in 0.1 M NaCl. The data are shown in fig. 42. The most significant change observed with respect to immersion time was the shift of the cathodic half of the polarization data to lower current densities. After long term exposures, e.g. 161 hours, the rate of the dominant

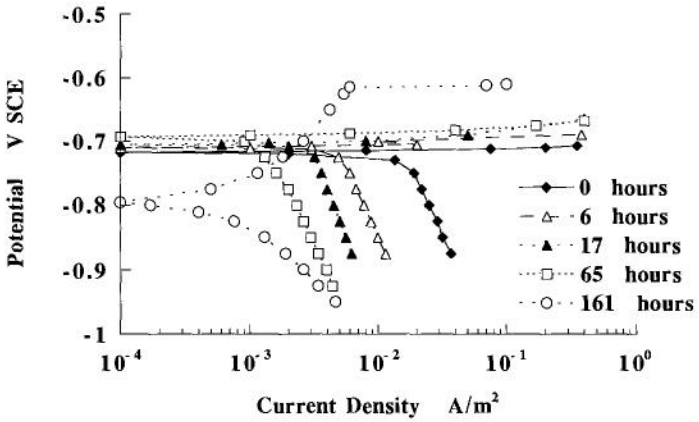

Fig. 42. Polarization data for 7075 Al alloy in 0.1 M NaCl after exposure to $CeCl_3$ solution for various times (after Hinton et al. 1986).

cathodic reaction, oxygen reduction, was markedly suppressed. This was associated with a significant reduction in I_{corr}. Also, E_{pit} increased by some 90 mV relative to that for the untreated specimen. Similar results have been observed for coatings produced in the same manner on an Al–1.8%Cu alloy and on pure aluminium (Hinton et al. 1986).

Auger analyses by Hinton et al. (1984, 1986) have shown that the coating produced on 7075 alloy by immersion in a solution containing 1000 ppm $CeCl_3 \cdot 7H_2O$ consists largely of hydrated Ce oxide (fig. 27). The Ce was thought to be in valency states 3 and 4. The analyses indicated that the coating was not of uniform thickness over the surface. The concentration of Ce in the coating increased with exposure time in the solution as the natural Al oxide film was replaced with the hydrated Ce oxide film. Mansfeld et al. (1991) have found that the coatings produced on 6061 alloy after immersion in 1000 ppm $CeCl_3$ contained a mixture of Al and Ce oxides to a depth of around 1500 Å. Clearly, the coatings produced by immersion in solutions of $CeCl_3 \cdot 7H_2O$ are based on Ce oxide, and the polarization data (fig. 42) suggest that a Ce oxide-based conversion coating, formed according to the mechanism identified in sect. 2.8 should have very good corrosion protection properties.

Wilson et al. (1993) produced such a Ce oxide coating on 7075 alloy weight-loss coupons by immersion in 1000 ppm $CeCl_3 \cdot 7H_2O$ solution for up to 200 hours. After subsequent immersion in 0.1 M NaCl for 7 days, the corrosion rate was only marginally less than that of the uncoated alloy, i.e. 5.7 cf. 6.4 $\mu g/m^2/s$. Moreover, the coated specimens were heavily pitted. Mansfeld et al. (1990b), using the same technique have coated various aluminium alloys and aluminium alloy metal matrix composites. The protective properties of the coating were then characterized by measuring the time at which corrosion pitting was first observed during immersion in 0.5 N NaCl. They found that immersion in 1000 ppm $CeCl_3$ for 7 days to exposure in the NaCl solution significantly prolonged the development of pitting (table 13).

Table 13
Times at which pits developed on aluminium alloys during immersion in 0.5 N NaCl after immersion in $CeCl_3$ solution for 7 days (after Mansfeld et al. 1990b)

Aluminium alloy	Surface preparation and time of immersion in $CeCl_3$ [a]	Time (days)
7075–T6	Deoxidize, 7 days	>24
6061	Deoxidize, 7 days	>3
6061 (30 days in $CeCl_3$)	Deoxidize, 30 days	>29
6061	Degrease, 7 days	>90
6061/SiC	Deoxidize, 7 days	>81
6061/graphite	Deoxidize, 7 days	>40

[a] Untreated specimens of all alloys pitted within 1 day after immersion in 0.5 N NaCl.

Mansfeld et al. (1990b) noted however that the performance of the coating depended on whether the substrate had been degreased or deoxidized in an acid based solution prior to immersion in the $CeCl_3$ solution (table 13). For example, degreasing of the 6061 alloy prior to immersion in the $CeCl_3$ solution rather than deoxidizing increased the time at which pitting was first observed from 3 to 90 days. Their deoxidizing process involves immersion in a nitric acid solution containing chromate inhibitor. Studies in the author's laboratory at ARL have shown that this deoxidizing treatment produces pits on the alloy surface associated with intermetallic particles in the microstructure. It is possible that these pits are again activated beneath the Ce oxide coating upon immersion in the NaCl solution. This could explain the improved performance of coatings formed in $CeCl_3$ on a degreased substrate observed by Mansfeld et al. (1990b).

Mansfeld et al. (1990a) also observed that immersion of a deoxidized 6061 alloy in $CeCl_3$ solution for 30 rather than 7 days, increased the time at which subsequent pitting was observed (from 3 to 29 days). Mansfeld et al. believe that with increasing time in $CeCl_3$ solution, the valency of Ce in oxide coating changes from predominantly 3^+ to 4^+. They consider the Ce 4^+ oxide to be the more stable of the two when immersed in NaCl solution.

For the pretreatment of 6061 Al alloy for 7 days in concentrations of different R chlorides between 10 and 30 mM, the subsequent reductions in rates of corrosion (fig. 43) were almost an order of magnitude less than the untreated 6061 and essentially independent of R chloride type and concentration (Mansfeld et al. 1991).

To overcome the lengthy and impractical periods of immersion, Mansfeld et al. (1991) and Mansfeld (1990) have developed a process, based on immersion, but including an anodizing step and much shorter treatment times. This process involves immersion in 5 mM $CeCl_3$ solution at 100°C for 2 hours followed by immersion in 5 mM $Ce(NO_3)_2$ solution at 100°C for 2 hours, then anodic polarization in de-aerated 0.1 M Na_2MoO_4 solution at +500 mV SCE for 2 hours. After applying this procedure to a deoxidized 6061 alloy specimen and then holding at 100°C in high humidity for 24 hours, a mixed oxide coating containing Al, Ce and small amounts of Mo (concentrated near the

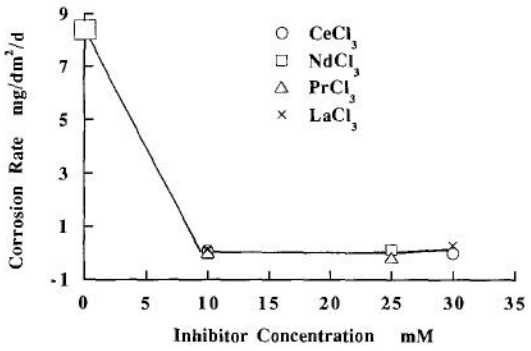

Fig. 43. Corrosion rates for 6061 Al alloy in 0.5 N NaCl with concentration of various R chlorides (after Mansfeld 1990). Negative values correspond to a weight gain.

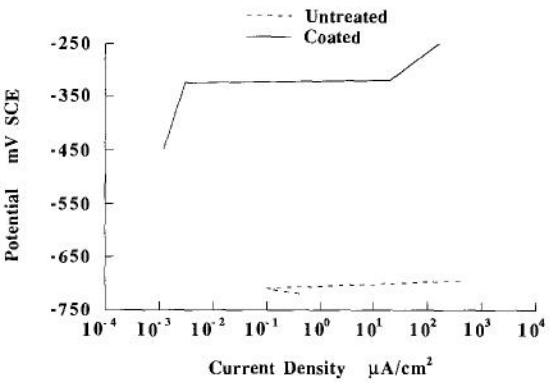

Fig. 44. Anodic polarization data for 6061 Al alloy in 0.5 N NaCl, untreated and coated by treating in $CeCl_3$, $Ce(NO_3)_3$ and Na_2MoO_4 (after Mansfeld 1990).

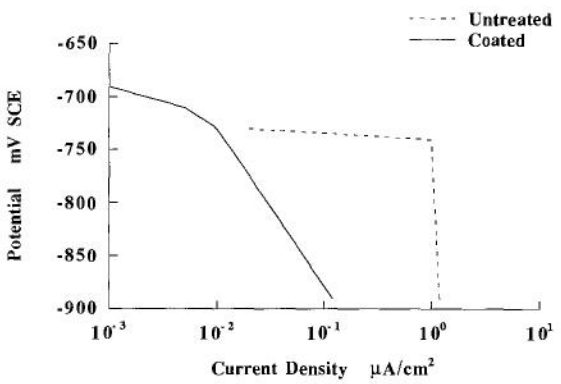

Fig. 45. Cathodic polarization data for 6061 Al alloy in 0.5 N NaCl, untreated and coated by treating in $CeCl_3$, $Ce(NO_3)_3$ and Na_2MoO_4 (after Mansfeld 1990).

outer layers of the film), developed on the surface. Subsequent exposure of the coated specimen in 0.5 N NaCl did not induce any pitting corrosion until after 60 days immersion (Mansfeld 1990). Uncoated 6061 specimens exposed to the same environment pitted within one day of immersion.

Figures 44 and 45 are polarization curves, obtained by Mansfeld (1990) for the 6061 alloy tested in 0.5 N NaCl solution with and without the R oxide coating. Anodic polarization data (fig. 44) indicate that when the coating is present the surface remains passive with increasing potential until around –320 mV when pitting occurs. By comparison the E_{pit} for the untreated specimen is close to E_{corr} at around –710 mV SCE. The presence of the coating also has a marked effect on the cathodic polarization curve fig. 45, reducing the rate of the cathodic oxygen reduction reaction by at least a factor of 10. Similar effects on both the anodic and cathodic reaction kinetics were earlier observed by Hinton et al. (1984). Both sets of data (Mansfeld 1990, Hinton et al. 1984) indicate that these R oxide coatings protect the Al surfaces from corrosion by inhibiting both halves of the corrosion reaction. Wilson and Hinton (1988) have now developed an immersion process which produces a R oxide coating on different metal substrates in minutes, rather than hours. It has been shown to be capable of protecting aluminium alloy surfaces from corrosion in strong chloride environments, and offers significant potential as a replacement for the chromate conversion coating.

4.1.1.2. *Cathodic deposition of the R oxide coating.* Hinton et al. (1986) have investigated the use of electrodeposition to reduce the times required to produce the Ce oxide coating. As described in sect. 2.6, these cerium oxide coatings are thought to be produced by a cathodic deposition mechanism. Hinton et al. (1986) reasoned that by cathodically polarizing the aluminium alloy substrate, the deposition of these oxide films could be accelerated. By polarizing galvanostatically, in 1000 ppm $CeCl_3 \cdot 7H_2O$ solution at current densities between 0.1 A m^{-2} and 2.8 A m^{-2} for 30 minutes, coatings were produced on a 7075 aluminium alloy substrate. These were found to contain mixtures of Ce and Al oxides to a depth of around 150 nm. While these coatings provided some short term protection to the substrate when immersed in a 0.1 M NaCl solution, they eventually failed because of small hemispherical defects in the film. These defects were thought to be associated with the R oxide precipitating over surfaced trapped hydrogen bubbles, which were simultaneously being evolved at the surface. They persisted even when the specimens were polarized at lower current densities (Hinton et al. 1986).

Hinton et al. (1987) have successfully produced, in 2–3 minutes, a Ce oxide coating on 7075 alloy by electrodeposition at high DC potentials (40–50 V). The electrolytes used were organic solvents such as butoxyethanol containing 10 000 ppm $CeCl_3$. XPS analysis (fig. 46) showed that the coatings consisted of a mixture of Ce and Al oxides to a depth of around 300 nm. Polarization studies (Hinton et al. 1986) show that these coatings could provide good corrosion resistance in NaCl solution. Their results indicate that the coating had a marked effect on the kinetics of the cathodic reaction (fig. 47). With increasing treatment time the cathodic curve was moved to lower current densities, indicating that the rate of the oxygen reduction reaction was being reduced. This had the effect of moving the E_{corr} away from the E_{pit} into the passive region for aluminium in this solution. The resultant gap between E_{corr} and E_{pit} was almost 250 mV SCE after an application time of 120 seconds.

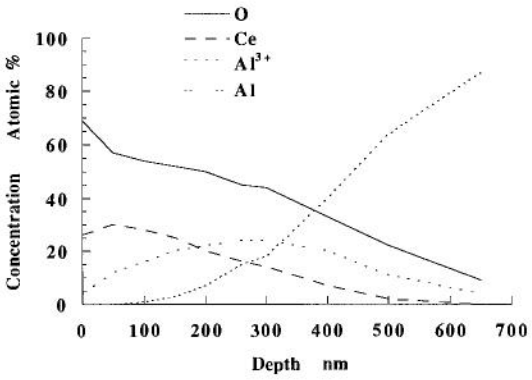

Fig. 46. X-ray photoelectron spectroscopy profiles of atomic concentration as function of sputter depth for 7075 Al alloy after cathodic treatment at 40 V for 150 s in butoxyethanol containing 10 000 ppm $Ce(NO_3)_3$ (after Hinton et al. 1987).

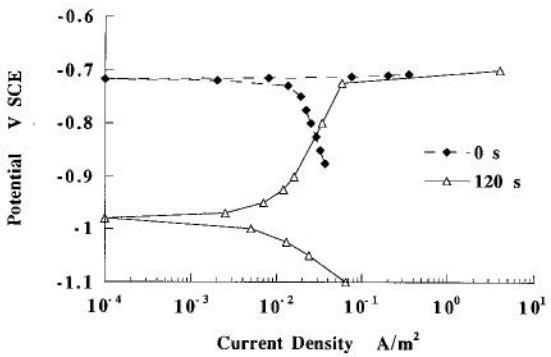

Fig. 47. Polarization data for 7075 Al alloy in 0.1 M NaCl after cathodic treatment at 50 V for 120 s in butoxyethanol containing 10 000 ppm $Ce(NO_3)_3$ (after Hinton et al. 1986).

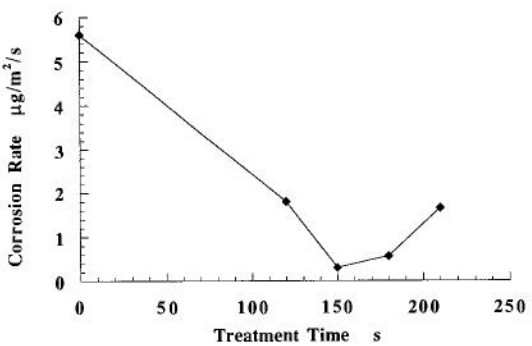

Fig. 48. Corrosion rate of 7075 Al alloy in 0.1 M NaCl, with treatment time at 40 V in butoxyethanol containing 10 000 ppm $Ce(NO_3)_3$ (after Hinton et al. 1986).

Corrosion rate data from weight-loss measurements shown in fig. 48 were obtained after immersing coated 7075 alloy specimens in 0.1 M NaCl solution for 3 weeks. These data indicate that a reduction in corrosion rate by a factor of 10 results from a treatment time of 150 s. With longer treatment times, the performance of the coating is not as good. This is attributed to a general thickening of the coating and associated cracking and spalling.

Although this coating was effective in protecting the surface of aluminium alloy from corrosion, the coating technique does present certain safety risks, most notably the use of volatile organic solvents and high DC voltages.

4.1.2. *Zinc substrates*

Hinton and Wilson (1989) have produced coatings on zinc and galvanized steel specimens by immersion in a solution of 1000 ppm $CeCl_3$ for 24 days or by heating the Zn substrate to 400°C and then quenching it into the same solution. Both techniques produce a thin transparent yellow film on the surface and on exposure to a 0.1 M NaCl solution for 21 days, the specimens corrode at a rate 25% less than the rate for untreated specimens.

4.2. *Summary*

The results obtained by both Mansfeld et al. and Hinton et al. are encouraging and suggest that a conversion coating based on a Ce oxide could be an attractive alternative to the chromate conversion coatings widely used to protect aluminium and zinc. However, as a practical commercial process, treatment times would need to be of the order of minutes, and the corrosion protection performance would need to be similar to that provided by the chromate conversion coating.

5. Corrosion control through exclusion of the environment

5.1. *Pigments in paint coatings*

The most common form of corrosion control is through the application of a paint coating. Most paint coatings have a dual role. Firstly, they introduce a barrier between the corrosive environment and the metal substrate and secondly, by incorporating partially soluble pigments, they provide corrosion inhibition. The most common and widely used inhibiting pigments are chromates. The suggestion to use them in paints was first recorded by Cushman (1907). McCloud (1931) later showed that zinc chromate pigment enhanced the corrosion protection performance of a phenolic resin varnish applied to aluminium, when tested under salt spray conditions.

When a chromate-containing paint is exposed to moisture, the chromate ions leach from the coating through to the substrate metal, where they are reduced to form a protective chromium oxide film. The most common inhibiting pigments used in primer paints are the slightly soluble salts of zinc, barium and strontium; they provide leachable chromate at a slow, controlled rate.

The restrictive laws relating to health and environment, which have brought about pressure to discontinue the use of chromate ions as inhibitors and in conversion coatings, are also forcing paint manufacturers to consider alternative corrosion inhibiting pigments in paint systems. The overall performance of R salts as corrosion inhibitors (described in

sect. 2), suggests that these compounds do have the potential to be used as alternatives to chromates, as inhibiting pigments in paints.

5.2. *Rare earth salts as pigments in paint coatings*

Baldwin et al. (1990) have investigated the protective effects of $Ce_2(MoO_4)_3$ or a mixture of $Ce_2(MoO_4)_3$ and $Ce_2(SO_4)_3$ added to epoxy polyamide primer paints at concentration levels similar to those used for chromate pigment. This is typically 20% by weight. They applied the primer (12–18 μm dry film thickness) to 2014 aluminium alloy panels and exposed the panels to 3 different environments:

(i) wet/dry cycle in 3% NaCl – 2 hours in solution and 2 hours in 80% RH air at 35°C;
(ii) wet/dry cycle in 3% NaCl buffered to pH = 8 – 2 hours in solution and 2 hours in 80% RH air at 35°C;
(iii) wet/dry cycle in 3% NaCl salt fog – 2 hours in the fog and 2 hours in air at 35°C.

The total period of exposure for each test was 1000 hours. After exposure of the panels, any corrosion damage beneath the paint coating was identified and rated on a scale of 0–9, with 9 being heavy corrosion. The distance corrosion had penetrated laterally from any through-thickness-scribe made in the paint was also measured. The results obtained are shown in figs. 49 and 50. These data include results for the same primer containing either TiO_2 as the control pigment, and Sr_2CrO_4 as a standard corrosion inhibiting pigment.

In all environments, none of the Ce salt pigments performed as well as the Sr_2CrO_4 additions. However, the results are significantly better than those with the control coating. Corrosion protection afforded by paint coatings containing leachable inhibitor pigments relies on the inhibitor being freely available at the substrate. The addition of the more soluble $Ce_2(SO_4)_3$ with the $Ce_2(MoO_4)_3$ did not make any significant difference to the corrosion protection performance (figs. 49, 50). The performance of inhibiting pigments also relies on the inhibitor being effective at low concentrations. Thus, chromates remain more effective inhibitors for aluminium at lower concentrations than the Ce salts (Baldwin et al. 1987).

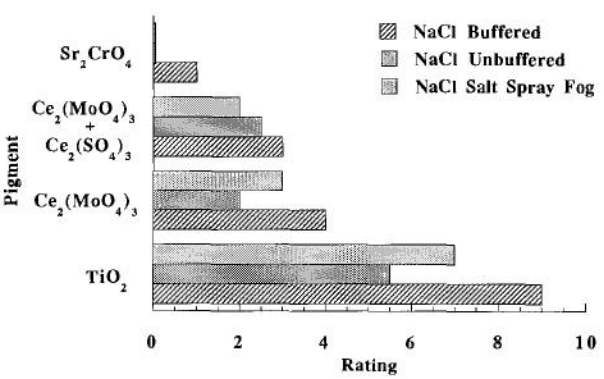

Fig. 49. Corrosion ratings for 2014 Al alloy panels coated with an epoxy polyamide paint containing various pigments, after exposure to three different NaCl environments. The higher ratings indicate a poor performance. (After Baldwin et al. 1990.)

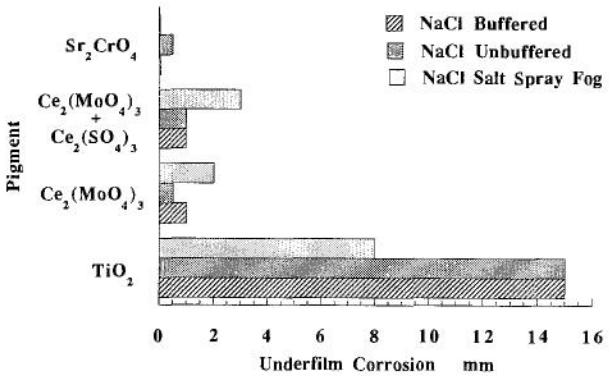

Fig. 50. The penetration distance of underfilm corrosion on 2014 Al alloy panels, from a scribe through an epoxy polyamide paint coating containing various pigments, after exposure to three different NaCl environments (after Baldwin et al. 1990).

Underfilm corrosion is understood to be driven by cathodic reactions such as oxygen reduction occurring at the exposed paint–metal interface. Thus, the better performance of the R pigments in the underfilm tests is likely associated with the ability of R salts to inhibit the cathodic reaction in the vicinity of the through-thickness-scribe, through the formation of an oxide or hydroxide. Consequently, the rate of dissolution (penetration) beneath the coating is much reduced.

5.3. *Rare earth salts adsorbed on other pigments in paint coatings*

Controlled release of inhibiting ions from pigments will always be a problem for paint formulators. Unfortunately, commonly available R compounds are either very soluble or completely insoluble. Therefore, they may not be suitable as pigment additions to paints. This problem might be overcome by synthesizing compounds with the required level of solubility. However, another approach for controlling the rate of release of highly soluble pigment salts has been developed by Goldie and McCarroll (1983, 1984). They adsorbed R cations onto particles of inorganic oxides, e.g. silica, alumina, iron oxide or tin oxide, by an ion exchange mechanism. The treated oxide particles were then included in the formulated paint. When water begins to diffuse through the paint film the ion exchange process is reversed, and the adsorbed R cation is displaced by hydrogen. The active R cation is then able to function in its inhibiting role at the metal surface. Using this technique, Goldie and McCarroll have successfully included soluble R nitrates into alkyd paints which have been applied to mild steel panels. These panels, scribed and tested in NaCl salt spray for 350 hours, exhibit high resistance to underfilm corrosion (see fig. 51). These findings are consistent with and are confirmed by the results of Baldwin et al. (1990).

The use of R salts as pigments in paint films does show some potential. However, much more research is required before R salts are available as alternative pigments to chromates. It is still possible that no single alternative to chromates will be found

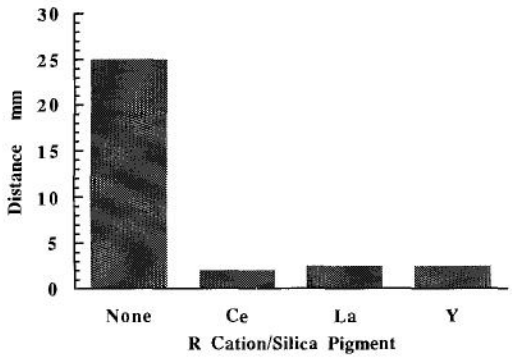

Fig. 51. Effects of R cation/silica pigment on the penetration of corrosion beneath an alkyd paint on mild steel (after Goldie and McCarroll 1983).

for some time. Perhaps more than one environmentally friendly inhibiting pigment will need to be incorporated into a paint film together with R salts, to promote synergistic inhibition effects, and thereby a level of corrosion protection comparable to that afforded by chromates.

6. Summary

6.1. *Rare earth salts, corrosion prevention and control*

Improved resistance to metallic corrosion can be achieved by

(i) modifying the chemical composition through selective alloying,
(ii) applying a more corrosion resistant metallic coating,
(iii) using a sacrificial metallic coating to corrode preferentially and thus protect the substrate,
(iv) modifying the aggressive environment by using corrosion inhibiting additions either in the bulk environment or in the paint film,
(v) introducing a barrier between the aggressive environment and the substrate metal using oxide coatings or paints incorporating corrosion inhibiting pigments.

It has been shown that R metals and compounds are capable of being used in many of these roles. Moreover, it is an area of application for R metals that is relatively new, and consequently, the reasons why they improve corrosion resistance are not completely understood. Clearly, in most of the areas described during the course of this chapter, considerably more research is required. However, there is one common factor which seems to be central to the whole topic of corrosion prevention and control with R metals and compounds, namely the effective formation/participation of a R oxide or hydroxide film.

The presence of the film is clearly responsible for the corrosion inhibition on a range of metals and alloys, when the corrosive environment is modified through the addition of R salts. The improved corrosion resistance of Mg and Al alloys containing additions of R metals appears in many cases to be associated with the formation of a R oxide

or hydroxide film on the surface. This is an obvious area for further research in future years.

The ex situ deposition of the oxide or hydroxide as a coating on a metal surface has also been shown to provide a significant level of corrosion protection. This is particularly so for aluminium alloys and aluminium alloy metal matrix composites. In the author's laboratory these coatings have been successfully produced on other alloys such as Zn, Cd and steel.

The inclusion of R metals in metallic Zn coatings not only improves the coating process itself but also produces improved corrosion resistance. R metal has been detected in the oxide coating on Zn and, thus, may well be associated with the improved corrosion resistance. Again, this is another area requiring further research.

The small amount of work, describing the addition of R salts to paint coatings as corrosion inhibiting pigments, indicates that they are capable of inhibiting corrosion at exposed areas of substrate. It can be reasonably assumed that the inhibition of corrosion results from the formation of a R oxide film. This concept has yet to be confirmed and the exact role of the film needs further clarification.

The use of R metals for corrosion protection in high temperature environments is well established and is the subject of another chapter (141) in this volume by Dr. N.E. Ryan. Their use for corrosion prevention and control in aqueous environments opens up a whole new range of applications for these metals. As industry is seeking more environmentally acceptable processes for corrosion prevention and control, the R compounds offer significant promise, particularly as replacements for chromates. R compounds are attractive as they are generally considered to be non-toxic (Seon 1989). Their availability is increasing and costs are reducing, as R production increases with the wider use of magnets, catalysts, and other materials. Attractive though they may be, the R compounds have yet to match the performance of chromates as inhibitors of corrosion. Therefore, considerably more research is required not only by corrosion engineers and scientists, but also from others such as chemists, electrochemists and ceramicists. The answer may lie not with a single alternative based on R compounds, but with a synergistic effect based on R compounds perhaps combined with other environmentally friendly inhibitors. This new role for R compounds offers an exciting new area for research and development in the coming decades, and will clearly make a significant impact on the future of the rare earth industry.

Acknowledgements

The author wishes to thank Dr. N.E. Ryan and Dr. L.F. Rose for helpful discussions during the preparation of this chapter, and Mr. P.N. Trathen and Mr. P. Haberecht for their technical assistance.

References

Ahmed, D.S., R.G.J. Edyvean, C.M. Sellars and H. Jones, 1990, Mater. Sci. & Technol. **6**, 469–474.

Ailor, W.H., 1971, Handbook on Corrosion Testing and Evaluation (Wiley, New York).

Angers, L., M.E. Fine and J.R. Weertman, 1987, Metall. Trans. A **18A**, 555.

Arnott, D.R., N.E. Ryan, B.R.W. Hinton, B.A. Sexton and A.E. Hughes, 1985, Appl. Surf. Sci. **22/23**, 236.

Arnott, D.R., B.R.W. Hinton and N.E. Ryan, 1987, Mater. Perform. **26**, 42.

Arnott, D.R., B.R.W. Hinton and N.E. Ryan, 1989, Corrosion **45**, 12.

Baldwin, K.R., P.L. Lane, M.A.H. Hewins and C.J.E. Smith, 1987, Metallic Cations as Corrosion Inhibitors for Aluminium–Copper Alloys, Royal Aircraft Establishment Technical Report 87052, September (UK Ministry of Defence).

Baldwin, K.R., M.C. Gibson, P.L. Lane and C.J.E. Smith, 1990, The development of alternatives to chromate inhibitors for the protection of aerospace Al alloys, in: Proc. 7th European Symp. on Corrosion Inhibitors, Ann. University Ferrara, N.S., Sez. V, Suppl. No. 9, 771–785.

Bennett, L.H., and J. Kruger, 1981, Economic Effects of Metallic Corrosion in the United States, National Bureau of Standards Special Publication 511-1, 2.

Biestek, T., and J. Weber, 1976, Electrolytic and Chemical Conversion Coatings (Portcullis Press, Surrey, UK) p. 4-127.

Blaser, R.W., 1976, Water pollution standards, in: Proc. American Hot-Dip Galvanisers Association Semi-Annual Meeting, Montreal, Canada.

Borgmann, C.W., 1937, Ind. Eng. Chem. **29**(7), 814.

Braun, A.H., 1979, Corrosion resistance of magnesium and magnesium alloys, in: American Society for Materials Metals Handbook, Vol. 2 (ASM, Metals Park, OH) pp. 596–609.

Bray, D.J., 1988, Mg alloy technology for aerospace applications, in: AGARD Conf. Proc. No. 144, New Light Alloys (NATO AGARD, Neuilly Sur Seine) pp. 27/1–27/9.

Bray, D.J., 1990, Cast and rapidly solidified magnesium alloys, in: AGARD Lecture Series No. 174, New Light Alloys (NATO, Neuilly Sur Seine) pp. 7–15.

Chang, C.F., S.K. Das, D. Raybould and A. Brown, 1986, Met. Powder Rep. **41**, 302–305.

Chang, C.F., S.K. Das, D. Raybould, R.L. Bye and E.V. Limoncelli, 1989, Recent developments in high strength PM/RS Mg alloys, A review, in: San Diego Conf. on Advances in Powder Metallurgy, Vol. 3 (Metal Powder Industries Federation, New Jersey) pp. 331–346.

Churchill, J.E., 1937, Trans. Electrochem. Soc. **76**, 341.

Cooke, G., P.J. Vore, C. Gumienny and G. Cooke Jr, 1990, A Study to Determine the Annual Direct Cost of Corrosion Maintenance for Weapon Systems and Equipment in the United States Air Force (Warner Robins Air Logistics Center, Robins AFB, GA, USA).

Cosgrave, M.C., and B.R.W. Hinton, 1991, Corrosion behaviour of boron–Al metal matrix composites, in: Corrosion 91, Proc. Annu. Conf. Australasian Corrosion Association, Sydney, Australia, p. F5.

Cushman, A.S., 1907, Proc. ASTM **3**, 211.

Davenport, A.J., H.S. Isaacs and M.W. Kendig, 1991a, Corros. Sci. **32**, 653–663.

Davenport, A.J., H.S. Isaacs and M.W. Kendig, 1991b, XANES Investigation of pH Effects during Ce Sealing of Anodised Al, Report No. 45674 (Brookhaven National Laboratory, Upton, NY).

Eliezer, D., M. Fass, D. Itzhak, Y. Kim and F.H. Froes, 1988, Corrosion behaviour of rapidly solidified Al–R alloys, in: Proc. 2nd Int. Conf. on Rapidly Solidified Materials, San Diego (ASM, Metals Park, OH) pp. 83–90.

Evans, U.R., 1924, J. Soc. Chem. Ind. London **43**, 315T.

Evans, U.R., 1961, The Corrosion and Oxidation of Metals: Scientific Principles and Practical Applications (Edward Arnold, London).

Fass, M., and D. Eliezer, 1989, J. Mater. Sci. Lett. **8**, 178–182.

Fass, M., D. Itzhak, D. Eliezer and F.H. Froes, 1987, J. Mater. Sci. Lett. **6**, 1227–1228.

Fass, M., D. Eliezer, D. Itzhak and F.H. Froes, 1988a, Environmental behaviour of rapidly solidified Al–R alloys, in: Proc. Int. Conf. on PM Aerospace Materials (MPR Publishing, Shrewsbury, UK) pp. 50–1.

Fass, M., D. Itzhak, D. Eliezer and F.H. Froes, 1988b, J. Mater. Sci. Lett. **7**, 76–78.

Frazier, W.E., E.W. Lee, M.E. Donnellan and J.J. Thompson, 1989, J. Met. **41**(May), 22–26.

Goldie, B.P.F., and J.J. McCarroll, 1983, Australian Patent AU-A-12527/83.

Goldie, B.P.F., and J.J. McCarroll, 1984, Australian Patent AU-A-32947/84.

Hatch, G.B., 1952, Ind. Eng. Chem. **44**(8), 1775.

Hawkins, D.T., and R. Hultgren, 1973, Constitution of binary alloys, in: ASM Metals Handbook, Vol. 8, Metallography, Structure and Phase Diagrams, eds J.R. Davis and J.D. Destefani (ASM, Metals Park, OH) p. 251.

Hehmann, F., R.G.J. Edyvean, H. Jones and F. Sommer, 1988, Effect of rapid solidification processing on corrodability of magnesium alloys, in: Proc. Conf. on Powder Metallurgy Aerospace Materials (MPR, Shrewsbury, UK).

Hehmann, F., F. Sommer, H. Jones and R.G.J. Edyvean, 1989, J. Mater. Sci. **24**, 2369–2379.

Hinton, B.R.W., 1989, New approaches to corrosion inhibition with rare earth salts, in: Corrosion 89, Proc. Annu. Conf. of the National Association of Corrosion Engineers (NACE), New Orleans, Paper 170.

Hinton, B.R.W., 1992, J. Alloys & Compounds **180**, 15–25.

Hinton, B.R.W., and D.R. Arnott, 1989, Microstructural Sci. **17**, 311.

Hinton, B.R.W., and L. Wilson, 1989, Corros. Sci. **29**, 967.

Hinton, B.R.W., D.R. Arnott and N.E. Ryan, 1984, Met. Forum **7**, 211.

Hinton, B.R.W., D.R. Arnott, N.E. Ryan, P.N. Trathen, L. Wilson and B.E. Wilson, 1985, Corros. Australasia **10**, 12.

Hinton, B.R.W., D.R. Arnott and N.E. Ryan, 1986, Mater. Forum **9**, pp. 161–173.

Hinton, B.R.W., D.R. Arnott and N.E. Ryan, 1987, Mater. Australasia 19, 1, pp 18–20.

Hinton, B.R.W., P.N. Trathen, L. Wilson and N.E. Ryan, 1988, The inhibition of mild steel corrosion in tap water by cerous chloride, in: Proc. 28th Australasian Corrosion Association Conf., Perth, Australia, November, 1988.

Hoar, T.P., 1971, Report of the U.K. Department of Trade Committee on Corrosion and Protection (HMSO, London).

Hubrecht, J., A.F. Skenazi, J. Vereecken and D. Coutsouradis, 1985, ATB Metall. **25**(3), 243–252.

Isaacs, H.S., A.J. Davenport and A. Shipley, 1991, J. Electrochem. Soc. **138**, 390–393.

Jha, S.C., T.A. Mozhi and R. Ray, 1989, J. Met. **41**(May), 27–30.

Kang, Z.C., and L. Eyring, 1992, J. Alloys & Compounds **181**, 483–487.

Khobaib, M., and S.D. Kirchoff, 1985, Corrosion Behaviour of Al–Fe–Ce Powder Metallurgy Alloys, AFWAL-TR-85-4068, Final Report Sept.-Dec. 1984 (Air Force Wright Aeronautical Laboratories, Wright-Patterson Air Force Base, OH).

King, J.J., 1990, in: New Advanced Magnesium Alloys, in: Advanced Materials Technology International, ed. G.B. Brook (Sterling Publications, London) pp. 12–19.

Krishnamurthy, S., E. Robertson and F.H. Froes, 1986, Mg–Nd alloys produced by rapid solidification, in: Proc. Symp. on Processing of Structural Metals by Rapid Solidification, eds F.H. Froes and S.J. Savage (ASM, Metals Park, OH) pp. 399–408.

Krishnamurthy, S., F.H. Froes and E. Robertson, 1988a, Investigation of rapidly quenched Mg–Ce alloys, in: Proc. 2nd Int. Conf. on Rapidly Solidified Materials: Properties and Processing, San Diego, eds P.W. Lee and J.H. Moll (ASM, Metals Park, OH) pp. 107–112.

Krishnamurthy, S., M. Khobaib, E. Robertson and F.H. Froes, 1988b, Mater. Sci. & Eng. **99**, 507–511.

Krishnamurthy, S., E. Robertson and F.H. Froes, 1988c, Rapidly solidified Mg alloys containing R additions, in: Advances in Mg Alloys and Composites, eds H. Paris and W.H. Hunt (The Minerals, Metals and Materials Society) pp. 77–88.

Kumar, B., and R. Sharan, 1979, J. Prod. Eng. **3**(3), 115.

Lake, D.L., 1988, Corros. Prev. Control **35**(4), 113.

Langenbeck, S.L., J.M. Cox and R.F. Simenz, 1986, Characterisation of Al–Fe–Ce alloys, in: Rapidly Solidified Powder Aluminium Alloys, ASTM STP 890, eds M.E. Fine and E.A. Starke (ASTM, Philadelphia, PA) pp. 450–463.

Lewis, R.E., A. Joshi and H. Jones, 1986, Rapidly solidified Mg alloys for high performance structural applications, a review, in: Proc. Symp. on Processing of Structural Metals by Rapid Solidification, eds F.H. Froes and S.J. Savage (ASM, Metals Park, OH) pp. 367–378.

Lichtenberger-Bajza, E., and I. Boczor, 1977, Mitteilung des Planungs-und Forschungsinstitutes der Aluminiumindustrie (Budapest) pp. 119–137.

Makar, G.L., J. Kruger and A. Joshi, 1988, in: Advances in Mg Alloys and Composites, eds H. Paris and W.H. Hunt (The Minerals, Metals and Materials Society) pp. 105–121.

Mansfeld, F., 1990, Environmentally-Induced Passivity of Al Alloys and Al Metal Matrix Composites, Final Report for the Period 10–1–87 to 9–30–90 for Office of Naval Research, AD-A231 350 (University of Southern California, Los Angeles, CA).

Mansfeld, F., S. Lin and H. Shih, 1990a, Corrosion Protection of Metal Matrix Composites, Final Report for US Army research Office, AD-A222 951 (University of Southern California).

Mansfeld, F., S. Lin, S. Kim and H. Shih, 1990b, J. Electrochem. Soc. **137**, 78–82.

Mansfeld, F., Y. Wang and H. Shih, 1991, Evaluation of the surface properties of Al alloys by electrochemical methods, in: Corrosion 91, Proc. NACE Annu. Conf., Paper 134.

Mayne, J.E.O., and J.A. Burkhill, 1980, in: Proc. 6th Symp. on Corrosion Inhibitors, University of Ferrara, Italy, Session 5, Supplement 8, pp. 117.

McCloud, J.L., 1931, Ind. Eng. Chem. **23**(12), 1334.

Mondolfo, L.F., 1979, Aluminium Alloys (Butterworths, London) pp. 883–893.

Polin, N.W., 1987, Corrosion, in: Corrosion of Copper and Copper Alloys, ASM Metals Handbook, 9th Ed., Vol. 13 (ASM, Metals Park, OH) p. 611.

Poole, S.W., and J.E. Franklin, 1978, High strength low alloy steels, in: ASM Metals Handbook, Vol. 9, Properties and Selection of Iron and Steel (ASM, Metals Park, OH) p. 411.

Popov, V.F., 1981, Izv. Vyssh. Uchebn. Zaved. Chern. Metall. **1**, 103–106.

Pourbaix, M., 1966, Atlas of Electrochemical Equilibria in Aqueous Solutions (Pergamon Press, London) pp. 183–198.

Rongzhang, T., S. Lianchao, C. Qian and J. Cixue, 1987, J. Cent. South Inst. Min. Metall. **18**, 432–428.

Savage, S.J., F.H. Froes and D. Eliezer, 1986, Microstructural characterisation of as cast rapidly solidified Al–Sm, Al–Gd, and Al–Er binary alloys, in: Proc. Int. Conf. on Rapidly Solidified Materials, eds P.W. Lee and R.S. Carbonara (ASM, Metals Park, OH) pp. 351–355.

Seon, F.M., 1989, J. Less-Common Met. **148**, 73–78.

Shreir, L.L., 1976, Corrosion, Vols. 1, 2, 2nd Ed. (Newnes-Butterworths, London).

Singh, I., and M. Singh, 1987, Corrosion **43**, 425–428.

Singh, R.N., N. Verma and W.R. Singh, 1989, Corrosion **45**, 222–229.

Thorne, P.C., and E.R. Roberts, 1954, Inorganic Chemistry, 6th Ed. (Oliver and Boyd, London) p. 418.

Thornhill, R.S., 1945, Ind. Eng. Chem. **37**, 706.

Towner, R.J., 1985, Met. Prog. **127**(5), 70.

Uhlig, H.H., 1963, Corrosion and Corrosion Control (Wiley, New York) pp. 307–315.

Unsworth, W., 1989, Int. J. Mater. & Product Technol. **4**(4), 359–378.

US Public Health Service, 1989, Toxicological Profile for Chromium, Report No. ATSDR/TP-88/10, July.

Vanysek, P., 1990–91, CRC Handbook of Chemistry and Physics, 71st Ed., ed. D.R. Lide (Chemical Rubber Company, Boston, MA) pp. 8-16–8-23.

Verma, N., W.R. Singh, S.K. Tiwari and R.N. Singh, 1990, Br. Corros. J. **25**, pp. 131–132.

Vyazovikina, N.V., V.N. Minakov, Y.N. Ivashchenko, V.V. Kovylyaev, S.S. Ponomarev and S.B. Prima, 1990, Prot. Met. **26**, 31–37.

Weinberg, F., M. Mager and L. Frederick, 1990, Can. Metall. Q. **29**, 163–166.

Wilson, L., and B.R.W. Hinton, 1988, Australian Patent PCT/Au88/00060.

Wilson, L., J. Hamilton, N.E. Ryan and B.R.W. Hinton, 1993, to be published.

Zhenyuan, C., Y. Zongsen, W. Yue and C. Xijin, 1987, J. Beijing Univ. Iron & Steel Technol. **9**(4), 1–7.

Zoccola, J.C., H.E. Townsend, A.R. Borzillo and J.B. Horton, 1978, Atmospheric corrosion behaviour of Al–Zn alloy coated steel, in: Atmospheric Factors Affecting the Corrosion of Engineering Metals, ASTM STP 646, ed. S.K. Coburn (ASTM, Philadelphia, PA) pp. 165–184.

Handbook on the Physics and Chemistry of Rare Earths
Vol. 21
edited by K.A. Gschneidner, Jr. and L. Eyring
Elsevier Science B.V.

Chapter 141

HIGH-TEMPERATURE CORROSION PROTECTION

N.E. RYAN
DSTO – Aeronautical Research Laboratory, Department of Defence, Australia

Contents

1. Introduction

Metallic components used for the construction of energy conversion/producing systems, petrochemical plants and gas turbines for aircraft propulsion are all required to operate

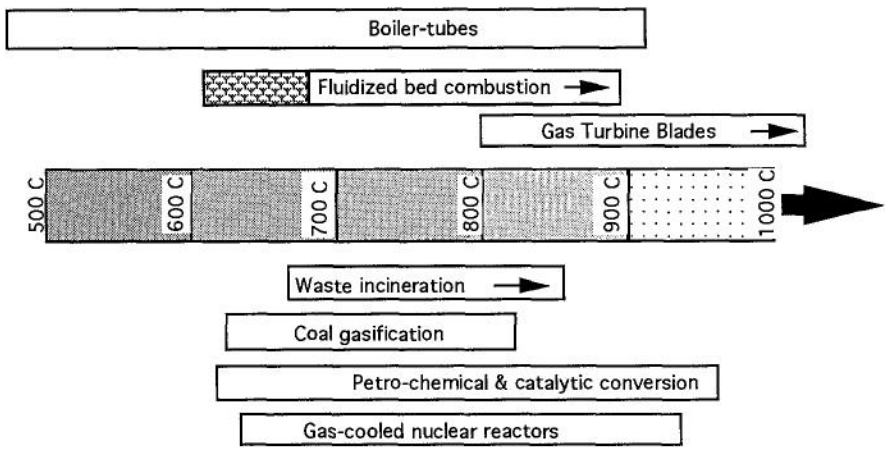

Fig. 1. Operating temperature ranges of energy conversion systems and industrial processes.

at elevated temperatures (see fig. 1) and are exposed to hostile environments in which oxygen is almost always present. Oxidation is thus a dominant form of high-temperature degradation in these materials. In systems used for coal gasification and fluidized-bed combustion, mixed-gas corrosion promoting degradation by sulphidation is encountered. In coal- or oil-fired boilers and gas-turbine energy conversion, particularly marine and land base turbines, molten hot-salt corrosion processes occur.

In developing alloys to resist ever increasing temperatures, in pursuit of increased productivity, cost-effectiveness, and fuel efficiency, the aim is to promote self-healing surface oxide or corrosion products, which act as barriers to the diffusion of the reactants from the environment to the metal, or between the metal and the environment, thereby protecting the substrate structural metal from catastrophic degradation.

In many instances demands for high-temperature strength, as for example in gas turbines, resistance to high-temperature oxidation/corrosion is compromised by strengthening alloy additions. Hence, oxidation/corrosion resistant coatings are required.

To retain structural integrity, excessive metal loss by oxide-scale formation or by internal oxidation/sulphidation must be avoided, as both lead to effective reductions in cross-section, thereby reducing the load-bearing capacity. Furthermore, the oxide barrier should also be resistant to spallation due to loss of adhesion or cracking, resulting from thermal cycling, as a consequence of differential (metal/oxide) elastic and thermal-expansion properties. Erosion by high-velocity particles is another cause of high-temperature oxidation/corrosion deterioration.

This review addresses the important role played by small additions of rare-earth elements in imparting enhanced oxidation/corrosion resistance to high-temperature materials. For the sake of completeness it is appropriate to first briefly outline the essential principles used to produce oxidation resistance in structural materials. More detailed accounts of the fundamentals of high-temperature oxidation/corrosion can be found, e.g., in publications by Birks and Meier (1983) and Kofstad (1988).

2. High-temperature oxidation/corrosion

2.1. *Oxidation*

When a metal is exposed at high temperature to atmospheres containing oxygen, metal-oxide scales develop,

$$M + \tfrac{1}{2}O_2 = MO. \tag{1}$$

This is believed to occur in two steps, in much the same way that a metal goes into aqueous solution. The metal is ionized by releasing electrons, e.g. for a divalent metal M,

$$M = M^{++} + 2e^{-} \tag{2}$$

and the electrons are absorbed by oxygen to produce an oxygen ion,

$$\tfrac{1}{2}O_2 + 2e^{-} = O^{--}. \tag{3}$$

The rate of growth of an oxide film is determined either by:

(a) outward diffusion of M^{++} ions and electrons through to the oxygen of the environment, promoting outward oxide growth from the oxide–air (gas) interface (fig. 2a).

(b) O^{--} ions diffusing through the oxide to promote slow oxide growth at the oxide/metal interface (fig. 2b).

(c) electrons moving slowly, because of the insulating characteristics of the oxide (e.g. the resistivity of Al_2O_3 is 10^9 > that of FeO). In this instance, the oxide may grow either from the metal/oxide or the oxide/air interface, or from within the oxide itself (fig. 2c).

Oxidation rates generally follow a linear or a parabolic law,

$$\begin{array}{ll} \text{Linear oxidation} & \text{Parabolic oxidation} \\ \Delta m = k_L t, & (\Delta m)^2 = k_p t. \end{array} \tag{4, 5}$$

where Δm is the weight-change with respect to time and k_L and k_p are, respectively, the linear and parabolic kinetic (or rate) constants, which increase exponentially with temperature, according to the conventional Arrhenius law,

$$k_L = A_L \exp\left(\frac{-Q_L}{RT}\right), \qquad k_p = A_p \exp\left(\frac{-Q_p}{RT}\right). \tag{6, 7}$$

The most effective protection is offered by reaction products which grow according to a parabolic rate law, those with the lowest temperature dependent parabolic rate constant

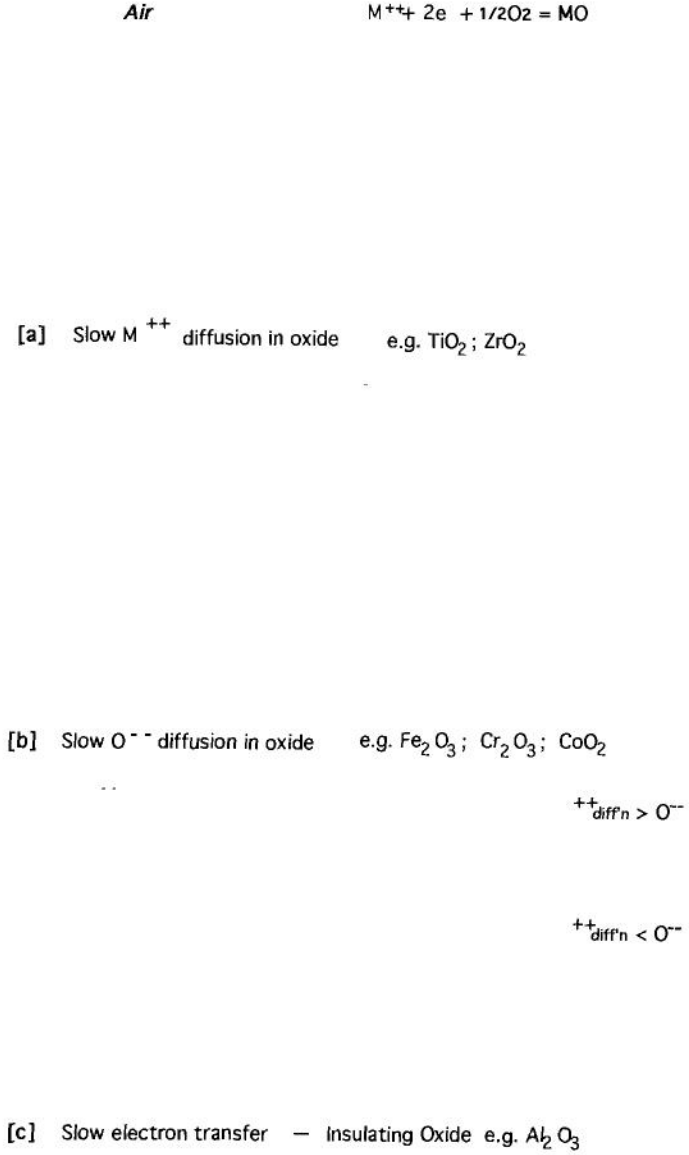

Fig. 2. Mechanisms of oxide formation and growth: (a) slow metal ion diffusion; (b) slow diffusion of oxygen ion; (c) slow electron transfer.

exhibiting the greatest level of high-temperature protection. Oxidation rate is generally expressed as change in weight per unit area:

$$\frac{\mathrm{d}(\Delta m/A)}{\mathrm{d}t} = \frac{k_\mathrm{p}}{2\Delta m/A}. \tag{8}$$

Oxide-film thickness increases with increasing time, creating a barrier between the metal and the hostile gas environment, provided that the oxide remains intact, adhering to the metal surface, that it does not crack, and moreover, that there is no alternative and easier diffusion path, other than through the solid oxide scale. Unfortunately, grain boundaries in the oxide scales do provide short-circuit paths for the diffusion of M^{++} ions and gaseous reactants such as O^{--}, $[SO_2]^{--}$ and S^{--}. The significance of oxide grain boundaries becomes more obvious upon investigation of the mechanism(s) by which rare earths function to increase oxidation resistance.

In creating alloys resistant to high-temperature oxidation, one uses elements with a high affinity for oxygen (as measured by their high negative free energy for oxide formation $-\Delta G^0$), the object being for the alloy addition to selectively oxidize over the base metal. For such alloys, eq. (1) is generalized as:

$$M_i + \tfrac{1}{2}O_2 = M_iO, \tag{9}$$

where $i = 1, 2, 3$, or more constituent elements in the alloy. If p_{O_2} denotes the partial pressure of oxygen in the environment, and $\Delta G^0_{M_iO}$ the free energy of oxide formation for the respective elements at different concentration or activity a_{M_i}, the equilibrium relation is

$$(p_{O_2})^{1/2}_{M_i-M_iO} = \frac{\exp(\Delta G^0_{M_iO}/RT)}{a_{M_i}}. \tag{10}$$

Each element will tend to form its oxide when the oxygen partial pressure exceeds the above equilibrium pressure.

Next, one must consider which oxide will form preferentially. The competition between elements for oxygen results in the selective oxidation of the most thermodynamically stable to eventually cover the alloy when exposed to the high-temperature oxidizing environment:

$$M_1O + M_2 = M_2O + M_1, \qquad \frac{a_{M_1}}{a_{M_2}} = \exp\left(\frac{\Delta G^0_{M_1O} - \Delta G^0_{M_2O}}{RT}\right). \tag{11, 12}$$

In practice, the preferred oxide does not form immediately, for there is always a *transition period* in which the base metal and other elements in the alloy nucleate surface oxides.

Figure 3 shows the free energies of formation of the oxides, nitrides and sulphides of a number of elements important to high-temperature alloy development. These diagrams show that the rare-earth elements all possess high affinities for oxygen (as well as for nitrogen and sulphur), greater than the oxygen affinities of silicon, chromium or aluminium. This is one reason why they have such a beneficial influence in improving the resistance of high-temperature alloys to hostile gaseous environments. However, they cannot be used as major alloying additions because of their relatively large atomic dimensions, for instance the yttrium atom is 46% larger than the nickel atom. This

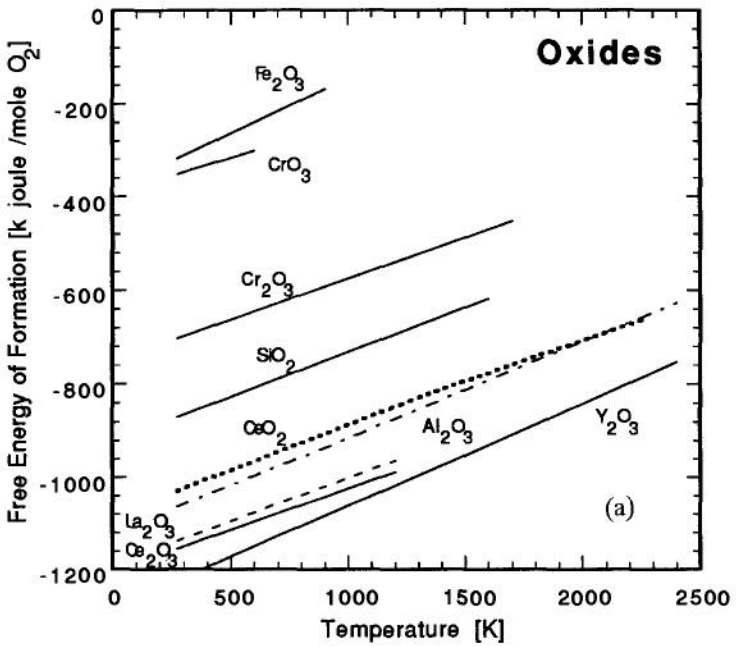

Fig. 3. Free-energy of formation for (a) oxides, (b) sulphides and (c) nitrides (Gschneidner et al. 1990).

size mismatch makes it difficult to achieve a homogeneous distribution of sufficient quantity (and activity level) as would be required to ensure the selective formation of a stable rare-earth oxide barrier, similar to that formed by Al, Cr or Si when added to Fe-, Co- or Ni-base alloys. Nevertheless, the rare earths do exhibit a marked influence on the transition periods during oxidation, by accelerating the nucleation and growth of protective scales, notably of alumina (Al_2O_3) or chromia (Cr_2O_3). They appear to behave in the same way as Cr does in the Al–Cr–Ni system, in which Cr aids in the preferential formation of Al_2O_3 with reduced concentrations of Al (see fig. 4). This beneficial behaviour results from preferred internal oxidation of rare-earth alloy additions, and also, when introduced by mechanical alloying, they are present as finely dispersed oxide particles.

Other factors influencing selective oxidation are the diffusion coefficients of (a) the preferred oxidizing element both in the substrate and in its oxide and (b) of oxygen in the substrate alloy and its oxide.

While a great deal of attention has been directed to obtain protective oxide barriers other than (i) alumina (Al_2O_3), (ii) chromia (Cr_2O_3), or (iii) silica (SiO_2), up to date none have been found. Silicon is not widely used, because in the amounts required to form continuous silica scales it forms either low-melting-point or brittle phases in the base structural alloys. Thus, high-temperature alloys are broadly classified as either alumina (Al_2O_3)- or chromia (Cr_2O_3)-forming alloys. This is an over-simplification, as a

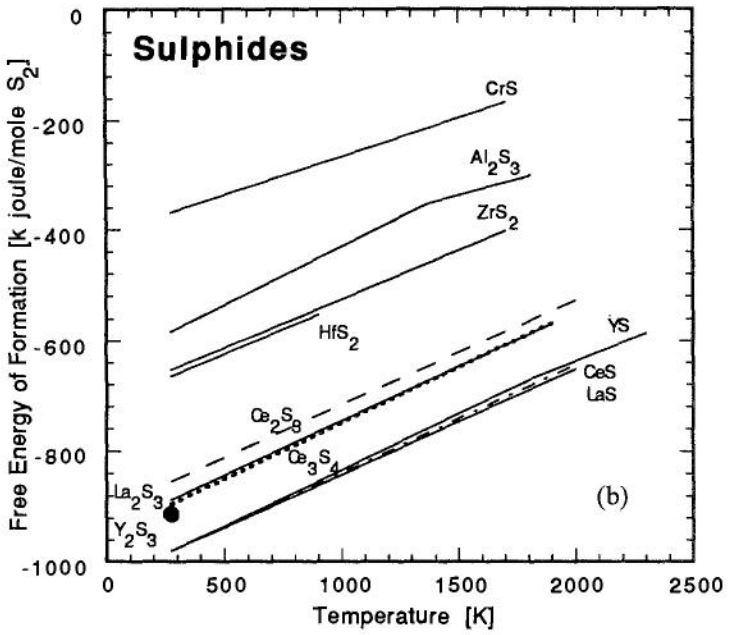
Sulphides
CrS
Al_2S_3
ZrS_2
HfS_2
YS
CeS
LaS
Ce_2S_3
Ce_3S_4
La_2S_3
Y_2S_3
(b)
Free Energy of Formation [k joule/mole S_2]
Temperature [K]
0
-200
-400
-600
-800
-1000
0
500
1000
1500
2000
2500

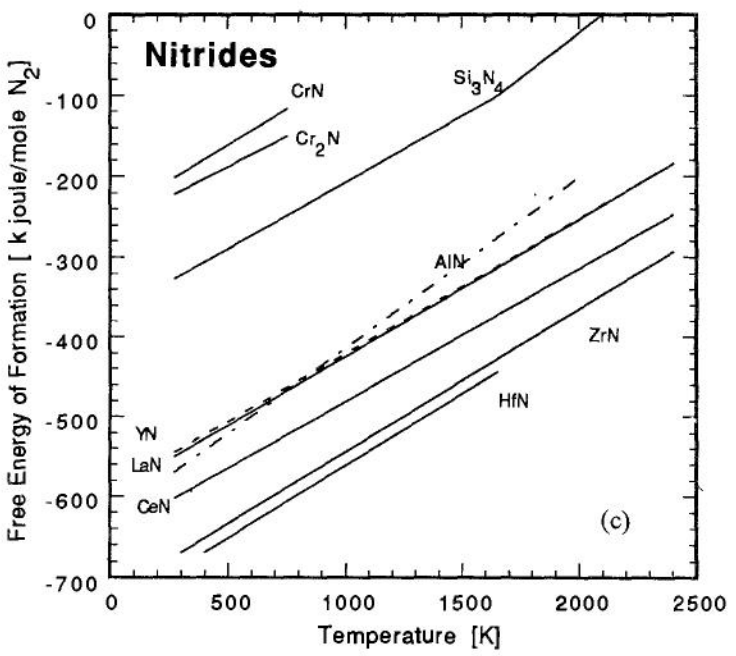
Nitrides
CrN
Cr_2N
Si_3N_4
AlN
ZrN
HfN
YN
LaN
CeN
(c)
Free Energy of Formation [k joule/mole N_2]
Temperature [K]
0
-100
-200
-300
-400
-500
-600
-700
0
500
1000
1500
2000
2500

Fig. 3bc.

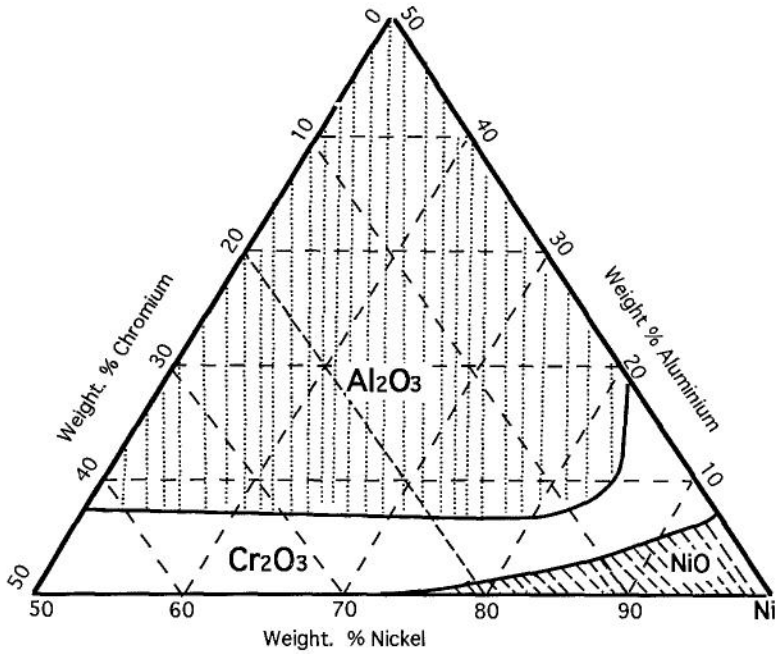

Fig. 4. Oxides of the ternary metal system Ni–Cr–Al forming at 950°C (Wallwork and Hed 1971).

wide range of other transitional oxides can form, especially spinels, but it does provide a convenient classification which will be adopted here. Characteristic features of these types of alloys can be summarized as follows:

(i) Cr_2O_3-formers generally follow a parabolic oxidation rate law at temperatures up to 950°C.

(ii) Al_2O_3 thickens at near logarithmic rates, much lower than for Cr_2O_3, and can provide protection in oxidizing atmospheres at temperatures up to 1350°C.

(iii) In high-velocity gas streams (i.e. turbine engines) Al_2O_3 scales are preferable to Cr_2O_3, as they are not susceptible to vaporization. The formation of volatile CrO_3 interferes with the protective integrity of Cr_2O_3 above $\approx$950°C. This is the principal reason why aluminide coatings are used on aircraft turbine blades. However, Al_2O_3 scales are more sensitive to spallation than Cr_2O_3.

(iv) Cr_2O_3 scales exhibit better resistance to sulphidation and hot-salt corrosion than Al_2O_3 scales.

The rare-earth elements, principally Ce and Y, play an important role in enhancing the oxidation/corrosion resistance of chromia (Cr_2O_3)- and alumina (Al_2O_3)-forming alloys.

2.2. *Loss of oxide adhesion*

Loss of adhesion arises when the volume of the oxide differs significantly from that of the substrate metal. With an increase in volume, the oxide layer will be in compression,

which will promote detachment or the formation of convoluted surface irregularities. With a decrease in volume, the oxide layer will generally crack to accommodate the induced tensile stress. Both situations lead to decreased protection, and to departure from a parabolic law for the rate of oxide growth.

Lack of adhesion can also arise as a consequence of the rapid outward diffusion of metal ions, leaving behind vacancies which coalesce to form (Kirkendall type) voids at the oxide/metal interface. By contrast, oxygen diffusion does not create vacancies, and thus the integrity of the oxide/metal adhesion is generally retained when this oxidation mechanism prevails.

2.3. *Sulphidation*

In mixed-gas environments, as occur in coal-conversion processes, the factors discussed above remain, but with the added complication of competition between the elements. In addition to oxygen, gases such as SO_2 and H_2S vie with each other to combine with the various elements in the substrate alloy.

The development of alloys resistant to mixed-gas corrosion also utilizes the selective oxidation principles, but the oxide scales must now act as barriers to the diffusion of other reactants as well, for instance sulphurous gases in addition to oxygen.

The concept of using elements capable of forming stable and slow-growing sulphide scales is a difficult option if they do not also form stable oxides. Molybdenum for instance is capable of forming a stable, slow growing, sulphide scale, but it also forms a volatile oxide (MoO_3). Again, there is good reason to examine the potential benefits of the rare earths which form stable oxides, sulphides and oxysulphides (see fig. 3).

2.4. *Hot-salt corrosion*

In gas-turbine engines, particularly those burning low-grade fuels, the presence of sulphur and vanadium in the fuel and of contaminants ingested from the air (especially from marine atmospheres) leads to the dissolution of otherwise protective oxides through the formation of low-melting-point deposits derived from Na_2SO_4, NaCl and V_2O_5.

Two forms of hot-corrosion are encountered: (a) Type I (high-temperature hot-salt corrosion) is prevalent in aircraft turbine engines operating at temperatures over 850°C; (b) type II (low-temperature hot-salt corrosion) occurs especially in industrial and marine turbine engines over the temperature range 700–800°C.

Degradation can occur by any of the following mechanisms:

(i) A fluxing reaction which removes an oxide-forming element. For example, chloride ions may selectively combine with, and thus remove, aluminium or chromium; or sulphur in Na_2SO_4 may induce sulphidation.

(ii) Dissolution of the protective oxide. This can occur by basic fluxing (Na_2O-rich) when the oxygen ions in the molten deposit react with the oxide, or by acidic fluxing (SO_3-rich) when oxygen ions are donated to the molten salt.

(iii) The formation of low melting-point eutectics. For example, Na_2SO_4 melts at 884°C, but it forms eutectic mixtures with $MgSO_4$ and with NaCl which melt at 660°C and 630°C, respectively.

Al_2O_3-forming alloys with less than 5 wt.% Al are susceptible to basic fluxing while Cr_2O_3-forming alloys are more resistant to hot-salt corrosion. Rare earths can improve the resistance to hot-salt corrosion by increasing the melting temperature of residues containing V_2O_5. Alternatively, rare earths introduced with the fuel can scavenge atomic oxygen, thereby inhibiting the formation of SO_3 and the consequent formation of sulphates which cause hot salt corrosion.

3. Rare earths in high-temperature alloys

3.1. *History*

Small additions of rare earths, particularly cerium (Ce) and yttrium (Y), for the purpose of reducing the rate of oxidation and preventing spallation of oxide scale in high-temperature alloys, was first applied by Pfeiffer (1957). Other early applications include (i) the development of Fe-base Cr–Al–Y alloys at General Electric Company by Collins et al. (1960), Felten (1961), Francis and Whitlow (1965, 1966) and Wukusick and Collins (1963, 1964); (ii) the development of FECRALLOY^{TM}, which possesses oxidation resistance up to 1350°C, at the United Kingdom Atomic Energy Research Establishment, by Antill and Peakall (1967). A more widely recognized use of Y is in the M–Cr–Al–Y overlay coatings or bond coats (where M = Fe, Co or Ni or combinations thereof), which are used for protecting high-temperature turbine blades, following the work of Talboom et al. (1970). However, it is over 50 years ago that Pfiel (1937) discovered that Ce-rich "mischmetal", used as a deoxidizer in preparing 80Ni–20Cr resistance-heating wire, also contributed to enhanced oxidation resistance as a consequence of residual rare earth. Pfiel (1945) was later granted a patent for the superficial application of rare-earth oxides to enhance the oxidation resistance of high-temperature alloys. Hagel and Seybolt (1961) demonstrated that fine dispersions of Y_2O_3 also enhanced the oxidation resistance of high-temperature metals (see also Hagel 1963, Seybolt 1966).

Because the rare-earth elements exhibit high negative free energies of formation for stable sulphides (fig. 3), they can also be expected to promote hot-corrosion resistance in mixed-gas sulphidizing environments.

Table 1 lists a wide range of commercial alloys and metallic coatings containing specific rare-earth metals.

In the applications just mentioned, rare earths impart their beneficial influence either when they are introduced into the high-temperature material as an alloy addition or finely dispersed oxide, or when they are applied to a metal substrate alloy as a coating. A third possibility, which has not been widely exploited to date, is to introduce the rare-earth element into the environment. These three application classifications are shown schematically in fig. 5.

Table 1
High-temperature alloys containing rare earths

Alloy type	Common designation	R	wt.%
High-temp. Fe-base alloy	FECRALLOY	Y	0.3
	253.MA	Ce	0.055
	MVMA	Ce	0.04
	Kanthal AF	Y	?
Ni-base superalloy	Hastelloy N	Y	0.26
	Hastelloy S	La	0.05
	Hastelloy T	La	0.02
	Haynes 214	Y	0.02
	Haynes 230	La	0.5
	Udimet 500+Ce	Ce	?
	Udimet 700+Ce	Ce	0.05–0.3
	Melni 19/22	La	0.17
	Nimonic 86	Ce	0.03
Co-base superalloy	Haynes 188	La	0.05
	Haynes 1002	La	0.05
	AiResist 213	Y	0.1
	AiResist 215	Y	0.17
	FSX 418	Y	0.15
	FSX 430	Y	0.03–0.1
	Melco series 2, 9, 10, 14	Y	0.1–0.2
Cr-base alloy	C-207	Y	0.15
	CI-41	Y+La	0.1 (total)
Mechanically-alloyed oxide dispersion strengthened (ODS) alloys			
High-temp. Fe-base alloy	MA 956	Y_2O_3	0.5
Ni-base superalloy	Haynes 8077	Y_2O_3	1.0
	MA 754	Y_2O_3	0.6
	MA 953	La_2O_3	0.9
	MA 6000	Y_2O_3	1.0
High-temperature metallic, overlay or bond-coatings			
Low-pressure plasma spray			
Fe-rich 25Cr–4Al	GE 2541	Y	1.0
Co-rich	GT	Y	1.0
Co-rich 25Cr–10Ni–5Ta–3Al	S 57	Y	0.5
Co-rich 25Cr–10Ni–5Ta–7Al	S 77	Y	0.5
Ni-rich 23Co–17Cr–12.5Al	Amperit 410	Y	0.45
Physical vapor (electron-beam) deposition			
Fe-rich 24Cr–8Al		Y	0.5
Co-rich 29Cr–6Al		Y	0.5
Ni-rich 22Cr–10Al		Y	0.5

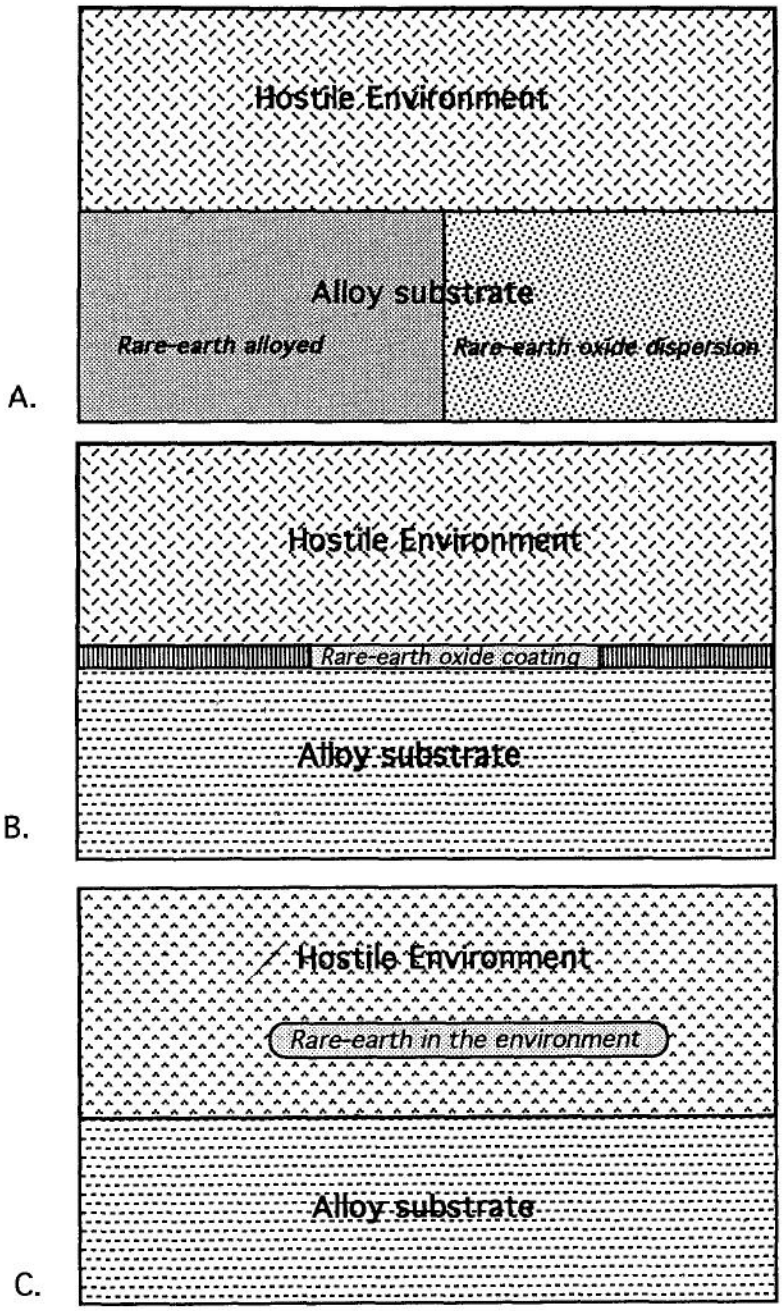

Fig. 5. Schematic, showing ways in which rare earths are used to impart improved oxidation resistance (a) as an alloy addition or finely dispersed oxide, (b) applied to the metal surface as a coating and (c) introduced into the hostile environment.

Ion bombardment for implanting rare-earth elements, as a special form of surface alloying, has also been used but mainly for mechanistic studies. Only rarely has the technique been applied for any practical purposes. Further details are covered in sect. 3.4.

3.2. *Application and benefit*

3.2.1. *Chromia (Cr_2O_3)-forming alloys*

3.2.1.1. *Rare earths as alloy additions.* The principal benefit provided by trace additions of rare-earth elements to Cr_2O_3-forming Fe- or Ni-base alloys is to reduce markedly the oxidation rate under isothermal oxidation conditions. Figure 6 shows results from studies conducted by Ecer and Meier (1979) for oxidation of Ni–50Cr in static air at 1100°C, and shows the marked reduction in rate of oxide growth achieved simply by the addition of 0.08 wt.% Ce. Under cyclic-oxidation conditions (fig. 6), the Cr_2O_3 scale spalls continuously in the absence of any Ce addition, but remains firmly adherent when Ce is present, with negligible weight change being recorded.

Similar features to these have also been demonstrated in Fe–27Cr alloys at temperatures between 1000°C and 1300°C by Wood and Boustead (1968) and by Wright and Wilcox 1974 in Fe–16Cr. Strafford and Harrison (1976) have examined Ni–15Cr-containing rare earths and Saito and Maruyama (1987) investigated rare-earth addition to a Ni–20Cr–1Si alloy. Rhys-Jones et al. (1987) have systematically examined the influence of Ce on the oxidation of Fe–Cr alloys at 1000°C, varying independently the Cr concentration and the Ce additions. The beneficial influence of Ce (in nucleating Cr_2O_3 and reducing rates of oxidation), increased with increasing Ce at constant Cr concentration, or at fixed Ce content with rising Cr concentration. The most significant effect of Ce was that it effectively induced the formation of Cr_2O_3 scales at concentrations of Cr lower than that required in the absence of the Ce additions.

In pure Cr the benefits of rare-earth additions are extended to also provide resistance to nitridation, which seriously embrittles chromium (see Hagel 1963, Seybolt 1966, Stephens 1972 and a study by Travadze et al. 1986 of Cr–La alloys in air at temperatures between 1100°C and 1400°C). These observations were repeatedly confirmed in the author's laboratory during the 1960's, in the development of ductile, high-strength chromium-base alloys (Mills and Ryan 1965).

Nagai et al. (1980a,b) demonstrated particular oxidation synergisms in a Fe–20Cr model alloy when more mobile Al and Si were added with other oxygen-reactive elements (Y, Gd, La, Zr and Ti). They noted that the formation of an internal (Si- or Al-rich) oxidation barrier, functioning to slow outward cation diffusion, was enhanced by the rare-earth alloy additions. This promoted improved oxidation resistance. The internal oxidation barrier was indirectly shown to result, not from any rare-earth enhanced metal diffusion in the substrate, but rather from changes in oxygen partial pressure at the metal/scale interface due to the presence of rare earths in the Cr_2O_3 scale. Similar results have been confirmed by Johansson et al. (1990) in stainless steels containing Si and treated with rare earths.

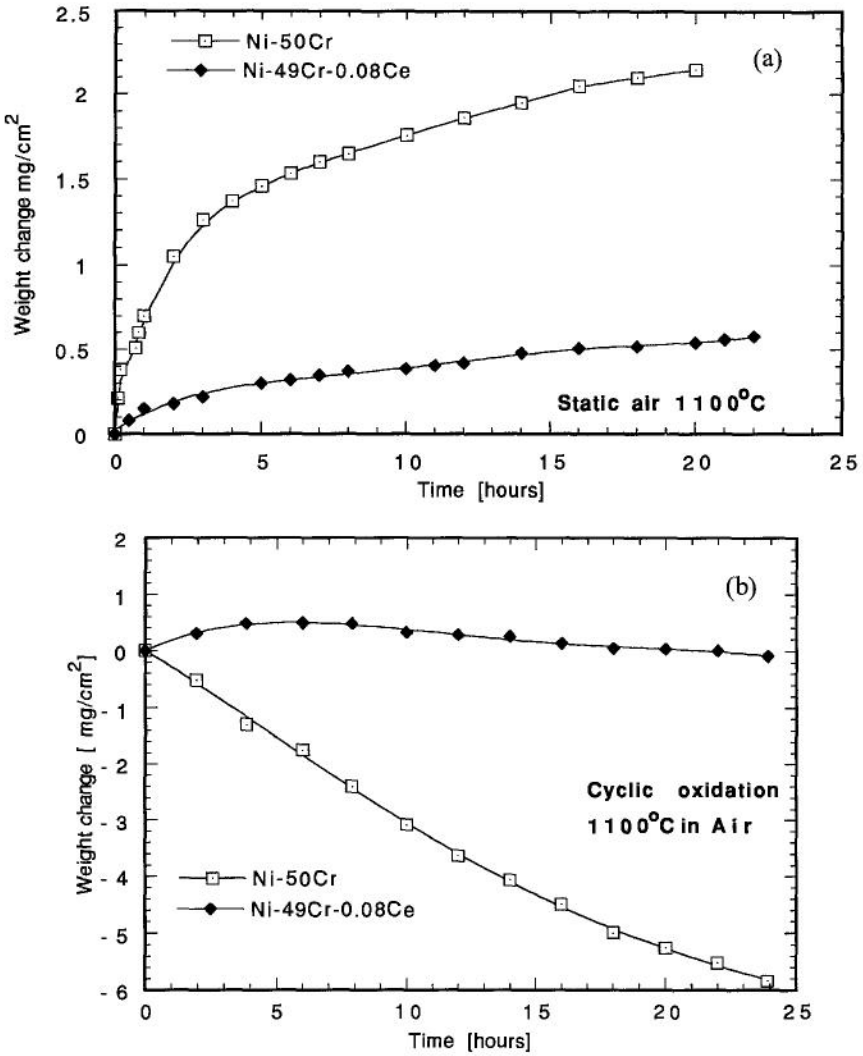

Fig. 6. Effect of Ce addition on the (a) static and (b) cyclic oxidation of Ni–50Cr alloy at 1100°C. (a) shows reduced rates of oxidation and (b) increased resistance to spallation (Ecer and Meier 1979).

3.2.1.2. *Rare earths as finely dispersed oxides.* One aspect of the mechanism by which rare-earth alloy additions improved resistance to oxidation is the ability to provide sites for the early nucleation of protective Cr_2O_3 films. Hence, it is plausible that they may function just as effectively in the form of fine oxide dispersions within the substrate alloy, and indeed this has elegantly been demonstrated by Rhys-Jones et al. (1987), Rhys-Jones and Grabke (1988). Figure 7 is a plot of the oxidation rate constant with respect to increasing weight% Ce metal, or CeO_2 dispersion, added to an Fe–10Cr alloy. The two curves are

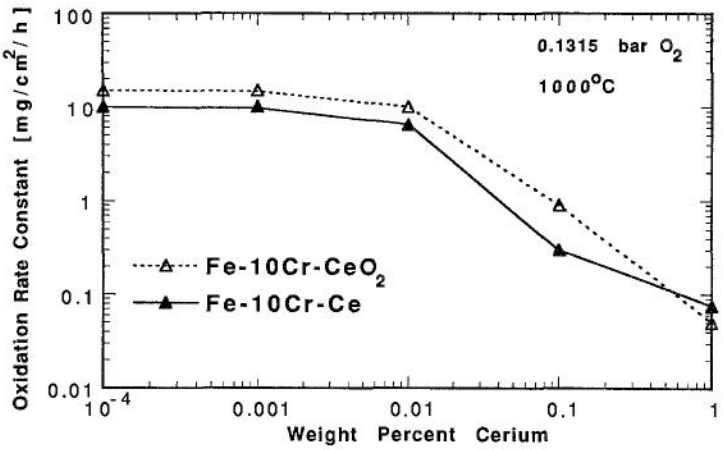

Fig. 7. Variation in the oxidation rate constant with wt.% Ce (or CeO_2) in Fe–10Cr alloy oxidized at 1000°C over 70 hours (Rhys-Jones et al. 1987).

closely parallel, showing a sharp reduction in oxidation rate constant, and thus, increased resistance to oxidation with additions of either Ce or CeO_2 above 0.01 wt.%.

These results confirm earlier practical demonstrations of the effect of fine rare-earth oxide dispersions in Ni–20Cr alloys (Stringer et al. 1972, Wright et al. 1975); in Fe–Cr alloys (Wright and Wilcox 1974, Nagai et al. 1981); in Co–21Cr (Stringer and Wright 1972) and in Cr-base alloys (Seybolt 1966, 1968). Attributes of the kind shown in these experimental materials are exhibited in modern mechanically-alloyed high-temperature materials, where the finely dispersed rare-earth oxide confers both increased strength, by virtue of its fine dispersion, as well as oxidation resistance and scale retention, on exposure to hostile high-temperature environments.

3.2.2. *Alumina (Al_2O_3)-forming alloys*

At temperatures above 1000°C, alumina (Al_2O_3)-forming alloys are preferred over the chromia (Cr_2O_3)-forming alloys which exhibit their best oxidation resistance at temperatures up to 950°C. Al_2O_3 is a highly stoichiometric oxide which possesses a low defect structure. Consequently, diffusion through Al_2O_3 is slow, and the Al_2O_3 protective film grows very slowly.

Both oxygen and aluminium ions diffuse, but the oxidation kinetics seem to be controlled mainly by grain-boundary inward diffusion of oxygen. Further, unlike Cr_2O_3, Al_2O_3 exhibits low volatility and is chemically inert in high-temperature oxidizing environments. However, its adhesion to the substrate is poor and the Al_2O_3 scale often develops a convoluted configuration; for more information see the review by Stott and Wood (1987).

Industrial attention focuses mainly upon iron-base (Fe–Cr–Al) alumina-forming alloys. For gas-turbine applications, Al_2O_3 scale formation is preferred, but the high-strength turbine-blade alloys do not possess adequate oxidation resistance and hence they must

be coated with either aluminide diffusion coatings, or with oxidation/corrosion resistant M–Cr–Al alloys containing up to 1 wt.% Y. These alloys are identified generically as MCrAlY overlay (or bond) coatings.

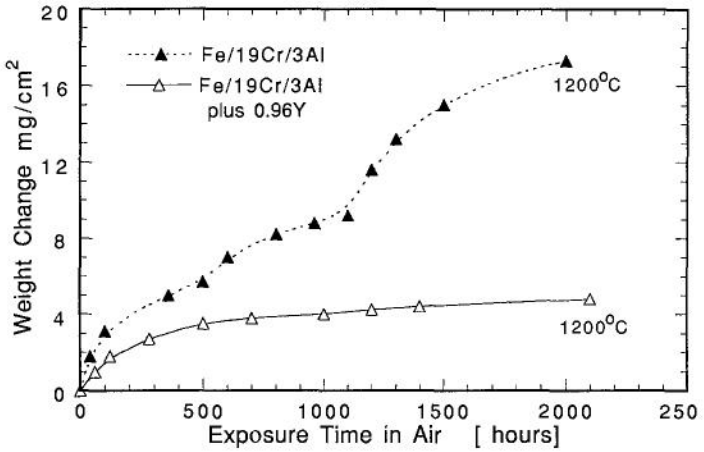

Fig. 8. Rates of oxidation in air of Fe–19Cr–3Al with and without Y. In the absence of Y, perturbations in the weight-change curve are associated with oxide cracking and spallation (Parshin et al. 1990).

3.2.2.1. *Influence of rare earths as alloy additions.* The addition of rare earths to Al_2O_3-forming alloys not only reduces the rate of oxidation as shown in fig. 8 (Parshin et al. 1990), but also enhances scale adhesion, particularly under cyclic conditions (see fig. 9, Tien and Pettit 1972). Golightly et al. (1976) and Wukusick and Collins (1964) have also studied the effect of Y additions on the oxidation of Fe–Cr–Al alloys in air, while Amano et al. (1979) have examined the influence of Ce additions. Jedlinski, Borchardt

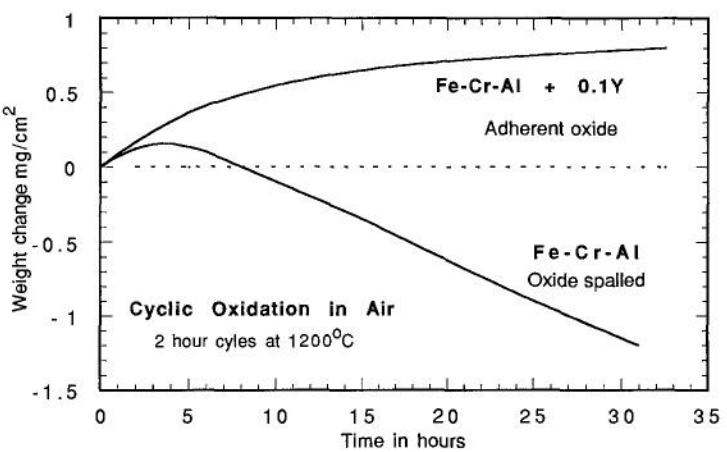

Fig. 9. Cyclic oxidation in air (2h cycles at 1200°C) of Fe–Cr–Al with and without 0.1% Y. Adherent Al_2O_3 is formed when Y is present. Oxide spallation results in the absence of Y (Tien and Pettit 1972).

and Mrowec (1991) in their study of Al_2O_3 scales on Fe–23Cr–5Al in air, over the temperature range 1200 to 1400°C, examined the influence of "mischmetal" additions, and of Y, introduced both by alloying and by ion implantation.

The effects of Y added to nickel-base alloys have been studied by Kuenzly and Douglass (1974) in Ni–13Al, and in Ni–10Cr–5Al by Kumar et al. (1974). Allam et al. (1978) have made a detailed study of Y additions in Co–Cr–Al alloys, while Giggins and Pettit (1975) have investigated both Co and Ni alloys containing 6Al with and without Y. A great deal of multi-nation attention continues to focus upon the mechanisms attached to Y for enhancing oxidation protection of the M–Cr–Al–Y series of overlay coating alloys, expanding the pioneering studies of Talboom, Elam and Wilson (1970).

3.2.2.2. *Rare earths incorporated into aluminide coatings.* The enhanced oxidation resistance and scale adhesion imparted to Al_2O_3 forming alloys has stimulated a quest for novel approaches for incorporating rare-earth elements into nickel–aluminide (β-NiAl) coatings on superalloy turbine-blade materials.

The simplest approaches are those resulting from diffusion heat-treatment of coatings derived from slurries containing Al, Cr, Ce and Y metal (~5 μm) powders, NH_4Cl and an organic binder. Using this slurry technology, Martinengo et al. (1977) produced a series of Cr-modified aluminide coatings and Cr-modified aluminides containing either Ce or Y. Enhanced oxidation/hot-corrosion resistance was demonstrated, particularly for chrome–aluminide coatings containing Y. More recent developments by Wang et al. (1989) of slurry deposited, Y-modified aluminide, again confirms improvement in scale adhesion and high-temperature oxidation.

Efforts to incorporate rare-earth elements during "pack-cementation" aluminide processing have also been attempted by Tu et al. (1986), and Takei et al. (1986). Success is generally hindered by the inappropriate thermochemical stabilities and/or volatility of rare-earth salts. Notwithstanding these difficulties, Olson et al. (1989) have been granted patents for producing Y-enriched aluminide on Co- and Ni-base alloys using Al–Y–Si(alloy)/Y_2O_3 powder-packs containing iodide activators. Mechanical entrapment of Y_2O_3 or CeO_2 from the pack-powder has demonstrated marginal benefit (Tu et al. 1986).

One novel and potentially practical approach, used for incorporating Ce and Y into aluminide coatings, has been demonstrated by He et al. (1990). They have successfully cathodically co-deposited Al/Ce and Al/Y coatings from molten-salt films. It should also be noted that the addition of up to 4 wt.% "mischmetal" in the molten aluminium used to aluminize steels, which are subsequently exposed to sulphidizing and carburizing environments at 850–950°C, results in markedly improved oxidation/corrosion resistance compared with standard aluminizing techniques for steel substrates (Long et al. 1975). Studies by Malik et al. (1991) have shown that it is possible to introduce rare-earth oxides into nickel–aluminide coatings applied to mild steel to achieve improved oxidation resistance.

3.3. *Surface-applied oxides*

The application of rare-earth oxides to the surfaces of high-temperature alloys to enhance their resistance to oxidation/corrosion has a long history, dating back to Pfiel (1945), and

is a highly cost effective approach. The simplest method has been to decompose thin films of a rare-earth soluble salt, derived from either aqueous or alcoholic solution, applying them to the substrate alloy and converting them to their corresponding rare-earth oxide (Skeldon et al. 1980, Landkof et al. 1985, Hou and Stringer 1987) or more sophisticated sol–gel techniques (Nelson et al. 1981, Fransen et al. 1984, 1985, Bennett 1984, 1989a) and also electrophoretic deposition from colloids of hydrous oxides or hydroxides (Polman et al. 1987, Haanappel et al. 1991).

When using the sol–gel route, the gel is developed directly on the metal substrate or applied after some degree of pre-oxidation, and then irreversibly converted by firing at up to 1000°C. The resulting oxide scale is more resistant than the oxide normally formed on the substrate alloy when exposed to hostile oxidizing/corrosive environment.

Rare-earth oxide films have also been applied by sputtering (Hussey et al. 1989, Graham 1991) and physical vapour deposition (PVD) routes (Adams et al. 1987, Onay and Saito 1990). For a detailed summary and history of methods used, see Moon and Bennett (1989).

Surface applied rare-earth oxides have mainly found application to Cr_2O_3-forming high-temperature alloys. The rare-earth oxides have clearly been shown to alter oxidation kinetics by changing the direction of reactive-ion transport from outward cation to inward anion diffusion, and as they become readily incorporated into the grain boundaries of the growing Cr_2O_3 scale, they also block these short-circuit diffusion paths. Furthermore, surface applied rare-earth oxides accelerate the development of the protective Cr_2O_3 scales (Bennett 1984, Rhys-Jones et al. 1987), and promote its formation at lower Cr concentrations (Goncel 1981, Landkof et al. 1985 and Rhys-Jones et al. 1987).

3.4. *Ion implantation*

Ion implantation provides a method for introducing chosen elements into the surface of a metal, thereby changing the surface alloy composition without recourse to melting procedures. Ion implantation is a useful tool for investigating surface behaviour relating to wear and corrosion protection. Although it can be applied to finished parts for practical industrial uses, it has mainly been adapted to investigate mechanisms of corrosion both in aqueous and high temperature environments (Was and Grabowski 1989, Bennett 1989b).

3.4.1. *Ion implantation into chromia-forming alloys*

Bennett, Dearnaley and their co-workers from UK-AEC Harwell Laboratories have pioneered many studies of ion implantation of rare earths, chiefly Ce and Y, but also La, Eu and Yb (Sc) in 20Cr–25Ni–Nb stabilized stainless steel (Antill et al. 1976, Bennett et al. 1984).

Ce and Y implanted at doses of 10^{15}–10^{17} ions per cm^2 greatly decrease the rate of oxidation in CO_2 atmospheres at temperatures up to 900°C and inhibit spalling. Benefits of reduced oxidation rate and scale adhesion have been conferred on Ni–25Cr above a critical dosage of 10^{16} ions per cm^2 (Hou and Stringer 1988). Patibandla et al. (1991)

have demonstrated that rates of oxidation in Ni–30Cr are reduced to one tenth of that of the unimplanted alloy when it is implanted with increasing doses of Ce ions (10^{14}, 10^{15} and 10^{16} per cm^2) and tested in a range of oxygen partial pressures (resulting from different CO–CO_2 gas mixtures), at temperatures between 900°C and 1100°C. Their detailed analysis of the Cr_2O_3 scales has provided excellent evidence contributing to a sound appreciation of the mechanism by which rare-earth elements impart increased resistance to oxidation.

In a 45Cr–Co-base alloy, Przybylski and Yurek (1988) have examined the beneficial influence of implanted Y ions. Implantation of Y into, and the effect on, the oxidation of pure Cr has been evaluated by Cotell et al. (1988).

These are but a small sample of a large number of studies on ion implantation for improved oxidation resistance; for further information the reader should refer to reviews by Bennett (1989b), Bennett and Tuson (1989) and Patibandla et al. (1991).

3.4.2. *Ion implantation into alumina-forming alloys*

Ion implantation into Al_2O_3-forming alloys has not been shown to be as useful in the study of oxidation mechanisms as it has for Cr_2O_3 formers. The reason for this is that Al_2O_3 scales tend to grow by inward oxygen diffusion, so that the initially implanted reactive element is quickly used up. The absence of a continuing supply at the oxide–metal interface leads eventually to the loss of adhesion of the oxide scale, although improved adhesion may have been imparted by the implanted Y ions. This kind of behaviour has been noted by Smeggil and Shuskus (1987) who compared the oxidation behaviour of a Co–Cr–Al–Y alloy and of Y ions implanted in Co–Cr–Al. Bennett et al. (1980a,b) noted similar features in Fe–15Cr–4Al at 1100°C. Jedlinski et al. (1989) have implanted Ce and Y ions into an aluminide (β-NiAl) on a nickel-base alloy and confirm that while initially the implanted reactive element effectively imparts increased scale adhesion, both in air and oxygen at 1000°–1200°C, the beneficial influence is not long lasting. They attributed this loss to the influence of the substrate Ni-base superalloy, since lasting benefits of reduced rates of oxidation and improved scale adherence were maintained when Y was implanted into bulk β-NiAl (Jedlinski and Mrowec 1987).

In an Fe–20Cr–5Al alloy, Quadakkers et al. (1991) have shown that implantation of Y ions at doses up to 10^{18} ions/cm^2 does not reproduce the same continuous benefits achieved by alloying with either Y or a fine dispersion of Y_2O_3, as, for example, in the mechanically-alloyed Fe–Cr–Al material – MA 956.

3.5. *Hot-salt corrosion*

3.5.1. *Rare earths in high-temperature superalloys*

The beneficial influence of dispersed rare-earth oxides in superalloys was demonstrated by Seybolt (1971). He emphasized the important benefit of the rare-earth oxides, as opposed to metallic alloy additions, proposing that, when exposed to molten Na_2SO_4, the rare-earth

oxides function to inhibit the formation of a low-melting-point Ni_3S_2–Ni eutectic or of liquid Ni_3S_2, the oxides acting to getter S in the form of stable oxysulphides R_2O_2S:

$$6CeO_2 + 3S \underset{(\text{from } SO_4)}{} + 4Cr = 3Ce_2O_2S + 2Cr_2O_3. \underset{(\text{from alloy})}{}$$

It is surprising that studies of this kind have not been extended in an effort to explain why relatively small fractions of rare-earth oxide (La_2O_3, CeO_2 and Gd_2O_3) dispersions function so effectively for long periods. Seybolt also conducted tests on a Ni-base superalloy containing a fine dispersion (0.5 wt.%) of CeO_2 and exposed at 940°C in a burner rig with 100 ppm NaCl being injected into the hot gas stream, which is converted to, and deposited as Na_2SO_4 on the alloy surface.

3.5.2. *Rare earths in aluminide coatings*

As referred to in sect. 3.2.2.2, attention has been given to incorporating Ce and Y into aluminide coatings by numerous novel methods. While enhanced oxidation resistance has been demonstrated, aluminide coatings containing rare earths must also exhibit improved resistance to hot-salt corrosion. This was shown to be the case for Cr–Ce and Cr–Y aluminides on IN738 and Hastalloy X (Martinengo et al. 1977) in crucible tests in fused Na_2SO_4–10NaCl salt mixes and by high-temperature (920°C) molten-salt electrochemical potentiodynamic experiments. While both Cr–Ce and Cr–Y aluminide coatings performed better than Cr-modified aluminide, the Y-containing aluminide generally exhibited better hot-salt resistance than the Cr–Ce aluminide coatings.

Similar behaviour has been obtained by He et al. (1990) for Al–Ce and Al–Y aluminide coatings produced by co-deposition onto a Ni substrate from molten-salt films. Figure 10 shows that both Ce–Al and Y–Al exhibit superior hot-salt corrosion, compared with

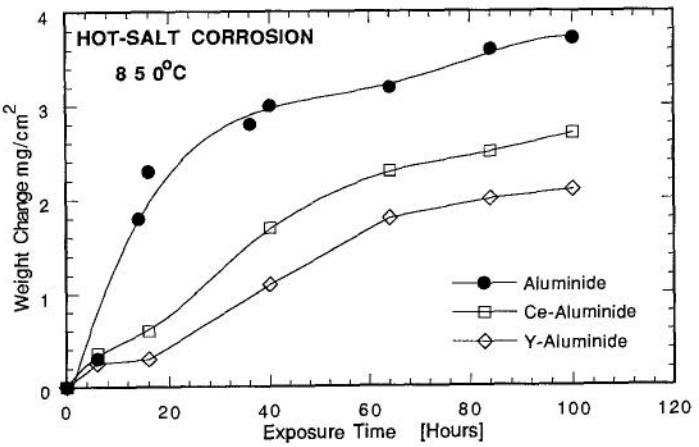

Fig. 10. Hot-salt corrosion of aluminide and co-deposited Al–Ce and Al–Y applied to 80Ni–20Cr Ni-chrome (He et al. 1990).

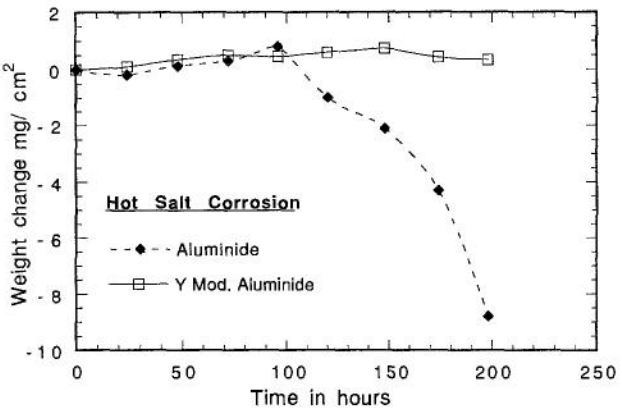

Fig. 11. Corrosion of aluminide coatings with and without yttrium at 750°C in 25% NaCl–75% Na_2SO_4 (Wang et al. 1989).

conventional aluminide coatings, when exposed at 850°C to a mixed Na_2SO_4–25NaCl coating. Y–Al was marginally more resistant that Ce–Al.

Wang et al. (1989) have shown (fig. 11), that an Y-modified aluminide produced by a slurry process onto IN738, clearly shows excellent hot-salt corrosion protection relative to conventional aluminide when exposed to cyclic hot-corrosion in molten Na_2SO_4–25NaCl.

In Japan, Takei et al. (1986) have examined Y-modified aluminide and Y-modified chromized coatings, where Y is first deposited by ion-plating followed by either Al or Cr pack-cementation. The beneficial influence of Y modification of both aluminide and chromized coatings on Ni-base superalloys (TM-49 and TM-321) has been confirmed in hot-salt, burner-rig and in an operational engine test.

3.5.3. *MCrAlY overlay coatings*

While a great deal of attention has been given to evaluation of the MCrAlY-type coatings with respect to their resistance to hot-salt corrosion generally, much less attention has been given to the specific influence of the Y addition. Lou et al. (1990) have examined Co–30Cr–6Al with and without 0.5Y having first been sputtered, using a planar magnetron apparatus, onto an IN738 Ni-base superalloy. Tests in molten-salt mixtures $75Na_2SO_4$–25NaCl at 850° (representative of Type I hot-salt corrosion), and in $75Na_2SO_4$–$25K_2SO_4$ at 900°C, clearly demonstrate the beneficial effect of the Y addition. Lou et al. attribute the beneficial influence of Y to the preferred formation of an Al_2O_3 oxide on Co–30Cr–6Al–0.5Y alloy inhibiting inward sulphur diffusion and thereby protecting the Ni-base substrate material from sulphidation. In the absence of Y, poorly adherent Cr_2O_3 forms and fails to effectively prevent sulphidation.

While these results show the favourable influence of Y, there remains evidence to show that Y can be leached from MCrAlY-type coatings and cast alloys with the formation of a complex oxy-sulphate $SO_3 + Y_2O_3 = Y_2O_2SO_4$ (Frances et al. 1988). Furthermore,

a French study (Vilasi et al. 1989), of a new Ni-rich γ–γ' overlay coating (Ni Co Cr Al Ta Y), showed that while Y, from M_5Y precipitates, promoted enhanced oxide-scale adhesion, and thus improved oxidation resistance, the Y addition provided no increased protection against acidic hot-salt corrosion. In this instance, the Y dissolved in the molten Na_2SO_4. Nevertheless, when this alloy, applied to a superalloy substrate by plasma spraying to form an overlay coating, was subjected to hot-salt corrosion testing at 850°C, the Y-containing material exhibited far greater resistance than the alloy without any Y. Results of this kind introduce the warning that behaviour of cast alloys does not necessarily provide a reliable guide in forecasting their performance as an overlay coating.

When MCrAlY coatings are exposed to vanadate impurities, derived from low-grade petroleum fuels, Kofstad and Seiersten (1987) have found that protective Al_2O_3 or Cr_2O_3 scale development is hindered by the presence of molten vanadates.

The chemistry of molten sulphate–vanadate deposits has been extensively investigated by Jones et al. (1985a,b, 1986), Jones and Williams (1987) and Jones (1988) in relation to both MCrAlY and stabilized-zirconia, thermal-barrier coatings. Their studies indicate that CeO_2 does not react to the same extent in V_2O_5, Na_3VO_4 or $NaVO_3$ as Y_2O_3 between 700°C and 900°C. Nevertheless, $Ce(SO_4)_2$ and Na_2SO_4 still combine to form low-melting eutectics in which V_2O_5 dissolves, leading to $CeVO_4$ precipitation. These studies were mainly concerned with the chemical interaction in molten-salt mixtures. Nevertheless, CeO_2 stabilized-zirconia was patented by Siemers and McKee (1982), in the belief that it was more resistant to hot-salt corrosion than the more common Y_2O_3 stabilized-zirconia. Destabilization of rare-earth-oxide stabilized zirconia thermal-barrier coatings by hot-salt corrosion still remains a serious problem.

3.6. *Sulphidizing and mixed gas atmospheres*

In studies of the beneficial effects of rare-earth elements in oxidizing atmospheres, attention is generally directed to temperature ranges exceeding 850°C. However, in mixed-gas atmospheres, characterizing coal gasification environments, significantly lower temperatures (often < 700°C) are encountered. At these lower temperatures, γ- or θ-alumina forms on the aluminium-containing alloys instead of the α-Al_2O_3 that forms at temperatures > 1000°C. On chromia-forming alloys, easy cation diffusion at the high sulphur (low oxygen) potentials, results in the formation of less protective (non-stoichiometric) sulphide scales of Fe, Ni, Cr, Al. While pre-oxidation, to form Al_2O_3 or Cr_2O_3 scales prior to exposure to mixed-gas atmospheres, affords some increased resistance as S^{--} diffusion proceeds, these oxides soon break down and the less protective sulphides develop. Since rare earths form stable sulphides (see fig. 3), and have clearly been shown to improve oxide-scale adhesion and reduce rates of oxidation in highly oxidizing environments, it would seem plausible that they might also impart benefits in sulphidizing environment.

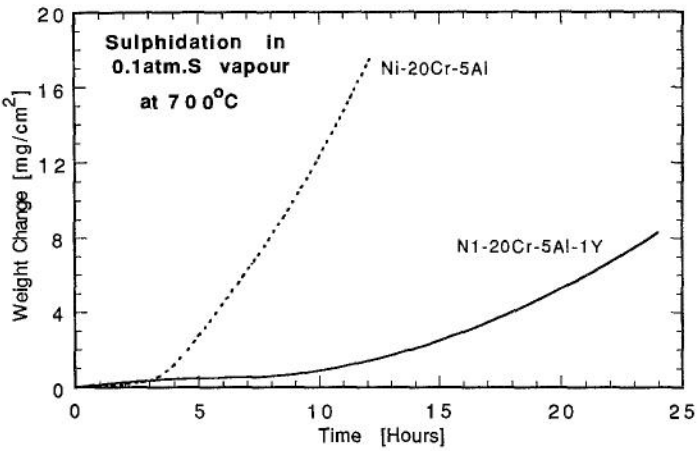

Fig. 12. Beneficial effect of yttrium on sulphidation of Ni–20Cr–5Al in 0.1 atm. sulphur vapour at 700°C (Vineberg and Douglass 1986).

3.6.1. *Rare earths for enhanced sulphidation resistance*

In pure S_2 vapour, at a pressure of 0.1 atm, Vineberg and Douglass (1986) demonstrated markedly reduced rates of sulphidation at 700°C (fig. 12) when 1 wt.% Y was added to a Ni–Cr–Al alloy. However, in mixed S_2–O_2 atmospheres at 500 to 700°C, Kung and Srinivasan (1990) failed to record any beneficial rare-earth effect when 1 wt.% Y was added to a model Fe–25Cr–6Al alloy.

A great deal more attention has focussed on modifying the Cr_2O_3-forming austenitic Fe–20Cr–32Ni alloy (Incoloy 800H). Both Ce and Y implantation have been investigated (Polman et al. 1987, Stroosnijder et al. 1989a,b, 1991). Direct exposure of this alloy to S–O–C bearing gas at 700°C, simulating a coal gasification atmosphere, normally results in serious degradation by severe external and internal formation of Fe and Cr sulphides. However, provided the Ce and Y implantation doses exceed 10^{16} ions per cm^2, significant sulphidation resistance ensues. A mass gain $\frac{1}{3}$ that of the unimplanted alloy, at a retarded rate of corrosion, corresponds with an observed increase in the Cr:Fe ratio in the mixed oxide/sulphide scale in the implanted alloy. This increase in the more stable sulphide-forming element (Cr_2S_3) parallels other observations derived from sulphidation of Fe–15Cr–4Al alloys containing Y (Saxena et al. 1987) and the influence of Ce, La or Y added to Fe–25Cr–40Ni (Shengtai et al. 1987). These latter authors show that Ce and Y additions of between 0.5 and 1 wt.% promote a 50% reduction in rate of sulphidation over that of the base alloy.

A more successful approach to sulphidation resistance is to induce pre-oxidation prior to exposure to the sulphur-rich gases. This has been shown by Polman et al. (1987), where Y-ion implantation into Fe–20Cr–32Ni (Incoloy 800H) proved insufficient to provide any improvement in its sulphidation resistance. However, pre-oxidation of the Y-implanted alloy, in oxygen at 1020°C, resulted in a 70% reduction in subsequent rate of sulphidation in mixed $95H_2$–$5H_2S$ and in $79Ar$–$20H_2$–$1H_2S$ gas mixtures at 560°C.

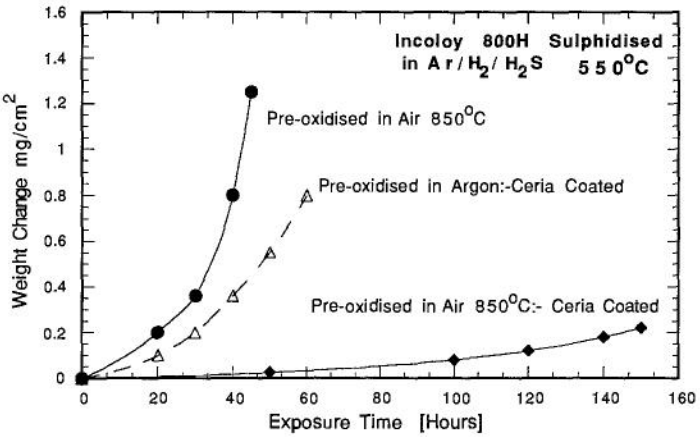

Fig. 13. High-temperature sulphidation of Incoloy 800H with and without ceria coating applied over a pre-oxidized substrate (Fransen et al. 1984).

Studies by Sidky and Hocking (1989) emphasise the importance of high-temperature (> 850°C) pre-oxidation to prolong the life of MCrAlY-type overlay alloys and MA956, when subsequently exposed both at the same (850°C) and at lower (450°C) temperatures in simulated coal-gasifier sulphidizing environments.

Natesan (1987) has given attention to M–Cr–Al coatings (applied by low-pressure plasma spraying) onto IN738 Ni-base superalloy. He has examined a range of M–Cr–Al compositions with and without Y and La exposed to ten different O_2–S_2 mixed-gas environments at two test temperatures 700°C and 871°C. Without the M–Cr–Al coating, IN738 is seriously degraded by sulphidation (Tiearney and Natesan 1982). Superior sulphidation resistance was provided by Co–Cr–Al–Y and Ni–Co–Cr–Y compositions over a wide range of S_2 pressures at low to intermediate pressures, but Ni–Cr–Al–La–Y and a Si-containing coating performed even better.

Benefits of the kind outlined above would suggest that the best resistance to sulphidation is achieved by oxide scales containing rare-earth elements (mainly Ce and Y). This being the case, one of the most cost-effective routes for enhancing resistance to sulphidation is to incorporate the rare-earth oxides by pre-oxidation of the substrates upon which rare-earth oxides have superficially been applied. The sequential development of this approach is illustrated in fig. 13, where the most effective sulphidation resistance is achieved on Incoloy 800H which has been pre-oxidized in air at 850°C and coated with CeO_2 (Fransen et al. 1985).

The particular benefits of pre-oxidation and coating with CeO_2, while not new, in relation to enhanced oxidation resistance, was noted by Fransen et al. in 1985, to also promote remarkably improved resistance to sulphidation in mixed-gases. Studies of this kind have continued in The Netherlands by Haanappel et al. (1991) who have exploited a technique involving electrophoretic deposition of a Ce-containing sol. Consideration of the influence of the sol solvent, concentration and thickness of the deposited layer, has

identified procedures capable of achieving optimum resistance to oxidation/sulphidation resistance in pre-oxidized (at 950°C) CeO_2-coated substrate (Incoloy 800H) exposed in an $Ar–19H_2–1H_2O–H_2S$ environment (simulating a coal-gasification atmosphere) over the temperature range 550°C to 700°C. While the CeO_2 surface-coated material exhibits resistance to thermal cycling, the benefits derived from CeO_2 coating are lessened by creep deformation; both actual strain and strain-rate effects induce cracks and consequent internal and localized external sulphidation (Stroosnijder et al. 1989a,b).

For a more detailed review of the influence of reactive elements, including the rare earths, on the resistance to high-temperature sulphidation, see Stott et al. (1989).

If the rare-earth oxides contribute to inhibiting sulphur diffusion by forming stable oxy-sulphides, as suggested by Seybolt (1971), it can more readily be appreciated that the ODS alloys containing rare-earth oxides perform well in sulphizing environments at 700°C, particularly when pre-oxidized at higher temperatures. This concept has been confirmed in Fe–25Cr–20Ni containing Y_2O_3 (Wright et al. 1989) and confirmed in the ODS alloys MA956 (see sect. 3.6.2).

3.6.2. *Commercial alloys containing rare earths in mixed gas systems*

Malik and Natesan (1990) have evaluated the performance of Al_2O_3-forming, oxide-dispersion-strengthened (ODS), ($Fe–20Cr–4.5Al–0.5Y_2O_3$) mechanically-alloyed material MA956, comparing it with other commercial Cr_2O_3-forming, Ni-base alloys, Incoloy 800H, C.101 and IN792, exposed to mixed oxygen/sulphur atmospheres over the temperature range 650–1200°C. Figure 14 clearly shows that MA956 alloy possesses superior resistance to sulphidation, exhibiting rates of sulphidation $\frac{1}{10}$ those of Incoloy 800H. This beneficial behaviour is attributed to the formation of an adherent Al_2O_3 film incorporating Y-containing M_2O_3 precipitates beneath an external sulphide. A development alloy similar to MA956 but with 16 wt.% Ni, to promote

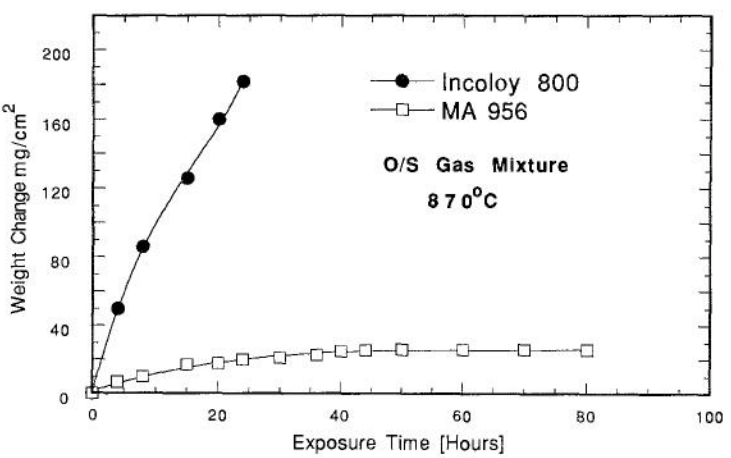

Fig. 14. Comparison between rates of oxidation of Incoloy 800 (Fe–21Cr–32Fe) and Y_2O_3 dispersion-strengthened MA956 ($Fe–20Cr–4.5Al–0.6Y_2O_3$) (Malik and Natesan 1990).

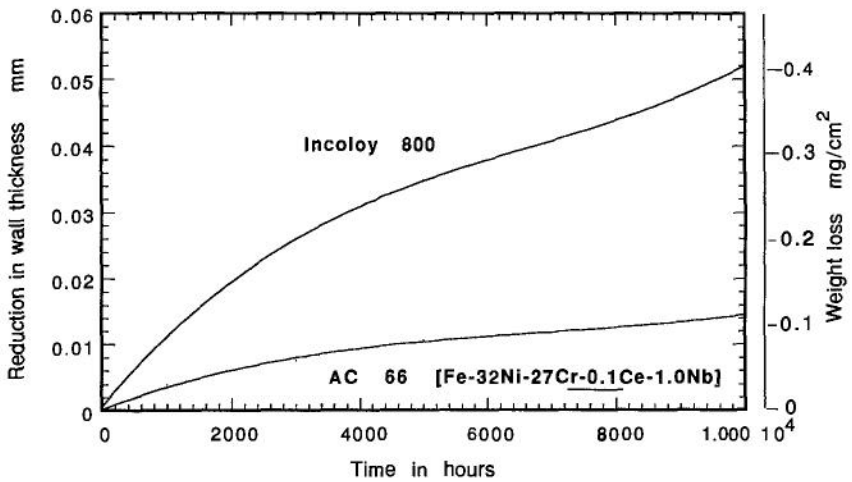

Fig. 15. High-temperature corrosion in fluidized bed process gas at 980°C (Bendick et al. 1990).

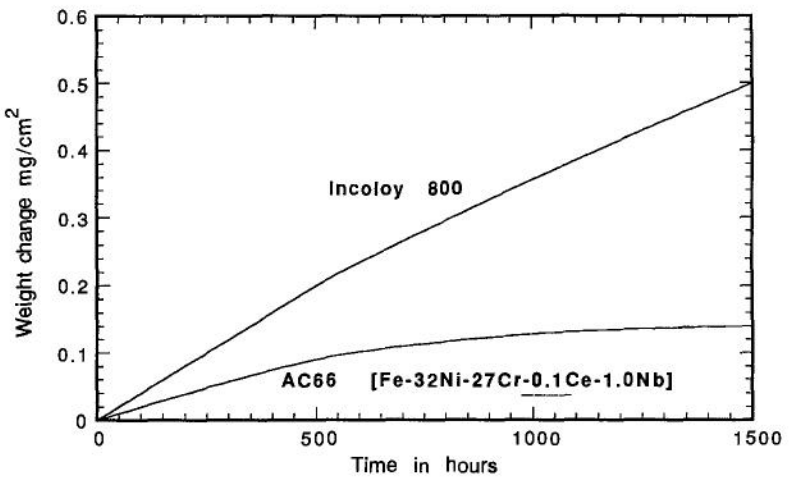

Fig. 16. High-temperature corrosion (wt.loss) in a $H_2/H_2O/HCl$ atmosphere at 980°C (Bendick et al. 1990).

Ni_3Al precipitation strengthening, was equally as resistant to sulphidation as the MA956 material. Malik and Natesan showed that further sulphidation resistance could be achieved by pre-oxidizing.

Particular attention is being given both in Europe and the USA to using Fe–20Cr–5Al-containing rare-earth additions as the substrate foil for automotive catalytic converters. The UK registered alloy FECRALLOY^{TM} exhibits corrosion resistance in oxidizing, sulphidizing and carburizing environments. In the USA, Sigler (1991) has examined the Fe–20Cr–5Al-containing Ce and La to improve oxide adherence. Exposed to moist

synthetic exhaust gas (a mixture of CO_2, H_2O, and N_2) significant temperature-dependent effects have been noted when both α- and θ-alumina tend to form at around 850°C.

In a German development (Bendick et al. 1990), an Fe–32Ni–27Cr–0.1Ce–1.0Nb alloy designated AC 66 exhibits excellent resistance to high-temperature sulphidizing corrosion in fluidized-bed process gas at 980°C (fig. 15). The Nb in this alloy, which of itself possesses a relatively high negative free energy for sulphide formation and very low rates of sulphidation (see e.g. Strafford and Bird 1979), most likely promotes a NbS_2 sub-scale, which acts as an internal diffusion barrier. This alloy (AC 66) also provides excellent high-temperature corrosion resistance, at 900°C, in mixed H_2/H_2O/HCl gases, representing a waste-incinerator environment (fig. 16).

4. Mechanisms for enhanced oxidation resistance

While the reactive-element (or rare-earth element) effects for enhancing oxidation resistance have been known for over 50 years, it is only over the last 10–15 years that serious, and extensive, consideration has been given to the mechanisms involved. Effort has been directed to identifying a single mechanism. However, it seems clear that several co-operative effects function to promote improved oxidation resistance. No generalized theory can account for all experimental observations. Rare earths influence oxide growth and transport behaviour on Cr_2O_3- and Al_2O_3-forming alloys differently, yet commonly lead to enhanced adhesion of the respective oxide scales.

The reader is directed to three comprehensive reviews and a conference publication, dealing with the reactive-element effects on oxidation: Whittle and Stringer (1980), Stott and Wood (1987), Moon and Bennett (1989) and Lang (1989), thus only a broad summary of proposed mechanisms, classified as either chemical, physical or mechanical effects is presented here. These may be further, or even alternatively, sub-divided into effects relating to (i) initial oxidation, (ii) growth-rate, (iii) scale adhesion, or (iv) cracking.

4.1. *Chemical effects*

4.1.1. *Chemical reactivity*

Reactive elements, as trace alloy additions, capable of enhancing metal-oxide bonding, characteristically possess large negative free energies of oxide formation (fig. 3, Nagai and Okabayashi 1981, Nagai et al. 1980b). This driving force might well confirm concepts proposed originally by Pfeiffer (1957) and Peters and Grabke (1984) for preferential rare-earth oxide formation. Similar ideas were put forward by McDonald and Eberhart (1965) and again by Smialek and Browning (1985).

This preferential formation of the rare-earth oxide, though conceded to occur, does not produce a continuous film. Rather, the local and preferential formation of rare-earth oxide is believed to exert a profound influence on initial stages of oxidation by (a) providing heterogeneous sites for the nucleation of the first formed oxide, (b) reducing the formation of transitional oxides, (c) promoting the growth of stable oxides (i.e. Cr_2O_3 and Al_2O_3),

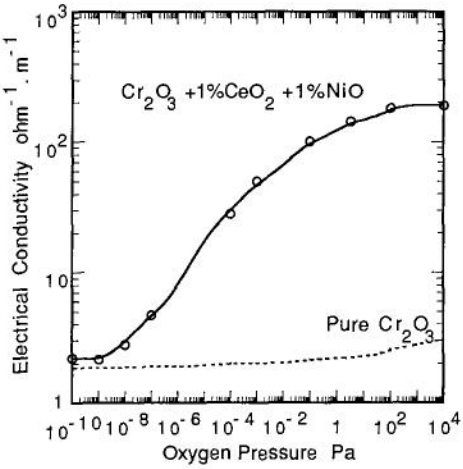

Fig. 17. Oxygen pressure dependence of the electrical conductivity of Cr_2O_3 at 1200°C (Nagai 1988).

(d) decreasing inter-nucleation spacing, (e) thereby promoting decreased oxide grain-size (Stringer et al. 1972, Ecer et al. 1982, Hou and Stringer 1987, and Saito and Maruyama 1987).

Meanwhile, theoretical studies by Anderson et al. (1985), who modelled molecular orbitals for possible bonding between Y, Al and Ni atoms (relative to metal and oxide clusters), predict that substantial bond enhancement occurs when a few mono-layers of Y become sandwiched between an Al_2O_3 scale and a Ni-base alloy substrate. However, no analytical evidence for any rare-earth enrichment at metal–oxide interfaces has yet been found, whereas analytical techniques have detected Ce and Y enrichment in both Cr_2O_3 and Al_2O_3 scale grain boundaries and more particularly in the outer regions of the oxide scales. Such observations are confirmed in studies by Przybylski et al. (1987, 1988), Yurek et al. (1987), Delaunay and Huntz (1982), Ramanarayanan et al. (1988), Bennett and Tuson (1989), Moon and Bennett (1989) and Wang et al. (1989).

Chemical effects relating to changes in ionic conductivity when rare earths are dissolved in oxides have been documented. For Cr_2O_3, Nagai (1988, 1989) has demonstrated changes from p- to n-type semiconductor behaviour when rare earths are dissolved in Cr_2O_3. This results in dramatic changes in electrical conductivity over a very wide range of oxygen pressures, as shown in fig. 17. The change to n-type semiconductivity should result in decreasing ion diffusion, and thus in reduced rates of oxidation.

Huntz (1988) has reported on studies of conductivity and chemical diffusion experiments conducted on synthetic Al_2O_3 doped with Y. Undoped Al_2O_3 behaves as an electron conductor, but this changes to an ionic conductor when doped with Y. He concludes that these observations confirm radioactive tracer studies which reveal that cation diffusion is enhanced by the presence of Y. Transport phenomena of this kind are very difficult to interpret, especially when it is recognized that Y_2O_3 is almost insoluble in Al_2O_3. Phase diagrams by Reser (1975) of Cr_2O_3–R_2O_3 and Al_2O_3–R_2O_3 indicate the likely

formation of perovskite-type oxides RMO_3 without dissolution in either Cr_2O_3 or Al_2O_3. Indeed $CeCrO_3$ oxide-scale grain-boundary precipitates have been identified in Cr_2O_3 by Saito and Maruyama (1987) and Graham (1991), and $YCrO_3$ by Przybylski et al. (1986). Choquet and Mevrel (1989) have identified $Y_3Al_3O_{12}$ (Y-garnet) particles in Al_2O_3 scales on a NiCoCrAlY alloy, confirming the 1984 results of Ramanarayanan et al. in Al_2O_3 formed on Fe–25Cr–4Al–0.5Y. Rare-earth enrichment of oxide-scale grain boundaries has been unequivocally established by transmission and scanning-electron-microscopy coupled with X-ray microprobe and other surface analytical approaches using radioactive tracer methods (Yurek et al. 1987, Przybylski et al. 1987, Cotell et al. 1990, Graham 1991).

4.1.2. *The effects of tramp elements (the sulphur effect)*

One of the main chemical influences associated with rare-earth enhancement of oxidation resistance, relates to scavenging of tramp impurities, principally S segregating to the metal/oxide-scale interface and interfering with scale adhesion. Smeggil et al. (1986) and Smeggil and Shuskus (1987) initially provided strong circumstantial evidence indicating the serious influence of S segregation upon the adhesion of Al_2O_3 scale. They showed that high-purity alloys with less than 10 ppm S exhibited high spallation resistance and argued that rare-earths (mainly Y) scavenged the S in the less pure alloys, or provided traps for S at internal Y_2O_3 particles. Further supporting evidence for impurity segregation has been provided by Lees (1987) who demonstrated that prior annealing of Cr in hydrogen improved the adhesion of Cr_2O_3 scales on pure Cr at 950°C. Lees also proposed that contamination of the Cr_2O_3 scale with S led to accelerated cation transport and voids at the oxide–metal interface. Thus, removal of S by hydrogen anneal before oxidation also resulted in a reduced rate of oxide growth with an associated change to anion (O^{--})-controlled growth direction.

Rising S contamination in Fe–20Cr has been shown by Rhys-Jones et al. (1987) and Rhys-Jones and Grabke (1988) to cause increased rates of oxidation and oxide spalling. Ce additions counteract these effects. Direct evidence for S segregation has now been reported by Luthra and Briant (1988), Bornstein et al. (1989), Khanna et al. (1989) and Smialek (1991). Figure 18 shows that even on S-free Ni–10Cr–8Al alloy, oxide spalling occurs. When a small trace (100 ppm) of S is present, the oxide scale remains attached, but exhibits an increased rate of oxide growth. A critical amount of Y is required to scavenge high S additions so as to maintain adhesion and a low rate of oxide growth. Evidence is now sufficiently strong to show that S is detrimental to the adherence of oxide scales, particularly on Al_2O_3-forming alloys.

A principal benefit (Ikeda et al. 1989) attributed to rare earths is their ability to scavenge the tramp S impurity as a stable sulphide. An appreciation of the thermochemistry of tramp element scavenging in relation to Al_2O_3 adherence has been outlined by Sigler (1989). While scavenging of the S impurity by rare earths is important, it cannot be considered as a single generalized mechanism, because it does not explain (a) changes in rates of oxidation, (b) direction of oxide growth, (c) the influence of

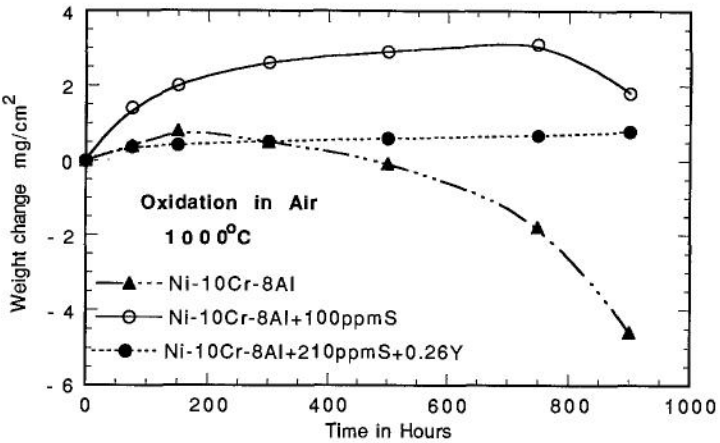

Fig. 18. Change in weight with respect to time at 1000°C in air for Ni–10Cr–8Al alloy with and without additions of sulphur and yttrium (Khanna et al. 1989).

dispersed rare-earth oxides (CeO_2, Y_2O_3), or (d) effects induced by superficially applied coatings.

4.2. *Physical effects*

The physical influences of rare-earth elements on rates and direction of growth and structural characteristics of oxide scales mainly result from the incorporation of the rare-earth compounds in the scale. Other influences relate to their capacity to nucleate more uniform fine-grained oxide, inhibit the formation of transitional oxides and promote, for instance, Cr_2O_3 formation where it would not normally be expected, as exemplified in studies by Stringer et al. (1972), Whittle et al. (1977), Rhys-Jones et al. (1987) and Rhys-Jones and Grabke (1988).

4.2.1. *Chromia-forming alloys*

On chromia-forming alloys, in the absence of any rare-earth element, oxide scales form essentially by outward cation diffusion with only minor inward oxygen diffusion through the oxide grain boundaries. This is explained by the fact that Cr^{3+} diffusion in Cr_2O_3 is almost 5 times faster than O^{--} diffusion (see table 2) but, as reported by King and Park (1989) and Park and Natesan (1990), grain-boundary diffusion is very much faster than bulk diffusion. They quote values at 1000°C of 10^{-11} cm^2/s and 10^{-14} cm^2/s, respectively, for an oxygen partial pressure in equilibrium with Cr/Cr_2O_3.

It has repeatedly been confirmed that in chromia-forming alloys, the mechanism of oxide-scale growth is changed in the presence of rare-earth elements from cation to anion control, and consequently the direction of growth also changes (Hussey et al. 1989, Graham 1991).

The rare-earth oxides, principally CeO_2 and Y_2O_3, are regarded as fast conductors of oxygen. For instance, in Y_2O_3 oxygen diffusion is 5 orders of magnitude faster than cation

Table 2
Coefficients of diffusion of cation (metal) and anion (oxygen) in alumina, chromia and rare-earth oxides

Oxide	Temperature (°C)	Coefficient of diffusion	
		Cation (metal) ($cm^2\ s^{-1}$)	Anion (oxygen) ($cm^2\ s^{-1}$)
Alumina (Al_2O_3)	700	9.4×10^{-18}	1×10^{-17}
Chromia (Cr_2O_3)	700	3.3×10^{-15}	4.6×10^{-22}
	1000	5.0×10^{-12}	9.4×10^{-17}
Ceria (CeO_2)	700	–	1.5×10^{-9}
	1000	–	2.8×10^{-8}
Yttria (Y_2O_3)	700	6.1×10^{-18}	2.2×10^{-11}
	1000	2.0×10^{-14}	2.6×10^{-9}
$LaCoO_3$ (perovskite)	1000	–	8×10^{-13}

References
Ishigaki et al. (1984)
Steele and Floyd (1971)
Hagel and Seybolt (1961)
Hagel (1965)

diffusion, and the same applies for some of the perovskite (RMO_3) type compounds, as can be seen in table 2. Thus, when present in Cr_2O_3, they would assist the inward diffusion of O^{--} to the metal/oxide interface. Furthermore, since CeO_2 or Y_2O_3 are likely to form preferentially, before other transitional oxides, the faster inward diffusion of oxygen would immediately be stimulated, inhibiting outward cation diffusion. Consequently, the coalescence of vacancies, which might otherwise lead to interfacial Kirkendall voids, is suppressed; hence, scale adhesion is enhanced.

Explanations of this kind take account of the change from cationic to anionic control of oxide growth direction (see e.g. the ^{18}O tracer oxidation studies of Cr by Cotell et al. 1990), but only partially account for the substantially reduced rates of growth. Therefore, the rare-earth enrichment of oxide grain boundaries and precipitation of RMO_3-type oxides must also function to block the grain-boundary short-circuit diffusion paths. Segregation of Y to Cr_2O_3 grain boundaries has been confirmed in a number of careful studies, e.g. by Yurek et al. (1987), and Ce enrichment by Papaiacovou et al. (1990). In addition, the presence of rare-earth oxide particles in the oxide grain boundaries function to interfere with grain-growth through so-called boundary "drag". This preserves a finer oxide grain-size, and thereby improved oxide-scale mechanical properties.

A good example of reduced oxide grain-size is shown in fig. 19. Part of this sample of IN738 was first coated with a CeO_2 sol from a 20% aqueous suspension of CeO_2 colloid and exposed for 100 hours in air at 900°C. A clear transition from fine to coarse oxide scale exists between the CeO_2 coated and uncoated areas on the IN738 specimen surface.

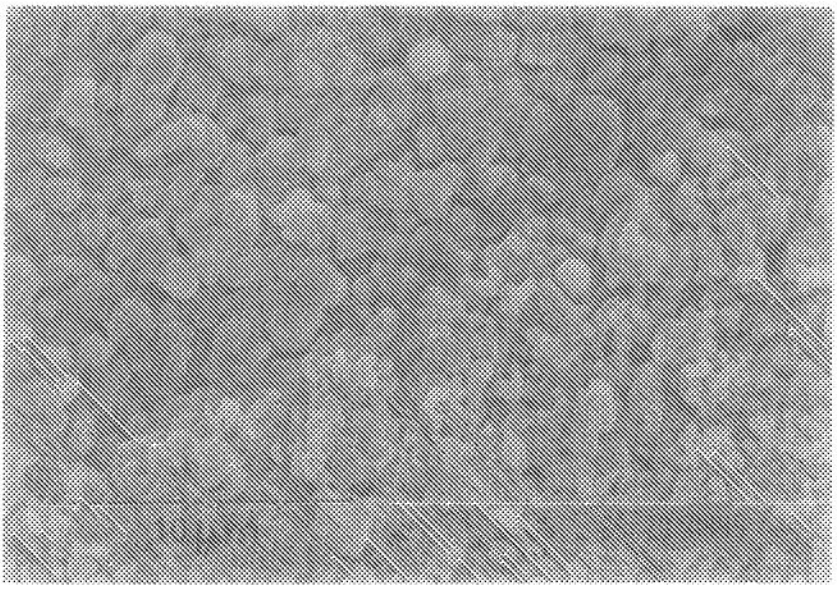

Fig. 19. Influence of CeO_2 sol–gel coating on the oxide grain size formed on IN738 superalloy. A clear delineation is seen in this micrograph between lower CeO_2-coated, and the upper CeO_2-free surface.

4.2.2. *Alumina-forming alloys*

Mechanisms for Al_2O_3 scale growth are not as clear cut as reported for Cr_2O_3 scales. Using standard marker techniques, differences in scale-growth direction have been noted in iron-base, α-alumina-forming alloys. Both inward oxygen diffusion (Tien and Pettit 1972) and cationic outward diffusion of Al (Quadakkers et al. 1989) has been reported in unmodified Fe–Cr–Al alloys (see table 3 for classification of authors reporting conflicting observations).

Careful ^{18}O tracer studies by Abderrazik et al. (1987) have revealed combined inward O^{--} diffusion and outward Al^{3+} diffusion, confirming the theories proposed by Golightly et al. (1976) and identifying the problems of internal-oxide formation within the growing oxide. This is also associated with convolutions in the oxide scale and poor adhesion. However, other inconclusive observations have been reported for Ni-base alloys. Reddy et al. (1982), using alternate exposure to ^{16}O and ^{18}O, reported inward O^{--} transport as the dominant growth mechanism for Al_2O_3 scales on NiCrAl alloys. Nevertheless, they did show that O^{--} diffused inward along grain-boundary short-circuit paths.

In the Al-rich β-NiAl Young and de Witt (1986) and Jedlinski and Mrowec (1987) observed substantial outward diffusion of Al^{3+}, which was further stimulated in the presence of Y. This is the reverse of the influence of rare earths in Cr_2O_3 scale. The one common feature for the influence of rare earths on either Cr_2O_3 or Al_2O_3 growth is clearly their separation into the oxide grain boundaries. Y being the more widely studied addition to alumina-forming alloys, $YAlO_3$ and $Y_3Al_5O_{12}$ (Y garnet) oxide grain-

Table 3
Transport mechanisms in thermally grown α-Al_2O_3

O_2 transport dominant (inward scale growth)	Both O_2- and Al^{3+} transport	Al^{3+} transport dominant (outward scale growth)
Tien and Pettit (1972)	Golightly et al. (1979, 1980)	Young and de Witt (1985)
Pettit and Felten (1976)		Young and de Witt (1986)
Hindam and Smeltzer (1980)		Abderrazik et al. (1987)
Whittle and Stringer (1980)		
Reddy et al. (1982)		
Ramanarayanan et al. (1984a,b)		
Moseley et al. (1984)		

boundary precipitates have been identified (Ramanarayanan et al. 1984a,b, Parshin et al. 1990, Choquet and Mevrel 1989).

Ce-modified alumina-forming alloys have been investigated by Amano et al. (1979) yielding evidence for dominant inward O^{--} diffusion in the presence of Ce.

With the aim of elucidating the influence of Y on transport mechanisms in Al_2O_3, studies have been conducted on doped and undoped solid Al_2O_3. El-Aiat and Kroger (1982) and Lesage et al. (1984) conclude that Y induces a change in conduction behaviour in Al_2O_3 from electron conductor (undoped) to ionic conductor (Y doped), which confirms other tracer studies reported by Huntz et al. (1984), wherein enhanced cation diffusion was noted in Y-doped poly-crystalline Al_2O_3. For these reasons Y_2O_3 is sometimes used as a sintering aid for consolidating ceramic aluminas. While these studies reveal that rare earths, and Y in particular, influence transport properties of solid Al_2O_3, they do not provide unequivocal evidence for the specific function of rare earths in thermally grown Al_2O_3 scales.

Researchers who have recognized preferential inward O^{--} diffusion as rate controlling for Al_2O_3 scale growth consider that Y suppresses Al^{3+} transport in the scale, prevents internal nucleation of Al_2O_3 and its consequent influence on internal stresses in the scale. Conversely, investigators recognising outward growth conclude that Y decreases O^{2-} diffusion. All agree however, that grain-boundary short-circuit diffusion in Al_2O_3 plays a significant role.

Two possible explanations are offered to account for seemingly conflicting results: (i) segregation of Y with its large ionic radius in Al_2O_3 lattice is capable of trapping Al vacancies and thereby slowing cationic diffusion, and/or (ii) grain-boundary precipitates modify the relative grain-boundary rates of Al^{3+} or O^{--} short circuit diffusion. Moreover, Y modifies (reduces) the size and shape of Al_2O_3-scale grains and external configuration, preventing the formation of poorly adherent convoluted scales. In this latter respect, rare earths act to reduce internal stress levels (see sect. 4.3.3).

4.3. *Mechanical effects*

Enhanced resistance to oxide spallation is a common benefit imparted by rare earths to both chromia and alumina-forming high-temperature alloys and some of the reasons for this improvement can be attributed to chemical or physical factors. However, reasons for spalling are factors derived mainly from mechanical influences: (i) thermal-mismatch stresses generated on cooling, (ii) interfacial voids, (iii) internal stresses developed during oxide growth, (iv) inherent oxide brittleness, and (v) defects and cracks developed in thickening oxide films.

4.3.1. *Oxide pegs*

The most notable of mechanical effects contributing to improved performance due to rare earths is oxide pegging. Protrusions associated with rare-earth-rich constituents act to peg the oxide scale and thereby increase its adhesion to the substrate. This concept was proposed as early as 1950 by Lustman (1950) and has received regular support from many researchers ever since (Felten 1961, Wukusick and Collins 1964, Allam et al. 1978, Hindam and Whittle 1982). However, since good adhesion can still be achieved in the absence of pegs (macro- or micro-), this cannot be regarded as a general mechanism to account for the rare-earth effect (Bennett 1984, Pivin et al. 1980).

4.3.2. *Increased oxide plasticity*

Mechanical effects derived from early speculation by Antill and Peakall (1967) concerned increased scale plasticity from dissolved rare-earth elements. Such concepts were also supported by Francis and Juston (1968). This increased oxide-scale plasticity is often attributed to rare-earth induced refinement of oxide grain-size. However, while this may apply to the relaxation of growth stresses by creep mechanisms such as grain-boundary sliding, during isothermal oxidation (Kofstad and Lillerud 1980), it remains a purely speculative proposal, for, even in the absence of Y, Choquet and Mevrel (1989) have shown that α-Al_2O_3 on NiCoCrAl (at 1100°C) is clearly quite plastic. Convoluted Al_2O_3 scale morphology identified by Golightly et al. (1976, 1980) might also be interpreted as evidence of oxide plasticity.

4.3.3. *Internal stresses in oxide scales*

Studies of Golightly et al. (1976) provide evidence for changes in internal stresses in oxide scale promoted by rare-earth elements. They argue that the formation of further Al_2O_3 within an existing scale resulting from inward diffusion O^{--} and Al^{3+} diffusing outward, must develop compressive growth stresses, and hence a ridged or convoluted scale. The addition of Y suppresses the outward diffusion of Al^{3+} and consequently reduces the development of high compressive oxide growth stresses.

Convincing evidence of rare-earth elements leading to reduced internal stresses in oxide scales has been obtained by X-ray measurements by Choquet and Mevrel (1989), and by deflection techniques by Delaunay et al. (1980) and Huntz (1988) using thin

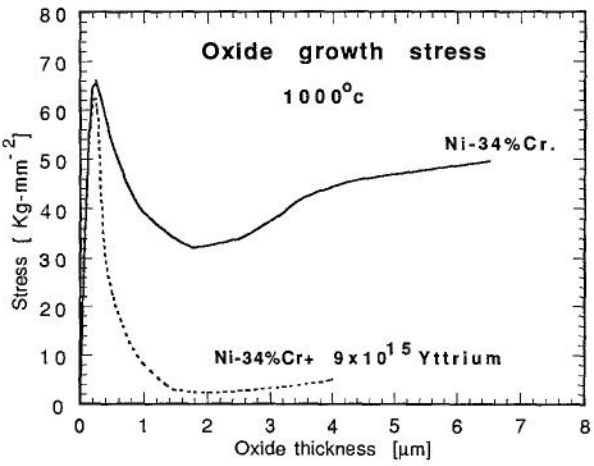

Fig. 20. Oxide growth stress as a function of thickness and yttrium ion-implantation (Huntz 1988).

strips of substrate alloy with and without rare-earth additions (see fig. 20). Following an initially high peak stress, the residual compressive level in the Cr_2O_3 scale formed on the Y implanted Ni–34Cr at 1000°C drops to a low relaxed level as the oxide grows compared to the high residual stress retained in Cr_2O_3 growing on the Y free Ni–34Cr.

4.3.4. *Changes in mechanical properties of oxides*

Lower growth rates result in thinner oxide scales which can more readily accommodate thermal-mismatch stresses on cooling and exhibit better resistance to spalling. However, Bennett and Tuson (1989) have unequivocally demonstrated that rare-earth additions are capable of promoting a five-fold increase in oxide thickness before the onset of any oxide spalling. This is associated with greatly increased times at temperature being necessary to build up to a specific thickness before spalling occurs. Results of this kind imply either an increase in oxide fracture strength/toughness or reduced defect size. The latter is regarded by Nicholls and Hancock (1989) to be consistent with the observed benefits imparted by active rare-earth elements, namely reduced distribution of defects (cracks, voids or open boundaries) in oxide scales. The absence of gross defects is exemplified in the studies reported by Rhys-Jones et al. (1987). Using these data, Nicholls and Hancock have plotted the equivalent critical crack (or defect) length a in a Cr_2O_3 scale versus Cr content, for Fe-Cr alloys with and without Ce (fig. 21). The beneficial effect of the 0.1% Ce addition for reducing the effective defect size is evident. Similar results have been found for the more dense (i.e. reduced defect size and distribution) Cr_2O_3 scales formed on Fe–20Cr–25Ni–Nb implanted with either Ce or Y ions. In the latter alloy the improvement in resistance to oxide fracture relates to a reduction in effective defect size of three orders of magnitude.

This analysis of reduced defect size and distribution due to rare-earth element effects, provides support for the concept that rare-earth oxides in oxide scales act as vacancy sinks preventing the formation of defects in oxides developed from voids or pores.

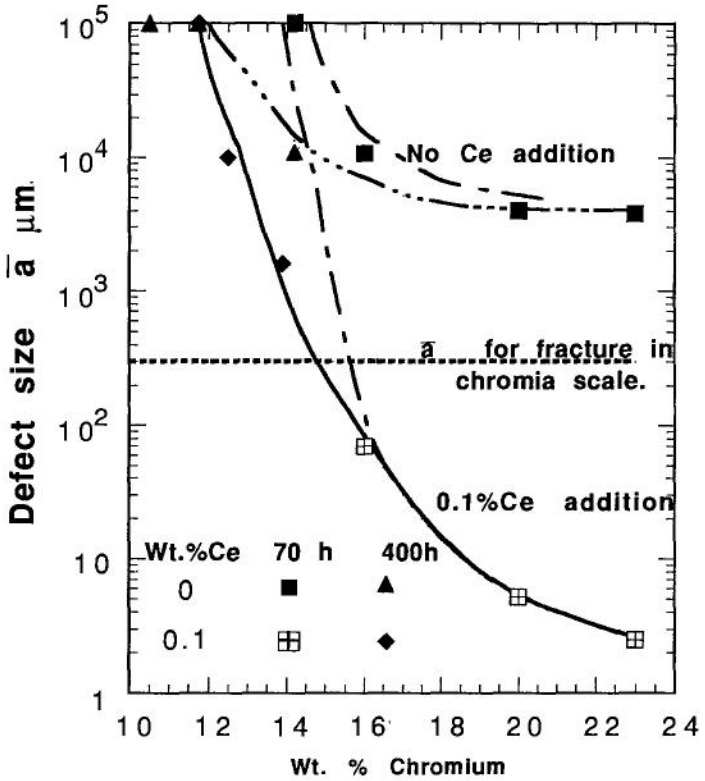

Fig. 21. Estimated values of an effective defect length a observed in oxides formed on Fe–Cr alloys with and without additions of cerium (Nicholls and Hancock 1989).

4.4. *Summary of mechanisms for rare-earth enhanced resistance to oxidation*

(1) Promotion of preferential nucleation and growth of stable, low diffusivity Cr_2O_3 or Al_2O_3 protective scales.
(2) Reduced rates of scale growth by modifying transport processes by (a) blocking outward cation diffusion, particularly along short-circuit grain-boundary paths, and/or (b) providing vacancy sinks which limit diffusional growth, thereby inhibiting the formation of interfacial voids.
(3) Prevention of spalling and fracture of the oxide scale by: (a) scavenging tramp elements, notably S, and (b) reducing internal stresses and defect size and increasing the mechanical strength/toughness of the oxide scale.

References

Abderrazik, B.G., G. Moulin and A.M. Huntz, 1987, Solid State Ionics **22**, 285.

Adams, R.O., A. Digiallonardo and C.W. Nordin, 1987, Thin Solid Films **154**, 101.

Allam, I.M., D.P. Whittle and J. Stringer, 1978, Oxid. Met. **12**(1), 35.

Amano, T., S. Yajima and Y. Saito, 1979, Trans. Jpn. Inst. Met. **20**, 431.

Anderson, A.B., S.P. Mehandra and J.L. Smialek, 1985, J. Electrochem. Soc. **132**, 1695.

Antill, J.E., and K.A. Peakall, 1967, J. Iron Steel Inst. London **205**, 1136.

Antill, J.E., M.J. Bennett, R.F.A. Carney, G. Dearnaley, F.H. Fern, P.D. Goode, B.L. Myatt, J.F. Turner and J.B. Warburton, 1976, Corros. Sci. **16**, 729.

Bendick, W., J. Lindeman and W. Schendler, 1990, Development of a new high-temperature alloy for coal gasification, cycle processes and waste incineration, in: High-temperature Materials for Power Engineering, Vol. 1, eds E. Bachelet, R. Brunetaud and D. Coutsouradis (Kluwer Academic Publishers, Dordrecht).

Bennett, M.J., 1984, J. Vac. Sci. & Technol. B **2**(4), 800.

Bennett, M.J., 1989a, Application and evaluation of ceramic coatings produced by sol–gel technology, in: Coatings for High-temperature Applications, ed. E. Lang (Applied Science Publishers, Barking, UK) ch. 6, p. 169.

Bennett, M.J., 1989b, Improved high temperature oxidation of alloys by ion-implantation, in: Environmental Degradation of Ion and Laser Beam Treated Surfaces, eds S. Was and K.S. Grabowski, p. 261.

Bennett, M.J., and A.T. Tuson, 1989, Mater. Sci. & Eng. A **116**, 79.

Bennett, M.J., G. Dearnaley, M.R. Houlton, R.W.M. Hawes, P.D. Goode and M.A. Wilkins, 1980a, Corros. Sci. **20**, 73.

Bennett, M.J., M.R. Houlton and G. Dearnaley, 1980b, Corros. Sci. **20**, 69.

Bennett, M.J., B.A. Bellamy, G. Dearnaley and M.R. Houlton, 1984, The influence of Eu, La, Sc, Yb, ion-implantation upon the oxidation behaviour of a 20Cr–25Ni–Nb stabilized stainless steel in carbon dioxide at 825°C, in: Proc. 9th Int. Congr. on Metals Corrosion, Ottawa, Vol. 2 (NRC, Canada) pp. 416–423.

Birks, N., and G.H. Meier, 1983, Introduction to High-Temperature Oxidation of Metals (Edward Arnold, London).

Bornstein, N.S., M.A. De Crescente and J.G. Smeggil, 1989, Mater. Sci. & Eng. A **120**, 175.

Choquet, P., and R. Mevrel, 1989, Mater. Sci. & Eng. A **120**, 153.

Collins, J.F., V.P. Calkins and J.A. McGurty, 1960, The Rare-Earths and Related Metals (ASM, Metals Park, OH) p. 499.

Cotell, C.M., G.J. Yurek, R.J. Hussey, D.F. Mitchell and M.J. Graham, 1988, Proc. Electrochem. Soc. **88**(5), 268.

Cotell, C.M., G.J. Yurek, R.J. Hussey, D.F. Mitchell and M.J. Graham, 1990, Oxid. Met. **34**(3/4), 173, 201.

Delaunay, D., and A.M. Huntz, 1982, J. Mater. Sci. **17**, 2027.

Delaunay, D., A.M. Huntz and P. Lacombe, 1980, Corros. Sci. **20**, 1109.

Ecer, G.M., and G.H. Meier, 1979, Oxid. Met. **13**, 159.

Ecer, G.M., R.B. Singh and G.H. Meier, 1982, Oxid. Met. **18**, 55.

El-Aiat, M.M., and F.A. Kroger, 1982, J. Am. Ceram. Soc. **65**(6), 280.

Felten, E.J., 1961, J. Electrochem. Soc. **108**, 490.

Frances, M., M. Vilasi, M. Mansour-Gabr and J.P. Steinmetz, 1988, in: Proc. 10th Int. Conf. on Met. Corr., Central Electrochemical Research Institute (Trans Tech Publications, Aedermannsdorf) Part 2, p. 1419.

Francis, J.M., and J.A. Juston, 1968, Corros. Sci. **8**, 445.

Francis, J.M., and W.H. Whitlow, 1965, Corros. Sci. **5**, 701.

Francis, J.M., and W.H. Whitlow, 1966, J. Iron & Steel Inst. London **204**, 355–359.

Fransen, T., M.A. de Jongh, M.M.A. Perik and P.J. Gellings, 1984, in: Proc. 9th Int. Congr. Metal Corrosion, Canada, **4**, 311.

Fransen, T., P.J. Gellings, J.C. Fuggle, G. van der Laan, J.M. Esteva and R.C. Karnatak, 1985, Appl. Surf. Sci. **20**, 257.

Giggins, C.S., and F.S. Pettit, 1975, ARL Report no. 75.0234 (Pratt and Whitney Aircraft, CT).

Golightly, F.A., F.H. Stott and G.C. Wood, 1976, Oxid. Met. **10**, 163.

Golightly, F.A., F.H. Stott and G.C. Wood, 1979, J. Electrochem. Soc. **126**(6), 1035.

Golightly, F.A., G.C. Wood and F.H. Stott, 1980, Oxid. Met. **14**(3), 217.

Goncel, O.T., 1981, in: Proc. Int. Congr. on Metal Corrosion, Vol. 1 (DECHEMA) p. 681.

Graham, M.J., 1991, Study of oxide scales using SIMS, in: Microscopy of Oxidation, Proc. Int. Conf., Cambridge, 1990, eds M.J. Bennett and G.W. Lorimer (Institute of Metals, London) p. 10.

Gschneidner Jr, K.A., B.J. Beaudry and J. Capellan, 1990, in: Metals Handbook, 10th Ed., Vol. 2 (ASM, Metals Park, OH) pp. 720–732.

Haanappel, V.A.C., T. Fransen, B. Geerdink, P.J. Gellings and M.F. Stroosnijder, 1991, Oxid. Met. **35**(5/6), 405.

Hagel, W.C., 1963, Trans. Am. Soc. Met. **56**, 583.

Hagel, W.C., 1965, J. Am. Ceram. Soc. **48**, 70.

Hagel, W.C., and A.U. Seybolt, 1961, J. Electrochem. Soc. **108**, 1146.

He, Y.D., R.Z. Zhu, W.Q. Zhang, W.P. Yu, X.Q. Ma and W.M. Deng, 1990, Mater. Sci. & Eng. A **123**, 117.

Hindam, H., and W.W. Smeltzer, 1980, Oxid. Met. **14**(4), 337.

Hindam, H., and D.P. Whittle, 1982, J. Electrochem Soc. **129**, 1147.

Hou, P.Y., and J. Stringer, 1987, Mater. Sci. & Eng. **87**, 295.

Hou, P.Y., and J. Stringer, 1988, Ion-implantation of Reactive Elements in Improving Adhesion of Thermally Grown Chromia Scales Report LBL - 25031, April 1988 (Lawrence Berkeley Laboratory, Berkeley, CA).

Huntz, A.M., 1988, Mater. Sci. & Technol. **4**, 1079.

Huntz, A.M., G. Moulin and B. Lesage, 1984, in: Proc. 9th Int. Congr. on Metallic Corrosion, Toronto, 3–7 June 1984, Vol. 2 (National Research Council of Canada, Toronto) p. 400.

Hussey, R.J., P. Papaiacovou, J. Shen, D.F. Mitchell and M.J. Graham, 1989, Mater. Sci. & Eng. A **120**, 147.

Ikeda, Y., M. Tosa, K. Yoshihara and K. Nii, 1989, Mater. Sci. & Eng. A **120**, 179.

Ishigaki, T., S. Yamauchi, J. Mizusaki and K. Fueki, 1984, J. Solid State Chem. **54**, 100.

Jedlinski, J., and S. Mrowec, 1987, Mater. Sci. & Eng. **87**, 281.

Jedlinski, J., K. Godlewski and S. Mrowec, 1989, Mater. Sci. & Eng. A **121**, 539.

Jedlinski, J., G. Borchardt and S. Mrowec, 1991, The effect of reactive elements on the oxidation behaviour of Fe–Cr–Al alloys, in: Microscopy of Oxidation, Proc. Int. Conf., Cambridge, 1990, eds M.J. Bennett and G.W. Lorimer (Institute of Metals, London) p. 278.

Johansson, R., J. Hamer, J. Redmond and R.M. Davison, 1990, Oxidation and high-temperature corrosion resistance of REM treated stainless steels (Corrosion 90, NACE) Paper 294.

Jones, R.L., 1988, Low quality fuel problems with advanced engine materials, in: Proc. Coatings for Advanced Heat Engines Workshop, May 1988, Session VI, ed. J.W. Fairbanks (US Department of Energy) pp. 1–8.

Jones, R.L., and C.E. Williams, 1987, Mater. Sci. & Eng. **87**, 353.

Jones, R.L., S.R. Jones and C.E. Williams, 1985a, J. Electrochem. Soc. **132**(6), 1498.

Jones, R.L., D.B. Nordman and S.T. Gadomski, 1985b, Metall. Trans. A **16**, 303.

Jones, R.L., C.E. Williams and S.R. Jones, 1986, J. Electrochem. Soc. **133**(1), 227.

Khanna, A.S., C. Wasserfuhr, W.J. Quadakkers and H. Nickel, 1989, Mater. Sci. & Eng. A **120**, 185.

King, W.E., and J.H. Park, 1989, in: Proc. 1988 MRS Spring Meeting (Materials Research Society, Pittsburgh, PA) Mater. Res. Soc. Symp. Proc. **123**, 193.

Kofstad, P., 1988, High-Temperature Corrosion (Elsevier, London).

Kofstad, P., and K.P. Lillerud, 1980, J. Electrochem. Soc. **127**, 2410.

Kofstad, P., and M. Seiersten, 1987, Mater. Sci. & Technol. **3**(7), 576.

Kuenzly, J.D., and D.L. Douglass, 1974, Oxid. Met. **8**, 139.

Kumar, A., M. Nasrallah and D.L. Douglass, 1974, Oxid. Met. **8**, 227.

Kung, S.-C., and V. Srinivasan, 1990, Oxid. Met. **33**(5/6), 481.

Landkof, M., A.V. Levy, D.H. Boone, R. Gray and E. Yaniv, 1985, Corrosion **41**, 344.

Lang, E., 1989, The Role of Active Elements in the Oxidation Behaviour of Higher-Temperature Metals (Applied Science Publishers, Barking, UK).

Lees, D.G., 1987, Oxid. Met. **27**, 75.

Lesage, B., A.M. Huntz, P. Ochin, B. Saadi and G. Petot-Ervas, 1984, Solid State Ionics **12**, 243.

Long, R.H., C.S. Morgan and H. Unger, 1975, Met. Prog. 1975(Feb.), 52.

Lou, H., F. Wang and L. Bai, 1990, Mater. Sci. & Eng. A **123**, 123.

Lustman, B., 1950, Trans. AIME **188**, 995.

Luthra, K.L., and C.L. Briant, 1988, Metall. Trans. A **19**, 2091.

Malik, A.U., and K. Natesan, 1990, Oxid. Met. **34**(5/6), 497.

Malik, A.U., R. Ahmad, Sh. Ahmad and S. Ahmad, 1991, Anti-Corrosion 1991(July), 4.

Martinengo, P.C., C. Carughi, U. Ducatti and G.L. Coccia, 1977, High temperature behaviour of protective coatings on Ni-base superalloys, in: Materials and Coatings to Resist High Temperature Corrosion, eds D.R. Holmes and A. Rahmel (Applied Science Publishers, Barking, UK) p. 293.

McDonald, J.E., and J.G. Eberhart, 1965, Trans. AIME **233**, 512.

Mills, T., and N.E. Ryan, 1965, Oxidation/nitridation resistance of chromium alloys containing rare-earth additions, unpublished data (DSTO-Aeronautical Research Laboratory).

Moon, D.P., and M.J. Bennett, 1989, Mater. Sci. Forum **43**, 269.

Moseley, P.T., K.R. Hyde, B.A. Bellamy and G. Tappin, 1984, Corros. Sci. **24**(6), 547.

Nagai, H., 1988, Influence of rare-earth oxide dispersion on the oxidation of Ni–Cr and Fe–Cr alloys, in: Proc. MRS Int. Meeting on Advanced Materials, Vol. 4, eds M. Doyama, S. Somiya and R.P.H. Chang (Materials Research Society, Pittsburgh, PA) p. 365.

Nagai, H., 1989, Mater. Sci. Forum **43**, 75.

Nagai, H., and M. Okabayashi, 1981, Trans. Jpn. Inst. Met. **22**, 101.

Nagai, H., T. Murai and H. Mitani, 1980a, Trans. Jpn. Inst. Met. **21**(9), 563.

Nagai, H., M. Okabayashi and H. Mitani, 1980b, Trans. Jpn. Inst. Met. **21**, 341.

Nagai, H., Y. Takebayashi and H. Mitani, 1981, Metall. Trans. A **12**, 435.

Natesan, K., 1987, Mater. Sci. & Eng. **87**, 99.

Nelson, R.L., J.D.F. Ramsay, J.L. Woodhead, J.A. Cains and J.A.A. Crossley, 1981, Thin Solid Films **81**, 329.

Nicholls, J.R., and P. Hancock, 1989, An alternative view of the effect of active elements on mechanical properties of scales, in: The Role of Active Elements in the Oxidation Behaviour of High-Temperature Metals, ed. E. Lang (Applied Science Publishers, Barking, UK) p. 195.

Olson, W.E., D.K. Gupta and M.S. Milaniak, 1989, Powder Mixture for Yttrium Enriched Aluminide Coatings, US Patent 5000782, March 1989.

Onay, B., and Y. Saito, 1990, Effects of reactive element/oxide addition methods on the growth and adherence of scales on Ni–Cr–Al alloys, in: Proc. MRS Int. Meeting on Advanced Materials, Vol. 4, eds M. Doyama, S. Somiyo and R.P.H. Chang (Materials Research Society, Pittsburgh, PA) p. 359.

Papaiacovou, P., R.J. Hussey, D.F. Mitchell and M.J. Graham, 1990, Corros. Sci. **30**(4/5), 451.

Park, J.H., and K. Natesan, 1990, Oxid. Met. **33**(1/2), 31.

Parshin, Yu.N., E.V. Kuznetsov and A.V. Ryabchenkou, 1990, Prot. Met. (Zach. Metallov) **26**(1), 76.

Patibandla, N., T.A. Ramanarayanan and F. Cosandey, 1991, J. Electrochem. Soc. **138**(7), 2176.

Peters, J., and H.J. Grabke, 1984, Werkst. Korros. **35**, 385.

Pettit, F.S., and E.J. Felten, 1976, Oxid. Met. **10**(3), 189.

Pfeiffer, H., 1957, Werkst. Korros. **8**, 574.

Pfiel, L.P., 1937, UK Patent No. 459848.

Pfiel, L.P., 1945, UK Patent No. 574088.

Pivin, J.C., C. Roques-Carmes, J. Chaumont and H. Bernas, 1980, Corros. Sci. **20**, 947.

Polman, E.A., T. Fransen and P.J. Gellings, 1987, Mater. Sci. & Eng. **88**, 157.

Przybylski, K., and G.J. Yurek, 1988, J. Electrochem. Soc. **135**(2), 517.

Przybylski, K., A.J. Garrett-Reed and G.J. Yurek, 1986, J. Am. Ceram. Soc. **69**, C-264.

Przybylski, K., A.J. Garrett-Reed, B.A. Pint, E.P. Katz and G.J. Yurek, 1987, J. Electrochem. Soc. **134**, 3207.

Przybylski, K., A.J. Garrett-Reed and G.J. Yurek, 1988, J. Electrochem. Soc. **135**, 509.

Quadakkers, W.J., H. Holzbrecher, K.G. Briefs and H. Beske, 1989, Oxid. Met. **32**, 67.

Quadakkers, W.J., J. Jedlinski, K. Schmidt, M. Krasovec, G. Borchardt and H. Nickel, 1991, Appl. Surf. Sci. **47**, 261.

Ramanarayanan, T.A., M. Raghava and R. Petkovic-Luton, 1984a, Oxid. Met. **22**(3/4), 83.

Ramanarayanan, T.A., M. Raghava and R. Petkovic-Luton, 1984b, J. Electrochem. Soc. **131**(4), 923.

Ramanarayanan, T.A., R. Ayer, R. Petkovic-Luton and D.P. Leta, 1988, Oxid. Met. **29**, 445.

Reddy, K.P.R., J.L. Smialek and A.R. Cooper, 1982, Oxid. Met. **17**(5/6), 429.

Reser, M.K., 1975, Phase Diagrams for Ceramists (American Ceramic Society, Columbus, OH).

Rhys-Jones, T.N., and H.J. Grabke, 1988, Mater. Sci. & Technol. **4**, 446.

Rhys-Jones, T.N., H.J. Grabke and H. Kudielka, 1987, Corros. Sci. **27**, 49; Werkst. Korros. **38**, 65.

Saito, Y., and T. Maruyama, 1987, Mater. Sci. & Eng. **87**, 275.

Saxena, D., S. Prakash, M.L. Mehta and I.P. Saraswat, 1987, Oxid. Met. **28**, 127.

Seybolt, A.U., 1966, Corros. Sci. **6**, 263.
Seybolt, A.U., 1968, Trans. Metall. Soc. AIME **242**, 1955.
Seybolt, A.U., 1971, Corros. Sci. **11**, 751.
Shengtai, S., H. Yuanwei and H. Yong, 1987, in: Proc. 10th Int. Congr. on Metal Corrosion (Madras, India) p. 1617.
Sidky, P.S., and M.G. Hocking, 1989, Corros. Sci. **29**(6), 735.
Siemers, P.A., and D.W. McKee, 1982, A Method of Coating a Superalloy Substrate, US Patent 4328285.
Sigler, D.R., 1989, Oxid. Met. **32**(5/6), 337.
Sigler, D.R., 1991, Oxid. Met. **36**(1/2), 57.
Skeldon, P., J.M. Calvent and D.G. Lees, 1980, Philos. Trans. R. Soc. London A **296**, 557.
Smeggil, J.G., and A.J. Shuskus, 1987, Surf. Coat. Tech. **32**, 57.
Smeggil, J.G., A.W. Fundkenbusch and N.S. Bornstein, 1986, Metall. Trans. A **17**, 923.
Smialek, J.L., 1991, Effect of sulphur content on Al_2O_3 scale adhesion, in: Microscopy of Oxidation, eds M.J. Bennett and G.W. Lorimer (Institute of Metals, London) p. 258.
Smialek, J.L., and R. Browning, 1985, NASA Tech. Memo 87168.
Steele, B.C.H., and J.M. Floyd, 1971, Proc. Br. Ceram. Soc. **19**, 55.
Stephens, J.R., 1972, Metall. Trans. **3**(8), 2075.
Stott, F.H., and G.C. Wood, 1987, Mater. Sci. & Eng. **87**, 267.
Stott, F.H., F.M.F. Chong and C.A. Stirling, 1989, Mater. Sci. Forum **43**, 327.
Strafford, K.N., and J.R. Bird, 1979, J. Less-Common Met. **68**, 223.
Strafford, K.N., and J.M. Harrison, 1976, Oxid. Met. **10**, 347.
Stringer, J., and I.G. Wright, 1972, Oxid. Met. **5**(1), 59.
Stringer, J., B.A. Wilcox and R.I. Jaffee, 1972, Oxid. Met. **5**(1), 11.
Stroosnijder, M.F., V. Guttmann, R.J.N. Gommans and J.H.W. de Witt, 1989a, Mater. Sci. & Eng. A **121**, 581.
Stroosnijder, M.F., J.F. Norton, V. Guttmann, M.J. Bennett and J.H.W. de Witt, 1989b, Mater. Sci. & Eng. A **116**, 103.
Stroosnijder, M.F., M.J. Bennett, V. Guttmann, J.F. Norton and J.H.W. de Witt, 1991, Oxid. Met. **35**(1/2), 19.
Takei, A., A. Ishida, K. Nii and M. Yamazaki, 1986, Corrosion Resistance of Composite Coatings for Gas Turbines (National Research Council of Canada) p. 86.
Talboom, F.T., R.C. Elam and L.W. Wilson, 1970, NASA Report CR.7813, PWA.405-A70.
Tiearney Jr, T.C., and K. Natesan, 1982, Oxid. Met. **17**, 1.
Tien, K.J., and F.S. Pettit, 1972, Metall. Trans. **3**, 1587.
Travadze, F.N., O.I. Mikadze, N.P. Keshelava and B.P. Bulia, 1986, Oxid. Met. **25**(5/6), 335.
Tu, D.C., C.C. Lin, S.J. Liao and J.C. Chou, 1986, J. Vac. Sci. & Technol. A **4**(6), 2601.
Vilasi, M., J. Steinmetz and P. Steinmetz, 1989, in: The Role of Active Elements in the Oxidation Behaviour of High Temperature Metals and Alloys, ed. E. Lang (Elsevier Applied Science Publishers, Barking, UK).
Vineberg, E.J., and D.L. Douglass, 1986, Oxid. Met. **25**(1/2), 1.
Wallwork, G.R., and A.Z. Hed, 1971, Oxid. Met. **3**, 171.
Wang, F., H. Lou, L. Bai and W. Wu, 1989, Mater. Sci. & Eng. A **121**, 387.
Was, G.S., and K.S. Grabowski, 1989, Environmental Degradation of Ion and Laser Beam Treated Surfaces (TMS).
Whittle, D.P., and J. Stringer, 1980, Philos. Trans. R. Soc. London Ser. A **295**, 309.
Whittle, D.P., M.E. El-Dahshan and J. Stringer, 1977, Corros. Sci. **17**, 879.
Wood, G.C., and J. Boustead, 1968, Corros. Sci. **8**, 719.
Wright, I.G., and B.A. Wilcox, 1974, Oxid. Met. **8**, 283.
Wright, I.G., B.A. Wilcox and R.I. Jaffee, 1975, Oxid. Met. **9**, 275.
Wright, I.G., J.A. Colwell, D.R. Baer and L.H. Schoenlein, 1989, Mater. Sci. & Eng. A **120**, 251.
Wukusick, C.S., and J.F. Collins, 1963, General Electric Co. NMPD, TM 63-7-3, June 1963.
Wukusick, C.S., and J.F. Collins, 1964, Mater. Res. Stand. **4**, 637.
Young, E.W.A., and J.H.W. de Witt, 1985, Solid State Ionics **16**, 39.
Young, E.W.A., and J.H.W. de Witt, 1986, Oxid. Met. **26**(5/6), 351.
Yurek, G.J., K. Przybylski and A.J. Garrett-Reed, 1987, J. Electrochem. Soc. **134**, 2643.

Handbook on the Physics and Chemistry of Rare Earths
Vol. 21
edited by K.A. Gschneidner, Jr. and L. Eyring

Chapter 142

RARE EARTH INTERMETALLICS FOR METAL–HYDROGEN BATTERIES

T. SAKAI
Osaka National Research Institute, Ikeda, Osaka, Japan

M. MATSUOKA and C. IWAKURA
University of Osaka Prefecture, Sakai, Osaka, Japan

Contents

List of symbols

$a(H_2O)$	activity of water
$a(H_2)$	activity of hydrogen
$\Delta a/a$	lattice expansion ratio of a-axis
C	normalized charge and discharge rates [= charge or discharge current (A)/nominal capacity (Ah)]
C_n	normal capacitive component
$\Delta c/c$	lattice expansion ratio of c-axis
E	electrode potential
E°	standard potential at 25°C
E_{eq}	equilibrium potential
$E_{eq}(H)$	equilibrium hydrogen potential
$E^0(H)$	standard electrode potential of a H_2O/H couple
$E^0(HgO/Hg)$	standard electrode potential of a HgO/Hg couple
EV	electric vehicle
ΔG	free energy change
H_{ad}	adsorbed atomic hydrogen
ΔH	enthalpy change
ΔH^0	enthalpy per mole H_2
i	current density
i_o	exchange current density
M	hydrogen storage alloy

Mm	mischmetal (mixture of rare-earth metals)	R_2	contact resistance between current collector and alloy
Ni–Cd	nickel hydroxide–cadmium battery	R_3	contact resistance between alloy particles
Ni–MH	nickel hydroxide–metal hydride battery	R_4	reaction resistance
P–C–T	pressure–composition–isotherm	SR	solidification rate
$P_{eq}(H)$	hydrogen equilibrium pressure	ΔS^0	entropy per mole H_2
P_{H_2}	hydrogen plateau pressure	T	absolute temperature
$P(H_2)$	hydrogen partial pressure	V	lattice volume
PTFE	polytetrafluoroethylene	$\Delta v/v$	volume expansion ratio
PVA	polyvinyl alcohol	W_4	Warburg impedance
Q_n	capacitive components in order to describe a depressed semi-circle	XPS	X-ray photoelectron spectroscopy
		β	symmetry factor
R	gas constant	$\gamma(H_2)$	fugacity coefficient
R_1	electrolyte resistance	η	overpotential

1. Introduction

The first metal–hydrogen system was the Pd/H_2 system (Wicke and Brodowsky 1978). Application of Pd as a rechargeable battery was also proposed (Barton et al. 1963). Since it is expensive, the palladium electrode has been utilized in limited areas such as a high purity hydrogen generator in which hydrogen produced by water electrolysis diffuses through the palladium, producing hydrogen with purity of more than 99.99%. In 1969, it was accidentally found during research on rare-earth magnets ($SmCo_5$) that rare-earth intermetallic compounds absorbed large amounts of hydrogen (Zijlstra and Westendorp 1969), opening a new scientific and technical field called "hydrogen storage alloys" (Buschow 1984). Immediately after this discovery, intermetallic compounds were applied as "hydrogen absorbing alloy electrodes", e.g. TiNi–Ti_2Ni by Justi et al. (1970) and Gutjahr et al. (1973), $LaNi_5$ by Ewe et al. (1973), and $LaNi_{5-x}M_x$ (M = Cu, Mn, Al, Cr) by Bronoel et al. (1976, 1978), Percheron-Guegan et al. (1978) and Van Rijswick (1978). Rechargeable nickel–metal hydride (Ni–MH) batteries composed of nickel hydroxide positive electrodes and metal hydride negative electrodes were constructed and evaluated using $LaNi_5$ by Markin et al. (1978, 1981) and Markin and Dell (1981). However, performance and cost of this new battery did not stimulate much scientific and industrial interest. In addition, there was little need for small rechargeable batteries. Detailed reviews of this early research work are given by Videm (1978), Bittner and Badcock (1983), and Iwakura (1985) and Iwakura and Sakai (1986).

After the oil crisis of 1974, hydrogen energy was proposed as the most promising clean energy system, creating a strong need for light, compact and safe storage tanks. Extensive research and development projects were carried out throughout the world on hydrogen storage alloys because they could store larger amounts of hydrogen (1000 cc/cc) per unit volume than liquid hydrogen (784 cc/cc at −273°C) and high pressure tanks (200 cc/cc

at 200 atm). Concentrated work was also carried out on a chemical heat-pump system which converted low-grade waste heat to a higher quality of heat using hydriding alloys. These applications required low cost alloys, and this stimulated work on alloys based on mischmetal (Mm, a mixture of rare-earth metals) and alloys based on titanium–zirconium. Large scale alloy production technologies were also developed and improved on during the late 1970's. Research results are summarized in books edited by Schlapbach (1988, 1992). The accumulated basic data and developed technologies made it possible for the metal hydride battery to make rapid progress after 1985.

Since 1980, another factor contributing to the development of metal hydride batteries was provided by progress in the area of battery materials and technologies for producing compact nickel–cadmium batteries. The social changes and consumerism of the 1980's led to a rapid popularization of light and compact cordless appliances such as video camera's, cellular phones, lap-top computers, shavers, toys, tools, etc. It created a strong demand for compact, high power, long life and maintenance-free rechargeable batteries. As a result, world production of small Ni–Cd cells increased rapidly (about 10% per year), amounting to 1.1 billion cells in 1990. However, the great demand for the Ni–Cd battery caused a serious shortage of cadmium and rapid rise in price because it was a sub-product of zinc production. Cadmium has one-order less available ore deposits than cobalt and two-orders less than nickel and rare earths. In addition, the wide-spread use of toxic cadmium in Ni–Cd batteries brought about environmental concerns for the future, followed by legal regulation in many countries.

Because of this, a tremendous research and development effort has been conducted on the MH electrode and the Ni–MH battery since 1985, leading to prominent progress in every area of performance. The good combination of both metal hydride technology and Ni–Cd technology resulted in the rapid commercialization of the sealed Ni–MH battery by the end of 1990. At present, an AA size Ni–MH cell has almost twice the capacity (1100 mAh) of a conventional Ni–Cd cell (600 mAh) (Ogawa et al. 1989, Nogami et al. 1989, Kanda et al. 1991). They are used in various cordless appliances, amounting to more than 200 million cells in 1994. In addition, serious air pollution by automobiles in city areas is strongly pushing the development of the electric vehicle (EV) and the need for improved battery performance. The key technology is to develop light and compact batteries with high power. Extensive research on large Ni–MH batteries is in progress for EV application (Sakai et al. 1991b, 1991e, 1993a, Muta et al. 1992, Ovshinsky et al. 1993, Matsumoto et al. 1993).

The research and development efforts on the hydrides and MH batteries have been reviewed in the following articles: Iwaki (1985, 1987), Osumi (1986), Kanda (1988), Ishikawa and Sakai (1989), Ohta (1989), Ohta et al. (1992), Iwakura (1989), Iwakura et al. (1989b, 1991, 1992b), Iwakura and Matsuoka (1990, 1991), Yonezu et al. (1989), Matsumoto (1989), Tamura (1992), Bennett and Sakai (1994) and Sandrock (1995). The technological development of Ni–MH batteries has made such good progress that scientific studies to clarify mechanisms could not keep up. The main objective of this chapter is to review the work carried out on rare-earth based alloys since 1984 and to encourage further scientific and technological efforts on the metal hydride battery.

Detailed information on the Zr–Ti–Ni-based alloys can be found in the following original papers: Wakao et al. (1984, 1987, 1989), Wakao and Sawa (1991), Fetcenko et al. (1988, 1990a,b, 1992), Venkatesan et al. (1988, 1989), Venkatesan and Reichman 1989, Moriwaki et al. (1989, 1991), Sawa et al. (1990, 1991), Sawa and Wakao (1990), Miyamura et al. (1992, 1994), Hirota et al. (1992), Coates and Wright (1992), Kajita and Uetani (1993), Kim and Lee (1994), Züttel et al. (1994a–d).

2. General features of Ni–MH batteries

2.1. *Charge–discharge mechanism*

Figure 1 illustrates the charge–discharge reactions. During charging, the nickel hydroxide $Ni(OH)_2$ positive electrode is oxidized to nickel oxyhydroxide NiOOH, while the alloy M negative electrode forms a hydride MH by water electrolysis. The reactions on each electrode proceed via solid state transitions of hydrogen. The overall reaction is expressed only by a transfer of hydrogen between alloy M and $Ni(OH)_2$:

$$\text{(Positive)} \quad Ni(OH)_2 + OH^- = NiOOH + H_2O + e^- \quad (E^0 = +0.490\text{V}), \tag{1}$$

$$\text{(Negative)} \quad M + H_2O + e^- = MH + OH^- \quad (E^0 \approx -0.828\text{V}), \tag{2}$$

$$\text{(Overall)} \quad Ni(OH)_2 + M = NiOOH + MH \quad (E^0 \approx 1.318\text{V}). \tag{3}$$

The mechanism for the Ni–MH battery is clearly distinguished from other batteries such as Ni–Cd, Ni–Zn, Ni–Fe, Pb–acid and Li batteries in which the dissolution and precipitation of the active materials such as Cd, Zn, Fe, Pb and Li occur on the electrodes during charge–discharge cycles, changing the electrolyte concentration and electrode morphology, for example for Ni–Cd:

$$2Ni(OH)_2 + Cd(OH)_2 = 2NiOOH + Cd + 2H_2O. \tag{4}$$

The morphological change associated with eq. (4) requires a porous electrode, thus reducing the practical energy density and also increasing the risk of a short-circuit and

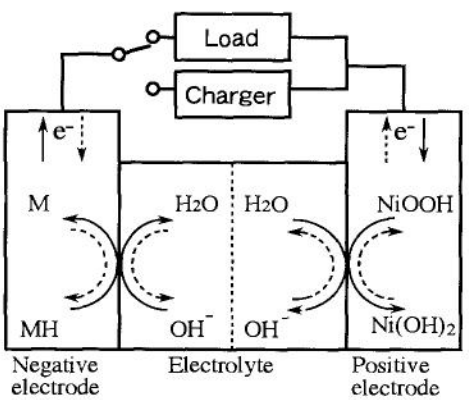

Fig. 1. Schematic drawing of the charge (dashed arrows) and discharge (solid arrows) reactions of a Ni–MH battery (Iwakura and Matsuoka 1990).

memory effects. The solid state transition mechanism allows the Ni–MH battery to have a more densely packed structure and a greater reliability. In addition, solid state batteries using proton conducting solid electrolytes can be realized (Mohri et al. 1986, Kuriyama et al. 1990a–d, 1992a). The replacement of Ni–Cd batteries by Ni-MH ones is facilitated by the fact that they have the same average discharge voltage (1.25 V).

2.2. *Overcharge reactions*

In the sealed cell, the MH electrode has a higher capacity than the $Ni(OH)_2$ electrode, thus facilitating a gas recombination reaction. During an overcharge situation, the MH electrode is charged continuously, forming hydride, while the Ni electrode starts to evolve oxygen gas according to eq. (5):

(Positive):

$$2OH^- = H_2O + \tfrac{1}{2}O_2 + 2e^- \quad (E^0 = +0.401\ \text{V}), \tag{5}$$

(Negative):

$$2M + 2H_2O + 2e^- = 2MH + 2OH^- \quad (E^0 \approx -0.828\ \text{V}), \tag{6}$$

$$2MH + \tfrac{1}{2}O_2 = 2M + H_2O, \tag{7}$$

$$H_2O + e^- = \tfrac{1}{2}H_2 + OH^- \quad (E^0 = -0.828\text{V}). \tag{8}$$

The oxygen diffuses through the separator to the MH electrode and there it reacts chemically, producing water (eq. 7) and preventing a pressure rise in the cell as shown in fig. 2. The electrolyte solution should be minimal to facilitate the diffusion of gas through

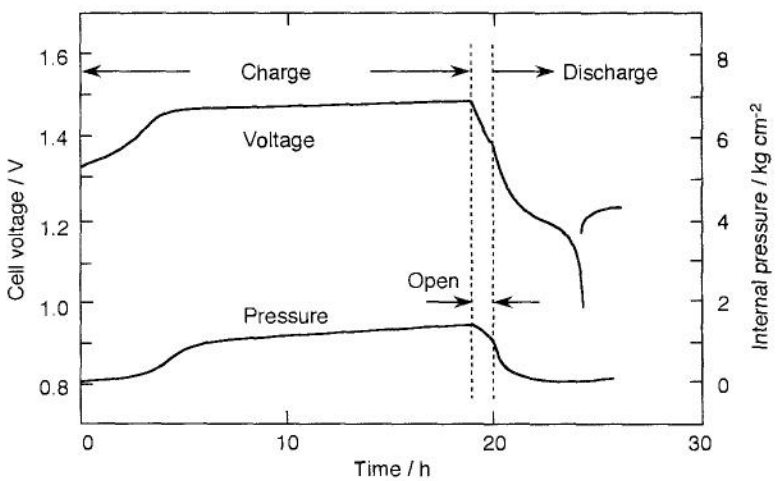

Fig. 2. Overcharge characteristics of a Ni–MH AA-size cell during the 30th cycle (current: 200 mA, temperature: 25°C) (Kanda et al. 1991).

the separator. If the charging rate is too high for hydrogen to form hydride, a sub-reaction for hydrogen gas evolution (eq. 8) occurs. A nearly comparable overcharge protection for the Ni–Cd battery has been obtained (Ogawa et al. 1989, Kanda et al. 1991, Sakai et al. 1991c).

2.3. *Overdischarge reactions*

During an overdischarge process, hydrogen gas starts to evolve at the Ni electrode (eq. 9). The hydrogen diffuses through the separator to the MH electrode and there it dissociates to atomic hydrogen by a chemical reaction (eq. 10), followed by a charge transfer reaction (eq. 11), ideally causing no pressure rise in the cell:

(Positive):
$$2H_2O + 2e^- = H_2 + 2OH^- \quad (E^0 = -0.828\ \text{V}), \tag{9}$$

(Negative):
$$H_2 + 2M = 2MH, \tag{10}$$

$$2OH^- + 2MH = 2H_2O + 2e^- + 2M \quad (E^0 \approx -0.828\text{V}). \tag{11}$$

The reactions at the MH electrode (eqs. 10–11) are the same as for the hydrogen diffusion electrode using platinum-containing carbon in an alkali fuel cell. Usually, the reaction

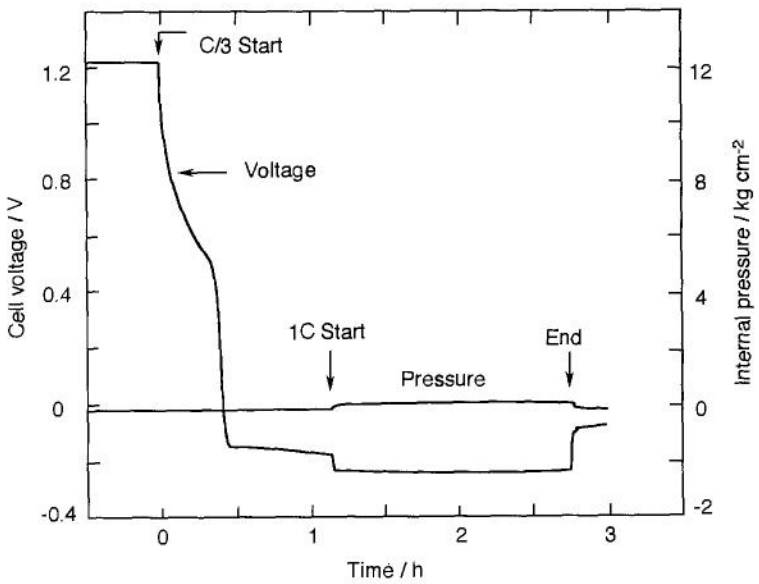

Fig. 3. Overdischarge characteristics of a Ni–MH AA-size cell; C = charge or discharge current (A)/nominal capacity (Ah) (Kanda et al. 1991).

rate of eq. (10) is not high, depending on the catalytic activity on the surface and also the electrode structure on which three phases (gas–solid–liquid) are in contact with each other. The overdischarge voltage, which is the total of the overpotentials of both reactions eq. (9) and eq. (11), was kept at around −0.2 V at low discharge rate without pressure rise (fig. 3) (Kanda et al. 1991, Sakai et al. 1992b).

The overdischarge protection is available only for hydrogen batteries and this has great merits for high voltage batteries composed of 100–300 cells, as for EV purposes.

2.4. *Battery structure of the sealed cell*

Figure 4 shows a schematic structure of a cylindrical sealed cell which is composed of a nickel hydroxide $Ni(OH)_2$ positive electrode, a polymeric separator (polyamide or hydrophilic polypropylene non-woven cloth), electrolyte solution (6–8 M KOH and 0.5–2 M LiOH aqueous solution) and a negative MH electrode. The lithium ions are intercalated into layers of $Ni(OH)_2$, improving the durability of the electrode. In a conventional $Ni(OH)_2$ electrode, the Ni ions are partly replaced by Co and Cd ions in order to improve the charging efficiency at temperatures above 40°C. A Cd-free nickel electrode was developed, using Zn ions instead of the Cd ions (Oshitani et al. 1989a,b). The component materials and production technologies for Ni–MH batteries are almost the same as those for Ni–Cd batteries (Ogawa et al. 1989, Nogami et al. 1990, Kanda et al. 1991, Sakai et al. 1987, 1991e–g, 1992a,b, Hasegawa et al. 1991, 1994, Kajita and Uetani 1993).

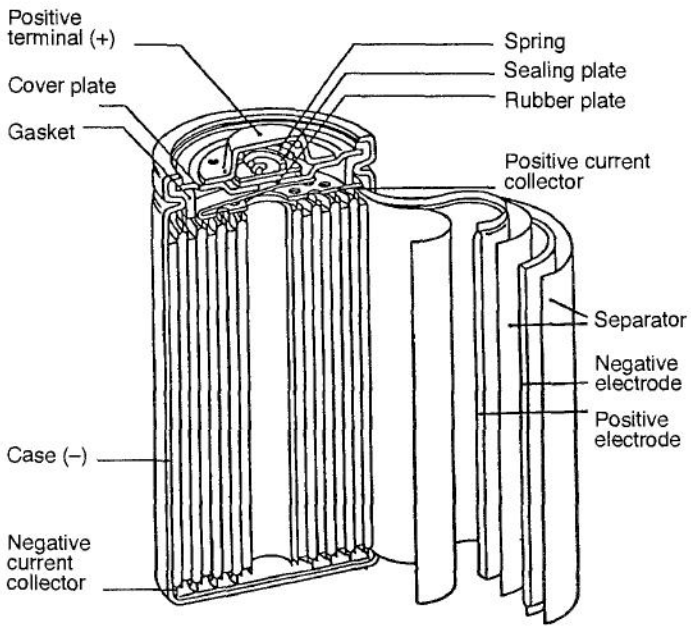

Fig. 4. Schematic structure of a cylindrical sealed Ni–MH cell (Furukawa 1993).

Table 1
Comparison of energy density of various batteries

Battery	Energy density			
	Wh kg^{-1}		Wh dm^{-3}	
	Actual	Theor.	Actual	Theor.
Pb/PbO_2	30–40	161	50–100	720
Cd/NiOOH	30–53	209	93–145	751
H_2/NiOOH	45–70	378	30–40	273
$LaNi_5H_6$/NiOOH[a]	55–75	216	180–210	1134
$LaNi_5H_6$/Air[a]	60–90	458	–	–

[a] Prototype.

2.5. *Features of the metal hydride battery*

Theoretical capacities are 375 mAh/g and 2600 mAh/cm^3 for $LaNi_5$ (1.4 wt.%H) because 1 gram of hydrogen provides 26.8 Ah of electric capacity. Practical capacities per volume of the MH electrodes, using rare-earth based alloys, are in the range of 900–1200 mAh/cm^3, depending on the kinds of alloys and preparation methods of the electrodes. Sintered electrodes using Ti (Zi)-based alloys were reported to exhibit higher capacity (1300 mAh/cm^3) (Venkatesan et al. 1988, Fetcenko et al. 1988). The capacities of MH electrodes are high compared to the values for Cd electrodes (500–700 mAh/cm^3) and $Ni(OH)_2$ electrodes (400–600 mAh/cm^3). Table 1 compares theoretical and practical

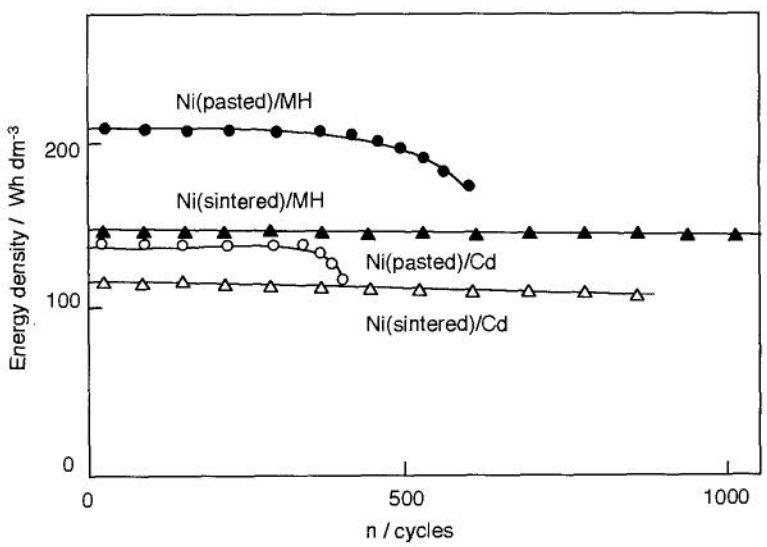

Fig. 5. Comparison of energy densities per volume and cycle lives for cylindrical sealed Ni–MH and Ni–Cd batteries (nominal capacity 1–3 Ah: charged at 0.25 *C* for 5 h and discharged at 0.3 *C* to 1 V); Ni (sintered) and Ni (pasted) stand for sintered-type and foamed-type nickel electrodes, respectively (Sakai et al. 1992b).

Table 2
Typical hydrogen storage alloys being tested up to date

AB_5-type (rare-earth system) alloys	Ti_2Ni
$LaNi_5$	$TiMn_{0.5}$
$LaNi_4Cu$	Ti_2Ni–TiNi-based multicomponent alloys; Ni partially substituted by V, Cr, Zr, Mn, Co, Cu, Fe, etc.
$LaNi_4Al$	$Ti_{1-y}Zr_yNi_x$ ($x=0.5$–1.45; $y=0$–1)
$LaNi_{2.5}Co_{2.5}$	*AB_2-type (Laves phase) alloys*
$La_{0.8}Nd_{0.2}Ni_2Co_3$	TiV_2
$La_{0.7}Nd_{0.2}Ti_{0.1}Ni_{2.5}Co_{2.0}Al_{0.5}$	$Ti_{2-x}Zr_xV_{4-y}Ni_y$
$La_{0.8}Nd_{0.2}Ni_{2.5}Co_{2.4}Si_{0.1}$	$Ti_{1-x}Cr_xV_{2-y}Ni_y$
$La_{0.9}Zr_{0.1}Ni_{4.5}Al_{0.5}$	$ZrNi_2$
$MmNi_5$	$ZrV_{0.4}Ni_{1.6}$
$MmNi_{3.55}Co_{0.75}Mn_{0.4}Al_{0.3}$	$ZrMn_{0.6}Cr_{0.2}Ni_{1.2}$
$MmNi_{4.2}Mn_{0.6}Al_{0.2}$	$LaNi_2$
$MmNi_{3.0}Co_{1.5}Al_{0.5}$	$CeNi_2$
$MmNi_{3.5}Co_{0.7}Al_{0.8}$	$Ti_{17}Zr_{16}V_{22}Ni_{39}Cr_7$
MmB_x ($x=4.55$–4.76; B = Ni, Co, Mn, Al)	
AB/A_2B-type (titanium system) alloys	
TiFe	
TiNi	

energy densities per weight (Wh/kg) and per volume (Wh/dm^3) for various rechargeable batteries. The Ni–MH battery has 20–30 wt.% and 50–100 vol.% higher energy density than a Ni–Cd battery and 400–500 vol.% higher density than a Ni-hydrogen battery using high pressure tank (30–50 atm). If the Ni electrode is replaced by an improved air electrode with higher rate capability, the weight density is expected to increase by more than 50% (Videm 1978, Sarradin et al. 1979, Folonari et al. 1980, Sakai et al. 1994b). Chemical charging of the MH electrode by hydrogen gas has been performed by Kuriyama et al. (1992c, 1994).

Cycle life of the Ni–MH sealed cell with higher capacity than the Ni–Cd cell was reported to be in the range of 500–2000 cycles (Ogawa et al. 1989, Sakai et al. 1991e–g, 1992a,b; fig. 5). The rate capability of the Ni–MH batteries was almost the same as that of the Ni–Cd battery (Nogami et al. 1990, Kanda 1991, Sakai et al. 1991e–g, 1992a,b). Muta et al. (1992) obtained more than twice the energy density per unit weight for a 140 Ah Ni–MH battery than for a lead–acid one at a power density of 65 W/kg. These results are encouraging for the application of Ni–MH batteries for electric vehicles. Charge retention was improved by changing the separator material from a polyamide to a polypropylene (Ikoma et al. 1987).

The MH electrode should satisfy all performance standards such as capacity, cycle life, charging and discharging efficiency, and charge retention. Research work on battery alloys has concentrated mainly on $MmNi_5$-based alloys, followed by $Ti_{1-x}Zr_xNi_{2+\alpha}$-based

(Laves phase) alloys. Several battery alloy compositions are listed in table 2. Battery performance depends on the alloys, electrode preparation methods, and battery assembly. The performances of alloys are changed by various factors such as alloy composition, casting conditions, grain boundary phases, surface modification, etc. The important point is that the Ni–MH battery does not have a fixed performance, opening the possibility for remarkable progress in the future.

In addition to the high performance, the battery can be free from environmental and resource problems. The battery does not contain hazardous elements such as Cd, Hg, Pb, Ag and Cr which are under severe legal regulation (Knoll et al. 1990). There is a wider choice of elements to be used in hydrogen storage alloys, in particular elements less dependent on specially limited resources such as Cd, Li, etc. The production of one billion AA-size cells requires about 10 000 tons of alloy. If 100 000 units of EV batteries (25 kWh) are produced, roughly 15 000 tons of alloy should be supplied. The available resources of rare earths and nickel are two orders higher than that of cadmium and will satisfy the huge future demands in cordless appliances and electric vehicles.

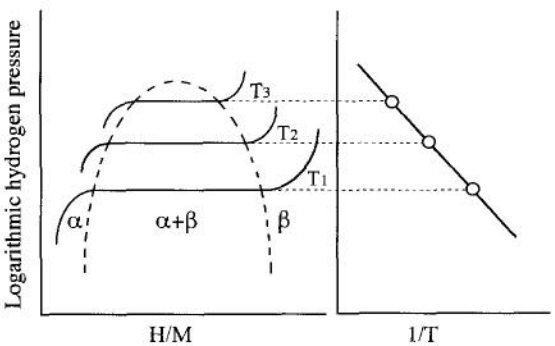

Fig. 6. Pressure–composition isotherms of the hydrogen storage alloy H system (Schlapbach 1988).

2.6. *Hydrogen storage alloys*

The temperature dependence of the hydrogen pressure–composition isotherms (P–C–T curves) is given in fig. 6. Initially, a small amount of hydrogen dissolves in the alloy as a solid solution (α-phase). The hydrogen occupies interstitial sites in the lattice and its concentration depends strongly on the hydrogen pressure. After the solid solution is saturated, a hydride phase (β-phase) nucleates and grows. During the α–β phase transition at a constant temperature, the equilibrium pressure ideally remains constant because the number of degrees of freedom is one, according to Gibbs' phase rule. After the α-phase is completely converted into the β-phase, the equilibrium pressure increases with increasing hydrogen concentration, forming a γ-phase as a solid solution in the hydride. The hydrogen plateau pressure (P_{H_2}) increases with increasing temperature according to the van't Hoff relation

$$\ln P_{H_2} = \frac{\Delta H^0}{RT} - \frac{\Delta S^0}{R}, \tag{12}$$

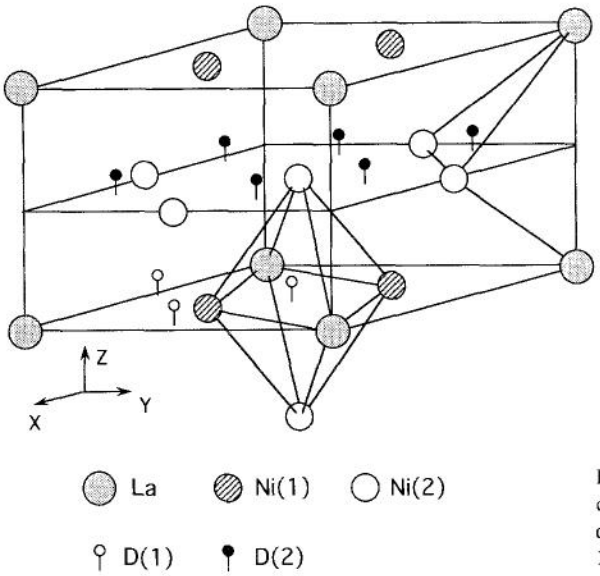

Fig. 7. Structure of the $LaNi_5$ intermetallic compound and the two different sites occupied by deuterium (Yartys' et al. 1982).

where R is the gas constant and ΔH^0 and ΔS^0 are the enthalpy and entropy change per mole H_2, respectively. These thermodynamic data characterize the alloy in an equilibrium state.

Crystal structures of $LaNi_5$-based alloys and their hydrides have been studied extensively, see the reviews by Buschow (1984) and Yvon and Fischer (1988). Figure 7 shows the $CaCu_5$ type structure for $LaNi_5$. The Ni atoms have two kinds of sites, 2c site at $z=0$ [Ni(1)] and 3g site at $z=\frac{1}{2}$ [Ni(2)]. The generally accepted model for the location of hydrogen atoms in the $LaNi_5H_x$ phase has the hydrogen atoms occupying two different sites: an octahedral site D(1) composed of two La, two Ni(1) and two Ni(2); and a tetrahedral site D(2) composed of two La and two Ni(2). The $LaNi_5$ stores three H atoms at the D(1) sites and three H atoms at the D(2) site, causing lattice expansion of the a-axis ($\Delta a/a$) by about 6% and of the c-axis ($\Delta c/c$) by about 6%, i.e., change of the cell volume (V) by 24.3%. The estimated volume of H in $LaNi_5H_6$ is 2.4 $Å^3$. The stability of the hydride phase increases with increasing cell volume of the alloy. The nickel can be replaced by such elements as Al, Mn, Si, Zn, Cr, Fe, Cu, and Co. Percheron-Guegan et al. (1985) reported that Al and Si replaced only the Ni atoms at the 3g site, causing the distortion of D(2) hydrogen occupation site and a resultant decrease in storage capacity. Fe, Mn, and Cu can also replace the Ni atoms at the 2c sites in addition to those at the 3g site. The replacement ratio increases in the order of Fe, Mn and Cu.

If La is replaced by smaller size elements such as Ce, Pr, Nd, Zr and Hf, the cell volume decreases, causing an increase in the hydrogen pressure. Since the usual mischmetals (Mm) are composed of La 20–30%, Ce 40–50%, Nd 10–20% and Pr 5–10%, $MmNi_5$ has a hydrogen pressure plateau higher by one order of magnitude than $LaNi_5$. The high equilibrium pressure can be reduced and controlled by partially replacing the

Ni by elements with larger metallic radius, such as Mn, Al, Cr, Si, Co, Cu, Zn and Fe (Sandrock 1978, Osumi et al. 1978, 1979a–c, 1981a,b, 1982, 1983). Elements such as Co, Cu, Zn and Fe can form continuous solid solutions with nickel over the whole range, but have less influence on the hydrogen pressure than elements such as Mn, Al, Cr and Si. The partial replacement of Ni also changes the decrepitation characteristics of the alloys. $MmNi_{4.5}Mn_{0.5}$ alloy shows a higher decrepitation rate and higher capacity for hydrogen, while $MmNi_{2.5}Co_{2.5}$ shows a lower decrepitation rate and much lower capacity. The partial replacement of Ni by Al causes a decrease in storage capacity, while that by Mn does not. Stoichiometric deviation also changes the pressure. The Mm-rich alloys shows lower pressure and higher capacity because of partial replacement of nickel by mischmetal and resultant increase in cell volume. The control of plateau pressure is the most important part in practical applications such as the hydrogen storage tank, chemical heat-pump and purification systems (Sandrock et al. 1992).

It is known that the surface of alloys decomposes into lanthanum oxide and metallic nickel clusters, bringing about a high catalytic activity for hydrogen dissociation (Schlapbach et al. 1979, 1980). The atomic hydrogen produced on the surface diffuses through the surface layer into the bulk and first forms a solid solution (α-phase), followed by precipitation of a hydride (β-phase). Hydrogen diffusivity in the $LaNi_5$ hydride is high, in the range of 10^{-7}–10^{-8} cm^2/s at 300 K (Richter et al. 1992). Because of this, hydrogen diffusion usually is not the limiting absorbing–desorbing reaction in a gas–solid system. Hydrogen storage alloys absorb hydrogen by an exothermic reaction and desorb it by an endothermic reaction as follows:

$$LaNi_5 + 3H_2 = LaNi_5H_6 + 21.6 \text{ kcal.} \tag{13}$$

The rate-determining step is heat removal from the reaction system, i.e. thermal conductivity of the system (Gerard and Ono 1992).

Videm (1978) pointed out that the following alloy properties need attention for optimum use as MH electrode:

(1) Chemical stability of component elements in KOH solution.
(2) Physical properties and mechanical stability.
(3) Overpotential at the desired current density.
(4) Hydrogen and electrical transport behaviors.

3. Metal hydride electrodes

3.1. *Equilibrium potential*

In the equilibrium state, the hydrogen partial pressure $P(H_2)$ on the electrode can be equal to the hydrogen equilibrium pressure $P_{eq}(H)$ of the MH as follows:

$$2M + H_2 = 2MH. \tag{14}$$

Therefore, an equilibrium potential $E_{eq}(H)$ could be related to the equilibrium hydrogen pressure of alloy according to the Nernst equation. The $E_{eq}(H)$ value against a HgO/Hg reference electrode is expressed as follows (Iwakura et al. 1988):

$$E_{eq}(H) \text{ vs. } E_{eq}(HgO/Hg) = \left[E^0(H) - E^0(HgO/Hg)\right] + \frac{RT}{2F}\ln\left(\frac{a(H_2O)}{a(H_2)}\right)$$
$$= \left[E^0(H) - E^0(HgO/Hg)\right] + \frac{RT}{2F}\ln\left(\frac{a(H_2O)}{\gamma(H_2)P_{eq}(H)}\right), \quad (15)$$

where $E^0(H)$ and $E^0(HgO/Hg)$ are the standard electrode potentials of the H_2O/H couple and the HgO/Hg couple, respectively; $a(H_2O)$ is the activity of water; $a(H_2)$ is the activity of hydrogen; and $\gamma(H_2)$ is the fugacity coefficient. Wakao and Yonemura (1983) reported that the plateau pressures obtained from electrochemical measurement for $LaNi_{5-x}M_x$ (M = Cu, Cr, Mn, Al) electrodes showed excellent agreement with those obtained by the gas method (Sieverts' method). Iwakura et al. (1988) calculated the equilibrium pressure according to eq. (15) using the standard potential, the activity of water and the fugacity coefficient in a concentrated KOH solution given by Balej (1985) as a function of temperature and concentration of KOH solution. The equilibrium potential at 20°C and 6 M KOH under 1 atm was expressed by the following equation, in good agreement with the data from the gas reaction (fig. 8):

$$E_{eq}(H) \text{ vs. } E_{eq}(HgO/Hg) = -0.9324 - 0.0291 \log P(H_2). \quad (16)$$

The electrochemical pressure–composition isotherms (P–C–T) were obtained at different temperatures for various alloys to evaluate the charged and discharged pressures of the electrodes (Sakai 1988, Sakai et al. 1990a,b). This method was quite useful to obtain the P–C–T curves of the MH electrode over a wide pressure range from 10^2 to 10^{-8} atm with a small amount of sample (at least several mg). This technique allowed one to evaluate hydrogen desorption behaviors in thin films of alloys (Sakai et al. 1989c, 1991d, Kamasaki and Okajima 1992) and amorphous alloys (Miyamura et al. 1989, 1991, 1992). Almost the same method was utilized by Jordy et al. (1991) and Meli et al. (1992) to study some of these alloys.

A pressure change of one-order corresponds to a potential change of 29 mV according to eq. (16). If the $E_{eq}(H)$ value changes from –0.93 V to –0.64 V vs. HgO/Hg, the $P_{eq}(H)$ changes from 1 atm to 10^{-10} atm. This means that it is not necessary to control exactly the alloy plateau pressure, as is generally the case for conventional applications such as storage tanks, chemical heat-pumps and purification systems (Sandrock et al. 1992). This allows a wider choice of alloys for Ni–MH batteries.

However, some control of the hydrogen pressure is still one of the important factors for electrode alloys. If the $P_{eq}(H)$ value is higher than the cell pressure, the charging efficiency of hydrogen decreases, leading to lower storage capacity and hydrogen gas evolution. The stability of $LaNi_5$ hydride at higher temperature was increased by partially replacing Ni by Cu, Cr, Al and Mn (Percheron-Guegan et al. 1978). On the other hand, a lower

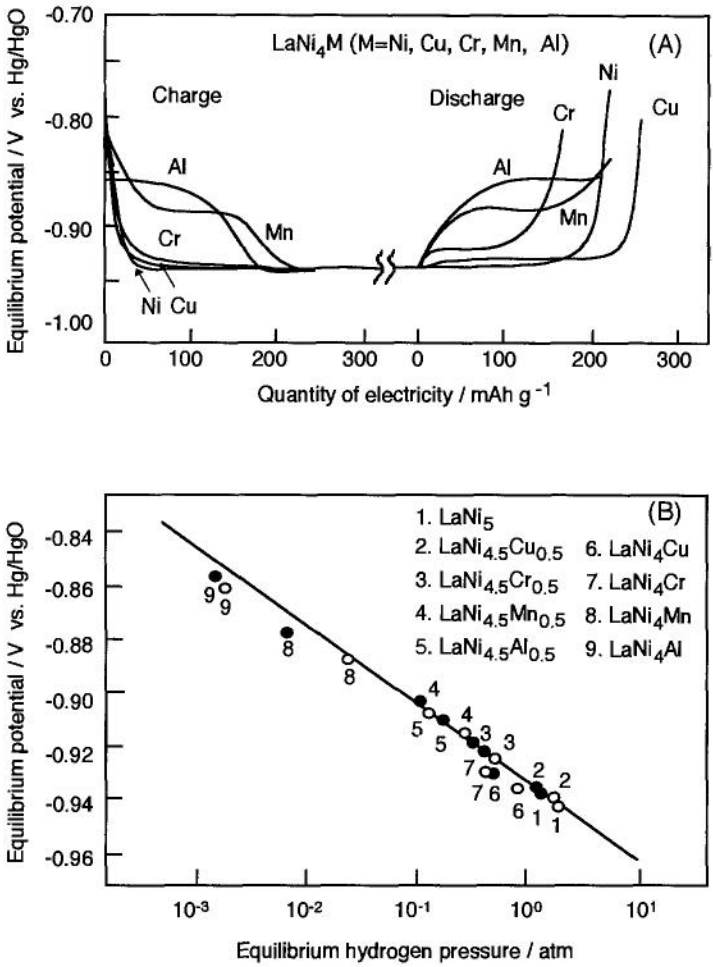

Fig. 8. (a) Variation of equilibrium potential with quantity of electricity of $LaNi_4M$ (M = Cu, Mn, Al, Cr); (b) plot of equilibrium potential against equilibrium hydrogen pressure of each plateau region for $LaNi_{4.5}M_{0.5}$ and $LaNi_4M$ negative electrodes. Open circles, charge (hydrogen absorption); solid circles, discharge (hydrogen desorption) (Iwakura et al. 1988).

equilibrium pressure causes a difficulty in activation as shown for a $LaNi_4Al$ electrode (Iwakura et al. 1988). The $P_{eq}(H)$ value should be controlled, depending on the purpose of the battery, e.g., high temperature use, low temperature use and high power use. For the usual batteries, the $P_{eq}(H)$ value should be below 1 atm at 60°C. The importance of suitable control of the plateau pressure for getting high charging efficiency was confirmed for $MmNi_{4.0}Mn_{0.2}Al_{0.2}Co_{0.6}$ by changing the rare-earth composition (La, Ce, Nd) in the Mm (Suzuki et al. 1993).

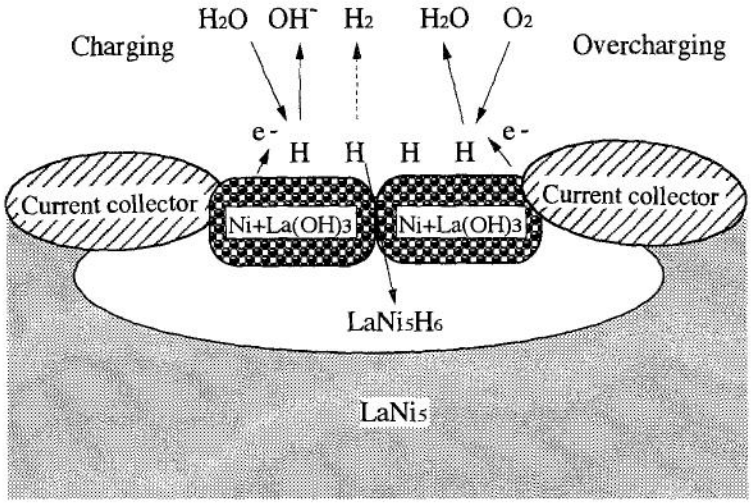

Fig. 9. Mechanism of hydrogen absorption and desorption at hydrogen storage alloy electrode.

3.2. *Kinetic properties*

The mechanism for charging–discharging the MH electrode is shown in fig. 9. First, charge transfer reaction produces adsorbed atomic hydrogen (H_{ad}) and OH^- on the electrode surface (Volmer process; eq. 17). If the diffusion rate of the atomic hydrogen can not follow the production rate, the hydrogen evolution reaction occurs (Tafel process; eq. 18). The atomic hydrogen has to diffuse from the surface to the bulk through the surface layer and grain boundaries before hydride formation in eq. (19):

$$H_2O + e^- = H_{ad} + OH^-(\text{Volmer process}), \tag{17}$$

$$2H_{ad} = H_2(\text{Tafel process}), \tag{18}$$

$$H_{ad\text{–surface}}(\text{diffusion process}) = \text{MH (Hydride)}. \tag{19}$$

The rate of the charge–discharge reaction is expected to depend on:

(1) surface conductivity of the alloy particles,
(2) effective surface area per unit weight of alloy or per unit area of electrode which is always changing by decrepitation, surface oxidation and dissolution of component elements,
(3) diffusivity of hydrogen from the surface to the bulk alloy,
(4) diffusivity of OH^- ion and H_2O to/from reaction surface,
(5) catalytic activity for the charge transfer reaction,
(6) contact resistance between alloy and current collector.

The potential difference between equilibrium and dynamic potentials, i.e. polarization, includes the total resistance resulting from the above factors as shown in fig. 10. Each

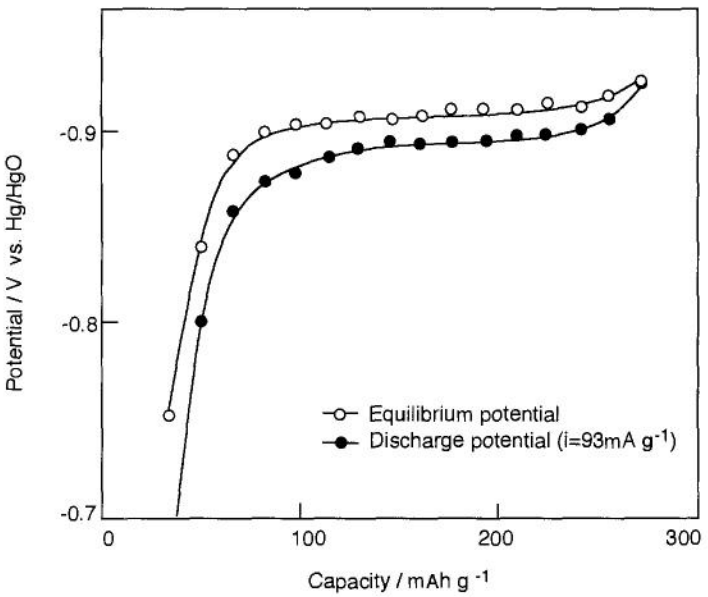

Fig. 10. Relationship of equilibrium or discharge potential and electrical capacity at 20°C for the $La_{0.9}Zr_{0.1}Ni_{4.5}Al_{0.5}$ negative electrode (Sakai et al. 1990a).

contribution from contact resistance, charge transfer resistance and diffusion resistance can be estimated separately by impedance analysis as described in sect. 3.3 (Kuriyama et al. 1992b, 1993b). However, the charge transfer resistance can be reduced by improving the surface conductivity, i.e., by enlargement of effective reaction area. It is difficult to separate both the effects from enlarged real reaction area and improved catalytic activity. Especially, the metallic nickel on the surface works as a good current collector and a good catalyst.

High electric conductivity at the alloy surface is necessary to provide electrons for the electrochemical reaction. Various methods of preparing electrodes have been tried since 1984. Willems (1984) made electrodes by pressing the mixture of alloy and copper powder in the weight ratio of 1 to 4. Iwakura et al. (1985) and Sakai et al. (1987, 1989a) used a 20 wt.% copper coated alloy developed by Ishikawa et al. (1985, 1986, 1989) to prepare the MH electrode, getting longer cycle life and better rate capability for the MH electrodes and sealed cells. A nickel coating was also used (Wakao et al. 1987, Sakai et al. 1991c). Wakao et al. (1984) made Ti–Zr–Ni-based electrodes by sintering the powder of the component elements. Fetcenko et al. (1988) developed a sintering method for Ti–Zr-based alloy powder to make the electrode sheet. Ikoma et al. (1986, 1988) and Ogawa et al. (1989) made electrodes by packing alloy powder into a foamed nickel matrix. Kanda et al. (1991) made electrodes by mixing the alloy with carbon and polymer. Hasegawa et al. (1991, 1994) mixed the alloy with cobalt or iron powder and filled it into a nickel fiber substrate. Park and Kirchheim (1992) developed a lower cost Cu-coating method

for the alloy electrode. Iwakura et al. (1992a, 1993) and Matsuoka et al. (1992, 1993a–d) chemically plated several metals on the MH electrodes or mixed the alloy powder with RuO_2 or Co_3O_4 powder or added chemical reducing agents such as KBH_4, H_3PO_2 to the KOH solution. Micro-composite particles of the alloy and copper were developed by mechanical mixing (Wada et al. 1993). In addition, various binding and/or pasting polymers such as polytetrafluoroethylene (PTFE), polyvinyl alcohol (PVA), silicon rubber (Sakai et al. 1991e), SEBS rubber (Hara et al. 1993), etc. are used. To obtain suitable electrode performances, various kinds of conductive powders such as Cu, Ni, Co, Fe and carbon (Yamashita et al. 1993), and matrices such as nickel foam and fiber are used. Surface insulation of alloy particles, which causes serious degradation of the performance, is expected to be caused by oxidation of metallic nickel, present in the surface layer of $LaNi_5$-based alloys; while it is caused mainly by formation of titanium and zirconium oxide films for TiZrNi-based alloys as described in sect. 3.11.

The reaction area is increased by decreasing the particle size and by cracking the particles. During the activation cycles the alloys are cracked by hydriding/dehydriding volume changes, allowing the diffusion of electrolyte solution inside the particles. The cracking also creates new fresh surfaces, free of oxidized layers. The addition of manganese in the alloys produces small equiaxed grains in the ingot, facilitating decrepitation and improving rate capability (Sakai et al. 1992a,b). Second phase formation in the grain boundaries was found to be effective sometimes in improving the rate capability. This improvement was mainly ascribed to an enhanced catalytic activity of the second phase (Notten and Hokkeling 1991), and facilitating the cracking of the alloys to increase the reaction area (Tadokoro et al. 1992, 1993). Alkali etching method was used for removing the surface oxide layer and also for increasing the effective surface area of the alloys (Ogawa et al. 1989). A gas atomizing method was used to get small particles of TiNi which is difficult to pulverize mechanically (Murata and Koshiro 1991).

Van Rijswick (1978) analyzed the rate-determining steps of the $LaNi_5$-based electrode, and concluded that the charge transfer becomes the rate-determining step for small particles, while the hydrogen diffusion dominates for larger particles. A potentiostatic discharge of the electrode showed a plateau of a high current density (520 mA/g) limited by the charge transfer, followed by a decrease in current due to the limitation of hydrogen diffusivity. The estimated diffusion coefficient (7×10^{-10} cm^2/s) was lower by one order of magnitude than the value obtained by the NMR method for $LaNi_5$. It was also observed that improvement of cycle life by partially replacing the nickel or lanthanum by Si, Al, Ti, Zr, caused a decrease in rate capability, suggesting lower diffusivity of hydrogen through the more protective surface layer (Willems 1984, Sakai et al. 1990a,b.)

Wakao and Yonemura (1983) analyzed current–overpotential curves of $LaNi_{5-x}Al_x$ and $LaNi_4Cu$ electrodes in terms of diffusion theory. The temperature dependence of the limiting current at large anodic polarization suggested that the main diffusion species changed from atomic hydrogen H in the alloy to hydroxide ion OH^- in the solution with decreasing enthalpy of hydride formation. The diffusion of OH^- ions and water is expected to become important at higher rates, depending on the porosity of the electrode. When the alloy was bound by polymeric binders, the discharge capability

greatly depended on the content of the polymer and the pressing pressure for making the electrode sheet (Sakai et al. 1990d, 1991b, Naito et al. 1993). On the other hand, when the electrodes were made by mixing and pressing $LaNi_5$ powder with 400% copper powder, no essential difference was found in the void volume range of 1.1 to 40.1% (Boonstra and Bernards 1990a). The rate-determining step of electrodes seems to depend greatly on the preparation methods. Kinetic properties of MH electrodes were also examined by Yayama et al. (1983, 1984, 1986, 1987, 1989). Electrochemical kinetic parameters of $LaNi_{4.8}Sn_{0.2}$ anodes were also evaluated by Ratnakumar et al. (1994).

3.3. *Impedance analysis*

Kuriyama et al. (1992b, 1993a,b) have conducted systematic analyses of the electrode reaction by using the electrochemical impedance spectroscopy. A Cole–Cole plot of

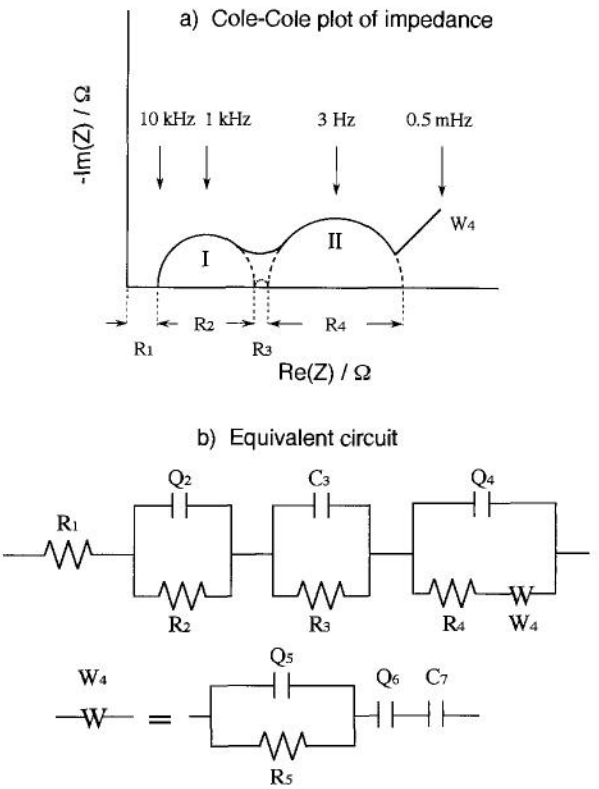

Fig. 11. Schematic representation of (a) a Cole–Cole plot and (b) an equivalent circuit for metal hydride electrodes. R_n, resistive components; C_n, normal capacitive component; Q_n, capacitive components in order to describe a depressed semicircle; W_4, Warburg impedance; Q_i, $Q_i(\omega) = [Y_{i_0}(j\omega)^n]^{-1}$, $(0 < n < 1)$ (Kuriyama et al. 1992b).

the impedance of an MH electrode using a copper-coated $MmNi_{3.5}Co_{0.7}Al_{0.8}$ alloy was well fitted by the equivalent circuit shown in fig. 11. R_1 was assigned to the electrolyte resistance. R_2 was ascribed to the contact resistance between current collector and alloy. R_3 was considered to be due to the contact resistance between alloy particles. R_4 was ascribed to the reaction resistance on the alloy surface. During 440 cycles, R_2 and R_3 did not change, showing that the copper layer on the alloy could preserve good electrical conductivity in the electrode, while R_4 increased significantly because of the degradation of the alloy surface. Even storage of the copper coated alloy in air for 6 months caused an increase in the R_4. The Warburg impedance (W_4) was related to the diffusion of hydrogen and electrolyte solution. When the electrode was made without copper coating, the contact resistances (R_2 and R_3) significantly increased with increasing discharge depth, and with increasing cycles. This result shows that a suitable electrode structure for giving the alloy powder a good conductivity, is important in order to test the electrode performance of the alloys.

Kuriyama et al. (1993a,b) compared the impedance spectra of Cu-coated alloys of $MmNi_{3.5}Co_{0.7}Al_{0.8}$ and $Ti_{0.5}Zr_{0.5}Ni_{1.1}V_{0.7}Al_{0.2}$. The reaction resistance R_4 for the titanium based alloy was higher by a factor of 7 than that of the Mm-based alloy, although the contact resistances R_2 and R_3 were almost the same for both. The Warburg impedance for the titanium-based alloy was about twice that of the mischmetal-based alloy. The surface insulation for the titanium-based alloys is a more serious problem than that for mischmetal-based alloys, requiring more caution for alloy treatments and electrode preparation. Impedance analyses were also reported by Agarwal et al. (1992).

3.4. *Surface activity*

The electrocatalytic activity of MH electrodes for hydrogen evolution reactions according to eqs. (17, 18) can be evaluated using the Tafel equation as follows:

$$\eta = E - E_{eq} = a - b\log i, \qquad a = \frac{2.3RT}{\beta F}\log i_0, \qquad b = \frac{2.3RT}{\beta F}\ \text{(Tafel slope)}. \quad (20)$$

where η is the overpotential, E the electrode potential at which hydrogen evolution occurs, E_{eq} the equilibrium potential, i the current density, i_0 the exchange current density, and β is a symmetry factor. The exchange current density increases with increasing electrocatalytic activity for charge transfer in eq. (17). However, we can get only an apparent current density per gram or area. This means that the exchange current density becomes a measure of surface activity, but it also includes both effects due to the effective reaction area and the catalytic activity. Hydrogen production mechanism on La(Mm)Ni_5-based alloy electrodes was shown to proceed through the Volmer–Tafel mechanism (Kitamura et al. 1981a,b, 1982a,b). Tamura et al. (1983) found that logarithmic exchange current densities ($\log i_0$) of $LaNi_5$ (−3.5) and $MmNi_5$ (−3.7) were much higher than the value of nickel (−5.1) and comparable to the value of Pt (−3.0) and Pd (−3.9). The much higher electrocatalytic activity of the alloys than those of their constituents such as nickel and

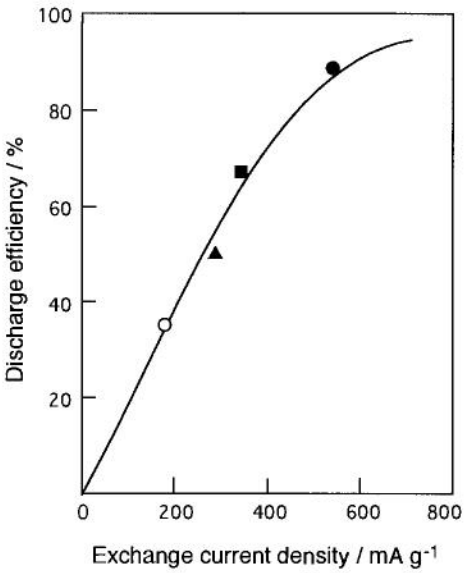

Fig. 12. Discharge efficiency under extreme conditions at 0°C and a high discharge current of 840 mA g^{-1} as a function of the exchange current density for the standard alloy (open circles), the pentaery $AB_{5.5}$ alloys (solid triangles, solid squares), and the Mo-containing $AB_{5.5}$ alloys (solid circles) (Notten and Hokkeling 1991).

lanthanum (mischmetal) suggested a synergistic effect by the alloying. The activation energy for hydrogen evolution was observed to increase with increasing heat of hydride formation for $LaNi_{5-x}Al_x$ and LaM_5 (M = Ni, Co, Fe, Cr). The synergistic effects for alloys were also pointed out by Machida et al. (1984, 1986). Catalytic activity of intermetallic compounds were discussed by Jaksic (1984, 1986a,b) based on the d-electron character. A detailed review of catalytic materials for hydrogen production was given by Hine (1987a,b).

Notten and Hokkeling (1991) found that the rate capability of MH electrodes increased when second phases (e.g. $MoCo_3$) were present in the $La_{0.8}Nd_{0.2}Ni_{2.5}Co_{2.4}Si_{0.1}$ alloy. They ascribed it to the enhanced catalytic activity on the surface due to the fact that a linear relationship between the rate capability and exchange current density exists (fig. 12).

Iwakura and coworkers (Iwakura et al. 1992a, Iwakura and Matsuoka 1992) pointed out that when the surface of the $MmNi_{3.6}Mn_{0.4}Al_{0.3}Co_{0.7}$ electrode was modified by electroless copper or nickel coating, the exchange current density increased from 240 mA/g to 460 mA/g with increasing of the rate capability of the MH electrode as shown in fig. 13. These results were ascribed to the effects of improving the current collecting ability. The same effect was found when the electrolyte solution (6 M KOH) contained a reducing agent such as 0.08 M H_3PO_2 (Iwakura et al. 1992a, Iwakura and Matsuoka 1992), or 0.001–0.1 M KBH_4 (Matsuoka et al. 1993a). The hydrogen, produced by the reducing agent, could reduce the surface nickel oxide, forming a nickel-rich surface layer which could give good surface conductivity and high catalytic activity. Part of the hydrogen was stored in the alloy, giving a volume change of 15% (fig. 14), although the amount of absorbed hydrogen depended on the concentration of reducing agent, treating time and temperature. They suggested that if the discharge reaction is

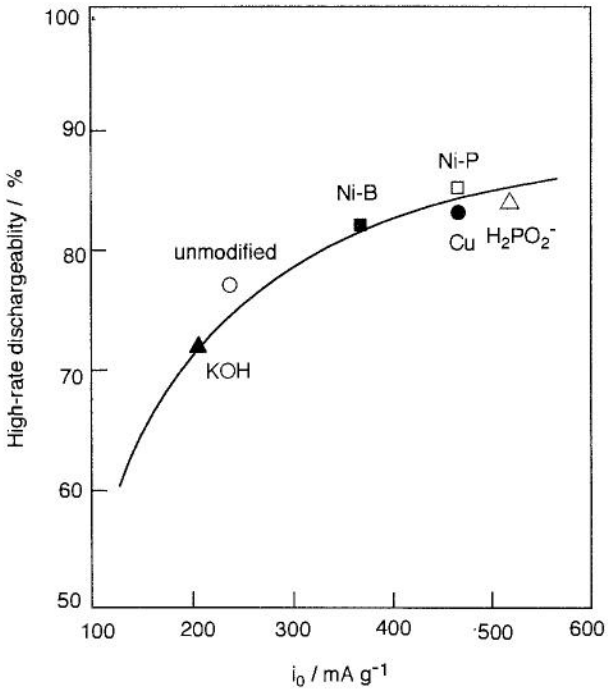

Fig. 13. Effect of surface modifications of MH electrode on high-rate dischargeability and exchange current density (i_0). Open circles, original one expressed by "unmodified"; solid circles, 10 wt.% copper plating (Cu); open squares, 10 wt.% nickel plating containing phosphorus (Ni–P); solid squares, 10 wt.% nickel plating containing boron (Ni–B); solid triangles, alkaline etching treatment by a 6 M KOH at 80°C; open triangles, reducing treatment at 80°C using 0.08 M reducing agent (H_3PO_2) contained in electrolyte solution. The high-rate dischargeability is defined as the capacity ratio at 1786 mA g^{-1} discharge to 178.6 mA g^{-1} discharge. (Iwakura et al. 1992a.)

limited by surface reaction, a linear dependence of rate capability on the exchange current density would be expected. The parabolic relationship in fig. 13 suggested that hydrogen diffusivity progressively becomes a rate-determining step with increase of the exchange current density. Matsuoka et al. (1993b) found that the rate capability was improved in the order of Fe, Ni, Co and Pd coating for the $Mm(Ni_{3.6}Mn_{0.4}Al_{0.3}Co_{0.7})_{0.92}$ electrode, but this was not true for $LaNi_5$ electrode. This result suggests that the rate-determining step is the surface reaction for the former alloy, while it is the hydrogen diffusivity for the latter alloy. Mixing of RuO_2 or Co_3O_4 powder was also effective to improve the rate capability (Iwakura et al. 1993, 1994). The modification by RuO_2 significantly increased the exchange current density as a result of enhanced Volmer reaction as shown in table 3.

Sakamoto and coworkers (Sakamoto et al. 1992, 1994, Sakamoto and Ishimaru 1994) simulated the discharge curves of Pd electrodes at various currents. By using the diffusion coefficient and the exchange current density, they obtained good agreement between the calculated and experimental curves. With increasing discharge rate, the rate-determining

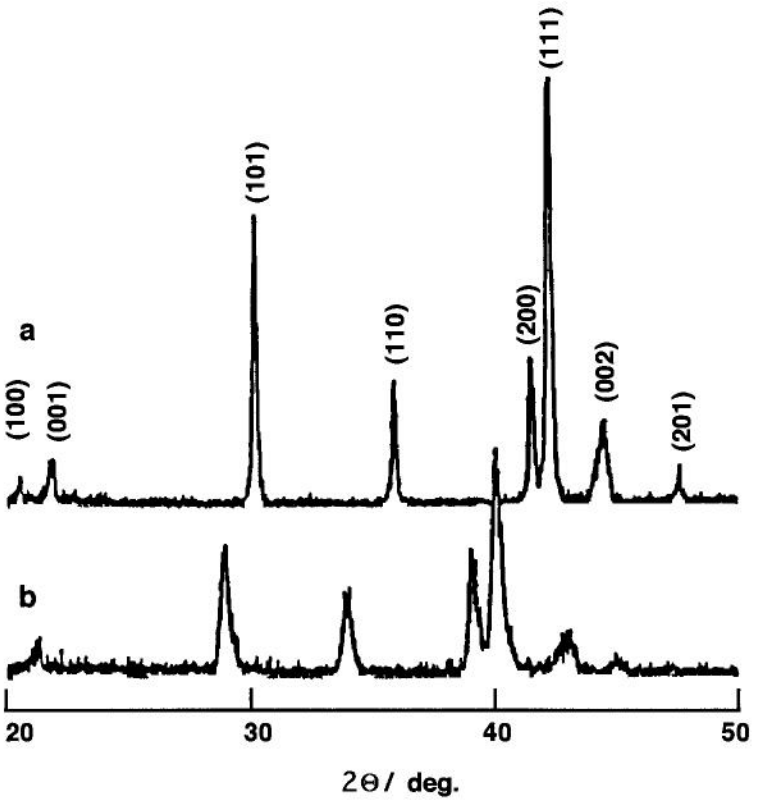

Fig. 14. Changes in X-ray diffraction patterns of $MmNi_{3.6}Mn_{0.4}Al_{0.3}Co_{0.7}$ alloy powder: (a) unmodified; (b) after treatment with reducing agent using 0.01 M KBH_4, 40°C (Matsuoka et al. 1993a).

Table 3
Kinetic parameters of the hydrogen electrode reaction on the negative electrode[a]

Alloys	$i_{0,\text{Volmer}}$ (mA g^{-1})	$i_{0,\text{Tafel}}$ (mA g^{-1})	$m_0 = i_{0,\text{Volmer}}/i_{0,\text{Tafel}}$
Unmodified	168.8	18.7	9.0
Co_3O_4 (5 wt.%)	179.9	10.7	16.8
RuO_2 (5 wt.%)	438.6	20.3	21.6
RuO_2 (10 wt.%)	478.2	20.9	22.9
RuO_2 (20 wt.%)	570.4	23.5	24.3

[a] Iwakura et al. (1993).

step changes from charge transfer to hydrogen diffusion. However, the same approach seems to be difficult to carry out on the $LaNi_5$-based alloys because they continue to crack and decompose, increasing the depth of oxygen penetration and changing the surface morphologies.

Viitanen (1993) developed a mathematical model to analyze the polarization behavior of the electrode under various conditions, in terms of physically measurable properties such as exchange current density, diffusivity of hydrogen, particle size of alloy, void fraction and electrode size.

3.5. *Pressure rise in a sealed cell*

When the charging reaction is limited by the diffusion process, hydrogen evolution (Tafel process) occurs, reducing charging efficiency. The hydrogen gas is not consumed quickly, so that the inner pressure of the sealed cell increases beyond the pressure limit (around 10 atm) of the safety vent. The gas release causes a drying out of the starved electrolyte, increasing the inner resistance of the battery and then limiting the cycle life of the sealed cell. The charging efficiency is expected to become higher for (1) larger effective reaction area, (2) higher hydrogen diffusivity through the surface layer, (3) higher catalytic activity for charge transfer (Volmer process) and (4) lower activity for recombination (Tafel process).

If the hydrogen pressure in the alloy becomes higher than the charging pressure, the driving force for hydrogen to diffuse to the inside would vanish, reducing the charging efficiency. The temperature rise during charging also affects charging efficiency, as does the possible formation of a diffusion barrier on the surface. The degradation of the alloy during cycling also causes hydrogen evolution in the sealed cell because the decomposition of alloy into oxides and Ni produces extra hydrogen in the MH electrode, reducing available capacity for electrolytic hydrogen (Kanda 1991).

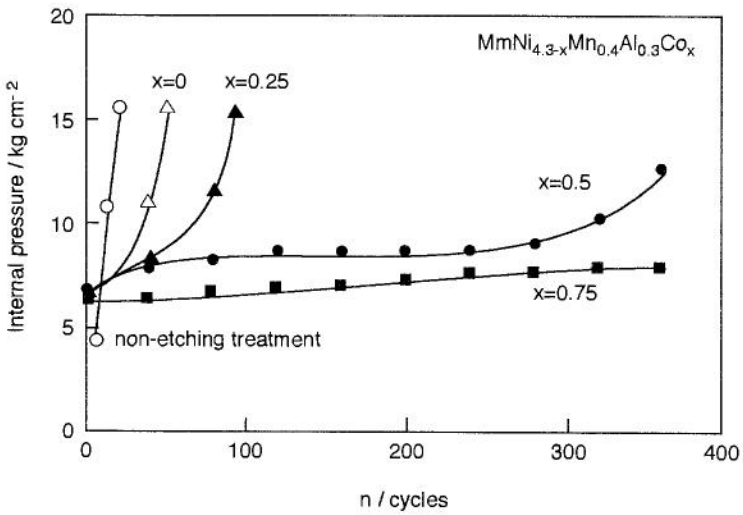

Fig. 15. Influence of Co content of $MmNi_{4.3-x}Mn_{0.4}Al_{0.3}Co_x$ alloy after alkaline etching treatment on the changes of internal gas pressure during standard charge–discharge cycles in the AA cell in comparison with non-treated alloy electrode (Ogawa et al. 1989).

Surface coating of the alloy by copper or nickel was found to be useful for improving the cycle life of the sealed cell (Sakai et al. 1987, 1991c, 1992b). Hydrogen evolution during high rate charging was greatly reduced by surface coating because the coated film gave the alloy a good surface conductivity, preventing passivation and enlarging the effective reaction area. Ogawa et al. (1989) reported that when $MmNi_{4.3-x}Mn_{0.4}Al_{0.3}Co_x$ alloy was impregnated into foamed nickel, an alkaline etching treatment was indispensable to prevent hydrogen evolution and to improve the cycle life of the sealed cell (fig. 15). This was ascribed to the formation of a nickel-rich surface which would work as good conductor and catalyst. Hasegawa et al. (1991, 1994) and Takashima et al. (1992) tested cells in which the MH electrode was made by packing an alloy ($MmNi_{3.7}Al_{0.9}Fe_{0.3}Cu_{0.1}$) into nickel fiber foam. The cycle life was quite short because the alloy surface was covered with corrosion product $Mm(OH)_3$, decreasing the electric conductivity by one order of magnitude. It was found that mixing cobalt powder with the alloy was effective to improve the cycle life, because cobalt could form conductive networks. Improvement of the charging efficiency at higher temperature is very important for high density batteries because the temperature rise becomes more serious.

3.6. *Chemical stability of $LaNi_5$*

Van Rijswick (1978) considered the chemical stability of alloys in alkaline solutions. There are three types of behavior for the elements: (1) immunity against oxidation when the metal is thermodynamically stable, (2) corrosion when the metal continuously oxidizes and dissolves in the solution, (3) passivation when the oxides or hydroxides are insoluble and form a protective layer. The behavior changes with both potential and pH of the solution (Pourbaix's potential–pH diagrams) (Pourbaix 1966). Metals with a strong affinity for hydrogen have a stronger affinity for oxygen (except palladium), forming stable oxides and hydroxides which are insoluble in the KOH solution. In the potential range over which hydrogen is charged and discharged in the KOH solution, the lanthanum is oxidized (although the solubility of the hydroxide is extremely low), while nickel is immune up to about 150 mV above the hydrogen potential after which it oxidizes to hydroxide, causing passivation. The cobalt is also immune up to about 100 mV above the hydrogen potential, but above that the oxidation product dissolves in the KOH solution. Iron and manganese continuously corrode because the oxides are soluble as ferrite ions and manganite ions. The effect of alloying results in a regularly packed structure of several kinds of atoms in which selective oxidation of the less noble metal (such as lanthanum) leaves a surface layer of the more noble metal (such as nickel and cobalt) which determines the corrosive properties of the alloys. This means that the major component metal should be thermodynamically stable against oxidation in the potential range, restricting the choice of the electrode alloy to nickel or cobalt-rich alloys, except for platinum group elements. However, if a major component metal oxidizes and passivates the alloy surface in the potential range, the oxide layer blocks the surface and locks the hydrogen in the alloys, causing irreversible storage. This model explains the surprisingly high chemical stability of $LaNi_5$ in the KOH solution.

3.7. *Deterioration mechanism of $LaNi_5$*

Willems (1984, 1986), Van Beek et al. (1984) and Willems and Buschow (1987) also examined the deterioration process of $LaNi_5$. During charge–discharge cycles the capacity of $LaNi_5$ electrodes declined drastically. After cyclic testing the electrode sample showed additional X-ray diffraction peaks due to $La(OH)_3$ and metallic nickel and a rapid increase in BET surface area due to the formation of $La(OH)_3$. From the thermodynamic aspect, the oxidation of lanthanum in the KOH solution is unavoidable. The free energy change of $LaNi_5$ oxidation, $\Delta G = -472$ kJ/mole, is almost two times the enthalpy change of $LaNi_5$ formation, $\Delta H = -273$ kJ/mole, giving the alloy a strong driving force for segregation in the aqueous solution. The surface layer, composed of lanthanum oxides and metallic nickel, would give the alloy a kinetic barrier for the further oxidation of lanthanum. However, the rare-earth-based hydriding alloys are brittle. The large lattice expansion (24 vol.%) of $LaNi_5$ during cycling causes cracking of the alloy, damaging the protective ability of the surface layer and forming continuously fresh surface. For example, during 1000 cycles of gas absorption–desorption $LaNi_5$ powder starting in the range of 100 to 200 μm was pulverized to fine powder with a specific surface area of 0.28 m^2/g which corresponded to 2.6 μm in diameter.

More detailed factors for $LaNi_5$ degradation were examined by Boonstra and co-workers (Boonstra et al. 1989, 1990, Boonstra and Bernards 1990a,b). When the $LaNi_5$ was partly oxidized by heating under oxygen atmosphere, a mixture of La_2O_3, La_2NiO_4 and Ni was formed, suggesting that the initially formed NiO would react with underlying $LaNi_5$ to produce the La_2NiO_4 and Ni. It was proposed that there was direct oxidation of $LaNi_5$ to $La(OH)_3$ and $Ni(OH)_2$ during cycling, followed by the reaction of the $Ni(OH)_2$ with the underlying $LaNi_5$. The decay rate decreased with increasing the initial oxygen content although the capacity greatly decreased. It was estimated that when only 40% of the alloy was oxidized, the discharge capacity became zero because the remaining alloy would be completely isolated from the current collector. The decay rate of the electrode increased with increasing contact time with the KOH solution. The decrease in the KOH concentration from 6 M to 0.6 M led to a drastic decrease in the discharge capacity because of the increase in electrolyte resistance. The capacity decay was also reduced by increasing the copper content from 80 to 99.3wt.% Cu in the electrode.

3.8. *Improvement of cycle life*

Willems (1984) examined the $LaNi_{5-x}Co_x$ system in order to confirm a hypothesis that a reduction of the lattice expansion during hydriding should lead to a more stable hydride electrode. The partial substitution of cobalt for nickel results in a considerable reduction of the volume expansion on hydrogen absorption (Van Mal et al. 1973). The stability of the electrodes, which was expressed by the capacity ratio of the initial cycle to the 400th cycle, became higher with increasing cobalt content from $x = 0$ to $x = 3.3$, i.e., with decreasing volume expansion ratio from 24.3% for $LaNi_5$ to 15.1% for $LaNi_{2.5}Co_{2.5}$ (table 4). The volume expansion ratio decreased especially in the c-axis direction, e.g.,

Table 4
Lattice expansion due to the formation of hydrides[a]

Compound	V (Å^3)	$\Delta a/a$ (%)	$\Delta c/c$ (%)	$\Delta V/V$ (%)
$LaNi_5$	86.66	7.8	6.9	24.3
$LaNi_4Co$	87.32	7.3	6.3	22.5
$LaNi_3Co_2$	87.74	7.0	5.3	20.5
$LaNi_{2.5}Co_{2.5}$	87.94	6.2	2.1	15.1
$LaNi_2Co_3$	88.02	5.9	0.9	13.3
$LaNi_{1.7}Co_{3.3}$	88.23	6.1	0.7	13.3

[a] Willems (1984).

from 6.9% for $LaNi_5$ to 2.1% for $LaNi_{2.5}Co_{2.5}$. The lattice expansion along the c-axis is expected to have more influence on cracking because the alloys have a layer structure with an ABAB stacking sequence. The same anisotropic effect of lattice expansion accompanied by stability improvement was reported for the substitution of Si for Ni by Meli et al. (1992).

In addition to volume expansion during hydrogen formation, i.e., internal stress, the decrepitation rate of $LaNi_5$-based alloys is expected to be closely related to the mechanical properties of the alloys. It was found by Sakai (1988) and Sakai et al. (1990c) that the decrepitation rate decreased with decreasing Vickers hardness in the order of M = Mn > Cu > Cr > Al > Co for $LaNi_{5-x}M_x$, thus increasing the cycle life of the alloys. The addition of Co was useful to improve the mechanical properties, i.e., to give the alloy some ductility in addition to the crystallographic effect described above. The $LaNi_{4.0}Al_{1.0}$ also showed long cycle life, although many activation cycles at 40°C were needed to get full capacity because of the low equilibrium pressure (10^{-4} atm at 20°C). The substitution of Mn provided the alloy with a more brittle character, giving a shorter cycle life. The importance of the mechanical properties is supported by the fact that such ductile metals as Pd and TiNi are not decrepitated during charge–discharge cycles. The replacement of La by Zr was effective for improving the cycle life because the addition of Zr in $LaNi_5$ prevented decrepitation (Sakai et al. 1989b, 1990a). Amorphous film electrodes of $LaNi_5$ and $LaNi_{2.5}Co_{2.5}$ showed less decrepitation rate and longer cycle life than the crystalline samples although the discharge capacities (80 mAh/g) were much lower than the crystalline ones (Sakai et al. 1989c, 1991d, Kamasaki and Okajima 1992). The alloy film absorbed the hydrogen only as a solid solution without hydride formation.

Miyamura et al. (1988, 1989, 1991, 1993a) found that amorphous alloys RNi_2 (R = La, Ce, Pr) had a long cycle life, but the discharge capacity was less than 100 mAh/g at room temperature. The $LaNi_2$ initially absorbed a large amount of hydrogen up to H/M = 1.6 with steeply sloped P–C–T curves, but only 20% of the hydrogen was dischargeable when the pressure changed from 1 to 10^{-8} atm. The discharge capacity increased with increasing temperature and with decreasing current, suggesting a diffusivity-limited reaction. The apparent diffusivity was measured in the $LaNi_2$ thin film electrode by a

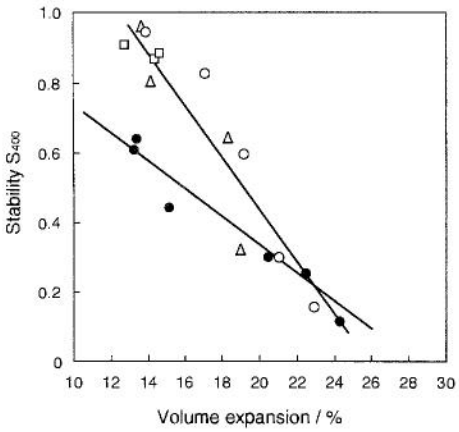

Fig. 16. Stability of $LaNi_5$-related hydride electrodes after 400 cycles S_{400}, as a function of the lattice volume expansion. Solid circles, $LaNi_{5-z}Co_z$; open triangles, $LaNi_{5-z}Co_zSi_{0.1}$; open circles, $LaNi_{5-z}Co_zAl_{0.1}$; open squares, others (Willems 1984).

potential step technique. The diffusivity (around 10^{-9} cm^2/s at 40°C) was two orders of magnitude lower than the value of crystalline samples and decreased with decreasing hydrogen concentration and temperature. It was concluded that the high stability of the RN_2 hydrides and low diffusivity of hydrogen caused the low rechargeable capacity. Long cycle life of ZrNi amorphous alloy was also reported (Ryan et al. 1991, Ciureanu et al. 1993).

Willems (1984) also reported that the stability of the cobalt-rich alloy was further improved by the addition of a small amount of aluminum and silicon, although these additions did not affect the stability of Co-free $LaNi_5$. The slope of the stability vs. volume expansion ratio for Al or Si-containing alloys was twice that of the $LaNi_{5-x}Co_x$ compounds (fig. 16), indicating higher sensitivity to mechanical stress. It was suggested that if the protective layer is not damaged by cracking of the alloy, a small addition of aluminum or silicon (only two atomic percent) could prevent the transport of lanthanum to the surface by the formation of a denser oxide layer. The replacement of La by Nd provided further improvement in the cycle life, developing a high stability alloy, $La_{0.8}Nd_{0.2}Ni_{2.5}Co_{2.4}Si_{0.1}$, although the rate capability was not enough for a practical battery. It was suggested that the diffusion of lanthanum to the surface was prevented by the different size of rare-earth elements in the lattice.

3.9. *Mischmetal-based alloys*

The high equilibrium pressure of the mischmetal-based alloy $MmNi_5$ requires the replacement of nickel by manganese or aluminum in order to decrease the pressure, leading to an alloy of the $MmNi_{4.3}(Al, Mn)_{0.7}$ composition (Ikoma et al. 1986). Ogawa et al. (1989) tested $MmNi_{4.3-x}Co_xAl_{0.3}Mn_{0.4}$ in a sealed cell. They found that the cycle life of the battery was improved by increasing the cobalt content and by an alkaline etching treatment (fig. 15), developing a practical alloy $MmNi_{3.55}Co_{0.75}Al_{0.3}Mn_{0.4}$. Nogami et al. (1990) also confirmed the effects of cobalt addition for improving the cycle life. They

Table 5
Amount of corresponding elements dissolved from the alloy after 200 cycles[a]

Alloys	La (wt.%)	Nd (wt.%)	Ni (wt.%)	Co (wt.%)	Mn (wt.%)	Al (wt.%)
$MmNi_{4.2}Mn_{0.6}Al_{0.2}$	0.6	0.8	0.5	–	24.8	< Det. limit
$MmNi_{3.6}Co_{0.6}Mn_{0.6}Al_{0.2}$	0.6	0.5	0.4	3.9	14.3	< Det. limit
$MmNi_{3.0}Co_{1.2}Mn_{0.6}Al_{0.2}$	0.3	0.3	0.3	3.2	6.5	< Det. limit

[a] Kanda et al. (1991).

reported that a stoichiometric deviation to the mischmetal-rich side ($x = 4.55$–4.75) for $Mm(NiCoAlMn)_x$ gave a higher capacity. Kanda and coworkers (Kanda et al. 1991, Kanda 1991) found that the $MmNi_{5-x}(MnAl)_x$ alloy showed continuous dissolution of Mn during cycles. As shown in table 5, after 200 cycles about 25wt.% of the total Mn in the $MmNi_{4.2}Mn_{0.6}Al_{0.2}$ was lost from the alloy and precipitated on the alloy surface as oxides. With increasing the Co content the dissolving ratio of manganese was greatly decreased to 14.3wt.% for $MmNi_{3.6}Co_{0.6}Mn_{0.6}Al_{0.2}$ and 6.5wt.% for $MmNi_{3.0}Co_{1.2}Mn_{0.6}Al_{0.2}$ although about 3–4wt.% of the total Co was found to precipitate on the surface oxide layer.

It was shown that by increasing the Ce and Nd content (R) in $La_{1-y}R_yNi_{5-x}(CoAl)_x$-based alloys the cycle life was significantly improved with much lower cobalt content, demonstrating the merit of low cost mischmetal (Sakai et al. 1991a, 1992a). With increasing the cobalt content in $MmNi_{4.2-x}Co_xAl_{0.8}$ the cycle life of the electrodes was much improved as shown in fig. 17a, while high rate capability was significantly reduced as shown in current dependencies of discharge capacity (fig. 17b), suggesting $MmNi_{3.5}Co_{0.7}Al_{0.8}$ as a suitable composition. Since the high equilibrium pressure of $MmNi_5$ requires the replacement of nickel by aluminum in order to decrease the pressure, reducing the cobalt content can be ascribed to the mixed effects of mischmetal, cobalt and aluminum. The alloy $MmNi_{3.5}Co_{0.7}Al_{0.8}$ (250 mAh/g) showed a capacity decay ratio of only 10% after 2000 cycles with only a little formation of $Mm(OH)_3$, while the previous La-based alloys $LaNi_{2.5}Co_{2.4}Al_{0.1}$ showed a decay ratio of 60% after 1000 cycles with significant formation of $La(OH)_3$.

Several long-life cobalt-free alloys have been proposed, such as $La_{0.9}Zr_{0.1}Ni_{4.5}Al_{0.5}$ by Sakai et al. (1990a) and $Mm_{0.9}Zr_{0.1}Ni_{4.2}Al_{0.7}V_{0.1}$ by Hazama et al. (1990) though they were tested only in half cell using 20 wt.% Cu-coated alloys. Hasegawa et al. (1991) developed an alloy $MmNi_{3.7}Al_{0.5}Fe_{0.7}Cu_{0.1}$, but a satisfactory cycle life was obtained only when the alloy powder was mixed with 16.7 wt.% cobalt powder or coated by nickel before packing it into a nickel fiber substrate. Meli et al. (1994) proposed a $MmNi_{4.2}Mn_{0.2}Al_{0.3}Si_{0.3}$ though it was tested only in a half cell using 75 wt.% Cu-mixed alloy. Additional tests in sealed cells will be needed to develop practical alloys without cobalt.

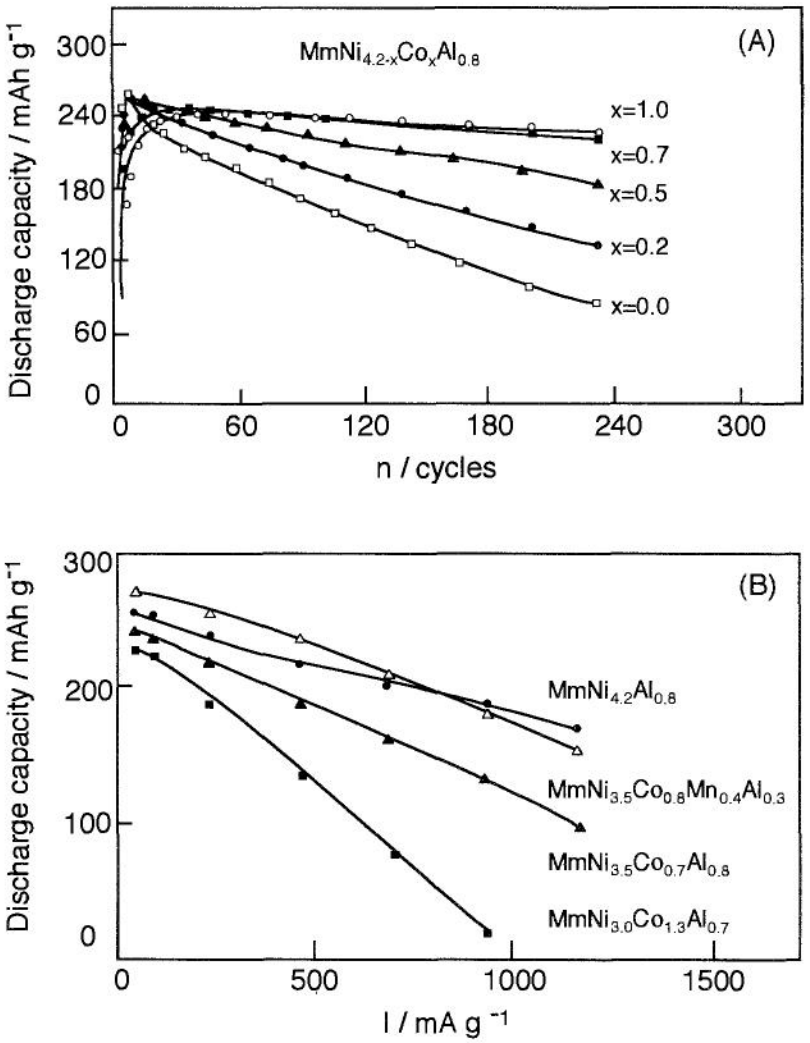

Fig. 17. (a) Influence of cobalt content on cycle life for $MmNi_{4.2-x}Co_xAl_{0.8}$ alloy electrodes at 20°C (charge 186 mA g^{-1} for 2 h; discharge, 93 mA g^{-1} to −0.6 V vs Hg/HgO); (b) influence of cobalt content on discharge capability for various $MmNi_5$ based alloy electrodes at 20°C (Sakai et al. 1991a).

3.10. *Casting condition of alloys*

It was found that the cycle life of the alloy $MmNi_{3.5}Co_{0.7}Al_{0.8}$ was sensitive to the cooling rate of the melt and the heat-treatment temperature (Sakai et al. 1991a, 1992a). At high solidification rate (SR) using a plate-like casting (SR = 10^2 K/s), a clear columnar structure with a smaller grain size (20–30 μm) formed and this led to an increased cycle life. Oriented crystal growth was observed to occur in the direction perpendicular to the *c*-axis.

The columnar structure showed less lattice strain and less pulverization. Heat-treatment at 1000°C caused a decrease in cycle life. This was ascribed to grain growth and the precipitation of excess elements at the grain boundaries. Since the cracking occurs first on the grain boundaries and then across the grains, it was believed that the protective surface layer formed on the smaller grain would remain more effective after decrepitation.

Melt spinning (SR = 10^5 K/s) resulted in a flake-like alloy with a much clearer columnar structure and a much smaller grain size (2–3 μm). This material showed a longer life, a lower decrepitation rate and a flatter pressure plateau as shown in fig. 18 (Mishima et al. 1993). Low-temperature heat-treatment at 400°C further improved the cycle life by removing lattice defects such as dislocations. A gas atomizing method (SR = 10^3–10^4 K/s), which produces spherical fine powders (30–40 μm) also had a small grain size (10 μm). This led to several improvements, such as fewer required activation cycles, higher rate capability and longer cycle life after a suitable heat-treatment, as compared to the samples prepared by conventional induction melting method (Kaminaka et al. 1992, Takeshita et al. 1992). The improvement was ascribed to a more homogeneous composition (without segregation) and smaller grain size.

The partial replacement of Al by Mn, such as $MmNi_{3.5}Co_{0.8}Al_{0.3}Mn_{0.4}$, significantly changed the metallurgical macrostructure (Sakai et al. 1992a). The addition of Mn resulted in an equiaxed structure composed of spherical fine grains, causing more sloped pressure plateau (more lattice strain). Even a sputter deposition of the Mn-containing alloy resulted in a polycrystalline alloy, although the Mn-free alloy became amorphous-like (Sakai et al. 1993c). This suggests that Mn facilitates nucleation. The lattice strain in the alloy gives a sloped pressure plateau and also facilitates the cracking of grains, depending on the casting methods. Sheet-like solidification by melt-spinning gave a flatter plateau than spherical solidification by gas atomization, suggesting that formation of spherical grains prevent the release of the lattice strain during solidification process (Sakai et al. 1994a). The high lattice strain and the high decrepitation rate of the Mn-containing alloys were ascribed to the formation of an equiaxed structure composed of fine grains. The high lattice strain should be released by heat-treatment in order to improve the cycle life. In addition, since the manganese tends to precipitate on the grain boundaries, the higher-rate solidification is useful to obtain more homogeneous compositions and smaller crystals with shorter diffusion paths for the segregated elements during heat-treatment.

The reduction–diffusion method is another method to prepare fine powders (around 20–50 μm) of alloys with low lattice strain because the alloy is prepared by heating the mixture of mischmetal oxides, the reductant (Ca) and the metal powder, such as Ni, Co, Mn, Al, at 900–1000°C (Takeya et al. 1993). Almost the same electrode performances as those of the samples prepared by the melting method were obtained for the Mn-containing alloys.

Prolonged mechanical grinding of $MmNi_{3.5}Co_{0.8}Al_{0.7}$ and cobalt powder caused a decrease in the discharge capacity because of amorphization of the alloy (Ikeya et al. 1993).

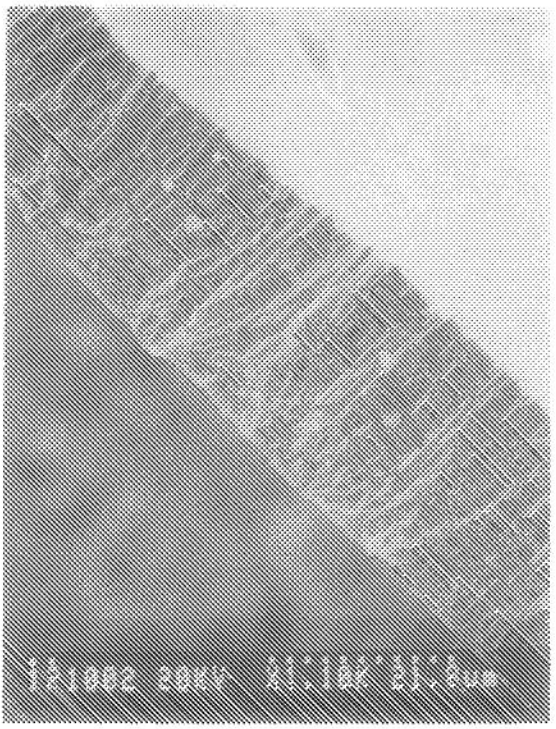

(a)

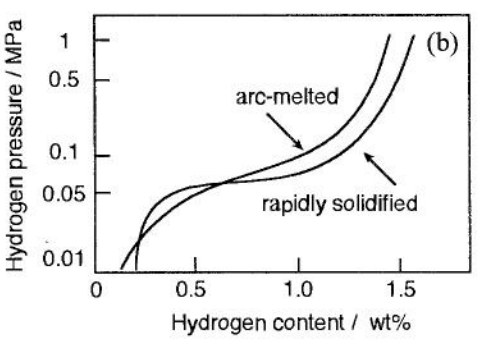

Fig. 18. (a) SEM image of a cross-section of rapidly solidified alloys of the $LaNi_4Co_{0.6}Al_{0.4}$ composition (Mishima et al. 1993). (b) Pressure–composition curves at 60°C of rapidly solidified and arc-melted alloys of the $LaNi_4Co_{0.6}Al_{0.4}$ composition (Mishima et al. 1993).

3.11. *Surface analysis*

Meli and coworkers (Meli and Schlapbach 1991, Meli et al. 1992–1995) have carried out a detailed and systematic surface analysis of the AB_5 electrode alloys before and after cycling, using X-ray photoelectron spectroscopy (XPS). When the $LaNi_5$ powder

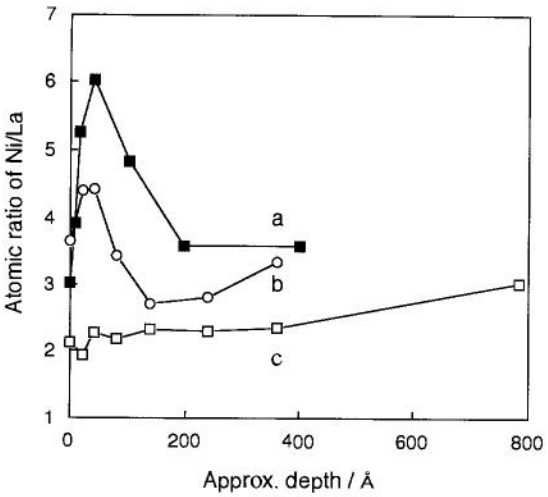

Fig. 19. XPS depth profile of (a) $LaNi_{4.5}Si_{0.5}$, (b) $LaNi_{4.7}Al_{0.3}$ and (c) $LaNi_5$ powder electrodes after 30 cycles in 6 M KOH. Atomic ratio of Ni/La is shown as a function of approximate sputter depth (2 keV Ar^+ about 4 Å min^{-1}) (Meli et al. 1993).

was exposed to air, the surface was contaminated to levels of 56 at.% oxygen and 15 at.% carbon. Nickel and lanthanum were oxidized to depths of 30 Å and 100 Å, respectively. Strong oxygen-induced lanthanum segregation was observed, giving a Ni/La ratio of 1.3 in agreement with earlier studies and an activation model by Schlapbach et al. (1979, 1980). When the $LaNi_5$ electrode was kept in 6 M KOH solution for 52 days, the nickel was found to exist as a hydroxide for the first 20 Å, as an oxide down to 200 Å and as a metal below that. The lanthanum was present as a hydroxide for the first 20 Å, as an oxide down to 1200 Å and as a metal below that. After 30 electrochemical cycles the nickel was found to become metallic below only 20 Å while the lanthanum remained oxidized to a depth of more 1000 Å. When the nickel was partly replaced by Al and Si, the oxygen penetration depth (about 500 Å and 400 Å, respectively) after 30 electrochemical cycles was clearly smaller than in undoped $LaNi_5$. This explains the lower capacity decay rate of $LaNi_{4.7}Al_{0.3}$ and $LaNi_{4.5}Si_{0.5}$, than that of $LaNi_5$. The partial replacement of Ni by Al and Si also caused higher enrichment of nickel in metallic state after 30 cycles on the surface layer in the depth of 20–50 Å and 10–100 Å, respectively, as shown in fig. 19. The added aluminum and silicon were not found down to 50 Å and 10 Å, respectively, showing that they dissolved into the KOH solution and did not take part in the formation of a "denser" surface oxide layer. It was suggested that the metallic nickel layer enriched on the surface would give a protective character on the alloy surface.

Meli et al. (1994) observed a lower rate capability and a slower activation when the nickel was partially replaced by a large amount of copper ($MmNi_{2.4}Cu_{2.0}Mn_{0.25}Si_{0.35}$). After 30 cycles the surface was covered with a thick nickel oxide layer (40 Å), and showed no enrichment of metallic nickel. Unlike nickel, the copper was completely metallic even at the top surface and enriched only slightly in the depth range of 4–200 Å. Metallic copper is expected to provide good electric conductivity, but the oxidized state of nickel would cause the decrease in catalytic activity, explaining the lower rate capability. The

composition of the rare earths (La, Ce and Nd) remained constant before and after cycling, suggesting a less important role for them on the surface.

The nickel enrichment on the surface was also reported for $Mm(NiCoMn)_5$-based alloys after alkaline etching treatments (Ogawa et al. 1989) and after electrochemical cycling (Kanda 1991). The manganese and cobalt were dissolved from the surface of the alloys.

For the Laves phase type $ZrV_{0.4}Ni_{1.6}$ electrode, Züttel et al. (1994a–d) found that after 30 cycles the surface vanadium, which had existed as an oxide, had completely disappeared; the nickel (metallic) was enriched, and the zirconium remained as a ZrO_2. These results suggest that dissolution of some elements in the KOH solution helps create the nickel-enriched surface layer. The metallic nickel layer is expected to work as good electric conductor, catalyst and protective layer in these Laves phase electrodes as previously described for the AB_5 electrodes.

Another effect of element dissolution was found by Kamasaki et al. (1993). The dissolution of Al and Co was accompanied by formation of $La(OH)_3$ whiskers on the alloy surface. An "anchor model" was proposed to the effect that the whiskers would work as anchors to prevent the peeling of the surface oxide layer from the bulk during electrochemical cycling, thus improving the cycle life. The formation of $La(OH)_3$ whiskers was also observed for the Si-containing alloys after alkaline treatment at 80°C (Meli et al. 1992). It is an interesting fact that the lower chemical stability improves the protective ability of the surface layer.

3.12. *Surface insulation*

In alkaline solutions, the oxidation potential of La, $E^0(La/La(OH)_3) = -2.90$ V, is less noble than that of hydrogen, $E^0(H_2/H_2O) = -0.828$ V, while the oxidation potential of Ni, $E^0(Ni/Ni(OH)_2) = -0.720$ V, is more noble than that of hydrogen, keeping the Ni in a metallic state in the pressure of hydrogen. If the electrode is deeply discharged below the oxidation potential of $Ni/Ni(OH)_2$, the surface nickel would be oxidized and passivated, causing the insulation of electrode and shorter cycle life. Kuriyama et al. (1992b) found that resistance due to surface activity of the alloy was greatly increased by a 100% discharge. Meli et al. (1992) observed that when the $LaNi_{4.5}Si_{0.5}$ electrode was kept at the oxidizing potential (0 V vs. Hg–HgO) in 6 M KOH at 22°C, a nickel oxide enriched surface was formed to a depth of 15 Å. The nickel oxide can be reduced during the charging process if the surface is not completely insulated by the coverage of nickel hydroxide.

High chemical stability of alloys tends to cause passivation (insulation) of the alloy surface. When fine powder (< 100 mesh) of $MmNi_{3.5}Co_{0.7}Al_{0.8}$ was stored in air for 1 month and mixed with 10 wt.% conducting powder such as Co, Cu, Ni, a low activation rate was observed (Sugahara et al. 1991, Sakai et al. 1994a). The number of required activation cycles decreased in the order of Ni powder-mixed, Cu powder-mixed, Co powder-mixed and Cu-coated alloys. Impedance analysis revealed that the electrode of Cu-coated alloy had much lower contact resistance between particles than that of Cu-mixed alloy (Kuriyama et al. 1992b).

When MH-electrode-limited Ni–MH batteries were held in completely discharged states at 40°C, a serious decrease in discharge capacity was observed for those electrodes mixed with conductive powders such as Ni, Cu or carbon, requiring reactivation cycling (Sakai et al. 1992b, 1993a, 1994a). The open circuit potential gradually decreased and approached 0 V (vs. NiOOH–$Ni(OH)_2$), suggesting the oxidation of surface nickel. The Cu-coated or Co-mixed MH electrodes did not show such a serious capacity decay. The cobalt could be dissolved before nickel oxidation and then precipitated easily during charging process, giving good conductive networks on the surface layer because the cobalt oxidation potential, $E^0(Co/Co(OH)_2) = -0.73$ V, was more negative than the nickel oxidation potential. When the alloy contained manganese, such a capacity decay after complete discharge was not observed, probably because of active dissolution of the manganese from the alloys. The continuous dissolution of some elements (Mn, V, etc.) from the alloys could keep the surface nickel in the metallic state, preventing insulation of the alloy surface.

3.13. *Microstructure on grain boundaries*

Buschow and Van Mal (1972) showed that a homogeneous $LaNi_5$ phase is obtained in the nickel-content range of 4.8–5.4. When a melt with higher nickel content is cooled, the $LaNi_5$ phase starts to solidify in contact with the nickel-enriched liquid of the eutectic composition. Finally, the alloy has nickel precipitates on the grain boundaries. Bronoel et al. (1976) found that $LaNi_5$ prepared in an alumina crucible had lower capacity than the alloy prepared in a cold crucible. They ascribed it to a stoichiometric deviation to the nickel-rich side.

Sakai et al. (1990e, 1992a) observed that the capacity decay rate of $MmNi_{3.5}Co_{0.7}Al_{0.8}$ depends on the quality of mischmetal; they ascribed this to the fact that the oxide impurity in mischmetal caused a stoichiometric deviation to the nickel-rich side, and a decrease in cycle life. The influence of stoichiometric deviation is shown in fig. 20. The deviation to the nickel-rich side caused preferential precipitation of aluminum–nickel compound ($AlNi_3$) on the grain boundaries, resulting in much lower cycle life, because the precipitate was highly reactive with the KOH solution. The low chemical stability was improved by heat-treatment at 1000°C although the capacity was decreased. The deviation to Mm-rich side caused a preferential precipitation of lanthanum and a slight decrease in cycle life. Almost the same results were observed for $MmNi_{3.5}Co_{0.8}Al_{0.3}Mn_{0.4}$ although the manganese addition resulted in somewhat different behaviors (Sakai et al. 1993b). The nickel-rich alloy had aluminum and manganese-enriched grain boundaries, while the mischmetal-rich alloy had lanthanum and manganese-enriched grain boundaries. The manganese tended to segregate on both sides of stoichiometry although the Mn, precipitated on the Mm-rich side, could diffuse into the bulk after heat-treatment at 1000°C.

When the La in $LaNi_{5-x}Al_x$ alloys was replaced by zirconium, the cycle life was greatly improved (Sakai et al. 1989b, 1990a, 1992a). This effect was later ascribed to the formation of a second phase $ZrNi_5$ network. Since the $ZrNi_5$ has a peritectic temperature

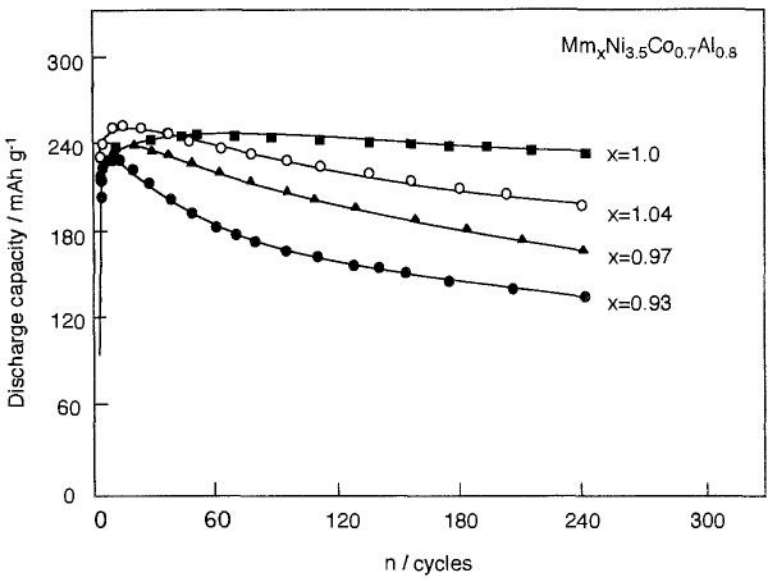

Fig. 20. Influence of the stoichiometric deviation of $Mm_xNi_{3.5}Co_{0.7}Al_{0.8}$ on capacity decay curves at 20°C (charge 186 mA g^{-1} for 2 h; discharge 93 mA g^{-1} to −0.6 V vs Hg/HgO) (Sakai et al. 1992a).

at 1300°C, the cooling down of the melt would start with the precipitation of $LaNi_5$ phase at 1325°C, followed by the precipitation of $ZrNi_5$. Ogura et al. (1991) reported that the Vickers hardness of $ZrNi_5$ (200) was much lower than that of $LaNi_5$ (800), clarifying that the second phase $ZrNi_5$ had much more tenacious properties than the bulk $LaNi_{5-x}Al_x$. It was expected that the network of the second phase would prevent the pulverization and oxidation of the bulk alloys. The same effect was observed for $Mm_{0.85}Zr_{0.15}Ni_{4.0}Al_{0.8}V_{0.2}$ in which almost complete segregation of Zr and V on the grain boundaries occurred, improving the cycle life (Sakai et al. 1991f).

The low rate capability of the alloy $La_{0.8}Nd_{0.2}Ni_{2.5}Co_{2.4}Si_{0.1}$ was improved by Notten and Hokkeling (1991); they changed the stoichiometry to the nickel-rich side, forming second phases such as electrocatalytic elements (Ni–Co) or a compound ($MoCo_3$) on the grain boundaries. The grain boundaries become good paths for hydrogen penetration, commencing the cracking of the alloys. The precipitates on the grain boundaries were expected to effectively take part in electrochemical reactions (fig. 21). The nickel-rich alloy ($AB_{5.5}(La_{0.8}Nd_{0.2}Ni_{3.0}Co_{2.4}Si_{0.1})$) showed a second phase of $NiCo_3$ solid solution. By solidifying the melt at higher rate the second phases were distributed homogeneously, decorating the surface of the grains. When Mo was introduced into the alloy with the composition of $La_{0.8}Nd_{0.2}Ni_{2.9}Mo_{0.1}Co_{2.4}Si_{0.1}$, a desired second phase of $MoCo_3$ with the $SnNi_3$-type structure was formed even though the enthalpy of formation for $MoNi_3$ was more negative than that of $MoCo_3$. This result was attributed to the higher thermodynamic stability of $LaNi_5$ than that of $LaCo_5$. The two phase alloy showed much higher rate capability than the single phase original alloy, increasing the exchange current density

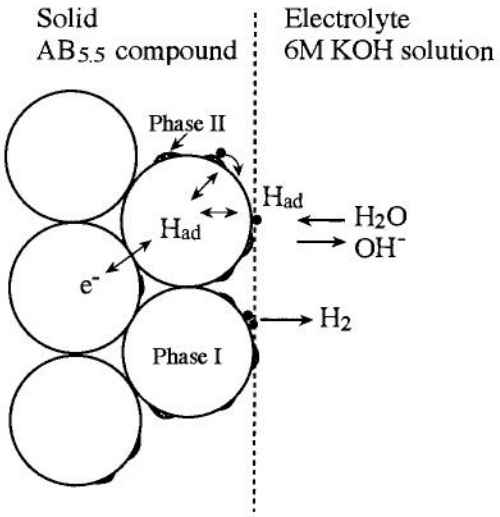

Fig. 21. Schematic representation of charge transfer reaction at the negative electrode consisting of two-phase alloy (Notten and Hokkeling 1991).

from 190 mA/g to 588 mA/g (fig. 12). The effect was ascribed to the higher catalytic activity of the $MoCo_3$ precipitate than the AB_5 matrix. However, the corrosion stability of the alloy was decreased by the second phase formation. When the $AB_{5.5}$ alloys were prepared by the melt-spinning method, an anisotropically deformed lattice (decrease in *a*-axis and increase in *c*-axis) was caused because the excess B elements were incorporated into the $CaCu_5$ structure (Notten et al. 1992). The alloys showed longer cycle life, but a poor rate capability. The annealing treatment at 900°C relaxed the deformed crystal lattice by segregating the excess B elements on the grain boundaries. These two phase alloys showed just opposite behavior: a higher rate capability, but a poor cycle life. Coene et al. (1992) reported that when the nickel-rich alloy $La(NiCu)_{5+x}$ became a single phase by suitable heat-treatment, the stoichiometric deviation (x) caused an increase in the *c*-axis and a decrease in the *a*-axis. Transmission electron microscopy studies showed that the La sites were partly replaced by dumbbell pairs of B atoms (Ni/Cu) oriented along the *c*-axis. Notten et al. (1994a–c) reported that the non-stoichiometric alloy showed longer cycle life and higher catalytic activity, although the capacity was considerably decreased.

Second phase formation by adding high melting point elements such as Zr, W, Ta, Mo, B into the $Mm(NiCoMnAl)_5$ based alloys was also reported to be effective in improving the rate capability in the order of above additives (Tadokoro et al. 1992, 1993, Kimoto et al. 1993 and Nogami et al. 1993a,b). These second phases facilitated the cracking of the alloys, increasing surface area from 260 to 440 cm^2/g. The cycle life was the longest for the boron addition. The second phase by boron addition was identified as a $MmCo_4B$ phase. With increasing boron content the capacity decreased, while rate capability increased, leading to the suitable composition $Mm(NiCoAlMn)_5B_{0.03}$. The specific surface area of the alloy increased rapidly after the first activation cycle. The sealed cell showed better rate capability and long cycle life (more than 500 cycles).

The beneficial effect of multiphase alloys was first proposed for TiNi–Ti_2Ni alloys by Justi et al. (1970). They cooled down the melt in the range of 33.3–50 at.% Ni, finding that the primarily precipitated TiNi grains were surrounded by peritectically formed Ti_2Ni. The TiNi is too hard and tough to pulverize, while the Ti_2Ni second phase is brittle, making it possible to mill the alloy. The second phase has a higher rate capability, but it degraded at a higher rate than the TiNi. The cycle life of TiZrNiCrV-based alloys was also improved by the multi-phase formation (Fetcenko et al. 1988, Hirota et al. 1992, Miyamura et al. 1992, 1994).

3.14. *Self-discharge*

Three reasons for MH battery self-discharge have been proposed. Two mechanisms are the same as for Ni–Cd batteries. The first is self-discharge of NiOOH. NiOOH reacts with water to produce oxygen, which diffuses to the MH electrode, oxidizing the hydride. The second is a shuttle effect of impurity ions from the separator (Ikoma et al. 1987, Fukunaga et al. 1993). Conventional polyamide (nylon) separator tends to produce an ammonium ion (NH_4^+) by hydrolysis in concentrated alkaline solution at higher temperature. The ammonium ion is oxidized to the nitrite ion (NO_2^-) on the NiOOH electrode, while the nitrite ion is reduced to the ammonium ion on the MH electrode as follows:

$$\text{(Positive)} \quad 6NiOOH + NH_4OH + OH^- \rightarrow 6Ni(OH)_2 + NO_2^-, \tag{21}$$

$$\text{(Negative)} \quad 6MH + NO_2^- \rightarrow 6M + NH_4OH + OH^-. \tag{22}$$

The shuttle reaction between ions of NO_2^- and NH_4^+ facilitates the self-discharge of both the electrodes. The reactivity of nitrite ions with MH is much higher than that with cadmium, causing a higher self-discharge rate of the Ni–MH sealed cell than that of the Ni–Cd cell. The impurity nitrate ion (NO_3^-) had the same influence because it was reduced to the nitrite ion on the MH electrode as follows:

$$2MH + NO_3^- \rightarrow 2M + NO_2^- + H_2O. \tag{23}$$

When the polyamide separator was replaced by a sulfonated-polypropylene separator, the charge retention of Ni–MH batteries with $MmNi_{3.5}Mn_{0.4}Al_{0.3}Co_{0.75}$ negative electrode was significantly improved as shown in fig. 22 (Ikoma et al. 1987). The battery temperature in a sealed cell tends to increase rapidly with increased charging and discharging rates because of starved electrolyte solution (Sakai et al. 1992b). High-temperature stability of the separator is more important for obtaining higher energy density and a higher charging rate.

Impurity metal ions such as V^{5+} (1400 ppm) and Cr^{6+} (400 ppm) had little influence on the self-discharge, while the existence of NO_2^-, NO_3^- and NH_4^+ ions significantly reduced the charge retention (Fukunaga et al. 1993). The charge retention of a sealed cell at 20°C for 30 days decreased from 80% at 10 ppm impurity of NO_2^- or NH_4^+ to about 60% at 1000 ppm impurity.

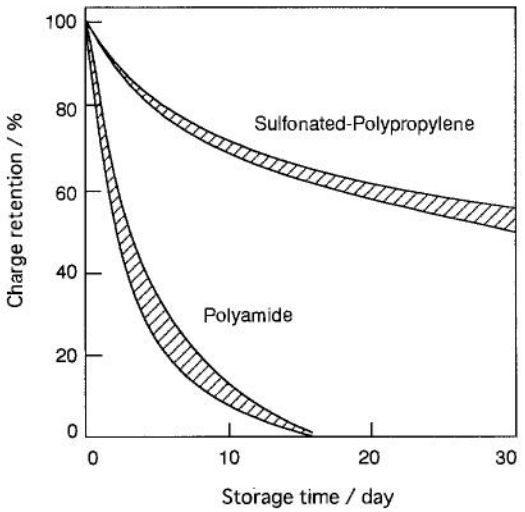

Fig. 22. Comparison of self-discharge rate at 45°C of Ni–MH cells using polyamide (PA) and sulfonated-polypropylene (S-PP) separators (Ikoma et al. 1987).

The third mechanism is the release of hydrogen from alloys by hydride decomposition. Iwakura et al. (1989a) observed that when MH electrodes, using $La(NiM)_5$ (M = Cu, Mn, Al, Cr), were stored in the fully-charged state, discharge capacity was decreased by both reasons of degradation of alloys (irreversible factor) and spontaneous release (reversible factor) of hydrogen from the hydride. Surface coating with copper was useful to prevent the degradation of alloys. Higher hydrogen equilibrium pressure than the cell pressure also facilitated the release of hydrogen (Anani et al. 1992). It was reported that the addition of small amounts of elements such as Si, Al, Cr, Ti, Zr, influenced the charge retention, suggesting the important role of the surface layer as a diffusion barrier against hydrogen release (Sakai et al. 1990a,b). The removal of lattice strain, i,e., flatness of pressure plateau, also improved the charge retention at 40°C for $Mm(NiCoMnAl)_5$ alloys (Sakai et al. 1994a). Thin films of $LaNi_5$ and $LaNi_{2.5}Co_{2.5}$ alloys, which absorb hydrogen in solid solution with strongly sloped P–C–T curves, showed a high self-discharge rate, suggesting that the formation of stable hydride is quite important (Sakai et al. 1991d).

4. Concluding remarks

We have so far described the research and development for nickel–metal hydride batteries in which a hydrogen storage alloy (metal hydride) is used as a negative electrode material. This type of battery has been attracting a great deal of attention as a new non-military battery because it is characterized by several advantages over the conventional secondary batteries:

(1) high energy density,
(2) high rate capability,
(3) durability against overcharge and overdischarge,

Table 6
Effects of various alloying elements on the behavior of metal hydride electrodes consisting of $La_{1-x}R_xNi_{5-y}M_y$ alloys (+, increase; 0, little effect; –, decrease)

Alloying element	Capacity	Plateau pressure	Cycle life	Rate capability	Initial activation	Decrepitation property	Precipitate formation
Substitutes for lanthanide metal							
Ce, Pr, Nd	–	++	+	0	0	0	0
Zr	––	+	+	–	++	–	++
Substitutes for transition metal							
B	––	0		+	++	+	++
Al	–	––	+	–	–	–	+
Si	––	–	+	–	–	–	+
Ti	––	–	+	–	+		++
V	––	–		+		++	
Cr	––	––	+	–		–	+
Mn	+	––	––	++	+	++	+
Fe	–	–	+	–			0
Co	–	–	++	––	––	––	0
Cu	–	–	0	–	0	+	0
Zn	–	–	0	–	0		0
Mo	––	0		+	++		++

(4) compatibility with a nickel–cadmium battery,
(5) cleanliness and freedom from toxic heavy metals,
(6) no consumption of the electrolyte solution during charge–discharge cycling.

Since the charge–discharge characteristics of the negative electrode can be widely altered depending on the kind and composition of alloys used, extensive R&D work has been conducted from this point of view. Effects of various alloying elements on the behavior of metal hydride electrodes are summarized in table 6. The bulk composition of alloys is usually modified by the partial substitution of some foreign elements for A- or B-sites in AB_5-type alloys or by adding a small amount of a third element. Bulk modification sometimes accompanies surface modification, especially when any other phases or segregations (precipitates) are formed on the alloy surface or at the grain boundaries, influencing the charge and discharge reactions. Thus, not only the properties of the alloy bulk but also those of the alloy surface greatly affect the charge–discharge characteristics of the negative electrodes. So, very often, surface modification techniques of the alloys are positively employed: e.g., (i) coating of alloy particles with nickel or copper by electroless plating, electro-deposition, or dry process; (ii) mixing of alloy particles with metal or metal oxide powder having electric conductivity, and (iii) chemical treatment of alloy particles by alkaline etching, alkaline-reducing agent treatment, or

anodic oxidation. These modifications may lead to the formation of the conductive, protective (passive) or catalytic layers on the alloy surfaces.

Although, in this text, we almost exclusively discussed AB_5-type alloys of the rare-earth system, the AB_2-type alloys of the Laves-phase system are another important series of compounds among the hydrogen storage alloys which are being put to practical use. Generally speaking, comparing these two types of alloys, the former shows superior high rate capability and initial activation, but the latter has a higher theoretical capacity per unit weight. In any alloy system, the biggest obstacle to this type of battery becoming more practical is the high cost of the alloys; however, a supply system for mischmetal which is low-cost and has fewer resource problems has been nearly established.

In conclusion, one could state that the development of a new hydrogen storage alloy of high performance and low cost is a key to further development of metal hydride batteries. It is needless to say that more scientific research such as thermodynamics, metallography and electrode kinetics, is important for this purpose.

5. Acknowledgments

The authors are greatly indebted to Dr. D. Noréus of Stockholm University, Dr. G. Sandrock of Suda Tech. Inc., and Prof. L. Schlapbach of the University of Fribourg, for their fruitful discussions and valuable comments.

References

Agarwal, P., M.E. Orazem and A. Hiser, 1992, in: Proc. Symp. on Hydrogen Storage Materials, Batteries and Electrochemistry, Vol. 92-5, eds D.A. Corrigan and S. Srinivasan (Electrochemical Society, Pennington) pp. 120–137.

Anani, A., A. Visintin, S. Srinivasan, A.J. Appleby, J.J. Reilly and J.R. Johnson, 1992, in: Proc. Symp. on Hydrogen Storage Materials, Batteries and Electrochemistry, Vol. 92-5, eds D.A. Corrigan and S. Srinivasan (Electrochemical Society, Pennington) pp. 105–119.

Balej, J., 1985, Int. J. Hydrogen Energy **10**, 365–374.

Barton, J.C., J.A.S. Green and F.A. Lewis, 1963, Nature **197**, 1293–1294.

Bennett, P.D., and T. Sakai, eds., 1994, Hydrogen and Metal Hydride Batteries, Proc. Vol. 94-27 (Electrochemical Society, Pennington).

Bittner, H.F., and C.C. Badcock, 1983, J. Electrochem. Soc. **130**, 193C–198C.

Boonstra, A.H., and T.N.M. Bernards, 1990a, J. Less-Common Met. **161**, 245–255.

Boonstra, A.H., and T.N.M. Bernards, 1990b, J. Less-Common Met. **161**, 355–368.

Boonstra, A.H., G.J.M. Lippits and T.N.M. Bernards, 1989, J. Less-Common Met. **155**, 119–131.

Boonstra, A.H., T.N.M. Bernards and G.J.M. Lippits, 1990, J. Less-Common Met. **159**, 327–336.

Bronoel, G., J. Sarradin, M. Bonnemay, A. Percheron-Guegan, J.C. Achard and L. Schlapbach, 1976, Int. J. Hydrogen Energy **1**, 251–254.

Bronoel, G., J. Sarradin, A. Percheron-Guegan and J.C. Achard, 1978, Mater. Res. Bull. **13**, 1265.

Buschow, K.H.J., 1984, in: Handbook on the Physics and Chemistry of Rare Earths, Vol. 6, eds K.A. Gschneidner Jr and L. Eyring (North-Holland, Amsterdam) pp. 1–111.

Buschow, K.H.J., and H.H. Van Mal, 1972, J. Less-Common Met. **29**, 203–210.

Ciureanu, M., D.H. Ryan, J.O. Ström-Olsen and M.L. Trudeau, 1993, J. Electrochem. Soc. **140**, 579–584.

Coates, D., and R.D. Wright, 1992, in: Proc. Symp. on Hydrogen Storage Materials, Batteries and

Electrochemistry, Vol. 92-5, eds D.A. Corrigan and S. Srinivasan (Electrochemical Society, Pennington) pp. 199–209.

Coene, W., P.H.L. Notten, F. Hakkens, R.E.F. Einerhand and J.L.C. Daams, 1992, Philos. Mag. A **65**, 1485–1502.

Ewe, H.H., E.W. Justi and K. Stephan, 1973, Energy Convers. **13**, 109–113.

Fetcenko, M.A., S. Venkatesan, K.C. Hong and B. Reichman, 1988, Power Sources **12**, 411.

Fetcenko, M.A., S.R. Ovshinsky, S. Venkatesan, K. Kajita, H. Kidou and K. Jeffries, 1990a, in: Proc. 3rd Int. Rechargeable Battery Seminar, Florida, USA, March 5–7.

Fetcenko, M.A., S. Venkatesan and S.R. Ovshinsky, 1990b, in: 34th Int. Power Sources Symp., New Jersey, USA.

Fetcenko, M.A., S. Venkatesan and S.R. Ovshinsky, 1992, in: Proc. Symp. on Hydrogen Storage Materials, Batteries and Electrochemistry, Vol. 92-5, eds D.A. Corrigan and S. Srinivasan (Electrochemical Society, Pennington) pp. 141–167.

Folonari, C., G. Iemmi, F. Manfredi and A. Rolle, 1980, J. Less-Common Met. **74**, 371–378.

Fukunaga, H., R. Nagai and K. Kajita, 1993, Extended abstracts presented at the 34th Battery Symp. in Jpn., p.241.

Furukawa, N., 1993, Molten Salts **36**, 225–241.

Gerard, N., and S. Ono, 1992, in : Hydrogen in Intermetallic Compounds II, ed. L. Schlapbach (Springer, Berlin) pp. 165–195.

Gutjahr, M.A., H. Buchner, K.D. Beccu and H. Säufferer, 1973, in: Power Sources, Vol. 4, ed. D.H. Collins (Oriel Press, Newcastle Upon Tyne) pp. 79–91.

Hara, T., N. Yasuda, Y. Takeuchi, T. Sakai, A. Uchiyama, H. Miyamura, N. Kuriyama and H. Ishikawa, 1993, J. Electrochem. Soc. **140**, 2450–2454.

Hasegawa, K., H. Mori and M. Oshitani, 1991, Yuasa-Jiho, No. 71, pp. 13–19.

Hasegawa, K., M. Ohnishi, M. Oshitani, T. Takeshima, Y. Matsumaru and K. Tamura, 1994, Z. Phys. Chem. NF **183**, 325–331.

Hazama, T., T. Sakai, H. Miyamura, N. Kuriyama, A. Kato and H. Ishikawa, 1990, Presented at 57th Meeting of Electrochemical Society, Japan, p. 245.

Hine, F., 1987a, Soda to Enso, No. 9, pp. 351–364.

Hine, F., 1987b, Soda to Enso, No. 10, pp. 397–410.

Hirota, M., S. Wada, R. Nagai, K. Kajita and M.A. Fetcenko, 1992, in: Proc. Symp. on Hydrogen Storage Materials, Batteries and Electrochemistry, Vol. 92-5, eds D.A. Corrigan and S. Srinivasan (Electrochemical Society, Pennington) pp. 210–219.

Ikeya, T., K. Kumai and T. Iwahori, 1993, J. Electrochem. Soc. **140**, 3082–3337.

Ikoma, M., Y. Umeo, H. Kawano, N. Yanagihara, Y. Ito and I. Matsumoto, 1986, Extended Abstract presented at 27th meeting of Battery Symp., Japan, p. 89.

Ikoma, M., Y. Ito, H. Kawano, S. Ikeyama, K. Iwasaki and I. Matsumoto, 1987, Extended abstract presented at 28th Battery Symp., Japan, p. 113.

Ikoma, M., Y. Ito, I. Matsumoto and H. Ogawa, 1988, Extended Abstract presented at the meeting of Electrochemical Society, No. 85, p. 174, Chicago.

Ishikawa, H., and T. Sakai, 1989, Tetu-to-Hagane, No. 11, 47–53.

Ishikawa, H., K. Oguro, A. Kato, H. Suzuki and E. Ishii, 1985, J. Less-Common Met. **107**, 105–110.

Ishikawa, H., K. Oguro, A. Kato, H. Suzuki and E. Ishii, 1986, J. Less-Common Met. **120** 123–133.

Ishikawa, H., K. Oguro, A. Kato, H. Suzuki, E. Ishii, T. Okada and S. Sakamoto, 1989, Z. Phys. Chem. NF **164**, 1409–1414.

Iwaki, T., 1985, Kogyo Zairyo **33**(11), 40–47.

Iwaki, T., 1987, Kino Zairyo, No. 7, 31–41.

Iwakura, C., 1985, in: Technologies and Economics of Fuel Cells, ed. S. Yoshizawa (CMC, Tokyo) pp. 178–208.

Iwakura, C., 1989, Bull. Inst. Future Tech. **3**(10), 35–56.

Iwakura, C., and M. Matsuoka, 1990, Kidorui (Rare Earths), No. 17, 11–36.

Iwakura, C., and M. Matsuoka, 1991, Prog. Batteries & Battery Materials **10**, 81–114.

Iwakura, C., and M. Matsuoka, 1992, Rep. Asahi Glass Foundation **60**, 197–206.

Iwakura, C., and T. Sakai, 1986, J. Hydrogen Energy Systems Soc., Jpn. **11**(2), 13–29.

Iwakura, C., T. Asaoka, T. Sakai, H. Ishikawa and K. Oguro, 1985, Denki Kagaku **53**, 722–725.

Iwakura, C., T. Asaoka, H. Yoneyama, T. Sakai, H. Ishikawa and K. Oguro, 1988, Nippon Kagaku Kaishi **1988**, 1482–1488.

Iwakura, C., Y. Kajiya, H. Yoneyama, T. Sakai, K. Oguro and H. Ishikawa, 1989a, J. Electrochem. Soc. **136**, 1351–1355.

Iwakura, C., T. Sakai and H. Ishikawa, 1989b, Kagaku Kogyo (Chemical Industry) **40**, 248–254.

Iwakura, C., M. Matsuoka, T. Sakai and H. Ishikawa, 1991, Kagaku To Kougyou **65**, 305–314; 346–350.

Iwakura, C., M. Matsuoka, K. Asai and T. Kohno, 1992a, J. Power Sources **38**, 335–343.

Iwakura, C., T. Sakai and H. Ishikawa, 1992b, Denki Kagaku **60**, 680–683.

Iwakura, C., Y. Fukumoto, M. Matsuoka, T. Kohno and K. Shinmou, 1993, J. Alloys & Compounds **192**, 152–154.

Iwakura, C., M. Matsuoka and T. Kohno, 1994, J. Electrochem Soc. **140**, 2306–2309.

Jaksic, M.M., 1984, Electrochim. Acta **29**, 1539–1550.

Jaksic, M.M., 1986a, J. Mol. Cat. **38**, 161–202.

Jaksic, M.M., 1986b, Int. J. Hydrogen Energy **11**, 519–532.

Jordy, C., A. Percheron-Guegan, J. Bouet, P. Sanchez, C. Chanson and J. Leonardi, 1991, J. Less-Common Met. **172/174**, 1236–1245.

Justi, E.W., H.H. Ewe, A.W. Kalberlah, N.M. Saridakis and M.H. Schaefer, 1970, Energy Conver. **10**, 183–187.

Kajita, K., and Y. Uetani, 1993, Battery Technology **5**, 84–90.

Kamasaki, K., and K. Okajima, 1992, Hyomen Gijyutsu **43**, 1077.

Kamasaki, S., H. Soh and Y. Misaki, 1993, Denki Kagaku **61**, 1455–1457.

Kaminaka, H., Y. Shida, Y. Hatakeyama, M. Hara, K. Koushiro, Y. Takeshita and N. Negi, 1992, Extended Abstract presented at 33rd Battery Symp., Japan, p. 157.

Kanda, M., 1991, in: Proc. 14th New Battery Design sectional meeting, pp. 11–22.

Kanda, M., M. Yamamoto, K. Kanno, Y. Satoh, H. Hayashida and M. Suzuki, 1991, J. Less-Common Met. **172/174**, 1227–1235.

Kanda, T., 1988, Denki Kagaku **56**, 13.

Kim, S.-R., and J.-Y. Lee, 1994, J. Alloys & Compounds **210**, 109–113.

Kimoto, M., M. Nogami, M. Tadokoro, K. Nishio, T. Saito and N. Furukawa, 1993, Proc. 183rd ECS Meeting, Hawai.

Kitamura, T., C. Iwakura and H. Tamura, 1981a, Chem. Lett. **1981**, 965.

Kitamura, T., C. Iwakura and H. Tamura, 1981b, Chem. Lett. **1981**, 1755.

Kitamura, T., C. Iwakura and H. Tamura, 1982a, Electrochim. Acta **27**, 1723–1727.

Kitamura, T., C. Iwakura and H. Tamura, 1982b, Electrochim. Acta **27**, 1729–1731.

Knoll, C.R., S.M. Tuominen, J.R. Peterson and T.R. McQueavy, 1990, in: Proc. Battery Waste Management Seminar, Deerfield Beach, FL.

Kuriyama, N., T. Sakai, H. Miyamura, A. Kato and H. Ishikawa, 1990a, Denki Kagaku **58**, 89–90.

Kuriyama, N., T. Sakai, H. Miyamura, A. Kato and H. Ishikawa, 1990b, J. Electrochem. Soc. **137**, 355–356.

Kuriyama, N., T. Sakai, H. Miyamura, A. Kato and H. Ishikawa, 1990c, Prog. Batteries & Solar Cells **9**, 265–268.

Kuriyama, N., T. Sakai, H. Miyamura, A. Kato and H. Ishikawa, 1990d, Solid State Ionics **40/41**, 906–909.

Kuriyama, N., T. Sakai, H. Miyamura, A. Kato and H. Ishikawa, 1992a, Solid State Ionics **53/56**, 688–693.

Kuriyama, N., T. Sakai, H. Miyamura, I. Uehara and H. Ishikawa, 1992b, J. Electrochem. Soc. **139**, L72-L73.

Kuriyama, N., H. Miyamura, T. Sakai, I. Uehara, H. Ishikawa and T. Iwasaki, 1992c, Extended Abstract presented at 33rd Battery Symp., Japan, p. 177.

Kuriyama, N., T. Sakai, H. Miyamura, I. Uehara and H. Ishikawa, 1993a, J. Alloys & Compounds **192**, 161–163.

Kuriyama, N., T. Sakai, H. Miyamura, I. Uehara and H. Ishikawa, 1993b, J. Alloys & Compounds **202**, 183–197.

Kuriyama, N., T. Sakai, H. Miyamura, I. Uehara and H. Ishikawa, 1994, in: Hydrogen Energy Progress X, Proc. 10th World Hydrogen Energy Conf., pp. 1713–1718.

Machida, K., M. Enyo, G. Adachi and J. Shiokawa, 1984, Electrochim. Acta **29**, 807.

Machida, K., M. Enyo, G. Adachi, H. Sakaguchi and J. Shiokawa, 1986, Bull. Chem. Soc. Jpn. **59**, 925.

Markin, T.L., and R.M. Dell, 1981, J. Electroanal. Chem. Interfacial Electrochem. **118**, 217–228.

Markin, T.L., N.J. Bridger, R. Bennett and R.M. Dell, 1978, in: Proc. 28th Power Sources Symp., Atlantic City, NJ, 12–15 June (Electrochemical Society, Pennington) pp. 136–138.

Markin, T.L., R. Bennett, N.J. Bridger and R.M. Dell, 1981, in: Power Sources, Vol. 8, ed. J. Thompson (Academic Press, London) pp. 445–457.

Matsumoto, I., 1989, Kino Zairyo, No. 11, 23–31.

Matsumoto, I., M. Ikoma, A. Ohota, H. Matsuda and Y. Toyoguchi, 1993, in: Proc. Symp. Batteries

and Fuel Cells for Stationary and Electric Vehicle Applications, Vol. 93-8, eds A.R. Landgrebe and Z. Takehara (Electrochemical Society, Pennington) pp. 240–49.

Matsuoka, M., H. Mori, K. Asai and C. Iwakura, 1992, Chem. Express **7**, 189–192.

Matsuoka, M., K. Asai, Y. Fukumoto and C. Iwakura, 1993a, Electrochim. Acta **38**, 659–662.

Matsuoka, M., T. Kohno and C. Iwakura, 1993b, Electrochim. Acta **38**, 787–791.

Matsuoka, M., M. Terashima and C. Iwakura, 1993c, Electrochim. Acta **38**, 1087–1092.

Matsuoka, M., K. Asai, Y. Fukumoto and C. Iwakura, 1993d, J. Alloys & Compounds **192**, 149–151.

Meli, F., and L. Schlapbach, 1991, J. Less-Common Met. **172/174**, 1252–1259.

Meli, F., A. Züttel and L. Schlapbach, 1992, J. Alloys & Compounds **190**, 17–24.

Meli, F., A. Züttel and L. Schlapbach, 1993, J. Alloys & Compounds **202**, 81–88.

Meli, F., A. Züttel and L. Schlapbach, 1994, Z. Phys. Chem. NF **183**, 371–377.

Meli, F., T. Sakai, A. Züttel and L. Schlapbach, 1995, J. Alloys & Compounds, in press.

Mishima, R., M. Miyamura, T. Sakai, N. Kuriyama, H. Ishikawa and I. Uehara, 1993, J. Alloys & Compounds **192**, 176–178.

Miyamura, H., T. Sakai, K. Oguro, A. Kato and H. Ishikawa, 1988, J. Less-Common Met. **146**, 197–203.

Miyamura, H., T. Sakai, K. Oguro, A. Kato and H. Ishikawa, 1989, in: Proc. MRS Int. Meeting on Advanced Materials, Vol. 2 (Materials Research Society) pp. 15–19.

Miyamura, H., N. Kuriyama, T. Sakai, K. Oguro, A. Kato and H. Ishikawa, 1991, J. Less-Common Met. **172/174**, 1205–1210.

Miyamura, H., T. Sakai, N. Kuriyama, K. Oguro, A. Kato and H. Ishikawa, 1992, in: Proc. Symp. on Hydrogen Storage Materials, Batteries and Electrochemistry, Vol. 92-5, eds D.A. Corrigan and S. Srinivasan (Electrochemical Society, Pennington) pp. 179–198.

Miyamura, H., N. Kuriyama, T. Sakai, K. Oguro, I. Uehara and H. Ishikawa, 1993a, J. Alloys & Compounds **192**, 188–190.

Miyamura, H., T. Sakai, N. Kuriyama, K. Oguro, I. Uehara and H. Ishikawa, 1994, Z. Phys. Chem. NF **183**, 347–353.

Mohri, M., Y. Tajima, H. Tanaka, T. Yoneda and M. Kasahara, 1986, Sharp Tech. Rev. **34**, 97–102.

Moriwaki, Y., T. Gamo, A. Shintani and T. Iwaki, 1989, Denki Kagaku **57**, 488–491.

Moriwaki, Y., T. Gamo, H. Seri and T. Iwaki, 1991, J. Less-Common Met. **172/174**, 1211–1218.

Murata, T., and K. Koshiro, 1991, GS Tech. Rep. **50**, 21–29.

Muta, M., A. Takagi, Y. Kajiyama, K. Kinoshita, A. Isogai, T. Sakai, H. Miyamura, N. Kuriyama, H. Ishikawa and I. Uehara, 1992, Abstract presented at 59th meeting of Electrochemical Society, Japan, p.229.

Naito, K., T. Matsunami, K. Okuno, M. Matsuoka and C. Iwakura, 1993, J. Appl. Electrochem. **23**, 1051–1055.

Nogami, M., T. Tadokoro, K. Inoue and N. Furukawa, 1989, Extended Abstract presented at 176th ECS Meeting, Florida, USA, p. 130.

Nogami, M., K. Moriwaki and N. Furukawa, 1990, in: Proc. 3rd Int. Rechargable Battery Seminar, March, Florida, USA.

Nogami, M., T. Tadokoro, M. Kimoto, Y. Chikano, T. Ise and N. Furukawa, 1993a, Denki Kagaku **61**, 1088–1093.

Nogami, M., T. Tadokoro, M. Kimoto, Y. Chikano, T. Ise and N. Furukawa, 1993b, Denki Kagaku **61**, 1094–1102.

Notten, P.H.L., and P. Hokkeling, 1991, J. Electrochem. Soc. **138**, 1877–1885.

Notten, P.H.L., J.L.C. Daams and R.E.F. Einerhand, 1992, Ber. Bunsenges. Phys. Chem. **96**, 656–667.

Notten, P.H.L., R.E.F. Einerhand and J.L.C. Daams, 1994a, Z. Phys. Chem. NF **183**, 267–279.

Notten, P.H.L., R.E.F. Einerhand and J.L.C. Daams, 1994b, J. Alloys & Compounds **210**, 221–232.

Notten, P.H.L., J.L.C. Daams and R.E.F. Einerhand, 1994c, J. Alloys & Compounds **210**, 233–241.

Ogawa, H., M. Ikoma, H. Kawano and I. Matsumoto, 1989, Power Sources **12**, 393–410.

Ogura, T., Y. Nomura, T. Kikuoka, R. Morinari and T. Horiba, 1991, Shin-Kobe Tech. Rep. No. 3, pp. 7–12.

Ohta, A., 1989, Prog. Batteries & Solar Cells **8**, 185–190.

Ohta, A., I. Matsumoto, M. Ikoma and Y. Moriwaki, 1992, Denki Kagaku **60**, 688–692.

Oshitani, M., M. Watada, H. Yufu and Y. Matsumaru, 1989a, Denki Kagaku **57**, 480–483.

Oshitani, M., H. Yufu, K. Takashima, S. Tsuji and Y. Matumura, 1989b, J. Electrochem. Soc. **136**, 1590–1593.

Osumi, Y., 1986, Soda to Enso, pp. 133–164.

Osumi, Y., H. Suzuki, A. Kato, K. Oguro, M. Nakane and Y. Miyake, 1978, Nippon Kagaku Kaishi **1978**, 1472–1477.

Osumi, Y., H. Suzuki, A. Kato, K. Oguro, M. Nakane and Y. Miyake, 1979a, Nippon Kagaku Kaishi **1979**, 45–48.

Osumi, Y., H. Suzuki, A. Kato, M. Nakane and Y. Miyake, 1979b, Nippon Kagaku Kaishi **1979**, 722–726.

Osumi, Y., A. Kato, H. Suzuki, M. Nakane and Y. Miyake, 1979c, J. Less-Common Met. **66**, 67–75.

Osumi, Y., H. Suzuki, A. Kato, K. Oguro and M. Nakane, 1981a, Nippon Kagaku Kaishi **1981**, 1493–1502.

Osumi, Y., H. Suzuki, A. Kato, K. Oguro and M. Nakane, 1981b, J. Less-Common Met. **79**, 207–214.

Osumi, Y., H. Suzuki, A. Kato and M. Nakane, 1982, J. Less-Common Met. **84**, 99–106.

Osumi, Y., H. Suzuki, A. Kato, K. Oguro, S. Kawai and M. Kaneko, 1983, J. Less-Common Met. **89**, 287–292.

Ovshinsky, S.R., M.A. Fetcenko and J. Ross, 1993, Science **260**, 176–181.

Park, C.-N., and R. Kirchheim, 1992, J. Alloys & Compounds **182**, 321–330.

Percheron-Guegan, A., J.C. Achard, J. Sarradin and G. Bronoel, 1978, in: Proc. Int. Symp. on Hydrides Energy Storage, eds A.F. Andresen and A.J. Maeland (Pergamon Press, Oxford) pp. 485–490.

Percheron-Guegan, A., C. Lartigue and J.C. Achard, 1985, J. Less-Common Met. **109**, 287–309.

Pourbaix, M., 1966, Atlas of Electrochemical Equilibria in Aqueous Solutions (Pergamon Press, Oxford).

Ratnakumar, B.V., C. Witham, B. Fultz and G. Halpert, 1994, J. Electrochem. Soc. **141**, L89–L91.

Richter, D., R. Hempelmann and R.C. Bowman Jr, 1992, in: Hydrogen in Intermetallic Compounds II, ed. L. Schlapbach (Springer, Berlin) pp. 97–163.

Ryan, D.H., F. Dumais, B. Patel and J.O. Ström-Olsen, 1991, J. Less-Common Met. **172/174**, 1246–1251.

Sakai, T., 1988, Sunshine J. **9**, 1–8.

Sakai, T., H. Ishikawa, K. Oguro, C. Iwakura and H. Yoneyama, 1987, J. Electrochem. Soc. **134**, 558–562.

Sakai, T., H. Miyamura and H. Ishikawa, 1989a, Prog. Batteries & Solar Cells **8**, 210–213.

Sakai, T., H. Miyamura, K. Oguro, A. Kato, N. Kuriyama and H. Ishikawa, 1989b, Denki Kagaku **57**, 612.

Sakai, T., H. Miyamura, K. Oguro and T. Ishikawa, 1989c, Z. Phys. Chem. NF **164**, 1539–1544.

Sakai, T., H. Miyamura, N. Kuriyama, A. Kato, K. Oguro and H. Ishikawa, 1990a, J. Electrochem. Soc. **137**, 795–799.

Sakai, T., H. Miyamura, N. Kuriyama, A. Kato, K. Oguro, H. Ishikawa and C. Iwakura, 1990b, J. Less-Common Met. **159**, 127–139.

Sakai, T., K. Oguro, H. Miyamura, N. Kuriyama, A. Kato, H. Ishikawa and C. Iwakura, 1990c, J. Less-Common Met. **161**, 193–202.

Sakai, T., A. Takagi, N. Kuriyama and H. Ishikawa, 1990d, Prog. Batteries & Solar Cells **9**, 269–279.

Sakai, T., T. Hazama, N. Kuriyama and H. Ishikawa, 1990e, in: Proc. Int. Symp. on Processing of Rare Metals, Kitakyushu, Jpn., pp. 381–384.

Sakai, T., T. Hazama, H. Miyamura, N. Kuriyama, A. Kato and H. Ishikawa, 1991a, J. Less-Common Met. **172/174**, 1175–1184.

Sakai, T., A. Takagi, K. Kinoshita, N. Kuriyama, H. Miyamura and H. Ishikawa, 1991b, J. Less-Commmon Met. **172/174**, 1185–1193.

Sakai, T., A. Yuasa, H. Ishikawa, H. Miyamura and N. Kuriyama, 1991c, J. Less-Common Met. **172/174**, 1194–1204.

Sakai, T., H. Ishikawa, H. Miyamura, N. Kuriyama, S. Yamada and T. Iwasaki, 1991d, J. Electrochem. Soc. **138**, 908–915.

Sakai, T., A. Takagi, T. Hazama, H. Miyamura, N. Kuriyama, H. Ishikawa and C. Iwakura, 1991e, in: Proc. 3rd Int. Conf. Batteries for Utility Energy Storage, Kobe, Jpn., March, 18–22, pp. 499–517.

Sakai, T., H. Miyamura, N. Kuriyama, A. Kato and H. Ishikawa, 1991f, Bull. Gov. Ind. Res. Inst., Osaka **42**, 69–101.

Sakai, T., H. Miyamura, N. Kuriyama and H. Ishikawa, 1991g, Battery Technology **3**, 88–99.

Sakai, T., H. Yoshinaga, H. Miyamura, N. Kuriyama and H. Ishikawa, 1992a, J. Alloy & Compounds **180**, 37–54.

Sakai, T., K. Muta, H. Miyamura, N. Kuriyama and H. Ishikawa, 1992b, in: Proc. Symp. on Hydrogen Storage Materials, Batteries and Electrochemistry, Vol. 92-5, eds D.A. Corrigan and S. Srinivasan (Electrochem. Soc., Pennington) pp. 59–91.

Sakai, T., H. Miyamura, N. Kuriyama, I. Uehara, M. Muta, A. Takagi, U. Kajiyama, K. Kinoshita and F.

Isogai, 1993a, J. Alloys & Compounds **192**, 158–160.

Sakai, T., H. Miyamura, N. Kuriyama, H. Ishikawa and I. Uehara, 1993b, J. Alloys & Compounds **192**, 155–157.

Sakai, T., H. Yoshinaga, H. Miyamura, N. Kuriyama, H. Ishikawa and I. Uehara, 1993c, J. Alloys & Compounds **192**, 182–184.

Sakai, T., H. Miyamura, N. Kuriyama, H. Ishikawa and I. Uehara, 1994a, Z. Phys. Chem. NF **183**, 333–346.

Sakai, T., T. Iwaki, Z. Ye, D. Noréus and O. Lindström, 1994b, in: Hydrogen and Metal Hydride Batteries, Proc. Vol. 94-27, eds P.D. Bennett and T. Sakai (Electrochemical Society, Pennington) pp. 393–402.

Sakamoto, Y., and N. Ishimaru, 1994, Z. Phys. Chem. NF **183**, 311–317.

Sakamoto, Y., K. Kuruma and Y. Naritomi, 1992, Ber. Bunsenges. Phys. Chem. **96**, 1813–1818.

Sakamoto, Y., N. Ishimaru and M. Hasebe, 1994, Z. Phys. Chem. NF **183**, 319–324.

Sandrock, G.D., 1978, in: Proc. 2nd World Hydrogen Energy Conf. (Pergamon Press, Oxford) pp. 1625–1656.

Sandrock, G.D., 1995, in: Hydrogen Energy System, Utilization of Hydrogen and Future Aspects, NATO ASI Series, ed. Y. Yürüm (Kluwer Academic Publishers, Dordrecht).

Sandrock, G.D., S. Suda and L. Schlapbach, 1992, in: Hydrogen in Intermetallic Compounds II, ed. L. Schlapbach (Springer, Berlin) pp. 197–258.

Sarradin, J., G. Bronoel, A. Percheron-Guegan and J.C. Achard, 1979, in: Power Sources, Vol. 7, ed. J. Thompson (Academic Press, London) pp. 345–351.

Sawa, H., and S. Wakao, 1990, Mater. Trans. **31**, 487–492.

Sawa, H., S. Wakao and J. Furukawa, 1990, Denki Kagaku **58**, 862–867.

Sawa, H., S. Wakao and J. Furukawa, 1991, Denki Kagaku **59**, 945–949.

Schlapbach, L., ed., 1988, Hydrogen in Intermetallic Compounds I; Electronic, Thermodynamic, and Crystallographic Properties, Preparation, Vol. 63 of Topics in Applied Physics (Springer, Berlin).

Schlapbach, L., ed., 1992, Hydrogen in Intermetallic Compounds II; Surface and Dynamic Properteis, Applications, Vol. 67 of Topics in Applied Physics (Springer, Berlin).

Schlapbach, L., A. Seiler, H.C. Siegmann, T.V. Waldkirch, P. Zürcher and C.R. Brundle, 1979, Int. J. Hydrogen Energy **4**, 21–28.

Schlapbach, L., A. Seiler, F. Stucki and H.C. Siegmann, 1980, J. Less-Common Met. **73**, 145.

Sugahara, H., T. Sakai, H. Miyamura, N. Kuriyama, H. Ishikawa and T. Toide, 1991, Rare Earth (Kidorui), No. 18, p. 184; paper presented at 19th Rare Earth Res. Conf., Kentucky, 1991.

Suzuki, K., N. Yanagihara, H. Kawano and A. Ohta, 1993, J. Alloys & Compounds **192**, 173–175.

Tadokoro, M., K. Moriwaki, K. Nishio, M. Nogami, N. Inoue, Y. Chikano, M. Kimoto, T. Ise, R. Maeda, F. Mizutaki, M. Takee and N. Furukawa, 1992, in: Proc. Symp. on Hydrogen Storage Materials, Batteries and Electrochemistry, Vol. 92-5, eds D.A. Corrigan and S. Srinivasan (Electrochemical Society, Pennington) pp. 92–104.

Tadokoro, M., M. Nogami, Y. Chikano, M. Kimoto, T. Ise, K. Nishio and N. Furukawa, 1993, J. Alloys & Compounds **192**, 179–181.

Takashima, M., Y. Matsumura, Y. Hasegawa, G. Kano, K. Hasegawa, M. Oshitani and Y. Matsumaru, 1992, Denki Kagaku **60**, 231–236.

Takeshita, Y., H. Kaminaka, Y. Shida, Y. Hatakeyama, K. Koushiro, M. Hara and N. Negi, 1992, Extended Abstract presented at 33rd Battery Symp., Japan, p. 159.

Takeya, K., Y. Tsugita, Y. Okajima, T. Sakai, H. Miyamura, K. Oguro, N. Kuriyama and H. Ishikawa, 1993, J. Alloys & Compounds **192**, 167–169.

Tamura, H., 1992, Shin Sozai **3**, 57.

Tamura, H., T. Kitamura and C. Iwakura, 1983, J. Less-Common Met. **89**, 567–574.

Van Beek, J.R., H.C. Donkersloot and J.J.G. Willems, 1984, Uncorrected Preprint, 14th Int. Power Sources Symposium, Brighton, UK.

Van Mal, H.H., K.H.J. Buschow and F.A. Kuijpers, 1973, J. Less-Common Met. **32**, 289–296.

Van Rijswick, M.H.J., 1978, in: Hydrides for Energy Storage, eds A.F. Andresen and A.J. Maeland (Pergamon Press, Oxford) pp. 261–271.

Venkatesan, S., and B. Reichman, 1989, in: Proc. 24th Intersociety Energy Conversion Engineering Conference, Crystal City, p. 1665.

Venkatesan, S., M.A. Fetcenko, B. Reichman, D. Magnuson and S. Dhar, 1988, in: Proc. 2nd Int. Rechargeable Battery Seminar, Florida, USA, p. 133.

Venkatesan, S., M.A. Fetcenko and B. Reichman, 1989, in: Proc. 24th Intersociety Energy Conversion Engineering Conference, Crystal City, p. 1659.

Videm, K., 1978, in: Hydrides for Energy Storage, eds A.F. Andresen and A.J. Maeland (Pergamon Press, Oxford) pp. 463–477.

Viitanen, M., 1993, J. Electrochem. Soc. **140**, 936–942.

Wada, M., H. Yoshinaga, O. Kajita, T. Sakai, M. Irikawa, H. Miyamura, N. Kuriyama and I. Uehara, 1993, J. Alloys & Compounds **192**, 164–166.

Wakao, S., and H. Sawa, 1991, Denki Kagaku **59**, 950–957.

Wakao, S., and Y. Yonemura, 1983, J. Less-Common Met. **89**, 481–488.

Wakao, S., Y. Yonemura, H. Nakano and H. Shimada, 1984, J. Less-Common Met. **104**, 365–373.

Wakao, S., H. Sawa, H. Nakano, S. Chubachi and M. Abe, 1987, J. Less-Common Met. **131**, 311–319.

Wakao, S., H. Sawa, H. Nakano, S. Chubachi and H. Nakano, 1989, Z. Phys. Chem. NF **164**, 1527–1532.

Wicke, E., and H. Brodowsky, 1978, in; Hydrogen in Metals II; Application-oriented Properties, eds G. Alefeld and J. Völki, Vol. 29 of Topics in Applied Physics (Springer, Berlin) pp. 73–155.

Willems, J.J.G., 1984, Philips J. Res. **39**(1).

Willems, J.J.G., 1986, Philips Tech. Rev. **43**, 22.

Willems, J.J.G., and K.H.J. Buschow, 1987, J. Less-Common Met. **129**, 13–30.

Yamashita, M., H. Higuchi, H. Takemura and K. Okuno, 1993, Denki Kagaku **61**, 729–730.

Yartys', V.A., V.V. Burnasheva, K.N. Semenenko, N.V. Fadeeva and S.P. Solov'ev, 1982, Int. J. Hydrogen Energy **7**, 957–965.

Yayama, H., O. Ichinomiya and K. Hirakawa, 1983, Jpn. J. Appl. Phys. **22**, L621–L623.

Yayama, H., K. Kuroki, K. Hirakawa and A. Tomokiyo, 1984, Jpn. J. Appl. Phys. **23**, 1619–1623.

Yayama, H., K. Hirakawa and A. Tomokiyo, 1986, Jpn. J. Appl. Phys. **25**, 739–742.

Yayama, H., A. Tomokiyo and K. Hirakawa, 1987, Oyo Busuri **56**, 216–219.

Yayama, H., A. Tomokiyo and K. Hirakawa, 1989, Jpn. J. Appl. Physics **28**, 530–534.

Yonezu, I., S. Kameoka, M. Nogami, K. Inoue, T. Matsumoto, T. Saito and N. Furukawa, 1989, J. Hydrogen Energy Systems Soc. Jpn. **14**, 21.

Yvon, K., and P. Fischer, 1988, in: Hydrogen in Intermetallic Compounds I, ed. L. Schlapbach (Springer, Berlin) pp. 87–138.

Zijlstra, H., and F.F. Westendorp, 1969, Solid State Commun. **7**, 857–859.

Züttel, A., F. Meli and L. Schlapbach, 1994a, Z. Phys. Chem. NF **183**, 355–363.

Züttel, A., F. Meli and L. Schlapbach, 1994b, J. Alloys & Compounds **203**, 235–241.

Züttel, A., F. Meli and L. Schlapbach, 1994c, J. Alloys & Compounds **206**, 31–38.

Züttel, A., F. Meli and L. Schlapbach, 1994d, J. Alloys & Compounds **209**, 99–105.

Handbook on the Physics and Chemistry of Rare Earths
Vol. 21
edited by K.A. Gschneidner, Jr. and L. Eyring

Chapter 143

CHEMICAL SENSORS

Gin-ya ADACHI and Nobuhito IMANAKA
Department of Applied Chemistry, Osaka University, 2-1 Yamadaoka, Suita, Osaka 565, Japan

Contents

List of symbols and abbreviations

A/F	air-to-fuel ratio	samaria	samarium oxide
calcia	calcium oxide	scandia	scandium oxide
EMF	electromotive force	SUMICERAM	brand name of inorganic adhesive agent
F	Faraday's constant		
ΔG	Gibbs free energy change	t_{90}	time necessary for 90% response
gadolinia	gadolinium oxide	t_{H^+}	proton transference number
IL1	primary limiting current	TMA	trimethylamine
IL2	secondary limiting current	UEGO	universal A/F ratio heated exhaust gas oxygen
ISE	ion selective electrode		
ISFET	ion sensitive field effect transistor	yttria	yttrium oxide
magnesia	magnesium oxide	zirconia	zirconium oxide
NASICON	Na^+ super ionic conductor	λ	ratio of (A/F) to $(A/F)_0$
R	gas constant	σ	conductivity

1. General remarks

With the substantial improvement of the standard of living and the availability of many appliances and devices, many kinds of sensors have been proposed and some have already become commercially available. A "sensor" is a device which detects physical or chemical quantities and transduces these quantities into electronic signals. Sensors which detect species and concentration of chemical substances are called "chemical sensors".

Chemical sensing is not a well investigated conventional research field. Research started just a few decades ago. However, some chemical sensors are already in widespread commercial use and contribute greatly to making our lives comfortable. Commercial sensors are roughly divided into three types according to the detection principle: (I) conductimetric type, (II) potentiometric type, (III) amperometric type.

The first commercial chemical sensor was a gas alarm sensor, which detects inflammable gases and prevents gas accidents. The sensor is simple, portable, and can be easily installed in most places. These features encourage mass production, and thus contribute to the production of an inexpensive device. The base materials for these sensors are mainly tin oxide (SnO_2) or zinc oxide (ZnO) semiconductors with type-I detection. When inflammable gases come in contact with the oxides, the electric conductivity changes and this change is used as a sensor output. The variation of the change is proportional to the gas concentration. In a practical semiconductive sensor, noble metals

such as palladium and platinum are added to the oxide as a sensitizer or catalyst. This addition appreciably improves response and sensitivity of the sensor. Since the type-I sensor detects gases by the conductivity change following gas adsorption on the surface, it is suitable for detecting small amounts of gas, such as in leaks. The sensor still has an ability to detect extensive gas leakage but not with such good accuracy.

Another widely used commercial sensor is the oxygen sensor for controlling the air-to-fuel (A/F) ratio in automobiles. The sensor is used to maintain the A/F ratio to the ideal value where the catalytic conversion of the pollutant gases is performed in an optimum condition. This sensor belongs to type II. The output is obtained as an electromotive force (EMF) from the oxygen gas concentration cell. The oxygen sensor is built with a stabilized zirconium oxide solid electrolyte. The only mobile carrier in the electrolyte is the oxygen anion, thereby enhancing the oxygen sensing characteristics appreciably.

The fluorine sensor is extensively used commercially. The fluorine content can also be detected by chemical sensing and the principle of this device also belongs to type II. The base material is lanthanum fluoride, which is an excellent fluorine conductor, and which is stable even in aqueous solution. A typical application is to measure the fluorine content in test water solutions. The principle of fluorine detection is based on the F^- concentration cell method. The detection limit is as low as 10^{-6} M, which covers most F^- concentrations in drinking water. A fast response is one of the typical characteristics of the type-II sensor: it is less than 3 minutes even if the F^{-1} content is as low as 10^{-6} M.

Humidity sensors are also widely applied in home electronic appliances. The representative material is $MgCr_2O_4$–TiO_2 ceramics. The adsorption of water molecules on the oxide results in a great conductivity increase, hence sensing is carried out by measuring the conductivity change with type I. The response time is just a few seconds. The ceramics are appropriate for the sensor material because adsorption and desorption of water molecules occurs smoothly. In addition, the conductivity change caused by the adsorption is very large, while the conductivity variation with temperature is small at practical operation temperatures (lower than 150°C). Furthermore, the ceramic materials have the advantage that they are strong enough to resist thermal shock.

In the bioscience field, enzyme-based sensors have already been commercially applied to measure glucose, acid, and urine content, etc. The most widely utilized sensor of this type is a glucose sensor (type III). In the glucose sensor probe, glucose reacts with oxygen, with the catalytic aid of enzyme, to form gluconolactone and hydrogen peroxide. The glucose content is obtained by measuring the amount of oxygen consumed in the reaction by an amperometric method (type III).

Several new types of unique sensors have been proposed. For humidity sensing, the operating temperature is generally around room temperature. However, a newly proposed sensor uses cerate ceramics and is applicable above 400°C. This feature enables sensing of water vapor content in various high temperature gas atmospheres. The sensor output is the EMF from the water-vapor gas concentration cell (type II), and the selectivity to water vapor is extremely high.

With the increase in environmental deterioration caused by acid precipitation, the on-site measurement of acid-forming gases is desirable. Attempts have been made to develop

a sensor for the detection of sulfur dioxide. The principle of detection is similar to the oxygen or the humidity sensor, with solid electrolyte in a gas concentration cell (type II). The operating temperature is as high as 700°C. Because the ionic state of SO_2 is a sulfate anion, SO_4^{2-}, and the gas content detection is made in an ionic conducting material which contains a sulfate anion, SO_2 sensing is carried out with a high selectivity. The gas concentration is immediately determined from the EMF output and it covers a wide range; from 30 ppm to 1%. In continuous operation, the response time is less than several minutes. The sensor with solid electrolyte offers great promise for on-site control of SO_2 gas emissions in the near future.

The carbon dioxide level has been rising considerably since the start of the Industrial Revolution. This steady CO_2 increase causes global warming. The most effective way of suppressing CO_2 exhaustion into the atmosphere is to control the emission amount of CO_2 at every exhausting site. For such a purpose, simple, inexpensive and portable sensors need to be developed. Barium cerate, which has been examined as a humidity sensor, can also be used as a CO_2 sensor, but in this case, the response is obtained by the type-I method. Tin oxide, which is a well known semiconductor for a commercial gas alarm sensor, has also been examined in CO_2 detecting applications. In this case, rare-earth doping into tin oxide contributes greatly to enhance the sensing characteristics. Rare-earth oxides, alone, have also been studied for use as a sensing material. The methods mentioned above belong to the type-I sensing.

Alcohol is contained in liquor, beer, and even in some tasty food dishes. Alcohol is one example of an interfering gas for the commercialized gas alarm sensor of type I. In addition, the number of drinking and driving violations is steadily increasing and can cause serious traffic accidents. Hence, the police need a portable and reliable alcohol sensor which can be carried in every police car. Some ceramic sensors for alcohol gas detection have been proposed, and research is still under progress. However, if the sensor's reliability is improved, the sensor can be installed in every police car.

The sensors mentioned above are all detectors of types I, II, or III. However, different sensing types, such as Ion Sensitive Field Effect Transistors (ISFETs) and optical chemical sensors have also been proposed. The variety of chemical sensors is still increasing steadily.

In this review, we focus on chemical sensors where rare-earth elements play an important role in chemical sensing and contribute to enhancing the sensing characteristics. The rare-earth impact upon the chemical sensor field is a main view point of this review article.

2. Oxygen sensors

2.1. *Introduction*

Air pollution by exhaust emission from automobiles has been increasing and causes a serious deterioration of the environment as the number of automobiles increases.

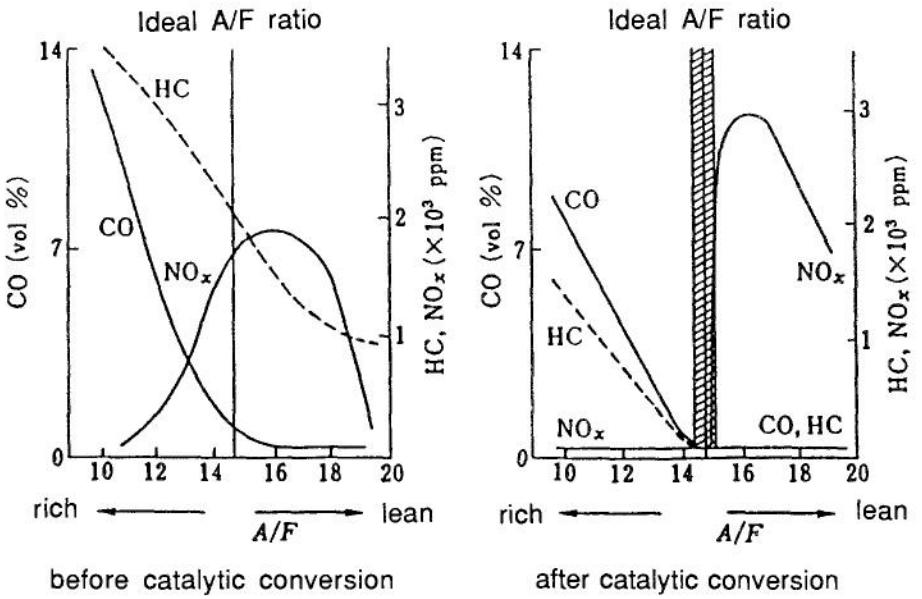

Fig. 1. Relation between A/F ratio and gas composition in exhaust gas (Oohata 1990). (Reprinted by permission of the publisher, The Rare Earth Society of Japan.)

Reduction in the amount of pollutant gases from automobile emissions is a worldwide concern. To decrease the amount of pollutant gases, a catalytic converter is installed into the exhaust gas stream of automobiles. The catalyst is called a three-way catalyst. The gases which cause air pollution in the exhaust are hydrocarbons, carbon monoxide and nitric oxides. The catalyst oxidizes both hydrocarbons and carbon monoxide into CO_2 and H_2O, and also reduces nitric oxides into nitrogen. Decrease of these three main pollutant gases is presented in fig. 1 (Oohata 1990, Adachi 1991).

Catalytic conversion is most efficiently achieved when the air-to-fuel (A/F) mixture is exactly that where the stoichiometric reactions for such oxidations and reduction occur. Beyond the point of the ideal A/F ratio, the oxygen content in exhaust gases drastically changes. Because the exhaust gas composition changes with several parameters (eg. throttle setting, speed, etc.) it is strongly desirable to have an oxygen sensor in the exhaust stream to keep the A/F ratio as close to the ideal as possible. Great efforts have been concentrated on the development of a reliable sensor for the purpose of precisely measuring the A/F ratio: by using a rapid feedback loop these data can be used to reduce the pollutant gases in the exhaust. One reasonable way to control the A/F ratio is to sense the oxygen gas content in the emission. The oxygen sensor based on the solid electrolyte type has been demonstrated to maintain an optimum condition for catalytic conversion. For such a purpose, rare-earth oxides are quite effective in improving the characteristics of the solid electrolyte, and especially, to stabilize the appropriate form for an ionic conduction as well as enhance the oxygen ionic

conductivity. The oxygen sensor has already been commercially used for consumer automobiles and has played a significant role in controlling the air/fuel ratio in the engine inlet manifold. Development of the oxygen sensor has led to a great reduction of pollutant gas emissions into the environment and has made the efficient and economic use of automobiles possible. Improvements of the sensing characteristics of the oxygen sensor have resulted in a more reliable and wider range performance along with a high reliability and a long durability, all of which is economically favorable. The electrolyte actually used is a stabilized zirconia. "Stabilized" means that some materials are mixed with zirconia to stabilize the appropriate structures. One representative and common rare-earth dopant for the stabilized zirconia oxygen sensor is yttrium oxide.

2.2. *Oxide anion conducting solid electrolytes*

2.2.1. *Zirconium oxide (zirconia)*

Pure zirconia exists in monoclinic form at room temperature. It transforms into a tetragonal phase at elevated temperatures, around 1100°C. On further heating, tetragonal ZrO_2 undergoes another phase transition to a cubic form at 2370°C. By adding yttrium oxide to zirconia, these high-temperature phases are stabilized, as shown in fig. 2 (Stubican et al. 1978, Stubican 1988, Pratt 1990). This is the reason why doped zirconia is called "stabilized zirconia". The yttrium ion maintains a stable trivalency. In this case, the trivalent cation substitutes for the tetravalent zirconium ion and oxygen vacancies are formed by charge compensation. These vacancies allow oxygen anions to migrate smoothly in the stabilized zirconia bulk. This clearly indicates that aliovalent cation doping into ZrO_2 is a superior way to obtain a good oxygen anion conducting solid electrolyte. The electric conductivity change for $ZrO_2$with several rare-earth cations is shown in fig. 3 (Adachi and Shimada 1982). In each case, there is an optimum doping amount. As more of the aliovalent cations are doped into ZrO_2, more oxygen vacancies form. However, the vacancies begin to form clusters when the amount of aliovalent doping exceeds a certain value. The conductivity increase by the rare-earth doping is different with each rare-earth cation. Figure 4 (Adachi 1988) presents the relationship between the conductivity and the ionic radius of the rare earths. It is clear from the figure that conductivity increases linearly with the decrease in ionic radius of the rare earth. The smaller the doped cation, the larger is the oxygen vacancy in bulk zirconia. The larger vacancy lets the oxygen anion migrate more smoothly, and results in the increase in oxygen ionic conduction.

The high oxygen ionic conductivity phase of zirconium oxide is cubic. To stabilize this form, an amount of 10–15 mol% of metal oxide such as Y_2O_3, CaO, or MgO has been added to ZrO_2. When we compare cubic zirconia stabilized by different metal oxide additions, Y_2O_3-mixed stabilized ZrO_2 shows a pure ionic conduction over a wider range of oxygen partial pressure than the CaO- or MgO-mixed stabilized varieties.

The zirconia sensor is installed between the engine and the catalytic converter in the exhaust system of automobiles. Hence, the oxygen sensor is exposed to severe conditions;

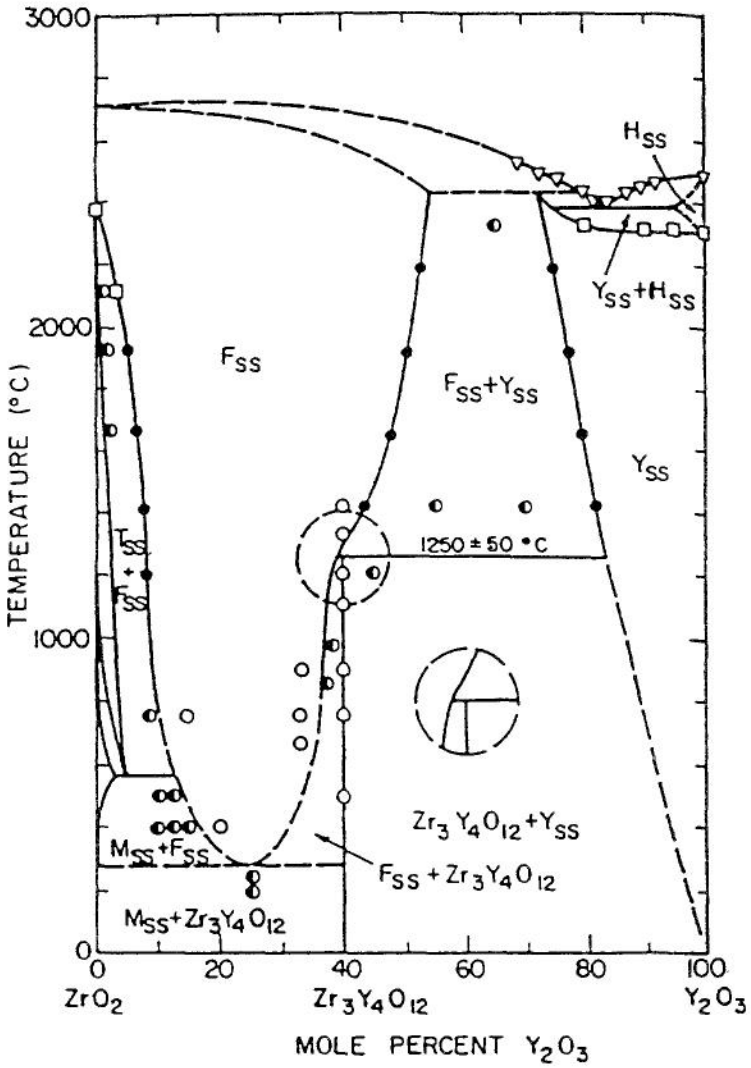

Fig. 2. Phase diagram for the system ZrO_2–Y_2O_3 (Stubican et al. 1978). (Reprinted by permission of the publisher, The American Ceramic Society.)

a high temperature gradient, vibration, salt exposure, large temperature changes, and it must operate continuously with a high reliability. Yttrium-doped zirconia yields the durable high performance solid electrolyte necessary for sensor material in such circumstances. The yttria (yttrium oxide) stabilized zirconia is widely applied as the solid electrolyte for the A/F sensor.

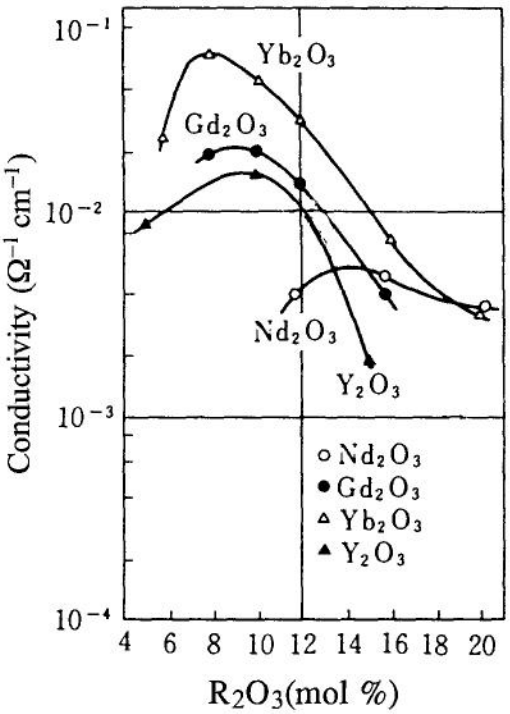

Fig. 3. Ionic conductivity of ZrO_2–R_2O_3 solid solutions at 800°C (Adachi and Shimada 1982).

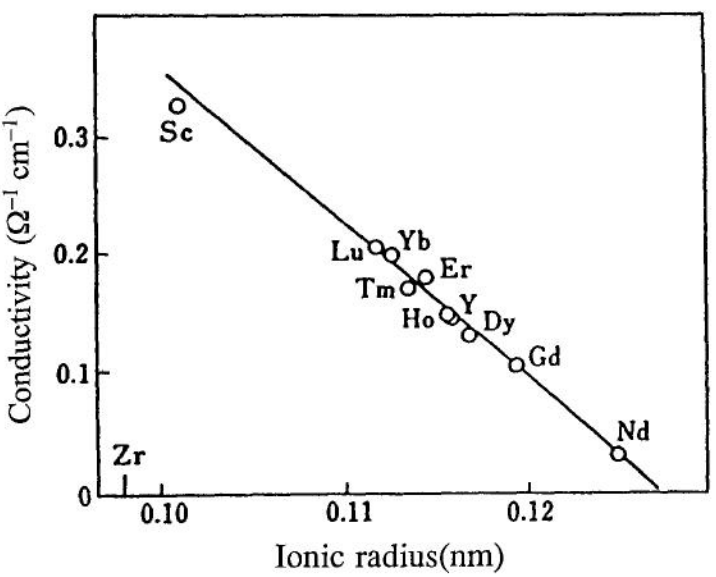

Fig. 4. Electric conductivity change by mixing of various rare-earth ions at 1273 K (10 mol% rare-earth oxide was mixed to make a solid solution) (Adachi 1988).

2.2.2. *Bismuth oxide*

Bismuth oxide crystallizes in two forms: the α-form is a monoclinic phase stable below 730°C, and the σ-form is a cubic phase, above this temperature. This high-temperature σ-form shows a considerably higher oxide ionic conductivity. The electric conductivity of Bi_2O_3 is approximately two orders of magnitude higher than that of stabilized zirconia. The σ-form possesses a considerable amount of oxide anion vacancies, expressed as $Bi_4O_6\square_2$, where □ represents the oxide ionic vacancy. This Bi_2O_3 material also easily forms a solid solution with some other metal oxides which results in filling the vacancies and stabilizing the σ-phase. One of the typical examples is the Bi_2O_3–Y_2O_3-system. Bismuth oxide alone shows a discontinuity in conductivity as a result of the phase transformation. However, by mixing 25 mol% Y_2O_3 with Bi_2O_3, the discontinuity is eliminated and the structure remains in the high oxide ionic conducting σ-form over the whole temperature range (Takahashi et al. 1975, Takahashi and Iwahara 1978). Y_2O_3-mixed Bi_2O_3 shows a considerably higher conductivity, and furthermore, the Bi_2O_3–Y_2O_3 system is easy to obtain as a dense bulk. However, Bi^{3+} in Y_2O_3–Bi_2O_3 electrolyte is easily reduced to the metallic state. In order to prevent such a reduction, the oxygen partial pressure should be higher than 10^{-13} atm to maintain the transference number over 0.99. In the Bi_2O_3–Y_2O_3 system, the conductivity decreases with the increase of the Y_2O_3 amount, and the optimum Y_2O_3/Bi_2O_3 mixing ratio is around ⅓. This is the lowest Y_2O_3/Bi_2O_3 ratio able to suppress the phase transition from the higher to the lower temperature phase and maintain the cubic σ-phase over a wide temperature range.

2.2.3. *Cerium oxide*

One of the rare-earth oxides, cerium oxide, can also become an oxide ionic conductor. Other rare-earth oxides mixed with CeO_2 also make a solid solution up to $x = 0.5$ in $Ce_{1-x}R_xO_{2-x/2}$. Kudo and Obayashi (1975) investigated the change of oxide ion transference number for the rare earth oxide–cerium oxide system. When Sm or Dy is used as the rare earth, the transference number saturates around 0.95–0.96. In the case of R = Nd, Gd, or Er in the $Ce_{1-x}R_xO_{2-x/2}$ solid solution, the transference number becomes almost unity. At temperatures below 600–700°C, the electrode reaction does not proceed smoothly and this greatly lowers the ionic conduction in the solid solution. Therefore, the transference number below 600°C is meaningless for comparisons in the CeO_2–R_2O_3 system. In the rare-earth series, Sc^{3+} (1.01 Å) (Shannon 1976), which possesses the smallest ionic radius, does not form a $Ce_{1-x}Sc_xO_{2-x/2}$ solid solution. The conductivity at 700°C of $Ce_{1-x}Gd_xO_{2-x/2}$, which shows an excellent transference number in the CeO_2–R_2O_3 system, is very similar with the value for stabilized zirconia at 1000°C (Kudo and Obayashi 1976). One of the crucial disadvantages of cerium oxide electrolytes is that the electronic conduction appears at lower oxygen partial pressures. For example, the oxide ionic transference number lowers to around 0.5 when the p_{O_2} is equal to ca. 10^{-8} Pa (1000°C).

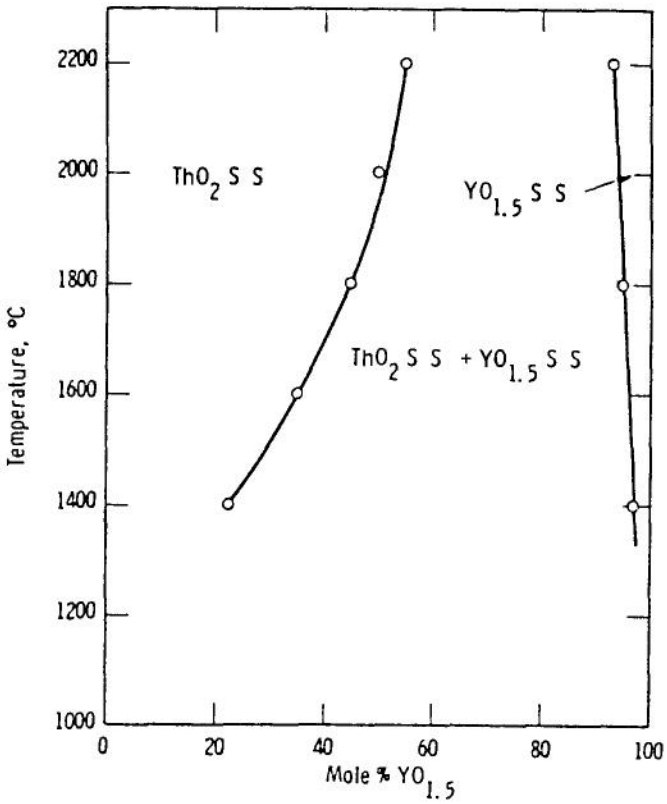

Fig. 5. Phase relationships in the system ThO_2–$YO_{1.5}$ (Subbarao et al. 1965). (Reprinted by permission the publisher, The American Ceramic Society.)

2.2.4. *Thorium oxide*

Thorium oxide exhibits the cubic fluorite form up to its melting point, at $T \approx 3220$°C. Oxygen ionic conduction in ThO_2 still persists at oxygen pressures well beyond the lower limit found for the oxide ionic conduction in the ZrO_2 electrolyte. Since ThO_2 maintains the cubic phase, there is no need to mix metal oxides to stabilize an appropriate form. However, the ThO_2 cubic form is a poorer ionic conductor than stabilized ZrO_2. Rare-earth oxides such as Y_2O_3 or La_2O_3 have been added, not to stabilize some phases but to increase the oxygen vacancies and enhance the conductivity to suitable levels. Rare earth-mixed ThO_2 systems form extensive solid solutions, as may be seen from the phase diagram (fig. 5) of ThO_2–$YO_{1.5}$ (Subbarao et al. 1965).

The mixing of di or trivalent metal oxides introduces a great number of anion vacancies. Table 1 (Etsell and Flengas 1970) shows the solubility of rare-earth oxides into ThO_2. In those rare-earth oxides, scandium oxide shows just a slight solubility because the ionic radius differs greatly between Sc^{3+} (1.01 Å) (Shannon 1976) and Th^{4+} (1.19 Å) (Shannon 1976). However, yttrium oxide and other rare-earth oxides are quite soluble

Table 1
Solubilities of di- and trivalent metal oxides in ThO_2 (Etsell and Flengas 1970) (reprinted by permission of the publisher, The American Chemical Society)

Oxide	Temperature (°C)	Solubility (% MO or M_2O_3)	Oxide	Temperature (°C)	Solubility (% MO or M_2O_3)
CaO	1700	10	Pr_2O_3	1400	54
	1800	>12	Nd_2O_3	1400	33
	1800	8		1500	33
SrO	1800	4	Sm_2O_3	1400	43
BaO	1800	<0.5	Eu_2O_3	1800	54
Sc_2O_3	1750	~0.5		1500	36
Y_2O_3	1200	18		1200	22
	1400	14	Gd_2O_3	1400	33
	2000	33		2000	45
	1400	12		800	19
La_2O_3	1300	35	Yb_2O_3	1400	5
	1400	32		1800	10
	1500	32		1000	3
	1950	39			
	1200	20			

in thorium oxide, with the highest value being obtained for the rare earth Pr^{3+} (1.27 Å) (Shannon 1976) and Gd^{3+} (1.19 Å) (Shannon 1976) whose rare-earth ionic radii are close to that of Th^{4+} (1.19 Å) (Shannon 1976). Figure 5 shows a ThO_2–$YO_{1.5}$ phase relation (Subbarao et al. 1965). As shown in fig. 5, three regions exist in the ThO_2–$YO_{1.5}$ system. ThO_2-type solid solution was found up to 50–55 mol% Y_2O_3 mixing at 2200°C. The Y_2O_3 solubility limit in ThO_2 monotonically decreases with a lowering of the preparation temperature.

The influence on the electric conductivity of Y_2O_3-mixing with ThO_2 of the ThO_2–Y_2O_3 system has been studied by Subbarao et al. (1965). In the ThO_2-type region, the conductivity increases with the Y_2O_3-mixing amount. Anion vacancies significantly increase by the Y_2O_3-mixing to form a ThO_2-type solid solution, and hence the conductivity of the solid solution is appreciably enhanced. However, as is well known, thorium oxide is radioactive and its commercial application is restricted.

2.2.5. *Hafnium oxide*

Hafnium oxide also forms a solid solution with various rare-earth oxides as shown in table 2 (Etsell and Flengas 1970). However, ionic conductivity of HfO_2 is appreciably lower than that of stabilized zirconia. Therefore, hafnium oxide has not yet been utilized for a practical application as a chemical sensor.

Table 2
Phase boundaries of cubic HfO_2-based solid solutions (Etsell and Flengas 1970) (reprinted by permission of the publisher, The American Chemical Society)

Oxide	Temperature (°C)	Boundaries (%MO or M_2O_3)
CaO	1800	12 and 22
	2500	10 and 20
	2000	12 and 20
Sc_2O_3	1500	14 and 15
Y_2O_3	1800	8 and >40
La_2O_3	1500	30 and 41 [a]
Nd_2O_3	1500	29 and 38 [b]
Eu_2O_3	1500	11 and 56
Gd_2O_3	2000	10 and 50
	1500	15 and 56
Ho_2O_3	1500	8 and 55

[a] Based on $La_2Hf_2O_7$. [b] Based on $Nd_2Hf_2O_7$.

2.3. *The characteristics of "stabilized zirconia" (phase relationship in the zirconia (ZrO_2)–yttria (Y_2O_3) system)*

The variation of lattice parameter of the cubic zirconia–yttria system with yttria amount was studied in detail by Stubican et al. (1978). By mixing Y_2O_3 with ZrO_2, the lattice parameter of the cubic ZrO_2 phase increases monotonically. This occurs because the ionic radius of Y^{3+} (1.16 Å) (Shannon 1976) is larger than that of Zr^{4+} (0.98 Å) (Shannon 1976). Around 3 mol% yttria-mixing, the monoclinic zirconia phase appears. By increasing the mixing amount to 4–5 mol%, there appear two phases, namely the monoclinic and the cubic ZrO_2 phases. For yttria content between 7 and 55 mol%, a single phase of yttria-mixed cubic stabilized zirconia was observed, as shown in fig. 6 (Duwez et al. 1951). For yttria mixing between 55 and 75 mol%, two phases again appear, but now one is the cubic zirconia structure and the other is the yttria one. The lattice parameter is constant in this two-phase region. At more than 80 mol% mixing with ZrO_2 the single phase of the yttria structure is found. This indicates that zirconia is also soluble in yttria, as shown in fig. 6.

Yttria also possesses a cubic structure similar to zirconia. This is the main reason for the formation of a solid solution in such a wide range of concentrations of the zirconia–yttria system. Yttria-stabilized zirconia can be obtained as a solid solution with an yttria content between 6 and 50 mol%. Other oxides, especially rare-earth oxides, are expected to have a similar cubic phase stabilizing effect. The oxides are scandia and rare-earth oxides with the atomic number from 62 to 71, since those metals are stable in the trivalent state. In fact, the cubic form of zirconia can be obtained in stable form by mixing any one of the rare-earth oxides such as scandia, samaria and gadolinia. The minimum amount of

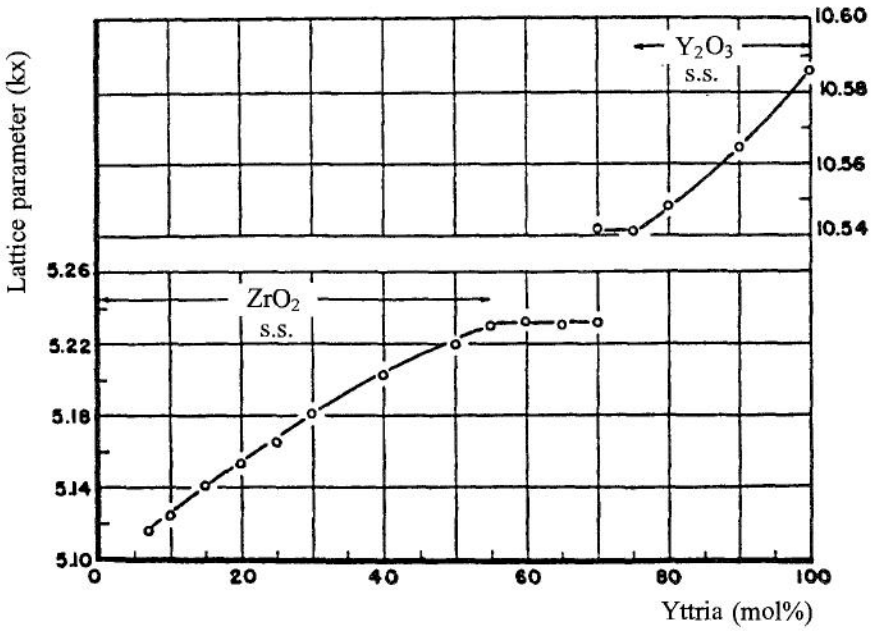

Fig. 6. Variation of lattice parameters of cubic zirconia and yttria solid solutions with yttria content (Duwez et al. 1951). (Reprinted by permission of the publisher, The Electrochemical Society Inc.)

the addition to stabilize the cubic structure is around 6 mol%, which is very close to the amount for the yttria-mixing.

2.4. *Mechanism of oxygen sensing with "stabilized zirconia"*

In the "stabilized zirconia" electrolyte, the only mobile ion is the oxygen anion. When two compartments with different oxygen concentrations are separated by a solid electrolyte, an oxygen gas concentration cell is formed as depicted in fig. 7 (Azad et al. 1992). There exists a driving force to move oxygen anions through the electrolyte, from the compartment with a higher oxygen concentration to the lower one. Air is used as a reference, thus the oxygen content is higher than that in the exhaust stream, the next half reaction occurs at the reference electrode,

$$O_2(\text{air}) + 4e^- \rightarrow 2O^{2-}. \tag{2.1}$$

On the other hand, the reverse half reaction occurs at the sensing electrode in the exhaust compartment,

$$O^{2-} \rightarrow O_2(\text{ex}) + 4e^-. \tag{2.2}$$

The overall reaction is expressed as

$$O_2(\text{air}) \rightarrow O_2(\text{ex}). \tag{2.3}$$

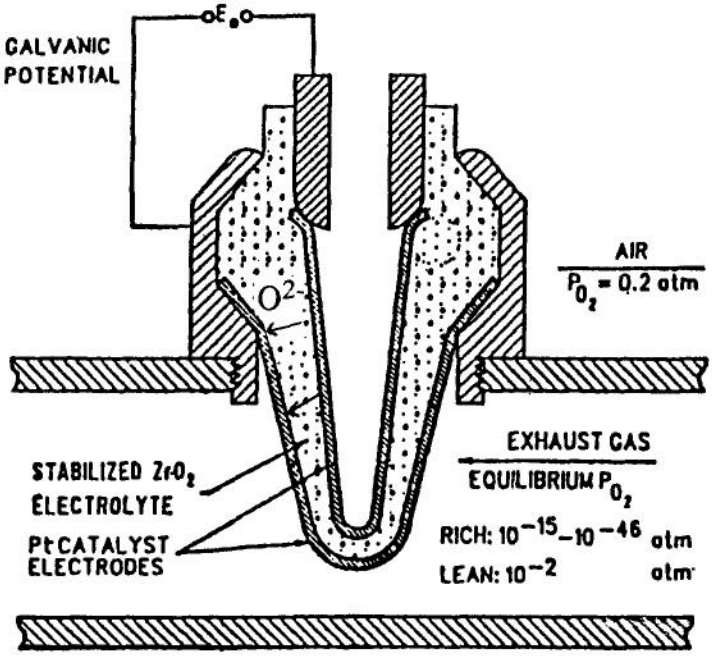

Fig. 7. Cross-sectional view of the oxygen gas sensor for automobiles (Azad et al. 1992). (Reprinted by permission of the publisher, The Electrochemical Society Inc.)

By applying the Nernst equation one derives the following equation:

$$E = \frac{RT}{4F} \ln \left(\frac{p_{O_2}(\text{air})}{p_{O_2}(\text{ex})} \right), \tag{2.4}$$

where R represents the universal gas constant, T is the absolute temperature, and F is Faraday's constant.

Because air is used as a reference, the oxygen pressure in the reference is constant at 0.21 atm, and the unknown oxygen content in the exhaust gas stream is directly calculated from eq. (2.4).

2.5. *Performance of oxygen sensors with "stabilized zirconia"*

The air-to-fuel ratio of the mixture introduced into an engine combustion chamber is called the A/F ratio. The ideal A/F ratio is where the fuel is consumed according to the stoichiometric reaction, and is expressed as $(A/F)_0$. The ratio of A/F to $(A/F)_0$ is called λ. In the case of $\lambda > 1$, excess oxygen exists in the ambient atmosphere. On the other hand, when $\lambda < 1$, most of the oxygen gas introduced into the engine combustion chamber reacts with fuel and the residual oxygen gas is very low. The oxygen content in the exhaust stream rapidly decreases when λ decreases from the fuel-lean region to the fuel-rich

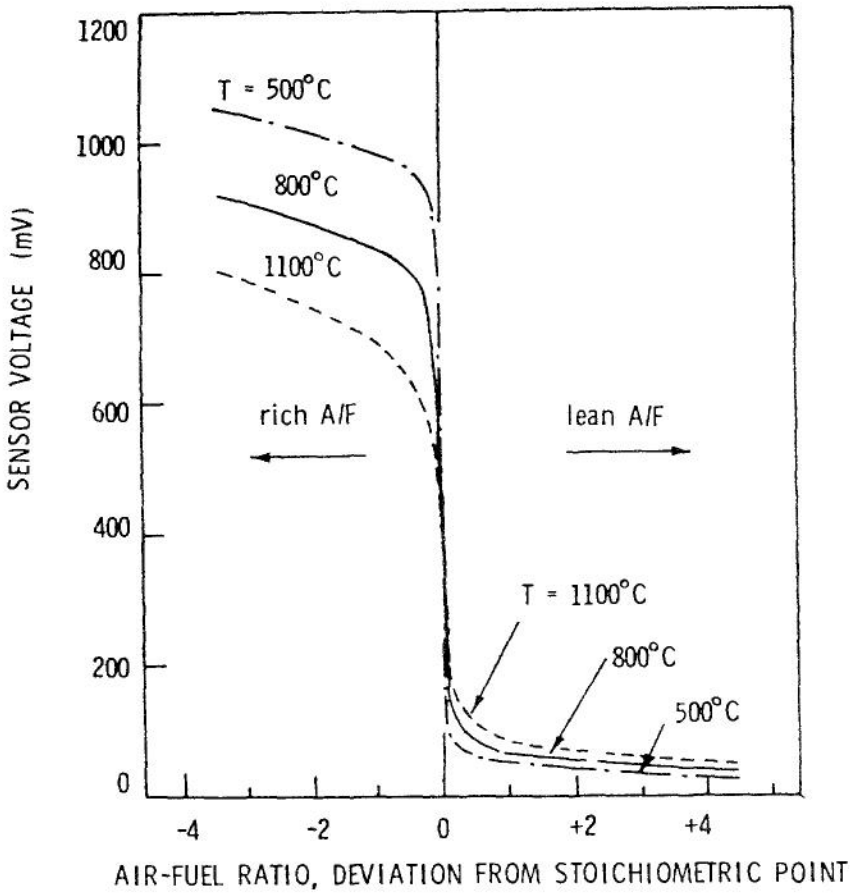

Fig. 8. Ideal sensor output curves (Fleming 1977). (Reprinted by permission of the publisher, The Electrochemical Society Inc.)

region. The EMF output according to eq. (2.4) also changes steeply at the point of $\lambda = 1$, as shown in fig. 8 (Fleming 1977). The shape of the curve in the figure is reminiscent of the shape of the letter λ and this why the A/F oxygen sensor is sometimes called "λ sensor". Reduction of pollutant gases is effectively realized by using the oxygen sensor to maintain the A/F ratio at an optimum value (see fig. 1). The quantities of pollution gases such as hydrocarbons, carbon monoxide, and nitrogen oxides are minimized and those that remain can be effectively converted into non-pollutant gases at the catalytic converter which is placed in the exhaust system as illustrated in fig. 9 (Adachi 1991).

As a practical electrolyte, yttria-doped zirconia is used. The yttrium doping contributes considerably to stabilizing high-temperature phases of zirconia with a high ionic conductivity and to obtain an excellent, durable material for surviving thermal shock. In a commercial oxygen sensor, a porous platinum electrode is placed on the zirconia

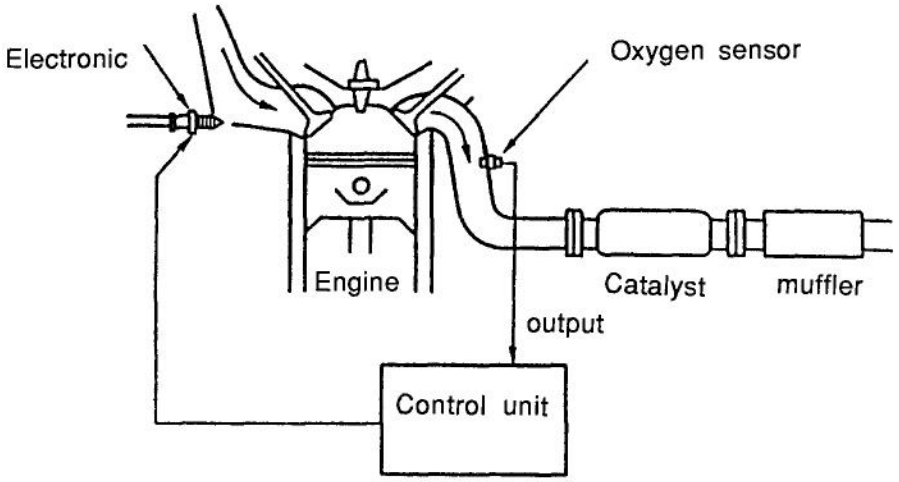

Fig. 9. Exhaust gas control system with oxygen sensor (Adachi 1991).

electrolyte with an alumina-based overlayer to prevent deterioration of the sensor by the combustion stream. Porosity and thickness of the layer directly influence the sensor characteristics, such as response and lifetime, etc. Efforts are being made to enhance the sensing ability and to widen the oxygen sensing range, while still maintaining a high durability and a low cost of production.

2.6. *Improvement of oxygen sensors for lean A/F control*

The fuel-lean region ($\lambda > 1$) is economical for fuel consumption. However, the EMF output for the normal Nernst-type oxygen sensor does not change appreciably in this range, as can be seen from fig. 8.

For fuel-lean operation, an oxygen sensor based on the principle of oxygen-pumping seems to be most promising. Two types of lean A/F sensors have been proposed. One is a pinhole-type, limiting-current oxygen sensor (Takeuchi and Igarashi 1988). The cross-sectional view of this type of oxygen sensor is presented in fig. 10 (Takeuchi and Igarashi 1988). In this sensor, yttrium-doped zirconia is also used as the solid electrolyte. However, one electrode is enclosed in a cover at a volume V. The gas in the enclosed ambient atmosphere is in contact with the outside through an aperture A. When a negative voltage is applied at the Pt electrode (cathode) inside the volume V, the transferred current forces the oxygen anion onto the electrode. The oxygen anions formed on the electrode, migrate in the zirconia electrolyte to pump the oxygen gas in the volume V to the other compartment. The reduction of oxygen pressure, inside the volume V, will cause oxygen diffusion into the volume through the aperture. As the applied voltage increases, a region appears where the current is constant (fig. 11) (Takeuchi and Igarashi 1988). This current is called a "limiting current", and this is why this oxygen sensor for the lean A/F control is called a "limiting-current sensor". At this stage, the flux of oxygen diffusion from

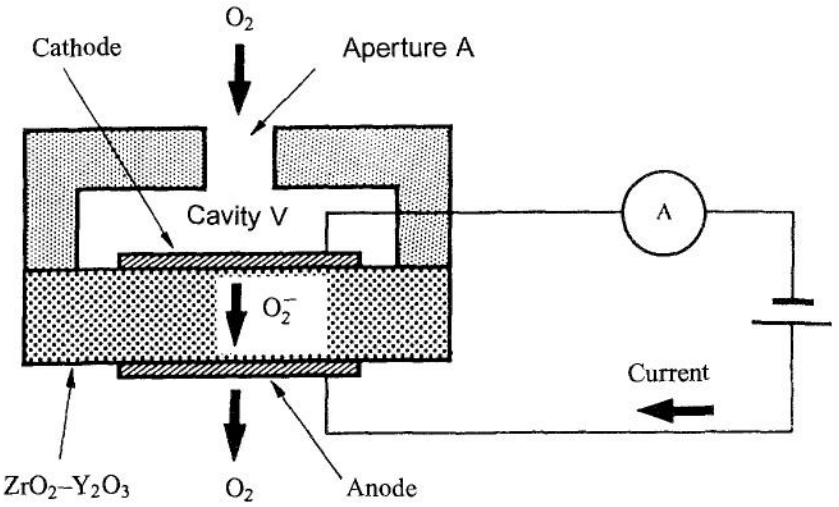

Fig. 10. Structure of a limiting-current oxygen sensor with pinhole (Takeuchi and Igarashi 1988). (Reprinted by permission of the publisher, Kodansha Ltd.)

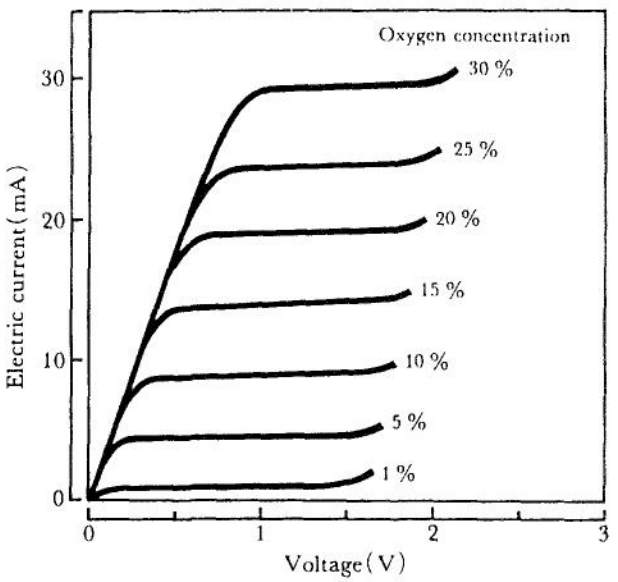

Fig. 11. Typical current–voltage characteristics of the sensor (Takeuchi and Igarashi 1988). (Reprinted by permission of the publisher, Kodansha Ltd.)

the aperture is equal to the oxygen pumped out of the volume V by the current. The relation between limiting current and oxygen pressure in the exhaust gas is almost linearly

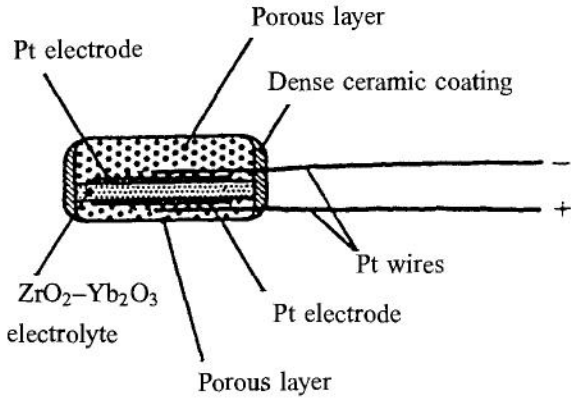

Fig. 12. Porous limiting-current type oxygen sensor (Takeuchi and Igarashi 1988). (Reprinted by permission of the publisher, Kodansha Ltd.)

proportional. This indicates that oxygen detection in the lean region is more sensitive when compared with the oxygen sensor of the Nernst type.

Other types of pumping sensors are also proposed for a lean A/F control sensor. One type is to cover the cathode electrode with a porous layer instead of the enclosure. The representative cross-section of this type of sensor is shown in fig. 12 (Takeuchi and Igarashi 1988). The advantage of the porous coating-type sensor is that the size becomes smaller and the structure is simpler than the pinhole-type sensor. In addition, a quick response can be expected because the inner space is very small.

One strong demand toward an improved oxygen sensor is a lower operating temperature. Two possible ways have been proposed. One is to reduce the sensor resistance by using higher conductivity oxide anion solid electrolytes. The other is to reduce the thickness of the solid electrolyte. The crucial problem caused by lowering the operating temperature of the limiting-current type oxygen sensor is a longer response time.

Several limiting-current oxygen sensors of advanced design have been proposed. One example uses two ZrO_2 cells. In this configuration, one cell is used for pumping and the other cell is used to measure the oxygen concentration. A design which uses two sheets of zirconia for the two cells is reviewed by Sheppard (1992).

The pumping-type sensor has the advantage of high accuracy, sensitivity, and repeatability in the lean region and, in comparison with the sensor of the Nernst-cell type, it is less sensitive to temperature change. Recently, an A/F sensor of the oxygen-pumping type which operates from the very rich to the very lean region has also been proposed. The device is called the UEGO (Universal A/F ratio heated Exhaust Gas Oxygen) sensor (Logothetis 1991), and the construction combines a heater with multilayer substrates of stabilized zirconia (Sheppard 1992). The UEGO sensor has the advantage that it can be used for both engine control and combustion monitoring in addition to controlling the A/F ratio. This means that the UEGO sensor is not only an oxygen sensor, but can also sense engine misfires and catalyst deterioration. However, the detailed behavior of this sensor is not yet understood. The development of oxygen sensors for

A/F control is still in progress, especially, in the areas of sensor performance, durability, continuous operation, and economy.

2.7. *Stabilized zirconia oxygen sensors for the steel industry*

Oxygen sensors based on a "stabilized zirconia" electrolyte are also employed to measure the oxygen content in steel melts. The sensor is directly immersed in the molten steel at a temperature around 1600°C, and therefore, a stabilized zirconia sensor which is highly resistant to thermal shock is used. In this case, magnesia (magnesium oxide) or calcia (calcium oxide) are doped into zirconia instead of yttria. Aliovalent calcium or magnesium doping into zirconia also stabilizes high-temperature phases of ZrO_2 and increases the conductivity in a manner similar to yttrium doping.

Zirconia, stabilized by magnesium oxide, has been widely used for the detection of oxygen in molten steel. However, MgO-stabilized zirconia has the disadvantage that electronic conduction in the electrolyte is rather high. This can cause short-circuiting and results in an unstable and unreliable sensor output. However, calcium oxide or yttrium oxide-stabilized zirconia maintains a low electronic conductivity, but their thermal resistance to insertion into molten steel is relatively poor for practical application. In order to apply the advanced merit of these stabilized zirconias, a double layer electrolyte has been developed. MgO-stabilized zirconia is applied as a matrix for the electrolyte tube and Y_2O_3-stabilized zirconia is used as the cover layer on the matrix electrolyte. By using this construction, these two types of zirconia electrolyte simultaneously provide a good thermal shock resistance and a low electronic conductivity (Liu et al. 1993). In this case, Cr–(10wt.%)Cr_2O_3 or Mo–(10wt.%)MoO_2 was used as a reference electrode. In particular, the oxygen sensor with a double layer electrolyte tube offers great advantages in the detection of oxygen in low concentration ranges.

In the oxygen sensor with stabilized zirconia, porous Pt is applied as the electrode. However, the Pt electrode is not satisfactory from the point of view of long term stability, and accurate response at temperatures higher than ca. 1100°C. Some attempts have been made to use oxides and mixed oxides as the electrode materials. For this purpose, non-stoichiometric oxides have been investigated to accelerate equilibrium with the oxygen present in the atmosphere. The non-stoichiometric ones have the advantage of a fast response and to lower impedance of the sensor cell.

Selected non-stoichiometric rare-earth oxides such as PrO_{2-x}, TbO_{2-x}, and CeO_{2-x} have been tested (Mari and Terzaghi 1983). The cell is expressed as RO_{2-x}/YSZ/Pt, where the non-stoichiometric oxide is used as the detecting electrode and Pt is applied as the reference. Of these rare-earth oxides, PrO_{2-x} sublimates at temperatures higher than 1100°C, which limits its temperature of application. In the rare-earth oxides examined, TbO_{2-x} was found to be the best candidate for the electrode at high temperatures around 1100°C.

To lengthen the sensor's lifetime, non-isothermal operation has also been investigated (Alcock et al. 1993). To maintain the temperature of the reference electrode a few hundred degrees lower than the temperature at the detecting electrode, a long stabilized

zirconia electrolyte rod is utilized. The details of this construction are reported by Alcock et al. (1993).

2.8. *Oxygen sensors with $LaYO_3$- and $LaAlO_3$-based materials*

Oxygen sensors with stabilized zirconia electrolytes can reliably measure oxygen pressure. However, at very low oxygen pressures, Zr^{4+} in the zirconia electrolyte is reduced, which results in an increased electronic conduction. An n-type electronic conduction appears in the electrolyte body and the sensor's output becomes unreliable. In the oxide ionic conductors, thorium oxide holds pure ionic conducting characteristics at lower oxygen partial pressures, compared to stabilized zirconia. However, as mentioned above, thorium oxide is radioactive and its commercial application is quite limited. For the purpose of measuring low oxygen partial pressures, a more suitable solid electrolyte is required. Perovskite oxides have been examined for this use, since they are based on oxides and are also very stable.

Candidates for use at a low oxygen content range are $LaYO_3$ and $LaAlO_3$ (Alcock et al. 1992a,b). Both oxides are very stable and show high melting points in addition to exhibiting a reasonably high ionic conductivity at elevated temperatures even in a low oxygen content region. In this case, Sr^{2+} doping at the La^{3+} site or Mg^{2+} doping at the Al^{3+} site in $LaAlO_3$ enhances the ionic conductivity several orders of magnitude. The conductivity is comparable to that of stabilized zirconia. A cell was constructed as follows:

$$\mathrm{Nb},\ \mathrm{NbO}/\mathrm{LaAl_{0.9}Mg_{0.1}O_{3-}}_x/\mathrm{Cr},\ \mathrm{Cr_2O_3}, \tag{2.5}$$

and the measured EMF of this cell agreed well with the EMF value calculated from the Gibbs free energy change for the following reaction (Alcock et al. 1992a):

$$\mathrm{Nb} + \tfrac{1}{3}\mathrm{Cr_2O_3} = \mathrm{NbO} + \tfrac{2}{3}\mathrm{Cr}. \tag{2.6}$$

As described above, oxide ionic vacancies are formed when one of the host cations is substituted with a cation of lower valence, and this enhances the ionic conductivity. The doped $LaAlO_3$ is expected to be a useful oxide ionic conductor at low oxygen partial pressures. The ionic conductivity of $LaYO_3$ can be enhanced by doping with rare earths such as Er, Ho, or Tm. These perovskite oxides are excellent oxygen ionic conductors even in the low oxygen pressure region where significant electronic conduction appears in the case of stabilized zirconia.

Rare-earth-containing perovskite oxides appear to be promising oxygen sensor material for measurement especially at lower oxygen pressure.

Recently, Post and Sanders (1993) have attempted to apply perovskite thin film (300 nm) of $Sr_{0.9}La_{0.1}FeO_{2.5+x}$ as an oxygen sensor. The films show a reversible reactivity which is specific to oxygen. An increase in UV-VIS transmittance of the film is observed with decreasing x, and the La-containing film can be used for oxygen sensing by measuring

the transmittance response. For the detailed characteristics of the La-containing perovskite films see Post and Sanders (1993).

2.9. *Oxygen sensing with lanthanum fluoride materials*

Lanthanum fluoride has been examined for use as a solid electrolyte for an oxygen sensor operating at room temperature. Most of the oxygen sensors in commercial use work at elevated temperature; the only exception is the electrochemical type which operates at room temperature. The sensor uses aqueous electrolytes and it is crucial to maintain the sensor in an appropriate condition at all times. Leakage and corrosion shorten the lifetime considerably.

An attempt has been made to measure oxygen concentration by using a fluorine conducting electrolyte (Yamazoe et al. 1987, Miura et al. 1987, 1989, Kuwata et al. 1984a,b). Yamazoe et al. (1987) proposed an oxygen gas sensor with a lanthanum fluoride single crystal electrolyte. Lanthanum fluoride is feasible in an aqueous environment and has been used to detect dissolved oxygen in water.

The set-up of the sensor is illustrated in fig. 13 (Yamazoe et al. 1987), where LaF_3 is used as a solid electrolyte. Both working and reference electrodes are necessary for the sensor, which is composed of three parts:

$$\mathrm{Sn},\ \mathrm{SnF_2/LaF_3/Pt},\ \mathrm{O_2}. \tag{2.7}$$

A typical sensing performance is shown in fig. 14 (Yamazoe et al. 1987). At the working electrode, the following two-electron reduction of oxygen occurs and the formed O^- exchanges the F^- anion at the F site:

$$\mathrm{O_2 + 2e^- \rightleftarrows 2O^-}, \qquad \mathrm{O^- + F_F^x \rightleftarrows O_F^x + F^-}. \tag{2.8, 2.9}$$

The overall chemical reaction at the working electrode is

$$\mathrm{O_2 + 2F_F^x + 2e^- \rightleftarrows 2O_F^x + 2F^-}. \tag{2.10}$$

Here, F_F^x and O_F^x represent the F^- and O^- (monovalent) ions at F^- sites of LaF_3, respectively.

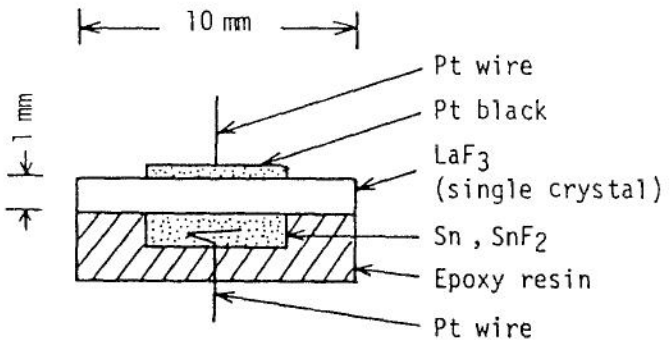

Fig. 13. Structure of the oxygen sensor element with an LaF_3 single crystal (Yamazoe et al. 1987). (Reprinted by permission of the publisher, Elsevier Sequoia S.A.)

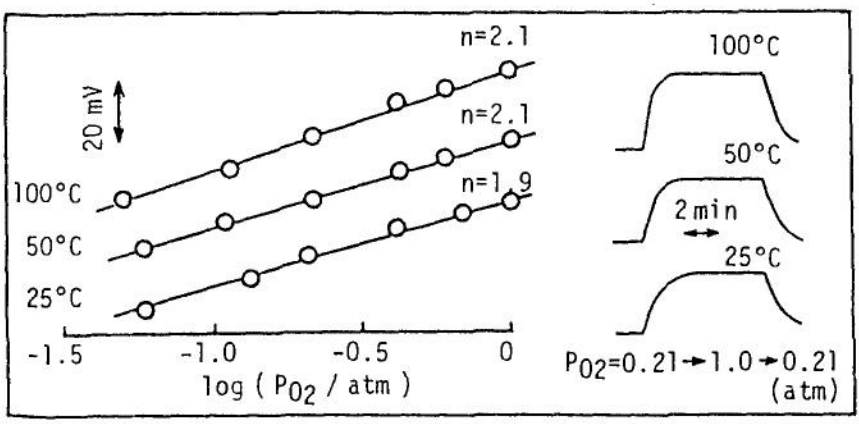

Fig. 14. Response curves of the oxygen sensor and dependence of EMF of the sensor on the oxygen partial pressure at various temperatures (Yamazoe et al. 1987). (Reprinted by permission of the publisher, Elsevier Sequoia S.A.)

The water vapor pretreatment, which changes the surface state of the LaF_3 electrolyte, enhances the sensing characteristics greatly. From IR spectra, the absorbance corresponds to the O–H stretching vibrations of $La(OH)_3$. The water vapor treatment forms $La(OH)_3$ on the electrolyte surface and this partial hydroxylation considerably contributes to enhancing the response.

The sensor also works well to detect oxygen dissolved in water, with a response time of 1 minute. In this case, the electrode reaction shows one electron per oxygen molecule as indicated below and the sensing electrode reactions are as follows:

$$O_2 + H_2O + e^- \rightleftarrows HO_2 + OH^-, \tag{2.11}$$

$$OH^- + F_F^x \rightleftarrows OH_F^x + F^-. \tag{2.12}$$

The overall reaction is written as

$$O_2 + H_2O + F_F^x + e^- \rightleftarrows HO_2 + OH_F^x + F^-. \tag{2.13}$$

Another difference between the sensing characteristics is that no pretreatment is necessary for oxygen detection in water.

The chemical reaction at the reference electrode is

$$SnF_2 + 2e \rightleftarrows Sn + 2F^-. \tag{2.14}$$

A sputtered LaF_3 film was also tested as a sensor electrolyte and the response rate was found to be faster than that of the single-crystal electrolyte. The non-stoichiometric nature of the sputtered film might accelerate the hydroxylation of the electrolyte surface.

The most advantageous features of this type of sensor are that it operates at room temperature, and a fast response. Rare-earth fluorides, which are used for fluoride sensing

(see sect. 3), can also work as a sensor for oxygen detection in the gas phase and even in an aqueous solution. These features are a consequence of the water-durable characteristics of the rare-earth fluoride.

2.10. *Carbon monoxide detection using a "stabilized zirconia"*

A unique proposed application for an yttria-stabilized zirconia is in carbon monoxide detection. A platinum electrode is attached on both sides of a zirconia electrolyte. One side is covered with a platinum catalyst on a porous alumina substrate and the Pt electrode is not in direct contact with the sample gas. Platinum on the substrate acts as a catalyst for CO oxidation. A cross-sectional view of the CO sensor is shown in fig. 15 (Okamoto et al. 1980) (the operating temperature is around 300°C). When carbon monoxide exists in the atmosphere, most will be catalytically oxidized by the oxygen in air during diffusion through the porous substance. Therefore, the gas that reaches the Pt electrode is not CO but a CO_2–O_2 mixture. On the other hand, on the surface of the platinum electrode without the catalyst, carbon monoxide is oxidized to CO_2 and causes an anomalous EMF. This potential shows a one-to-one correspondence to the CO concentration. The typical performance of the CO sensor in air at 300°C is shown in fig. 16 (Okamoto et al. 1980). The EMF output increases with the CO content, but the slope of the curve decreases gradually. This sensor can operate at temperatures between 260 and 350°C and no special O_2 reference gas is necessary.

Li et al. (1993) have recently reported a carbon monoxide sensor which uses CuO–ZnO instead of Pt-dispersed Al_2O_3 as the catalyst. Here, platinum is used as the electrodes. A CuO–ZnO mixture is coated on one electrode. CuO–ZnO–Al_2O_3 is a well known industrial catalyst used for water–gas generation and methanol synthesis. Carbon monoxide is strongly chemisorbed on CuO but rather weakly on ZnO. The ZnO addition to CuO contributes to enhance the mechanical strength and chemical stability. The response is appreciably fast, and in less than 2 minutes reaches 90% of the steady state value. However, it takes about 18 minutes to recover to the baseline value. The highest response was obtained operating at 450°C. At temperatures lower than 450°C, the EMF output appears even though no CO is present, indicating that the operating temperature of the sensor is restricted to temperatures higher than 450°C. A linear relationship between

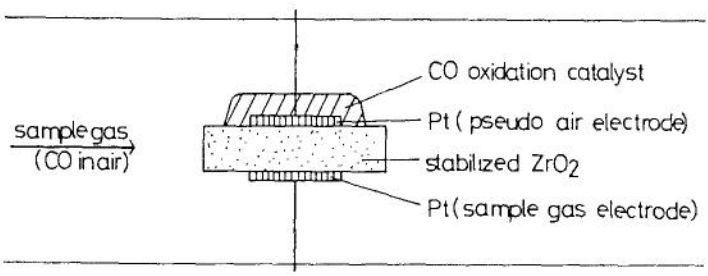

Fig. 15. Structure of the new CO gas sensor (Okamoto et al. 1980). (Reprinted by permission of the publisher, Elsevier Science Publishers B.V.)

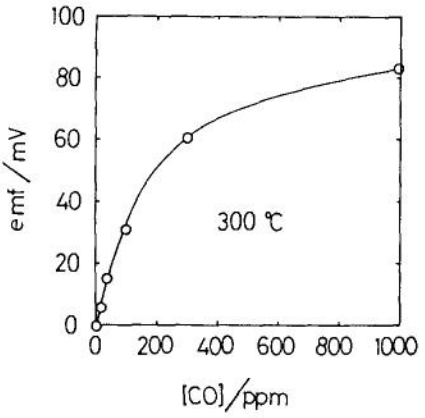

Fig. 16. Variation of the EMF response of the CO gas sensor with CO concentration (Okamoto et al. 1980). (Reprinted by permission of the publisher, Elsevier Science Publishers B.V.)

the sensor output and the CO content is obtained in the range from 0 to approximately 1500 ppm for the sensor with the CuO–ZnO catalyst, while the linear region for the sensor with the Pt–Al_2O_3 catalyst is from 0 to about 200 ppm. The differences between the two sensors are the operating temperature and the catalyst.

The CO sensing characteristics with Y_2O_3 mixed stabilized zirconia electrolyte have been appreciably improved by using the CuO–ZnO catalyst instead of Pt-dispersed Al_2O_3, and by raising the operating temperature to 450°C.

3. Fluorine sensors

3.1. *Introduction*

In the Ion Selective Electrode (ISE) field, the most popular and extensively used sensor is the glass electrode which is sensitive to a hydrogen ion. One of the other commercial sensors is a fluorine sensor, which is not as well known as the glass electrode.

Fluorine is widely distributed and found in sea waters, rocks, fossils, minerals and waste materials. Interest in the measurement of the fluorine content in these substances is related to the investigation of effects of fluorine ingestion over prolonged time periods. Furthermore, in the biomedical field, it is necessary to know the fluorine content in substances such as bone and tooth enamel after mineralization, and to monitor the uptake and metabolism in plants and animals in order to provide feedback to ongoing treatment. Therefore, the development of a simple and portable fluorine sensor, based upon the ISE, would be an important contribution in this field.

The discovery of the lanthanum fluoride electrode by Frant and Ross (1966) resulted in an appreciable improvement in the detection of fluorine. Metal–fluoride compounds, especially light rare-earth fluorides, show an excellent ionic conduction. The carrier in the solid fluoride is mainly anionic fluorine with some electronic conduction. This means that the material is a fluorine conducting solid electrolyte, a feature which highly enhances the

selective F^- sensing. Rare-earth fluorides such as LaF_3 and CeF_3 also can be excellent F^- ionic conductors. In these fluorides, aliovalent cation mixing into the rare-earth fluoride appreciably increases the F^- ionic conductivity. In the rare-earth series, europium doping into rare-earth fluorides appreciably improves the fluorine sensing characteristics (Lingane 1967, Lakshminarayanaiah 1976, Rechnitz 1967).

The fluoride ion can migrate in a solid more easily than the oxide anion because the ionic radius of F^- is very close to O^{2-} while the valency of F^- is half that of O^{2-}.

Another common fluoride ionic conductor is calcium fluoride. In order to increase the fluoride ionic vacancies, an aliovalent cation has to be mixed with CaF_2. In this case, trivalent rare-earth cations such as La^{3+}, Gd^{3+} are used as the mixing ion. In addition to these fluoride electrolytes, β-PbF_2 also shows a good F^- ionic conduction. The details of these two fluorine conducting electrolytes are described below.

3.2. *Several types of fluorine conducting solid electrolytes*

3.2.1. *Calcium fluoride*

The best known fluoride electrolyte is calcium fluoride which shows similar conductivity to zirconium oxide. There is anti-Frenkel-type disorder (F^- interstitials and vacancies) in CaF_2 and CaF_2 doped with YF_3. The doping of YF_3 in CaF_2 causes Schottky disorder as well as anti-Frenkel-type disorder, with vacancies on the cation sublattice; this doping offers little advantage. CaF_2 is chemically reactive at high temperatures, and is readily oxidized and hydrolyzed. Therefore, it is essential to keep the electrolyte in a dry protective atmosphere so as to prevent the deterioration of the pure fluorine ionic conducting characteristics.

3.2.2. *Lead fluoride*

One of the other widely investigated fluorine ionic conductors is lead fluoride. It exists in two crystallographic forms. One is α-PbF_2 which is orthorhombic, the other is β-PbF_2 which exhibits cubic symmetry. The lead fluoride which is used is often a mixture of both forms. Comparing these two forms, the β-form is more stable than the α-form at room temperature. Lead fluoride of the β-form also shows a high fluorine ionic conductivity. When the ionic conductivity between β-PbF_2 and CaF_2 is compared, the higher fluorine ionic conduction is found for β-PbF_2 because of the high polarizability of the Pb^{2+} ion.

The detailed properties of other common rare-earth fluoride conductors are described below.

3.3. *Characteristics of rare-earth fluorides*

Solid electrolyte candidates for a fluorine anion sensor are materials with the F^- anion. Some rare-earth fluorides show good F^- ionic conductivity. Rare-earth fluorides, in general, crystallize in two phases, one being hexagonal and the other orthorhombic as shown in fig. 17 (Thoma and Brunton 1966). Lanthanide trifluorides can be divided into four groups from the crystal structure point of view (Sobolev et al. 1976).

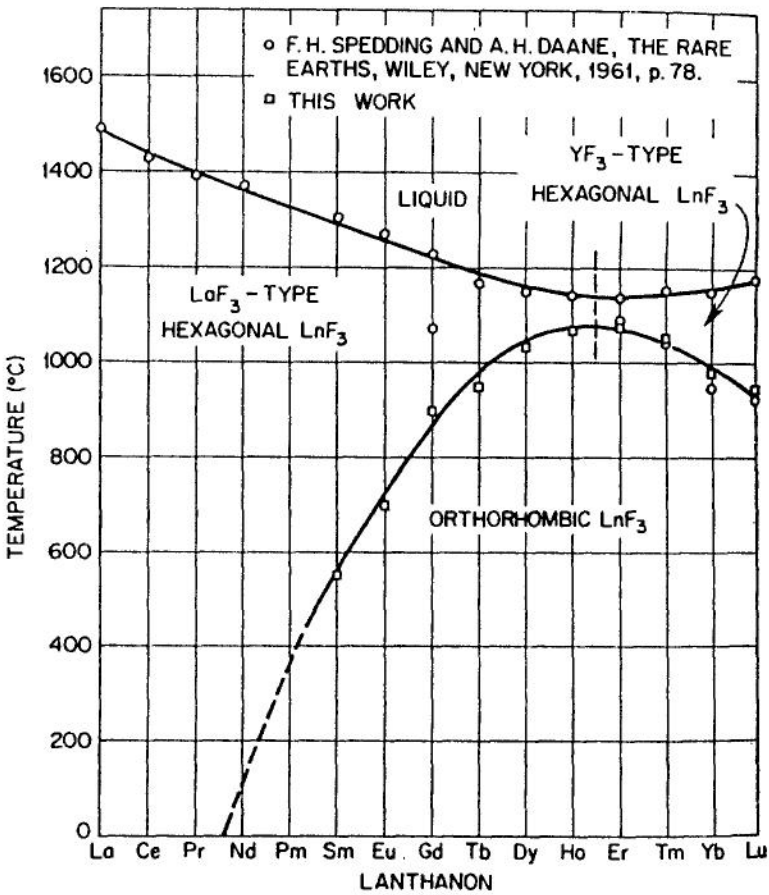

Fig. 17. Dimorphism among the rare-earth trifluorides (Thoma and Brunton 1966). (Reprinted by permission of the publisher, The American Chemical Society)

Group I includes the fluorides of the rare-earth elements from La to Nd, which, from liquid nitrogen to the melting temperature, crystallize in the tysonite LaF_3 structure. With increasing atomic number, the melting temperature decreases monotonically. Group II shows a dimorphic form from Sm to Gd: these fluorides are orthorhombic at lower temperatures (type β-YF_3), while they can take a tysonite LaF_3 structure at higher temperature. With increasing atomic number the α–β transformation temperature increases sharply and the fusion temperature decreases, while the temperature range where a stable tysonite can form becomes narrow. Group III contains TbF_3, DyF_3, and HoF_3, which crystallize only as orthorhombic β-YF_3, except at temperatures near the melting point. Group IV consists of the trifluorides from Er to Lu and Y. These RF_3 materials take dimorphic forms. At lower temperature the modification is the β-YF_3 form (orthorhombic), while at high temperature the structure is isostructual with the α-YF_3 form (hexagonal). The α–β transformation temperature decreases considerably from

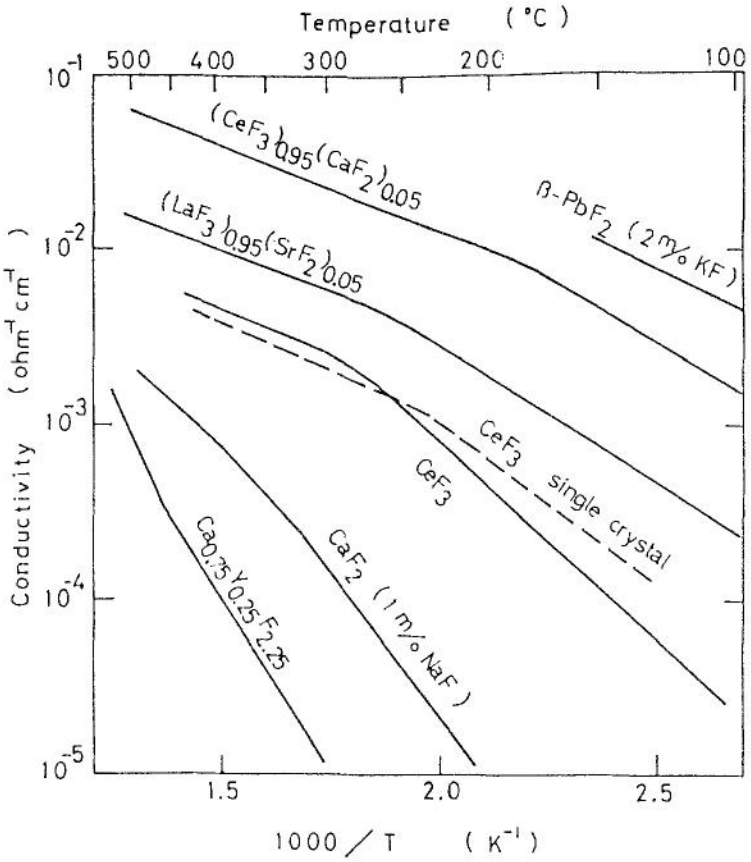

Fig. 18. Comparison of conductivities for various fluoride electrolytes (Takahashi et al. 1977). (Reprinted by permission of the publisher, The Electrochemical Society. Inc.)

ErF_3 to LuF_3. With increasing atomic number of the lanthanide, the characteristics, such as ionic radius, basicity, and polarization, decreases. The decrease in ionic radius results in the tendency for the coordination number (CN) to decrease. The CN of La^{3+} is equal to 11 in the tysonite form. The number becomes 9 in the orthorhombic β-YF_3 and decreases further to 8 in the hexagonal α-form.

Cerium trifluoride is hydrolyzed to cerium oxide in humid air at high temperature. Of the tysonite-type fluorides, cerium oxide mixed with calcium fluoride (5 mol%) shows the highest fluorine ionic conductivity as presented in fig. 18 (Takahashi et al. 1977).

As described above, the fluorides of the light rare earths from La to Nd have the hexagonal structure, while the fluorides of the rare earths from Sm to Lu exist in the orthorhombic form at room temperature. However, those with an orthorhombic structure transform to a hexagonal lattice at higher temperatures.

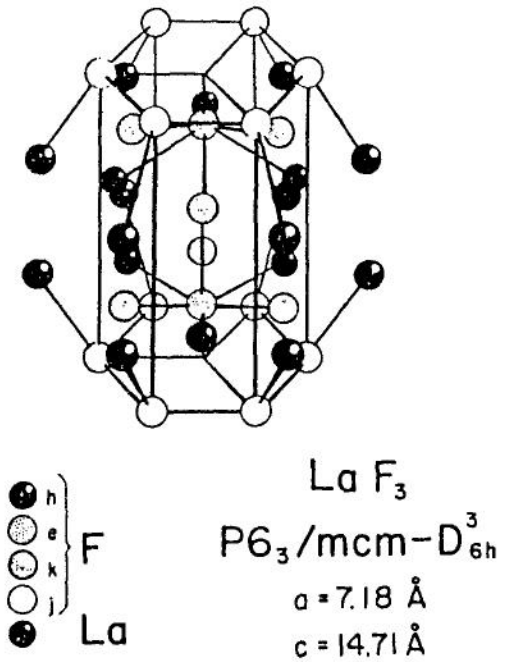

Fig. 19. Half of the unit cell of LaF_3 (Sher et al. 1966). (Reprinted by permission of the publisher, The American Physical Society)

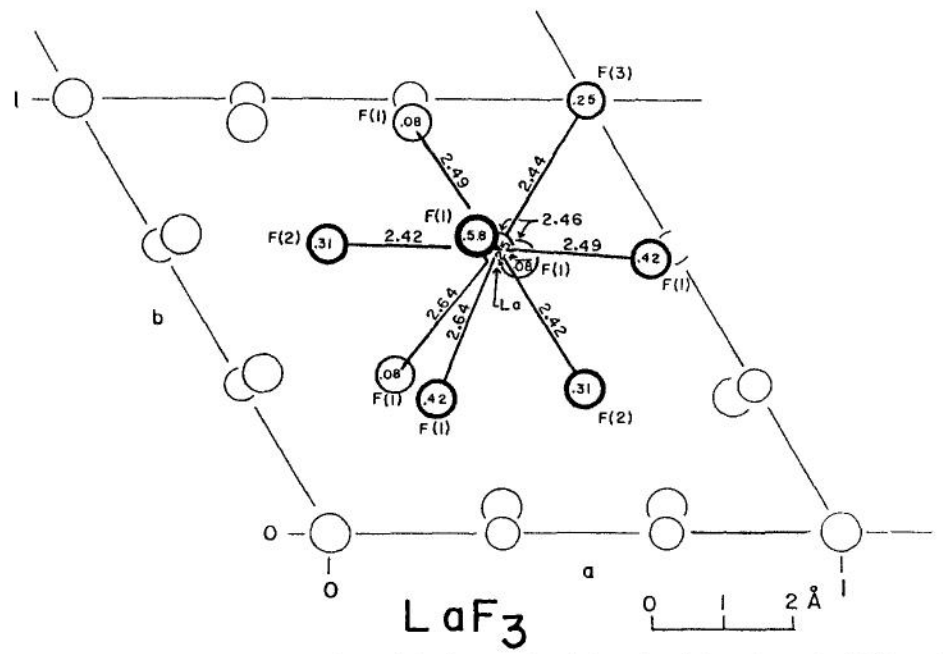

Fig. 20. Nine-fold coordination of lanthanum in lanthanum trifluoride as viewed down the *c*-axis (Zalkin et al. 1966). (Reprinted by permission of the publisher, The American Chemical Society.)

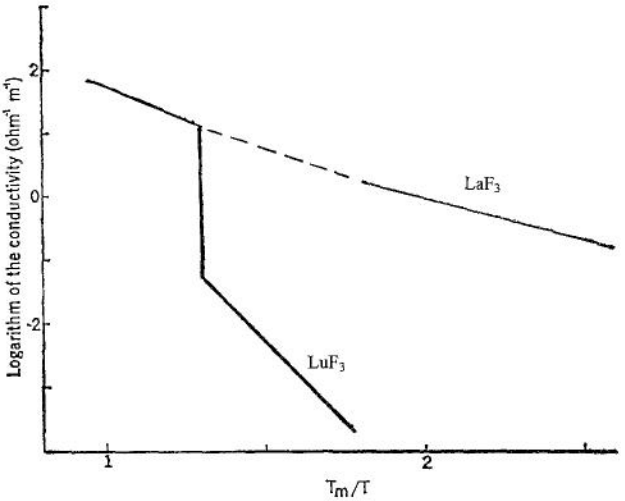

Fig. 21. Logarithms of specific conductivities of LaF_3 and LuF_3 as a function of the ratio (melting temperature/temperature) (O'Keeffe 1973). (Reprinted by permission of the publisher, The American Association for the Advancement of Science.)

The hexagonal crystal structure and the view down along the *c*-axis for RF_3 are presented in figs. 19 (Sher et al. 1966) and 20 (Zalkin et al. 1966). $F^-(2)$ and $F^-(3)$ in fig. 20 exist between the hexagonal lattice consisting of the La^{3+} cation and six $F^-(1)$ anions. Both $F^-(2)$ and $F^-(3)$ have been found, by F^{19} NMR measurement (Goldman and Shen 1966), to be equivalent, from an ionic migration point of view. The fluorine conduction occurs through Schottky defects which appear at $F^-(2)$ and $F^-(3)$ sites, and this hexagonal structure with defects is very effective for fluorine anion migration in the fluoride bulk. Representative conductivity results for LaF_3 and LuF_3 are shown in fig. 21 (O'Keeffe 1973). The electric conductivity of LaF_3 gradually decreases with a reduction in temperature. However, the conductivity of LuF_3 abruptly decreases by more than two orders of magnitude in cooling from high temperature. LaF_3 retains a hexagonal form, while hexagonal LuF_3 transforms to orthorhombic as indicated in fig. 17. The phase transformation from hexagonal to orthorhombic is the main reason for the sudden decrease in conductivity. The hexagonal LaF_3 retains a hexagonal phase even at room temperature. If we extrapolate the conductivity of LaF_3 toward a higher-temperature region, as indicated by a dashed line in the figure, the conductivity of the hexagonal LaF_3 is almost consistent with that of the hexagonal LuF_3. This means that the rare-earth fluorides, in the hexagonal form, are excellent electrolytes for F^- ionic conduction.

One of the main applications of the fluorine conductor in the sensor field is the measuring of the fluorine content in test solutions. In most cases, the operating temperature is around room temperature because solutions are aqueous. Therefore, the candidate electrolytes for the sensor are the rare-earth fluorides which retain the hexagonal structure at room temperature. In addition, the fluoride electrolytes should be water stable

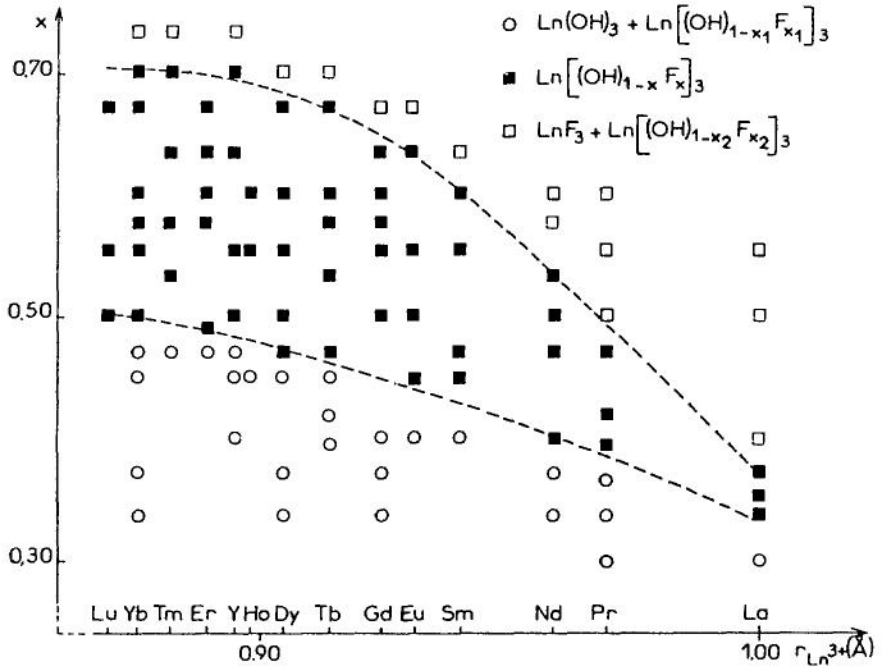

Fig. 22. Limiting compositions of $R[(OH)_{1-x}F_x]_3$ phases as a function of the R element at 450°C and $4k_B$ (Marbeuf et al. 1971). (Reprinted by permission of the publisher, Academic Press, Inc.)

since they are immersed in aqueous solution. Hence, the fluorides suitable for the sensor material are restricted to those of the lighter rare earths from La to Nd or Sm, which retain a hexagonal phase. In those rare earths, LaF_3 is the material of preference. Other rare-earth fluorides, such as hexagonal NdF_3 and SmF_3, are also suitable but these are not commercially used because they are too expensive to prepare as membranes. In addition, the fluorides of Nd and Sm are less stable than LaF_3, as shown in fig. 22 (Marbeuf et al. 1971).

The LaF_3 sensors are made of single crystals. Polycrystalline LaF_3 is not suitable as a sensor component because of its high rate of solubility. The strong bonding between the atoms in the single crystal results in a low solubility. In the commercial application, divalent europium is doped into the LaF_3 single crystal and embedded within the sensor component to make a practical electrolyte. Europium doping is important to increase the ionic conductivity in order to improve the fluorine sensing characteristics.

3.4. *Detection mechanism of fluorine sensors*

The base material used as a solid electrolyte is lanthanum fluoride. In the fluoride, the only permeable carrier is the fluorine anion in the single-crystal membrane. The inside of the tube is filled with a standard fluoride solution (Lingane 1967) and, when the sensor is

immersed into test solutions with unknown F^{-1} ion content, fluorine ions migrate through the LaF_3-based electrolyte from the compartment with a higher fluorine concentration to the lower one. The Nernst equation is as follows:

$$E = C_1 + \frac{RT}{F}\ln\left(\frac{(F^-)_{\text{internal}}}{(F^-)_{\text{external}}}\right) \quad (C_1 = \text{constant}). \tag{3.1}$$

Since the fluorine concentration in the internal standard is known, eq. (3.1) simplifies to

$$E = C_2 - \frac{RT}{F}\ln(F^-)_{\text{external}} \quad (C_2 = \text{constant}). \tag{3.2}$$

Because C_2 is constant and independent of the F^- content in test solutions, the F^- concentration in the test solution is simply calculated from eq. (3.2) by the direct measurement of the sensor's EMF output.

3.5. *Performance of the sensor*

Figure 23 (Frant and Ross 1966) shows the practical EMF response to the F^- variation, with a response which follows the Nernst equation from 1 to 10^{-6} M. In drinking water, the average F^- content is around 5×10^{-4} M, so this type of sensor is well suited for the analysis of most drinking water. One of the great advantages of using a LaF_3 electrolyte is that no serious interferences are observed for the most common anions coexisting in the solution. The major interfering anion is the hydroxide anion. For example, the sensor output as a function of pH with several fluorine concentrations is shown in fig. 24 (Frant and Ross 1966). In the higher pH region, the EMF output corresponding to the F^- content for both 10^{-3} and 10^{-5} M test solutions changes with pH. It is clear from the results that the OH^- concentration influences F^- sensing, and that the hydroxide anion interferes more seriously in dilute solutions.

The mechanism of hydroxide anion interference is as follows. When the LaF_3-based ISE is immersed in water, the following reaction will occur on the LaF_3 solid surface (Koryta and Stulik 1983, Portier 1976):

$$LaF_3 + H_2O \rightleftarrows LaOF + 2HF. \tag{3.3}$$

Since O^{2-} and OH^- anionic radii are slightly larger than F^-, they can diffuse through the fluoride lattice and change the LaF_3 properties on the surface (Zachariasen 1951). When the hydroxide anions are present in a test solution, various solid solutions of $La[(OH)_{1-x}F_x]_3$ are formed (Marbeuf et al. 1971, Portier 1976). Consequently, the presence of hydroxide anions in solution significantly interferes with F^- sensing. Several cations such as Al^{3+}, Be^{2+}, or Fe^{3+} also interfere with F^- sensing by forming a complex with fluoride anions. The details of the cation interference have been described by Bock and Strecker (1968), Mesmer (1968), and Baumann (1968). However, even in the presence

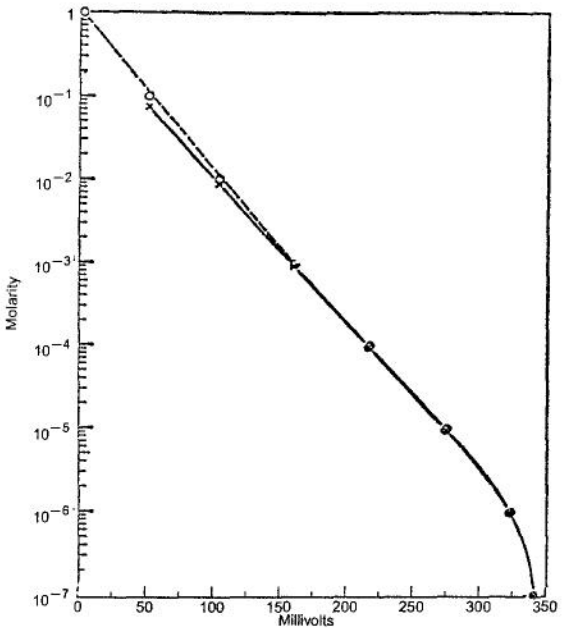

Fig. 23. Electrode response to fluoride concentration (dashed line) and calculated activity (solid line) in pure KF solutions (Frant and Ross 1966). (Reprinted by permission of the publisher, The American Association for the Advancement of Science.)

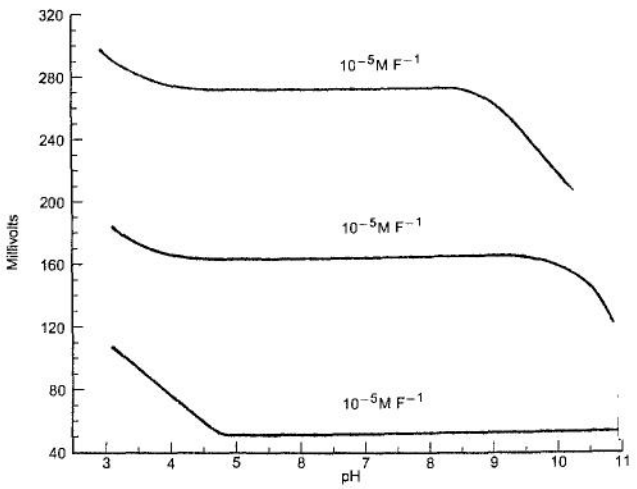

Fig. 24. Electrode response as a function of pH and fluoride concentration. Hydroxyl ion interference depends on the fluoride level (Frant and Ross 1966). (Reprinted by permission of the publisher, The American Association for the Advancement of Science.)

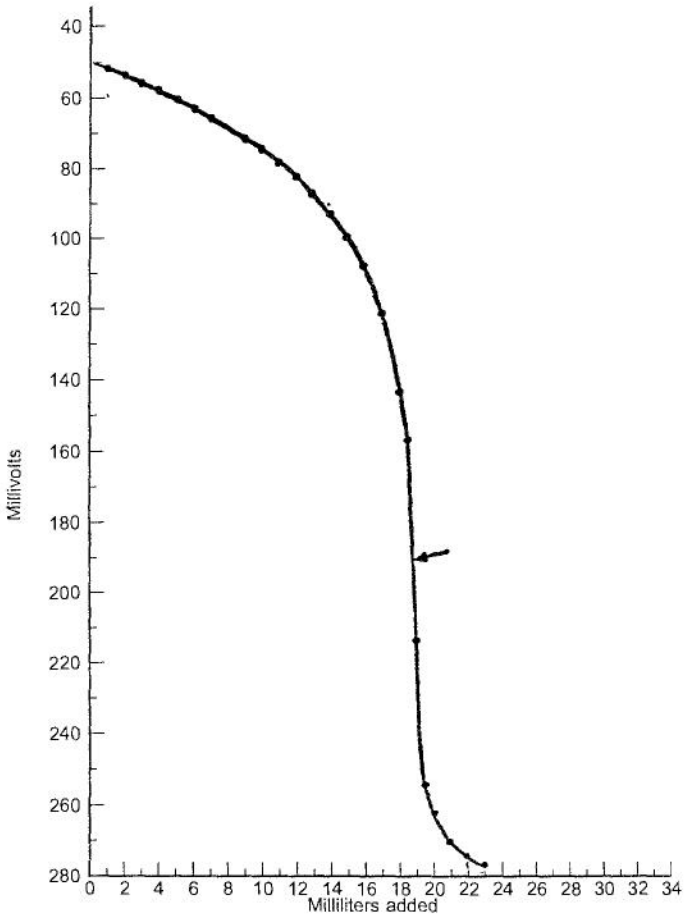

Fig. 25. Titration of NaF with $La(NO_3)_2$ (Frant and Ross 1966). (Reprinted by permission of the publisher, The American Association for the Advancement of Science.)

of such interfering cations, it is possible to measure the fluorine content accurately by eliminating those cations by precomplexing with phosphoric acid.

The response time of the sensor is also a function of the fluorine concentration. It is less than half a second for solutions higher than 10^{-3} M and shorter than 3 minutes at 10^{-6} M (Koryta and Stulik 1983, Srinivasan and Rechnitz 1968).

Another interesting application of this F^{-1} sensor is its use as the end point indicator for a titration. Figure 25 (Frant and Ross 1966) presents the result of NaF titration with $La(NO_3)_3$. The sensor clearly indicates an end point.

In many applications rare earths are used as additives. As mentioned in sect. 2, yttrium oxide is doped into zirconia to stabilize the appropriate structure for ionic conduction.

However, in this fluorine sensor, the base electrolyte is composed of the lanthanum cation with the fluorine anion. In addition, one unusual property is that the sensor can operate even when directly immersed into aqueous solutions at room temperature. The realization of the application is greatly dependent on two facts: LaF_3 is stable in water and it shows an excellent fluorine conduction even at room temperature. These remarkable characteristics permit the use of LaF_3 as a simple and portable sensor and have led to its commercial use on a worldwide scale.

3.6. *Other gas sensing with lanthanum fluoride*

Lanthanum fluoride has also been used at ambient temperatures as a constituent of a solid-state electrode for reducible gases by constructing thin-film metal/lanthanum fluoride/metal cells. By biasing the cell above a certain characteristic potential, which depends on the electron affinity of the gases, the cell conductivity increases with the gas content. For gases such as CO_2, SO_2, and NO, the current output increases with increasing gas concentration. The lifetime of the sensor is limited to several months, due to electrode degradation. However, the electrodes are regenerated by heating to 300°C in a high vacuum for a few hours. The details of the sensing properties have been described by LaRoy et al. (1973).

4. Humidity sensors

4.1. *Introduction*

Humidity essentially exists everywhere on earth. It is necessary for most living things to have water in some form to survive. The maintenance of proper humidity is important in the growing of decorative plants and crops and it is desirable to control humidity to obtain the best flavor when food is being cooked. Control of humidity to obtain amenable conditions in working and leisure activities for high productivity and a more comfortable environment is also preferred. These are incentives to develop a compact, inexpensive water vapor detector. Installation of these sensors at specific sites would be effective to monitor and control humidity.

The three conventional methods of measuring humidity utilize electrolytes, organic compounds, or metal oxides, respectively. The electrolyte humidity sensors either form an electrolyte solution by absorption of water vapor or electrolyze water vapor on the sensing element to obtain the water vapor concentration by measuring the total amount of electric current required. These electrolyte sensors use water in solution or water absorbed on the element, and so the operating temperatures are restricted to ambient temperature. The second type of humidity sensor uses organic compounds; the detecting method uses the resistance, the capacitance, or the weight change by water absorption. The third type uses a metal oxide as a sensing material. A typical example is the chromium oxide–magnesia (magnesium oxide) humidity sensor, which is used in electric appliances. In

Table 3
Application areas by industry, with operational temperature and humidity ranges (Fagan and Amarakoon 1993) (reprinted by permission of the publisher, The American Ceramic Society)

Application area	Operating temperature (°C)	Humidity range (% RH)	Remarks
Home electric appliances			
Airconditioners	5–40	40–70	air-conditioning
Dryers	80	0–40	drying of clothing
Microwaves	5–100	2–100	cooking control
VTRs	−5–60	60–100	dew prevention
Automobiles			
Rear window defogger	−20–80	50–100	dew prevention
Medical			
Medical treatment equipment	10–30	80–100	respiratory equipment
Incubators	10–30	50–80	air-conditioning
Industry			
Textile	10–30	50–100	spinning
Dryers	50–100	0–50	ceramic, timber drying
Powder humidity	5–100	0–50	ceramic material
Dried foodstuff	50–100	0–50	–
Electronic parts	5–40	0–50	magnetic heads, LSI's, IC's
Agriculture, forestry, stockbreeding			
Greenhouse air-conditioning	5–40	0–100	air-conditioning
Dew prevention in tea-leaf growing	−10–60	50–100	dew prevention
Broiler farming	20–25	40–70	health control
Measurement			
Thermostatic bath	−5–100	0–100	precision measurement
Radiosonde	−5–40	0–100	precision meteorological measurement
Hygrometer	−5–100	0–100	control recorders
Others			
Soil humidity	–	–	plant growing, landslides

practice, TiO_2 is mixed with $MgCr_2O_4$ to increase the thermal and mechanical strength. Water vapor is first absorbed on the oxide surface and a proton is formed. The number of protons increases with humidity and the resistance of the sensor element monotonically decreases with increasing humidity. In most cases, the hydroxide absorbed on the metal-oxide surface is difficult to remove. However, water vapor on the $MgCr_2O_4$–TiO_2 solid solution is easily removed.

Table 3 (Fagan and Amarakoon 1993) lists representative and potential uses for humidity sensors. There still are some limitations. Ceramic sensors require regeneration

and cleaning with continuous use. For polymeric sensors, frequent recalibration is also needed, especially in atmospheres with relative humidities of more than 50%.

Since the 1980's, a new type of humidity sensor, based on a solid electrolyte, has been under development. The sensor uses a protonic conductor as a base component and makes a galvanic cell of a water vapor gas concentration type. When the characteristics of this new type of sensor are compared with conventional humidity sensors, two representative advantages of this sensor are seen. The sensor output is an EMF change, and is suitable for continuous operation with a fast response. The sensor can operate at higher temperatures, because the solid electrolyte is stable even at elevated temperatures. These features are expected to accelerate the development of this type of sensor. The base material is a perovskite-type strontium cerate $SrCeO_3$. The pure cerate is not a protonic conductor.

Doping of a trivalent rare earth into $SrCeO_3$ is a key point in applying the cerate as the electrolyte for a humidity sensor.

4.2. *Protonic conducting solid electrolytes*

There are several types of protonic conductors. One of the representative protonic conductors is uranyl phosphoric acid hydrate ($HUO_2PO_4 \cdot 4H_2O$:HUP). The electrolyte is based on the hydrate. Protonic conductivity occurs through the interexchange of hydrogen by the rotation of H_2O or H_3O^+ molecules in the hydrates. Therefore, the protonic conductivity of these solid electrolytes decreases with reducing humidity. These electrolytes are restricted to use around room temperature, since they cease to be protonic conductors if they are dehydrated.

Another type of protonic conductor is H_3O^+ or NH_4^+ β- or β″-alumina. In the β- or β″-alumina, the mobile ion species are Na^+ ions. Therefore, Na^+ ions are exchanged by H_3O^+ or NH_4^+ in the H_3O^+ or NH_4^+ β- or β″-alumina.

Recently, a protonic conductor based on strontium or barium cerate ($SrCeO_3$, $BaCeO_3$) has been developed. In these cerates, protons do not exist in the solid at all. This feature is apparently different from the two electrolytes mentioned above. One of the specific characteristics of the cerate electrolytes is that they can work as effective conductors at elevated temperatures compared with the hydrate protonic conductor and the ionically exchanged H_3O^+ or NH_4^+ β- or β″-alumina.

4.3. *The characteristics of $SrCeO_3$-based materials*

Pure strontium cerate, $SrCeO_3$, is not a protonic conductor, and the oxide is low in electronic conductivity. However, by substitution on the Ce^{4+} site with a trivalent rare-earth cation such as Yb^{3+}, Sc^{3+}, or Y^{3+}, the doped $SrCeO_3$ shows a p-type conduction when neither hydrogen nor water vapor exist in the atmosphere. This means that hole conduction appears in the solid. When the oxide ceramics are heated to several hundred degrees centigrade in the presence of water vapor or hydrogen gas, protonic conduction appears and the electronic conduction is reduced. The tetravalent cations are the rare-earth

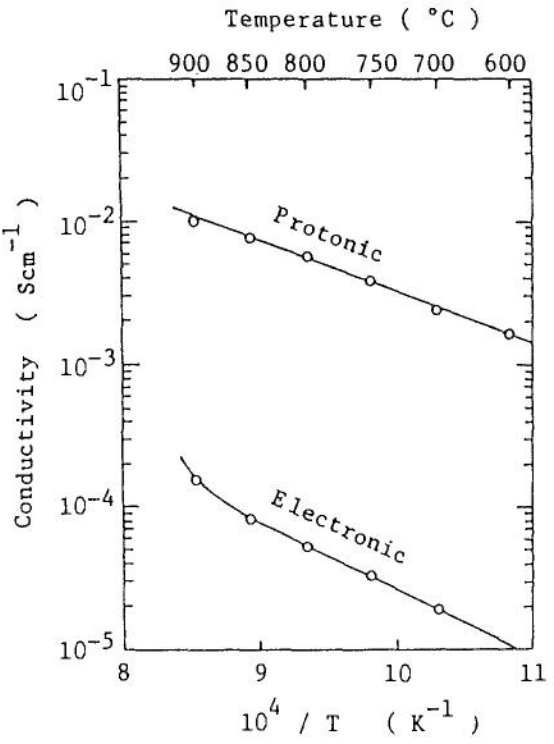

Fig. 26. Electric conductivity variation with temperature for $SrCe_{0.95}Yb_{0.05}O_{3-x}$ in hydrogen atmosphere (Iwahara et al. 1986). (Reprinted by permission of the publisher, Elsevier Science Publishers B.V.)

Ce^{4+} ions, so the best candidates for the dopant are stable trivalent rare earths whose ionic radii are almost the same size as Ce^{4+}.

The electric conductivity of one representative rare-earth substituted $SrCeO_3$ materials is shown in fig. 26 (Iwahara et al. 1986); these measurements were carried out in a humid hydrogen atmosphere. The conductor is almost purely ionic. The electronic conductivity is about two orders of magnitude lower than the ionic conductivity. Since chemisorbed water does not exist on the oxide surface at the temperature where this electrolyte is applied, protons conduct, not on grain boundaries, but through the bulk lattice. In the cerate electrolyte, the most mobile ions are the protons and this feature enhances the selectivity to humidity sensing. The originality of this new humidity sensor is that the sensor beneficially applies the properties of the solid electrolyte to greatly improve the sensing ability. In addition, this electrolyte is moderate in its hardness and is less porous in pellet form (< 5%). These properties eliminate the gas leakage through the electrolyte which is a critical problem in practical applications. These appreciable advantages greatly encourage researchers to proceed with further experiments for practical applications of this material as a humidity sensor.

Figure 27 (Iwahara 1988) shows the σ vs. T^{-1} relationship of representative protonic conductors. The demand is greatly increasing to precisely control humidity at high temperatures in the textile, wood and food industries. A protonic conductor which is

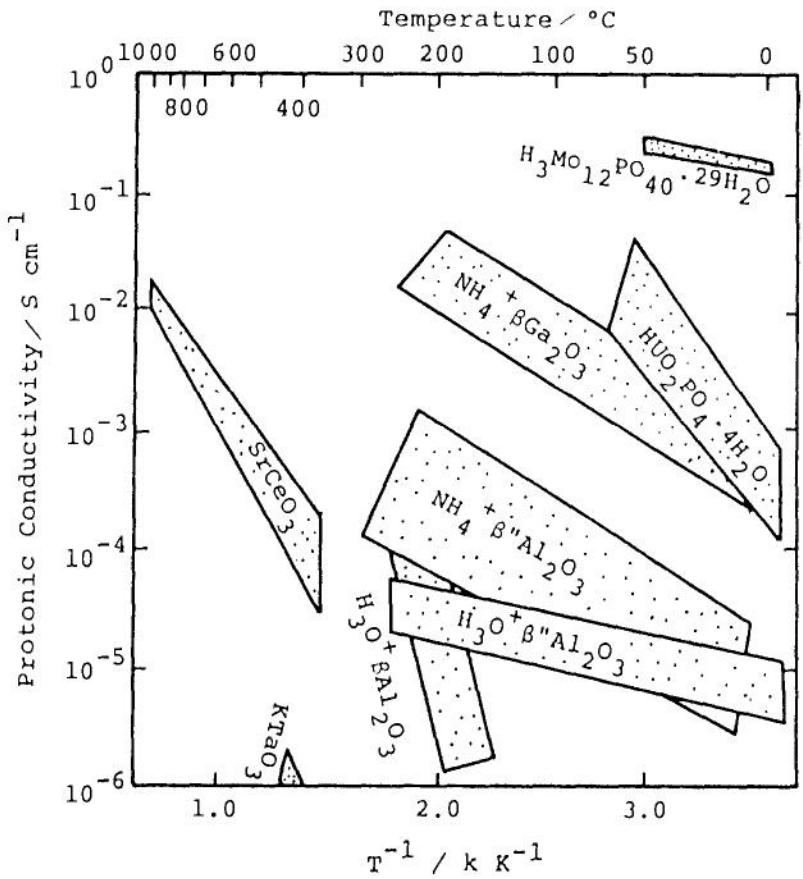

Fig. 27. Conductivity variations with temperature for representative protonic conductors (Iwahara 1988). (Reprinted by permission of the publisher, Elsevier Science Publishers B.V.)

stable at elevated temperatures is suitable for such a usage. All the electrolytes, except $SrCeO_3$ and $KTaO_3$ electrolytes, are not stable above 400°C. Since $KTaO_3$ is considerably lower in conductivity, the only protonic conducting candidate for a practical sensor is $SrCeO_3$-based. In the $SrCeO_3$-based materials, useful cerates are the electrolytes with higher conductivity. These high-conductivity electrolytes accurately detect the ambient humidity with a fast response.

In order to increase the electric p-type conductivity, several rare-earth cations were doped into the Ce site of the $SrCeO_3$ electrolyte. The highest conductivity was observed for the cerate with Yb substitution (Iwahara et al. 1981). Of the three rare-earth cations, Yb^{3+}, Y^{3+}, and Sc^{3+}, Yb^{3+} has the closest ionic radius to Ce^{4+}. It is easily concluded that the best candidate dopant is Yb. Since the hole concentration produced by the substitution is closely related to the humidity sensing mechanism, the hole concentration in the solid electrolyte directly influences the applicability for the humidity sensor. The

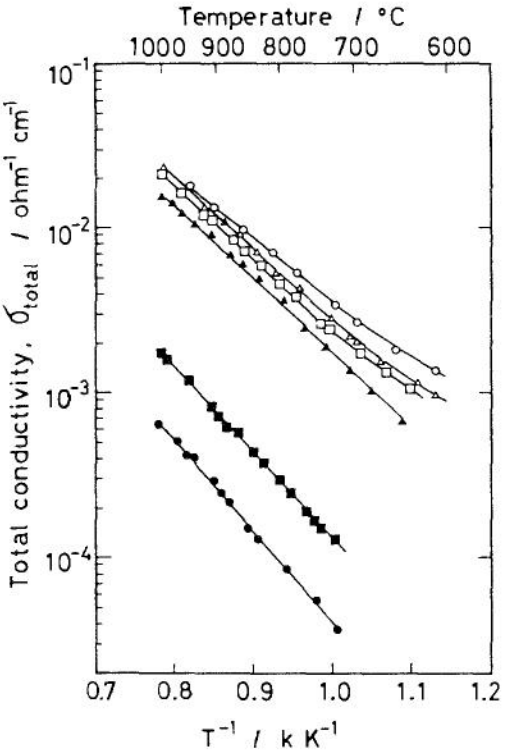

Fig. 28. Total conductivity changes with temperature of $SrCe_{1-x}Yb_xO_{3-x}$ in air dried with P_2O_5. Solid circle, 0 ("nominally pure"); solid square, 0.02, solid triangle, 0.03; open square, 0.05; open triangle, 0.07; open circle, 0.10 (Uchida et al. 1983). (Reprinted by permission of the publisher, Elsevier Science Publishers B.V.)

optimum amount of Yb doping in the cerate is clear from the conductivity results. (The measurements were conducted in a non-humid condition.) With Yb doping, holes are produced in the electrolyte and the conductivity increases appreciably as shown in fig. 28 (Uchida et al. 1983). The monotonic increase in conductivity saturates at approximately 5 at.% Yb, but this is enough to obtain a cerate with high electric conductivity.

One of the representative methods to check the ionic conductivity of the solid cerate is to measure the transference number of the mobile ion. (The proton transference number, t_{H^+} is measured by the water vapor gas concentration cell by changing the oxygen pressures on both sides of the cell and keeping the water pressure constant.) Figure 29 (Uchida et al. 1982) shows the results. The transference number of hydrogen monotonically decreases with the increase of oxygen pressure. The increase in oxygen pressure causes an enhancement of the hole concentration in the solid, while the protonic conduction is independent of the oxygen pressure. The total conductivity increases without changing the ionic conductivity and consequently decreases the hydrogen transference number. When no oxygen exists in either compartment, t_{H^+} becomes almost unity at lower temperatures.

A three-dimensional illustration of the total and the protonic conductivity is shown in fig. 30 (Uchida et al. 1983). The hydrogen transference number increases with increasing

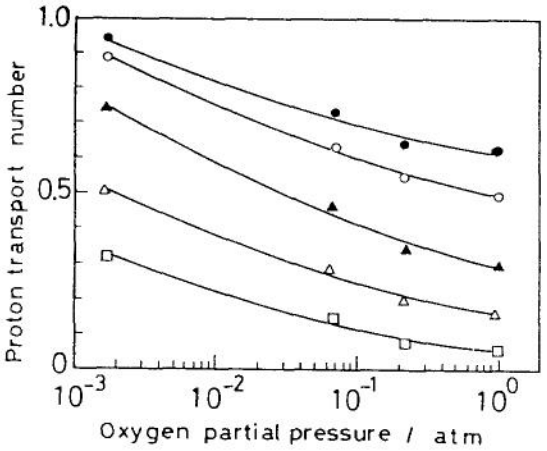

Fig. 29. Proton transport number with oxygen partial pressure for $SrCe_{0.95}Yb_{0.05}O_{3-x}$. Solid circles, 600°C; open circles, 700°C; solid triangles, 800°C; open triangles, 900°C; open squares, 1000°C (Uchida et al. 1982). (Reprinted by permission of the publisher, Chapman and Hall.)

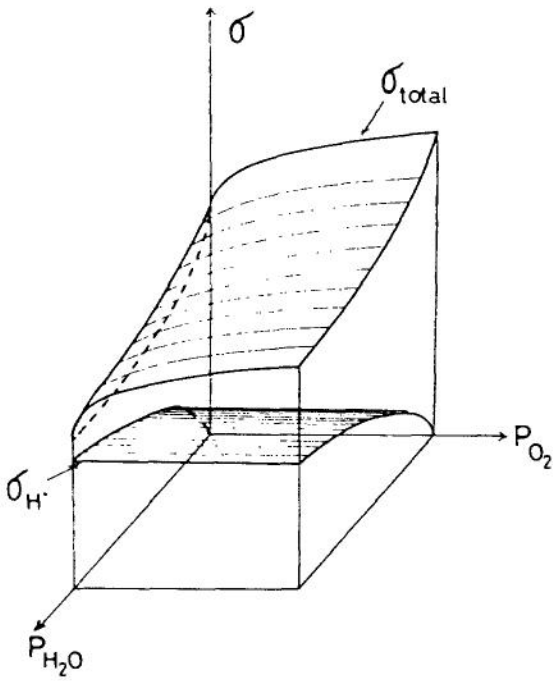

Fig. 30. Schematic illustration of the three-dimensional representation of total conductivity σ_{total} and the proton conductivity σ_H as a function of p_{O_2} and p_{H_2O}. (Uchida et al. 1983). (Reprinted by permission of the publisher, Elsevier Science Publishers B.V.)

p_{H_2O}, while the total conductivity decreases as the p_{H_2O} increases. The number of holes produced by Yb doping in $SrCeO_3$, is reduced by the reaction with water vapor and lowers the total conductivity. However, the reaction between holes and water vapor produces protons and increases the t_{H^+} as a result. In the $SrCe(Yb)O_3$ solid, no proton is present in the electrolyte. The cerate becomes a protonic conductor, when hydrogen atoms enter the structure as protons. Therefore, hydrogen solubility in the $SrCe(Yb)O_3$ solid electrolyte

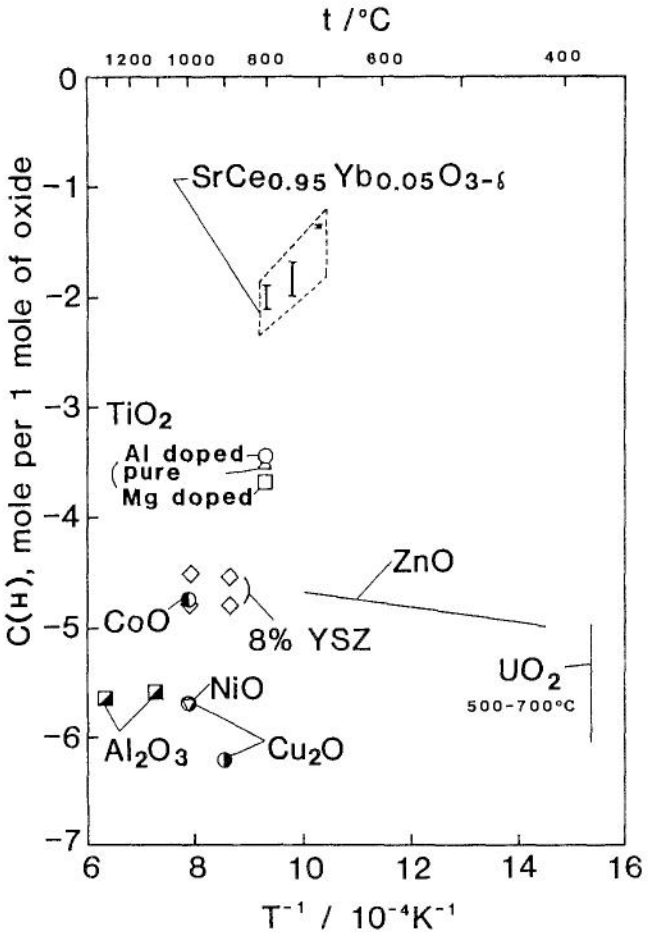

Fig. 31. Solubility of hydrogen in various oxides (Ishigaki et al. 1986). (Reprinted by permission of the publisher, Elsevier Science Publishers B.V.)

should be closely related to the protonic conduction characteristics of the electrolyte, and appreciably influence the humidity sensing performance. Figure 31 (Ishigaki et al. 1986) presents a comparison of the hydrogen solubility in $SrCe(Yb)O_3$ with other oxides. We can easily find that an extremely large amount of hydrogen can be dissolved in the $SrCe(Yb)O_3$ electrolyte. The high solubility of hydrogen is expected to greatly enhance the protonic conduction of the cerate electrolyte.

4.4. *The principle of humidity detection*

The humidity sensor is also based on a galvanic gas concentration cell as shown in fig. 32 (Iwahara et al. 1983a). By the doping of aliovalent rare-earth cations into $SrCeO_3$,

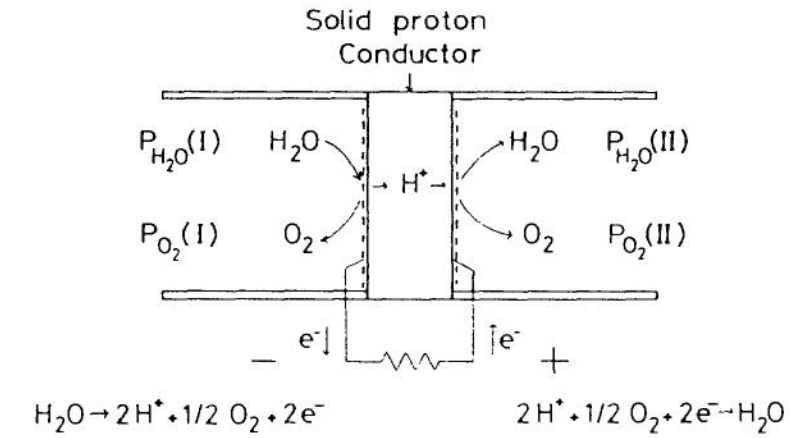

Fig. 32. Mechanism of a steam concentration cell using a solid protonic conductor $PH_2O(I) > PH_2O(II)$ (Iwahara et al. 1983a). (Reprinted by permission of the publisher, Chapman and Hall.)

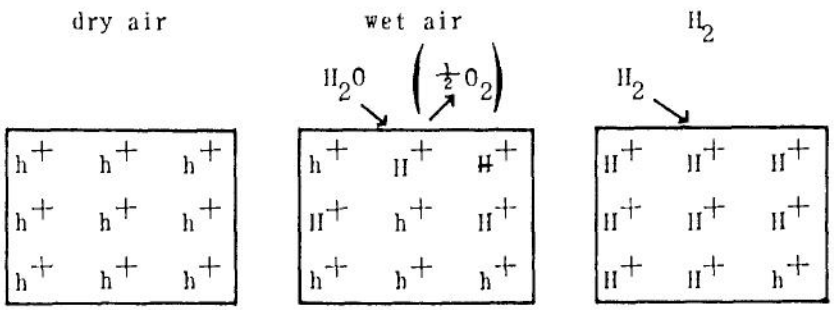

Fig. 33. Appearance of protonic conduction in $SrCeO_3$-based oxides (Iwahara 1988). (Reprinted by permission of the publisher, Elsevier Science Publishers B.V.)

electron holes are produced by charge compensation as shown in fig. 33 (Iwahara 1988). When water vapor exists in the atmosphere, holes in p-type $SrCe(Yb)O_3$ react with water vapor as indicated in the following equation and produce protons to become a protonic electrolyte:

$$H_2O + 2h^+(\text{oxide}) \rightleftarrows 2H^+(\text{oxide}) + \tfrac{1}{2}O_2. \tag{4.1}$$

This equation can be rewritten as

$$H_2O \rightleftarrows 2H^+ + \tfrac{1}{2}O_2 + 2e^-. \tag{4.2}$$

In the case of the water vapor concentration of compartment (I) being higher than that of compartment (II), the half reaction is described by the equations shown in fig. 32.

Combining the two half reactions, the theoretical EMF is obtained by the following equation:

$$E = \frac{RT}{2F} \ln \left(\frac{p_{H_2O}(I)}{p_{H_2O}(II)} \right) \left(\frac{p_{O_2}(II)}{p_{O_2}(I)} \right)^{1/2}. \tag{4.3}$$

When $p_{O_2}(I)$ and $p_{O_2}(II)$ are almost equal, e.g. similar to the atmospheric oxygen pressure, the EMF equation simplifies to

$$E = \frac{RT}{2F} \ln \left(\frac{p_{H_2O}(I)}{p_{H_2O}(II)} \right). \tag{4.4}$$

When $p_{H_2O}(I)$ is controlled at a constant pressure, the unknown humidity in compartment (II) can be easily calculated from this equation.

4.5. *Humidity sensing performance*

The cross-sectional view of the apparatus used for the experimental measurements is illustrated in fig. 34 (Iwahara et al. 1983a). Two types of the sensor were tested. The two compartments were divided by a solid electrolyte pellet in both cells. In the A-type, a gas with constant p_{H_2O} was passed through the tube. In the B-type sensor a molecular sieve serves as a water vapor reservoir. The representative EMF results are shown in fig. 35 (Iwahara et al. 1983a). A stable and almost linear relation was observed between the EMF output and the logarithm of p_{H_2O}. A good agreement between the measured EMF and the theoretical EMF of eq. (4.4) is obtained in the lower p_{H_2O} region.

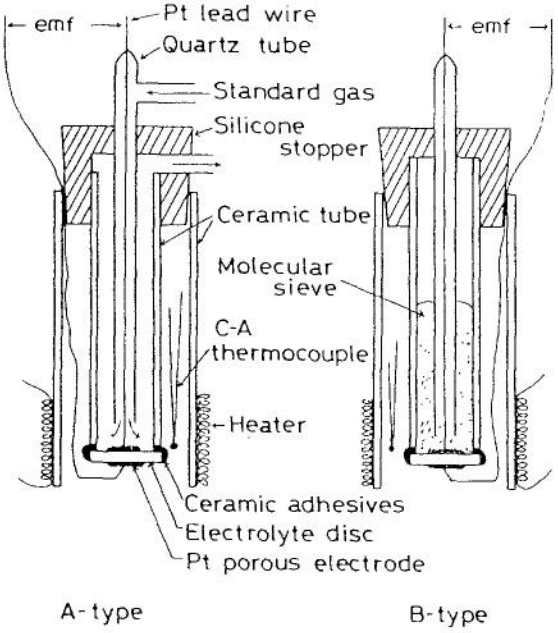

Fig. 34. Cross-sectional views of the galvanic cell-type humidity sensors (Iwahara et al. 1983a). (Reprinted by permission of the publisher, Chapman and Hall.)

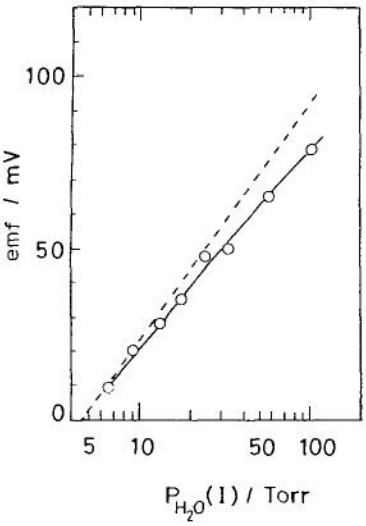

Fig. 35. EMF response of the A-type sensor to p_{H_2O}(I). Working temperature is 400°C (dashed line shows theoretical EMF) (Iwahara et al. 1983a). (Reprinted by permission of the publisher, Chapman and Hall.)

The response to humidity is a key factor for practical applications. The sensor response was monitored with both increasing and decreasing p_{H_2O}. Both EMF outputs respond accurately to the humidity change. The humidity sensor response was also checked for quickly changing water temperatures, by pouring hot water into the vessel where the sensor was attached (Iwahara et al. 1983a). The EMF output increased steeply and a stable EMF was obtained within half a minute. The B-type sensor also shows a linear response to the EMF-logarithm of the p_{H_2O} relationship. However, in both types, the conductive species in the solid electrolyte are not protons alone. The relation between the EMF output and transference number is

$$E = t_{H^+} \times E_0, \tag{4.5}$$

where E_0 is EMF when the transference number is unity. The exact t_{H^+} is shown in fig. 30. The accurate humidity can be obtained by calculation, using eqs. (4.4) and (4.5). Other gases may influence the selective humidity sensing. A small amount of hydrogen, butane, or carbon dioxide gas was injected with the humid air into the vessel for the B-type sensor. The results are listed in table 4 (Iwahara et al. 1983a). The coexistence of CO_2 does not influence humidity detection. Butane causes a decrease in EMF. This occurs because of the adsorption of butane on the electrode surface. However, the decrease is quite small, as shown in table 4. The presence of hydrogen resulted in an EMF increase. Since the solid electrolyte is a protonic conductor, one can predict that hydrogen will influence the EMF of the sensor.

The performance test of the humidity sensor has been carried out under the condition that the gases in the test and the reference compartments are based on moisturized air. The oxygen partial pressures on both sides are considered to be almost equal and eq. (4.4) is used for the calculation of EMF for the $SrCeO_3$-based humidity sensor. However, even

Table 4
Deviation of EMF from the usual humidity response caused by impurity gas injection (Iwahara et al. 1983a) (reprinted by permission of the publisher, Chapman and Hall)

Impurity gas	Maximum deviation of the EMF (%)	
	300°C	400°C
H_2	+0.78	+17.0
C_4H_{10}	−1.7	−6.3
CO_2	±0.0	±0.0

in the case when the oxygen pressure in each compartment is different, we can easily obtain the exact humidity from eq. (4.3) by measuring the individual oxygen pressures. For this purpose, a galvanic yttrium-doped zirconia oxygen sensor (sect. 2) can be used to measure the oxygen concentration accurately.

4.6. *Other applications of $SrCeO_3$-based solid electrolytes*

Yb-doped $SrCeO_3$ becomes a protonic conductor in a hydrogen-containing atmosphere as well as in a humid atmosphere, as mentioned earlier. The other application of this sensor is, of course, the detection of hydrogen. The cell arrangement is the same as the humidity sensor. When we set up the concentration cell with different hydrogen content, $p_{H_2}(I)$ and $p_{H_2}(II)$, the theoretical EMF is obtained by the following equation:

$$E = \frac{RT}{2F} \ln \left(\frac{p_{H_2}(II)}{p_{H_2}(I)} \right). \tag{4.6}$$

A stable and a linear relationship was observed, as presented in fig. 36 (Iwahara et al. 1983b). Since both electronic and protonic conduction occur, the slope of the line is less than that calculated from eq. (4.6). The hydrogen transference number obtained from the figure is between 0.92 and 0.98. Since the exact hydrogen transference number at a certain temperature is known from fig. 30, it is quite simple to calibrate the EMF output

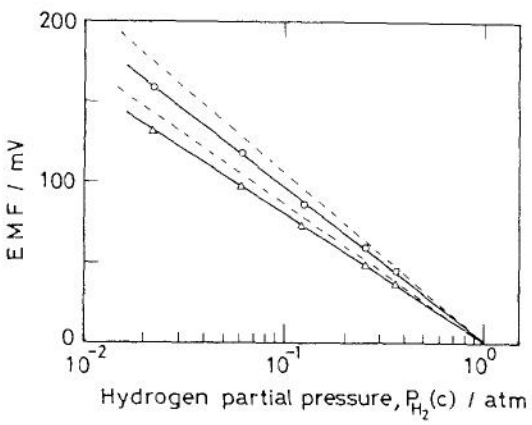

Fig. 36. EMF response of the hydrogen concentration cell to p_{H_2O}(c). H_2(1 atm), $Pt/SrCe_{0.95}Yb_{0.05}O_{3-x}/Pt$, $H_2(p_{H_2}(c))$. Open circles, 800°C; open triangles, 600°C (broken line shows theoretical EMF) (Iwahara et al. 1983b). (Reprinted by permission of the publisher, Elsevier Science Publishers B.V.)

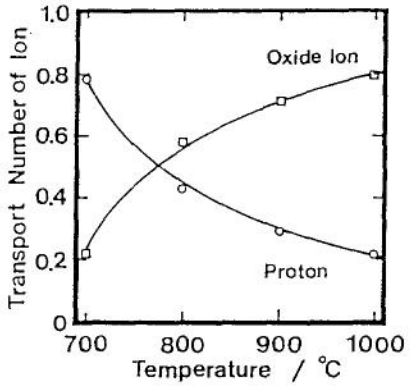

Fig. 37. Transference numbers of proton and oxide ion in $BaCe_{0.9}Nd_{0.1}O_{3-x}$ under fuel cell condition (Iwahara et al. 1991).

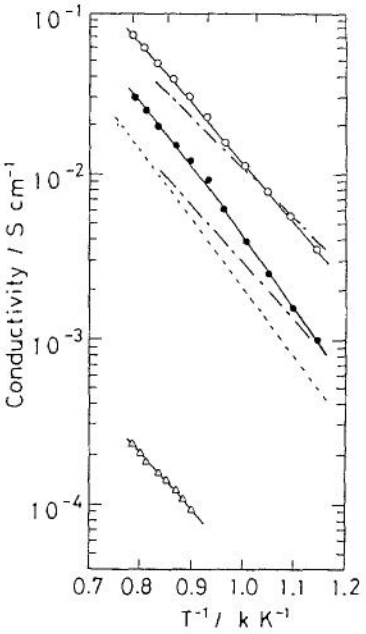

Fig. 38. Conductivity of $BaCe_{1-x}Nd_xO_{3-x}$ in wet air. Open circles, $x=0.10$; solid circles, $x=0.05$; open triangles, $x=0$. The dashed line is the data for $SrCe_{0.95}Yb_{0.05}O_{3-x}$ in wet air (Iwahara et al. 1988). (Reprinted by permission of the publisher, The Electrochemical Society Inc.)

to obtain the accurate hydrogen concentration as mentioned in sect. 4.5. Therefore, the performance as a hydrogen sensor is reliable enough to apply Yb-doped $SrCeO_3$ as the electrolyte for hydrogen sensing.

Rare-earth doped barium cerate, $BaCe(R)O_3$ (R = rare earths), also shows a p-type conduction similar to strontium cerate in the absence of hydrogen or water vapor. However, barium cerate is different from strontium cerate in two unusual characteristics. One is that barium cerate becomes an oxide ionic conductor as well as a protonic conductor at elevated temperatures as shown in fig. 37 (Iwahara et al. 1991). The other is that the electric conductivity of $BaCeO_3$ is appreciably higher than that of $SrCeO_3$ (fig. 38) (Iwahara et al. 1988). Research has been done to apply these cerates for fuel cell applications (Iwahara et al. 1983c, 1989a, 1990a,b, 1991, Iwahara 1988) and for hydrogen extraction by steam electrolysis (Iwahara et al. 1981, 1986, 1988). The details are described in the references.

The barium cerate electrolyte has also been investigated for application in a carbon dioxide gas sensor. The details of the sensing performance are described in sect. 6.

Molten aluminum alloys react with water vapor in the ambient atmosphere and absorb hydrogen during casting, fabrication and so on. The hydrogen solubility is greatly different between the liquid and the solid metal. Incorporated hydrogen in aluminum alloys made the cast alloy porous. Since hydrogen can be easily absorbed by reaction with water vapor in the ambient atmosphere, the hydrogen content in the alloy is continuously changing. The reduction of hydrogen concentration in molten alloys is essential for the

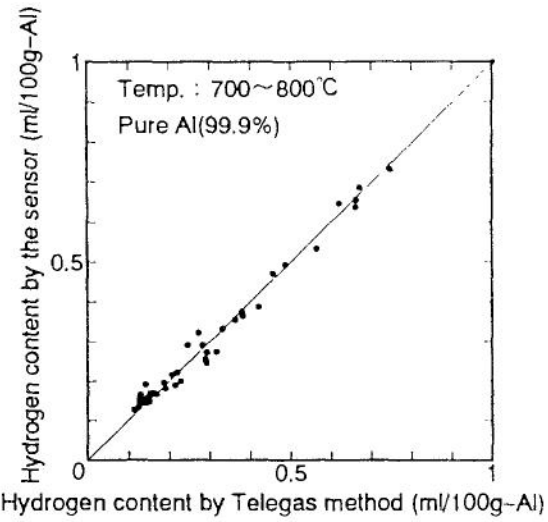

Fig. 39. Comparison of hydrogen content in molten aluminum obtained by the hydrogen sensor and by the Telegas method (Yajima et al. 1992).

purpose of obtaining a high quality aluminum product. Therefore, in situ hydrogen content measurements are the most appropriate way to detect the content accurately.

There is a linear relation between the solubility of hydrogen in molten aluminum and the square root of hydrogen pressure in the ambient gas, as follows:

$$S = K p_{H_2}^{1/2}. \tag{4.7}$$

The hydrogen content in the molten aluminum can then be obtained from eqs. (4.6, 4.7).

A stable EMF is obtained soon after inserting the sensor into molten aluminum (Iwahara et al. 1989b). Figure 39 (Yajima et al. 1992) shows the relationship between the hydrogen content in molten aluminum obtained by the sensor, and that obtained by the conventional Telegas method. This type of sensor has merit in measuring the hydrogen content in various metal alloys.

Another type of hydrogen sensor is obtained by use of rare-earth fluorides which are commonly applied as a fluorine sensor. The fluoride electrolyte used here is calcium-doped cerium fluoride. As a reference, $Bi(BiF_3)$ was used which was covered with epoxy resin to separate it from the sample gases. A linear relationship was obtained between the sensor output and the hydrogen concentration (Mingmei and Yufang 1992). The output decreases linearly with an increase in hydrogen pressure in the sample gas. These results clearly indicate that rare-earth fluoride can also work well as a hydrogen sensor.

Lanthanum fluoride has also been investigated as a hydrogen sensor. The sensor consists of the following cell:

$$\text{Sn, } SnF_2 \ / \ LaF_3 \ / \ \text{Pt black.} \tag{4.8}$$
[reference electrode / solid electrolyte / sensing electrode]

The time necessary for attaining 90% response at 20°C for a 1.3% hydrogen atmosphere is 3 minutes (Kuwata et al. 1984c). In the case where the sensor is inserted in an atmosphere

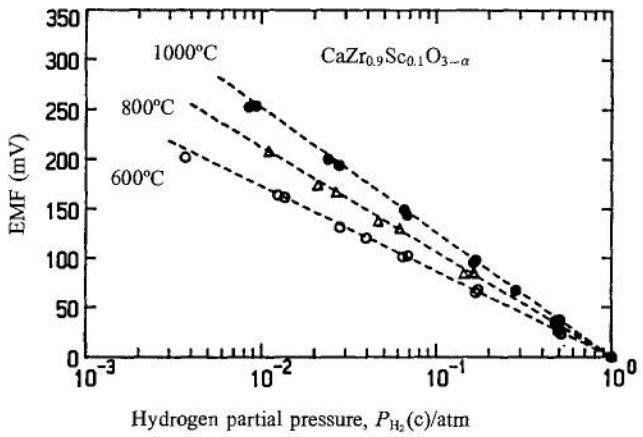

Fig. 40. EMF response of the following hydrogen concentration cell: PH_2(1 atm),Pt/$CaZr_{0.9}Sc_{0.1}O_{3-\alpha}$/Pt,$PH_2$(c). Dashed lines, theoretical value; solid circles, 1000°C; open triangles, 800°C; open circles, 600°C (Yajima et al. 1991). (Reprinted by permission of the publisher, Elsevier Science Publishers B.V.)

of hydrogen diluted with nitrogen, no response was obtained. Oxygen presence in the ambient atmosphere is essential for this type of sensor when used for hydrogen sensing. The hydrogen sensor with lanthanum fluoride also responds to CO. However, the response is sluggish compared with that for hydrogen sensing.

Another representative protonic conductor at elevated temperatures is calcium zirconate. Strontium cerate and barium cerate protonic conductors are not stable and decompose into the starting materials of $SrCO_3$ or $BaCO_3$ and CeO_2 in a CO_2-containing atmosphere below about 800°C (Gopalan and Virkar 1993). This becomes a crucial disadvantage in practical applications. The ionic conductivity of $CaZrO_3$ is not high and the treatment by aliovalent cation doping is effective in raising the conductivity. EMF measurement of hydrogen gas concentration cells using scandium-doped $CaZrO_3$ solid electrolyte, for the temperature range from 600°C to 1000°C, is presented in fig. 40 (Yajima et al. 1991). From this figure, we can estimate the proton conduction and the proton transport number. The EMF obtained was closely consistent with the theoretical value calculated from the Nernst equation, showing that the protonic transport number of $CaZr(Sc)O_3$ is almost unity in the temperature range examined.

The $CaZrO_3$-based sensor is more stable than alkali earth cerates for the detection of hydrogen or water vapor in a CO_2-containing atmosphere (Koide et al. 1992).

4.7. *Other types of humidity sensors*

One type of humidity sensor utilizes porous perovskite-type ceramic materials. Perovskite-type metal oxides are good candidates because their surfaces can be easily modified in order to obtain water adsorptive properties by choosing an appropriate cation in the oxides. In addition, the perovskite-type oxides do not require thermal treatment. Also, no influence is expected in sample gases from coexisting CO_2. As the metals in perovskite

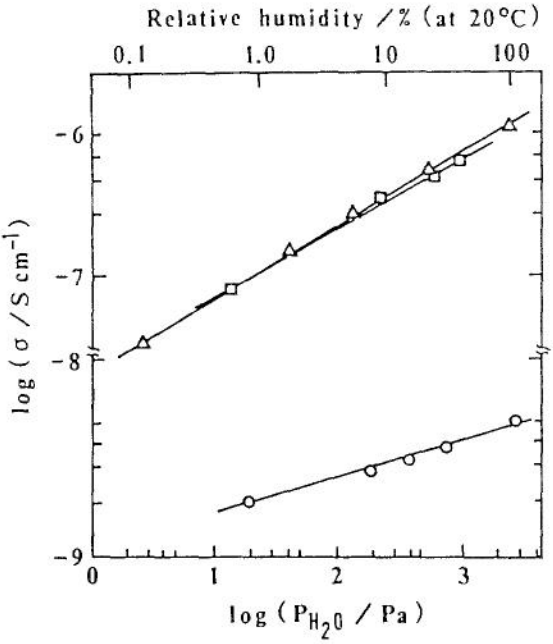

Fig. 41. Effects of partial substitution of La^{3+} for Sr^{2+} in $SrSnO_3$ on humidity-sensing characteristics: open circles, $SrSnO_3$; open triangles, $Sr_{0.95}La_{0.05}SnO_3$; open squares, $Sr_{0.9}La_{0.1}SnO_3$ (Shimizu et al. 1989). (Reprinted by permission of the publisher, The Electrochemical Society Inc.)

oxides, alkaline-earth ions show a strong affinity for water molecules. The conductivity change of perovskite oxide is based on the chemisorption of water molecules, and water vapor is an electron donor in the semiconductor. Enhancement of sensitivity to water vapor was investigated by substituting the Sr site with La in perovskite-type $SrSnO_3$. The substitution produces electrons and enhances n-type characteristics. In this type of sensors, the typical operating temperature is 400°C (Arai et al. 1983).

Humidity sensors which use ionic oxides operate at around room temperature. The output of such a humidity sensor changes gradually with time. However, humidity sensors of the semiconductor type work well at elevated temperatures and maintain a stable output although there is interference from reducing gas, particularly ethanol. When the water vapor content increases, interference from reducing gases becomes smaller. The rare earth lanthanum also plays an important role in the perovskite-type humidity sensor. The rare earth enhances the interaction between the adsorbed species and the oxides at the surface (Shimizu et al. 1985).

The humidity sensing performance of $SrSnO_3$ with Sr partially substituted with La is shown in fig. 41 (Shimizu et al. 1989). The conductivity of the sample increases with increasing humidity. A logarithmic plot of conductivity and humidity is linear:

$$\sigma = \sigma_1 p_{H_2O}^{\alpha}, \tag{4.9}$$

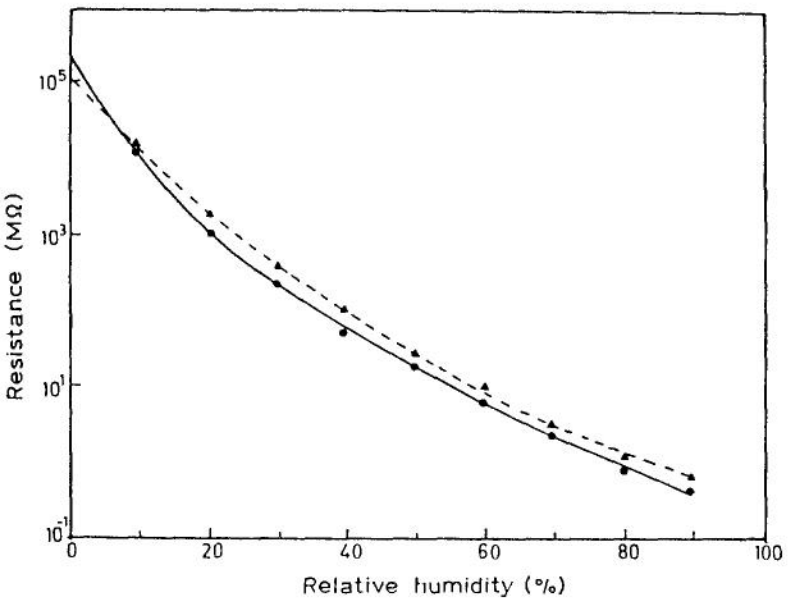

Fig. 42. Change in resistance of $BaTiO_3$ film as a function of relative humidity. Solid line, 100 nm thick film; dashed line, 800 nm thick film (Ardakani et al. 1993). (Reprinted by permission of the publisher, Chapman and Hall.)

where σ_1 denotes the conductivity for $p_{H_2O} = 1$ Pa. Figure 41 illustrates the sensitivity enhancement resulting from the partial Sr site substitution with La^{3+}. The conductivity increase is approximately one order of magnitude over the whole water-vapor region examined. There is almost no difference between the samples with La partial substitutions of 5 and 10 mol%. The increase in conductivity results from the increase in the electron concentration caused by the substitution. This indicates that lanthanum solubility in the perovskite $SrSnO_3$ oxide is around 5 mol% La mixing. The lanthanum mixing enhances an electronic interaction on the surface of the semiconductor, and results in improved humidity sensing. In such a semiconductor sensor, the preparation conditions, such as sintering temperature, play an important role in the sensing characteristics. In the La-substituted $SrSnO_3$ case, conductivity of the sample increases with an increase in the sintering temperature. However, α decreases with increasing sintering temperature. The increase in conductivity is ascribed to a contact resistance decrease between adjacent sintered particles. The higher sintering causes a decrease in surface area, where active adsorption sites exist, and this results in a decrease of α.

A similar perovskite oxide, $Ba_{1-x}La_xTiO_3$, has also been examined as humidity sensor material. The oxide was deposited on a quartz substrate as a film. The performance of a representative sensor film of $BaTiO_3$ is presented in fig. 42 (Ardakani et al. 1993). With an increase of relative humidity, the sensor resistance greatly decreases. Also, the sensor response was essentially independent of the film thickness. This indicates that the sensing

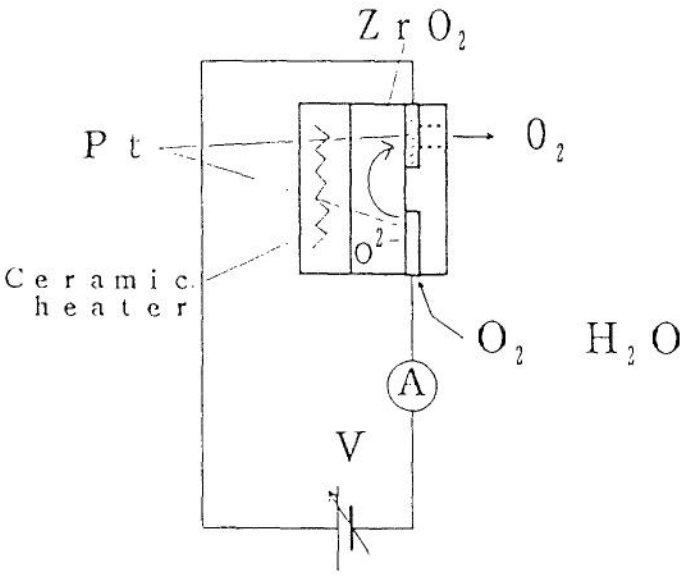

Fig. 43. Structure of the new limiting-current type plane oxygen sensor (Yagi and Horii 1992). (Reprinted by permission of the publisher, The Electrochemical Society Japan.)

occurs mainly on the surface of the oxide layer. The oxide with low La doping shows a good humidity sensing performance.

A limiting-current type sensor, which is very common in oxygen sensing as described in sect. 2, has also been investigated for the detection of humidity at high temperatures. The structure of the limiting-type humidity sensor is presented in fig. 43 (Yagi and Horii 1992, Yagi and Ichikawa 1992a,b, Yagi 1993). The platinum electrode is porous the pores control the gas diffusion. Yttrium oxide (8 mol%) was mixed with zirconia to obtain a stabilized zirconia. Both anode and cathode are on the same plane, and this feature greatly contributes to obtaining a more compact sensor probe.

The principle of the humidity detection mechanism is as follows. The sensor detects the additional oxygen produced by the water vapor decomposition, and the selectivity for water vapor is high. Since this sensor also uses an oxide ionic conductor, it also responds to an oxygen concentration change. However, if the applied voltage is higher than 1.4 V, the water vapor in the ambient atmosphere decomposes by electrolysis, and produces oxygen. With the formation of additional oxygen, the sensor output changes and the water vapor content in the atmosphere is detected. The operating temperature is around 500°C, hence the sensor can be operable at a temperature higher than the boiling point of water at 1 atm.

The sensor's I–V response is shown in fig. 44 (Yagi and Horii 1992, Yagi and Ichikawa 1992a,b, Yagi 1993). The temperature of the sensor element is controlled at 500°C. When the applied voltage is lower than approximately 1.4 V, the primary limiting current (IL1) decreases with a water vapor increase. Contrarily, when the applied voltage is higher

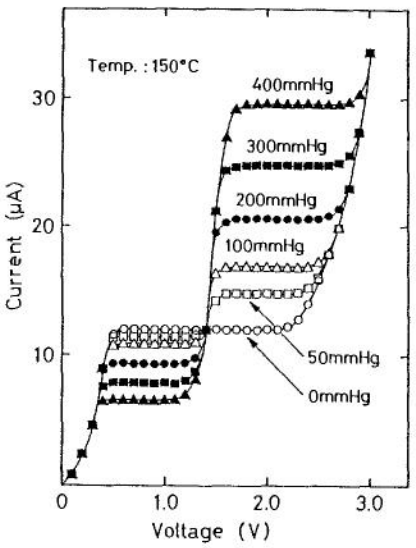

Fig. 44. *I–V* characteristics of the plane oxygen sensor operated at 500°C in air–H_2O mixed gas kept at 150°C (Yagi and Horii 1992). (Reprinted by permission of the publisher, The Electrochemical Society Japan.)

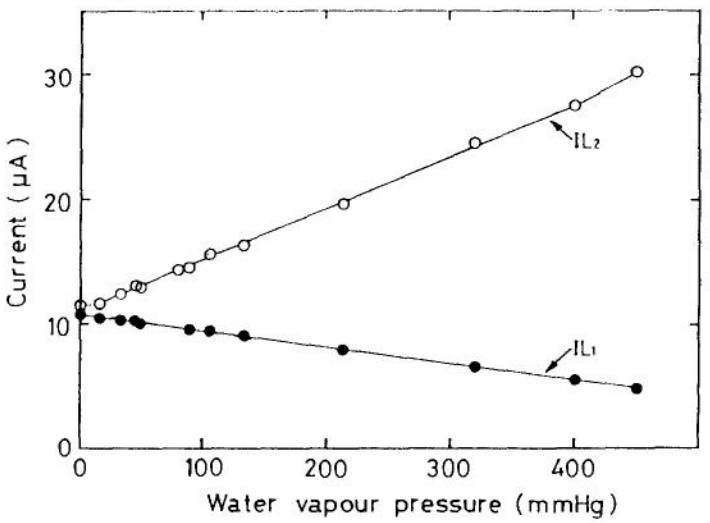

Fig. 45. Relation between IL1, IL2 and water vapor pressure of the plane oxygen sensor (Yagi and Horii 1992). (Reprinted by permission of the publisher, The Electrochemical Society Japan.)

than 1.4 V, the secondary limiting current (IL2) increases with a water vapor increase. The relation between IL1, IL2 and the water vapor concentration is presented in fig. 45 (Yagi and Horii 1992, Yagi and Ichikawa 1992b, Yagi 1993). If the water vapor pressure increases, the partial pressure of oxygen in the ambient atmosphere decreases. Then, the IL1 value will decrease with the water vapor increase. In the IL2 region, water vapor is electrolyzed and produces oxygen. Therefore, the IL2 output increases with the water

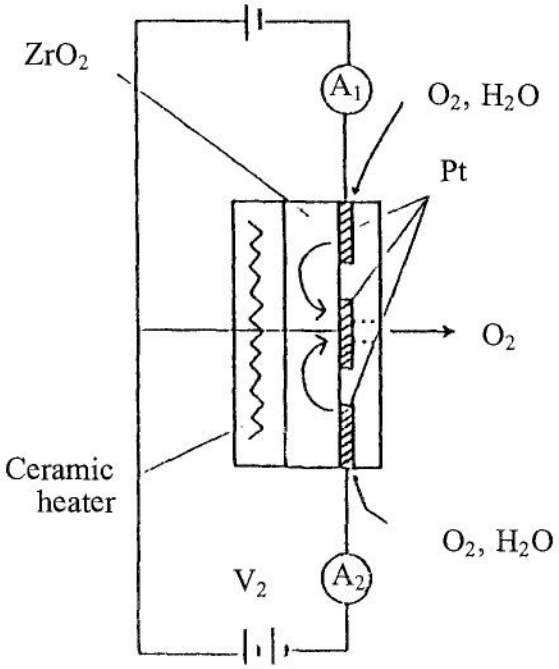

Fig. 46. Structure of the multisensor using the plane oxygen sensor (Yagi and Ichikawa 1992b).

vapor pressure enhancement. Response is around several minutes. Even if deterioration of the sensor element occurs, the ratio of IL2/IL1 is still the same because both IL1 and IL2 are related to the oxygen content. The sensor output variation is different in each sensor probe. However, by using the ratio, the sensor's output can be normalized. One of the representative and beneficial merits is that the sensor can work well even in an atmosphere with a continuously changing oxygen content. Since the output of IL1 and IL2 corresponds to the oxygen content with and without water vapor electrolysis, the humidity in the ambient atmosphere is easily obtained by correcting for the oxygen content variation. The details are discussed in the reference.

Conventional humidity sensors utilize phenomena such as resistance or capacitance changes caused by water adsorption, and so the sensing characteristics greatly deteriorate at relative humidities over 90%. However, the limiting-current type sensor operates around 500°C, and can be applied as a humidity sensor even up to 100% relative humidity. The material used in this type of sensor is stabilized zirconia. As described in sect. 2, stabilized zirconia has also been practically applied as an oxygen gas sensor for automobiles in the past few decades. Therefore, the humidity sensor of the limiting-current type also has an excellent stability in an exhaust gas atmosphere. Since stabilized zirconia is a well known material for an oxygen sensor, a multi-functional gas sensor such as the one presented in fig. 46 (Yagi and Ichikawa 1992b) can be fabricated to simultaneously detect both oxygen and water vapor content in the ambient atmosphere.

5. Sulfur dioxide sensors

5.1. *Introduction*

Environmental deterioration by acid precipitation is becoming a serious problem in addition to global warming. The pollutants are mainly sulfur dioxide and nitric oxides. There is an urgent need to reduce the emission of these gases into the environment. Several instrumental techniques such as an infrared absorption method already have been applied in commercial analysis. These elemental analyses are accurate and sensitive enough to detect the SO_2 concentration. However, some pretreatment is needed to remove the gases which interfere with SO_2 sensing. For reliable on-site measurements, it is necessary to maintain and calibrate the apparatus. Also, the size of the equipment is relatively large. Especially, it is quite difficult to monitor SO_2 emissions from moving vehicles. To control emission of pollutant gases from all sources, a simple and inexpensive SO_2 monitoring sensor should definitely be located at every emitting site.

One way to avoid other gases interfering with accurate detection, is to design the sensor setup from a sensing mechanism point of view. To get a real-time output, one suitable way for gas detection is to measure electric outputs, such as potentiometric, amperometric, or conductometric signals. From the selective sensing point of view, the application of a solid electrolyte, like the stabilized zirconia electrolyte for the oxygen sensor in sect. 2, is expected to be the most advantageous way of detection. The potentiometric method requires setting up the detecting gas concentration cell in an appropriate configuration. Up to now, several candidates for the solid electrolyte have been proposed. Prototype sensors have also already been fabricated and their sensing performance tested.

The composition of the solid electrolyte is a key point for effective detection. The ionic form of SO_2 gas is, of course, the SO_4^{2-} sulfate anion. However, this extremely bulky anion has difficulty in migrating into the solid phase. What can be considered next is to move not the anion but rather the cation in the solid. The candidate cations are those with ionic radii which are appreciably small, and in particular, the alkali metal cations are considered to be appropriate. Taken in combination, this results in the selection of alkali metal sulfates as promising candidates for the electrolyte component of the chemical SO_2 sensor. Sodium sulfate (Jacob and Rao 1979, Imanaka et al. 1983a–c, 1984, 1985a,b, 1986a–c, 1987a,b, 1988) is the most promising electrolyte, since lithium sulfate is hygroscopic and potassium sulfate shows the lowest conductivity. Other alkali sulfates, such as Li_2SO_4 (Worrell 1983, Worrell and Liu 1984, Liu and Worrell 1988), and K_2SO_4 (Gauthier and Chamberland 1977, Gauthier et al. 1977, 1981, Gauthier and Bale 1983) have been investigated for application as the solid electrolyte.

In the case of applying sodium sulfate as the electrolyte, doping of a rare-earth element is essential in obtaining a suitable electrolyte for a SO_2 sensor. Here, rare-earth doping also improves the electrical characteristics markedly, as previously mentioned in sect. 2.

Another way of SO_2 sensing, without the sulfate electrolyte, is to use an excellent alkali metal ionic conducting solid electrolyte such as β-alumina (Na^+) (Itoh et al.

1984, Sugimoto and Kozuka 1988) and NASICON [Na^+ Super Ionic Conductor: $(Na^+)(Na_3Zr_2Si_2PO_{12})$] (Saito et al. 1983, 1984b, Maruyama et al. 1985).

In these solid electrolytes, the species migrating in the solid phase are sodium ions and not sulfur oxides. Therefore, by using this chemistry, we can devise an appropriate sensor arrangement. The gas to detect is SO_2 and the ionic state of SO_2 gas is SO_4^{2-}. As Na^+ is the mobile cation in the solid electrolyte, sodium sulfate, which is the combination of both Na^+ and SO_4^{2-}, should be formed on the solid electrolyte surface. In the sulfur dioxide gas sensor with those solid electrolytes, sodium sulfate is used to detect SO_2 gas.

5.2. *The characteristics of sodium sulfate*

Sodium sulfate shows five polymorphisms (Kreidl and Simon 1958, Saito et al. 1981). The sulfate exists as the Na_2SO_4–V phase at room temperature. On heating, it transforms to the metastable Na_2SO_4–III phase and finally to the Na_2SO_4–I phase. The I phase is a high Na^+ conducting material. By cooling the I phase, it transforms to the III phase through an unstable II phase. It takes around several months to transform from the III to the V phase. The existence of moisture in the atmosphere accelerates the III to V transition.

Figure 47 (Saito et al. 1982) presents the thermal analysis of undoped and yttrium-

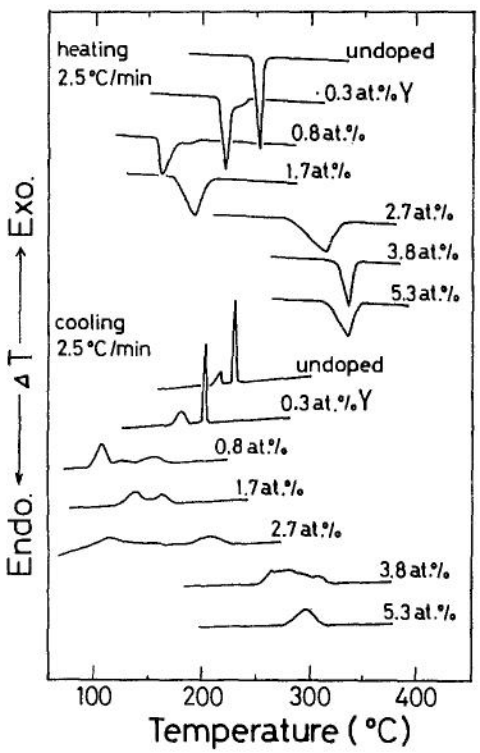

Fig. 47. DTA curves of the undoped and yttrium-doped sodium sulfate (Saito et al. 1982). (Reprinted by permission of the publisher, Elsevier Science Publishers, B.V.)

doped sodium sulfate. The Y doping less than 1.7 at.% lowered the III–I transition temperature. By doping between 2.7 and 5.3 at.%, the transition temperature is raised. On cooling, the two exothermic peaks corresponding to I → II and II → III transition coalesce in the samples of 2.7 and 3.8 at.% Y doping. In the case of 5.3 at.% Y doping, only one exthothermic peak was observed. With Y doping of more than 3.8 at.%, the high-temperature phase was obtained by quenching, even at room temperature. This indicates that the rare-earth yttrium doping suppresses the high- to low-temperature phase transformation and facilitates the quenching process.

Aliovalent cations such as rare earths, can replace the Na^+ site in sodium sulfate and can form vacancies up to 30%. Doping of di or trivalent cation increases the ionic conductivity of sodium sulfate. The conductivity increase is closely related to the number of vacancies and not to the size or valency of the substituting ion (Höfer et al. 1981). The conductivity maximum appears at approximately 7% □ (□ = vacancy) (Höfer et al. 1978) and is independent of temperature. The maximum conductivity is two orders of magnitude higher than that of the pure sodium sulfate (I) phase. In the low cation vacancies region, aliovalent cation doping causes defect formation. This results in a conductivity increase, which becomes larger as the doping amount increases. In the higher defect region, interactions, such as cluster formation (Y^{3+}□, □Y^{3+}□), occur and this reduces the conductivity (Saito et al. 1984a). The ionic conductivity of the Y_2O_3-doped Na_2SO_4(I) solid solution is not as high as the well known superionic conductors such as β-alumina and NASICON. However, it shows a relatively good Na^+ conductivity and is applicable for the solid electrolyte in a chemical SO_2 sensor.

5.3. *Principle of SO_2 detection*

The principle of the SO_2 gas detection with the sulfate-based solid electrolyte, is as follows. Two compartments, each with a different SO_2 gas concentration, are divided by the solid electrolyte.

In the compartment with lower SO_2 content, sodium sulfate decomposes into $2Na^+$, SO_3 and $\frac{1}{2}O_2$ on the surface of the electrolyte, and thereby increases the SO_2 concentration. On the other surface of the electrolyte, the reverse chemical reaction proceeds to form sodium sulfate. So, the overall chemical reaction is expressed as follows:

$$SO_3 + \tfrac{1}{2}O_2 \rightleftarrows SO_3 + \tfrac{1}{2}O_2. \tag{5.1}$$

The Nernst equation is written as

$$E = \frac{RT}{2F}\ln\left(\frac{p'_{SO_3}p'^{1/2}_{O_2}}{p''_{SO_3}p''^{1/2}_{O_2}}\right), \tag{5.2}$$

where R, T, and F represent gas constant, absolute temperature, and Faraday constant, respectively.

$$SO_3 \rightleftarrows \tfrac{1}{2}O_2 + SO_2. \tag{5.3}$$

$$K_1 = p_{SO_2} \frac{p_{O_2}^{1/2}}{p_{SO_3}}. \tag{5.4}$$

By combining eqs. (5.2) and (5.4) one obtains the following equation:

$$E = \frac{RT}{2F} \ln \left(\frac{(p'_{SO_2})_{in} (p'_{O_2})^{1/2}}{(1 + K_1/p'^{1/2}_{O_2})(p''_{SO_3})(p''_{O_2})^{1/2}} \right). \tag{5.5}$$

In most of the samples for analysis, the SO_2 gas is present in ambient atmosphere, so that p'_{O_2} and p''_{O_2} are almost equal to 0.21 atm. Then, eq. (5.5) simplifies to

$$E = \frac{RT}{2F} \ln \left(\frac{(p'_{SO_2})_{in}}{(1 + K_1/0.21^{1/2})(p''_{SO_3})} \right). \tag{5.6}$$

Since the SO_2 concentration of the reference compartment is controlled, we can calculate the SO_2 gas concentration in the test atmosphere from eq. (5.6).

5.4. *Characteristics of rare-earth doped Na_2SO_4 solid electrolytes*

When alkali metal sulfate undergoes a phase transformation, the result is microcracks in the sulfate electrolyte body. These cracks cause a gas leakage between compartments and make it difficult to detect the SO_2 content accurately. Suppression of the transformation in the bulk sulfate is essential in its application as the solid electrolyte for the gas sensor. Here, the rare-earth elements are used as dopants to suppress the phase transition in the sulfate electrolyte and to stabilize a high temperature sulfate phase, thus maintaining a high ionic conductivity, similar to the case of yttrium doping in stabilized zirconia. Rare-earth doping into sulfate enhances the conductivity and greatly improves the SO_2 sensing characteristics. The doping of a rare earth into the sodium sulfate electrolyte has been well investigated. Several kinds of rare earths have been tried, to improve the properties of the sulfate as a sensor electrolyte.

Figure 48 (Imanaka et al. 1985a) shows one of the representative σT–T^{-1} relationships for sodium sulfate and sodium sulfate doped with various amounts of yttrium sulfate with silicon dioxide. The SiO_2 addition prevents the sodium sulfate from becoming ductile. By doping a rare earth in the form of yttrium sulfate into sodium sulfate, the conductivity is greatly enhanced and the phase transition which causes the decline in the σT–T^{-1} curve disappears except at the lowest $Y_2(SO_4)_3$ mixing of 4.9 mol%. This result indicates that the rare-earth mixing in sulfate with silicon dioxide contributes greatly to suppressing the phase transition in sodium sulfate as well as increasing the ionic conductivity.

It is well known that, chemically, there are two types of elements in the rare-earth series. One type forms cations which retain stable trivalency. The other type consists of elements which have di- or tetravalency in addition to trivalency. As described earlier in this section, the rare-earth mixed sodium sulfate is an ionic conductor. It is necessary to eliminate any electronic short circuit in the electrolyte in order to reduce as much as

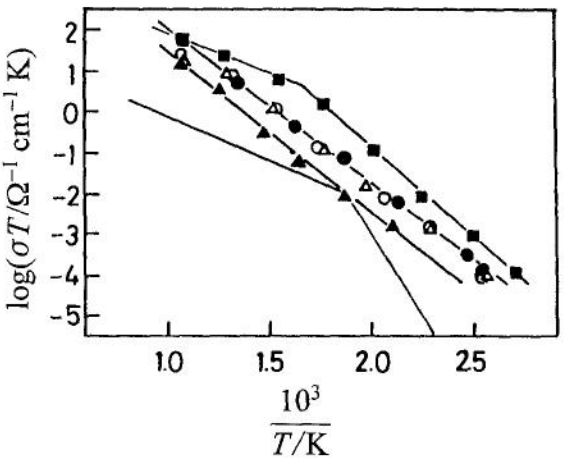

Fig. 48. Temperature dependence of electric conductivity for Na_2SO_4–$Y_2(SO_4)_3$–SiO_2. Solid squares, 55.1:4.9:40.0; open circles, 52.2:7.7:40.1; solid circles, 50.1:9.9:40.0; open triangles, 48.1:11.8:40.1; solid triangles, 45.1:14.8:40.1; solid line, Na_2SO_4 (Imanaka et al. 1985a).

possible the electronic conduction components. The valency change between trivalent and di- or tetravalent rare-earth elements causes electronic conduction in the electrolyte body. Therefore, the only appropriate candidates for the dopant are those rare earths, such as Y^{3+}, which hold a stable trivalent state.

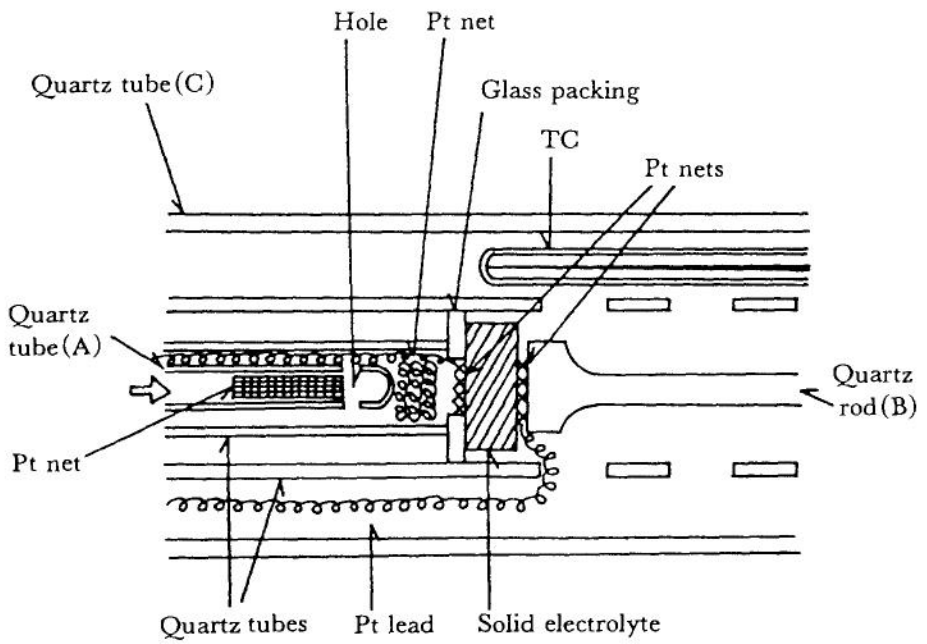

Fig. 49. Apparatus for EMF measurement with a given SO_2 content gas flow as a reference (Imanaka et al. 1986a).

5.5. *SO_2 gas detection with a reference SO_2 gas circulation*

A typical SO_2 gas concentration cell was fabricated with the sulfate base electrolyte which contained rare-earth ions, and the SO_2 sensing characteristics were investigated. The apparatus used to examine this method is depicted in fig. 49 (the test gas flowed from the inner quartz tube A, and the reference gas was passed through the outer quartz tube B) (Imanaka et al. 1986a,d). Platinum mesh is placed inside tube A to promote the oxidation from SO_2 to SO_3 in the test gas for accurate SO_2 detection. The SO_2 gas sensing results of this type of sensor at 823 K are shown in fig. 50 (Imanaka et al. 1986a,d). Here, −4.0 and −2.0 in $\log(p_{SO_2})_{in}$ correspond to 100 ppm and 1% in the SO_2 content, respectively. The EMF output obtained is almost consistent with the calculated EMF value from eq. (5.6). This means that rare-earth doping into the sodium sulfate electrolyte suppresses the phase transition in the electrolyte body and also the microcracks, and thus contributes to accurate SO_2 sensing. From these results, it is clear that the SO_2 gas concentration cell with a rare-earth mixed sodium sulfate electrolyte can detect the SO_2 concentration, precisely and in continuous operation.

The application of the gas concentration cell method is appropriate to show the effectiveness of the materials as the solid electrolyte for SO_2 measurement. However, the apparatus is relatively complicated since regulation of the SO_2 content in the reference compartment is always necessary for the measurements.

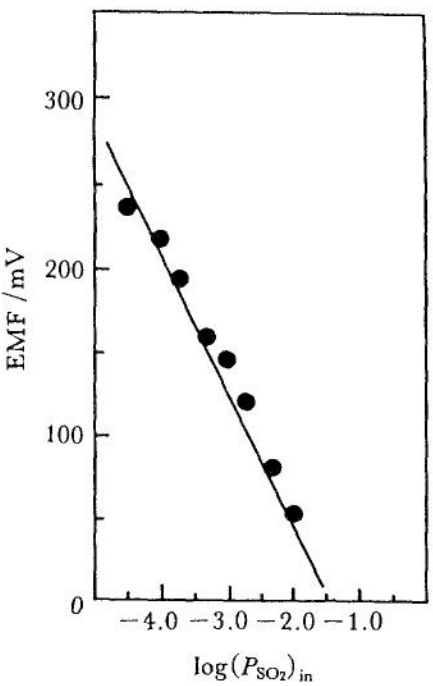

Fig. 50. Sensor output (EMF) variation with several SO_2 gas concentrations at 823 K. Solid line, calculated EMF (Imanaka et al. 1986a).

5.6. *SO_2 sensing performance with a solid reference reservoir*

To maintain the SO_2 reference gas circulation content at a known constant value is a critical barrier in using this type of SO_2 sensor in a commercial application. In order to approach more practical sensing, devices using a solid (rather than a gaseous) SO_2 reference have been investigated. For instance, a metal sulfate/metal oxide mixture can be used to provide such a stable SO_2 content gas reservoir.

The principle of obtaining a certain SO_2 content is as follows. There exists the following chemical equilibrium in the metal sulfate/metal oxide mixture at the reference side:

$$MSO_4 \rightleftarrows MO + SO_3, \qquad K_2 = p_{SO_3} = \exp(-\Delta G/RT). \tag{5.7, 5.8}$$

At a certain measuring temperature, ΔG is obtained as a fixed value. From eqs. (5.6) and (5.8) we can obtain the following equation:

$$E = \frac{RT}{2F} \ln \left(\frac{(p'_{SO_2})_{in}}{(1 + K_1/0.21^{1/2})(\exp(-\Delta G/RT))} \right). \tag{5.9}$$

Since both ΔG and K_1 are fixed at a certain temperature, the SO_2 gas concentration in the test atmosphere is directly calculated from the EMF output in eq. (5.9).

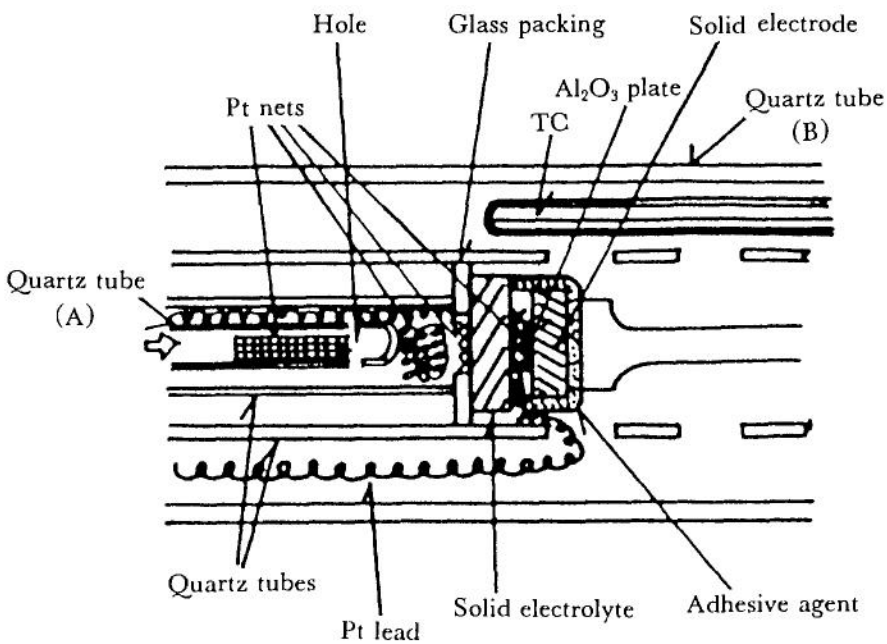

Fig. 51. Sectional view of the apparatus for SO_2 gas detection using the solid reference electrode method (Imanaka et al. 1986a).

A cross-sectional view of the apparatus for the SO_2 sensor with the solid state reference reservoir is shown in fig. 51 (Imanaka et al. 1985b, 1986a,b, 1987b). In this case, a pellet of the metal sulfate/metal oxide mixture is placed beside the electrolyte with a platinum current collecting electrode. Between the sulfate–oxide mixture and the electrolyte, an alumina plate was fixed to prevent a chemical reaction between them. In order to eliminate interference from ambient atmosphere, the solid state reservoir is covered with an inorganic adhesive agent SUMICERAM. Small apertures exist in the platinum electrode since a mesh-type Pt electrode is employed. The outer quartz tube (B) in fig. 51 is filled with air, so oxygen pressure in the reference compartment with the inorganic adhesive coverage is kept constant at 0.21 atm. In this measurement, the test gas flows in the same way as that shown in fig. 49.

There are several limitations in applying a metal sulfate as the solid reference. One is the need to use an appropriate metal sulfate which produces a proper SO_2 content in the reference at the operating temperature. Another is the need to use a metal sulfate which decomposes only to the metal monoxide so that eq. (5.7) can be applied. It is possible to exploit other metal sulfate decomposition reactions which are different from eq. (5.7). However, the Gibbs free energy change of a more complicated reaction is less accurate and causes higher uncertainty of the sensor output. For candidate metal sulfates, nickel, or cobalt sulfate were selected. One of the typical SO_2 sensing results, with $NiSO_4$–NiO as the reference, is shown in fig. 52 (Imanaka et al. 1987b). Excellent and consistent data were obtained between the measured and the calculated EMF output. This clearly indicates

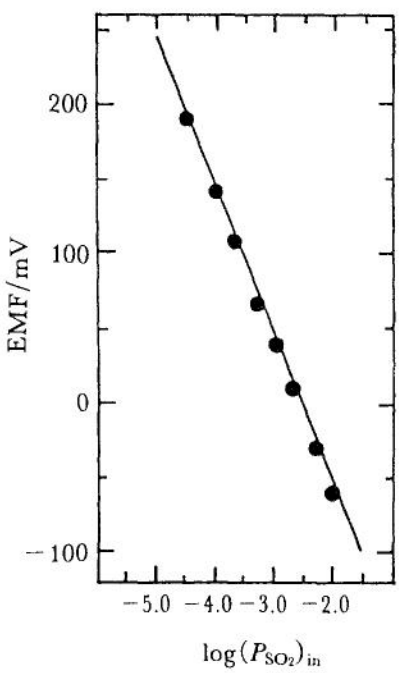

Fig. 52. Sensor output variation with the SO_2 gas concentration at 973 K. Solid line, calculated EMF (Imanaka et al. 1986a).

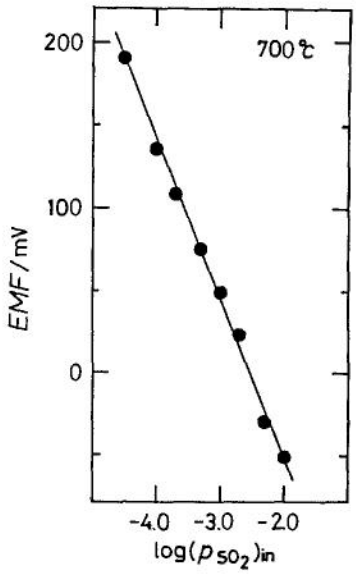

Fig. 53. Sensor output variation with the several SO_2 gas concentrations at 973 K. Solid line, calculated EMF (Imanaka et al. 1988). (Reprinted by permission of the publisher, The Chemical Society of Japan.)

that the application of such a metal sulfate/metal oxide mixture as the SO_2 reference reservoir is suitable in place of gas circulation in the reference compartment. By using a solid on the reference side instead of gas circulation, the sensor can be designed more simply, and also it can be made portable, thus approaching more closely the requirements for a practical application.

One of the eagerly desired features is to widen the range in operating temperature. The same EMF output, as the calculated value, can be obtained even at 923 K, which is 50 K lower in operating temperature compared with the result in fig. 52. The sensor can also detect the concentration accurately over a wide range, from 30 ppm to 1%, and was found to exhibit the same characteristics as demonstrated in the sensor with the gas circulation method.

A platinum mesh metal has been used in the gas introducing tube as a catalyst for the oxidation from SO_2 to SO_3 (see figs. 49 and 51). It is necessary to reduce the amount of Pt used in the sensor construction in order to reduce production costs. One way is to use another catalyst such as inexpensive V_2O_5 instead of platinum. One experiment is to mix V_2O_5 directly with the sulfate solid electrolyte. The SO_2 sensing characteristics of the SO_2 sensor with both the V_2O_5 catalyst and solid reference, is shown in fig. 53 (no platinum catalyst was applied; Imanaka et al. 1988). From the figure, it is easily seen that the sensor device can detect SO_2 content with the same sensing performance as in the case shown in fig. 52. The application of the V_2O_5 catalyst shows a satisfactory sensing performance which is similar to that obtained with a platinum catalyst.

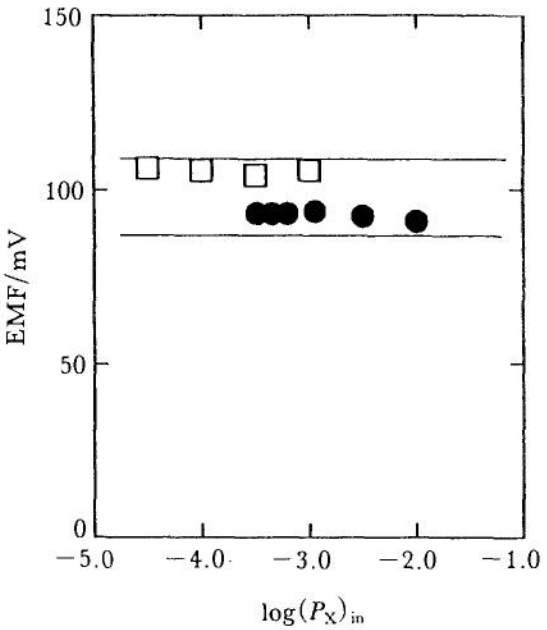

Fig. 54. Sensor output variation with the NO_2 or CO_2 gas concentration. Open squares, NO_2(SO_2 content: 230 ppm); solid circles, CO_2 (SO_2 content: 330 ppm); solid lines, calculated EMF (Adachi and Imanaka 1991). (Reprinted by permission of the publisher, Kodansha Ltd.)

5.7. *Selective SO_2 sensing with a sulfate electrolyte and rare earths*

When we apply these sensors in practice, the selective sensing to accurate detection with various coexisting gases is an important feature. Gases expected to coexist with sulfur dioxide are, of course, nitrogen oxides which are a main cause of acid precipitation, and carbon dioxide, produced by combustion. Figure 54 (Adachi and Imanaka 1991) shows the EMF deviation with a change of NO_2 or CO_2 content under the condition of a controlled SO_2 concentration at a constant value. From the figure, it can be easily seen that there is no deviation in the EMF output with the variation of the NO_2 or the CO_2 concentration. This clearly indicates that the coexistence of such gases has little influence upon the SO_2 selectivity.

One of the representative applications of this SO_2 sensor is the measurement of volcanic emissions. In this case, hydrogen sulfide gas will coexist with SO_2, and its effect upon the sensor has been tested. The result is shown in fig. 55 (Adachi and Imanaka 1991). With H_2S gas coexistence lower than approximately 1000 ppm, the EMF value deviates to a lower value in comparison to the calculated (dashed) line. In this measurement, H_2S is mixed with air with a fixed SO_2 gas content. Therefore, H_2S can be expected to be oxidized by the oxygen in the test atmosphere. The relation between the EMF output and the SO_2 content is replotted in fig. 56 (Adachi and Imanaka 1991) as EMF vs. the total amount of SO_2. The total amount corresponds to the sum of SO_2 gas initially introduced and the SO_2 gas produced by the oxidation, assuming that the introduced H_2S gas is completely oxidized. The

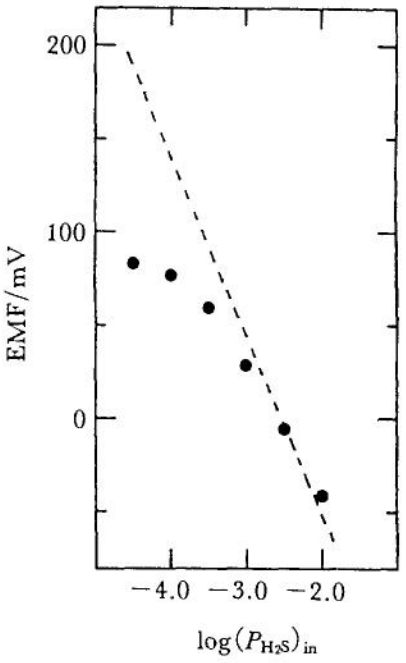

Fig. 55. Sensor output variation with several H_2S concentrations at 973 K. Dashed line, calculated EMF (Adachi and Imanaka 1991). (Reprinted by permission of the publisher, Kodansha Ltd.)

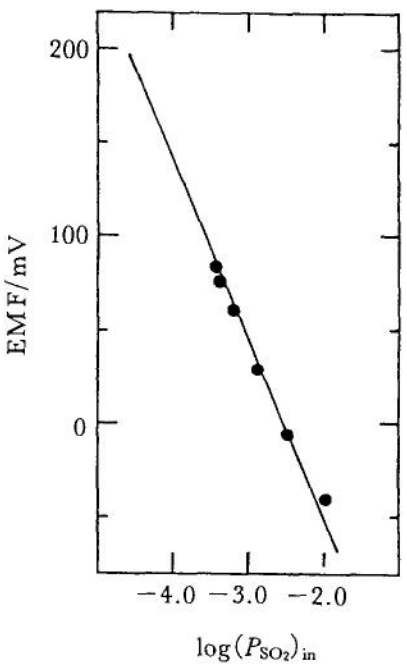

Fig. 56. Sensor output variation with total SO_2 gas concentration. Line, calculated EMF (Adachi and Imanaka 1991). (Reprinted by permission of the publisher, Kodansha Ltd.)

replotted EMF values in fig. 56 exactly coincide with the calculated line. This means that the H_2S gas introduced in the compartment was totally oxidized into SO_2. Water vapor is also produced from the introduced H_2S gas, as shown by the combustion reaction ($H_2S + \frac{3}{2}O_2 \rightarrow H_2O + SO_2$). This also indicates that water vapor (produced by the H_2S combustion at approximately 30 ppm to 1%) has little influence on the selective SO_2 detection of the sensor.

5.8. *SO_2 detection with a prototype sensor*

As a practical test for on-site application of the sensor for SO_2 detection, a prototype probe sensor was fabricated. A sectional view of the probe sensor is illustrated in fig. 57 (Adachi and Imanaka 1991). In this type of probe, a mullite tube is utilized instead of the more expensive quartz tube. In order to prevent the chemical reaction between the sulfate electrolyte and the solid reference, an alumina plate was placed between them, as for the case of the SO_2 sensor with the solid reference reservoir (sect. 5.6). The measurement was

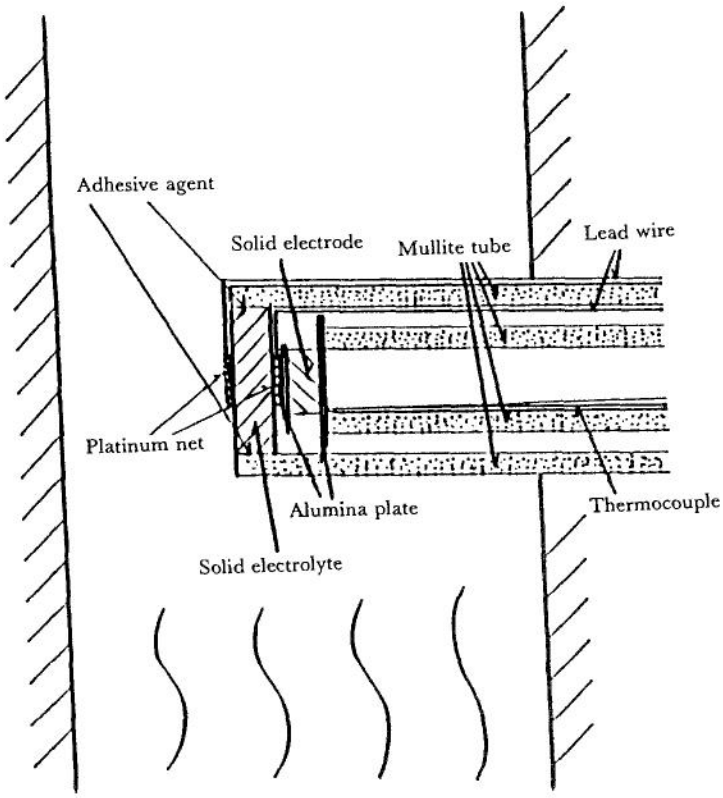

Fig. 57. Sectional view of the SO_2 sensor probe (Adachi and Imanaka 1991). (Reprinted by permission of the publisher, Kodansha Ltd.)

conducted with the probe directly attached to the detecting gas flowing tube. The probe was found to detect the concentration accurately (Adachi and Imanaka 1991) for a varying SO_2 content, as in the case of the experiments reported in figs. 52, 53. The probe-type sensor also retains excellent selective SO_2 sensing characteristics in the presence of NO_2 or CO_2 gas (Adachi and Imanaka 1991). The SO_2 sensor probe shows a good sensing performance with high selectivity by using the gas concentration cell method with a solid reference reservoir.

Most of the recent progress in the detection of SO_2 has been achieved with a sensor based on a solid electrolyte. Other solid electrolytes such as β-alumina (Itoh et al. 1984, Sugimoto and Kozuka 1988) and NASICON (Na^+ Super Ionic Conductor) (Saito et al. 1983, 1984b, Maruyama et al. 1985) are also promising candidates for a practical SO_2 sensor.

6. Carbon dioxide sensors

6.1. *Introduction*

Global warming has become a serious world-wide problem in addition to the environmental deterioration by acid precipitants. The wavelength of light from the sun is between 0.2 μm and 2 μm, with the highest intensity in the visible range from 0.4 μm to 0.8 μm. The sunlight is incident on the surface of the earth which then reflects the infrared rays of wavelength from 4 μm to 30 μm. The atmosphere does not absorb most of the visible light, but with the exception of wavelengths between 8 μm and 12 μm, it does absorb the infrared radiation and this results in heat production. The phenomenon of heat accumulation near the ground is quite similar to that found in a greenhouse. This is the reason why the warming of the earth is sometimes called the "greenhouse effect". The cause of the warming is the emission of gases such as carbon dioxide, methane, freon and nitrous oxide into the air atmosphere. Of those gases, carbon dioxide has the highest content in the atmosphere and the concentration of the gas has appreciably increased since the Industrial Revolution. The concentration of CO_2 before this period was 280 ppm, while today it is around 350 ppm. This great increase has mainly resulted from the consumption of fossil fuel. The most effective way to reduce the CO_2 emission into the atmosphere is to reduce the individual amounts exhausted from each emission site. For such an application, the development of simple and inexpensive sensors is essential.

One representative method for CO_2 detection is by infrared absorption analysis. An accurate measurement can be achieved by this method, but the equipment is relatively large-scale and expensive. Continuous maintenance is required to maintain calibration and precision. In addition, detection by the infrared method is not simple since practical measurements require the removal of other gases which influence the infrared absorption.

6.2. *CO_2 sensing with barium cerate electrolytes*

The barium cerate solid electrolyte which has already been described in sect. 4, has also been applied to carbon dioxide gas sensing.

The principle of detection is as follows. On the surface of the Ba–Ce–Y–O electrolyte, barium oxide exists as a result of the decomposition of the protonic conductor. Barium oxide reacts with water vapor in a humid atmosphere and forms barium hydroxide on the surface. This hydroxide absorbs carbon dioxide to form a carbonate, and as a result, the conductivity decreases.

The setup of the sensor is shown in fig. 58 (Hibino and Iwahara 1992a). A linear response between sensitivity and concentration is obtained as shown in fig. 59 (Hibino and Iwahara 1992a). In this case, neither proton nor oxide ionic conducting characteristics in the $BaCeO_3$ solid electrolyte has anything to do with the CO_2 sensitivity.

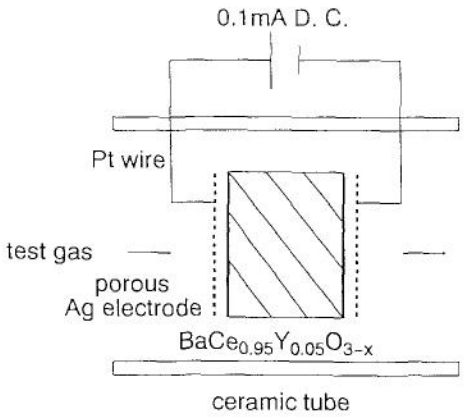

Fig. 58. Set-up of the CO_2 sensor (Hibino and Iwahara 1992a). (Reprinted by permission of the publisher, The Chemical Society of Japan.)

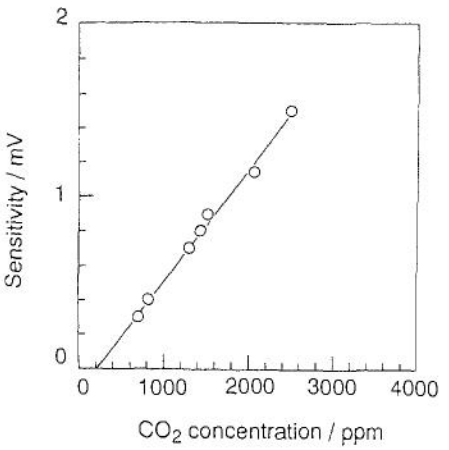

Fig. 59. Relation between sensitivity and CO_2 concentration (Hibino and Iwahara 1992a). (Reprinted by permission of the publisher, The Chemical Society of Japan.)

6.3. *CO_2 sensing with rare-earth oxides*

Rare-earth oxides such as Sm_2O_3 or Y_2O_3 are also found to be suitable sensor materials for carbon dioxide detection. Addition of sodium carbonate enhances the CO_2 sensing characteristics and addition of barium carbonate improves the humidity tolerance of the sensor element. Addition of barium carbonate also contributes greatly to preventing the sensor from deteriorating. The best composition for the rare-earth based sensor is Na_2CO_3(20 wt.%)–$BaCO_3$(20 wt.%)–CaO(10 wt.%)–Y_2O_3(50 wt.%). The performance of the sensor based on yttrium oxide is presented in fig. 60 (Sugai and Matsuzawa 1992).

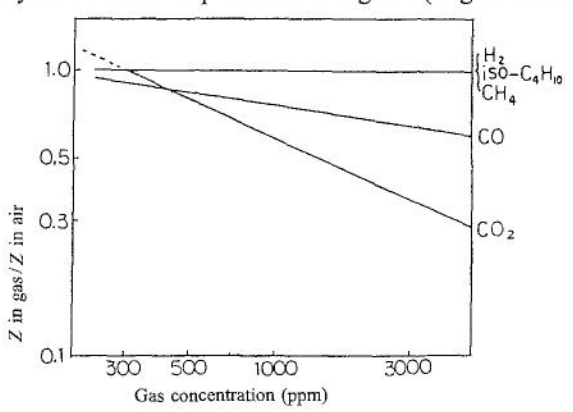

Fig. 60. Output change of (Na_2CO_3(20 wt.%)–$BaCO_3$(20 wt.%)–CaO(10 wt.%)–Y_2O_3(50 wt.%)) sensor with CO_2 variation at around 500°C (Sugai and Matsuzawa 1992). (Reprinted by permission of the publisher, Japan Association of Chemical Sensors.)

This type of sensor is insensitive to inflammable gases such as H_2, CH_4, and i-C_4H_{10}, but it also responds to carbon monoxide as well as carbon dioxide. The response ratio for CO is about half that for carbon dioxide.

6.4. *CO_2 sensing with tin dioxide*

Tin dioxide is another oxide applicable as base material for carbon dioxide sensors. On pure SnO_2, the adsorption of CO_2 increases the resistance of the oxide. But, when water vapor is present on the SnO_2 surface, the material does not function as a CO_2 sensor (Tamaki et al. 1990a).

By adding some metal oxides to SnO_2, a response can be obtained. Of the metal oxides examined, the highest sensitivity was observed for addition of lanthanum oxide, and the response time is much shortened (Mizuno et al. 1992). For the La_2O_3(4.2 wt.%)-loaded SnO_2 sensor, the 90% response times with CO_2 turned on and off are 0.4 min and 2 min, respectively. By exposing the sensor element to an atmosphere containing carbon dioxide, the resistance of the sensor decreases. This phenomenon occurs due to the desorption of O^- or O_2^- caused by the adsorption of carbon dioxide, and produces oxygen molecules and free electrons (Yoshioka et al. 1991).

The sensing performance is dependent on the operating temperature. The sensitivity has its maximum at 673 K, while the response time is shortened with increasing operating temperature. The sensitivity slightly decreases above 623 K. The sensor's performance is also influenced by the amount of La_2O_3 loading, with a maximum obtained at a loading level of 4.2 wt.% of La_2O_3. An example of the sensor output with CO_2 concentration is presented in fig. 61 (Mizuno et al. 1992). The resistance of the sensor output monotonically increases with increasing CO_2 concentration in the composition region below 2080 ppm.

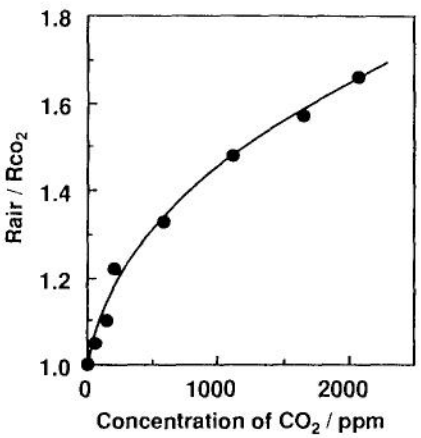

Fig. 61. Output variation of (La_2O_3(2.7 wt.%)-loaded SnO_2) sensor with CO_2 concentration at 673 K (Mizuno et al. 1992). (Reprinted by permission of the publisher, Japan Association of Chemical Sensors.)

7. Alcohol and hydrocarbon sensors

7.1. *Alcohol sensors*

7.1.1. *Introduction*

The application of an alcohol sensor to detect the concentration of alcohol in breath is very effective in enforcing the drinking and driving laws. The development of a portable sensor with simple and fast operation is desired for use in police vehicles to aid in apprehending offenders, and reduce the number of traffic offenses.

Several types of alcohol sensors have been proposed. One uses calorimetric methods based upon the reductive properties of ethanol. Another is to measure the current produced during the electro-oxidization of alcohol to acetic acid (Bay et al. 1972). In addition, an n-type semiconductor such as ZnO has been examined for measurement of the conductivity change due to ethanol adsorption (McArthur et al. 1973). However, those methods are not yet satisfactorily developed for application.

Rare-earth based perovskite oxides, $(R,M)BO_3$, are found to show a high electric conductivity and a large increase in resistivity when they come in contact with a reducing gas such as alcohol (Obayashi et al. 1976, Obayashi and Kudo 1980).

7.1.2. *Mechanism of alcohol sensing*

Rare-earth based perovskite oxides are p-type semiconductors. The resistivity of the oxide increases in a reducing gas atmosphere. However, the increase in resistivity is different for each reducing gas. For example, the increase is small for hydrogen and carbon monoxide, but a large increase in resistivity is observed for ethanol. This is why the perovskite oxide can be operative as an alcohol sensor.

7.1.3. *Sensing performance of perovskite oxides with rare earths*

The perovskite oxide sensitive to ethanol is $(R,M)BO_3$ where R corresponds to a rare earth and M and B represent an alkaline earth metal and Fe, Co, and Ni, respectively.

In general, a higher response ratio is obtained for the oxide with Fe, and a faster response for the samples with Co and Ni. The response ratio is defined as $(R_{sat}-R_0)/R_0$, where R_{sat} and R_0 represents the resistance at a saturated condition and the resistance at an initial stage, respectively. A typical response ratio for the ethanol concentration is shown in fig. 62 (Obayashi et al. 1976). Here, lanthanum occupies one of the perovskite sites. The time necessary to attain the 90% response is monotonically shortened with increasing temperature as tabulated in table 5 (Obayashi et al. 1976). Partial Ni site substitution with Fe in $LaNiO_3$ greatly increases the response ratio as shown in fig. 63 (Obayashi et al. 1976). Perovskite oxides with other rare earths are also effective in obtaining a good response to ethanol. Table 6 (Obayashi et al. 1976) shows the response ratio to 90% response time for the samples which contain various rare earths. The response ratio monotonically increases with a decrease in rare-earth ionic radius, while the 90% response needs more time. The characteristic performance for a prototype ethanol sensor is summarized in

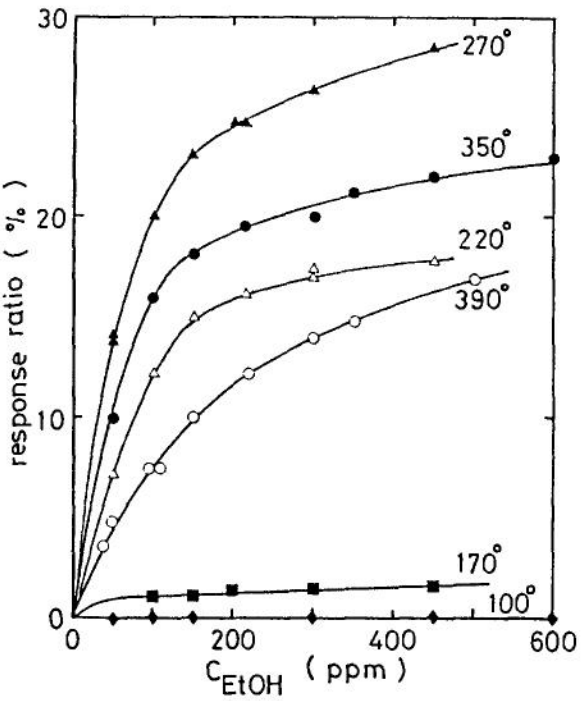

Fig. 62. Response ratio of $LaNiO_3$ against ethanol vapor at varied temperatures (Obayashi et al. 1976). (Reprinted by permission of the publisher, Academic Press, Inc.)

Table 5
Ninety percent response time (t_{90}) of $LaNiO_3$ elements for 150 ppm EtOH (Obayashi et al. 1976) (reprinted by permission of the publisher, Academic Press, Inc.)

Temperature (°C)	t_{90} (s)
100	Inactive ($=\infty$)
150	$>10^5$
170	$\sim 10^4$
220	$\sim 10^3$
270	120–150
330	40–60
350	5–10
390	<5

table 7 (Obayashi et al. 1976). The coexistence of 5 vol% H_2O and/or 1 vol% CO_2 does not influence the ethanol sensing. Because the resistivity change caused by the oxidation of ethanol on the sensor surface directly influences the sensor output, CO and other organic compounds which change the resistivity of the oxide also affect the sensor output. However, the temperature where the oxidation occurs is different for each gas. It is easy to eliminate such interference by selecting an appropriate operating temperature.

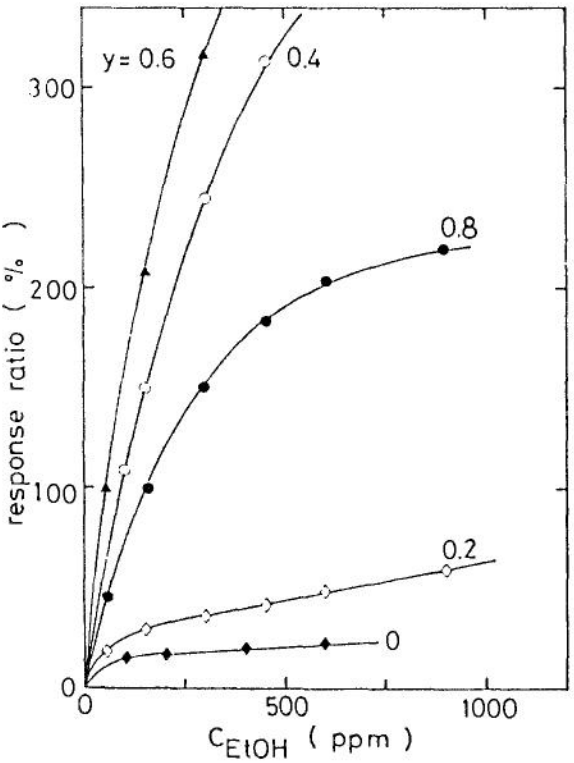

Fig. 63. Response ratio of $LaNi_{1-y}Fe_yO_3$ against ethanol vapor at 350°C (Obayashi et al. 1976). (Reprinted by permission of the publisher, Academic Press, Inc.)

Table 6
Response ratio of $R_{0.5}Sr_{0.5}CoO_3$ for 150 ppm EtOH and related compounds at 330°C (Obayashi et al. 1976) (reprinted by permission of the publisher, Academic Press, Inc.)

Compound	Response ratio (%)	t_{90} (s)
$La_{0.5}Sr_{0.5}CoO_3$	25	50
$Nd_{0.5}Sr_{0.5}CoO_3$	40	150
$Sm_{0.5}Sr_{0.5}CoO_3$	50	100
$Gd_{0.5}Sr_{0.5}CoO_3$	90	250
$Sm_{0.5}Sr_{0.5}Co_{0.8}Fe_{0.2}O_3$	130	–
$Sm_{0.5}Sr_{0.5}Co_{0.5}Fe_{0.5}O_3$	400	–
$Sm_{0.5}Sr_{0.5}FeO_3$	1200	–

Another unusual alcohol sensing method is based on using the $BaCeO_3$-based protonic conductor which is used as an electrolyte for humidity sensing (sect. 4). A cross-sectional view of the sensor is presented in fig. 64 (Hibino and Iwahara 1992b, Iwahara and Hibino 1993). The operating temperature is 723 K and the sensor response with various alcohol

Table 7
Some characteristics of a prototype ethanol sensor based on $LaNiO_3$ (Obayashi et al. 1976) (reprinted by permission of the publisher, Academic Press, Inc.)

Response ratio	Sensitivity	t_{90}	Ethanol on–off cycle	Heat cycle (r.t.~400°C)	400°C keep
20% against 200 ppm EtOH	30 ppm	≈5 s	$>1.2\times10^4$	$>5\times10^3$	>2000 hr

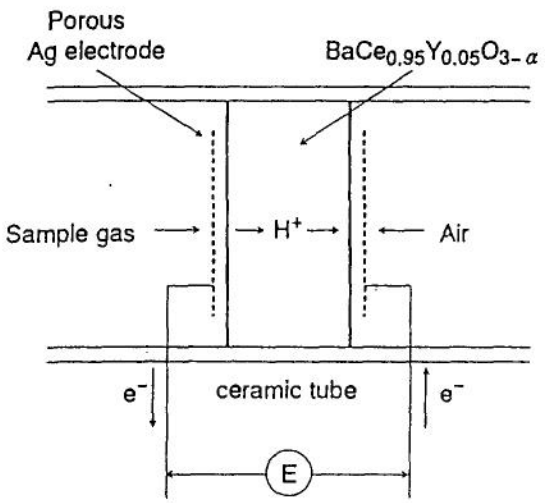

Fig. 64. Schematic illustration of the gas cell (Hibino and Iwahara 1992b). (Reprinted by permission of the publisher, The Chemical Society of Japan.)

concentrations is shown in fig. 65 (Hibino and Iwahara 1992b, Iwahara and Hibino 1993). The EMF output increases monotonically with the concentration. The time necessary for the attainment of 90% response is 10 seconds after ethanol exposure starts and a few minutes to recover when ethanol exposure stops.

The mechanism of alcohol sensing is proposed as follows. Ethanol is subject to dehydrogenation on $BaCeO_3$ and produces CH_3CHO and H_2. The sensor detects the hydrogen produced at the protonic conductor surface.

Another type of alcohol sensor where a rare earth is mixed to enhance the sensing characteristics has also been proposed. A typical sensor element is illustrated in fig. 66 (Matsushima et al. 1989). A paste of rare-earth oxide mixed with tin oxide powder was mounted on an alumina tube with two platinum coil electrodes and then a heat treatment was conducted. The ethanol sensing characteristics of La_2O_3-loaded SnO_2 increased by a factor of 43 compared with an unloaded SnO_2 element. However, there was no difference in the response transient to ethanol. Also, the time necessary to recover stable output when ethanol is removed from the ambient atmosphere is greatly shortened by rare-earth doping. Figure 67 (Matsushima et al. 1989) shows the ethanol (1000 ppm) sensitivities of various metal-oxide doped elements as a function of the electronegativity of the dopant

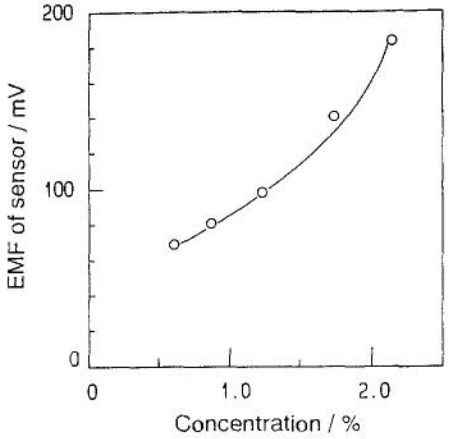

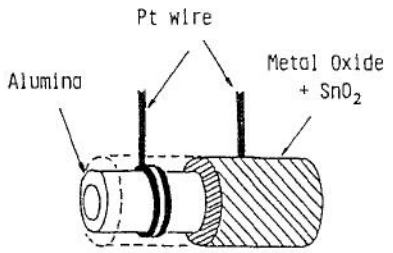

Fig. 66. Schematic view of the gas sensor element (Matsushima et al. 1989). (Reprinted by permission of the publisher, The Chemical Society of Japan.)

Fig. 65. EMF as a function of concentration of ethanol at 723 K (Hibino and Iwahara 1992b). (Reprinted by permission of the publisher, The Chemical Society of Japan.)

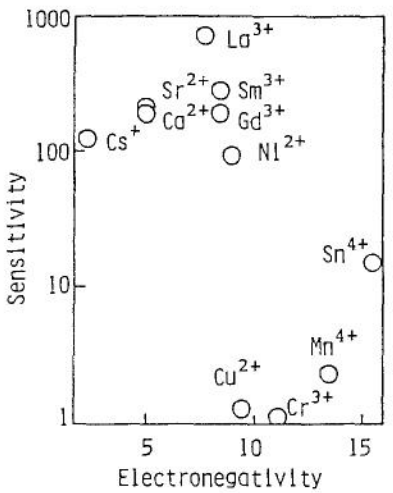

Fig. 67. Gas sensitivities of 5 wt.% metal oxide loaded-SnO_2 elements to 1000 ppm ethanol in air at 300°C as correlated with the electronegativities of loaded metal cations (Matsushima et al. 1989). (Reprinted by permission of the publisher, The Chemical Society of Japan.)

metal cation. It can be seen from the figure that a high ethanol sensitivity is obtained for the basic oxides containing alkali, alkaline-earth or rare-earth elements. Pd addition to the La_2O_3–SnO_2 system contributes to shorten the response time, but simultaneous Pd and La_2O_3 doping into SnO_2 increases the electric resistance of the element. This increase makes it difficult to apply the conventional circuitry to measure sensor response.

Indium oxide shows appreciably lower resistivity than SnO_2, so In_2O_3 was substituted for SnO_2 in order to mitigate this difficulty. In addition, the structure of the sensor element was changed from the bulk-layer type to that of a thick film, resulting in the enhancement of both the sensitivity and the selectivity. The 90% response time was about 35 seconds and the sensitivity to ethanol further increased by a factor of 84 compared with unloaded

Table 8
The sensitivity of a Pd–La_2O_3–In_2O_3 thick film element to various gases (300°C, 1000 ppm in air) (Tamaki et al. 1990b) (reprinted by permission of the publisher, The Chemical Society of Japan)

Gas	Sensitivity
C_2H_5OH	1994
CO	34
H_2	32
CH_4	6
i-C_4H_{10}	22

SnO_2. Selective ethanol sensing is also achieved by addition of both Pd and La_2O_3 to In_2O_3. As listed in table 8 (Tamaki et al. 1990b), the sensor response to ethanol is exceptionally high compared with other gases, such as CO, H_2, CH_4 or i-C_4H_{10}. The addition of La_2O_3 and Pd to In_2O_3 has brought a remarkable enhancement in sensitivity and selectivity, and shortened the response time to ethanol, together with an appropriate resistivity, suitable for practical applications.

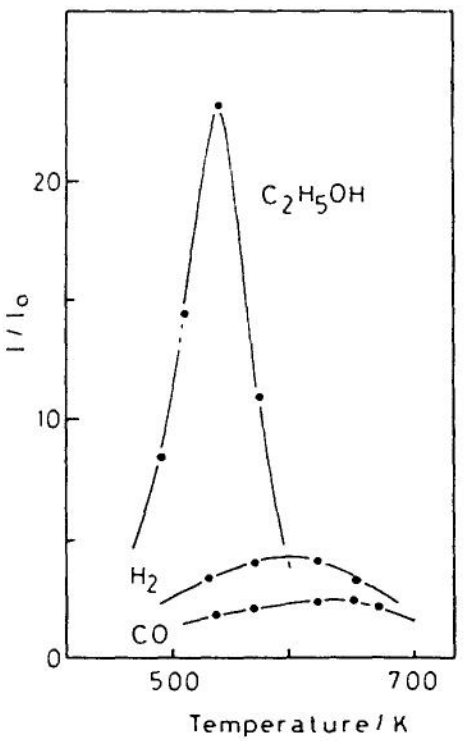

Fig. 68. $Sm_{0.8}Sr_{0.2}MnO_3/SnO_2$ sensitivity vs. temperature curves (Mitsuoka et al. 1992). (Reprinted by permission of the publisher, Elsevier Sequoia S.A.)

In the rare-earth series from La to Sm, R_2CuO_4 shows the highest ethanol sensitivity. Both R_2CuO_4 (R = La, Nd, Sm) and SnO_2 were pelletized and placed in mechanical contact to make a heterojunction. The I–V characteristics of R_2CuO_4/SnO_2 were measured by applying a bias potential of 0.5 V between the combined pellets. Of the R_2CuO_4 compounds examined, La_2CuO_4/SnO_2 shows the highest activity. This is ascribed to the formation of an excellent p–n junction by combining p-type La_2CuO_4 and n-type SnO_2 (Makimoto and Arakawa 1992).

Another type of ethanol sensor uses a similar heterojunction. In this case, tin oxide is combined with a rare-earth manganate. Hydrogen gas reacts with the oxygen of non-stoichiometric perovskite oxides and adsorbed oxygen on SnO_2. This results in a change of interface such as the Fermi contact level, space charge, etc. Figure 68 (Mitsuoka et al. 1992) shows the temperature dependence of the sensor sensitivity to various gases (about 0.5 ml carbon monoxide, hydrogen, 3 µl ethanol when the sensor is biased with a potential of 0.5 V; I and I_0 represent the current produced in a sample gas and in air, respectively). From the figure, the sensing is in the order of $C_2H_5OH > H_2 > CO$. Because sensor detection is clearly related to the reactivity of the adsorbed oxygen on SnO_2 or perovskite oxides, as well as the reactivity of the oxygen of non-stoichiometric perovskite oxides, the selectivity can be improved by changing the combination of perovskite oxides and metal oxides.

7.2. *Hydrocarbon sensors*

A protonic conductor such as $CaZr_{0.9}In_{0.1}O_{3-x}$ can be applied to sense hydrocarbon gases. In this case, two different electrodes were used. One is silver metal which is a material inert to hydrocarbons and the other is a perovskite-type oxide ($La_{0.6}Ba_{0.4}CoO_3$) which contains rare earth and accelerates the combustion of hydrocarbons. The chemical reaction occurring in the sensor is shown in fig. 69 (Hibino and Iwahara 1994). Hydrocarbons in the ambient atmosphere do not react on the Ag electrode. On the contrary, hydrocarbons react with oxygen and form water vapor and carbon dioxide on the oxide electrode surface.

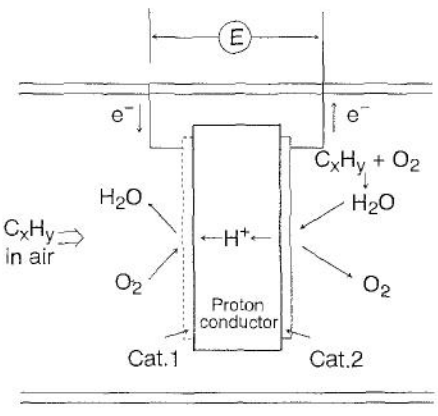

Fig. 69. Principle of the hydrocarbon sensor using a protonic conductor as a solid electrolyte: Cat. 1 and 2 show the electrode materials which are inert to hydrocarbons and catalyze their combustion, respectively (Hibino and Iwahara 1994).

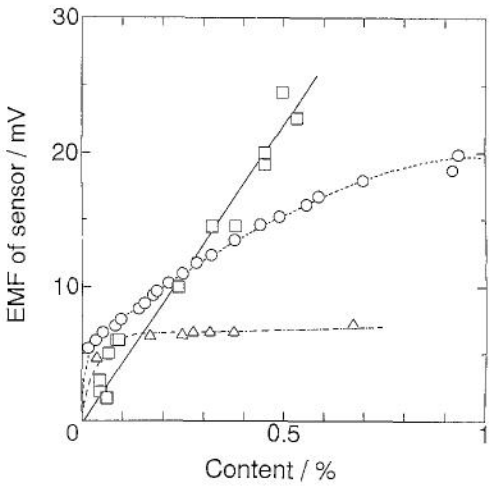

Fig. 70. Variation of EMF of the sensor element with CH_4 (open circles), C_2H_6 (open triangles) and C_3H_8 (open squares) gas composition (Hibino and Iwahara 1994).

The water vapor content of each electrode is different, and so a water vapor concentration cell can be fabricated by using a protonic conductor as described in sect. 4, for a high-temperature humidity sensor. In this type of concentration cell, the water vapor in the ambient atmosphere is applied as a reference. No effort is necessary to establish a standard electrode. The time necessary for 90% response is less than 1 min. The water vapor pressure at the oxide electrode is higher than that on the Ag electrode. By using different electrodes, the water vapor pressure on each of them differs.

The sensor output change at 770°C when exposed to several hydrocarbons (CH_4, C_2H_6, C_3H_8) is shown in fig. 70 (Hibino and Iwahara 1994). From the figure, it is easy to find that the sensor works well for the gases CH_4 and C_3H_8, but not for C_2H_6. This is because, on the Ag electrode surface, C_2H_6 is oxidatively dehydrogenated and forms water vapor. This does not result in a clear difference of water vapor content between two electrodes. For the accurate detection of C_2H_6, we should choose a material which does not cause hydrocarbon combustion and which is inert to the oxidative dehydrogenation of C_2H_6. The sensitivity and reactivity toward hydrocarbons are different for every electrode material. This indicates that the response, sensitivity and selectivity can be controlled by choosing the appropriate combination of two electrodes.

The outstanding merits of this type of hydrocarbon sensor are as follows. Firstly, the sensing characteristics are enhanced by choosing the appropriate combination of electrodes. Secondly, a standard electrode material is not necessary for detection because the water vapor which initially exists in the atmosphere is applied as the reference material.

An attempt has been made to develop a long-lasting, ambient-temperature, solid state, amperometric sensor with high resistance against humidity (Zaromb et al. 1993). The sensor uses the solid electrolyte $Ce_{0.95}Ca_{0.05}F_{2.95}$ and comprises a sensor cell of $Sn/Ce_{0.95}Ca_{0.05}F_{2.95}/Pt$. For the detection of gaseous species, the sensing electrode potential necessary to elicit a response to oxidizable compounds such as CO or $CH_3N_2H_3$

is only about 0.4 V. On the contrary, a potential of 0.8 V or higher is necessary to obtain a response to CH_4. In order to detect CH_4, the sensor also responds to more easily oxidizable compounds such as CO and $CH_3N_2H_3$, as well as CH_4, since a higher potential is needed for the detection. So, to determine the accurate CH_4 concentration, two sensors are required. One is biased at higher potential for the detection of both CH_4 and more oxidizable compounds. The other is biased to sense only the oxidizable compounds. At present, the sensitivity of the sensor is apt to degrade with time. However, the $Ce_{0.95}Ca_{0.05}F_{2.95}$ based sensor still shows a response to methane after a period of eight months.

8. Nitrogen oxide sensors

8.1. *Introduction*

Nitrogen oxides are emitted mainly during the combustion of fossil fuel. There are two representative generating sources. One is the combustion facilities and the other is moving vehicles, such as automobiles and trucks. The exhaust nitrogen oxides cause acid rain and photochemical smog. As a result of these phenomena, environmental pollution has been spreading on a global scale. In practical situations, instrumental methods such as chemiluminescence and infrared analysis have been extensively applied for NO_x detection. The methods are suitable to measure the gas content, but the apparatus is expensive and quite difficult to install at every combustion facility. On-site NO_x monitoring is very effective in suppressing the total amount of combustion exhaust into the air. For such an application, oxide semiconductors have been heavily investigated for use as sensor components.

In 1986, Bednorz and Müller (1986) discovered a high-temperature oxide superconductor of $(La_{1-x}Ba_x)_2CuO_4$ with its critical temperature above 30 K. After the discovery, another oxide superconductor was discovered with the composition $YBa_2Cu_3O_{7-x}$ (123 phase). In this 123 phase, the superconducting properties remain in the cases where Y is completely substituted with other rare-earth ions except for praseodymium. These two types of superconductor show p-type conducting properties. After their discovery, n-type oxide superconductors were also discovered. The oxide is $R_{2-x}R'_xCuO_4$ (R = Pr, Nd or Sm, R′ = Ce). In the n-type superconductors, praseodymium can be a constituent of the superconductor, and in the rare-earth series, the only exception is Sc.

One of the representative applications of the superconductors based on cuprate oxides is their use as a component of the NO_x sensor.

8.2. *Nitrogen oxide sensing*

There have been some attempts to apply the cuprate oxide superconductors to chemical sensing. When gases such as NO, NO_2, N_2O exist in the ambient atmosphere, the resistivities of $YBa_2Cu_3O_{7-y}$ and $Eu_{1+x}Ba_{2-x}Cu_3O_{7-y}$ increase remarkably (Munakata

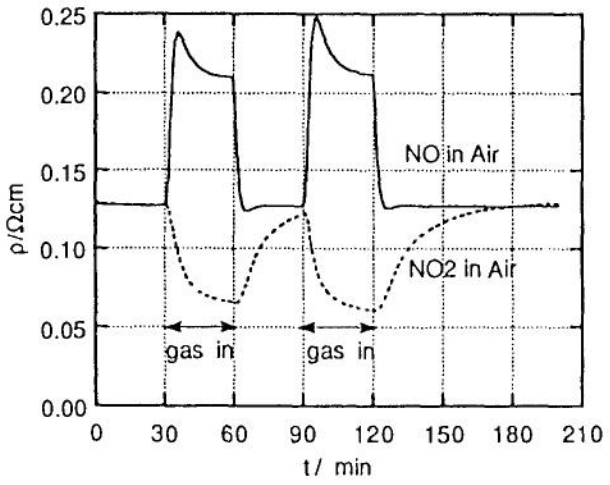

Fig. 71. La_2CuO_4 resistivity changes at 400°C by NO_x gases (3000 ppm) in air (Morita et al. 1993). (Reprinted by permission of the publisher, The Electrochemical Society Inc.)

et al. 1992). In these cases, NO or NO_2 was adsorbed on the surface of the oxide superconductors. NO and NO_2 were chemisorbed in the positive charged state. The existence of N_2O also enhances the resistivity through the catalytic decomposition of N_2O on the oxide surface. These results indicate that the oxides have a potential for application as a NO_x sensor.

Lanthanum cuprate is well known from the discovery of the oxide high-temperature superconductor. Application of oxide superconductors as chemical sensor material has been investigated. La_2CuO_4 shows metallic behavior with a hole-type conduction. The effect of NO or NO_2 gas presence on the resistivity of La_2CuO_4 is shown in fig. 71 (Morita et al. 1993). The resistivity starts to change when it comes in contact with nitrogen oxides. The direction of the change is opposite for NO and NO_2. It increases in the presence of NO, and decreases in the presence of NO_2. This indicates that NO gas is adsorbed on the oxide surface in a positive-charge state, while the NO_2 gas is in a negative state. By using this feature, it is possible to sense NO and NO_2 separately. Response time is a few minutes for NO but clearly longer for NO_2.

La_2NiO_4 is isostructual with La_2CuO_4, and the resistivity of both oxides is quite similar. However, the response of the resistivity change in the presence of NO_x is considerably lower, by as much as $1/10$ (Morita et al. 1993). The existence of copper in the oxide is essential in NO_x sensing.

The sensor material used for this experiment is not high in density and has larger grain size. By controlling these parameters during the preparation process, an improvement of the NO_x sensing characteristics is expected.

$YBa_2Cu_3O_{7-x}$, which is one of the familiar high-temperature oxide superconductors with rare earths, reacts with NO and then decomposes (Huang et al. 1992). When n-type $Nd_{1.85}Ce_{0.15}CuO_{4-x}$ oxide superconductor is used, no sensor response is observed in NO_x or CO_x existing atmospheres.

The nitrogen oxides are pollutant gases from industrial facilities. One of the characteristics of pollutant gases from living things is odor. A representative odor is trimethylamine (TMA) which comes from rotting fish. TMA penetrates to the neck of sintered SnO_2 particles and increases the resistivity. La_2O_3 addition into SnO_2 suppresses the catalytic activity of the TMA oxidation (Nishizaka et al. 1992). Excess addition of La inhibits neck formation and results in low TMA sensitivity. Here, a common rare-earth application is doping which is effective to enhance the odor sensing characteristics.

9. Concluding remarks

It is not commonly known that rare earths play such an important role in the chemical sensor field and have been extensively used in applications world-wide. One of the most common applications is the use of rare earths as a dopant to improve material characteristics. Rare-earth addition as a dopant is very effective in stabilizing an appropriate phase for sensor material as mentioned in sect. 2 for stabilized zirconia in the oxygen sensor. In these applications, one of the typical characteristics is that most rare earths effectively maintain a stable trivalency. Doping of a stable trivalent rare earth into an aliovalent site produces ionic vacancies and appreciably enhances the ionic conduction. The increase in conductivity is closely related to the enhancement of the sensing characteristics. In stabilized zirconia, yttrium is selected as the dopant. Yttrium doping makes it possible to stabilize the high-temperature phase of zirconia with a high conduction. Yttrium is not a base component element, but just a dopant. However, doping results in a remarkable improvement of the sensing characteristics.

In a humidity sensor, ytterbium doping into the rare-earth cerium base material is the key point to obtaining a suitable solid electrolyte for humidity detection. Cerium site substitution of the ytterbium trivalent cation produces holes in the cerate and it becomes an excellent protonic conductor in the presence of hydrogen or water vapor. Rare-earth doping in the cerate is essential to obtain a solid electrolyte for the humidity sensor.

Doping of rare-earth elements into a sulfate electrolyte also contributes appreciably to obtaining a good ionic conductor similar to the case for stabilized zirconia. Doping causes retention of the high-temperature phase for superior ionic conduction. One different feature between stabilized zirconia and the sulfate electrolyte is that the trivalent rare earth substitutes a monovalent cation site in the sulfate electrolyte, while the tetravalent zirconium site is replaced with trivalent yttrium in zirconia. In the sulfate electrolyte, the vacancy produced is not an anion vacancy but a cation vacancy. Their production also enhances the cationic conduction which reflects in the improvement of the sensing characteristics.

One other rare-earth application is their direct use as a base material of the sensor. One typical application is with rare-earth fluorides. The fluorides are excellent fluorine ionic conductors even at room temperature and also very stable in an aqueous solution. These features make the commercial use in fluorine sensing in a solution possible. A practically used material is lanthanum fluoride. Other rare earths also show similar

properties. However, these fluorides are too expensive and less stable than the lanthanum fluoride electrolyte. In a practical fluoride sensor, europium, which is one of the most expensive rare-earth elements, is used as a dopant. This doping, a typical application of rare earth elements in the chemical sensor field, also appreciably increases the F^{-1} sensing ability. Another application of a rare earth as a base component is in the strontium cerate electrolyte for humidity sensors. In this material, tetravalent cerium is used as a base component. This type of sensor is an example of the uncommon case where rare earths are not only applied as a dopant, but also as a base material.

A base material used for alcohol sensing is the perovskite oxide with rare-earth elements, which shows p-type semiconducting properties. The most commonly used rare earth is lanthanum. In this case, to retain a perovskite structure with semiconducting characteristics is important. Other rare earths are used instead of lanthanum. However, lanthanum is the most reasonable choice of the rare-earths series from the expense viewpoint. Methane sensing is also attempted by using the rare-earth-containing perovskite oxide. The perovskite oxide does not act as base material but as the auxiliary electrode to accelerate methane combustion.

There have been some attempts to examine rare-earth oxides or rare-earth-containing oxides as sensors for carbon dioxide or nitrogen oxides. In these cases, the absorption or adsorption of the gases on the surface of the sensor element plays a significant role in detecting the gases.

Many kinds of rare-earth elements have already been used in commercial production and have been proposed in prototype sensors. The rare-earth series is composed of scandium, yttrium, and fifteen lanthanoid elements. So, except for Pm, there are sixteen elements from which to select. The ionic radii of the rare earths are quite similar because of the lanthanide contraction, in addition to maintaining a stable trivalency. Furthermore, some of the rare earths show di- or tetravalency in addition to trivalency. This valency change results in a change in ionic radius even for the same rare-earth cation. This variation in ionic radius widens the application of rare earths as a dopant in addition to their use as a base material, and makes possible the selection of an appropriate rare-earth element for a chosen application. Rare-earth usage in the chemical sensor field has been making steady progress and new and unique types of sensors with rare earths can be expected to be developed. The rare-earth series is a promising elemental group and plays a "Saviour" role in the Periodic Table; to improve materials characteristics significantly as a dopant and to develop new materials which will make a great and unique contribution, not only in the chemical sensor field, but also in our life style.

Acknowledgement

The authors greatly wish to express their thanks to Dr. Michael Post of the National Research Council of Canada for his advice in preparing the article.

References

Adachi, G., 1988, Seramikkusu **23**, 435.

Adachi, G., 1991, Kidorui Monogatari (Sangyo Tosho), p. 101. In Japanese.

Adachi, G., and N. Imanaka, 1991, Chem. Sens. Tech. **3**, 131.

Adachi, G., and M. Shimada, 1982, Mukizairyou Kagaku (Kagaku-Dojin), p. 66.

Alcock, C.B., B. Li, J.W. Fergus and L. Wang, 1992a, Solid State Ionics **53–56**, 39.

Alcock, C.B., J.W. Fergus and L. Wang, 1992b, Solid State Ionics **51**, 291.

Alcock, C.B., B. Li and L. Wang, 1993, Solid state galvanic oxygen sensors (25–1600°C), in: Proc. Symposium on Chemical Sensors II, 1993, eds M. Butler, A. Ricco and N. Yamazoe (Electrochemical Society, Pennington) pp. 174–181.

Arai, H., S. Ezaki, Y. Shimizu, O. Shippo and T. Seiyama, 1983, Semiconductive humidity sensor of perovskite-type oxides, in: Proc. Int. Meeting on Chemical Sensors, eds T. Seiyama, K. Fueki, J. Shoikawa and S. Suzuki (Kodansha/Elsevier) pp. 393–398.

Ardakani, H.K., S.S. Shushtarian, S.M. Kanetkar, R.N. Karekar and S.B. Ogale, 1993, J. Mater. Sci. Lett. **12**, 63.

Azad, A.M., S.A. Akbar, S.G. Mhaisalkar, L.D. Birkefeld and K.S. Goto, 1992, J. Electrochem. Soc. **139**, 3690.

Baumann, E.W., 1968, Anal. Chim. Acta **42**, 127.

Bay, H.W., K.F. Blurton, H.C. Lieb and H.G. Oswin, 1972, Nature **240**, 52.

Bednorz, J.G., and K.A. Müller, 1986, Z. Phys. B **64**, 189.

Bock, R., and S. Strecker, 1968, Z. Anal. Chem. **235**, 322.

Duwez, P., F.H. Brown Jr and F. Odell, 1951, J. Electrochem. Soc. **98**, 356.

Etsell, T.H., and S.N. Flengas, 1970, Chem. Rev. **70**, 339.

Fagan, J., and V.R.W. Amarakoon, 1993, Am. Ceram. Soc. Bull. **72**, 119.

Fleming, W.J., 1977, J. Electrochem. Soc. **124**, 21.

Frant, M.S., and J.W. Ross Jr, 1966, Science **154**, 1553.

Gauthier, M., and C.W. Bale, 1983, Metall. Trans. **14B**, 117.

Gauthier, M., and A. Chamberland, 1977, J. Electrochem. Soc. **124**, 1579.

Gauthier, M., A. Chamberland, A. Belanger and M. Poirier, 1977, J. Electrochem. Soc. **124**, 1584.

Gauthier, M., R. Bellemare, A. Belanger and M. Poirier, 1981, J. Electrochem. Soc. **128**, 371.

Goldman, M., and L. Shen, 1966, Phys. Rev. **144**, 321.

Gopalan, S., and A.V. Virkar, 1993, J. Electrochem. Soc. **140**, 1060.

Hibino, T., and H. Iwahara, 1992a, Chem. Lett., p. 1221.

Hibino, T., and H. Iwahara, 1992b, Chem. Lett., p. 1225.

Hibino, T., and H. Iwahara, 1994, J. Appl. Electrochem. **24**, 268.

Höfer, H.H., W. Eysel and U. v. Alpen, 1978, Mater. Res. Bull. **13**, 265.

Höfer, H.H., W. Eysel and U. v. Alpen, 1981, J. Solid State Chem. **36**, 365.

Huang, X.J., L.Q. Chen and J. Schoonman, 1992, Solid State Ionics **57**, 7.

Imanaka, N., G. Adachi and J. Shiokawa, 1983a, Denki Kagaku 51, 93. In Japanese.

Imanaka, N., G. Adachi and J. Shiokawa, 1983b, Na_2SO_4 doped with $NaVO_3$ and/or $Ln_2(SO_4)_3$ (Ln = rare earths) as an SO_2 solid electrolyte sensor, in: Proc. Int. Meeting on Chemical Sensors, eds T. Seiyama, K. Fueki, J. Shiokawa and S. Suzuki (Kodansha/Elsevier) pp. 348–352.

Imanaka, N., G. Adachi and J. Shiokawa, 1983c, Chem. Lett. 287.

Imanaka, N., G. Adachi and J. Shiokawa, 1984, Bull. Chem. Soc. Jpn. **57**, 687.

Imanaka, N., Y. Yamaguchi, G. Adachi and J. Shiokawa, 1985a, Bull. Chem. Soc. Jpn. **58**, 5.

Imanaka, N., Y. Yamaguchi, G. Adachi and J. Shiokawa, 1985b, J. Electrochem. Soc. **132**, 2519.

Imanaka, N., G. Adachi and J. Shiokawa, 1986a, A solid electrolyte for sulfur dioxide detection, sodium sulfate mixed with rare earth sulfates and silicon dioxide, ACS Symposium on Chemical Sensors – Fundamentals and Applications (American Chemical Society) p. 121.

Imanaka, N., Y. Yamaguchi, G. Adachi and J. Shiokawa, 1986b, J. Electrochem. Soc. **133**, 1757.

Imanaka, N., Y. Yamaguchi, G. Adachi, J. Shiokawa and H. Yoshioka, 1986c, Solid State Ionics **20**, 153.

Imanaka, N., Y. Yamaguchi, G. Adachi and J. Shiokawa, 1986d, J. Electrochem. Soc. **133**, 1026.

Imanaka, N., K. Kuwabara, G. Adachi and J. Shiokawa, 1987a, Solid State Ionics **23**, 15.

Imanaka, N., Y. Yamaguchi, G. Adachi and J. Shiokawa, 1987b, J. Electrochem. Soc. **134**, 725.

Imanaka, N., K. Kawai, J. Shiokawa and G. Adachi, 1988, Chem. Lett. 1133.

Ishigaki, T., S. Yamauchi, K. Kishio and K. Fueki, 1986, Solid State Ionics **21**, 239.

Itoh, M., E. Sugimoto and Z. Kozuka, 1984, Trans. Jpn. Inst. Met. **25**, 504.

Iwahara, H., 1988, Solid State Ionics **28–30**, 573.

Iwahara, H., and T. Hibino, 1993, New gas sensors using high temperature proton conducting ceramics, in: Proc. Symp. on Chemical Sensors II, 1993, eds M. Butler, A. Ricco and N. Yamazoe (Electrochemical Society, Pennington) pp. 464–473.

Iwahara, H., T. Esaka, H. Uchida and N. Maeda, 1981, Solid State Ionics **3/4**, 359.

Iwahara, H., H. Uchida and J. Kondo, 1983a, J. Appl. Electrochem. **13**, 365.

Iwahara, H., H. Uchida and N. Maeda, 1983b, Solid State Ionics **11**, 109.

Iwahara, H., H. Uchida and S. Tanaka, 1983c, Solid State Ionics **9–10**, 1021.

Iwahara, H., T. Esaka, H. Uchida, T. Yamauchi and K. Ogaki, 1986, Solid State Ionics **18–19**, 1003.

Iwahara, H., H. Uchida, K. Ono and K. Ogaki, 1988, J. Electrochem. Soc. **135**, 529.

Iwahara, H., H. Uchida, K. Morimoto and S. Hosogi, 1989a, J. Appl. Electrochem. **19**, 448.

Iwahara, H., H. Uchida, T. Nagano and K. Koide, 1989b, Denki Kagaku 57, 992.

Iwahara, H., H. Uchida and K. Morimoto, 1990a, J. Electrochem. Soc. **137**, 462.

Iwahara, H., H. Uchida and K. Morimoto, 1990b, Denki Kagaku **58**, 178.

Iwahara, H., T. Yajima, H. Uchida and K. Morimoto, 1991, SOFC using perovskite-type oxide $BaCe_{0.9}Nd_{0.1}O_{3-x}$ as a solid electrolyte, in: Proc. 2nd Int. Symp. on Solid Oxide Fuel Cells, Athens, Greece, 1991 (Commission of the European Communities) pp. 229–235.

Jacob, K.T., and D.B. Rao, 1979, J. Electrochem. Soc. **126**, 1842.

Koide, K., T. Yajima and H. Iwahara, 1992, Characteristics of hydrogen and stream sensors using proton conducting ceramics, in: Technical Digest, 4th Int. Meeting on Chemical Sensors, 1992, pp. 710–711.

Koryta, J., and K. Stulik, 1983, Ion-Selective Electrodes, 2nd Ed. (Cambridge University Press, Cambridge) p. 144.

Kreidl, E.L., and I. Simon, 1958, Nature **181**, 1529.

Kudo, T., and H. Obayashi, 1975, J. Electrochem. Soc. **122**, 142.

Kudo, T., and H. Obayashi, 1976, J. Electrochem. Soc. **123**, 415.

Kuwata, S., N. Miura, N. Yamazoe and T. Seiyama, 1984a, Nippon Kagaku Kaishi, p. 1232.

Kuwata, S., N. Miura, N. Yamazoe and T. Seiyama, 1984b, Chem. Lett., p. 981.

Kuwata, S., N. Miura, N. Yamazoe and T. Seiyama, 1984c, Chem. Lett., p. 1295.

Lakshminarayanaiah, N., 1976, Membrane Electrodes (Academic Press, New York) p. 127.

LaRoy, B.C., A.C. Lilly and C.O. Tiller, 1973, J. Electrochem. Soc. **120**, 1668.

Li, N., T.C. Tan and H.C. Zeng, 1993, J. Electrochem. Soc. **140**, 1068.

Lingane, J.J., 1967, Anal. Chem. **39**, 881.

Liu, Q., and W.L. Worrell, 1988, Solid State Ionics **28–30**, 1668.

Liu, Q., K. Huang, Y. Xia, W. Liu, W.L. Worrell and H. Clauss, 1993, Oxygen sensor with double layer electrolyte for low oxygen measurement of steel melts, in: Proc. Symp. on Chemical Sensors II, 1993, eds M. Butler, A. Ricco and N. Yamazoe (Electrochemical Society) pp. 281–286.

Logothetis, E.M., 1991, Automotive oxygen sensors, Chemical Sensor Technology, Vol. 3 (Kodansha/Elsevier) p. 89.

Makimoto, O., and T. Arakawa, 1992, Sensing properties of Ln_2CuO_4/SnO_2 (Ln= rare earth) having the heterojunction, in: Technical Digest, 4th Int. Meeting on Chemical Sensors, 1992, pp. 664–665.

Marbeuf, A., G. Demazeau, S. Turrell, P. Hagenmuller, J. Derouet and P. Caro, 1971, J. Solid State Chem. **3**, 637.

Mari, C.M., and G. Terzaghi, 1983, Thick films of non-stoichiometric oxides: new electrodes for high temperatures solid state oxygen meters, in: Proc. Int. Meeting on Chemical Sensors, eds T. Seyama, K. Fueki, J. Shiokawa and S. Suzuki (Kodansha/Elsevier) pp. 273–278.

Maruyama, T., Y. Saito, Y. Matsumoto and Y. Yano, 1985, Solid State Ionics **17**, 281.

Matsushima, S., T. Maekawa, J. Tamaki, N. Miura and N. Yamazoe, 1989, Chem. Lett., p. 845.

McArthur, D.P., H. Bliss and J.B. Butt, 1973, J. Catal. **28**, 183.

Mesmer, R.E., 1968, Anal. Chem. **40**, 443.

Mingmei, W., and R. Yufang, 1992, Sens. Actuators B **8**, 179.

Mitsuoka, M., A. Otofuji and T. Arakawa, 1992, Sens. Actuators B **9**, 205.

Miura, N., J. Hisamoto, S. Kuwata and N. Yamazoe, 1987, Chem. Lett., p. 1477.

Miura, N., J. Hisamoto, N. Yamazoe, S. Kuwata and J. Salardenne, 1989, Sens. Actuators **16**, 301.

Mizuno, N., T. Yoshioka and M. Iwamoto, 1992, CO_2 sensing characteristics of SnO_2 element modified by La_2O_3, in: Technical Digest, 4th Int. Meeting on Chemical Sensors, 1992, pp. 542–545.

Morita, T., M. Miyayama, J. Motegi and H. Yanagida, 1993, NO_x gas sensing properties of La_2CuO_4 ceramics II, in: Proc. Symp. on Chemical Sensors II, 1993, eds M. Butler, A. Ricco and N. Yamazoe (Electrochemical Society, Pennington) pp. 450–455.

Munakata, F., K. Shinohara, M. Kobayashi, K. Furuya, M. Yamanaka and H. Takao, 1992, Gas sensory properties of $R_{1+x}Ba_{2-x}Cu_3O_{7-y}$, in: Technical Digest, 4th Int. Meeting on Chemical Sensors, 1992, pp. 580–581.

Nishizaka, Y., C. Yokoyama, K. Inumaru, T. Okuhara and M. Misono, 1992, Effect of additives and particle size on the sensitivity of SnO_2-based sensor for offensive-odor components, in: Technical Digest, 4th Int. Meeting on Chemical Sensors, 1992, pp. 418–421.

Obayashi, H., and T. Kudo, 1980, Nippon Kagaku Kaishi, p. 1568.

Obayashi, H., Y. Sakurai and T. Gejo, 1976, J. Solid State Chem. **17**, 299.

Okamoto, H., H. Obayashi and T. Kudo, 1980, Solid State Ionics **1**, 319.

O'Keeffe, M., 1973, Science **180**, 1276.

Oohata, T., 1990, Kidorui **17**, 37.

Portier, J., 1976, Angew. Chem. Int. Ed. Engl. **15**, 475.

Post, M.L., and B.W. Sanders, 1993, Oxygen sensing using the bulk properties of perovskite thin-films, in: Proc. Symp. on Chemical Sensors II, 1993, eds M. Butler, A. Ricco and N. Yamazoe (Electrochemical Society, Pennington) pp. 358–362.

Pratt, J.N., 1990, Metall. Trans. A **21**, 1223.

Rechnitz, G.A., 1967, Chem. Eng. News (June 12), p. 146.

Saito, Y., K. Kobayashi and T. Maruyama, 1981, Solid State Ionics **3/4**, 393.

Saito, Y., K. Kobayashi and T. Maruyama, 1982, Thermochim. Acta **53**, 289.

Saito, Y., T. Maruyama, Y. Matsumoto and Y. Yano, 1983, Electromotive force of the SO_2–O_2–SO_3 concentration cell using NASICON ($Na_3Zr_2Si_2PO_{12}$) as a solid electrolyte, in: Proc. Int. Meeting on Chemical Sensors, eds T. Seiyama, K. Fueki, J. Shiokawa and S. Suzuki (Kodansha/Elsevier) pp. 326–331.

Saito, Y., T. Maruyama and K. Kobayashi, 1984a, Solid State Ionics **14**, 265.

Saito, Y., T. Maruyama and S. Sakai, 1984b, Rep. Res. Lab. Eng. Mater. (Tokyo Institute of Technology) 9, 17.

Shannon, R.D., 1976, Acta Crystallogr. A **32**, 751.

Sheppard, L.M., 1992, Ceram. Bull. **71**, 905.

Sher, A., R. Solomon, K. Lee and M.W. Muller, 1966, Phys. Rev. **144**, 593.

Shimizu, Y., M. Shimabukuro, H. Arai and T. Seiyama, 1985, Chem. Lett., p. 917.

Shimizu, Y., M. Shimabukuro, H. Arai and T. Seiyama, 1989, J. Electrochem. Soc. **136**, 1206.

Sobolev, B.P., P.P. Fedorov, K.B. Seiranian and N.L. Tkachenko, 1976, J. Solid State Chem. **17**, 201.

Srinivasan, K., and G.A. Rechnitz, 1968, Anal. Chem. **40**, 1818.

Stubican, V.S., 1988, Adv. Ceramics **24**, 71.

Stubican, V.S., R.C. Hink and S.P. Ray, 1978, J. Am. Ceram. Soc. **61**, 17.

Subbarao, E.C., P.H. Sutter and J. Hrizo, 1965, J. Am. Ceram. Soc. **48**, 443.

Sugai, T., and T. Matsuzawa, 1992, Rare earth metal oxide based CO_2 gas sensor, in: Technical Digest, 4th Int. Meeting on Chemical Sensors, 1992, pp. 550–553.

Sugimoto, E., and Z. Kozuka, 1988, Nippon Kogyo Kaishi **104**(1200), 89.

Takahashi, T., and H. Iwahara, 1978, Mater. Res. Bull. **13**, 1447.

Takahashi, T., H. Iwahara and T. Arao, 1975, J. Appl. Electrochem. **5**, 187.

Takahashi, T., H. Iwahara and T. Ishikawa, 1977, J. Electrochem. Soc. **124**, 280.

Takeuchi, T., and I. Igarashi, 1988, Limiting current type oxygen sensor, Chemical Sensor Technology, Vol. 1 (Kodansha/Elsevier) p. 79.

Tamaki, J., M. Akiyama, C. Xu, N. Miura and N. Yamazoe, 1990a, Chem. Lett., p. 1243.

Tamaki, J., T. Maekawa, S. Matsushima, N. Miura and N. Yamazoe, 1990b, Chem. Lett., p. 477.

Thoma, R.E., and G.D. Brunton, 1966, Inorg. Chem. **5**, 1937.

Uchida, H., N. Maeda and H. Iwahara, 1982, J. Appl. Electrochem. **12**, 645.

Uchida, H., N. Maeda and H. Iwahara, 1983, Solid State Ionics **11**, 117.

Worrell, W.L., 1983, The application of solid-sulfate electrolytes in SO_2/SO_3 sensors, in: Proc. Int. Meeting on Chemical Sensors, eds T. Seiyama, K. Fueki, J. Shiokawa and S. Suzuki (Kodansha/ Elsevier) pp. 332–337.

Worrell, W.L., and Q.G. Liu, 1984, J. Electroanal. Chem. Interfacial Electrochem. **168**, 355.

Yagi, H., 1993, Humidity sensors using ceramic materials, in: Proc. Symp. on Chemical Sensors II, 1993, eds M. Butler, A. Ricco and N. Yamazoe (Electrochemical Society, Pennington) pp. 498–509.

Yagi, H., and K. Horii, 1992, Denki Kagaku **60**, 220.

Yagi, H., and K. Ichikawa, 1992a, J. Ceram. Soc. Jpn. **100**, 282.

Yagi, H., and K. Ichikawa, 1992b, Humidity sensing characteristics of a limiting current type plane oxygen sensor for high temperature, in: Technical Digest, 4th Int. Meeting on Chemical Sensors, pp. 104–107.

Yajima, T., H. Kazeoka, T. Yogo and H. Iwahara, 1991, Solid State Ionics **47**, 271.

Yajima, T., K. Koide, N. Fukatsu, T. Ohashi and H. Iwahara, 1992, A new hydrogen sensor for molten aluminum, in: Technical Digest, 4th Int. Meeting on Chemical Sensors, pp. 796–797.

Yamazoe, N., J. Hisamoto, N. Miura and S. Kuwata, 1987, Sens. Actuators **12**, 415.

Yoshioka, T., N. Mizuno and M. Iwamoto, 1991, Chem. Lett., p. 1249.

Zachariasen, W.H., 1951, Acta Crystallogr. **4**, 231.

Zalkin, A., D.H. Templeton and T.E. Hopkins, 1966, Inorg. Chem. **5**, 1466.

Zaromb, S., M.E. Moehlenkamp and J.X. Tull, 1993, Humidity-resistant ambient-temperature solid-electrolyte amperometric sensors, in: Proc. Symp. on Chemical Sensors II, 1993, eds M. Butler, A. Ricco and N. Yamazoe (Electrochemical Society, Pennington) pp. 162–173.

Handbook on the Physics and Chemistry of Rare Earths
Vol. 21
edited by K.A. Gschneidner, Jr. and L. Eyring

Chapter 144

CRYSTAL FIELD IN NON-METALLIC (RARE EARTH) COMPOUNDS

Denis GARCIA[1] and Michèle FAUCHER[2]
Laboratoire de Chimie et Physico-Chimie Moléculaire et Minerale,
URA 1907 du CNRS, Ecole Centrale Paris, Grande Voie des Vignes,
92295 Chatenay Malabry Cedex, France
[1]*e-mail: 100541.363@compuserve.com*
[2]*e-mail: faucher@pcm.ecp.fr*

Contents

List of symbols and abbreviations

A^k	intrinsic parameter	HF	Hartree–Fock
B_q^k	crystal field parameters	ℓ	orbital quantum number
e	electron charge	LCCF	analogous to SCCF, with $\boldsymbol{s}_i \cdot \boldsymbol{S}$ replaced by $\boldsymbol{l}_i \cdot \boldsymbol{L}$
F^k	Slater integrals		
g	two electron Hamiltonian part	$M^{(n)}$	electrostatic n-pole
H_{CF}	crystal field Hamiltonian	n	principal quantum number
h	one-electron Hamiltonian part	N	number of electrons

$\boldsymbol{R}$	coordinates of a ligand	$\alpha^{(n)}$	n-polar polarizability
$\boldsymbol{r}$	coordinates of an electron	β	Trees' second parameter
$\hat{r}$	angular coordinates of $\boldsymbol{r}$	γ	Trees' third parameter
SCCF	spin-correlated crystal field	ζ	spin–orbit coupling constant
t	three-electron Hamiltonian part	σ_k	shielding factor of rank k
T^i	Judd's parameters	φ	atomic or ionic one electron wavefunction
t_i	three-electron operators		
V	electrostatic potential	$\begin{pmatrix} \ell_1 & \ell_2 & \ell_3 \\ m_1 & m_2 & m_3 \end{pmatrix}$	$3-j$ symbol
α	Trees' first parameter		

1. Introduction

Trivalent lanthanide free ion spectra have been recorded, unambiguously identified and ascribed to the degenerate levels $^{2S+1}L_J$ of the f^N configuration. When such an ion is embedded in a medium, two effects appear:

(1) the $2J+1$ degeneracy of the $^{2S+1}L_J$ levels disappears, partially or totally;

(2) the $^{2S+1}L_J$ barycenter energy moves.

These two phenomena are referred to as "crystal field effects in rare earth compounds" and "crystal field" may be defined as *any action that breaks the spherical symmetry of the free ion.*

The word "field" alludes to the electric field which was suspected to be the source of the observed Stark splittings when the effect was discovered. Presently, we know that electrostatic effects are weak and even negligible in many cases.

In spite of the term "crystal", well organized solids are not the only media which present the effect: glasses, organic non-crystals, or even liquids reveal, by non-equivocal optical signals, the lowering of local symmetry. But crystals, having long since acquired their letters of nobility for services rendered, keep their privileged status.

The "rare earths" are not the only elements concerned with the crystal field: actinides have their own, as have more generally all the unsaturated ℓ^N configurations. But the amount of information contained in a lanthanide optical spectrum is a hundred times more detailed than that delivered by a d^N spectrum.

The goal of this chapter is to give an insight into the methods which have been worked out to classify, model, and predict the crystal-field effects. Whenever possible, practical examples are given. After an overview on the principles, the first part will deal with the fittings of phenomenological parameters, ending with correlated mechanisms. The second part is reserved for ab initio methods.

2. The effective Hamiltonian

The complex spectrum of a trivalent lanthanide ion in most compounds is composed of many transitions between a large number of sublevels. In order to compare and classify

the spectra, it is necessary to reduce all these data to a small number of parameters which are easy to handle: the process is summarized in the two following subsections.

2.1. *Atomic energy levels*

Solving the Hartree or Hartree–Fock Hamiltonian for the $n\ell^N$ configurations gives a set of wave functions that can be written for one electron as the product of a radial part, $R_{n\ell}(r)$ by a spherical harmonic, $Y_m^\ell(\theta, \varphi)$, and a spin-up ($\alpha$) or spin-down ($\beta$) function. The complete functions representing the $n\ell^N$ configuration are the $C_{2(2\ell+1)}^{2(2N+1)}$ Slater determinants built from the $2(2\ell+1)$ functions $R_{n\ell}(r)\, Y_m^\ell(\theta, \varphi)\,(\alpha \text{ or } \beta)$: they all have the same energy $E_{n\ell}$.

This degeneracy is first broken by the electrostatic interaction between electrons, expressed as

$$H_{\text{electrostatic}} = \sum_k F^k \sum_{i<j} C^{(k)}(i)\, C^{(k)}(j), \tag{1}$$

where i and j label two different electrons, $C^{(k)}$ is a spherical tensor of rank k,

$$C_q^k = \sqrt{\frac{4\pi}{2k+1}}\, Y_q^k,$$

and F^k are the Slater parameters:

$$F^k = \iint \frac{r_<^k}{r_>^{k+1}} R_{n\ell}^2(1)\, R_{n\ell}^2(2)\, \mathrm{d}r_1\, \mathrm{d}r_2,$$

with $r_<$ ($r_>$) the smallest (greatest) of r_1 and r_2.

The diagonalization of this new Hamiltonian leads to the new wave functions $|S\, M_S L\, M_L\rangle$, where S is the total spin and L the total orbital momentum. They correspond to energies depending on S and L and are linear combinations of the previous Slater determinants.

Taking into account the spin–orbit interaction (which originates from relativistic effects) and the associated spin–orbit coupling constant ζ gives the $|\gamma^{2S+1} L_J M_J\rangle$ functions as linear combinations of the previous versions ($|S\, M_S L\, M_L\rangle$). The γ label stands for other useful labels (namely irreducible representations of the G_2 and R_7 groups).

2.2. *Crystal-field parameters*

We suppose that the crystal-field effects originate from a potential which operates on each of the N electrons so that the corresponding Hamiltonian can be written as

$$H_{\text{CF}} = \sum_i V(i), \tag{2}$$

where the sum runs over the N electrons.

Taking V as a linear combination of the $r^k C_q^k(\theta, \varphi)$ functions permits verification of the gauge condition $\Delta V = 0$ as for an electric potential. Let b_q^k be the coefficient of the combination; we then get

$$V(\boldsymbol{r}) = \sum_{k,q} b_q^k r^k C_q^k(\theta, \varphi), \qquad H_{\mathrm{CF}} = \sum_{k,q} b_q^k \sum_i r_i^k C_q^k(\theta_i, \varphi_i) \tag{3, 4}$$

Strictly speaking, this is the correct form of the expression giving the first-order crystal-field effects. In practice, the matrix elements of H_{CF} between $|\gamma^{2S+1}L_J M_J\rangle$ functions have a constant part which depends only on the radial wave function $R_{n\ell}(r)$ so that the literature always gives

$$H_{\mathrm{CF}} = \sum_{k,q} B_q^k \sum_i C_q^k(i), \tag{5}$$

where $B_q^k = b_q^k \langle r^k \rangle_{n\ell}$. Here $\langle r^k \rangle_{n\ell}$ is the mean value of r^k relative to the $R_{n\ell}$ function, i.e., $\langle r^k \rangle_{n\ell} = \int_0^{+\infty} r^k R_{n\ell}^2(r)\, \mathrm{d}r$.

Expression (5) for the first-order crystal-field parameters is utilized in 99.95% of the practical studies. Before introducing further complications, we shall pause for a while to describe their properties and their determination.

Since we are dealing with ℓ electrons, only a few B_q^k values are useful: k must be even and smaller than 2ℓ. B_0^0 may be ignored since it corresponds to a global energy shift. The Hamiltonian must be hermitic, therefore $B_q^{k*} = (-1)^q B_{-q}^k$.

Additional symmetry conditions may require some B_q^k to cancel since H_{CF} must be invariant under local symmetry operators. For instance, if the local symmetry contains a fourfold axis, then the only non-zero values are B_0^2, B_0^4, B_4^4, B_0^6 and B_4^6 for $\ell = 3$. The crystal field depends therefore on only five parameters.

The complete spectra are generated by a set of atomic parameters plus the crystal field parameters:

Parameters	Comments
Atomic parameters	
$F^2, \ldots, F^{2\ell}$	or their equivalents $E_0, E_1, \ldots$, for the electronic interaction
ζ	for the spin–orbit coupling
α, β, γ	for Trees' parameters (f electrons)
...	other parameters for spherical operators
Crystal-field parameters	
B_q^k	$2 \leqslant k \leqslant 2\ell$ and $\lvert q \rvert \leqslant k$

Table 1
Relationship between the tensor operator parameters B_q^k and the operator-equivalent parameters $A_q^k\langle r^k\rangle$ (following Kassman 1970 and Newman and Ng 1989)

B_q^k	Equivalent	B_q^k	Equivalent
B_0^2	$2A_2^0\langle r^2\rangle$	B_0^6	$16A_6^0\langle r^6\rangle$
B_2^2	$(\frac{1}{3})(6)^{1/2}A_2^2\langle r^2\rangle$	B_2^6	$(\frac{16}{105})(105)^{1/2}A_6^2\langle r^6\rangle$
B_0^4	$8A_4^0\langle r^4\rangle$	B_3^6	$-(\frac{8}{105})(105)^{1/2}A_6^3\langle r^6\rangle$
B_2^4	$(\frac{2}{5})(10)^{1/2}A_4^2\langle r^4\rangle$	B_4^6	$(\frac{8}{21})(14)^{1/2}A_6^4\langle r^6\rangle$
B_3^4	$-(\frac{2}{35})(35)^{1/2}A_4^3\langle r^4\rangle$	B_6^6	$(\frac{16}{231})(231)^{1/2}A_6^6\langle r^6\rangle$
B_4^4	$(\frac{4}{35})(70)^{1/2}A_4^4\langle r^4\rangle$		

For a detailed account of the atomic theory of complex atoms we refer the reader to the papers by Racah (1942, 1943, 1949) and the books by Judd (1963) and Wybourne (1965).

Kibler (1979) has worked out a symmetry-adapted crystal field parametrization scheme but it has not supplanted the usual B_q^k, probably because the fitting programs have existed for years and every author is reluctant to make changes in a highly tested routine. Rudowicz and Bramley (Rudowicz and Bramley 1985, Rudowicz 1986) have proposed a standardization of the crystal-field Hamiltonian in the case of orthorhombic or monoclinic site symmetries in order to allow comparisons between apparently different crystal-field parameter sets. The chosen reference frame is the one for which the ratio between second-order parameters dwells in a given range. The procedure has been applied by Gajek et al. (1993).

Steven's normalisation to express the B_q^k has coexisted for a long time with Wybourne's formalism, but in the last few years the latter seems to prevail. Yet, both are still utilized and the correspondence is given in table 1.

2.3. *On the utility of the crystal field parameters*

There are two connected approaches to the *cfp*: the *ab initio* and the *parametric* approach. We shall examine in sect. 4 the theories which have been worked out to evaluate the contributions to the ligand field *ex nihilo*. None of these can be considered faultless. What they can do at most is to give starting values for a fitting procedure: the second (parametric) approach with which we are going to deal now.

The main question is: what exactly is the interest of *cfp* fitting? Firstly, it permits to evaluate quantitatively how close the model predictions comes to reality and to try to understand and correct it if possible. Secondly, as mentioned in the introduction, the *cfp* are perfect tools to order, to classify the rare earth spectra. One can plot curves of some property versus the *cfp* strength and correlate both quantities.

Besides, the *cfp* may be the starting point of other developments such as paramagnetic behaviour. Indeed, coming with the *cfp* are the Hamiltonian eigenvectors. The behaviour

of a rare-earth ion under a weak magnetic field (Zeeman effect) depends only on the eigenvectors and eigenvalues of the unperturbed Hamiltonian. The following formula, due to Van Vleck, gives the paramagnetic susceptibility as a function of the absolute temperature:

$$\chi = \frac{N}{\sum_i e^{-E_i/kT}} \sum_i \left\{ \left[\frac{|\langle \psi_i | H_M | \psi_i \rangle|^2}{kT} - \sum_{i' \neq i} \frac{2 |\langle \psi_i | H_M | \psi_{i'} \rangle|^2}{E_i - E_{i'}} \right] e^{-E_i/kT} \right\}, \quad (6)$$

where N is the number of atoms per cm^3, ψ_i is the ith eigenvector with eigenvalue E_i and H_M the total Hamiltonian including crystal field effects.

Another important utilisation of the eigenvectors is the calculation of line intensities. The widely admitted electric dipolar mechanisms for lanthanides have been worked out by Judd (1962), Ofelt (1962) and Jørgensen and Judd (1964).

2.4. *The fitting of atomic parameters*

We mentioned previously the following atomic parameters: the Slater parameters F^k, spin–orbit parameter ζ, Trees' α, β, γ, Judd's three-particle operators T^2, T^3, T^4, T^6, T^7, T^8, and other magnetic parameters like M_k and P_k. They vary from one compound to another and linked to them are the level barycenters. Before introducing any *cfp* fitting, the barycenters have to be connected as precisely as possible with the experimental values and therefore the spherical parameters have to be refined at first. Practically, the convergence of the procedure is rather quick, but the fitted parameters interact with each other, and there remains some uncertainty because of their mutual coupling. Judd and Crosswhite (1984) proposed an alternate set of parameters which corresponds to an orthogonalized set of operators for the f shell. The main result is that the conventional Hamiltonian

$$\begin{aligned} H =& e_0 E^0 + e_1 E^1 + e_2 E^2 + e_3 E^3 \\ &+ \alpha L(L+1) + \beta G(G_2) + \gamma G(R_7) \\ &+ t_2 T^2 + t_3 T^3 + t_4 T^4 + t_6 T^6 + t_7 T^7 + t_8 T^8 \end{aligned} \quad (7)$$

may be rewritten as

$$\begin{aligned} H =& e_0 E^{0\prime} + e_1' E^{1\prime} + e_2 E^{2\prime} + e_3 E^{3\prime} \\ &+ \alpha' e_\alpha' + \beta' e_\beta' + \gamma' e_\gamma' + \\ & t_2' T^{2\prime} + t_3 T^{3\prime} + t_4 T^{4\prime} + t_6 T^{6\prime} + t_7 T^{7\prime} + t_8 T^{8\prime} \end{aligned} \quad (8)$$

(the primes indicate values or operators which changed from one formula to the other). The consequences are:

- introducing new orthogonalized operators in the fitting process does not disturb the already fitted ones,

– the mean error on one parameter quickly decreases as new parameters are introduced.

As to spherical parameters, at least the Slater integrals and the spin–orbit coupling constant, it should be possible to evaluate them with precision from the radial part of the f-electron wave function obtained by solving the Hartree or Hartree–Fock equations. Unfortunately, the F^k calculated this way are 30–50% greater than the fitted ones. It seems that the lanthanides are almost alone (even if there are fourteen elements!) in the Periodic Table in displaying such pronounced misbehaviour. Elements to help understand this may be found in a paper by Rajnak and Wybourne (1963) who showed that the effects of configuration interactions in ℓ^N configurations may be represented by

- a shielding of the Slater parameters,
- two-electron operators of odd rank, mathematically equivalent to Trees' operators (Trees 1951)
- three-particle operators examined by Judd (1966) who limited the number of effective operators to six.

The shielding of the Slater F^k parameters is expressed in terms of very intricate integrals involving radial wavefunctions, the relative energies of the configurations, six-J symbols and infinite summation over the configurations and intermediate integer-loop indexes. There is no way to calculate it.

Anyway, since the 4f wavefunction of rare-earth ions has an internal localization with respect to the lower-energetic 5s and 5p, the radial integrals are supposed to be maximum and so is the shielding. The strength of this shielding is also related to the energy difference between configurations, which depends on the host compound. Therefore, it is expected to vary from one compound to the other, which is indeed observed (see a rather complete review on the "nephelauxetic effect" by Reisfeld and Jørgensen 1977).

Another trail has been explored by Morrison (1974, 1979) who related the configuration energy shift and Slater parameter shielding to the host structure using an electrostatic model based on the polarizability of the medium.

2.5. *cfp fitting*

Extracting the *cfp* from the experimental data consists in getting a starting set of parameters and refining them so as to minimize the mean deviation between calculated levels and observed ones. The atomic parameters are frozen at first; then, if the number of experimental lines is sufficient, all the parameters are allowed to vary simultaneously. In practice, the convergence is rather fast. The ways to obtain starting values are described in sect. 4, the most utilized being the electrostatic model, but the covalo-electrostatic model (sect. 4.4) gives better results. A relative accuracy of the starting values and correctness of the level assignments are crucial requirements. Due to the improvement of the experimental design, the number of observed lines has nearly doubled since two decades so that the fits have gained in precision.

We shall give experimental results for lanthanides and actinides before describing some "bugs" and giving elements for the ab initio calculations. A large number of compounds

have been examined so far and the list given in table 2 has not the ambition of being exhaustive.

The compounds are classified in families and are given along with their *crystal-field strength.* This parameter was defined first by Auzel (1979), then modified by Chang et al. (1982) and by Kibler (1983). We shall utilize the form we obtained by expressing in a B_q^k form the sum of the squared barycentered energies of individual 4f orbitals weighted by their number (Faucher et al. 1986). In the process, the spherical contribution of the ligand field disappears as usual.

$$\overline{E} = \left[(2l+1) \sum_{k \neq 0} \frac{1}{2k+1} \begin{pmatrix} l & l & k \\ 0 & 0 & 0 \end{pmatrix}^2 |B^k|^2 \right]^{1/2} . \tag{9}$$

In table 2, the $\overline{E}^k$ ($k = 2, 4, 6$) are the components of $\overline{E}$ such as

$$\overline{E} = \left[\sum_{k \neq 0} \left| \overline{E}^k \right|^2 \right]^{1/2} . \tag{10}$$

The crystal-field strength is a rotational invariant and Leavitt (1982) showed that the shifts in the centers of gravity of the free-ion levels due to J-mixing is related to this parameter. Yeung and Newman (1985) extended this concept towards higher-order invariants.

When a whole family or the whole series of lanthanides was investigated, only the Nd^{3+} and/or the Eu^{3+} data are reported. When several references for the same compound exist in the literature, the most recent is quoted. While listing these numerical data, the authors noted that for the same rare earth doped in similar hosts, the variations in E^4 and E^6 *always* occur in opposite directions, the most frequent trend being that when the lanthanide–ligand distance shortens, E^4 decreases while E^6 increases. Why??? Answering this question is left to the reader.

The examples given in table 2 concern lanthanide or lanthanide doped compounds in which the optically active ion has the same valence as the host ion. This is not the case when, for instance, trivalent lanthanides are introduced in fluorite structures such as CaF_2. Then, the local arrangement around the lanthanide ion is unknown. A study of Yeung (1992) addresses the problem of fitting spin and distorsion parameters of Gd^{3+} in the charge-compensated compound Gd^{3+}:CaF_2.

2.6. *The "bugs"*

The mean deviation resulting from experimental/calculated fits is usually satisfactory. The accuracy does not depend only on the number of levels (for instance 91 versus 364 for trivalent praseodymium and neodymium, respectively), but also on the strength of the crystal field. While the deviation is ~6 cm^{-1} and ~10 cm^{-1} for Pr^{3+} and Nd^{3+} doped in $LaCl_3$ respectively, it rises up to 31 and 15 cm^{-1} in Y_2O_3.

Table 2
Crystal-field strengths for some rare-earth or rare-earth-doped compounds

Compound	$\overline{E}^2$	$\overline{E}^4$	$\overline{E}^6$	Ref.
Fluorides				
$Nd^{3+}:LaF_3$	61	170	252	1
NdF_3	75	154	277	2
$Nd^{3+}:LiYF_4$	96	278	198	3
$Eu^{3+}:KY_3F_{10}$	127	205	69	4
Chlorides				
$Nd^{3+}:LaCl_3$	41	52	142	5
$Nd^{3+}:Cs_2NaYCl_6$	0	413	125	6
Oxychlorides				
NdOCl	212	171	131	7
$Eu^{3+}:LaOCl$	296	219	100	8
$Eu^{3+}:YOCl$	188	196	170	8
Oxybromides				
$Eu^{3+}:LaOBr$	349	234	111	9
$Eu^{3+}:GdOBr$	246	211	140	9
$Tm^{3+}:LaOBr$	29	177	70	10
Oxides				
Nd_2O_3	193	335	168	11
$Nd^{3+}:Y_2O_3$	273	490	188	12
$Eu^{3+}:BaY_2O_4$	181	440	239	13
	102	475	214	13
Borate				
$NdBO_3$	75	288	268	14
$Eu^{3+}:GdAl_3(BO_3)_4$	181	440	239	15
Aluminates				
$Nd^{3+}:LaAlO_3$	51	124	339	16
$NdAlO_3$	111	104	355	17
$Nd^{3+}:LuAlO_3$	200	261	318	18
$Nd^{3+}:YAlO_3$	188	272	295	19
$Nd^{3+}:Y_3Al_5O_{12}$	167	532	444	20
	110	484	343	21
$Ca_{0.8}Nd_{0.2}Mg_{0.2}Al_{11.8}O_{19}$	109	62	299	22
Gallates				
$Pr_3Ga_5O_{12}$	12	502	276	23
$Pr^{3+}:Gd_3Ga_5O_{12}$	4	496	304	23
$Pr^{3+}:Y_3Ga_5O_{12}$	27	495	312	23
$Tm^{3+}:Gd_3Ga_5O_{12}$	65	313	196	24

continued on next page

Table 2, *continued*

Compound	$\bar{E}^2$	$\bar{E}^4$	$\bar{E}^6$	Ref.
Antimonate				
$Nd_3Sb_5O_{12}$	295	331	125	25
Vanadates, phosphates, arsenates				
Nd^{3+}:YVO_4	31	224	164	26
$NdVO_4$	16	232	137	27
Eu^{3+}:$GdVO_4$	15	162	107	28
Eu^{3+}:YVO_4	25	151	118	28
Eu^{3+}:YPO_4	69	148	103	28
Eu^{3+}:$LuPO_4$	46	162	91	28
Eu^{3+}:$GdAsO_4$	3	124	115	28
Eu^{3+}:$YAsO_4$	28	145	110	28
$NdPO_4$	155	177	211	28
$LiNdP_4O_{12}$	134	170	127	29
$LiErP_4O_{12}$	100	104	137	29
Sulfide				
γ-Nd_2S_3	48	255	132	30
Oxysulfide				
Nd_2O_2S	45	226	101	31
Nitrates				
$Nd(NO_3)_3 \cdot 6H_2O$	69	112	242	32
$Eu_2Zn_3(NO_3)_{12} \cdot 24H_2O$	34	71	326	33
Silicates				
Eu^{3+}:D–$Y_2Si_2O_7$	233	363	167	34
Eu^{3+}:D–$Lu_2Si_2O_7$	232	340	169	34
Eu^{3+}:C–$Y_2Si_2O_7$	235	373	180	35
Eu^{3+}:C–$Lu_2Si_2O_7$	247	372	186	35
Tellurides				
$Nd_2Te_4O_{11}$	105	251	125	36
Molybdates, tungstates				
$Na_5Eu(MoO_4)_4$	46	179	86	37
$Na_5Eu(WO_4)_4$	42	178	85	37
Tm^{3+}:$NaLa(MoO_4)_2$	110	166	86	38

continued on next page

However, some deviations are systematically higher than the average values. Indeed, when most experimental misinterpretations have been eliminated, it turns out that often, large deviations remain, mainly originating from one particular level. If one eliminates this

Table 2, notes

References

(1) Carnall et al. (1988a,b)
(2) Caro et al. (1981)
(3) Da Gama et al. (1981)
(4) Porcher and Caro (1976)
(5) Crosswhite et al. (1976)
(6) Reid and Richardson (1985)
(7) Aride (1981)
(8) Hölsä and Porcher (1981)
(9) Limburg et al. (1992)
(10) Mazurak et al. (1994)
(11) Caro et al. (1979)
(12) Chang et al. (1982)
(13) Taibi et al. (1994)
(14) Antic-Fidancev et al. (1992a)
(15) Görller-Walrand et al. (1994)
(16) Faucher and Garcia, unpublished
(17) Antic-Fidancev et al. (1980)
(18) Faucher et al. (1989c)
(19) Karayianis et al. (1976c)
(20) Gruber et al. (1990)
(21) Burdick et al. (1994)
(22) Alablanche et al. (1992)
(23) Antic-Fidancev et al. (1992b)
(24) Lupei et al. (1994)
(25) Antic-Fidancev et al. (1991a)
(26) Guo et al. (1987)
(27) Antic-Fidancev et al. (1991b)
(28) Linarès et al. (1977)
(29) Mazurak and Gruber (1992)
(30) Gruber et al. (1983)
(31) Beaury and Caro (1990)
(32) Caro et al. (1977)
(33) Görller-Walrand et al. (1992)
(34) Chateau et al. (1989)
(35) Chateau et al. (1990)
(36) Cascales et al. (1992)
(37) Huang et al. (1984)
(38) Merkle et al. (1992)

level from the experimental set, the mean deviation drops to normal values. By *normal values*, we mean that the average deviation within each level is not too far from the value of the global deviation.

The misbehaving levels provide a bulk of empirical information betraying higher-order effects. Here is a short list of the most famous "taletellers":

- the $^1D_2$ level of Pr^{3+} in $LaCl_3$ (the overall experimental and calculated splittings amount to 150 and 110 cm^{-1}, respectively);
- the $^3K_8$ level of Ho^{3+} in $LaCl_3$ (123/78 cm^{-1});
- the ^5D multiplet of Eu^{3+} (113/62 and 148/79 cm^{-1} for $^5D_1$ and $^5D_2$, respectively, in Y_2O_3);
- the $^2H(2)_{11/2}$ of Nd^{3+} and Er^{3+} (280/97 cm^{-1} in Nd_2O_3) [the (2) stands for special quantum numbers, eigenvalues of Casimir operators for groups G_2 and R_7 that distinguish twin levels $^2H_{11/2}$ with the same quantum numbers SLJ];
- the $^8S_{7/2}$ of Gd^{3+} (1.65/0.877 cm^{-1} (!) in Gd_2O_3);
- the sharp drop of the sixth-order *cfp* in the second half of the rare-earth series.

The discrepancy of the $^8S_{7/2}$ level of Gd^{3+} is a tiny bug but has continuously puzzled solid-state spectroscopists. This $L = 0$ state can only be split through second-order crystal-field effects. The small experimental splittings can be obtained by EPR techniques or by optical measurements when the crystal field is strong enough (Antic-Fidancev et al. 1982). Either the ordering of the levels is opposite in calculated and experimental splittings, or, when they agree, the calculated splitting is too small. The case is discussed in detail in the papers by Newman and Urban (1972) and Newman and Ng (1989); they propose an interpretation in terms of the superposition model.

As experimental designs improve and explored spectral ranges spread higher, more bugs will certainly be detected, giving supplementary information.

Two questions then arise. Why are there deviant levels? How can they be integrated in the parametric scheme? We shall partially answer the first question in the second part of this paper which deals with the physical origin of the crystal field.

The answer to the second question is that the crystal field Hamiltonian (3), though usually efficient in a large part of the compounds under study, is not sufficient to describe the reality completely. It is necessary to add terms accounting for higher-order effects.

3. Multielectronic crystal field

Just remember what the free ion Hamiltonian is: it represents all the possible interactions an electron can experience in a spherical environment. We encountered:

- a one-electron operator which is the spherical potential created by the nucleus electric field: $V(r)$;
- a one-electron operator which represents a relativistic correction: $\zeta(r)\,\boldsymbol{l}\cdot\boldsymbol{s}$, where $\zeta(r)$ is proportional to $r^{-1}\,(\mathrm{d}V/\mathrm{d}r)$;
- two-electron operators which represent the electron–electron electrostatic interaction and a part of configuration interaction: $\{C^{(k)}(1)\otimes C^{(k)}(2)\}^{(0)}$;
- three-electron operators which represent elements of the configuration interaction:

$$\left\{\left\{C^{(k_1)}(\hat{\boldsymbol{r}}_1)\otimes C^{(k_2)}(\hat{\boldsymbol{r}}_2)\right\}^{(k_3)}\otimes C^{(k_3)}(\hat{\boldsymbol{r}}_3)\right\}^{(0)};$$

- more-than-three-electron operators we have no idea of ...

All these free-ion operators transform like the irreducible representation $\langle 0\rangle$ of R_3 or, in other words, they are all invariant under any rotation of the system.

But what happens when the same ion is embedded in a crystal: the local symmetry is no longer that of R_3: let us call it Λ. The operators describing the behaviour of the ion only need to be invariant under Λ symmetries and then, each operator in the above list can display non-spherical components such as

- one electron: ${}^1B_q^k(r)\,C_q^k(\hat{\boldsymbol{r}})$ to complete the spherical $V(r)$, which can be written as ${}^1B_0^0(r)\,C_0^0(\hat{\boldsymbol{r}})$ since $C_0^0=1$;
- the case of the spin–orbit operator $\zeta(r)\boldsymbol{l}\cdot\boldsymbol{s}$ is more complex since we have to go back to the initial expression $\boldsymbol{s}\cdot(\boldsymbol{p}V)\wedge\boldsymbol{p}$ in order to take into account the aspherical part of V: the case may be desperate due to the complexity of the resulting operators!
- two electrons: ${}^2B_q^{(k_1,k_2)k}(r_1,r_2)\left\{C^{(k_1)}(\hat{\boldsymbol{r}}_1)\otimes C^{(k_2)}(\hat{\boldsymbol{r}}_2)\right\}_q^k$;
- three electrons:

$${}^3B_q^{((k_1,k_2)K,k_3)k}(r_1,r_2,r_3)\left\{\left\{C^{(k_1)}(\hat{\boldsymbol{r}}_1)\otimes C^{(k_2)}(\hat{\boldsymbol{r}}_2)\right\}^{(K)}\otimes C^{(k_3)}(\hat{\boldsymbol{r}}_3)\right\}_q^k.$$

Here ${}^NB_q^{(k_1,\ldots)k}(r_1,\ldots,r_N)$ is the radial part of the N-electron operators.

We see easily that the modification of the F^k and α, β, γ parameters is related to the values of the ${}^2B_q^{(k_1,k_2)k}(r_1,r_2)$, the modification of the T^i is related to the ${}^3B_q^{((k_1,k_2)K,k_3)k}(r_1,r_2,r_3)$, etc.

We have no similar equivalence for the change in spin–orbit constant because of the lack of a formula for the non-spherical spin–orbit interaction.

The relationship between the ${}^{N}B_q^k$ and the spherical parameters may be found in Ng and Newman (1987a).

Last but not least: as stated before, the matrix elements of these operators include the radial integral of the ${}^{N}B_q^{(k_1,\ldots)k}(r_1, \ldots, r_N)$ functions, so we can consider these integrals ${}^{N}B_q^{(k_1,\ldots)k}$ as parameters.

Let us say a few words about the ${}^{2}B_q^{(k,0)k}$. The corresponding "two"-electron operators are $\left\{C^{(k)}(\hat{r}_1) \otimes C^{(0)}(\hat{r}_2)\right\}_q^k$. Since $C^{(0)} = 1$, this operator simply reduces to $C_q^k(\hat{r}_1)$. As a consequence, when we are fitting the *cfp*, we are not looking for ${}^{1}B_q^k$ parameters but for the infinite summation

$$ {}^{1}B_q^k + {}^{2}B_q^{(k,0)k} + {}^{3}B_q^{((k,0)k,0)k} + \cdots $$

But we must still investigate the non-trivial ($k_2 \neq 0$) two-electron operators, i.e. the correlated crystal field.

3.1. *Correlated crystal field*

The term "correlated" crystal field designates the two-electron part of the crystal field Hamiltonian. Although a concept of the 1970s, correlation is a keyword of the late 1980s and 1990s.

The first set of the operators we met above are the

$$ {}^{2}B_q^{(k_1,k_2)k}(r_1, r_2)\left\{C^{(k_1)}(\hat{r}_1) \otimes C^{(k_2)}(\hat{r}_2)\right\}_q^k $$

first proposed by Bishton and Newman(1968). Their paper contains most of the basic notions, in particular the formulation of the correlation crystal field compared with the one-electron expression, and the calculation of the matrix elements between product states of the $n\ell$ shell. The total number of correlated parameters is scandalously high: 637 for the lowest site symmetry, since k_1 and k_2 run from 2 to 6, k runs from $|k_1 - k_2|$ to $k_1 + k_2$, and q runs from $-k$ to $+k$. And in octahedral site symmetry there are still 41 left!

An important point must be stressed here, i.e., the prediction that correlated parameters for $k = 2$ and 4 should be the most important. The demonstration is made that the correlated crystal field can be formally accounted for by a *term dependent* one-electron crystal field and also that the superposition principle holds for separate ligand contributions as for the one-electron crystal field. This allows a drastic reduction of the number of correlated parameters; however, there are still 23 for each metal–ligand distance.

The "ordinary" correlated crystal-field operators as defined above are not mutually orthogonal as are the one-electron operators. Besides the conceptual disturbance, a practical inconvenience is the instability of numerical fit procedures. Judd (1977a) has described the two-electron crystal field operators on a group-adapted basis insuring their

mutual orthogonality. The paper by Reid (1987) brings minor changes to Judd's operators $g_2'^{(K)}$ and $g_3^{(K)}$ in order to correct residual unorthogonalities. Kooy and Reid (1993) give useful transformation relations between the ordinary correlated crystal-field operators and Judd's $g_i^{(K)}$. The complete set of transformations has been worked out by Kooy (1994).

The transformation to orthogonal operators does not change the total number of parameters involved, which is enormous as we have just seen. In an investigation on actinide ligand field, Judd (1977a) selected a smaller and more handy set of operators and associated parameters. The physically plausible assumption is made that charge transfer towards the ligand selectively affects the f symmetry orbitals. The process can be mimicked by a small set of effective two-electron operators acting on unmodified f orbitals. The supplementary set of parameters just doubles the number of ordinary *cfp*. Unfortunately, attempts to improve the fits for the hexahalide complexes of uranium were unsuccessful.

3.1.1. *Spin-correlated crystal field*

Searching along the lines of selective modification of the radial wavefunctions, Newman (1970) and Judd (1977b) found another source of correlated crystal field in the exchange forces between 4f electrons with similarly directed spins. They introduce a correction of the type $\boldsymbol{s}_i \cdot \boldsymbol{S}$ (where $\boldsymbol{s}_i$ is the ith electron spin and $\boldsymbol{S}$ the total spin) as a multiplicative factor to apply to the $C^{(k)}$ operators. The effective crystal field Hamiltonian therefore becomes:

$$H_{\mathrm{CF}} = \sum_i B_q^k \left(1 + c_k \boldsymbol{s}_i \cdot \boldsymbol{S}\right) C_q^k(\hat{\boldsymbol{r}}_i), \tag{11}$$

where the c_k are experimentally adjustable parameters. The number of supplementary parameters is at most equal to the number of ordinary *cfp*. The spin-correlated crystal field (SCCF) is proportional to the ordinary crystal field for terms of maximum multiplicity so that the c_k have to be fitted from terms of non-maximum multiplicity only. Reid (1987) gives the relationship between the $\boldsymbol{s} \cdot \boldsymbol{S}\, C^{(k)}$ and the $g_i^{(K)}$ $(i = 1, 2, 3)$.

Even if the effects of these new operators seem interesting in some cases, Judd (1979) concluded that the parameters c_k "can only be of marginal significance at best". Crosswhite and Newman (1984), however, do not agree since they eliminate with the SCCF the discrepancy of the $^3K_8$ levels of Ho^{3+} doped in $LaCl_3$. Moreover, they identify the SCCF (which provide positive contributions to the c_k) as responsible for the sudden decrease of sixth-order parameters in the second half of the rare-earth series. The results obtained with c_k values fitted for Gd^{3+} and Ho^{3+} are consistent with this hypothesis. A similar attempt was subsequently made for actinide doping of $LaCl_3$ (Newman and Ng 1988) but apparently without the same success. Yeung and Newman (1986), applying the model to Ho^{3+}:YPO_4, Er^{3+}:$YAlO_3$ and Nd^{3+}:$PbMoO_4$, came to the conclusion that the most significant contribution comes from the rank-six spin-correlated crystal field. Reid (1987) made the same statement (investigating Gd^{3+} and Ho^{3+} in $LaCl_3$). Besides, spin correlation added to the ordinary crystal field does not significantly improve the fits for $Cs_2NaLnCl_6$ (Reid and Richardson 1985). Jayasankar and Richardson (1989)

and Jayasankar et al. (1989) investigating eight trivalent rare earths in $LiYF_4$ stated a significant improvement when SCCF is included especially for Er^{3+} and Tm^{3+}. It seems therefore that the point is not clear-cut.

3.1.2. *Orbitally correlated crystal field*

This section, in addition to the LCCF responding to the definition given in the first paragraph hereafter will also deal with the more general correlation combining the orbital momenta of the two electrons.

The LCCF is a trademark. First introduced by Yeung and Newman (1987), it is based on a concept analogous to the spin-correlated crystal field, and consists in replacing $\boldsymbol{s}_i \cdot \boldsymbol{S}$ by $\boldsymbol{l}_i \cdot \boldsymbol{L}$ in the above formula. This model proved its efficiency in eliminating the discrepancy of the $^1D_2$ levels of Pr^{3+} in $LaCl_3$. Reid (1987) showed that $\boldsymbol{l} \cdot \boldsymbol{L}\, C^{(k)}$ is a combination of all Judd's $g_i^{(K)}$ except those for $i = 4, 6, 8, 10$. Van Siclen (1982) states that the Coulombic interaction of two open-shell electrons via polarizable ligands leads to two-electron *cfp* or to term-dependent one-electron *cfp*. He evaluated the effect ab initio for Pr^{3+} in ethylsulfates and trichlorides and also for heavier rare earths, Eu^{3+} and Tb^{3+}, to check whether it could account for the decrease of the sixth-order crystal-field parameters. The result was rather disappointing.

The most glaring discrepancy quoted at the beginning of this section is the case of the $^2H(2)_{11/2}$ level of triply ionized neodymium. It persisted for a long time in spite of clear experimental evidence (see for instance Caro et al. 1981). Faucher and Garcia (1988) and Faucher et al. (1989a,b) showed that the anomaly touched the rank-four crystal field only; they suspected that it concerned twin levels only and proposed an empirical rule to take it into account for any neodymium compound within the classical one-electron *cfp* fitting. The same type of correction applies to the $^2H(2)_{11/2}$ level of trivalent erbium in the complementary $4f^{11}$ configuration (Moune et al. 1991).

A further analysis due to Li and Reid (1990) showed that this effect could be well interpreted via the correlated crystal field, by selecting mainly one among Judd's fourth-rank orthogonal crystal field operators $g_i^{(K)}$, namely $g_4^{(10)}$. This operator arises reportedly from $4f \rightarrow nf$ excitations considered by Ng and Newman (1987a,b). Besides rare earths, successful fits were also performed on actinide compounds (Reid and Li 1991). Recently, Faucher et al. (1993) utilized a complete set of fourth-rank (non-orthogonal) correlated operators. The transformation of the final fitted parameters into Judd's orthogonal set did not seem to show the *exclusive* occurrence of one particular operator. Correlation crystal field parameters built as combinations $\left\{U^{(k_1)}(\hat{\boldsymbol{r}}_1) \otimes U^{(k_2)}(\hat{\boldsymbol{r}}_2)\right\}^k$ with k_1, k_2 odd and even are efficient to eliminate discrepancies. Combinations of Wybourne's $C^{(k)}$ (which arise in the development of $1/r$) are not, since combinations with k_1, k_2 odd lead to vanishing matrix elements.

3.1.3. *Conclusion on the correlated crystal field*

In fact, spin-correlated and orbitally correlated crystal field are not two different correlation actions: both are part of the more general correlated crystal field described

by Kibler and Grenet (1985, 1986a,b), and Kibler and Katriel (1990) for d^n and f^n ions. It involves the spin as well as the orbital parts of the wavefunctions. See the general formula (24) for the weak field case in the paper of Kibler and Grenet (1985).

3.2. *Configuration interaction and crystal field*

Rajnak and Wybourne (1964) investigated the effects of interference between configuration interaction and crystal-field effects. Using a perturbation treatment, they showed that the $n\ell^N$–$n\ell^{N-1}n'\ell'$ mixing through the Coulombic operator causes a LS dependence of the crystal-field parameters. The basic hypothesis of such a calculation is that configurations are far enough from each other and that one can consider them to be condensed on their barycenter: this is not true if we consider $4f^2$ and $4f^15d^1$ of trivalent praseodymium: the energy difference is 60 000 cm^{-1} whereas the 4f5d extent is about 20 000 cm^{-1}. And this situation is worsened all along the trivalent rare-earth series: the energy difference is 80 000 cm^{-1} for trivalent neodymium ($4f^3$) while the breadth of $4f^25d^1$ is ~50 000 cm^{-1}.

The only way to take into account configuration interaction is to perform an exact calculation of the total system including the two interacting configurations. In the case of $4f^N/4f^{N-1}5d^1$ interaction, the only coupling operator is the crystal-field Hamiltonian: since the two configurations are of opposite parity, Coulombic interaction matrix elements are zero. On the contrary, the matrix elements of the crystal field between $4f^N$ and $4f^{N-1}5d^1$ contains B_q^k parameters with odd k values.

Until this point, when talking about *cfp*, we were dealing with the B_q^k parameters for $k=2$, 4 and 6 because of selection rules on 4f functions. But B_q^k is only the mean value over the 4f radial wavefunction of the function $B_q^k(r)$. So we have:

$$B_q^k = \langle B_q^k(r) \rangle_{4f} \quad k \text{ even}; \qquad B_q^k = \langle B_q^k(r) \rangle_{4f,\,5d} \quad k \text{ odd}. \tag{12, 13}$$

In order to take into account configurations with the same parity as $4f^N$, such as $4f^{N-1}6p$, one must introduce different B_q^k parameters for the same k even values:

$$B_q^k = \langle B_q^k(r) \rangle_{4f}, \qquad B_q^{k\prime} = \langle B_q^k(r) \rangle_{4f,\,6s}. \tag{14}$$

The additional *cfp* may be treated exactly like the primary ones, i.e., one can perform a fitting procedure on these new parameters, once the matrix elements for the configuration interaction are included in the routines.

The program ATOME (Garcia 1988) has been developed to include these matrix elements. In fact, ATOME is rather different from the other programs since it manipulates Slater determinantal functions instead of $^{2S+1}L_J$ states: let the machine do the tough jobs!

Garcia and Faucher (1989) applied configuration interaction ($4f^2$/4f5d) to the deviant case of trivalent praseodymium in $PrCl_3$ (the problem of the $^1D_2$ level) because of the reduced size of the system: the high symmetry imposes no more than four even *cfp* and two odd *cfp*. Most of the discrepancy of the $^1D_2$ multiplet is eliminated with only two

supplementary parameters (the two odd-rank *cfp*) whereas Yeung and Newman (1987) needed four additional parameters with a correlated crystal field.

The covalo-electrostatic model (see sect. 4.4) gave excellent starting values for the fitting procedure.

Of course, the k-even *cfp* fitted this way are different from those traditionally evaluated inside the $4f^N$ configuration alone. In the case of $PrCl_3$, the difference reaches 30% for B_0^4. So it is more and more questionable to look for 'the' model to calculate *cfp* ab initio: which *cfp*? The *cfp* on $4f^N$ or the *cfp* on $4f^N + 4f^{N-1}5d$ and involving possibly still higher excited configurations? It seems to make no sense to take the standard (i.e. without configuration interaction) fitted *cfp* as an absolute reference for ab initio calculation, at least when deviant levels exist.

Another advance permitted by configuration interaction is a precise calculation of other properties such as the magnetic behaviour under weak fields. The Zeeman effect in $PrCl_3$ is totally reproduced by the configuration interaction parameters (Garcia and Faucher 1989). Unfortunately, the same parameters permit only partial reproduction of the electronic transition oscillator strength (Garcia and Faucher 1992).

Let us go back to the basics of the program ATOME: the determinantal approach. It is less sophisticated than the tensorial algebra of Racah, but both methods are time consuming.

Working with tensorial algebra requires calculation of new tricky tables for each new operator and each f^N configuration or to relate this new operator to known ones. On the contrary, in the determinantal approach, 1 or N electrons is the same problem since only integrals for one, two or three electron operators between the corresponding number of orbitals (two, four or six, respectively) are needed whatever the number of electrons.

The advantage of the determinantal approach is decisive if you are interested in a multiconfigurational system. Just try to calculate

$$\left\langle 4f^{4^{2S+1}}L_J \left| 1/r_{12} \right| 4f^3 5d^{1^{2S'+1}}L'_{J'} \right\rangle !!$$

If you work with determinants, you only need calculating integrals of the type $\langle \varphi_1 \varphi_2 | 1/r_{12} | \varphi_3 \varphi_4 \rangle$, where the φ_i are 4f or 5d wavefunctions, which is straightforward. The main advantage of the tensorial method is to allow a reduction of the matrix size in order to spare computer time; but today, we have more and more powerful computers so that time and memory are no longer a problem.

And finally, the determinantal method permits one to be closer to the physical interaction than the tensorial way. The $^{2S+1}L_J$ levels are only abstractions whereas all the known interactions are defined as one-, two- or three-electron operators ($1/r_{12}$, $\boldsymbol{l}\cdot\boldsymbol{s}$, ...).

4. Ab initio calculations

Up to this point, we have not talked about the physical origin of the crystal-field effects. All we can say is that they look like Stark effects: splitting of the $(2J+1)$ degenerated $^{2S+1}L_J$ levels of the trivalent rare-earth ions.

Of course, the challenging point is to understand the physics of the process so as to be able to calculate either the complete spectra or, at least, the *cfp* the same way we can evaluate the falling point of a baseball given its initial position, speed and acceleration!

In the following, we shall review the Superposition Model, the Angular Overlap Model, the Electrostatic Model, the Covalo–Electrostatic Model and unnamed models still under development. These are all meant to help ab initio calculations of *cfp* values from the structural data of each compound, i.e. the ion positions and the physical properties of each ion such as its size, polarizability, etc.

4.1. *The superposition model (SM)*

The idea of building the crystal field of transition-metal and lanthanide compounds as a superposition of single ligand contributions was first expressed by Griffith (1964), but it was effectively introduced by Bradbury and Newman (1967) and developed in subsequent work. It is utilized to standardize the analysis of crystal field data. A large amount of information on and beyond the subject appears in a review paper by Newman and Ng (1989) which stresses the relationship of the superposition model with the angular overlap model often preferred for d electrons.

The main hypothesis of the superposition model is that the *cfp* may be written as a sum of individual contributions from the ions in the crystal, each one being the product of a purely angular part [$C^{(k)}(\hat{\boldsymbol{R}})$, where $\hat{\boldsymbol{R}}$ stands for the angular coordinates Θ and Φ of the vector $\boldsymbol{R}$] and a radial part which depends on the rare earth/ion distance. The resulting expression is

$$B_q^k = \sum_j A^k(R_j)\, C_q^k(\hat{\boldsymbol{R}}_j), \tag{15}$$

where the sum runs over all ions j of the crystal at positions $\boldsymbol{R}_j$. In eq. (15), the functions $A^k(R)$, called *intrinsic parameters,* are supposed to decrease quickly with R so that the summation may be limited to the first neighbors. Newman (1977) proposed expressing the R dependence of the intrinsic parameters A^k as a power law: ligands at a same distance from the rare earth nucleus are grouped in sets S, and expression (15) becomes

$$B_q^k = \sum_S A^k(R_0) \left(\frac{R_0}{R_S}\right)^{t_k} K_q^k(S), \tag{16}$$

where the coordination factor $K_q^k(S)$ is the sum of the tensor operators $C_q^k(\hat{\boldsymbol{R}}_j)$ for set S. Entire freedom is left for the choice of R_0 which is an arbitrarily fixed distance. It seems that Newman and Ng (1989) chose R_0 equal to the shortest metal–ligand distance in the compound (see equation 3-2 in their paper). All the angular dependences are included in the terms $K_q^k(S)$ and can be readily evaluated utilizing the crystalline data of the compound. The quantities to fit are then t_k $(k = 2, 4, 6)$, which makes a total

of 3 unknowns per ligand species. For axial symmetries, when there are two different kinds of ligands, and only one second-rank parameter B_0^2, it is impossible to derive the corresponding t_2. For that reason, few determinations of A^2 can be found in the literature. For instance, in Eu^{3+}:YOCl, where the local symmetry of the trivalent europium is C_{4v}, the non-zero B_q^k correspond to $q = 0$ or $q = 4$ whereas there are three nearest-neighbor species: four oxygens at 2.2776 Å, four chlorines at 3.024 Å and one chlorine at 3.018 Å. Even if we group all the chlorines together, we have to extract the intrinsic parameters A^2(2.2776 Å) for the oxygens and A^2(3.020 Å) for the chlorines whereas we have only one crystal-field parameter B_0^2 at our disposal, i.e., one equation and two unknown intrinsic parameters. The electrostatic model (EM), which we shall examine in a further section, is a particular case of the superposition model. Expressions linking both models show that for repulsive interactions between the ligands and the open-shell electrons, the A^k should be positive.

A number of crystal-field data sets have been analysed by the superposition model, for rare-earth substituted garnets by Newman and Stedman (1969), for CaF_2, SrF_2 and $LaCl_3$ by Newman (1971, 1978), for $LaAlO_3$, La_2O_3 and La_2O_2S by Linarès and Louat (1975), for vanadates, arsenates and phosphates by Linarès et al. (1977), etc. Some examples (intrinsic parameters and power law when determined) are listed in table 3.

The superposition model often works well, rather better for A^4 than for A^6. For parent compounds with similar chemical characteristics, quite similar values of intrinsic parameters and power laws are obtained. The difficulty consists in explaining the discontinuous jumps from one family to another. Aiming towards this goal, Newman (1978) discussed a standardization of the reference distances and power laws for various ligands. But this seems difficult in view of the results listed in table 3. For instance, how can one reconcile, without adding some additional postulate, the power laws for A^4 in Er^{3+}:SrF_2 ($t_4 = 6.3$) and in Er^{3+}:LaF_3 ($t_4 = 11.1$)?

Noting the diversity of the results for compounds with oxygen ligands, Newman mentions the probable important role of ionicity of the metal–oxygen bond which is likely to change in view of the bonding of oxygens with the other ions of the compound. One remark which can be made is that instead of indirectly deriving the intrinsic parameters from the fitted crystal-field parameters, creating a cascade of arithmetic approximations, it would be better to directly fit the parameters of the superposition model from the spectra, and that is indeed the procedure recommended by Newman. In fact it is seldom practised since most fitting routines are fixed once and for all.

For low site symmetries systematic *angular* discrepancies sometimes occur between the experimental field parameters and those deduced from the superposition model. It is namely the case for rare earth substituted Y_2O_3 in which B_2^6 is far too strong for all the members of the series. The distortion cannot be accounted for by any power law since the crystal structure is precisely known at low temperature and shows that the six oxygen first neighbours are nearly equidistant from the rare earth.

As a conclusion we shall say that the superposition model, alone, does not constitute an ab initio predictive method but it is an important part of it. Besides, its value comes

Table 3
Some results of the superposition model: standard distance R_0, intrinsic parameters A^k and power laws t^k ($k=4,6$)

Host	Ln^{3+}	R_0	A^4	t_4	A^6	t_6	Ref.
Fluorides							
CaF_2	Gd^{3+}		86.8	10.7	27.8	21.6	1
SrF_2	Tb^{3+}	2.410	75.9	6.3	20.3	10.1	1
SrF_2	Er^{3+}	2.373	75.9	6.3	20.3	10.1	1
BaF_2	Tb^{3+}	2.410	75.9	6.3	20.3	10.1	1
	Er^{3+}	2.373	75.9	6.3	20.3	10.1	1
LaF_3	Er^{3+}	2.42	74	11.1	19.4	8.7	1,5,6
KY_3F_{10}	Eu^{3+}	2.19	78.4	16.6	19.7	9.1	1
Chlorides							
$LaCl_3$	Pr^{3+}	2.953	38.8		15.8		2
$LaCl_3$	Eu^{3+}	2.98	34	5–7	20.5	5–7	4
$Cs_2NaPrCl_6$	Pr^{3+}	2.673	82.4	7.9	52.8	12.1	1
Oxides							
$Y_3Ga_5O_{12}$	Dy^{3+}	2.407	75.9	11	21.2	10.9	1
$Y_3Ga_5O_{12}$	Er^{3+}	2.377	75.9	11	21.2	10.9	1
La_2O_2S	Eu^{3+}	2.423	88	10	18.5	11	4
La_2O_3	Eu^{3+}	2.54	70	10	8.6	11	4
$LaAlO_3$	Eu^{3+}	2.68	35	10	16.4	11	4
$CaWO_4$	Er^{3+}	2.466	51		17		1
YPO_4	Eu^{3+}	2.313	47.8	8	n.d.[a]		3
$YAsO_4$	Eu^{3+}	2.300	40	8	n.d.[a]		3
YVO_4	Eu^{3+}	2.291	57.3	8	n.d.[a]		3

[a] n.d., not determined.

References
(1)Newman (1978)
(2) Curtis and Newman (1969)
(3) Linarès et al. (1977)
(4) Linarès and Louat (1975)
(5) Yeung and Newman (1985)
(6) Stedman and Newman (1971)

from its universality and philosophical strength: in the field of ab initio methods for calculating the *cfp*, a contribution does or does not satisfy the superposition model; it can be considered as a criterion for classifying all the proposed theories as well as a basis for additive models in which the total *cfp* is a sum over various contributions.

4.1.1. *Application*

Let us finish this section by giving a practical example: application of the superposition model to the compound Nd_2O_3. The space group is $P\bar{3}m1$, the parameters of the hexagonal cell refined at 4 K by Faucher et al. (1982) are $a=3.8277$ Å, $c=5.9908$ Å, with the positional parameters $u=0.2463$, $v=0.6469$. The site symmetry of the rare earth is

Table 4
Crystal-field parameters of Nd_2O_3

Set	B_0^2	B_0^4	B_3^4	B_0^6	B_3^6	B_6^6	Source
1	−836	634	−1606	752	237	672	Caro et al. (1979)
2	−807	594	−1607	681	457	719	unpublished fit utilizing the levels of Caro et al. (1979)

Oxygen ligand sets, distances, angles and coordination factors in Nd_2O_3 [a]

Set	Nb	R (Å)	Θ (°)	Φ	(k,q)				
					(4, 0)	(4, 3)	(6, 0)	(6, 3)	(6, 6)
1	1	2.3999	0.	0	1.	0.	1.	0.	0.
2	3	2.3007	73.853	0, ±120	0.3335	1.0936	0.2519	−1.0178	1.1192
3	3	2.6572	123.731	180,±60	−1.0960	1.4173	0.7874	0.2404	0.4715

[a] The standard reference distance R_0 is equal to 2.3 Å. The intrinsic parameters and the power laws giving the best solutions for the system of equations (16) are:

$A^4 = 935\,(117)\,\text{cm}^{-1}$; $A^6 = 500\,(31)\,\text{cm}^{-1}$.
$t_4 = 5.7$ $t_6 = 5.9$

C_{3v}. The experimental crystal-field parameters have been determined by Caro et al. (1979), but we use another set determined with a procedure that empirically corrects the $^2H(2)_{11/2}$ levels. The corresponding parameters (in Wybourne's formalism) are reported in table 4, as well as the ligand distances and angles with respect to the rare earth and the corresponding coordination factors $K_q^k(S)$ for set S.

The values in Stevens normalisation are between parentheses. The results are quite different from those obtained by Linarès and Louat (1975) for Eu^{3+} in La_2O_3 (see table 3), both for the intrinsic parameters and for the power laws. The main reason is that the shortest metal–ligand distance (2.3 Å) has been taken as reference here, while the mean distance (2.42 Å) was chosen in the study by Linarès and Louat (1975). This rather mild difference changes the results drastically. It is useful to keep this in mind when applying and interpreting the superposition model.

4.2. *The angular overlap model (AOM)*

The original angular overlap model (AOM) due to Jørgensen et al. (1963) was initially dedicated to the treatment of d elements. The papers by Schäffer and Jørgensen (1965) and Jørgensen (1965) improved the model. A review of the AOM may be found in Gerloch and Woolley (1984).

The basic idea is to work on 4f orbitals. It is proposed to write the antibonding energy of a 4f orbital interacting with its first neighbors (ligands) orbitals as:

$$E = \Xi^2 \sigma^* = \Xi^2 e_\sigma/(2l+1), \tag{17}$$

where Ξ is a purely geometric factor including the local symmetry and σ^* (or e_σ) a *contact term* which represents the effects of a single ligand. e_σ is supposed to be proportional to the square of the overlap integral between the radial functions of the central metal and a ligand and therefore to decrease exponentially with the internuclear distance. The extension of expression (17) to π, φ, ... effects is described by Schäffer and Jørgensen (1965):

$$E = \sum_{e=\sigma,\pi,\varphi,\ldots} \Xi_e^2 e^*, \tag{18}$$

where the coefficients e^* also depend on the ligand chemical nature so that the sum runs also over the different ligand species.

The cross relations due to Kibler (1971, 1974, 1975) between the coefficients of the Angular Overlap model e^* (up to φ effects), the electrostatic model (EM) crystal field parameters, and the superposition model (SM), translate in familiar *cfp* terminology the contribution of one overlap type λ with ligand L to the B_q^k. It is written as

$$B_q^k(L) = \sum_{-3 \leqslant \lambda \leqslant 3} (-1)^\lambda \frac{2k+1}{2l+1} \begin{pmatrix} l & l & k \\ -\lambda & \lambda & 0 \end{pmatrix} \Big/ \begin{pmatrix} l & l & k \\ 0 & 0 & 0 \end{pmatrix} e_\lambda \cdot C_q^{k*}(\hat{\boldsymbol{L}}) \tag{19}$$

so that the *cfp* B_q^k and the coefficients e_λ are related by the following formula:

$$\begin{aligned} B_q^2 &= \sum_L \left(\tfrac{5}{7} e_\sigma(L) + \tfrac{15}{14} e_\pi(L)\right) C_q^{2*}(\hat{\boldsymbol{L}}), \\ B_q^4 &= \sum_L \left(\tfrac{9}{7} e_\sigma(L) + \tfrac{3}{7} e_\pi(L)\right) C_q^{4*}(\hat{\boldsymbol{L}}), \\ B_q^6 &= \sum_L \left(\tfrac{13}{7} e_\sigma(L) - \tfrac{39}{14} e_\pi(L)\right) C_q^{6*}(\hat{\boldsymbol{L}}), \end{aligned} \tag{20}$$

where the interactions δ, φ, ... have been neglected. The sum runs over the ligands L at angular position $\hat{\boldsymbol{L}}$. The neglect of high-order overlaps is justified for oxygen ligands for which significant overlaps occur only with the s and p valence shells. e_σ represents the essential part of the anti-bonding effects and is therefore positive. Jørgensen (1965) states that in halides e_π is 20–25% of e_σ, but for some ligands, e_π may be negative. However tempting in view of its link with familiar quantities, this transformation does not meet with unanimous support, the problem lying apparently in the fact that the genuine parameters

of the AOM are defined with respect to tesseral harmonics whereas the *cfp* B_q^k work on the basis of spherical harmonics. The relations (20) derived by Kibler (1975) assume that the metal–ligand interactions are axially symmetric, therefore, they presumably do not represent faithfully the parameters of the early AOM when the compound possesses a site symmetry likely to mix up individual orbitals $|\ell, m|$ and $|\ell, m'|$. The point is stressed by Linarès et al. (1981) who give an numerical evaluation of the errors which are committed by utilizing expressions (20). Newman and Ng (1989) also insist that although the angular overlap model has narrow connections with the superposition model, it differs conceptually. The single-ligand interactions as originally defined by Jørgensen (1965) for the AOM have a C_{2v} symmetry whereas they display a $C_{\infty v}$ symmetry in the SM.

As we pointed out for the Superposition Model, it is preferable to fit the parameters of the AOM directly from the spectroscopic observations. However, since the fitting routines are adapted to yield the *cfp* B_q^k (following the formalism of Wybourne or Stevens), the process is often made in two steps (or three): firstly the determination of the B_q^k, then:

(1) the best fit of the e_λ if Kibler's method is applied.
(2) or determination of the individual orbital energies, and the application of Jørgensen's equations.

The majority of AOM studies reported in past years deals with σ and π contact terms only. Urland (1977–1979, 1981) has devoted several papers to careful analyses of lanthanide *cfp* data along the lines of the AOM. Different ligand effects are mainly investigated in $LaCl_3$ doped with the whole series of lanthanides. The value of e_σ is close to 200 cm^{-1} and the ratio e_π/e_σ ranges from 0.19 to 0.39 with a mean value equal to 0.27. For scheelite, $CaWO_4$, e_σ decreases steadily along across the lanthanide series from 376 cm^{-1} for Nd^{3+} to 244 cm^{-1} for Yb^{3+}, in agreement with overlap calculations. Besides, the mean e_σ values in hydroxides and hydrated ethylsulfates are equal to 279 and 174 cm^{-1}, respectively, giving (Urland 1979)

$$H_2O(174) < Cl^-(202) < OH^-(279) \leqslant O^{2-}(293) \qquad \text{for } e_\sigma;$$
$$H_2O(30) < Cl^-(73) \leqslant OH^-(78) < O^{2-}(104) \qquad \text{for } e_\pi.$$

Linarès et al. (1981) re-examined also the data for $LaCl_3$ doped with the whole series of lanthanides, $KY_3F_{10}:Eu^{3+}$, $NdAlO_3$, and a series of hydroxides. As in the SM, the ligands at a same distance from the rare earth nucleus are grouped in sets. An approximate power law $e_\lambda(R_n)/e_\lambda(R_{n'}) = (R_{n'}/R_n)^{t_\lambda}$ is derived. A test of the validity of the method is the recalculation of B_0^2 for comparison with the experimental value once the parameters of the AOM have been determined.

Faucher et al. (1986) analyzed the data for eleven rare-earth compounds utilizing Kibler's expressions for the *cfp* due to the AOM. The contact terms e_λ are determined so as to make equations (20) fit as well as possible with the experimental *cfp*. The ratio e_π/e_σ ranges between 0.16 and 0.56 but the most frequent ratio is slightly lower than 0.4. Looking for the physical origin of the antibonding energies, Jørgensen et al. (1986) evaluated the proportionality constant $K = e_\sigma/S^2_{Ln-L}$ and noted that the mean value of K is 168 eV for 31 Nd–O contacts. This large value can only be compared with the angular

Table 5
Compound, number of contacts, rare-earth–ligand distance, value of the contact term e_σ, power law exponent t_σ for the e_σ term, ratio e_π/e_σ, power law exponent t_π and references

Compound	Contact	R (Å)	e_σ	t_σ	e_π/e_σ	t_π	Ref.
$LaCl_3:Pr^{3+}$	Pr–9Cl	2.953	191	n.a.[a]	0.19	n.a.[a]	1
$LaCl_3:Nd^{3+}$	Nd–9Cl	2.953	240	n.a.[a]	0.25	n.a.[a]	1
$LaCl_3:Nd^{3+}$	Nd–9Cl	2.953	257	n.a.[a]	0.25	n.a.[a]	2
$LaCl_3:Eu^{3+}$	Eu–9Cl	2.953	227	n.a.[a]	0.17	n.a.[a]	1
$LaCl_3:Eu^{3+}$	Eu–9Cl	2.953	254	n.a.[a]	0.22	n.a.[a]	2
$YOCl:Eu^{3+}$	Eu–4O	2.278	549	n.a.[a]	0.39	n.a.[a]	3
	Eu–5Cl	3.017	90		<0		
$KY_3F_{10}:Eu^{3+}$	Eu–4F	2.190	467	9.7	0.60	18.3	2
	Eu–4F	2.331	258		0.35		
$KY_3F_{10}:Eu^{3+}$	Eu–4F	2.190	455	11	0.40	9.8	3
	Eu–4F	2.331	236		0.43		
$LiYF_4:Nd^{3+}$	Nd–4F	2.246	505	(0.5)	0.16	<0	3
	Nd–4F	2.293	500		0.29		
$NdAlO_3$	Nd–3O	2.386	475	9.3	0.12	19	2
	Nd–6O	2.659	239	7	0.20		
	Nd–3O	2.936	118		0.16		
Nd_2O_3	Nd–3O	2.301	705	10.7	0.48		3
	Nd–O	2.400	450	4	(0.48)		
	Nd–3O	2.657	259		<0		
Nd_2O_2S	Nd–4O	2.362	507		0.44	n.a.[a]	3
	Nd–3S	2.964	90		0.56	n.a.[a]	
$Y_2O_3:Eu^{3+}$	Eu–4O	2.25	881	23	0.41	33	3
	Eu–2O	2.33	391		0.29	n.a.[a]	
$CaWO_4:Nd^{3+}$	Nd–4O	2.438	376	7	0.24	7	4
	Nd–4O	2.479	335		0.24		
$CaWO_4:Er^{3+}$	Nd–4O	2.438	262	7	0.37	7	4
	Nd–4O	2.479	233		0.24		
$Gd(OH)_3$	Nd–9OH	2.46	422		0.21		2
$Tb(OH)_3$	Nd–9OH	(2.45)	(394)		0.44		2
$Dy(OH)_3$	Nd–6OH	2.429	386	9	0.49	60	2
	Nd–3OH	2.452	355		0.30		
$Er(OH)_3$	Nd–6OH	2.402	318	9	0.45		2
	Nd–3OH	2.439	277		0.21		

[a] n.a., not applicable: the ligands are at the same distance from the nucleus and there is no power law.

References

(1) Urland (1978)
(2) Linarès et al. (1981)
(3) Faucher et al. (1986)
(4) Urland (1979)

part of the f-electron kinetic energy so that a large part of the anti-bonding effects seems due to this operator. However, the conclusion is that the experimental results are best reproduced by the addition of π to σ effects. Some results from the papers quoted above are reported in table 5.

We refer the reader back to a paper by Gajek and Mulak (1992) to get an insight into the performance of the AOM when applied to actinide compounds. The ratio e_π/e_σ is always close to 0.35. Gajek and Mulak advise adding an empirical and tunable lattice-dependent e_δ contribution varying regularly inside a homologous and isostructural series. Comparing AOM with ab initio calculations, the authors list the microscopic contributions to the usually neglected e_δ effect.

4.2.1. *Application*

Let us again analyze the experimental *cfp* of Nd_2O_3, but this time in terms of the AOM. If ligands sets 1 and 2 are grouped as above, there are six equations and four unknown quantities $e_{\sigma 1,2}$, $e_{\sigma 3}$, $e_{\pi 1,2}$ and $e_{\pi 3}$:

$$
\begin{array}{rrrrcr}
-0.1086e_{\sigma 1,2} & -0.1628e_{\pi 1,2} & -0.0803e_{\pi 1,2} & -0.1205e_{\pi 3} & = & -807 \\
1.7144e_{\sigma 1,2} & 0.5715e_{\pi 1,2} & -1.4091e_{\pi 1,2} & -0.4697e_{\pi 3} & = & 595 \\
1.4061e_{\sigma 1,2} & 0.4687e_{\pi 1,2} & 1.8222e_{\pi 1,2} & 0.6074e_{\pi 3} & = & -1607 \\
2.3249e_{\sigma 1,2} & -3.4874e_{\pi 1,2} & 1.4622e_{\pi 1,2} & -2.1933e_{\pi 3} & = & 457 \\
2.0785e_{\sigma 1,2} & 3.1177e_{\pi 1,2} & 0.8756e_{\pi 1,2} & -1.3134e_{\pi 3} & = & 719
\end{array}
$$

The solutions are

$e_{\sigma 1,2} = 602\ (705, 450)\ \mathrm{cm}^{-1}$ $\quad e_{\pi 1,2} = 274\ (338, 216)\ \mathrm{cm}^{-1}$

$e_{\sigma 3} = 353\ (259)\ \mathrm{cm}^{-1}$ $\quad e_{\pi 3} = 83\ (<0)\ \mathrm{cm}^{-1}$

The values in parentheses were obtained by Faucher et al. (1986) who separated the three sets of ligands. The present set is coherent with the former one but gives a more probable (*positive*) value for the π anti-bonding contact term of the most remote ligands. The fact which emerges is that π effects are vanishingly small in Nd_2O_3 at the interatomic distance 2.65 Å.

4.3. *The electrostatic model (EM)*

Bethe (1929) is the father of the electrostatic model. Although it is the oldest model, it is maybe still the most popular one because it is based on a clear idea that permits one to calculate the *cfp ex nihilo* in a straightforward way. However, as in politics, popularity is not synonymous with efficiency and the model fails in predicting exact crystal-field parameters. However, the EM presents some interesting features and we are going to describe it quite precisely.

The main hypothesis of the electrostatic model is that crystal-field effects originate from electrostatic interaction of the 4f electrons with the rest of the crystal. So we can write the crystal-field Hamiltonian as

$$H_{\mathrm{CF}} = \sum_i -eV(\boldsymbol{r}_i), \tag{21}$$

where the sum runs over the 4f electrons and $\boldsymbol{r}_i$ is the coordinate vector of the ith electron.

All we have to do is to express the potential $V(\boldsymbol{r})$ as a function of the crystal characteristics. Let $\rho_j(\boldsymbol{\tau}$ be the charge density corresponding to the jth ion of the crystal of coordinate $\boldsymbol{R}_j$; we get:

$$V(\boldsymbol{r}) = \sum_j \iiint \frac{\rho_j(\boldsymbol{\tau})}{|\boldsymbol{r} - (\boldsymbol{R} + \boldsymbol{\tau})|} \, \mathrm{d}^3\tau. \tag{22}$$

Let us assume that we can write, if $|\boldsymbol{r}| < |\boldsymbol{R} + \boldsymbol{\tau}|$, which means that the 4f electron never enters the distribution of charge ρ:

$$\frac{1}{|\boldsymbol{r} - (\boldsymbol{R} + \boldsymbol{\tau})|} = \sum_{n=0}^{\infty} \frac{1}{n!} \tau^{(n)} \cdot \nabla_{\boldsymbol{R}}^{(n)} \left(\frac{1}{|\boldsymbol{R} - \boldsymbol{r}|} \right) \tag{23}$$

where $\tau^{(n)}$ is the nth-rank tensor built on $\boldsymbol{\tau}$ and $\nabla_{\boldsymbol{R}}^{(n)}$ is the nth-rank tensor built on the derivative operator with respect to $\boldsymbol{R}$. We get:

$$V(\boldsymbol{r}) = \sum_j \frac{1}{n!} \iiint \rho_j(\boldsymbol{\tau}) \, \tau^{(n)} \cdot \nabla_{\boldsymbol{R}}^{(n)} \left(\frac{1}{|\boldsymbol{R} - \boldsymbol{r}|} \right) \tag{24}$$

or

$$V(\boldsymbol{r}) = \sum_j M_j^{(n)} \cdot \nabla_{\boldsymbol{R}}^{(n)} \left(\frac{1}{|\boldsymbol{R} - \boldsymbol{r}|} \right), \tag{25}$$

with

$$M^{(n)} = \frac{1}{n!} \iiint \rho(\boldsymbol{\tau}) \, \tau^{(n)} \, \mathrm{d}^3\tau.$$

$M^{(n)}$ is a nth-rank tensor and is called the 2^n-pole moment of the charge distribution. $M^{(0)}$ is a scalar and gathers the total net charge of the distribution. $M^{(1)}$ is a vector and is called the dipole, $M^{(2)}$ is the quadrupole.

Taking into account the development relation

$$\frac{1}{|\boldsymbol{R}-\boldsymbol{r}|}=\sum_{k} r^{k}\, C^{(k)}(\hat{\boldsymbol{r}})\cdot C^{(k)}(\hat{\boldsymbol{R}})/R^{k+1} \tag{26}$$

and the fact that

$$\nabla_m^n(C_q^k(\hat{\boldsymbol{R}})/R^{k+1})=(-1)^q\left[\frac{(2k+2n+1)!}{(2k+1)!2^n}\right]^{1/2}\begin{pmatrix} k & k+n & n\\ -q & q-m & m\end{pmatrix}\frac{C_{q-m}^{k+n}(\hat{\boldsymbol{R}})}{R^{k+n+1}} \tag{27}$$

we get

$$V(\boldsymbol{r})=\sum_{k=0}^{\infty} r^k C^{(k)}(\hat{\boldsymbol{r}})\cdot\sum_{j}\sum_{n=0}^{\infty}(-1)^k\left[\frac{(2k+2n+1)!}{(2k+1)!2^n}\right]^{1/2}\left\{M_j^{(n)}\otimes C^{(k+n)}(\hat{\boldsymbol{R}}_j)\right\}^{(k)}/R_j^{k+n+1} \tag{28}$$

and finally

$$B_q^k=e\langle r^k\rangle\sum_{j}\sum_{n=0}^{\infty}(-1)^{k+1}\left[\frac{(2k+2n+1)!}{(2k+1)!2^n}\right]^{1/2}\left\{M_j^{(n)}\otimes C^{(k+n)}(\hat{\boldsymbol{R}}_j)\right\}^{(k)}/R_j^{k+n+1}, \tag{29}$$

where e is the electron charge and $\langle r^k\rangle$ is the expectation value of r^k with respect to the 4f radial wavefunction.

This is the basic equation for the electrostatic model. It shows that the electrostatic *cfp* are the sum of multipolar contributions. A similar expression was worked out by Malta (1979).

The contribution of 0th rank is called the point charge contribution. It was the only one included in the first version of the model which was, for this reason, designated as the point charge electrostatic model (PCEM). This contribution is written as:

$$B_q^{k(0)}=e\langle r^k\rangle\sum_{j}(-1)^{k+1}\frac{q_j}{R_j^{k+1}}C_q^k(\hat{\boldsymbol{R}}_j). \tag{30}$$

This form shows clearly that the PCEM enters the superposition model with:

$$A^k(R)=e\langle r^k\rangle(-1)^{k+1}\frac{q}{R^{k+1}}. \tag{31}$$

Following the PCEM, Newman's intrinsic parameters should be positive for negatively charged ligands.

Given the structural data $\boldsymbol{R}_j$ (from X-ray for instance) and the $\langle r^k \rangle_{4f}$ (from Hartree-Fock calculations), the first problem is to choose the point charge q_j. Shall we take the nominal charge $-2e$ for the oxygens, $+3e$ for the europium, ... or less?

Let us examine the values of the bonding ionicities as given by Pauling (1960). The rare-earth–oxygen bonding ionicity is ~0.74, of the same order of magnitude as for nickel–fluor (0.70). Based on a RMN study, Shulman and Sugano (1963) showed that the wave-function mixing is weak so that we can use the nominal charges for the rare-earth ion and its ligands.

Another problem consists in determining the $M_j^{(n)}$ values (n-polar moment of the jth ion of the crystal). The crystal field modifies the charge distribution which, in turn, creates an opposite electric field. On each ion of the medium, the electrostatic field created by all the other ions enables the same phenomenon. To a first-order approximation, the electrostatic field creates an electrostatic dipole directly related to the applied electric field through the dipolar polarizability tensor $\alpha^{(1)}$:

$$M^{(1)} = \alpha^{(1)} \boldsymbol{E}, \tag{32}$$

where $\boldsymbol{E} = -\nabla^{(1)} V$ is the sum of the field generated by all the other point charges and all the other dipoles of the medium. In the same way, the electrostatic field gradient generates an electrostatic quadrupole related to the applied gradient through the quadrupolar polarizability:

$$M^{(2)} = \alpha^{(2)} \nabla^{(1)} \boldsymbol{E}. \tag{33}$$

Of course the total field is the sum of the electrostatic fields created by the other point charges, dipoles and quadrupoles and the total field gradient is the sum of the electrostatic field gradients created by the other point charges, dipoles, quadrupoles, and so on ... It seems reasonnable to stop there because the terms of the series are supposed to decrease quickly but also because we have no precise idea of the magnitude of a "hexadecupolar" polarizability! The dipole and quadrupole moments are finally determined writing the electric equilibrium of the crystal and their values are introduced into expression (29).

A lot of works exist in the literature aiming to make the empirical B_q^k *cfp* fit with PCEM values. The most elaborate consider multipolar contributions. Hutchings and Ray (1963) opened the way, Weenk and Harwig (1977) and Bijvank and den Hartog(1980) introduced self-consistently calculated point dipoles in ionic lattices for various purposes, in particular to correct the fields or to evaluate *cfp*. Morrison et al. (1981) found significant contributions of self-induced dipoles through polarizable ligands to the one-electron crystal field. The calculation was applied to $LaCl_3$.

Faucher and Garcia (1982) focussed on the determination of electrostatic *cfp* of lanthanides, including the contributions of point charges, of consistently calculated dipoles and quadrupoles. The comparison between experimental and calculated *cfp* values is not easy, given the large number of parameters to consider; it is therefore useful to determine objective criteria to qualify the model. Two performance indexes close to those

Table 6
Mean values over thirteen compounds of the reliability and scale factors obtained with the electrostatic model

	Reliability factors			Scale factors		
	$R^{(2)}$	$R^{(4)}$	$R^{(6)}$	$S^{(2)}$	$S^{(4)}$	$S^{(6)}$
Point charges (PC)	59	8.4	22.0	1.36	1.49	4.04
PC + dipoles (D)	36	9.2	26.0	0.61	1.46	3.62
PC + D + quadrupoles	41	18.5	33.0	0.54	1.25	3.00

utilized for X-ray methods are defined: a scale factor and a reliability factor. The *cfp* B_q^k is considered as a generalized vector with $2q+1$ components. Its length is equal to

$$B^k = \left[\sum_{-k \leqslant q \leqslant k} B_q^k \cdot B_q^{k*} \right]^{1/2} . \tag{34}$$

Then the scale factor emerges naturally as the ratio between the lengths of the experimental and calculated vectors:

$$S^{(k)} = \left| B^{(k)}(\text{expt}) \right| / \left| B^{(k)}(\text{calc}) \right| , \tag{35}$$

while the angle between the two generalized vectors $B^{(k)}(expt)$ and $B^{(k)}(calc)$ represents a reliability factor:

$$R^{(k)} = \arccos \left[\frac{B^{(k)}(\text{expt}) \cdot B^{(k)}(\text{calc})}{|B^{(k)}(\text{expt})| \cdot |B^{(k)}(\text{calc})|} \right] . \tag{36}$$

A perfect agreement would yield $S^{(k)}=1$ and $R^{(k)}=0$ degree. Faucher and Garcia (1982) report for 16 rare-earth compounds reliability and scale factors which are far from these ideal values. Mean values for 13 compounds are given in table 6.

The values of $R^{(4)}$ and (to a lesser extent) $R^{(6)}$ are not too bad, which is just a consequence of the superposition principle. The addition of dipolar contributions slightly improves $R^{(2)}$ (for axial symmetry, it is equal to 0 or 180 degrees according to whether the sign of B_0^2 is correct or not). $R^{(4)}$ and $R^{(6)}$ worsen especially when quadrupoles are added. The scale factors are extremely fluctuant, depending on the compound, and extreme values are hidden in the averages listed in table 6. The mean values of $S^{(4)}$ and especially $S^{(6)}$ are obviously too large. The mean dipolar/point charge contribution is 1.4, 0.15 and 0.15 for $k=2$, 4 and 6, respectively, while the quadrupolar/point-charge contribution is 1.4, 0.54 and 0.63, respectively. With the literature polarizabilities values, the multipolar series diverges (as confirmed by an approximate evaluation of the octupolar contribution) and this explains the improvement of the scale factors with the addition of the quadrupolar contribution.

Thus are openly stated the defects of the Electrostatic Model. Efforts have been made to moderate the defeat and two corrections are likely to help.

First, we already mentioned that the Hartree–Fock Slater integrals F^k do not match the fitted ones: the ab initio values are 1.1 to 1.5 timesthe phenomenological ones. This difference can be taken into account by an expansion of the rare earth radial wavefunction which, in counterpart, gives higher radial integrals $\langle r^k \rangle$. If λ is the mean ratio between the phenomenological F^k and the Hartree–Fock ones, then $\langle r^k \rangle / \lambda^k$ may replace the simple $\langle r^k \rangle$ of eq. (29). This intervention results in an increase of the calculated B_q^k hence an improvement of the scale factors, except $S^{(2)}$ which becomes too small.

A second source of correction comes from the other shells: the 4f shell is responsible for the spectroscopic properties of the rare-earth ion, but the 5s and 5p shells, which are lower in energy, also experience crystal-field effects and are no longer "spherical"; they create an electrostatic field that tends to cancel the applied crystal field. This shielding effect is taken into account by the shielding factor σ_k which represents the ratio between the applied electrostatic field (or its $(k-1)$th derivative) and the induced ionic field. Applying the electrostatic $(k-1)$ gradient $E^{(k)}$, the outer electronic shells re-create the gradient $-\sigma_k E^{(k)}$ so that the total resulting gradient experienced by the 4f electrons is $(1-\sigma_k)E^{(k)}$. Rewriting eq. (28) as

$$V(\boldsymbol{r}) = \sum_k b^{(k)} r^k C^{(k)}(\hat{\boldsymbol{r}}) \tag{37}$$

leads to

$$E^{(k)} = -\nabla^{(k)} V(\boldsymbol{r}) = \left[\frac{(2k)!}{2^k}\right]^{1/2} b^{(k)}. \tag{38}$$

The original $b^{(k)}$ are replaced by the expression $(1-\sigma_k)\,b^{(k)}$. The last two corrections permit one to write a new version of eq. (29):

$$B_q^k = \frac{e(1-\sigma_k)\langle r^k \rangle}{\lambda^k} \sum_j \sum_{n=0}^{\infty} (-1)^{k+1} \left[\frac{(2k+2n+1)!}{(2k+1)!\,2^n}\right]^{1/2} \left\{M_j^{(n)} \otimes C^{(k+n)}(\hat{\boldsymbol{R}}_j)\right\}^{(k)} / R_j^{k+n+1}. \tag{39}$$

Some values for σ_k can be found in the papers by Sternheimer (1966), Sternheimer et al. (1968), Barnes et al. (1964), Sengupta and Artman (1970), Burns (1962) or Gupta and Sen (1973).

This second correction mainly lowers the second-order parameters, therefore increasing $S^{(2)}$. The combined effect of the two corrections is an improvement of the scale factors. Although some satisfying results have been obtained in this way (Faucher et al. 1980), it unfortunately requires special tailoring to fit individual cases.

Karayianis, Leavitt, Morrison and Wortman (Karayianis et al. 1973, 1976a,b, 1977, Karayianis and Morrison 1975, Leavitt et al. 1975, 1982, Morrison et al. 1976, 1977a–c, 1980, Wortman et al. 1976a–c, 1977) were the strongest advocates of this modified form of the PCEM which they call the three-parameter theory. They write

$$B_q^k = \tau^{-k}(1-\sigma_k)\langle r^k\rangle A_q^k, \tag{40}$$

where A_q^k is a lattice sum and τ is the scaling factor which expands the 4f wavefunction. They published a number of crystal-field studies on compounds with different chemical characteristics, namely arsenates, yttrium aluminate, YAG, lanthanum fluoride, $LiYF_4$, $Y_2SiBe_2O_7$, $Cs_2NaLnCl_6$, scheelite, etc. For covalent compounds they recognized the necessity to tune the ionic charges, so arriving at coherent results. They established series of smoothed B_q^k for lanthanide doping in a given compound.

While the genuine electrostatic model definitely does not give satisfactory ab initio *cfp*, it may be used in its modified form to produce "not too bad" starting values preliminary to the fitting of phenomenological parameters.

4.3.1. *Addendum 1: Direct determination of multipolar moments*

Direct determination of multipolar moments is the key of the multipolar electrostatic model. Garcia and Faucher (1986) related the electronic multipole magnitude to the X-ray factor structure:

$$f(\boldsymbol{k}) = \sum_n (\mathrm{i}\boldsymbol{k})^{(n)} \cdot M^{(n)}, \tag{41}$$

where the only multipole different with respect to eq. (29) is $M^{(0)}$ which excludes the nucleus point charge in the X-ray diffusion process. This formula when applied to the $LaCl_3$ data (Morosin 1968) gives multipoles two orders of magnitude lower than those calculated using literature polarizabilities. Even if this kind of calculation is not very precise, it seems that the consistently determined multipoles are incompatible with the X-ray data.

4.3.2. *Addendum 2: Extended charge contribution*

One of the assumptions of eq. (23) is that $|\boldsymbol{r}| < |\boldsymbol{R}_j + \boldsymbol{\tau}|$, which means that 4f electrons never enter the electronic distribution of the jth ion. This may be considered true for the main part of the crystal but what about the nearest neighbors? They are the main contributors to $k=4$ and $k=6$ parameters because of the rapidly decreasing $1/R^{k+1}$ factor but the electronic distribution overlaps the 4f electrons so that charge penetration cannot be neglected. The exact Coulombic interaction between the extended charge distributions of a rare-earth 4f electron and its ligands closed electronic shells was calculated and compared to the point-charge effect by Garcia and Faucher (1984). The main conclusions are that the ratio between extended-charge parameters and point- charge parameters ranges, depending on the rare-earth–ligand distance, from 0.9 to 1.0 for B^2,

0.5 to 1.0 for B^4 and −0.15 to 0.70 for B^6. This shows clearly that the PCEM results are even worsened if we make an "exact" electrostatic calculation. A conclusion is that the point-charge electrostatic model is adequate to represent the electrostatic effects of the crystal on the rare-earth ion except for the nearest-neighbor interactions.

4.4. *The covalent models*

The key to most covalent models is the Linear Combination of Atomic Orbitals treatment or LCAO. Its principles, as carefully detailed by Roothaan (1951) are closely connected to Hartree–Fock calculations described by Slater (1960) and Cowan (1981). Let us recall the basic formulae and hypothesis:

- the LCAO treatment applies to a cluster formed, for instance by a central ion and its closest ligands;
- each electron of the system is described by a wavefunction ψ_i built as a linear combination of all the atomic orbitals φ_λ of the cluster, i.e., $\psi_i = \sum_\lambda \varphi_\lambda e_{\lambda i}$, where $e_{\lambda i}$ are numerical coefficients, $\psi_i = \varphi e_i$ in matrix notation,
- the complete Hamiltonian is written as $F = \sum_\mu h_\mu + \sum_{\mu,\nu} g_{\mu\nu}$, where h is a one-electron Hamiltonian (kinetic energy plus electrostatic nuclei interactions ...) and g is a two-electron Hamiltonian (Coulombic repulsion).
- the e_i are obtained by solving

$$e_i(H + 2\sum_j (J_j - K_j) - \varepsilon_i S) = 0, \tag{42}$$

with ε_i the eigenvalues of the system, $H_{\lambda\mu} = \langle \varphi_\lambda | h | \varphi_\mu \rangle$ and $J_{ij} = \langle \varphi_i \varphi_j | g | \varphi_i \varphi_j \rangle$ are the Coulombic integrals, $K_{ij} = \langle \varphi_i \varphi_j | g | \varphi_j \varphi_i \rangle$ the exchange integrals, and $S_{\lambda\mu} = \langle \varphi_\lambda | \varphi_\mu \rangle$ the overlap integrals.

In fact, the part h of the Hamiltonian contains more than the kinetic energy plus the electrostatic potential of the nuclei: in this case, it includes the electrostatic crystal field created by the rest of the crystal, the cluster under study excepted. Depending on the evaluation of the J_{ij} and K_{ij} integrals, i.e., depending on whether they are effectively calculated or neglected, one may include corrective terms in the one-electron Hamiltonian h.

The result of eq. (42) is a set of eigenvectors e_i and eigenvalues ε_i. Some of the eigenvectors are mainly (more than 80%) rare-earth functions and permit one to obtain the *cfp* that would produce the same splitting for this function set. The choice of the set of starting wavefunctions φ_i is rather important. Usually, one takes the 4f functions, and the *n*s and *n*p functions for each ligand. But we can also integrate the 5d wavefunction of the rare-earth ion as well as its 5s and 5p ones.

A considerable contribution to ab initio calculations is due to Newman and coworkers. More than twenty years ago, they evaluated the contribution of a variety of mechanisms to the one-ligand one-particle crystal field, namely overlap and exchange effects (Ellis and Newman 1967), exchange charge effects (Bishton et al. 1967), charge penetration (Ellis and Newman 1968), and ligand–ligand overlap effects (Curtis and Newman 1969).

The work of this period has been gathered and discussed in a lengthy paper by Newman (1971). The calculations are made by means of perturbative processes and attention is paid to the renormalization of the wavefunctions (Bishton and Newman 1968). The latter set is restricted to the 4f of the central ion, and the *n*s and *n*p functions of the ligand.

A Russian team of scientists has been working on a parallel track for years, preferring the evaluation of ab initio effects to model calculations. Their initial interest was in d elements. Their techniques are described in the papers by Eremin and Kornienko (1972, 1975, 1977), Levin and Cherepanov (1979) and Eremin (1981). The contributions of two-particle operators are calculated with the help of the second quantization method.

Gajek et al. (1987) published ab initio evaluations of the crystal field in the actinide compounds: $CsUF_6$, Cs_2UCl_6 and U^{4+}:UCl_4. The various contributions could be directly compared with the results of Newman (1971) for Pr^{3+}:$LaCl_3$. A large discrepancy beween experimental and calculated values was stated for U^{4+}:UCl_4.

Some years ago, Ng and Newman (1985, 1987a,b), calculated all the contributions up to second order in perturbation theory to the crystal-field and Slater parameters. A complete list of perturbations are described in clearly organized tables. The perturbation basis contains the ligand outer orbitals and 49 metal states. The electronic excitations which are considered are the following:

(1) electrostatic and overlap contributions;
(2) ligand to valence shell (includes the classical covalency);
(3) metal core to valence shell (includes shielding);
(4) ligand to metal excited states (ligand polarization);
(5) metal core to excited states;
(6) valence to excited states.

The method was applied to the system Pr^{3+}:$LaCl_3$. The authors identified new contributions to rank-6 crystal field one-electron *cfp* originating from the correlated mechanisms $B_0^k(k_1, k_2)$. They stated that neither covalency nor ligand polarization could significantly contribute to the reduction of Slater parameters in crystals and identified probable influential excitations namely $4f \rightarrow nf$. The quality of the final match between experimental and calculated intrinsic parameters is moderate: 180/607, 38.8/30.3 and 15.8/9.12 cm^{-1} for A^2, A^4 and A^6, respectively, in Pr^{3+}:$LaCl_3$. The paper is rather a theoretical reference to be consulted as to which process contributes most to the *cfp* and which one is therefore worth calculating.

Garcia and Faucher (1984, 1985) applied the cruder *covalo-electrostatic* model which contains kinetic-energy and electrostatic contributions. The interaction matrix includes all the ligands' valence shells so that renormalization is automatically accounted for. This limited LCAO model has been applied to a series of twelve rare-earth or rare-earth-doped compounds. Exchange and Coulombic integrals are replaced by electrostatic interaction. The calculation of extended charge contributions is detailed in Garcia and Faucher (1984). The integrals were calculated using Hartree–Fock radial wavefunctions. The parameters of the method are the one-electron ionization energies of the lanthanide and ligands.

In spite of these drastic simplifications, the results are not too bad. Average reliability and scale factors as defined in sect. 4.3 are reported in table 7 and compared with

Table 7
Mean values over ten compounds of the reliability and scale factors obtained by the electrostatic model, the covalo–electrostatic model, and the covalo–electrostatic model with contribution of next-nearest neighbours

	Reliability factors			Scale factors		
	$R^{(2)}$	$R^{(4)}$	$R^{(6)}$	$S^{(2)}$	$S^{(4)}$	$S^{(6)}$
EM (PC + dipoles)	38	6	22	0.61	1.27	3.31
Covalo–Electr.	54	12	16	1.57	1.01	1.05
NNB-Covalo–Electr.	29	8	13	0.94	1.39	0.96
					1.07[a]	

[a] If Nd^{3+}:$Ca_{0.8}Mg_{0.2}Al_{11}O_{19}$ is excluded.

the results obtained by the electrostatic model. The *cfp* are in the ratio imposed by the superposition model so that the reliability factors are not much changed. The small increase of $R^{(4)}$ ($6 \rightarrow 12$%) and the slight decrease of $R^{(6)}$ ($22 \rightarrow 16$%) are not significant. On the other hand, the scale factors are significantly improved (closer to 1) even if some extreme values are stated ($S^{(6)} = 2$ for $NdAlO_3$).

An effort to improve the model consists in including the effects of the next-nearest neighbours of the rare earth (Faucher et al. 1991, 1992). The following interaction scheme is proposed: lanthanide $\leftrightarrow$ ligands $\leftrightarrow$ next-nearest neighbours. The principle is the same as above but the interaction sphere stretches out to a larger distance from the central ion. The corresponding reliability and scale factors are also reported in table 7 for a comparison with former values. Assumptions are made concerning the ionization energy of the interacting species and their apparent dependency on the rare-earth–ligand distance. The process improves the sixth-order parameters. The resulting scale factors are close to unity and $R^{(6)}$ is lowered. Even if "blind-eyed" calculations still lack accuracy, the next-nearest-neighbour track is certainly a good one to follow in order to deliver more precise estimations. Recently, Shen and Holzapfel (1994) examined the distance dependence of the intrinsic parameters for Pr^{3+}:$LnCl_3$ under high pressure; the values they found for the experimental power laws are twice smaller than calculated earlier ($t_4 = 6.0$, $t_6 = 6.9$). They state that the agreement with theoretical values calculated by Newman's model is improved if the Madelung potential is scaled by the metal–ligand distance.

Mironov and Rosov (1992a,b) recently worked out a many-electron, semi-empirical crystal field calculation for the f^n shells, where the valence subsystem of the f-cluster is treated by a MO-LCAO method while the f^n free-ion interactions are described by empirical parameters.

4.5. *The configuration interaction model (CIM)*

We have already met the configuration interaction with its effects on the crystal-field parameters (see sect. 3.2).

Now, we are dealing with configuration interaction as a tool to simulate, to calculate rare-earth spectra, the crystal field parameters no longer being useful.

This step is the one logically following the LCAO we have just described. The point is that the LCAO step gives a basis of orthonormal one-electron wavefunctions $\{\psi_i\}$. We can dispatch the system electrons in many ways on this basis. Each different electron configuration is a state represented by a Slater determinant built on the $\{\psi_i\}$ basis. Among these configurations, some are corresponding to $4f^N$ (N electrons on functions which are mainly 4f), others to $4f^{N+1}np^5$ where np is the outer shell of the ligands. The two kinds of configurations may interact freely through a Coulombic repulsion operator.

The program ATOME (already mentioned in sect. 3.2) has been used for this purpose since it is able to manipulate determinantal states defined on an orthonormal basis; one just needs to give it the way to calculate (the notations are evident) the matrix elements:

one electron $\langle\psi_i|h|\psi_j\rangle$

two electrons $\langle\psi_i\psi_j|g|\psi_k\psi_l\rangle$

three electrons $\langle\psi_i\psi_j\psi_k|t|\psi_l\psi_m\psi_n\rangle$

Then we have $F = \sum_\lambda h_\lambda + \sum_{\lambda\mu} g_{\lambda\mu} + \sum_{\lambda\mu\nu} t_{\lambda\mu\nu}$, where F is the total Hamiltonian of the system which is divided into three parts: one-electron h, two-electron g and three-electron t. ATOME currently handles up to three-electron operators.

Faucher and Garcia (1990) studied the system constituted by a trivalent neodymium ion and a single oxygen ligand with charge $-2e$. The $4f^32p^6$ vs $4f^42p^5$ interaction calculation involves a total of 6370 levels. The results of the calculation is a series of energies: the 364 lowest energies correspond to $4f^3$ and may be considered as an experimental spectrum for which it is possible to fit crystal-field parameters: the corresponding deviation is mediocre ($19\,cm^{-1}$) compared to standard values ($14\,cm^{-1}$ and $11\,cm^{-1}$ for Nd_2O_3 and $NdAlO_3$). This implies that this configuration-interaction process is responsible for two-electron correlation effects that cannot be fitted by standard crystal-field theory (sect. 3.1). It is noteworthy that all the fitted parameters, i.e. the Slater integrals, spin–orbit coupling constant, Trees' and Judd's parameters, are modified by the interaction of the lanthanide with the oxygen ligand via configuration mixing.

The configuration-interaction model simulated by ATOME was utilized by Parent et al. (1994) to prove the reality of copper pairs in $CuZr_2(PO_4)_3$: they carried out a calculation on the Cu^+–Cu^+ system and reproduced in a quite satisfactory way all the data of the luminescence spectra, i.e. band positions and transition intensities.

It seems that this "extended" configuration method is a possible way to interpret, with the only help of the Coulombic repulsion between rare-earth and ligand electrons:

- a level splitting,
- a change in free ion parameters.

Even if the actual simulations are still qualitative, this trail undoubtedly promises new developments in the interpretation of crystal-field splitting.

5. Actinides

We mentioned actinides several times since the methods developed for the $4f^n$ can be directly applied to $5f^n$ compounds. Conversely, the usually bad performance of crystal-

field studies on actinides have triggered theoretical studies finally profitable to lanthanides. Optical data on $5f^n$ actinide elements are much sparser than for $4f^n$ lanthanides. Unlike lanthanides, the triply ionized state is not the most frequently encountered: for instance, optical transitions for degrees of oxidation from +3 to +7 have been observed for plutonium. A survey of optical properties of tetravalent actinides has been given by Edelstein (1987).

Carnall (1986) reminds that the increasing of atomic numbers enhances the localisation of inner f orbitals, provoking a change from delocalized to localized behaviour, which means that heavier actinides behave more like lanthanides than lighter ones.

Yet it is the systematic spectral analysis of the trivalent series of actinides in $LaCl_3$, which, in the eighties, provided the solid anchoring for studies in the area. Crosswhite et al.(1980) and Carnall et al. (1980) were successful in determining a complete set of free ion and crystal field parameters for U^{3+}, Np^{3+} and Pu^{3+}. A recent review by Carnall (1992) sums up and completes the results on the trivalent series up to Cf^{3+}. The values (in cm^{-1}) of the crystal field parameters for U^{3+} and Nd^{3+} ($5f^3$ and $4f^3$ respectively), in $LaCl_3$, are:

Ion	B_0^2	B_0^4	B_0^6	B_6^6
U^{3+}	287	−662	−1340	1070
Nd^{3+}	163	−336	−713	462

The crystal-field parameters for uranium are almost exactly twice the values for the rare earth. The mean error of the fit is 29 cm^{-1} for 82 levels (against 8 cm^{-1} for 101 levels for Nd^{3+}). This was in fact a real success which is not always met in the analysis of actinide spectra. As stressed by Crosswhite et al. (1980), many obstacles hamper the analysis: firstly the spin–orbit coupling parameter is twice that of neodymium (1623/880 cm^{-1}) while the electrostatic interactions are about two times smaller (39715/33537/23670 cm^{-1} respectively for $F^2/F^4/F^6$ in U^{3+} against 72780/54450/38123 in Nd^{3+}. The levels are more mixed up making the assignment more difficult. Besides, absorption is high above 20 000 cm^{-1}, where the levels of the first excited configuration $5f^{n-1}6d$ appear (Edelstein et al. 1991), and the coupling with the lattice is strong, producing numerous vibronic sidebands. Hubert et al. (1993) and Thouvenot et al. (1994) have performed a comparative analysis of Am^{3+}, Eu^{3+} and Cm^{3+} in cubic ThO_2.

The success met with trivalent ions prompted the extension of studies towards tetravalent actinides. As pointed out by Carnall et al. (1991), most spectroscopic analysis studies were performed until now on U^{4+} since the stability of tetravalent actinide compounds decreases along the series. Unlike the trivalent case, both the free-ion and the crystal-field interactions are strong in the tetravalent case, which brings further difficulties in the interpretation of the spectra. The work of Soulié (1977) gives information on the crystal field of some pentavalent uranium compounds, namely UF_6Cs, UCl_6Cs and UF_6NO. We find, in the middle eighties, contributions from Krupa et al. (1983) on Pa^{4+} ($5f^1$) in the low-symmetry site compounds $ThBr_4$ and UCl_4, from Delamoye et

Table 8
Crystal field in uranium or uranium doped compounds[a]

Ion	Compound	N'_v	n	σ
U^{3+}	$LaCl_3$	602	82	29
U^{4+}	UF_4	2200	69	31
	UCl_4	1602	60	26
	$ThCl_4$	1560	46	25
	α-$ThBr_4$	1564	30	77
	β-$ThBr_4$	1543	36	26
	$ThSiO_4$	1617	71	25
	Cs_2UCl_6	3360		
U^{5+}	UF_6Cs	10074		
	UF_8Cs_3	8854		

[a] Symbols: N'_v, strength of the field calculated as by Carnall et al. (1991); n, number of assigned lines; σ, mean deviation if available.

al. (1983a,b) on U^{4+} ($5f^2$) in $ThBr_4$. In the latter case, 38 levels are assigned and the deviation of the parametric adjustment is equal to $39\,cm^{-1}$. Khan Malek et al. (1986) gave a comparative study of U^{4+} in $ThCl_4$, UCl_4 and $ThSiO_4$, all three of which have the same crystal structure while Simoni et al. (1988) examined the properties of the host α-$ThBr_4$. The $5f^3$ configuration of Np^{4+} was analysed by Lahalle et al. (1986) in $ThSiO_4$ and ThO_2. Rajnak et al. (1984) investigated $Np(BD_4)_4$. More recently Carnall et al. (1991) analysed the UF_4, NpF_4, and PuF_4 spectra with the complication due to a multiple-site symmetry for the actinide ion. The study was later extended to heavier actinides: Am^{4+}, Cm^{4+} and Bk^{4+} (Liu et al. 1994). Table 8 gives for U^{n+} ($n=3,4,5$), which is the most investigated actinide, and for various compounds, the overall crystal field strength N'_v, the number of observed absorption lines and the experimental/calculated deviation. The strength of the crystal field is magnified approximately by four at each step of oxidation. A recent correlated crystal field analysis on Np^{3+}:$LaCl_3$ lowered the standard deviation between calculated and experimental levels from 19.7 to $6.6\,cm^{-1}$ (Reid and Li 1991).

6. Conclusion

Many theoretical applications have been done on praseodymium in $LaCl_3$; the reason is obvious: the Pr^{3+} configuration is the first non-trivial one of the rare-earth series and yet of moderate dimensions. As for $LaCl_3$, it is a model compound belonging to the historical series from which Dieke deduced the famous charts of rare-earth energy levels. The extension of high-resolution investigations towards higher energies is facilitated by modern spectroscopic tools. Besides, the calculation of parametric rare-earth configurations is now fast and commonplace. Therefore interest is transferring towards heavier rare earths, in particular Nd^{3+} in which more than 75% of the configuration

can be experimentally observed, for instance 148 out of 182 Stark levels in Nd^{3+}:YAG (Burdick et al. 1994).

Not all crystal-field studies are performed on insulating crystals, and we should at least evoke crystal-field studies on dark, conducting or superconducting materials which have been developing these last years supported by neutron inelastic scattering experiments (Goodman et al. 1991, Soderholm et al. 1991, Mesot et al. 1991).

In our account of the crystal field, we have tried to separate clearly the predictive and the deductive (parametric) methods, however our goal is imperfectly attained. The same occurs in real life, and for two reasons: firstly because user-ready predictive methods often fail and then experimenters find some comfort in fitting parameters, and secondly the theoreticians adore looking for "effective" operators, thus encouraging the process.

There are two approaches to the study of electronic structures, formally and traditionally distinct but equivalent in essence: the molecular-orbital calculations in which one performs a global energy minimization, and the conventional perturbative crystal-field theory which deals with the details of rare-earth spectra. Some attempts have been done to merge the two approaches (Goodman 1992, Gerard 1993).

A lot of work is still ahead. Besides complete ab initio models, and simplified semi-empirical models, we shall assist in the development of a new class of calculations: complete spectrum calculation avoiding the intermediate crystal-field parameters. We are still far from dealing with all the configuration interactions necessary to simulate a complete crystal field (including next-nearest neighbours in a large cluster) but with the accelerating development of modern computers, the project might not stay unrealistic.

It is clear that the knowledge of the rare-earth level energies is incomplete if it is not accompanied by the corresponding intensities. The transition probabilities are mainly accounted for by dynamic ligand polarization effects (Jørgensen and Judd 1964, Mason et al. 1974, Malta and de Sá 1980) and a configuration-interaction perturbation treatment (Judd 1962, Ofelt 1962) progressively improved by the consideration of third-order effects (Burdick et al. 1993). Garcia and Faucher (1989) show that the exact $4f^2/4f5d$ mixing permits one to reproduce only partially the oscillator strength of the trivalent praseodymium transition in $PrCl_3$.

Do we have to look towards rare earth/ligand mixing to find the missing intensities? We do not know yet. But it seems evident that the key of the problem is a global approach since the splitting effects represented by the B_q^k crystal-field parameters and the intensity effects are closely connected.

We cannot end this chapter without mentioning the developing quark model of the f shell (Judd and Lister (1993) which is presently in a stage of group-theoretical analysis and has certainly not yet disclosed all its possibilities.

References

Alablanche, S., A. Kahn-Harari, J. Thery, B. Viana, D. Vivien, J. Dexpert-Ghys and M. Faucher, 1992, J. Solid State Chem. **98**, 105.

Antic-Fidancev, E., M. Lemaitre-Blaise, L. Beaury, G. Teste de Sagey and P. Caro, 1980, J. Chem. Phys. **73**, 4613.

Antic-Fidancev, E., M. Lemaitre-Blaise and P. Caro, 1982, J. Chem. Phys. **76**, 2906.

Antic-Fidancev, E., M. Lemaitre-Blaise, P. Porcher and J.C. Krupa, 1991a, Eur. J. Solid State Inorg. Chem. **28**, 77.

Antic-Fidancev, E., J. Hölsä, M. Lemaitre-Blaise and P. Porcher, 1991b, J. Phys.: Condens. Matter **3**, 6829.

Antic-Fidancev, E., J. Aride, J.P. Chaminade, M. Lemaitre-Blaise and P. Porcher, 1992a, J. Solid State Chem. **97**, 74.

Antic-Fidancev, E., J. Hölsä, J.C. Krupa, M. Lemaitre-Blaise and P. Porcher, 1992b, J. Phys.: Condens. Matter **4**, 8321.

Aride, J., 1981, Ph.D. Thesis (Bordeaux).

Auzel, F., 1979, Mater. Res. Bull. **14**, 223.

Barnes, R.G., R.L. Mössbauer, E. Kankeleit and J.M. Poindexter, 1964, Phys. Rev. **136**, A175.

Beaury, L., and P. Caro, 1990, J. Phys. France **51**, 471.

Bethe, H., 1929, Ann. Phys. **3**, 133.

Bijvank, E.J., and H.W. den Hartog, 1980, Phys. Rev. B **22**, 4121.

Bishton, S.S., and D.J. Newman, 1968, J. Chem. Phys. Lett. **1**, 616.

Bishton, S.S., M.M. Ellis, D.J. Newman and J. Smith, 1967, J. Chem. Phys. **47**, 4133.

Bradbury, M.I., and D.J. Newman, 1967, Chem. Phys. Lett. **1**, 44.

Burdick, G.W., H.J. Kooy and M.F. Reid, 1993, J. Phys.: Condens. Matter **5**, L323.

Burdick, G.W., C.K. Jayasankar, F.S. Richardson and M.F. Reid, 1994, Phys. Rev. B **50**, 16309.

Burns, G., 1962, Phys. Rev. **128**, 2121.

Carnall, W.T., 1986, J. Less-Common Met. **122**, 1.

Carnall, W.T., 1992, J. Chem. Phys. **96**, 8713.

Carnall, W.T., H. Crosswhite, H.M. Crosswhite, J.P. Hessler, N. Edelstein, J.G. Conway, G.V. Shalimoff and R. Sarup, 1980, J. Chem. Phys. **72**, 5089.

Carnall, W.T., G.L. Goodman, K. Rajnak and R.S. Rana, 1988a, A systematic analysis of the spectra of the lanthanides doped into single crystal LaF_3, Report ANL-88-8 (Argonne National Laboratory, 9700 South Cass Av., Argonne, IL 60439).

Carnall, W.T., G.L. Goodman, K. Rajnak and R.S. Rana, 1988b, J. Chem. Phys. **90**, 3443.

Carnall, W.T., G.K. Liu, C.W. Williams and M.F. Reid, 1991, J. Chem. Phys. **95**, 7194.

Caro, P., D.R. Svoronos, E. Antic and M. Quarton, 1977, J. Chem. Phys. **66**, 5284.

Caro, P., J. Derouet, L. Beaury and E. Soulié, 1979, J. Chem. Phys. **70**, 2542.

Caro, P., J. Derouet, L. Beaury, G. Teste de Sagey, J.P. Chaminade, J. Aride and M. Pouchard, 1981, J. Chem. Phys. **74**, 2698.

Cascales, C., E. Antic-Fidancev, M. Lemaitre-Blaise and P. Porcher, 1992, J. Phys.: Condens. Matter **4**, 2721.

Chang, N.C., J.B. Gruber, R.P. Leavitt and C.A. Morrison, 1982, J. Chem. Phys. **76**, 3877.

Chateau, C., J. Hölsä and P. Porcher, 1989, Z. Phys. Chem. NF **166**, 211.

Chateau, C., J. Hölsä and P. Porcher, 1990, J. Chem. Soc., Dalton Trans., p. 1575.

Cowan, R.D., 1981, The Theory of Atomic Structure and Spectra (University of California, Berkeley, CA).

Crosswhite, H., and D.J. Newman, 1984, Phys. Status Solidi b **126**, 381.

Crosswhite, H.M., H. Crosswhite, F.W. Kaseta and R. Sarup, 1976, J. Chem. Phys. **61**, 1981.

Crosswhite, H.M., H. Crosswhite, W.T. Carnall and A.P. Paszek, 1980, J. Chem. Phys. **72**, 5103.

Curtis, M.M., and D.J. Newman, 1969, J. Chem. Phys. **52**, 1340.

Da Gama, A.A., G.F. de Sá, P. Porcher and P. Caro, 1981, J. Chem. Phys. **75**, 2583.

Delamoye, P., J.C. Krupa, J.G. Conway and N. Edelstein, 1983a, Phys. Rev. B **28**, 4913.

Delamoye, P., K. Rajnak, M. Genet and N. Edelstein, 1983b, Phys. Rev. B **28**, 4923.

Edelstein, N., 1987, J. Less-Common Met. **133**, 39.

Edelstein, N., W.K. Kot and J.C. Krupa, 1991, J. Chem. Phys. **96**, 1.

Ellis, M.M., and D.J. Newman, 1967, J. Chem. Phys. **47**, 1986.

Ellis, M.M., and D.J. Newman, 1968, J. Chem. Phys. **49**, 4037.

Eremin, M.V., 1981, Opt. Spektrosk. **51**, 136.

Eremin, M.V., and A.A. Kornienko, 1972, Sov. Phys. Solid State **14**, 644.

Eremin, M.V., and A.A. Kornienko, 1975, Sov. Phys. Solid State **17**, 206.

Eremin, M.V., and A.A. Kornienko, 1977, Phys. Status Solidi b **79**, 775.

Faucher, M., and D. Garcia, 1982, Phys. Rev. B **26**, 5451.

Faucher, M., and D. Garcia, 1988, C.R. Acad. Sci. Paris **II-307**, 2015.

Faucher, M., and D. Garcia, 1990, J. Lumin. **46**, 375.

Faucher, M., J. Dexpert-Ghys and P. Caro, 1980, Phys. Rev. B **21**, 3689.

Faucher, M., J. Pannetier, Y. Charreire and P. Caro, 1982, Acta Crystallogr. B **38**, 344.

Faucher, M., D. Garcia and C.K. Jørgensen, 1986, Chem. Phys. Lett. **129**, 387.

Faucher, M., D. Garcia, P. Caro, J. Derouet and P. Porcher, 1989a, J. Phys. France **50**, 219.

Faucher, M., D. Garcia and P. Porcher, 1989b, C.R. Acad. Sci. Paris **II-308**, 603.

Faucher, M., D. Garcia, E. Antic-Fidancev and M. Lemaitre-Blaise, 1989c, J. Phys. & Chem. Solids **50**, 1227.

Faucher, M., D. Garcia and O.K. Moune, 1991, J. Lumin. **51**, 341.

Faucher, M., D. Garcia and O.K. Moune, 1992, J. Alloys & Compounds **180**, 243.

Faucher, M., O.K. Moune and D. Garcia, 1993, J. Phys. II (France) **3**, 961.

Gajek, Z., and J. Mulak, 1992, J. Phys.: Condens. Matter **4**, 427.

Gajek, Z., J. Mulak and M. Faucher, 1987, J. Phys. & Chem. Solids **48**, 947.

Gajek, Z., J. Mulak and J.C. Krupa, 1993, J. Solid State Chem. **107**, 413.

Garcia, D., 1988, Program ATOME, unpublished.

Garcia, D., and M. Faucher, 1984, Phys. Rev. B **30**, 1703.

Garcia, D., and M. Faucher, 1985, J. Chem. Phys. **82**, 5554.

Garcia, D., and M. Faucher, 1986, C.R. Acad. Sci. Paris **II-303**, 333.

Garcia, D., and M. Faucher, 1989, J. Chem. Phys. **91**, 7461.

Garcia, D., and M. Faucher, 1992, J. Alloys & Compounds **180**, 239.

Gerard, I., 1993, Thesis, IPNO-T-93.02 (Orsay) unpublished.

Gerloch, M., and R.G. Woolley, 1984, Prog. Inorg. Chem. **31**, 371.

Goodman, G.L., 1992, J. Alloys & Compounds **181**, 33.

Goodman, G.L., C.K. Loong and L. Soderholm, 1991, J. Phys.: Condens. Matter **3**, 49.

Görller-Walrand, C., I. Hendrickx, L. Fluyt, M.P. Gos, J. d'Olieslager and G. Blasse, 1992, J. Chem. Phys. **96**, 5650.

Görller-Walrand, C., E. Huygen, K. Binnemans and L. Fluyt, 1994, J. Phys.: Condens. Matter **6**, 7797.

Griffith, J.S., 1964, Phys. Rev. Lett., p. 576.

Gruber, J.B., R.P. Leavitt and C. Morrison, 1983, J. Chem. Phys. **79**, 1664.

Gruber, J.B., M.E. Hills, T.H. Allik, C.K. Jayasankar, J.R. Quagliano and F.S. Richardson, 1990, Phys. Rev. **41**, 7999.

Guo, M.D., A.T. Aldred and S.K. Chan, 1987, J. Phys. & Chem. Solids **48**, 229.

Gupta, R.P., and S.K. Sen, 1973, Phys. Rev. **A7**, 850.

Hölsä, J., and P. Porcher, 1981, J. Chem. Phys. **75**, 2108.

Huang, J., J. Loriers, P. Porcher, G. Teste de Sagey, P. Caro and C. Levy-Clément, 1984, J. Chem. Phys. **80**, 6204.

Hubert, S., P. Thouvenot and N. Edelstein, 1993, Phys. Rev. B **48**, 5751.

Hutchings, M.T., and D.K. Ray, 1963, Proc. Phys. Soc. London **81**, 663.

Jayasankar, C.K., and F.S. Richardson, 1989, Phys. Status Solidi b **155**, 221.

Jayasankar, C.K., M.F. Reid and F.S. Richardson, 1989, Phys. Status Solidi b **155**, 559.

Jørgensen, C.K., 1965, J. Phys. **26**, 285.

Jørgensen, C.K., and B.R. Judd, 1964, Mol. Phys. **8**, 281.

Jørgensen, C.K., R. Pappalardo and H.H. Schmidtke, 1963, J. Chem. Phys. **39**, 1422.

Jørgensen, C.K., M. Faucher and D. Garcia, 1986, Chem. Phys. Lett. **128**, 250.

Judd, B.R., 1962, Phys. Rev. **127**, 750.

Judd, B.R., 1963, Operator Techniques in Atomic Spectroscopy (McGraw-Hill, New York).

Judd, B.R., 1966, Phys. Rev. **141**, 4.

Judd, B.R., 1977a, J. Chem. Phys. **66**, 3163.

Judd, B.R., 1977b, Phys. Rev. Lett. **39**, 242.

Judd, B.R., 1979, J. Lumin. **18/19**, 604.

Judd, B.R., and H. Crosswhite, 1984, J. Opt. Soc. Am. B **1**, 255.

Judd, B.R., and G.M. Lister, 1993, J. Alloys & Compounds **193**, 155.

Karayianis, N., and C.A. Morrison, 1975, Local distortion, Harry Diamond Laboratories Report HDL-TR 1682.

Karayianis, N., R.P. Leavitt, C.A. Morrison and D.E. Wortman, 1973, Scheelites, Harry Diamond Laboratories Report HDL-TR 1648.

Karayianis, N., D.E. Wortman and C.A. Morrison, 1976a, YVO_4, Harry Diamond Laboratories Report HDL-TR 1775.

Karayianis, N., C.A. Morrison and D.E. Wortman, 1976b, YPO_4, Harry Diamond Laboratories Report HDL-TR 1776.

Karayianis, N., D.E. Wortman and C.A. Morrison, 1976c, Solid State Commun. **18**, 1299.

Karayianis, N., D.E. Wortman and C.A. Morrison, 1977, $Y_3Ga_5O_12$, Harry Diamond Laboratories Report HDL-TR 1793.
Kassman, A.J., 1970, J. Chem. Phys. **53**, 4118.
Khan Malek, C., J.C. Krupa, P. Delamoye and M. Genet, 1986, J. Less-Common Met. **122**, 75.
Kibler, M., 1971, J. Chem. Phys. **55**, 1989.
Kibler, M., 1974, J. Chem. Phys. **9**, 3859.
Kibler, M., 1975, Int. J. Quantum Chem. **9**, 403.
Kibler, M., 1979, in: Recent Advances in Group Theory and their Application to Spectroscopy, ed. J.C. Donini (Plenum, New York) p. 1.
Kibler, M., 1983, Phys. Lett. A **98**, 343.
Kibler, M., and G. Grenet, 1985, Int. J. Quantum Chem. **28**, 213.
Kibler, M., and G. Grenet, 1986a, Int. J. Quantum Chem. **29**, 11.
Kibler, M., and G. Grenet, 1986b, Int. J. Quantum Chem. **29**, 485.
Kibler, M., and J. Katriel, 1990, Phys. Lett. A **147**, 417.
Kooy, H.J., 1994, Two-body operators and rare-earth spectroscopy, Ph.D. Thesis (University of Hong Kong).
Kooy, H.J., and M.F. Reid, 1993, J. Alloys & Compounds **193**, 197.
Krupa, J.C., S. Hubert and M. Foyentin, 1983, J. Chem. Phys. **78**, 2175.
Lahalle, M.P., J.C. Krupa and R. Guillaumont, 1986, J. Less-Common Met. **122**, 65.
Leavitt, R.P., 1982, J. Chem. Phys. **77**, 1661.
Leavitt, R.P., C.A. Morrison and D.E. Wortman, 1975, Three parameter theory of crystal fields, Harry Diamond Laboratories Report HDL-TR 1673.
Leavitt, R.P., J.B. Gruber, N.C. Chang and C.A. Morrison, 1982, J. Chem. Phys. **76**, 4775.
Levin, L.I., and V.I. Cherepanov, 1979, Sov. Phys. Solid State **21**, 1204.
Li, C.L., and M.F. Reid, 1990, Phys. Rev. B **42**, 1903.
Limburg, H.-J., J. Hölsä, P. Porcher, G. Herzog, D. Starick and H. Wulff, 1992, J. Solid State Chem. **98**, 404.
Linarès, C., and A. Louat, 1975, J. Phys. **36**, 49.
Linarès, C., A. Louat and M. Blanchard, 1977, Structure and Bonding **33**, 179.
Linarès, C., A. Louat and M. Blanchard, 1981, Chem. Phys. (Neth.) **68**, 453.
Liu, G.K., W.T. Carnall, G. Jursich and C.W. Williams, 1994, J. Chem. Phys. **101**, 8277.
Lupei, A., V. Lupei, S. Grecu, C. Tiseanu and G. Boulon, 1994, J. Appl. Phys. **75**, 4652.
Malta, O.L., 1979, Mol. Phys. **38**, 1347.
Malta, O.L., and G.F. de Sá, 1980, Chem. Phys. Lett. **74**, 101.
Mason, S.F., R.D. Peacock and B. Stewart, 1974, Chem. Phys. Lett. **29**, 149.
Mazurak, Z., and J.B. Gruber, 1992, J. Phys.: Condens. Matter **4**, 3453.
Mazurak, Z., A. Garcia and C. Fouassier, 1994, J. Phys.: Condens. Matter **6**, 2031.
Merkle, L.D., J.B. Gruber, M.D. Seltzer, S.B. Stevens and T.H. Allik, 1992, J. Appl. Phys. **72**, 4269.
Mesot, J., P. Allenspach, U. Staub, A. Furrer, R. Osborn, S. Bennington and A.D. Taylor, 1991, Physica C **185–189**, 2167.
Mironov, V.S., and S.P. Rosov, 1992a, Phys. Status Solidi b **169**, 463.
Mironov, V.S., and S.P. Rosov, 1992b, Phys. Status Solidi b **170**, 199.
Morosin, B., 1968, J. Chem. Phys. **49**, 3007.
Morrison, C.A., 1974, Phys. Lett. A **51**, 49.
Morrison, C.A., 1979, J. Chem. Phys. **72**, 1001.
Morrison, C.A., N. Karayianis and D.E. Wortman, 1976, $Y_2SiBe_2O_7$, Harry Diamond Laboratories Report HDL-TR 1766.
Morrison, C.A., N. Karayianis and D.E. Wortman, 1977a, Predicting spectra and intensities, Harry Diamond Laboratories Report HDL-TR 1816.
Morrison, C.A., N. Karayianis and D.E. Wortman, 1977b, $YAlO_3$, Harry Diamond Laboratories Report HDL-TR 1788.
Morrison, C.A., D.E. Wortman and N. Karayianis, 1977c, Pentaphosphates, Harry Diamond Laboratories Report HDL-TR 1779.
Morrison, C.A., R.P. Leavitt and D.E. Wortman, 1980, J. Chem. Phys. **73**, 2580.
Morrison, C.A., G.F. de Sá and R.P. Leavitt, 1981, J. Chem. Phys. **76**, 3899.
Moune, O.K., D. Garcia and M. Faucher, 1991, J. Phys. & Chem. Solids **52**, 513.
Newman, D.J., 1970, J. Chem. Phys. Lett. **6**, 288.
Newman, D.J., 1971, Adv. Phys. **20**, 197.
Newman, D.J., 1977, Aust. J. Phys. **30**, 315.
Newman, D.J., 1978, Aust. J. Phys. **31**, 79.
Newman, D.J., and B. Ng, 1988, J. Phys. C **21**, 3273.
Newman, D.J., and B. Ng, 1989, Rep. Prog. Phys. **52**, 699.
Newman, D.J., and G.E. Stedman, 1969, J. Chem. Phys. **51**, 3013.
Newman, D.J., and W. Urban, 1972, J. Phys. C **5**, 3101.

Ng, B., and D.J. Newman, 1985, J. Chem. Phys. **83**, 1758.
Ng, B., and D.J. Newman, 1987a, J. Chem. Phys. **87**, 7096.
Ng, B., and D.J. Newman, 1987b, J. Chem. Phys. **87**, 7110.
Ofelt, G.S., 1962, J. Chem. Phys. **37**, 511.
Parent, C., P. Boutinaud, G. le Flem, B. Moine, C. Pedrini, D. Garcia and M. Faucher, 1994, Opt. Mater. **4**, 107.
Pauling, L., 1960, The Nature of the Chemical Bond (Cornell University Press, Ithaca, NY).
Porcher, P., and P. Caro, 1976, J. Chem. Phys. **65**, 89.
Racah, G., 1942, Phys. Rev. **62**, 438.
Racah, G., 1943, Phys. Rev. **63**, 367.
Racah, G., 1949, Phys. Rev. **76**, 1352.
Rajnak, K., and B.G. Wybourne, 1963, Phys. Rev. **132**, 280.
Rajnak, K., and B.G. Wybourne, 1964, J. Chem. Phys. **41**, 565.
Rajnak, K., R.H. Banks, E. Gamp and N. Edelstein, 1984, J. Chem. Phys. **80**, 5951.
Reid, M.F., 1987, J. Chem. Phys. **87**, 2875.
Reid, M.F., and C.L. Li, 1991, Eur. J. Solid State Inorg. Chem. **28**, 171.
Reid, M.F., and F.S. Richardson, 1985, J. Chem. Phys. **83**, 3831.
Reisfeld, R., and C.K. Jørgensen, 1977, Lasers and Excited States of Rare Earths (Springer, Berlin).
Roothaan, C.C.J., 1951, Rev. Mod. Phys. **23**, 69.
Rudowicz, C., 1986, J. Chem. Phys. **84**, 5045.
Rudowicz, C., and R. Bramley, 1985, J. Chem. Phys. **83**, 5192.
Schäffer, C.E., and C.K. Jørgensen, 1965, Mol. Phys. **9**, 401.
Sengupta, D., and J.D. Artman, 1970, Phys. Rev. B **1**, 2986.
Shen, Y.R., and W.B. Holzapfel, 1994, J. Phys.: Condens. Matter **6**, 2367.
Shulman, R.G., and S. Sugano, 1963, Phys. Rev. **130**, 506.
Simoni, E., S. Hubert and M. Genet, 1988, J. Phys. (France) **49**, 1425.
Slater, J.C., 1960, Quantum Theory of Atomic Structure, Vol. 11 (McGraw-Hill, New York).
Soderholm, L., C.K. Loong, G.L. Goodman and B.D. Dabrowski, 1991, Phys. Rev. B **43**, 7923.
Soulié, E., 1977, Thesis, Report CEA-R-4849, unpublished.
Stedman, G.E., and D.J. Newman, 1971, J. Phys. & Chem. Solids **32**, 109.
Sternheimer, R.M., 1966, Phys. Rev. **146**, 140.
Sternheimer, R.M., M. Blume and R.F. Peierls, 1968, Phys. Rev. **173**, 376.
Taibi, M., J. Aride, E. Antic-Fidancev, M. Lemaitre-Blaise and P. Porcher, 1994, Phys. Status Solidi a **144**, 453.
Thouvenot, P., S. Hubert and N. Edelstein, 1994, Phys. Rev. B **50**, 9715.
Trees, R.E., 1951, Phys. Rev. **83**, 756; **84**, 1089.
Urland, W., 1977, Chem. Phys. Lett. **50**, 445.
Urland, W., 1978, Chem. Phys. Lett. **53**, 296.
Urland, W., 1979, Chem. Phys. Lett. **62**, 525.
Urland, W., 1981, Chem. Phys. Lett. **83**, 116.
Van Siclen, C. De W., 1982, J. Phys. C **15**, 4117.
Weenk, J.W., and H.A. Harwig, 1977, J. Phys. & Chem. Solids **38**, 1047.
Wortman, D.E., N. Karayianis and C.A. Morrison, 1976a, $LiYF_4$, Harry Diamond Laboratories Report HDL-TR 1770.
Wortman, D.E., N. Karayianis and C.A. Morrison, 1976b, $YAsO_4$, Harry Diamond Laboratories Report HDL-TR 1772.
Wortman, D.E., C.A. Morrison and N. Karayianis, 1976c, $Y_3Al_5O_12$, Harry Diamond Laboratories Report HDL-TR 1773.
Wortman, D.E., C.A. Morrison and N. Karayianis, 1977, $CaWO_4$, Harry Diamond Laboratories Report HDL-TR 1794.
Wybourne, B.G., 1965, Spectroscopic Properties of Rare Earths (Wiley, New York).
Yeung, Y.Y., 1992, J. Phys.: Condens. Matter **4**, 9741.
Yeung, Y.Y., and D.J. Newman, 1985, J. Chem. Phys. **84**, 4470.
Yeung, Y.Y., and D.J. Newman, 1986, J. Phys. C **19**, 3877.
Yeung, Y.Y., and D.J. Newman, 1987, J. Chem. Phys. **86**, 6717.

Handbook on the Physics and Chemistry of Rare Earths
Vol. 21
edited by K.A. Gschneidner, Jr. and L. Eyring

Chapter 145

SOLVATION AND ANION INTERACTION IN ORGANIC SOLVENTS

Jean-Claude G. BÜNZLI and Anita MILICIC-TANG
Université de Lausanne, Institut de chimie minérale et analytique, BCH 1402 1015 Lausanne, Switzerland

Contents

List of symbols and abbreviations

AN	acetonitrile	$\bar{n}$	average number of coordinated ligands
ARDF	atomic radial distribution function		
B_k^q	crystal-field parameter	NMR	nuclear magnetic resonance
t-ButOH	*tert*-butanol	Ns	first solvation number
CN	coordination number	PC	propylene carbonate
DMA	N, N-dimethylacetamide	*n*-PrOH	*n*-propanol
DMF	N, N-dimethylformamide	q	concentration ratio T_L/T_R
DMSO	dimethylsulfoxide	R	rare earth
EPR	electron paramagnetic resonance	R_L	$[L]_t/[R(III)]_t$
Et_4NClO_4	tetraethylammoniumperchlorate	S	total solvation number (1st + 2nd sphere)
EtOH	ethanol		
EXAFS	extended X-ray absorption fine structure	ΔS	entropy change
		T	total concentration
FT-IR	Fourier transform infrared	T_λ	Judd–Ofelt intensity parameter
ΔG	Gibbs energy change	TBP	tributyl phosphate
$g(r)$	radial distribution function	triflate	trifluoromethanesulfonate
ΔH	enthalpy change	Z	atomic number
I	ionic strength	α_j	partial mole fraction
K_n	stepwise stability constant	β	nephelauxetic parameter
L	ligand	β_n	overall or cumulative stability constant
MeOH	methanol		

1. Scope of the review

The trivalent 4f-block elements, plus Y(III), Sc(III) and La(III), form an extended series of cations with the same formal charge and with similar chemical properties, mostly due to very weak ligand-field effects. The $4f^n5s^25p^6$ electronic configuration ensures that the bonding and stereochemistry of R(III) complexes and solvates are largely determined both by the predominantly ion–dipole bonding interaction between the cation and the ligands, and by the steric repulsion between the coordinated ligands. As a result, in the solid state, coordination numbers ranging from 3 to 14 have been reported (Jørgensen 1979). Early indications that the preferred hydration number of R(III) ions may be nine came with the publication of the structures of neodymium ethylsulfate and bromate (Lincoln 1986).

An understanding of the properties of solutions of metal salts requires the knowledge of the composition and structure of the first coordination sphere. Thus, considerable effort has been expended in determining the hydration number of both d- and f-transition metals. The latter stirred a long and intense debate whether or not they sustain a change in coordination number. Recent X-ray and neutron diffraction data have now firmly

established this change, from 9 to 8 (Lincoln 1986, Cossy and Merbach 1988, Rizkalla and Choppin 1991). In non-aqueous solutions, the study of solvation processes is more tractable, the ligand exchange rates being slower. However, due to the difficulty of working under anhydrous conditions with the water-hungry R(III) ions, progress in this field has been rather slow. In fact numerous studies have been performed either in mixed aqueous solvents, or with hydrated salts, resulting in ambiguous interpretation.

In this chapter we review the interaction between rare-earth cations and both inorganic anions and simple, monodentate neutral molecules in anhydrous organic solutions. Some of the work in mixed solvents is also taken into account. The literature is surveyed until April 1994.

2. Solvation and coordination numbers

Since ions in solution always react in solvated form, and since most of the reactions are accompanied by a change in the ion solvation shell, knowledge of the composition and structure of the solvated ions is one of the fundamental conditions for a thorough understanding of all chemical processes in solution. There are several ways to define the solvation phenomena. One of the most general is given by Krestov (1991): "*Solvation should be considered as the sum of energetic and structural changes occurring in a system in the process of transferring gaseous ions (or atomic-molecular particles) into the liquid solvent, resulting in the formation of homogeneous solution having a fixed chemical composition and structure*".

The most essential feature of ion solvation is the chemical bonding of solvent molecules of the immediate surroundings and their coordination to the ion. Furthermore, in the process of ion–solvent interaction a considerable change of solvent structure takes place. There are two general approaches to interpreting ionic solvation: thermodynamics and kinetics. The thermodynamic approach is based on the calculation of the ion–solvent interactions, and the solvation is described in terms of coordination numbers and thermodynamic (equilibrium) properties including enthalpy, entropy, heat capacity and Gibbs energy changes. The kinetic method takes solvent–solvent interaction into account and is related to the theories of kinetic stability of the ion–solvent associate, determined by the activation energy for the exchange of the solvent molecules. This approach considers solvation not as the binding of solvent molecules by metal ions but, rather, as the influence of the electric field generated by the cations on the translation motion of the adjacent solvent molecules.

The most common model of ion solvation is the concentric shell model, postulating the existence of several coordination shells around the solvated ion (Enderby and Neilson 1981). However, there remains controversy over the precise definition of primary and secondary solvation shells and numbers, especially for those ions where movement of solvent molecules between shells and bulk solvent is very fast. To avoid ambiguity, the term *inner (or first) coordination sphere* is used here to refer to both the solvent and the ligand molecules which are in direct contact with the central ion.

The total number of bonds with solvent and ligand molecules in the first coordination sphere is the *coordination number (CN)* of the ion. The *first solvation number (Ns)* is the number of solvent molecules in the first coordination sphere. Such a time-independent definition needs, however, a complementary time-dependent definition of the first coordination sphere. Therefore, a solvent molecule in the first coordination sphere may be defined as having a long residence time in comparison to its correlation time in subsequent coordination spheres or in the bulk. Undoubtedly, the solvation residence time varies with the lability of the metal ion. The *solvation number (S)* is defined as the number of solvent molecules under the influence of the electric field generated by the central ion, and following the ion's motion in the solution.

Another aspect which is dealt with in this review refers to the complexation reactions between the metal ion, R^{3+}, and different neutral or charged ligands, L^{n-}. In general, two types of complexes may be formed in solution: *outer-sphere* species $[RS_x]^{3+}L^{n-}$ in which the cation and the ligand are separated by one or several solvent molecules S. The expulsion of the solvent molecules leads to the formation of an *inner-sphere* complex $[RLS_y]^{(3-n)+}$ in which the anion and the cation are in direct contact. Lanthanide cations form both inner- and outer-sphere complexes, and with some ligands both types of complexes may be present simultaneously. The rare-earth complexation reactions are consistent with the Eigen multi-step mechanism

$$R^{3+}_{solv} + L^{n-}_{solv} \overset{\text{Step 12}}{\rightleftarrows} [RS_x]^{3+}L^{n-} \overset{\text{Step III}}{\rightleftarrows} [RLS_y]^{(3-n)+}. \quad (1)$$

Step 12 involves diffusion-controlled outer-sphere complex formation, followed by the loss of bound solvent from the ligand solvation shell to form a second outer-sphere complex. Step III is the loss of solvent from the cation solvation shell followed by the cation–ligand bond formation. If a change in coordination number occurs during the complexation reaction, it is most often coupled to step III.

Several criteria help to distinguish between inner- and outer-sphere complexes, although not always unambiguously. For instance, Choppin (1971) and Choppin and Bertha (1973) have used the thermodynamic ΔH and ΔS parameters. They have assigned, in aqueous solutions, a predominantly outer-sphere character to Cl^-, Br^-, I^-, ClO_3^-, NO_3^-, sulfonate and trichloroacetate complexes and an inner-sphere character to F^-, IO_3^-, SO_4^{2-} and acetate complexes. Moreover, these authors have related this ordering to the pK_a values of the ligands. On the other hand, a group of Russian authors have postulated that inner- and outer- sphere complexes may be studied separately by spectrophotometric methods, but this is subject to some doubt (*vide infra*).

3. Characterization of complex equilibria

3.1. *Equilibrium constants*

Different kinds of equilibrium constants are in use in the literature (Beck and Nagypal 1990). Unfortunately, there is no united symbolism in connection with even the simplest

equilibrium constants. In this section, we recall the basic definitions and make explicit the abbreviations used in the text. All the constants we will be using are concentration constants, that is, the activity coefficients are supposed to be unity for all the species in equilibrium.

The stepwise formation of complexes may be described by the following set of equilibrium constants, which characterize the stability of the complexes (charges are omitted):

$$\mathrm{R} + \mathrm{L} \rightleftarrows \mathrm{RL}, \qquad K_1 = \frac{[\mathrm{RL}]}{[\mathrm{R}] \cdot [\mathrm{L}]}, \tag{2}$$

$$\mathrm{RL} + \mathrm{L} \rightleftarrows \mathrm{RL_2}, \qquad K_2 = \frac{[\mathrm{RL_2}]}{[\mathrm{RL}] \cdot [\mathrm{L}]}, \tag{3}$$

$$\mathrm{RL}_{n-1} + \mathrm{L} \rightleftarrows \mathrm{RL}_n, \qquad K_n = \frac{[\mathrm{RL}_n]}{[\mathrm{RL}_{n-1}] \cdot [\mathrm{L}]}. \tag{4}$$

The inner-sphere complex formation is in fact accompanied by the displacement of solvent molecules from the coordination sphere of the metal ion and should be described by the following more general equation:

$$\mathrm{RS}_x + \mathrm{L} \rightleftarrows [\mathrm{RS}_{x-i}\mathrm{L}] + i\mathrm{S}. \tag{5}$$

Accordingly, the process actually taking place should be described by the equilibrium constant defined by

$$K_1^* = \frac{[\mathrm{RS}_{x-i}\mathrm{L}] \cdot [\mathrm{S}]^i}{[\mathrm{RS}_x] \cdot [\mathrm{L}]}. \tag{6}$$

Therefore, special attention must be paid when interpreting K data since solvation may influence the values of the stability constants. When a distinction between inner- and outer-sphere complexes is possible, the stability constant K may be written as the sum of two contributions:

$$K_n = K_n^{\mathrm{in}} + K_n^{\mathrm{out}}, \tag{7}$$

where K_n^{in} and K_n^{out} are distinct constants for inner- and outer-sphere complex formation.

The products of the individual stability constants also give characteristic constants, called overall or cumulative formation constants, usually denoted by

$$\beta_1 = K_1, \tag{8}$$

$$\beta_2 = K_1 \cdot K_2 = \frac{[\mathrm{RL_2}]}{[\mathrm{R}] \cdot [\mathrm{L}]^2}, \tag{9}$$

$$\beta_n = \prod_{i=1}^{n} K_n = \frac{[\mathrm{RL}_n]}{[\mathrm{R}] \cdot [\mathrm{L}]^n}. \tag{10}$$

Finally, the dissociation constant β_n^{d} is defined as inverse of the overall stability constant β_n. In order to avoid any confusion, we encourage authors to explicitly write the chemical equilibrium and the definition of the stability constants they are using.

Various factors influence the values of the stability constants. Among them, the most important are: (i) external factors such as the ionic medium and the ionic strength, temperature and pressure; (ii) parameters related to the properties of the metal ion (ionic radius, ionization potential and electronegativity, electronic configuration); (iii) the properties of the donor atoms of the ligand. The ionic strength and the ionic medium modify the activity coefficients and create specific interactions with both the metal and the ligand. Indeed, the law of mass action is strictly valid only when activities are used instead of concentrations, so that the calculation of the thermodynamic equilibrium constants requires either the knowledge of the activity coefficients or that they remain constant. The most commonly used *constant ionic medium method* is based on the fact that the activity coefficient of a given solute is the same in all solutions of the same ionic strength. Alkali metal or tetraalkylammonium perchlorates are usual salts for fixing the ionic strength. Perchlorate was long considered a non-coordinating anion. This has been shown to be untrue, especially for rare-earth ions in organic solvents having a weak to moderate donor strength. It is now well established that perchlorate interacts with these ions to form inner-sphere complexes of moderate stability (sect. 5.1.).

Stability constants and temperature are connected by the following thermodynamic relationship:

$$\Delta G = -RT \log K, \qquad \Delta G = \Delta H - T\Delta S. \tag{11}$$

3.2. *Distribution curves*

To characterize the extent of the complex formation, Bjerrum (1920) has introduced the concept of the average ligand number $\bar{n}$ defined as follows:

$$\bar{n} = \frac{T_L - [L]}{T_R}, \tag{12}$$

where T_L and T_R are the total concentrations of ligand and metal ions, respectively, and [L] is the equilibrium concentration of the ligand; $\bar{n}$ can also be expressed by means of the overall or stepwise stability constants

$$\bar{n} = \frac{\sum_{j=1}^{N} j\beta_j[L]^j}{\sum_{j=0}^{N} \beta_j[L]^j} \quad \text{or} \quad \bar{n} = \frac{\sum_{j=1}^{N} \prod_{i=1}^{j} K_i[L]^j}{\sum_{j=0}^{N} \prod_{i=0}^{j} K_i[L]^j}. \tag{13,14}$$

Equations (13, 14) show that stability constants may be calculated through the experimental determination of at least N different $\bar{n}$ and [L] data pairs (N is the maximum number of ligands that can be coordinated to the metal ion). The average number $\bar{n}$ depends only on the equilibrium concentration of the free ligand [L] and is independent of both the total ligand and metal concentrations. *Corresponding solutions* are defined as having different T_L and T_R values, but the same values of [L] and, consequently, $\bar{n}$.

Another set of important parameters used to describe complex equilibria are the partial mole fractions α_j,

$$\alpha_j = \frac{\beta_j[\mathrm{L}]^j}{\sum_{k=0}^{N} \beta_k[\mathrm{L}]^k}, \tag{15}$$

which depend solely on the equilibrium concentration of the ligand and are a function of all the formation constants.

Equilibria in complex systems can be illustrated by the concentration distribution curves, obtained by plotting the α_j versus the equilibrium concentration or the logarithm of the equilibrium concentration of one of the components. We shall consider a two-component system in a dilute solution, so that the formation of polynuclear species is avoided. The system is described by the following equations:

$$T_{\mathrm{R}} = \sum_{0}^{N} [\mathrm{RL}_j] = [\mathrm{R}] \sum_{0}^{N} \beta_j[\mathrm{L}]^j, \tag{16}$$

$$T_{\mathrm{L}} = [\mathrm{L}] + [\mathrm{R}] \sum_{0}^{j} j\beta_j[\mathrm{L}]^j = [\mathrm{L}] + \bar{n}T_{\mathrm{R}}. \tag{17}$$

At constant concentration ratio $q = T_{\mathrm{L}}/T_{\mathrm{R}} = [\mathrm{L}]/T_{\mathrm{R}} + \bar{n}$, the parameter T_{R} can be

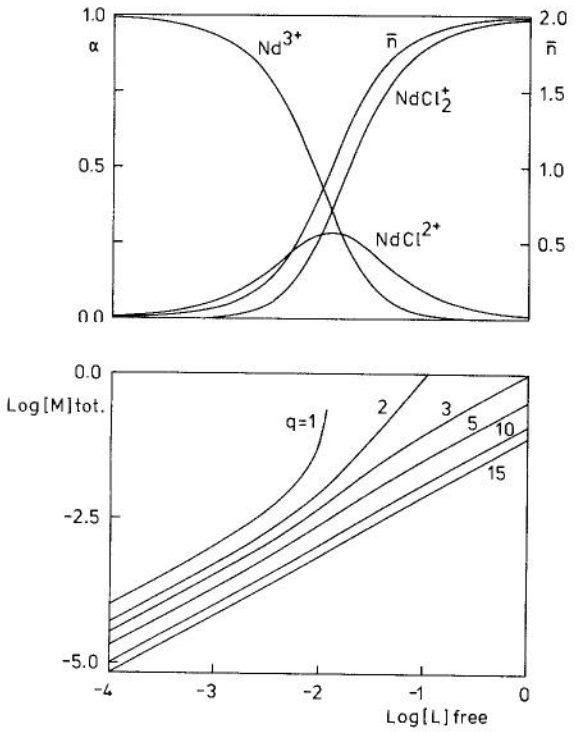

Fig. 1. Distribution curves $\alpha_j = f(\log[\mathrm{L}])$ and $\bar{n}$ and $\log T_{\mathrm{R}} = f(\log[\mathrm{L}])$ for various values of $q = T_{\mathrm{L}}/T_{\mathrm{R}}$ for the Nd^{3+}–Cl^- system in methanol.

expressed as a function of the equilibrium concentration of the ligand:

$$T_R = \frac{\sum_0^N \beta_j [L]^{j+1}}{\sum_0^N (q-j)\beta_j [L]^j}. \tag{18}$$

Usually the distribution curves, $\alpha_j = f(\log[L])$ and $\bar{n}$ on one hand, and $\log T_R = f(\log[L])$ for various q values on the other hand, are plotted in two facing diagrams, as shown in fig. 1 for the Nd^{3+}–Cl^- system in methanol.

3.3. *Spectrophotometric determination of stability constants*

Spectrophotometric methods are widely used to determine stability constants and the associated thermodynamic parameters. For a two-component system, the following methods, which differ from one another in the way the total concentrations are varied, are generally applied:

(i) spectrophotometric L-method (T_R is kept constant and T_L is varied),
(ii) spectrophotometric R-method (T_L is kept constant and T_R is varied),
(iii) continuous variation or Job's method ($T_L + T_R$ is kept constant but T_L/T_R is varied),
(iv) stoichiometric-dilution method (T_L and T_R are varied, but T_L/T_R is kept constant),
(v) corresponding-solutions method (T_L and T_R are varied so that the relationship $T_L = [L] + \bar{n}T_R$ is satisfied at constant [L] and $\bar{n}$ values).

Since a substantial number of stability constants of lanthanide complexes in anhydrous solutions has been determined using the spectrophotometric L-method, an important remark has to be made. The basic equation upon which the method relies gives the apparent absorption coefficient ε of a solution of mononuclear complexes as a function of the ligand concentration:

$$\varepsilon = \frac{\sum_{n=0}^N \varepsilon_n \beta_n [L]^n}{\sum_{n=0}^N \beta_n [L]^n}. \tag{19}$$

If $N = 1$, eq. (19) becomes

$$\varepsilon = \frac{\varepsilon_0 + \varepsilon_1 \beta_1 [L]}{1 + \beta_1 [L]} \tag{20}$$

and may be rearranged to a linear relationship as follows

$$\frac{\varepsilon - \varepsilon_0}{[L]} = \varepsilon_1 \beta_1 - \varepsilon \beta_1 \quad \text{or} \quad \frac{[L]}{\varepsilon - \varepsilon_0} = \frac{1}{(\varepsilon_1 - \varepsilon_0)\beta_1} + \frac{[L]}{\varepsilon_1 - \varepsilon_0}. \tag{21, 22}$$

The relevance of this method was discussed by Johansson (1971), who pointed out that several factors may induce errors in the calculation of the stability constants: neglect

of higher complexes RL_n, accidental reduction of eq. (20), or influence of experimental errors. We shall discuss the separation of inner- and outer-sphere complex formation in some detail.

Outer-sphere complexation affects mainly the charge transfer bands in the UV part of the spectra, leaving the visible spectra unaffected. This feature provides the possibility to distinguish outer- from inner-sphere complexation. However, the misconception has occasionally arisen that the degrees of outer- and inner-sphere complexation can be determined separately by spectrometry for a given system. For instance, a group of Russian authors (Kozachenko and Batyaev 1971a,b, Kozachenko et al. 1970, 1973) have calculated for several RL systems an outer-sphere formation constant from the UV portion of the spectra, and an inner-sphere formation constant from the visible part of the spectra (f–f transitions). They propose the following treatment:

$$R + L \rightleftarrows R \cdots L, \qquad \omega_{01} = \frac{[R \cdots L]}{[R] \cdot [L]}, \tag{23}$$

$$R + L \rightleftarrows [RL], \qquad \beta_1 = \frac{[RL]}{[R] \cdot [L]}, \tag{24}$$

where $R \cdots L$ and RL are the outer- and inner-sphere complexes, respectively, and ω_{01} and β_1 the corresponding equilibrium constants. These constants are related to the molar absorption coefficients of the solution ε and to the molar fractions of the various complexes by the following equations:

$$\varepsilon = \varepsilon_0 \alpha_0 + \varepsilon_{01} \alpha_{01} + \varepsilon_1 \alpha_{11}, \tag{25}$$

$$\varepsilon = \frac{\varepsilon_0 [R]}{[R]_t} + \frac{\varepsilon_{01} [R \cdots L]}{[R]_t} + \frac{\varepsilon_1 [RL]}{[R]_t}, \tag{26}$$

$$\varepsilon = \frac{[R][L]}{[R]_t} \left(\frac{\varepsilon_0}{[L]} + \varepsilon_{01} \omega_{01} + \varepsilon_1 \beta_1 \right). \tag{27}$$

Replacing $[R]_t = [R] + [R \cdots L] + [RL]$ gives

$$\frac{\varepsilon - \varepsilon_0}{[L]} = \varepsilon_{01} \omega_{01} + \varepsilon_1 \beta_1 - \varepsilon (\omega_{01} + \beta_1). \tag{28}$$

It is seen from the last equation that $(\omega_{01} + \beta_1)$ and $(\varepsilon_{01} \omega_{01} + \varepsilon_1 \beta_1)$ can be obtained from a plot of $\varepsilon - \varepsilon_0/[L]$ vs. ε. The resulting constants are different at different wavelengths. The interpretation given by Kozachenko et al. is that the UV portion of the spectra yields the sum of the constants for both inner- and outer-sphere complexes, $\omega_{01} + \beta_1$, while the measurements in the visible region yield solely the inner-sphere formation constant β_1. However, this interpretation is erroneous. If both inner- and outer-sphere RL complexes were formed (but no higher complexes RL_n), eq. (19) becomes

$$\varepsilon = \frac{\varepsilon_0 + (\varepsilon_{01} \omega_{01} + \varepsilon_{11} \beta_1)[L]}{1 + (\omega_{01} + \beta_1)[L]}. \tag{29}$$

The denominator of eq. (29) is derived only from the stoichiometry of the system and is completely independent of wavelength. Johansson (1971) concludes that at higher

wavelengths ε_{01} is close to ε_0, and that only the values of $\omega_{01}+\beta_1$ are obtained at any wavelength.

Although the equilibrium constants obtained by the spectrophotometric L-method have to be considered carefully, they are included in this review. Note that the values reported in the tables or discussed in the text correspond to the $\omega_{01}+\beta_1$ values in the original articles.

4. Investigation methods and techniques

There is a great variety of methods and experimental techniques which can be applied to the study of ion solvation or complexation phenomena. In principle, they can be divided in two categories: (i) direct methods which probe either the metal ion or the ligands bonded in the first coordination sphere and (ii) indirect methods which measure bulk phenomena such as solute–solvent or solvent–solvent interactions (Lincoln 1971). The first group of methods distinguish bonded ligands on the basis of their distance from the metal ion, and the number of bonded molecules within contact distance of the metal ion is taken as the coordination number. Depending upon the lability of the metal ion, CN determinations may be made over a fraction of the ligand exchange half-life or over many half-lives. The corresponding experimental methods are time-independent and are represented by diffraction methods. A second category of direct methods (e.g. nuclear magnetic resonance, isotopic dilution, ion exchange) utilize the fact that the residence time of a bonded ligand is often significantly longer than its correlation time in the bulk solvent, which allows one to distinguish between solvent molecules in these two environments. Other direct methods, such as vibrational spectroscopy, produce an average picture of the metal-ion environment while indirect methods yield solvation numbers.

4.1. *Diffraction techniques*

Diffraction studies of solutions are technically no more difficult than those of crystalline solids, but the processing of the experimental data and the subsequent interpretation of the radial distribution functions $g(r)$ is considerably more tedious. In addition, they may only be performed on concentrated solutions (typically 0.5–3 M), which favours anion interaction. Direct metal–ligand distances obtained from $g(r)$ are the structural parameters which diffraction studies provide with great reliability. X-ray diffraction is the more commonly used method, but neutron diffraction offers the great advantage of locating hydrogen (or, rather, deuterium) atoms and thus of providing information about the orientation of bonded ligands. Calculation of the coordination numbers is more critical since it requires the help of a structural model and is more easily influenced by systematic errors due to experimental measurements or introduced by the data treatment. The existence of some order beyond the first coordination shell has been definitely demonstrated for most of the cations, but the parameters describing the second coordination shell are uncertain and not always given in the papers.

A large number of X-ray and neutron diffraction studies have been performed on rare-earth ion solutions in water (Rizkalla and Choppin 1991, Helm and Merbach 1991). These investigations clearly point to changes in the hydration number throughout the lanthanide series. A pulsed neutron diffraction study by Yamaguchi et al. (1991), carried out on 2 M aqueous perchlorate solutions of Pr(III), Nd(III), Tb(III), Dy(III), Tm(III), and Yb(III), confirmed the change in the hydration number from ~9–10 for the light lanthanide ions to ~8 for the heavier ones. The application of diffraction methods to organic solutions has been less extensive. However, the existence of $[NdCl_2(CH_3OH)_6]^+$ and $[La(CH_3OH)_8]^{3+}$ species in concentrated methanolic solutions of lanthanide chlorides has been reported by Steel and Wertz (1977) and Wertz and Finch (1979). More recently, Johansson et al. (1991) have studied the structure of solvated Er(III) and Y(III) nitrates and chlorides in dimethylsulfoxide.

Another useful experimental technique is EXAFS, which was used to establish a decrease in the hydration number between Nd (9.5) and Lu (7.7) in 2 M solutions of lanthanide perchlorates (Yamaguchi et al. 1988).

4.2. *Electronic absorption and emission spectroscopy*

UV-visible absorption spectroscopy is most frequently used as a method for characterizing chemical equilibria. There are, however, some difficulties associated with its use for investigating the successive formation of lanthanide coordination compounds. The molar absorption coefficients of f–f transitions are very low (typically 0.1–10 $\ell\,mol^{-1}\,cm^{-1}$) and the shifts upon stepwise complexation are very small, typically a few cm^{-1} only, so that absorption spectra of complexed species generally overlap.

Analysis of f–f absorption spectra is usually made to obtain the crystal-field (B_k^q), nephelauxetic (β) and intensity (T_λ) parameters for a given coordination compound. This analysis turns out to be somewhat difficult for solution species because of the insufficiently resolved fine structure of the absorption bands. The nephelauxetic parameter β can be considered as the spectroscopic covalency parameter of the metal–ligand bond in the complex (Jørgensen and Reisfeld 1982). Intensity (T_λ) parameters have been mostly considered as empirical data and calculated from a fit of the experimental intensities. The parameters T_4 and T_6 change only slightly within the lanthanide series and they are rather insensitive to variations in the coordination environment. On the other hand, T_2 is significant only for hypersensitive transitions corresponding to $|\Delta J| = 2$; it varies sharply with changes in the first coordination sphere (Carnall et al. 1965, Henrie et al. 1976).

The commercial availability of powerful tunable lasers, operating in either continuous or pulsed mode, has prompted new interest in the use of luminescence techniques for the study of coordination properties (Bünzli 1989). The highly luminescent Eu(III) and Tb(III) ions may be excited around 580 and 488 nm, respectively, by readily available dye lasers. These ions are ideal luminescent stains to probe their coordination environment, in spite of their low molar absorption coefficients and the efficient quenching of their luminescence by high energy vibrations. The high selectivity of the laser light and its large intensity, as well as high sensitivity of photon counting, largely compensate the

first disadvantage, while measurements in deuterated solvents may offset the second one. Monitoring changes in luminescence intensity, lifetime or energy transfer efficiency when a complexing agent is added to the solution indicates whether or not the ligand penetrates into the first coordination sphere, and in favourable cases, coordination numbers as well as stability constants can be calculated. On the other hand, luminescence data reflect the coordination properties of the Ln(III) ions in the excited state. Since the lifetime of excited states is long (0.1–several milliseconds), the excited species reach thermodynamic equilibrium with the ligands in solution and therefore have to be treated as separate entities with individual chemical properties (Choppin 1984). There has been some concern that dissociation and coordination number changes occur during the lifetime of these species (Marcantonatos et al. 1981, Vuilleumier et al. 1982, Marcantonatos et al. 1982). However, it has been shown that luminescence measurements and FT-IR data, which provide information about the ground state, give the same coordination numbers for several anhydrous lanthanide solutions (Bünzli et al. 1982a, Mabillard 1983). The number of ligand molecules in the inner-coordination sphere of the metal ion, is usually calculated using Stern–Völmer plots (Bünzli 1989) or by taking advantage of the difference in quenching between deuterated and non deuterated ligands (Sudnick and Horrocks 1979). The accuracy with which CN's can be estimated is ± 0.3 to ± 0.5 units.

Other techniques, such as magnetic circular dichroism (Görller-Walrand and Godemont 1977, Görller-Walrand et al. 1982), circularly polarized luminescence (Dyer et al. 1986, Glover et al. 1992) or magnetic circularly polarized luminescence (Richardson and Brittain 1981, Foster and Richardson 1983, Stephens et al. 1986) have also been used for the study of Eu and Tb complexes.

4.3. *Vibrational spectroscopy*

Vibrational spectra are sensitive to the local symmetry of coordinated and uncoordinated species. It is therefore possible to distinguish between these entities in solution. In addition, coordination induces a variation in the force constants of the vibrations, resulting in substantial shifts of the bands. Quantitative determinations are feasible, provided a good calibration curve is established and the cell thickness is determined before each measurement.

Several determinations of the average coordination number of lanthanide ions in non-aqueous and mixed solutions have been made, using both grating infra-red spectroscopy (Lugina and Davidenko 1980, Batyaev et al. 1985) and FT-IR difference spectra (Bünzli et al. 1982b, Bünzli and Mabillard 1986a, Bünzli and Kasparek 1991, Milicic-Tang and Bünzli 1992). With the latter technique, a spectroscopic accuracy of ± 0.01 unit of absorbance can be reached and coordination numbers may be determined to ± 0.3 unit.

Raman spectroscopy is an appropriate complement to IR vibrational studies, although it requires more concentrated solutions. It has been successfully used for several aqueous systems and glasses (Knoeck 1969, Egorov and Kuzinets 1977, Kanno and Hiraishi 1984). With the development of both powerful lasers and FT-Raman techniques, there is little

doubt that this spectroscopy will become an important tool in lanthanide coordination chemistry.

4.4. *Ultrasonic absorption*

The velocity of elastic ultrasonic waves in solution is strongly influenced by solute–solvent and solute–solute interactions which, in turn, are determined by the chemical structure of the solute and solvent molecules. Adiabatic compressibility β for a system having the density ρ, is related to the measured ultrasonic velocity u by the following equation:

$$\beta = (u^2\rho)^{-1}. \tag{30}$$

The total solvation number can be calculated from the β value, provided the following two assumptions hold: (i) the solvated (or complexed) ion is incompressible, (ii) the compressibility of the free solvent is the same as that of the pure solvent. On the other hand, the ultrasonic absorption of a system undergoing chemical relaxation is given by

$$\frac{\alpha}{f^2} = \sum_i \frac{A_i}{1 + (f/f_{Ri})^2} + B, \tag{31}$$

where α is the absorption coefficient; f the frequency; f_{Ri} the relaxation frequency for each reaction step; A_i the relaxation amplitude for each step; B the experimental background. The important quantity is the excess of absorbance μ, defined as $\mu = (a/f^2 - B)f^2\lambda$. Because of their high lability, the relaxation times for the complexation reactions of the R(III) ions are of the same order of magnitude as the ultrasonic absorption times, which makes this technique suitable for the study of lanthanide systems. Most of the ultrasonic absorption measurements on the rare-earth cations have been made by Silber and co-workers and by a Polish group (Jezowska-Trzebiatowska et al. 1978). Most of the investigated systems are aqueous and mixed aqueous solutions. The interaction between chloride (Silber and Mioduski 1984), nitrate (Silber and Campbell 1989), perchlorate (Silber and Pezzica 1976) and R(III) ions was studied.

4.5. *Nuclear magnetic resonance*

One of the most informative techniques about solvation and complexation processes is NMR spectroscopy. Under optimal conditions, the chemical shift of the coordinated ligand is different from that of the free moiety, giving clear evidence of the complexation reaction. The ratio of the areas under the two signals provides direct information on the number of coordinated molecules. However, the essential condition for the observation of separate NMR signals is that ligand exchange reactions must be slow, which is obviously not the case for R(III) ions. It is therefore usually necessary to work at low temperature, −60 to −120°C. If the NMR signals of bonded and free molecules cannot be separated,

the measurement of the relaxation time T_2 vs temperature or the plot of the chemical shift of the coalesced signals as a function of the concentration of the ligand, provide information about the coordination.

A large number of nuclei such as ^{1}H, ^{15}N, ^{17}O, ^{35}Cl have been employed to probe lanthanide coordination properties (e.g. Brucher et al. 1985, Fratiello et al. 1991). Special interest was taken in the DMF solutions, where solvent exchange reactions have been characterized at variable temperature and pressure (Cossy and Merbach 1988). Information about the coordination environment of R(III) ions can also be gained by directly observing the R(III) nuclei, which is possible for ^{89}Y (Fratiello et al. 1989a), and ^{139}La (Bünzli et al. 1987).

4.6. *Electron paramagnetic resonance*

Compared to NMR, EPR spectroscopy is more sensitive, and work is possible with solutions as dilute as 10^{-3} to 10^{-4} M. For rare earths, Gd(III) and Eu(II) with a half-filled f shell and no orbital angular momentum (to the first approximation) are the only lanthanides whose EPR spectra can be observed routinely at room temperature (Stephens 1989). EPR and spin-echo modulation experiments have been performed on R(III) frozen solutions in methanol and aqueous ethanol at 4.2 K (R = Ce, Nd, Yb, Er; Mims and Davis 1976, Janakiraman and Kevan 1981).

4.7. *Thermodynamics of ion solvation*

Thermodynamic data constitute one of the most important aspects of ion solvation phenomena. Energy changes during solvation are mostly characterized by enthalpy and structural ones by entropy changes. Enthalpies of solvation provide the simplest indicator of the ion–solvent interaction strength (Carvalho and Choppin 1967, Spedding et al. 1977a); other data, however, such as entropy (Bertha and Choppin 1969, Spedding et al. 1977b), heat capacity (Spedding et al. 1979), partial molal volume, or activity coefficients (Rard and Spedding 1982) are available and give useful information about R(III) ions in aqueous solutions. Semi-empirical correlations have been developed, in which, for example, partial molal hydration volumes can be related to their charge, radius and hydration number. The application of these ideas to hydrated lanthanide ions enhanced the hypothesis of a change in their hydration number in the middle of the series (Spedding et al. 1975). Thermodynamic data allow one to distinguish between inner- and outer-sphere interaction. If outer-sphere complexes are formed, the change in enthalpy is favourable and the change in entropy unfavourable (Choppin and Strazik 1965). The opposite is true for inner-sphere complexation (Choppin and Graffeo 1965).

Most of the available thermodynamic data refer to aqueous solutions, although some measurements have also been done for organic solutions (Burgess and Kijowski 1981).

4.8. *Other experimental methods*

A large number of other experimental methods are available for the investigation of ion solvation and complexation processes. Some are related to the determination of motion inside the solution and enable the estimation of the effective volume of the moving solvated ion and, consequently, the solvation number. The motion may be spontaneous (e.g. diffusion), mechanically produced (e.g. viscosity) or electrically produced (e.g. conductivity). Conductivities and mobilities, which are closely related, provide a measure of the resistance of the complexed ions to motion through the solvent. Other methods include extraction, chromatography and isotopic dilution.

4.9. *Simulation techniques*

Monte Carlo or molecular dynamics calculations can be applied in the study of the structure of the solvated ions, and calculations on lanthanide ions are in progress (Meier et al. 1990, Troxler and Wipff 1994).

5. Interaction with anions

5.1. *Interaction with perchlorate*

Information has been newly obtained about the properties and structure of anhydrous lanthanide perchlorates and trifluoromethanesulfonates (triflates). A synthetic method was proposed for preparing anhydrous perchlorates, which uses Cl_2O_6 as a powerful perchlorating agent (Favier and Pascal 1991, 1992, Favier 1992). IR and Raman measurements show that $R(ClO_4)_3$ (R = Y, La, Nd, Sm, Gd, Yb) are isostructural, with three perchlorate ions bonded in a bridging tridentate manner, which implies CN = 9 for the metal ion. Similar results are obtained for anhydrous lanthanide triflates, leading to the same CN = 9 (Hamidi 1992).

Inner-sphere interaction with perchlorate ions does not occur in strong donors such as dimethylformamide (DMF) or dimethylsulfoxide (DMSO), as revealed by conductimetric, absorption, luminescence, NMR, and FT-IR data (Lugina et al. 1973, Pisaniello et al. 1982, 1983, Bünzli and Yersin 1982). In the absence of water, however, perchlorate interacts with lanthanide ions to form inner-sphere complexes in organic solvents having a weak to moderate donor strength. Evidence of this interaction has been brought by several experimental techniques. Conductimetric measurements show $R(ClO_4)_3$ (R = Nd, Eu, Er) to be 2:1 electrolytes in anhydrous methanol (Zholdakov et al. 1971), anhydrous acetonitrile (Bünzli and Mabillard 1986b), and methanol-containing water (Legendziewicz et al. 1986). Absorption and emission spectra of $Eu(ClO_4)_3$ are consistent with an inner-sphere interaction between perchlorate and Eu(III) ions (Haas and Stein 1971a,b), while ultrasonic measurements of $R(ClO_4)_3$ solutions in methanol:water mixtures (R = Nd, Gd, Er) point to the simultaneous presence of inner- and outer-sphere

Table 1
Perchlorate vibrations

>Cl–O···Ln (C_{3v})		ClO_4^- (T_d)	>Cl(O)(O)Ln (C_{2v})	
ν_4(E)	δ_{as}(ClO) 1160 cm^{-1}		ν_8(B_2)	ν_{as}(ClO_2) 1200 cm^{-1}
		ν_3(T_2) ν_{as}(ClO) 1090–1100 cm^{-1}	ν_6(B_1)	ν_{as}(ClO_2) 1140 cm^{-1}
ν_1(A_1)	ν_s(ClO_3) 1030 cm^{-1}		ν_1(A_1)	ν_s(ClO_2) 990 cm^{-1}
ν_2(A_1)	ν(ClO) 930 cm^{-1}	← ν_1(A_1) ν_s(ClO) Raman only, 930 cm^{-1} →	ν_2(A_1)	ν_s(ClO_2) 930 cm^{-1}
ν_3(A_1)	δ_s(ClO_3) 650 cm^{-1}		ν_3(A_1)	δ_s(ClO_2) 650 cm^{-1}
		ν_4(T_2) δ_{as}(ClO_2) 625 cm^{-1}	ν_7(B_1)	ρ(ClO_2) 640 cm^{-1}
ν_5(E)	δ_{as}(ClO_3) 620 cm^{-1}		ν_9(B_2)	ρ(ClO_2) 610 cm^{-1}
			ν_4(A_1)	δ_s(ClO_2) 450 cm^{-1}
ν_6(E)	ρ(ClO_2) 470 cm^{-1}	← ν_2(E) δ_s(ClO_2) Raman only, 460 cm^{-1}		
			ν_5(A_2)	torsion, Raman only
	6 modes	4 modes		9 modes

complexes (Silber and Pezzica 1976). The existence of these species has been confirmed by FT-IR spectroscopy in anhydrous acetonitrile (Bünzli and Kasparek 1991) and by ^{139}La NMR measurements in anhydrous methanol (Bünzli et al. 1987). Absorption and luminescence spectra have been reported for solutions of lanthanide perchlorates (R = Pr, Nd, Eu, Dy) in various alcohols and amides (Legendziewicz et al. 1984, 1986, 1988). The intensities of the absorptions were analyzed using the Judd–Ofelt theory, and the oscillator strengths of the f–f absorption bands were determined.

Bünzli and collaborators have studied the inner-sphere interaction between perchlorate and lanthanide ions in anhydrous acetonitrile using FT-IR difference spectroscopy (e.g. Bünzli et al. 1982a,b, Bünzli and Kasparek 1991). Besides two IR active modes of unassociated perchlorate (u, local symmetry T_d, cf. table 1), the FT-IR difference spectra of $R(ClO_4)_3$ solutions 0.05 M display absorption bands which can be assigned to monodentate (m, C_{3v}) and bidentate (b, C_{2v}) perchlorates (fig. 2). A detailed analysis of the FT-IR spectra (fig. 3) reveals that both ClO_4^- (m) and ClO_4^- (b) are bonded in the first coordination sphere of the R(III) ions. The strength of the R(III)/ClO_4^- interaction is reflected in the value of the $\tilde{\nu}_4$–$\tilde{\nu}_1$ splitting (fig. 4). There is a slight decrease from La(III) to Gd(III), followed by a steep increase up to Tm(III). Outer-sphere perchlorate ions do not give rise to distinct absorptions, the estimated $\tilde{\nu}_4$–$\tilde{\nu}_1$ splitting being < 50 cm^{-1} (Bünzli and Kasparek 1991) so that the corresponding vibrations fall within the envelope of the ν_1(u) vibration. With respect to the variation of the average number of uncoordinated perchlorates per R(III) ion, $\bar{n}_u$, the lanthanides can be divided into three groups: La, Pr–Gd and Tb–Yb, for which 48±1%, 61±2% and 69±2% of the perchlorate anions are uncoordinated, respectively.

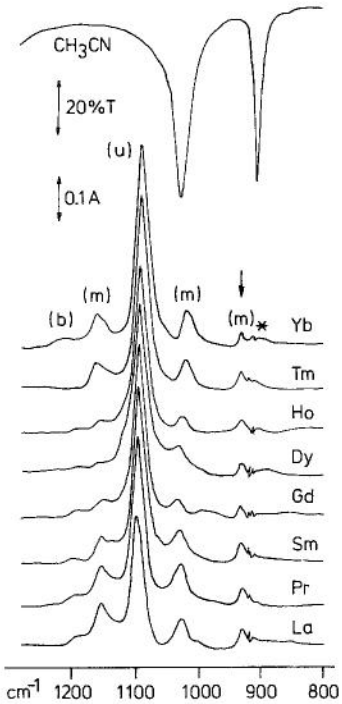

Fig. 2. FT-IR difference spectra of $R(ClO_4)_3$ solutions 0.05 M in anhydrous acetonitrile, in the spectral range of the main perchlorate vibrations. The arrow points to absorption from the coordinated solvent. *, solvent absorptions not completely compensated; u, unassociated; m, monodentate; b, bidentate (Bünzli and Kasparek 1991).

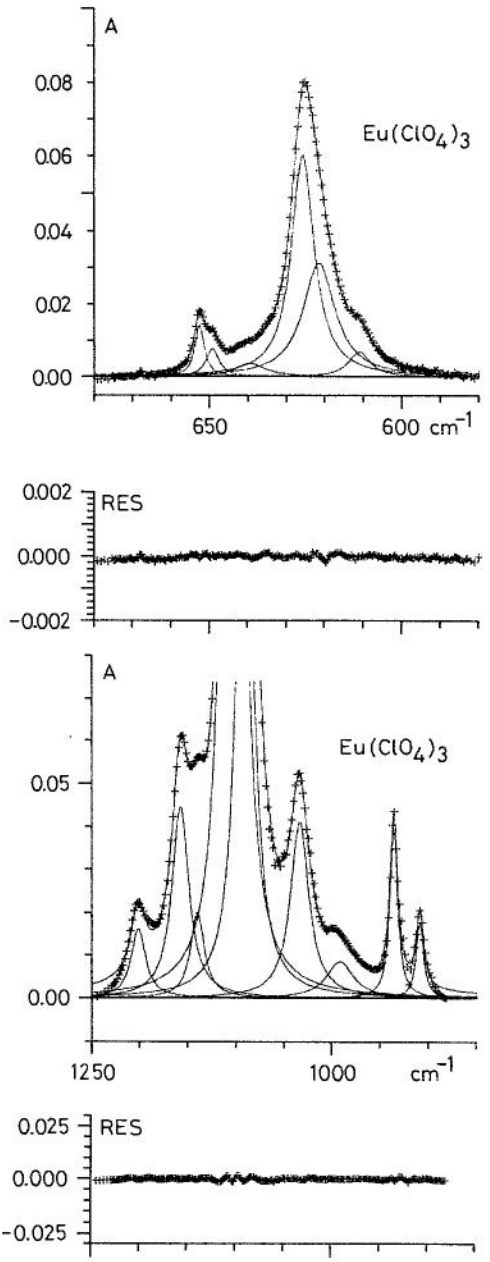

Fig. 3. Curve analysis of the FT-IR difference spectrum of an $Eu(ClO_4)_3$ solution 0.05 M in anhydrous acetonitrile, with residuals at the bottom (Bünzli and Mabillard 1986a).

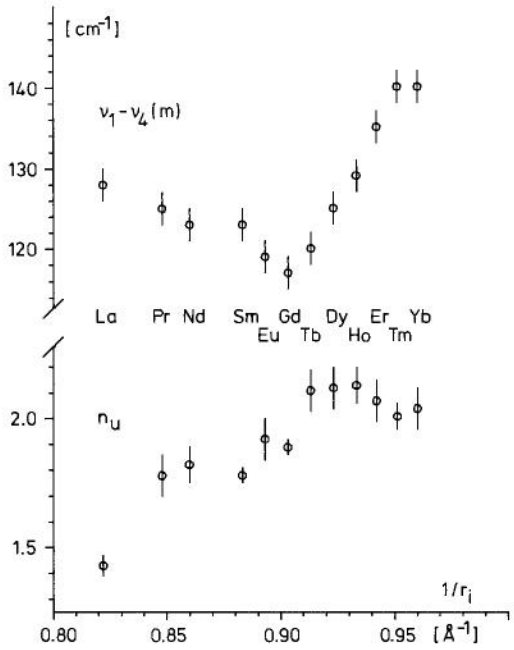

Fig. 4. Splitting $\tilde{\nu}_4$–$\tilde{\nu}_1$ [cm^{-1}] of monodentate perchlorate (top) and average number of uncoordinated perchlorate ions per R(III) ions, n_u (bottom), in $R(ClO_4)_3$ solutions 0.05 M in anhydrous acetonitrile vs. the reciprocal ionic radii for CN = 9 (Bünzli and Kasparek 1991).

In order to rationalize the data with respect to the R(III)/ClO_4^- interaction, the authors consider the following simplified equilibria, disregarding the coordination mode (monodentate or bidentate) of the perchlorate anions in the inner coordination sphere:

$$[R_{solv}]^{3+} + ClO_4^- \overset{K_{01}}{\rightleftarrows} \{[R_{solv}]^{3+}ClO_4^-\} \overset{K_1'}{\rightleftarrows} [R(ClO_4)_{solv}]^{2+}, \tag{32}$$

$$[R(ClO_4)_{solv}]^{2+} + ClO_4^- \overset{K_{12}}{\rightleftarrows} \{[R(ClO_4)_{solv}]^{2+}ClO_4^-\} \overset{K_2'}{\rightleftarrows} [R(ClO_4)_{2solv}]^{+}. \tag{33}$$

The variation of $\bar{n}_u$ along the series is interpreted as reflecting a gradual displacement of the above equilibria towards the left. The change of both $\bar{n}_u$ and $\tilde{\nu}_4$–$\tilde{\nu}_1$ vs. the atomic number of the lanthanide (fig. 4) is explained taking into account steric factors and the increase in electronic density with decreasing ionic radius. For La, the solution contains approximately 25% bisperchlorato and 75% monoperchlorato species. The proportion of the former decreases drastically for Pr (ca. 10%), then remains approximately constant until the middle of the series, and finally vanishes for Tb. Steric effects cause a lengthening in the Ln–ligand distance and, as a result, the $\tilde{\nu}_4$–$\tilde{\nu}_1$ splitting decreases, despite the increasing electron density. The difference observed for $\bar{n}_u$ between La and Pr does not reflect a coordination number change but, rather, the displacement of equilibria 32 and 33. However, speaking in terms of *average* CN, the change may be described as reflecting a CN variation of ca. 0.5 unit. The discontinuities occurring at Gd may be interpreted

Table 2
Apparent stability constants for the formation of monoperchlorato species in $R(ClO_4)_3$ solutions 0.05 M ($\log K_1$) and of *tris*(triflate) species in $R(SO_3CF_3)_3$ solutions 0.01 to 0.03 M ($\log K_3$) in anhydrous acetonitrile

R	$\log K_1$ ClO_4^-	Ref.	$\log K_3$ $SO_3CF_3^-$	Ref.
Gd	n.a.	–	2.5	3
Tb	1.9±0.4	1	2.6	3
Dy	1.8±0.4	2	2.5	3
Ho	1.8±0.3	2	2.5	3
Er	2.1±0.4	1	2.5	3
Tm	2.7±0.5	2	2.4	3
Yb	n.a.	–	2.3	3
Lu	n.a.	–	2.3	3
Yb	2.4±0.4	2		

References
(1) Bünzli and Mabillard (1986a,b) (2) Bünzli and Kasparek (1991) (3) Di Bernardo et al. (1993)

as expressing the displacement of an equilibrium involving two species differing by the number of coordinated acetonitrile molecules:

$$[R(ClO_4)(solv)_x]^{2+} \rightleftarrows [R(ClO_4)(solv)_{x-1}]^{2+} + solv. \tag{34}$$

The apparent equilibrium quotients $K_1 = K_{01}K_1'$ have been evaluated for the heavier lanthanide ions (table 2), under the assumption that the experimental $\bar{n}_u$ values are not biased by the presence of outer-sphere perchlorate ions (*vide supra*). The $R(III)/ClO_4^-$ interaction in acetonitrile is moderate ($\log K_1 \approx 2$) and similar to the interaction evidenced in methanol for La(III) by ^{139}La NMR spectroscopy (Bünzli et al. 1987) with $\log K_1 = 2.6 \pm 0.2$. However, this interaction is strong enough to be taken into account when interpreting stability constants determined in the presence of a large excess of perchlorate as supporting electrolyte.

The composition of the first coordination sphere of Ce(III) in anhydrous solutions 10^{-3} M in methanol, propanol, isopropanol and butanol has been characterized by studying the interconfiguration transitions $4f^{n-1}5d \leftrightarrow 4f^n$. In addition to the inner-sphere monoperchlorato complex, a solvated species $[Ce(solv_8)]^{3+}$ was observed, the photophysical properties of which are very similar to those of $[Ce(H_2O)_8]^{3+}$ (Svetashev and Tsvirko 1991).

5.2. *Interaction with trifluoromethanesulfonate*

The instability of anhydrous lanthanide perchlorates in the presence of organic material or traces of impurities like grease or acid can lead to dangerous accidents (Raymond 1983). Consequently, most scientists prefer to use the safer trifluoromethanesulfonate

(triflate) anion $SO_3CF_3^-$. Lanthanide triflates can be easily prepared by reacting the oxides with trifluoromethanesulfonic acid. Progressive heating under vacuum (10^{-6} mmHg/80°) of the white crystals leads to anhydrous salts. The triflate ion is believed to be poorly coordinating. However, Pilloud and Bünzli (1987) have shown lanthanide triflate solutions in propylene carbonate to be 2:1 electrolytes, pointing to inner-sphere complexation. Another study has demonstrated that the affinity of triflate for lanthanum in methanol is approximately similar to that of perchlorate (Bünzli et al. 1987).

The nature and the extent of the interaction between R(III) cations and the triflate anion has been studied in anhydrous acetonitrile by the same FT-IR technique described for the perchlorate interaction (Di Bernardo et al. 1993). Solubility problems were encountered for the lighter lanthanide ions (La–Eu, $< 10^{-1}$ M) so that only the heavier lanthanide ions were investigated. Conductimetric measurements on a Yb(III) triflate solution indicate a 1:1 electrolyte. The 1000–1300 cm^{-1} region of the mid-infrared spectrum contains the main triflate vibrations and the $\nu_{as}(SO_3)$ mode is particularly well suited for a quantitative study. The number of uncoordinated triflate ions per R(III) ion, $\bar{n}_{trif}$, was determined with the help of a calibration curve, after curve resolution of the spectra (fig. 5). It is always

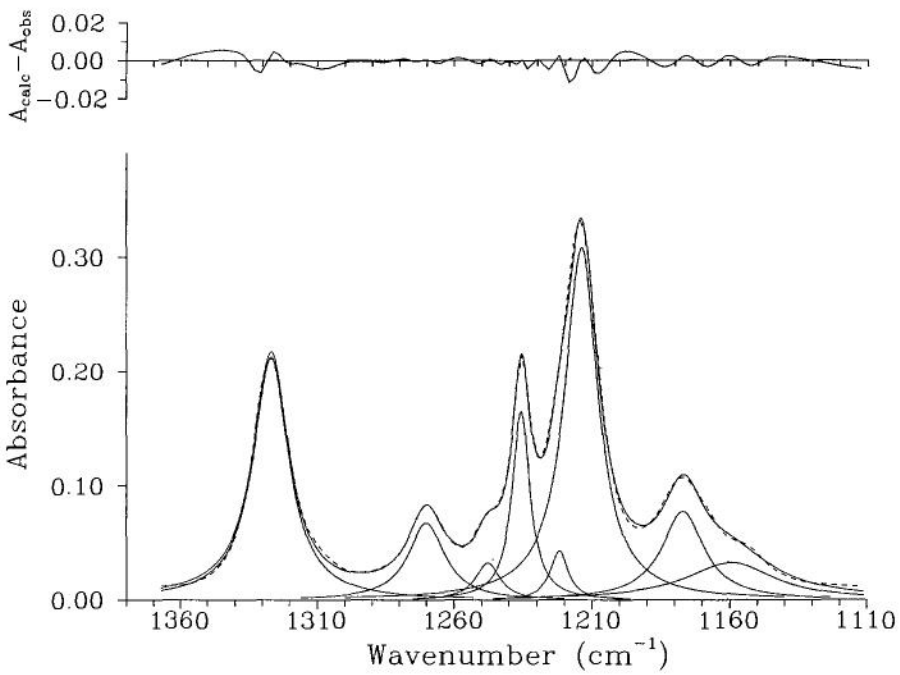

Fig. 5. Curve analysis for a 33.9 mmol dm^{-3} $Lu(CF_3SO_3)$ solution in anhydrous acetonitrile. Eight Lorentzian functions were employed to simulate the experimental spectrum. The residuals are reported at the top of the figure (Di Bernardo et al. 1993).

larger than 2 and the apparent equilibrium constants for the following complexation reaction could be determined (table 2):

$$[R(SO_3CF_3)_2(solv)_x]^+ + SO_3CF_3^- \overset{K_3}{\rightleftarrows} [R(SO_3CF_3)_3(solv)_y]. \quad (35)$$

Within the experimental uncertainties (± 0.1) the $\log K_3$ values display a consistent small decrease with increasing atomic number. This probably results from an increase in steric crowding as the third ligand is added, since the charge density of the ions increases with Z.

5.3. *Interaction with halides*

5.3.1. *Solutions in acetonitrile and propylene carbonate*

Absorption spectra of the chloro complexes formed in anhydrous propylene carbonate (PC) were investigated for R = Pr, Sm, Nd in the near UV, visible and near infrared spectral ranges by Hamze et al. (1989). After testing three theoretical models to fit the experimental data, the authors concluded that lanthanide chloride solutions 0.015 M in PC contain two chloro-species only: $[RCl(solv)_x]^{2+}$ and $[RCl_2(solv)_y]^+$. If a third, neutral chloro complex is introduced, the fit improves, but improper calculated spectra are generated for the latter species. In general, significant bathochromic shifts are observed with the increase of the complexation degree of R(III): 1–4 nm in the near UV, 4–11 nm in the visible, and 5–30 nm in the near IR. The calculated individual electronic spectra of the two chloro complexes display a very small bathochromic shift only, suggesting that no important conformational change occurs in the inner coordination sphere in going from the solvate to the mono- and di-chloro complexes. The overall stability constants for R = Pr, Nd, and Sm are: $\beta_1 = 54$, 92, 80; $\beta_2 = 1.6\times10^3$, 5.2×10^3, 1.0×10^3, respectively. These values are consistent with a moderate R(III)/Cl^- interaction and reflect a stabilization of the chloro complexes with respect to methanolic solutions (cf. table 3). This spectroscopic study was performed in the presence of perchlorate and the perchlorate coordination was not taken into account in the calculation of the β's by Hamze et al. (1989). Therefore, the stability constants for the chloro complexes are underestimated. For instance, Bünzli and Kasparek (1991) calculated from FT-IR data $\log K_{Cl} = 2.6\pm0.7$ for the Er(III) monochloro complex in anhydrous acetonitrile, taking into account the formation of perchlorato complexes.

5.3.2. *Alcoholic solutions*

In order to determine the chemical environment of lanthanide cations in solution, Freed and his group (Sayre et al. 1957) investigated the spectral properties of selected lanthanides in crystals, aqueous and anhydrous media. For anhydrous europium chloride, a C_{2v} local symmetry was evidenced in methanol and ethanol. Lowering of the symmetry of the ionic environment from D_{2h} in water to C_{2v} in alcohol was interpreted in terms of the presence of associated anions in the alcoholic solutions (Sayre et al. 1957). The

Table 3
Overall stability constants for the formation of lanthanide chloro- and bromo-complexes in anhydrous methanol, ethanol, and propanol, as determined by spectrophotometry

X/R	$\beta(RX^{2+})$	$\beta(RX_2^+)$	Conditions		Ref.
			T (°C)	solution	
Methanol					
Cl–La	1500±200	–	23		1[a]
Cl–Pr	5.4	4.4		$LiClO_4$ 4 M	2
	7.10±0.30	–	25	$LiClO_4$ 3 M	3
Cl–Nd	16.8	26.8		$LiClO_4$ 4 M	2
	8.35±0.25	–	25	$LiClO_4$ 3 M	3
	63±1	100±2		Isomolar mixtures of LiCl and $LiClO_4$ (0.5 M)	4
Cl–Sm	13.0	35		$LiClO_4$ 4 M	2
	9.16±0.24	–	25	$LiClO_4$ 3 M	3
Cl–Ho	6.60±0.20	–	25	$LiClO_4$ 3 M	3
Cl–Er	5.15±0.20	–	25	$LiClO_4$ 3 M	3
Ethanol					
Cl–Ho	8.65±0.55	–	25	$LiClO_4$ 3 M	5
Cl–Er	6.16±0.55	–	25	$LiClO_4$ 3 M	5
n-Propanol					
Cl–Pr	298±15	–	25	$LiClO_4$ 1 M	6
	288±14	–	25	$LiClO_4$ 1 M	7
Cl–Nd	10.8±14.9	–	25	$LiClO_4$ 1 M	6
Cl–Ho	12.37±0.62	–	25	$LiClO_4$ 1 M	6
Cl–Er	4.32±0.22	–	25	$LiClO_4$ 1 M	6
Methanol[b]					
Br–Pr	1.33±0.30	–	25	$LiClO_4$ 3 M	8
Br–Nd	1.55±0.22	–	25	$LiClO_4$ 3 M	8
Br–Sm	1.87±0.25	–	25	$LiClO_4$ 3 M	8
Br–Ho	0.97±0.14	–	25	$LiClO_4$ 3 M	8
Br–Er	0.70±0.15	–	25	$LiClO_4$ 3 M	8
Methanol[c]					
Br–Pr	4.84±0.90	–	25	$LiClO_4$ 3 M	8
Br–Er	3.30±0.30	–	25	$LiClO_4$ 3 M	8
n-Propanol					
Br–Pr	9.50±0.48	–	25	$LiClO_4$ 1 M	6
Br–Nd	4.30±0.22	–	25	$LiClO_4$ 1 M	6
Br–Ho	17.50±0.88	–	25	$LiClO_4$ 1 M	6
Br–Er	9.06±0.45	–	25	$LiClO_4$ 1 M	6

continued on next page

Table 3, notes

[a] By ^{139}La-NMR spectroscopy. [b] Aqueous methanol, 50% water. [c] Aqueous methanol, 10% water.

References

(1) Bünzli et al. (1987)
(2) Hamze et al. (1986)
(3) Kozachenko and Batyaev (1971a)
(4) Zholdakov et al. (1971)
(5) Kozachenko and Batyaev (1971b)
(6) Krutous and Batyaev (1974)
(7) Krutous and Batyaev (1973)
(8) Kozachenko et al. (1973)

formation of chloro complexes in anhydrous alcoholic solutions was later confirmed by several authors.

5.3.2.1. *Methanol.* Solutions of $LaCl_3$ 1.95 M in methanol were studied by X-ray diffraction and ^{139}La and ^{35}Cl NMR spectroscopy (Smith et al. 1976). The analysis of the first two peaks in the atomic radial distribution function (ARDF) allowed the authors to evaluate the average number of La–O and La–Cl interactions per La(III) ion. These amount to $n_{La-O} = 5.0 \pm 0.2$ and $n_{La-Cl} = 3.0 \pm 0.1$. The average inner coordination sphere complex appears to be the 8-coordinate species $[LaCl_3(CH_3OH)_5]$, with La–O and La–Cl distances of 2.48 Å and 2.95 Å, respectively. However, long-range interactions in the ARDF between 3.9 and 6.7 Å were interpreted as reflecting the presence of a pseudo-cubic, dichloro-bridged species $[La_2Cl_4(CH_3OH)_{10}]^{2+}$ as the average solute species. The NMR data confirm the inner-sphere La–Cl interaction and indicate that the solvates undergo rapid exchange reactions. Anhydrous solutions of $NdCl_3$ 1.95 M in methanol were also investigated by X-ray diffraction (Steel and Wertz 1977). The Nd(III) ion is, on average, 8-coordinate, $[NdCl_2(CH_3OH)_6]^+$ being the average inner coordination sphere complex. The mean Nd–O and Nd–Cl bonding distances are 2.41 Å and 2.78 Å, respectively, while the ion-pair Nd···Cl distance is ca. 4.9 Å. Somewhat different conclusions are drawn from electron spin echo modulation studies carried out for Nd(III) 0.005 M in methanol glasses at 4.2 K. By using partially deuterated methanols Janakiraman and Kevan (1981) found that Nd(III) is coordinated by nine equivalent methanol molecules with distances Nd–H(OH) of 3.1 Å and Nd–H(CH3) of 4.0 Å. According to this analysis, a Nd–Cl interaction is precluded in this highly diluted medium, which is not in contradiction with the X-ray diffraction study, since the stability of the chloro complexes is rather small.

Available stability constants for the formation of various chloro complexes in anhydrous methanol are reported in table 3. Kozachenko and Batyaev (1971a) investigated the inner- and outer-sphere chloride complex formation in absolute and aqueous methanol for all the lanthanides which have absorption bands in the UV and visible parts of the spectrum. Stability constant data for absolute methanol reveal a slight increase in the degree of complex formation in the series Pr–Nd–Sm, followed by a decrease for the heavier lanthanide ions, Ho and Er. The stability constants are approximately three times larger than in 50% methanol and 8–9 times larger than in water. The estimated β_1's (± 0.1) amount to 0.71 (Nd), 0.82 (Nd), 1.24 (Sm), 0.50 (Ho), and 0.47 (Er).

More recently, Hamze et al. (1986) demonstrated the formation of weak chloro complexes for Pr, Nd, and Sm 0.038–0.09 M in anhydrous methanol with the help of

a numerical treatment of several thousand experimental absorbances covering the absorption ranges from UV to near-IR. The bathochromic shifts produced by an increase in chloride-ion concentration, observed for all electronic transitions, are interpreted as reflecting the formation of two chloro complexes. Individual electronic spectra are calculated for these complexes and point to similar structures for the solvates and mono- and di-chloro complexes.

In all these experiments, the supporting electrolyte was $LiClO_4$ 3–4 M, but perchlorate coordination was disregarded in the calculation of the overall stability constants. On the other hand, Zholdakov et al. (1971) have calculated the stability constants for $[NdCl(CH_3OH)_x]^{2+}$ and $[NdCl_2(CH_3OH)_y]^{+}$ complexes, taking into account the possibility of perchlorate association on the metal ion: $K_1 = 63$ and $K_2 = 100\ M^{-1}$. These constants are ~3.7 times larger compared to those reported by Hamze et al. (1986), but they are in excellent agreement with the relative stability constant $K_{Cl/ClO_4} = 3.82$ obtained by Bünzli et al. (1987) for La(III) in anhydrous methanol with the help of ^{139}La NMR spectroscopy. Using the Nd data of Zholdakov et al. (1971), a calculation for a 0.005 M solution indicates that 42% of the metal remain uncomplexed by chloride, while 28 and 30% are split between mono- and di-chloro complexes, respectively. Assuming a coordination number of 9 for the solvate (*vide supra*) and 8 (or 9) for the chloro complexes, $\bar{n} = 7.5$ (or 8.1) methanol molecules would be coordinated, on average, to the metal ion. In the interpretation given by Janakiraman and Kevan (1981) for the spin echo measurements, the authors mention that the fit for $\bar{n} = 9$ is somewhat better than for $\bar{n} = 8$ or 10. Since the fit involved two other parameters ($r_{Nd-H(OH)}$ and the hyperfine coupling constant α) and since contributions from alcohol molecules in the outer shell cannot be completely neglected, it is understandable that the Nd–Cl interaction has neither been evidenced nor taken into account. Nevertheless, data obtained with widely different techniques, namely spectrophotometry, X-ray diffraction, and electron paramagnetic resonance, and gathered under rather different experimental conditions, point to a coherent overall picture, with a weak lanthanide–chloride interaction in methanol and a coordination number of the solvate and chloro complexes ranging between 8 and 9.

The interaction between bromide and lanthanide ions was also studied, but experimental data are available for aqueous methanol solutions only (Kozachenko et al. 1973). Using a spectrophotometric method, the formation of rather weak outer-sphere bromo complexes was evidenced, and their stability constants for Pr, Nd, Sm, and Ho were determined in water and in 50% and 90% methanol (table 3). For solutions in 50% methanol, the stability of the outer-sphere bromo complexes is larger for Pr, Nd, and Sm ($K_1 = 1.3$–1.9) compared to Ho (0.97) and Er (0.70). Kozachenko et al. (1973) explained this behaviour as reflecting a higher stability for the solvates of the heavier lanthanide ions. A similar trend was observed in the stability constants of the chloro complexes in absolute methanol (*vide supra*). Finally, the stability of the bromo complexes of the lanthanides increases as the dielectric constant of the medium is reduced.

The interaction between Cl^-, Br^-, NCS^- and trivalent cerium has been studied in anhydrous methanol by analyzing the interconfiguration transitions $4f^{n-1}5d \leftrightarrow 4f^n$. Inner-

sphere mono complexes are predominant in the concentration range 10^{-4} to 10^{-2} M (Svetashev and Tsvirko 1991).

5.3.2.2. *Ethanol.* Kozachenko and Batyaev (1971b) studied the inner- and outer-sphere lanthanide complex formation (R = Pr, Nd, Sm, Eu, Ho, and Er) with chloride ions at a constant ionic strength ($LiClO_4$ 3 M) in aqueous and absolute ethanol. The stability constants for the formation of the $[RCl(C_2H_5OH)_x]^{2+}$ could be calculated for Ho and Er (table 3). They are similar to those found for methanolic solutions. The symmetry of the hexachloro-europate(III) anion in anhydrous ethanol has been investigated by magnetic circular dichroism measurements (Görller-Walrand et al. 1982). The authors concluded to the presence of an 8-coordinate species with pseudo-D2 symmetry, $[EuCl_6(EtOH)_2]^{3-}$.

5.3.2.3. *Propanol.* The formation of Pr and Nd chloro complexes in anhydrous *n*-propyl alcohol has been investigated spectrophotometrically by Krutous and Batyaev (1973), who interpret their data assuming the presence of monochloro complexes only. The increase of the overall stability constant of the Pr complex with decreasing ionic strength has been determined in the presence of both lithium perchlorate and chloride using the UV portion of the spectrum. With LiCl as supporting electrolyte, extrapolation to zero ionic strength yields $\log K_1(I=0) = 4.3 \pm 3.1$ for Pr ($0.3–1.6 \times 10^{-3}$ M), while $\log \beta_1$, estimated from an analysis of the f–f transitions, ranges between 0.4 ± 1.1 and 0.65 ± 1.4. Thermodynamic parameters were tentatively estimated from the temperature dependence of K_1 to be: $\Delta H^0_{298} = 11.5\ \text{kJ mol}^{-1}$ and $\Delta S^0_{298} = 71\ \text{J K}^{-1}\ \text{mol}^{-1}$. The Nd chloro complex has been less extensively studied; $\log K_1$ is smaller, ranging between 0.7 ± 1.30 (I(LiCl) = 6.6) and 1.8 ± 0.5 (I(LiCl) = 0.8).

The interaction between Pr, Nd, Ho, and Er with chloride, bromide and nitrate ions in *n*-propanol was spectrophotometrically studied by Krutous and Batyaev (1974) at 25°C and constant ionic strength equal to 1 ($LiClO_4$). The stability constants of the rare-earth complexes (table 3) are larger than in both ethanol and methanol, in good agreement with the decrease in the dielectric constant of the medium (20.1 at 25°C vs. 24.3 and 32.6, respectively) and the decrease in the dipole moment, 1.64 for the *n*-propanol molecule, as compared to 1.69 and 1.70 for ethanol and methanol, respectively. It is noteworthy that the changes in the stability constants for different anions and lanthanides do not show regular trends. This may be explained by two different factors: (i) the use of concentrations instead of the activity values, and (ii) the R–ClO_4^- interaction, which is not taken into account.

5.3.3. *Solutions in DMF, DMA and DMSO*

5.3.3.1. *N, N-dimethylformamide (DMF).* The complexation of rare-earth ions (R = La–Lu) by chloride has been studied in DMF by titration calorimetry at 25°C in the presence of 0.2 M Et_4NClO_4 (Ishiguro and Takahashi 1991). The formation of $[RCl]^{2+}$, $[RCl_2]^{+}$, $[RCl_3]$ and $[RCl_4]^{-}$ complexes has been evidenced for all the metal ions, except La for which the $[LaCl]_4^-$ complex hardly forms (table 4). A small but sizable ionic medium

Table 4
Stability constants for the formation of $[RX_n]^{(3-n)+}$ complexes ($X = Cl^-$, Br^-) in DMF containing 0.2 M Et_4NClO_4, at 25°C, as determined by titration calorimetry; $[R]_t$ between 0.003 and 0.03 M. Uncertainties refer to three standard deviations

R	$\log K_1$	$\log K_2$	$\log K_3$	$\log K_4$	Ref.
R/Cl⁻ (inner-sphere)					
Y	2.3±0.2	2.1±0.2	1.4±0.3	1.1±0.2	1
La	3.04±0.06	2.15±0.08	0.43±0.16	–	2
Ce	3.25±0.09	2.16±0.08	1.36±0.13	0.24±0.29	
Pr	3.25±0.09	2.13±0.09	1.42±0.14	0.49±0.14	2
Nd	3.26±0.10	2.01±0.09	1.35±0.13	0.63±0.12	2
Sm	3.00±0.11	1.89±0.10	1.50±0.13	0.95±0.09	2
Eu	3.15±0.23	2.05±0.15	1.66±0.17	1.03±0.10	2
Gd	2.80±0.13	1.97±0.12	1.44±0.18	1.11±0.13	2
Tb	2.63±0.16	2.17±0.14	1.38±0.20	1.34±0.15	2
Dy	2.57±0.11	2.19±0.11	1.46±0.13	1.43±0.08	2
Ho	2.61±0.21	2.39±0.19	1.63±0.21	1.46±0.16	2
Er	2.47±0.2	2.42±0.20	1.81±0.10	1.41±0.09	2
Tm	2.57±0.2	2.76±0.15	2.04±0.10	1.55±0.06	2
Yb	2.70±0.2	2.61±0.18	2.35±0.13	1.73±0.05	2
Lu	2.82±0.2	2.48±0.15	2.41±0.11	1.71±0.06	2
R/Br⁻ (outer-sphere)					
Y	1.8±0.4	–	–	–	1
La	1.4±0.2	0.4±0.3	–	–	1
Nd	1.6±0.3	0.5±0.3	–	–	1
Tb	1.6±0.5	1.0±0.4	–	–	1
Tm	2.1±0.4	–	–	–	1

References
(1) Takahashi and Ishiguro (1991) (2) Ishiguro and Takahashi (1991)

effect was found when the concentration of the supporting electrolyte was varied over the range 0.1–0.4 M, suggesting that R(III) ions form solvent-separated ion pairs with perchlorate ions. The species distributions calculated by using the stepwise formation constants show that $[LaCl]^{2+}$ and $[LaCl_2]^+$ form extensively, but $[LaCl_3]$ does not. For Ce, Pr and Nd (cf. fig. 6) the $[RCl_3]$ complex also forms extensively, but the concentration of $[RCl_4]^-$ remains small. With the intermediate ions Sm–Er, formation of $[RCl]^{2+}$ is gradually suppressed, while that of $[RCl_4]^-$ is gradually enhanced: $\log K_4$ increases from 0.24 for Ce to about 1.7 for Yb and Lu. The same authors (Takahashi and Ishiguro 1991) have also studied the formation of bromo- and iodo-complexes of Y(III), La(III), Nd(III), Tb(III), and Tm(III). Bromide forms monobromo and dibromo inner-sphere complexes only (table 4). The corresponding $\log K_n$ values are smaller than for the

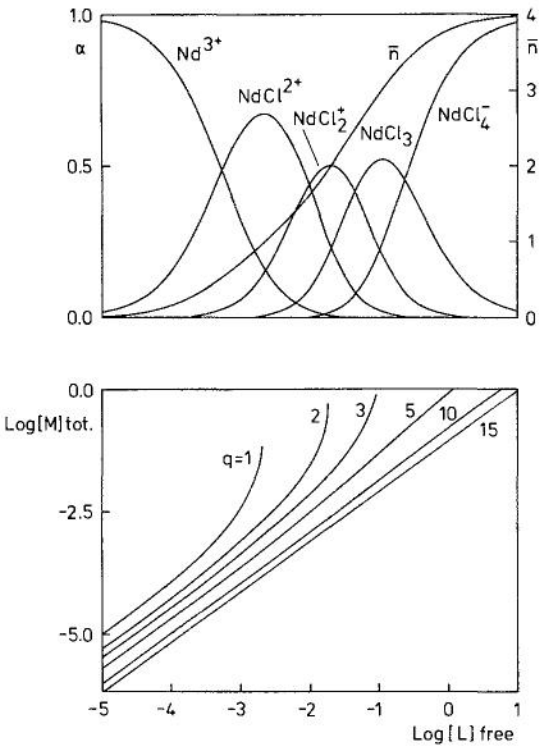

Fig. 6. Distribution curves $\alpha_j = f(\log [L])$ and $\bar{n}$ and $\log T_R = f(\log [L])$ for various values of $q = T_L/T_R$ for the Nd^{3+}–Cl-system in DMF.

chloro complexes, as expected. The stepwise formation constant could not be determined for iodide complexation since the enthalpies of reaction were very small (but surprisingly negative).

The large and positive enthalpy and entropy values (table 5) reflect the formation of inner-sphere chloro-complexes for all the R(III) ions, with displacement of solvated DMF molecules. The ΔH_1^0 and ΔS_1^0 values decrease with atomic number for La–Nd, while they gradually increase again between Sm and Er. For Tm, Yb, and Lu, the ΔH_1^0 and ΔS_1^0 values are large and similar. The variation of $T\Delta S_1^0$ along the R(III) series is similar to that of ΔH_1^0, i.e. $T\Delta S_1^0$ compensates ΔH_1^0. However, this compensation is not perfect: a linear $\Delta H_1^0/T\Delta S_1^0$ relationship is observed only for the lighter lanthanides (La–Nd). The variation of ΔH_1^0 and ΔS_1^0 along the series may be interpreted by taking into account the presence of two differently solvated species. Indeed, Pisaniello et al. (1983) and Cossy and Merbach (1988) have demonstrated by ^{1}H-NMR spectroscopy that the following equilibrium occurs for solutions of La, Ce, Pr and Nd perchlorates:

$$[R(DMF)_8]^{3+} + DMF \rightleftarrows [R(DMF)_9]^{3+}. \tag{36}$$

This equilibrium shifts to the right in the order La > Ce > Pr > Nd, and Ishiguro and Takahashi (1991) observed a systematic decrease in the ΔH_1^0 and ΔS_1^0 values for the

Table 5
Thermodynamic parameters ΔH_n^0 (kJ mol^{-1}) and ΔS_n^0 (J K^{-1} mol^{-1}) for the formation of $[RX_n]^{(3-n)+}$ complexes (X = Cl$^-$, Br$^-$) in DMF containing 0.2 M Et_4NClO_4, at 25°C, as determined by titration calorimetry; [R]$_t$ between 0.003 and 0.03 M

R^{3+}	ΔH_1^0	ΔH_2^0	ΔH_3^0	ΔH_4^0	ΔS_1^0	ΔS_2^0	ΔS_3^0	ΔS_4^0	Ref.
R/Cl⁻ (inner-sphere)									
Y	19±1	27±6	–	–	108±2	131±16	–	–	1
La	21.2±0.4	12.1±1.1	72.0±1.9	–	129±1	82±3	249±62	–	2
Ce	16.4±0.2	11.1±0.7	16±4	120±73	118±1	79±2	79±11	–	2
Pr	14.1±0.3	10.3±1.1	18±5	85±22	109±1	75±2	87±16	292±72	2
Nd	13.2±0.2	13.2±1.2	20±6	63±17	107±1	83±2	94±19	224±56	2
Sm	13.6±0.3	19.8±2.5	15±7	51±10	103±1	102±6	79±21	188±34	2
Eu	13.1±0.4	19.5±2.6	13±6	55±11	104±3	104±6	74±19	206±35	2
Gd	15.1±0.4	23.4±3.0	20±10	46±15	104±1	116±7	95±30	177±50	2
Tb	15.5±0.5	23.7±2.4	25±11	31±15	102±2	121±6	111±34	131±49	2
Dy	17.8±0.8	25.8±3.1	20±10	24±10	109±1	129±8	95±30	106±32	2
Ho	18.0±0.8	24.6±2.9	20±9	32±11	110±2	128±6	98±26	136±35	2
Er	22.2±1.4	24.2±3.6	21±6	35±7	122±2	127±1	106±20	145±24	2
Tm	27.4±2.0	16.6±2.8	21±4	20±3	141±4	109±7	108±12	98±12	2
Yb	25.8±1.5	22.4±3.4	14±4	31±2	138±2	125±9	92±13	137±9	2
Lu	26.8±1.0	21.9±2.8	17±4	23±2	144±2	121±7	104±11	109±8	2
R/Br⁻ (outer-sphere)									
Y	1.0±0.4	–	–	–	38±6	–	–	–	1
La	5±1	25±15	–	–	42.9±0.7	–	–	–	1
Nd	2.8±0.8	11±8	–	–	40±2	–	–	–	1
Tb	1.3±0.7	1±2	–	–	35±17	24±4	–	–	1
Tm	0.7±0.2	–	–	–	42±8	–	–	–	1

References
(1) Takahashi and Ishiguro (1991) (2) Ishiguro and Takahashi (1991)

monochloro complexes in the same sequence. Observed ΔH_1^0 and ΔS_1^0 values thus change depending on the equilibrium constant between the 8- and 9-coordinate solvates. As both ΔH_1^0 and ΔS_1^0 values for the above equilibrium are negative (–14.9 kJ mol^{-1} and –69 J K^{-1} mol^{-1} for Nd, Ishiguro and Takahashi 1991), the chloro complexation of $[R(DMF)_9]^{3+}$ will be more endothermic than that of $[R(DMF)_8]^{3+}$. This implies that the equilibrium is shifted to the right to a greater extent. For Sm–Lu the 8-coordinate species $[R(DMF)_8]^{3+}$ prevail in DMF solutions (Cossy and Merbach 1988). Thus, ΔS_1^0 values for Sm–Ho are practically the same, which is consistent with the unvarying geometries of the solvates. The ΔH_1^0 values increase gradually with Z, which suggests that metal–DMF bonds in $[R(DMF)_8]^{3+}$ are strengthened monotonically as the ionic radii of the R(III) ions decrease. Finally, Ishiguro and Takahashi (1991) explained the particularly large values

of ΔH_1^0 and ΔS_1^0 observed for Tm, Yb and Lu systems as being related to the solvent exchange mechanism. Cossy and Merbach (1988) have shown this mechanism to be of the interchange type for Tb, Dy, and Ho, while it is dissociative for Tm and Yb, with a cross-over occurring at erbium.

The variation of ΔH_2^0 with Z is significantly different, and a cross-over with ΔH_1^0 occurs: $\Delta H_1^0 > \Delta H_2^0$ for La–Pr and Tm–Lu, while the opposite is true for Sm–Ho. A similar entropy cross-over takes place, suggesting that the number of expelled solvent molecules varies with the nature of the R(III) ion. It is noteworthy that the overall $\Delta H_{\beta 4}^0$ and $\Delta S_{\beta 4}$ values for Sm–Lu are almost constant with average values of 95.3 kJ mol^{-1} and 476 J K^{-1} mol^{-1}, respectively. The $\Delta S_{\beta 4}$ value provides evidence for extensive desolvation of the R(III) ions and suggests that the geometry of the R(III) solvates varies substantially upon complexation.

The enthalpies of formation of the monobromo complexes of these metal ions are also positive, but smaller than those of the chloro complexes. They decrease smoothly in the order La > Nd > Tb > Tm. It is thus found that the formation enthalpies change in the sequence $\Delta H^0(\mathrm{Cl}) > \Delta H^0(\mathrm{Br}) > \Delta H^0(\mathrm{I})$, which would be unusual for hard metal(III) ions. This implies that, unlike the chloride ion, the bromide ion (and most certainly the iodide ion) forms outer-sphere complexes with the R(III) and Y(III) ions in DMF. The $\log K_1$, ΔH_1^0 and ΔS_1^0 values of the monochloro complex of Y(III) in DMF are close to those of Ho(III) and Er(III), as expected from their similar ionic radii. The $\log K_1$, ΔH_1^0 and ΔS_1^0 values for the monobromo complex of Y(III) are smaller than those of the monochloro complex, as in the case of lanthanide ions. Evidence for either an inner- or outer-sphere complex was obtained from ^{89}Y-NMR spectra for $Y(ClO_4)_3$, YCl_3, and YBr_3 in DMF at room temperature.

5.3.3.2. *N, N-dimethylacetamide (DMA).* By using incremental calorimetric titrations, Volpe et al. (1980) studied the formation of the inner-sphere complexes $[RCl]^{2+}$ and $[RCl_2]^+$ in DMA. The equilibrium constants K_1 and K_2 and the molar enthalpy changes ΔH_1 and ΔH_2 are reported in table 6. The variation of enthalpy is endothermic and suggests the formation of weakly bonded species in this medium. The $\log K$ and ΔH values present a break at gadolinium, which can be interpreted as being due to the electronic effects and the change in coordinating ability of the lanthanide. Airoldi et al. (1982) measured the formation constants and the respective variations of enthalpy for the La and Nd complexes with bromide. Thermochemical data were collected for the 1:1 and 1:2 species, which are less stable than the corresponding chlorospecies (table 6). The order of stability $Cl^- > Br^-$ was established for both La species, while the order is $Br^- > Cl^-$ for the 1:1 Nd complexes. Both $[NdCl_2]^+$ and $[NdBr_2]^+$ species were not detected. The authors interpret their results as reflecting the formation of inner-sphere complexes with both chloride and bromide.

5.3.3.3. *Dimethylsulfoxide (DMSO).* The solvation of the Pr ion in aqueous DMSO containing 0 to 100% DMSO and a constant $PrCl_3$ concentration of 0.0183 M has been

Table 6
Stability constants and ΔH_1 and ΔH_2 values for the formation of chloro- and bromo-complexes in DMA at 298 K

R	K_1 (mol^{-1} ℓ)	K_2 (mol^{-1} ℓ)	ΔH_1 ($kJ\,mol^{-1}$)	ΔH_2 ($kJ\,mol^{-1}$)	Ref.
R/Cl⁻					
Y	156±1	220±31	20.4±0.1	30.7±0.3	1
La	212±1	62±9	26.1±0.1	36.0±0.4	1
Ce	242±1	37±5	28.2±0.1	27.7±0.3	1
Pr	167±1	30±4	35.5±0.2	37.8±0.4	1
Nd[a]	58±1	–	24.1±0.1	–	1
Sm	109±1	21±3	25.9±0.1	18.9±0.2	1
Eu	81±1	50±7	23.4±0.1	21.5±0.2	1
Gd	17±1	51±9	13.2±0.1	–0.111±0.001	1
Tb	128±1	38±5	17.7±0.1	22.2±0.2	1
Dy	66±1	144±20	17.4±0.1	18.1±0.2	1
Ho	190±1	166±23	17.8±0.1	26.1±0.3	1
Er	205±1	57±8	9.9±0.1	9.5±0.1	1
Tm	284±1	232±33	22.1±0.1	35.9±0.4	1
Yb	221±1	1462±205	17.4±0.1	22.8±0.2	1
Lu	293±1	233±33	30.7±0.2	49.0±0.5	1
R/Br⁻					
La	165±1	48±7	32.6±0.2	45.6±0.4	2
Nd[a]	115±1	–	33.6±0.2	–	2

[a] The $[NdX_2]^+$ species could not be detected.

References
(1) Volpe et al. (1980) (2) Airoldi et al. (1982)

studied by electronic absorption spectroscopy (Borina 1988). As the DMSO concentration in the solution is raised, a shift is observed for all the Pr absorption bands towards longer wavelengths, together with an increase in their oscillator strength. This points to significant changes in the coordination environment of the Pr ion, which are interpreted as a gradual change from $[Pr(H_2O)_9]^{3+}$ to $[Pr(DMSO)_8]^{3+}$. No Pr–Cl interaction was evidenced. Luminescence lifetime measurements on Eu solutions (Tanaka et al. 1988) also point to a preferential solvation by DMSO over H_2O and chloride. X-ray diffraction measurements on 1 M $ErCl_3$ solutions in DMSO, carried out by Johansson et al. (1991), established the formation of inner-sphere chloride complexes, with about 1.3 chloride ions directly bonded to Er. The Er–Cl bond length is 2.57 Å and Er–O(DMSO) and Er–S(DMSO) distances are 2.36 and 3.45 Å, respectively. The total coordination number for the Er(III) ion is 6.5(3), which is lower than the value of 9 found in the nitrate solutions (*vide infra*).

5.4. *Interaction with thiocyanate*

The study of the molecular structure of thiocyanato complexes is interesting in view of the variety of coordinated forms and the occurrence of bridging structures. The ability of the thiocyanate ion to form complexes with d and f transition elements in a mono (M–NCS, M–SCN) or bidentate (M–NCS–M) coordination has been extensively investigated. In the majority of reported cases however, the NCS group is coordinated to the metal as a monodentate ligand.

Recently, De Paoli et al. (1993a,b) reported the crystal and molecular structure of the homologous complexes $R(NCS)_3(THF)_4$, in which the unusual dual behaviour of the NCS ligand is evidenced. The thiocyanate complexes $R(NCS)_3(THF)_4$ with R = Nd, Eu, and Er crystallize in the monoclinic space group $P2_1/a$, with a ranging from 19.279(9) Å for Nd to 18.980(9) Å for Er. (b, c, and β have almost constant values: $b = 8.11 \pm 0.01$ Å, $c = 17.68 \pm 0.05$ Å and $\beta = 111.0 \pm 0.03°$. The specific features of these complexes are the octa-coordination, their dimeric nature and the fact that the NCS groups are coordinated both as mono (R–NCS) and bidentate (R–NCS–R) ligands. The structural units assume an almost undistorted square antiprismatic coordination geometry, resulting from an association through NCS bridges of two $R(NCS)_3(THF)_4$ units. The R–N and R–O distances decrease regularly going from Nd to Er, according to the lanthanide contraction. The R–S distances range from 3.10 Å (Nd) to 3.26 Å (Er) and correspond to rather weak bond interactions. For Ln = Yb, a monomeric complex is obtained. The coordination geometry of the metal ion consists of a slightly distorted pentagonal bipyramid in which two nitrogen atoms are in the apical positions and four oxygen atoms from the THF molecules as well as one nitrogen atom from a NCS anion lie in the equatorial plane.

The interaction between lanthanide and thiocyanate ions has been investigated most in aqueous solution and very few data about anhydrous solutions are available. Takahashi and Ishiguro (1992) reported the formation of thiocyanato complexes of Y(III) and R(III) (R = La, Nd, Tb, Ho, Tm, Yb) ions in N, N-dimethylformamide containing 0.2 M $(C_2H_5)_4NClO_4$ at 25°C, using calorimetry, ^{89}Y-NMR and Raman spectroscopy. The data are satisfactorily explained in terms of the formation of a series of mononuclear $[R(NCS)_n]^{(3-n)+}$ complexes, the formation constants, reaction enthalpies and entropies of which were determined. The $\log K_1$ values for the formation of $[R(NCS)]^{2+}$ complexes (~ 1.5–1.8 $\ell\,mol^{-1}$) do not significantly differ from one metal ion to the other. Furthermore, the ΔH_1^0 (~ 7.4–9 kJ mol^{-1}) and ΔS_1^0 (~ 57–66 J mol^{-1} K^{-1}) parameters are also virtually independent of the metal ion. The ΔH_1^0 value is positive, and much smaller than that of the analogous $[RCl]^{2+}$ complexes, but slightly larger than that of the $[RBr]^{2+}$ complexes (cf. sect. 5.3.3.). In general the following relationship holds: $\Delta H_1^0(Cl) \gg \Delta H_1^0(NCS) > \Delta H_1^0(Br)$. The thermodynamic parameters of the thiocyanato complexes are rather similar to those of the bromo complexes, which are outer-sphere complexes in anhydrous DMF. However, ^{89}Y-NMR spectra suggest that the thiocyanate ion is bonded in the Y(III) inner coordination sphere.

When the NCS^- ion behaves as a bidentate ligand, the CS vibration band shifts to a higher or lower frequency relative to that of the free (solvated) NCS^- ion upon coordi-

nation through the N or S end, respectively. With lanthanide ions, this band is always shifted to a higher frequency, indicating that the NCS^- ion binds to the metal ion through its N end. The magnitude of the shift becomes larger with increasing atomic number, as expected for an electrostatic R(III)–NCS^- interaction. The near constancy of the thermodynamic parameters for the various thiocyanato complexes arises from the fact that the N end of the NCS^- ion is relatively small and thus practically no geometry change occurs along the lanthanide series. The CS stretching vibrational band of NCS^- bound to La(III), Ce(III), Tm(III), Yb(III) and Lu(III) ions is resolved into two Lorentzian components, suggesting that a solvation equilibrium is established in these metal systems, i.e. the solutions contain two distinct species differing in the number of coordinated solvent molecules.

Inner-sphere complexation between Ce(III) and thiocyanate ions has also been evidenced by absorption and luminescence measurements of anhydrous alcoholic solutions (Svetashev and Tsvirko 1991), while Buslaev et al. (1980) have shown that the shifts of the ^{45}Sc-NMR signals of $Sc(NCS)_3$ solutions in acetonitrile depend linearly on the number of NCS^- bonded to the metal ion.

5.5. *Interaction with nitrate*

Nitrate is an effective coordinating anion and it interacts strongly with the hard R(III) cations, even in water. This was demonstrated as early as 1928 by Quill and colleagues who found that absorption spectra of several R(III) ions undergo substantial modifications upon addition of nitric acid (Quill et al. 1928). Luminescence spectra and lifetimes also clearly point to inner-sphere complexation in water (Bünzli and Yersin 1979). The complexation between rare-earth and nitrate ions has been studied in several solvents (mostly mixed solvents) by various experimental techniques.

5.5.1. *Solutions in acetonitrile*

The lanthanide–nitrate interaction in anhydrous acetonitrile was investigated by means of conductimetry, vibrational spectroscopy, and luminescence measurements which are very sensitive to changes in the first solvation sphere of the metal ion (Bünzli and Choppin 1989). Conductimetric data on 0.0001–0.01 M solutions of europium or terbium trinitrate in anhydrous acetonitrile indicate that no dissociation occurs. The vibrational spectra show the presence of coordinated acetonitrile and the nitrato group frequencies are consistent with bidentate anions of approximate C_{2v} local symmetry (Bünzli et al. 1978). When the concentration of nitrate is increased, the formation of $[R(NO_3)_n]^{(3-n)+}$ species ($n > 3$) is clearly evidenced in the FT-IR spectra (Mabillard 1983). The coordination numbers determined for Nd, Eu, Tb and Er in solutions containing an excess of nitrate are constant (9.9 ± 0.3) and correspond to the formation of pentanitrato $[R(NO_3)_5]^{2-}$ species, in which the nitrate ions are bonded in a bidentate fashion and which do not contain any coordinated acetonitrile molecule. The strong nitrate/europium interaction is evidenced when water is added to acetonitrile solutions of europium trinitrate. The first two acetonitrile molecules are quantitatively replaced by water molecules, but the replacement of the remaining solvent molecules is difficult to achieve and requires

$R_{H_2O} = [H_2O]_t/[R]_t = 8$. FT-IR difference spectra of solutions with $R_{H_2O} = 18$ show that all the nitrato groups are still coordinated. The apparent equilibrium ratios K_n for the following equilibria:

$$[R(NO_3)_{n-1}]^{(4-n)+}_{solv} + NO_3^- \rightleftarrows [R(NO_3)_n]^{(3-n)+}_{solv} \tag{37}$$

have been estimated for Eu(III). The values found are $K_1 = 23\pm3$, 15 ± 5 and $5\pm1\ M^{-1}$ for $R_{H_2O} = 44$, 94 and 304, respectively, while $K_2 = 17$ and $10\ M^{-1}$ for $R_{H_2O} = 44$ and 94, respectively (Bünzli and Yersin 1984).

Using FT-IR spectroscopy, Bünzli et al. (1993) investigated the lanthanide–nitrate interaction in anhydrous acetonitrile for selected light (La, Nd), intermediate (Sm, Eu, Gd, Tb, Dy) and heavy (Er, Yb) lanthanide cations. The mean coordination number of the R(III) ions and the structural properties of the various nitrato species were determined in the presence of an excess of nitrate. In all $R(NO_3)_3$ solutions, the nitrate ion is bonded in a bidentate fashion and displays C_{2v} local symmetry, as proved by Raman polarization studies. This leads to a splitting of the ν_3 and ν_4 vibration modes of ionic nitrate. The strength of the metal–nitrate interaction is best characterized by the splitting of the $\nu_3(E')$ mode: $\tilde{\nu}_1(A_1)$–$\tilde{\nu}_4(B_2)$. Most of the absorption bands assigned to nitrate vibrations contain at least two components which can be explained by the presence of inequivalent NO_3^- ions, e.g. coordinated at slightly different distances. Significant differences in this inequivalency are observed depending on the R(III) ions: the three nitrates are equivalent for La and Yb, while one of the nitrates is different from the two others for the Eu ion (Mabillard 1983). Since the ν_1 vibration band could not be mathematically decomposed, the $\tilde{\nu}_1$–$\tilde{\nu}_4$ splittings have been determined from the experimental data. Two splittings have been defined for each ion. They are based on the two main components of ν_1 and ν_4, defined with respect to the ν_3 vibration of the free nitrate ion: the smaller ("internal") splitting corresponds to nitrates interacting more weakly (i.e. with longer R–NO_3^- distances) while the larger ("external") is related to nitrates interacting more strongly (i.e. with shorter R–NO_3^-distances). The average $\tilde{\nu}_1$(ext)–$\tilde{\nu}_4$(ext) and $\tilde{\nu}_1$(int)–$\tilde{\nu}_4$(int) splittings amount to 230 ± 4 and $193\pm13\ cm^{-1}$, respectively, and are both well within the range accepted for bidentate coordination. They point to a rather strong R–nitrate interaction in anhydrous acetonitrile solutions.

When increasing amounts of $AgNO_3$ are added to anhydrous solutions of lanthanide perchlorates, the quantitative formation of successive $[R(NO_3)_n]^{(3-n)+}$ species ($n = 1$–5) is evidenced by the FT-IR spectra. The nitrate vibrations ν_2, ν_4, and ν_6 undergo a hypsochromic shift as $R_{NO_3^-} = [NO_3^-]_t/[R]_t$ increases, while ν_1 and ν_3 experience a bathochromic shift. Depending upon the R ion and the ratio $R_{NO_3^-}$, some of the vibrational modes are split into 2–3 components. It is noteworthy that for $R_{NO_3^-} = 5$, the absorption bands of the bonded NO_3^- ions are symmetrical and, therefore, comprised of one component only. For the La and Yb ions, the $\tilde{\nu}_1$–$\tilde{\nu}_4$ splitting decreases with increasing R_{NO_3}'s, which may be interpreted as reflecting the lengthening in the lanthanide–nitrate distances, when more nitrate ions are coordinated. Moreover, the increase in the mean $\tilde{\nu}_1$–$\tilde{\nu}_4$ splitting vs. Z, points to an increased R(III)–nitrate interaction with increasing electron

density of the metal ion. Finally, the addition of an excess of nitrate leads to the formation of ten-coordinated species $[R(NO_3)_5]^{2-}$ exclusively, regardless of the lanthanide ion. No hexanitrato species is observed, even for La. There is no decrease in CN for heavier ions, which is consistent with observations made for solid pentanitrates.

5.5.2. *Solutions in alcohols*

The lanthanum–nitrate interaction was studied in anhydrous methanol by ^{139}La NMR (Bünzli et al. 1987), but the absolute stability constants could not be evaluated. The interaction with neodymium, europium and erbium was investigated by UV–VIS spectroscopy in aqueous methanol by Silber et al. (1990) and Silber and Strozier (1987). Stability constants, as well as thermodynamic parameters were calculated. Table 7 lists the stability constants available for solutions with a low water content.

In aqueous methanol, Eu(III) forms $[Eu(NO_3)]^{2+}$, $[Eu(NO_3)_2]^{+}$ and $[Eu(NO_3)_3]$ solvated complexes (Silber and Strozier 1987). As the water mole fraction increases, the magnitude of each of the equilibrium constant decreases. In water, the *tris*-complex is not present. Under the same experimental conditions, the stoichiometries of the nitrate complexes are different for Nd(III) and Er(III) compared to Eu(III) (Silber et al. 1990). These differences persist as the solvent composition is varied. At low water mole fractions, Eu(III) and Er(III) form complexes up to the *tris* complex, whereas Nd(III) forms complexes up to the dinitrato compound only. Analyzing both the equilibrium and ultrasonic data, Silber et al. (1990) predict which complexation step causes a change in the coordination number. For Er(III), the ultrasonic maximum occurs around a water mole fraction $x = 0.4$, which is the solvent composition where the *tris* complex starts to appear; henceforth, the addition of the third nitrate to the inner coordination sphere of Er(III) induces a reduction in the coordination number. For Nd(III), the coordination number changes as the *bis* complex forms. The ultrasonic maximum for Eu(III) does not correspond to any change in the complex stoichiometry, so that the change in coordination number for this cation occurs with all the nitrato complexes. The enthalpy and entropy of complexation show major differences between Nd(III) and other lanthanides, which is explained by the extent of the outer-sphere complexes present for Nd(III). These equilibrium studies demonstrate that, under the same reaction conditions, different lanthanide–ligand interactions may occur within the lanthanide series. The extent of inner- versus outer-sphere complexation also creates differences in the complexation thermodynamics. Using the latter data, one can explain which ligand causes a sufficient steric crowding in the inner solvation shell to lead to a reduction of the coordination number. Silber et al. (1990) also found that the effect of the weak perchlorate interaction on the stability constants of the nitrato complexes is negligible at $x = 0.26$: the equilibrium constants determined in the presence and in absence of added perchlorate are within experimental error. We note however that in anhydrous methanol at 23°C, Bünzli et al. (1987) determined a relative stability constant equal to $K_{NO_3^-/ClO_4^-} = 13.2$ for La(III).

The formation of nitrato complexes by Pr, Nd, Ho and Er has been studied in *n*-propanol at 25°C and constant ionic strength (1 M lithium perchlorate) by a spectrophotometric

Table 7
Stability constants of lanthanide–nitrate complexes in various organic solvents

R	Solvent[a]	Conditions			K_1	K_2	K_3	Ref.
		T (°C)	I	electrolyte				
Methanol[a]								
Nd	$x_w = 0.04$	25	3.0	$NaNO_3$, KNO_3	83.12±1.4	5.56±1.0	–	1
Eu	$x_w = 0.01$	25	3.0	$NaClO_4$	168.4±14.8	114.6±5.2	41.1±3.6	2
Er	$x_w = 0.13$	25	3.0	$NaNO_3$, KNO_3	110.15±15.05	40.83±5.59	12.27±1.40	1
n-Propanol								
Pr		25	1.0	$LiClO_4$	1.24–3.57	–	–	3
Nd		25	1.0	$LiClO_4$	3.13–8.54	–	–	3
Ho		25	1.0	$LiClO_4$	2.29	–	–	3
Er		25	1.0	$LiClO_4$	3.76	–	–	3
N, N-Dimethylacetamide								
La		25			17±1	16±2	–	4
Nd		25			25±1	92±13	–	4

[a] x_w is the water mole fraction; the data for other water mole fractions and other temperatures are available in the given references.

References

(1) Silber et al. (1990)
(2) Silber and Strozier (1987)
(3) Krutous and Batyaev (1974)
(4) Airoldi et al. (1982)

method (Krutous and Batyaev 1974). The stability constants of the mononitrato complexes have been calculated from the shifts of the absorption bands, from the change in their intensity maxima, or from the change in the band area (table 7). As the nitrate ion absorbs in the UV region, the stability constants were determined using the f–f transitions in the visible part of the spectra.

5.5.3. *Solutions in water–acetone and water–methanol*

The extent of inner-sphere complexation between nitrate and lanthanide ions has been recently determined by ^{15}N-NMR spectroscopy in various aqueous mixtures, such as water–acetone and water–methanol containing dichlorodifluoromethane (Freon-12) for R = Ce (Fratiello et al. 1992b), Pr (Fratiello et al. 1993), Nd (Fratiello et al. 1992a), and Er (Fratiello et al. 1991). In the temperature range –95°C to –110°C, the ligand exchange is slow enough to enable the direct observation of distinct ^{15}N signals for nitrate ions in the R^{3+} solvation shell and in the bulk medium (fig. 7). For erbium in water–acetone mixtures, ^{15}N signals are observed at low nitrate to Er^{3+} mole ratios for both the mono- and dinitrato complexes, but only the *bis* complex forms at higher anion concentrations. No spectral evidence for the *tris* complex was seen at any nitrate concentration. In water–

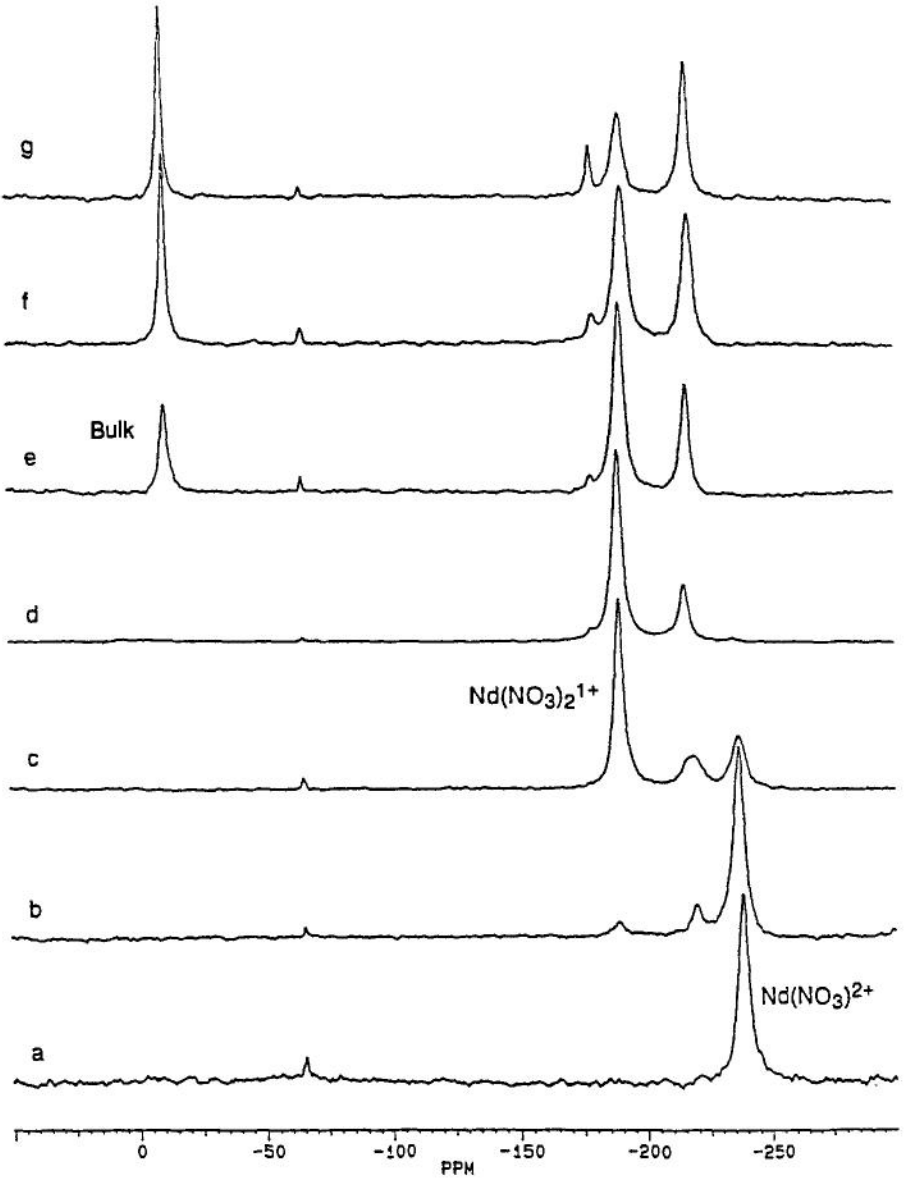

Fig. 7. The ^{15}N-NMR spectra of Nd salts containing enriched $Na^{15}NO_3$ in 1:20:7, water:acetone:Freon-12 mixtures, recorded at −110°C. The samples contained (a) 0.50, (b) 1.0, (c) 2.0 and (d) 3.0 moles of $Na^{15}NO_3$ per mole of $Nd(NO_3)_3$. The small peak at −65 ppm is assigned to nitrogen gas. The spectra are not reproduced to scale (Fratiello et al. 1992b).

methanol–acetone mixtures, signals for the mono- and dinitrato complexes persist even at higher nitrate concentrations, indicating a reduced tendency to inner-sphere complexation

with increasing dielectric constant. For cerium in water–acetone–Freon-12 mixtures and for mole ratios up to 3:1, $[Ce(NO_3)]^{2+}$ and $[Ce(NO_3)_2]^{+}$ are clearly preponderant, but one or more higher-order species are also present in small amounts. The nitrato complexes do not form consecutively and at higher nitrate to cerium mole ratios (>8) Fratiello et al. conclude to the presence of tetranitrato with either penta- or hexanitrato species. Finally, for neodymium in aqueous mixtures with acetone and Freon-12, resonance signals for $[Nd(NO_3)]^{2+}$, $[Nd(NO_3)_2]^{+}$, and two higher complexes are observed. Signal areas indicate that the latter species are possibly a combination of the tetra-, penta- and hexanitrato complexes, but not the trinitrato. In all these systems, contact ion-pairing involves the nitrate ion exclusively, without competition from perchlorate or triflate ion.

A direct, low-temperature nitrogen-15 (^{15}N) NMR technique has also been applied to the study of inner-shell complex formation between Pr(III) and nitrate ion in aqueous solvent mixtures (Fratiello et al. 1993). In water–acetone–Freon-12 mixtures at 110°C to −115°C, four coordinated nitrate signals are generally observed, and a very small signal for an additional complex, or an isomer of one of the others, appears at the highest nitrate concentration. Signals for the mono- and dinitrato complexes are unambiguously identified, but with the exception of the trinitrato complex, several possible assignments exist for the remaining peaks.

To overcome excessive signal broadening due to viscosity, measurements in methanol and ethanol are possible only if triflate is used as starting salt. Coordinated nitrate signals in aqueous and anhydrous methanol are observed only for the mono- and dinitrato species, and signal areas indicate that at most two moles of nitrate per Pr(III) are complexed. A third signal is seen in the spectra of the ethanolic solution, and the presence of this higher complex was confirmed by area measurement of the fraction of bound nitrate. The extent of complex formation in these solvent systems is attributed to differences in the dielectric constants. A comparison of the complexing tendencies of Pr(III) with those of other lanthanide ions studied by this NMR method suggests the possibility of a change in coordination number across the lanthanide series.

5.5.4. *Solutions in DMF, DMA and DMSO*

5.5.4.1. *Dimethylformamide.* According to conductimetric measurements, europium or terbium nitrates are 2:1 (<0.02 M), or 1:1 (>0.02 M) electrolytes in DMF solutions (Bünzli and Yersin 1982, Bünzli and Vuckovic 1983). Krishnamurthy and Soundararajan (1966) also determined that the first solvation sphere contains one or two nitrato groups. Abrahamer and Marcus (1968) later deduced from the study of the absorption spectra that the R(III)/nitrate interaction in DMF was outer-sphere. Finally, using IR, Raman, and electronic absorption spectroscopic data Bünzli and Vuckovic (1984) concluded to inner-sphere R(III)/nitrate interaction in DMF solutions. Upon addition of nitrate, equilibria take place which involve mono-, di-, and possibly trinitrato complexes. For $[Nd(NO_3)_n]^{(3-n)+}$ and $n=1$, the apparent equilibrium ratio is estimated as $K_1 \approx 110 \pm 30\ M^{-1}$. A more complicated situation occurs for Eu(III) (Bünzli and Yersin 1982). Diluted solutions (0.05 M) contain at least three different solvates; the predominant

species is $[Eu(NO_3)_2(DMF)_y]^+$ (80% of the total Eu concentration) and this is more stable than $[Eu(NO_3)(DMF)_x]^{2+}$. The neutral complex $[Eu(NO_3)_3(DMF)_z]$ is also present, as inferred from a high-resolution analysis of the $^5D_0 \rightarrow {}^7F_0$ luminescence band. The average number of coordinated nitrate ions per europium ion, $\bar{n}$, could be determined thanks to a linear relationship between the intensity of the hypersensitive $^5D_0 \rightarrow {}^7F_2$ transition and this number. Its value is 1.8 for a 0.047 M solution.

5.5.4.2. *Dimethylacetamide.* The stability constants and enthalpy values for lanthanide–nitrate interactions in anhydrous DMA (R = La, Nd) have been determined by means of calorimetric titration (Airoldi et al. 1982). The experimental results support the existence of the inner-sphere mono- and dinitrato complexes with the following formation constants: $K_1 = 17$, $K_2 = 16$ for lanthanum and $K_1 = 25$, $K_2 = 92$ for neodymium (cf. table 7). The enthalpies of formation ΔH_1 (La: 48.2, Nd: 1.0 kJ mol^{-1}) and ΔH_2 (La: 23.1, Nd: 8.3 kJ mol^{-1}) are all endothermic, although rather small. Finally, mononitrato complexes appear to be less stable for both La(III) and Nd(III) ions compared to the corresponding chloro- and bromo complexes (cf. tables 6, 7).

5.5.4.3. *Dimethylsulfoxide.* Johansson et al. (1991) reported the structure of solvated Er(III) and Y(III) nitrates in dimethylsulfoxide. These measurements confirm that Er(III) and Y(III) form isostructural solvates in DMSO. Therefore, the intensity difference curve for two solutions of identical composition can be used to eliminate non-metal interactions and to derive precise information on the structure around the metal ions. Radial distribution functions for erbium and yttrium nitrate and chloride solutions in DMSO are shown in fig. 8. In 1 M nitrate solutions, each metal ion is coordinated to an average of about 1.5 nitrate ions and 6 DMSO molecules. The bonding of the nitrate ion is bidentate and probably slightly asymmetric with an M–O1 bond length of 2.38 Å and an M–O2 bond of 2.57 Å. In view of the standard deviations obtained in the least-squares refinement, however, the deviation from a symmetric arrangement is not significant. The Er(Y)–O(NO_3) bond length, 2.47 (2.46)Å, in solution is similar to 2.47 (2.43) Å for Er(Y)–O(NO_3) found in the crystalline phase (Aslanov et al. 1972a,b). The average R–O(DMSO) bond length of 2.31 Å is shorter than the average value of 2.47 Å for the R–O(NO_3) bonds. The overall coordination number for the Er(III) ion is close to 9, in agreement with the structure of crystalline $Er(NO_3)_3(DMSO)_3$ and with the data gathered in acetonitrile solution of erbium nitrate in presence of DMSO (Bünzli et al. 1990).

5.6. *Relative complexation ability of anions*

The results discussed above unequivocally demonstrate that in moderately dissociating solvents, such as acetonitrile or propylene carbonate, most anions are involved in inner-sphere coordination to rare earth ions, in particular perchlorate and triflate. In this section, we examine the data pertaining to the relative complexing abilities of various anions.

The relative complexation strength of chloride *versus* perchlorate has been determined for La, Nd, Eu and Er (Bünzli and Kasparek 1991). Tetraethylammonium chloride

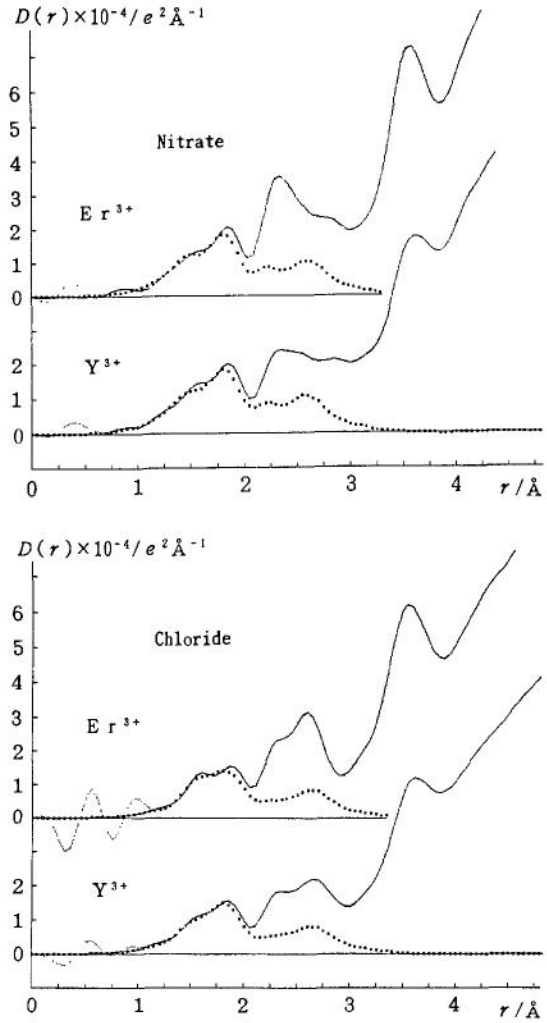

Fig. 8. Radial distribution functions $D(r)$ (solid lines), for the erbium and yttrium solutions. Dotted lines show the $D(r)$ functions before corrections for spurious peaks below ~1 Å. Theoretical values (dots) include contributions from intramolecular interactions in DMSO and nitrate ions (Johansson et al. 1991).

was added to perchlorate solutions in anhydrous acetonitrile and the concentration of uncoordinated perchlorate was determined by means of FT-IR spectrometry. As chloride is added, the concentration of free perchlorate increases. The quantitative data were interpreted using the following simplified model:

$$[R(ClO_4)_2(solv)]^+ + Cl^- \overset{K'_{Cl/ClO_4}}{\rightleftarrows} [RCl(ClO_4)(solv)]^+ + ClO_4^-, \tag{38}$$

$$[R(ClO_4)(solv)]^{2+} + Cl^- \overset{K_{Cl/ClO_4}}{\rightleftarrows} [RCl(solv)]^{2+} + ClO_4^-. \tag{39}$$

Equation (38) could be applied to La and Nd and equation (39) to Er. The $\log K'_{Cl/ClO_4}$ values are 1.1 ± 0.2 for La and 1.2 ± 0.2 for Nd, while $\log K_{Cl/ClO_4}$ amounts to 0.5 ± 0.3 for Er.

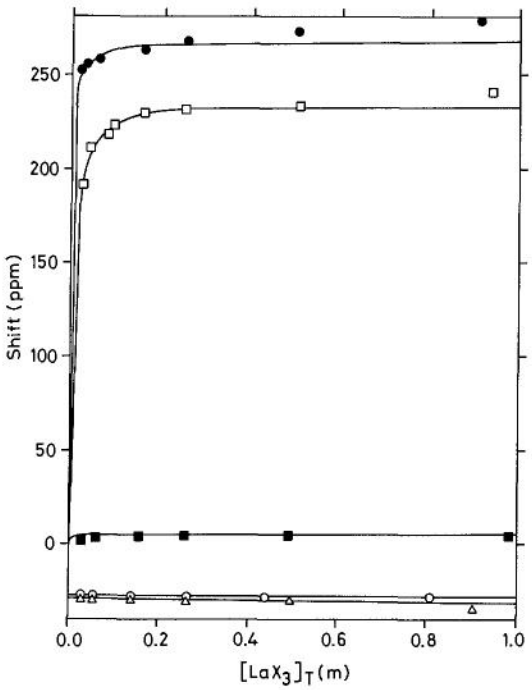

Fig. 9. ^{139}La NMR chemical shifts as a function of LaX_3 concentration in anhydrous methanol at 23°C (Bünzli et al. 1987).

Table 8
Estimated stability constants for the equilibria $La^{3+} + X^- \rightleftarrows [RX]^{2+}$ in anhydrous methanol at 23°C[a]

X	K_X	$\log K_X$
ClO_4^-	390±60	2.6±0.2
$CF_3SO_3^-$	450±60	2.7±0.1
Br^-	460±70	2.7±0.2
Cl^-	1500±200	3.2±0.1

[a] Bünzli et al. 1987.

More recently, Di Bernardo et al. (1993) have determined, by the same FT-IR method, the affinity of the perchlorate ion for lanthanide bis(triflate) complexes in anhydrous acetonitrile:

$$[R(SO_3CF_3)_2(solv)]^+ + ClO_4^- \overset{K_{mix}}{\rightleftarrows} [R(SO_3CF_3)_2(ClO_4)(solv)]. \quad (40)$$

The reported values of $\log K_{mix}$ are 1.6±0.1 for both Tb and Lu. Since the apparent formation constants of the tris(triflate) complexes are 2.6 and 2.3, respectively (cf. table 2), the affinity of the perchlorate ion for the bis(triflate) complexes is about ten times lower than the one of the triflate itself.

Table 9
Relative stability constants for the equilibria $LaX^{2+} + Y^- \rightleftarrows LaY^{2+}$ in anhydrous methanol at 23°C[a]

X	Y	$K_{Y,X}$	$\log K_{Y,X}$	$\log \bar{K}_{Y,X}$[b]
ClO_4^-	Cl^-	3.82	0.58	0.60
ClO_4^-	Br^-	1.27	0.10	0.07
ClO_4^-	NO_3^-	13.2	1.12	1.13
Cl^-	NO_3^-	3.32	0.52	0.53
Br^-	NO_3^-	11.7	1.07	1.06
$CF_3SO_3^-$	Br^-	1.06	0.02	0.01
$CF_3SO_3^-$	Cl^-	3.26	0.51	0.54

[a] Bünzli et al. 1987.
[b] $\log \bar{K}_{Y,X}$ is the average of $\log K_{Y,X} = \log K_{Y,Z} + \log K_{Z,X}$, etc.

The coordination of several ions to La(III) in methanol has been studied by ^{139}La NMR (Bünzli et al. 1987). The chemical shift of the ^{139}La-NMR resonance is indeed governed by the composition of the inner coordination sphere. The chemical shifts measured for several LaX_3 methanolic solutions are shown in fig. 9. The large variation of these shifts versus the concentration of the salts is indicative of the presence of a significant inner-sphere interaction between La(III) and all the anions studied to form complexes of the type $[LaX_n(solv)_x]^{(3-n)+}$. The absolute stability constants K_x (table 8) for the anion complexation can be obtained from the following equations, where x is the mole fraction of LaX^{2+}, and where the solvation has been neglected:

$$La^{3+} + X^- \rightleftarrows [LaX]^{2+}, \qquad \delta_{obs} = (1-x)\,\delta_{La^{3+}} + x\,\delta_{LaX^{2+}}. \tag{41, 42}$$

Due to rapid exchange processes, the ^{139}La-NMR spectrum of an equimolar mixture of LaX_3 and LaY_3 displays only one resonance with the average chemical shift:

$$\delta_{obs} = x\,\delta_{LaX^{2+}} + (1-x)\,\delta_{LaY^{2+}}. \tag{43}$$

The relative equilibrium constants $K_{Y,X}$ for the 1:1 complexes (table 9),

$$LaX^{2+} + Y^- \overset{K_{Y,X}}{\rightleftarrows} LaY^{2+} + X^- \tag{44}$$

point to the interaction between La(III) and X^- increasing in the order

$$CF_3SO_3^- \approx ClO_4^- < Br^- < Cl^- < NO_3^-.$$

The same order prevails in water for nitrate, chloride and perchlorate (Chen Zhigang and Detellier 1992).

The influence of chloride, bromate and perchlorate on the absorption spectra of methanolic solutions of Nd, Eu, and Er has been studied by Davidenko et al. (1972).

The shape of the spectra depends on the nature of the anion, especially for Nd and, to a lesser extent, for Eu and Er. The decrease in the influence of the anion, from Cl^- to ClO_4^- and from Nd to Er, is accompanied by an increase in the similarity of the absorption spectra of aqueous and methanolic solutions. Measurements of the electric conductivity in methanol (Zholdakov et al. 1971) confirm the replacement of the perchlorate ion by chloride.

In DMF solutions, conductivity and ^{35}Cl-NMR measurements confirm the absence of perchlorate complexation for the whole series of R^{3+} ions (Pisaniello and Merbach 1982). The mono-, di-, and trinitrato complexes have been evidenced for Eu (Bünzli and Yersin 1982) and possibly Nd solutions (Bünzli and Vuckovic 1984). Inner-sphere complexes are clearly evidenced with Cl^- ions, but outer-sphere complexes are formed with bromide ions (Takahashi and Ishiguro 1991).

Finally, in DMA solutions the following order of stability was established (Airoldi et al. 1982):

$$\text{La}: \ Cl^- > Br^- > NO_3^-; \qquad \text{Nd}: \ Br^- > Cl^- > NO_3^-.$$

5.7. *Relative solvent affinity*

Information about the relative strength of the interaction between terbium and aqueous and non-aqueous solvents was obtained by Batyaev et al. (1975). Terbium perchlorate solutions (0.0036 M) in water, deuterated water, pyridine–water, *n*-propanol–water, acetonitrile–water, DMF–water, and methanol were studied by relaxation spectroscopy. An affinity series could be established, which is parallel to the donor number of the solvents:

$$H_2O > C_5H_5N \approx CH_3OH > HCON(CH_3)_2 > CH_3(CH_2)_2OH > CH_3CN.$$

On the other hand, the following affinity sequence for $Tb(ClO_4)_3$ and $Tb(NO_3)_3$ has been established by Bünzli and Vuckovic (1983) on the basis of absorption and luminescence data:

$$NO_3^- > DMSO > DMF \approx H_2O > (CH_3)_2CO > CH_3CN.$$

This sequence is in agreement with the relative basicity of the various donors.

The solvent effect on intensities of hypersensitive transitions of $R(ClO_4)_3$ (R = Nd, Ho, Er) has been investigated by Legendziewicz et al. (1982). The molar refractivities and oscillator strengths of hypersensitive bands are reported for water, alcohols, DMSO, DMF and diethylformamide. Intensities of the f–f bands and the nephelauxetic effect of the alcoholic solvates of the heavy-lanthanide chlorides with Ho(III) and Er(III) have also been reported (Keller et al. 1982). The intensity T_2 parameter increases as follows:

Er : *n*-propanol > ethanol > methanol > water;

Nd : ethanol > *n*-propanol > methanol > water.

In any case, the nephelauxetic effect is very small, in agreement with the expected hard–hard interaction with alcohols, which precludes a covalent contribution to the R–alcohol

Table 10
Enthalpies of solution at 298 K of anhydrous Sc, Y, La, Gd and Yb trichlorides in water and various non-aqueous solvents[a]

XY_3	Enthalpy of solution ($kJ\,mol^{-1}$)						
	Water	MeOH	EtOH	DMSO	DMF	PC	Et.-glycol
$ScCl_3$	−205.1±1.7	−155.4±1.9		−160.5±1.9			
YCl_3	−226.1±4.2	−164.9±2.3		−213.2±2.5			
$LaCl_3$	−135.7±3.6	−92.6±0.3	−65[b]				−103±9[c]
$GdCl_3$	−181.1±1.6	−156.7±2.5		−211.5±2.7	−193.3±3.3		
$YbCl_3$	−218.7±1.9	−167.4±3.1		−231.8±3.1			
YBr_3	−253.3±3.2						
$LaBr_3$	−173.0±3.1						
$YbBr_3$	−239.5±1.4						
ScI_3	−261.3±2.7	−217.2±2.0		−393.0±1.1			
YI_3	−262.1±3.6	−255.7±2.9		−316.2±3.9			
LaI_3	−206.9±3.2	−237.9±3.4	−227.5±2.0	−338.8±3.6	−303.6±2.3	−293.9±6.0	
GdI_3	−249.4±2.3	−266.6±3.4		−365.5±3.2			

[a] Burgess and Kijowski (1981). [b] Estimated.
[c] $LaCl_3$ dissolved only with difficulty in this solvent.

bond. The spectroscopic results for Nd suggest that a change in the number of alcohol molecules takes place for *n*-propanol, whereas for the heavier lanthanide ions possibly all solvates have a lower coordination number.

Absorption and emission spectra of europium perchlorate and nitrate have been measured in protonated and deuterated solvents: water, DMSO, methanol and acetonitrile (Haas and Stein 1971a,b). With nitrate as the anion, the complexing ability decreases in the order water > methanol > acetonitrile.

Finally, the enthalpies of solution of rare-earth halides were studied in a series of non-aqueous solvents (Burgess and Kijowski 1981); they are given in table 10. The enthalpies of solution of the trichlorides in methanol are markedly less negative than in water. The difference is assigned to a less favourable solvation both of the lanthanide cation and the chloride ions. Ethylene glycol is intermediate between water and methanol, judging from the value for the enthalpy of solution of $LaCl_3$. Enthalpies of solution of the trichlorides in DMSO are slightly more negative than those in water. We note that chloride ions are much less solvated in DMSO than in water, while the reverse is true for lanthanide ions (cf. for instance the apparent formation constants for the mononitrato complex of europium in DMSO and water: 200 and 900 M^{-1}, respectively (Bünzli et al. 1982a). Similar comments apply to dimethylformamide solutions for which the enthalpies of solution of lanthanum, gadolinium, and ytterbium trichlorides have also been reported (Blandamer et al. 1982).

6. Interaction with neutral donor molecules

6.1. *Acetonitrile (AN)*

The weak donor acetonitrile interacts with R(III) ions to form solvates which may be isolated in presence of weakly coordinating anions such as BF_4^- or $AlCl_4^-$. The first synthesis was carried out by the $NOBF_4$ oxidation of metallic Eu in acetonitrile (Thomas et al. 1986) and yielded $[Eu(CH_3CN)_3(BF_4)_3]_x$. Molecular weight, conductivity and ^{11}B- and ^{19}F-NMR measurements point to an interaction between BF_4^- and Eu(III), as well as to the existence of a dimer in AN ($x=2$). More recently, Hu Jingyu et al. (1990) reacted rare-earth anhydrous chlorides with aluminium chloride in AN to obtain $[Ln(CH_3CN)_9][AlCl_4]_3 \cdot CH_3CN$, with Ln = La, Pr, Nd, Sm, Eu, Gd, Tb, Ho, Yb. The molecular and crystal structure of the Sm solvate could be solved and shows all nine AN molecules coordinated to the Sm(III) ion with distances of 2.53–2.55 Å (Shen Qi et al. 1990).

In solution, AN molecules bonded in the inner coordination sphere of the R(III) ions give rise to distinct vibrational bands in the FT-IR difference spectra (Bünzli et al. 1982b). The latter are shifted towards higher wavenumbers with respect to the free AN vibrations and have been observed in solutions of nitrates (Bünzli and Mabillard 1986a,b, Bünzli et al. 1990), triflates (Di Bernardo et al. 1993), and perchlorates (Bünzli and Kasparek 1991). The more convenient spectral region to study the R(III)–AN interaction is 2250–2350 cm^{-1}, in which both the ν_2 and $(\nu_3 + \nu_4)$ vibrations occur. For lanthanide perchlorates, the hypsochromic shifts range from 25 (La) to 34 (Yb) cm^{-1} for ν_2, and from 15 (La) to 22 (Yb) for $(\nu_3 + \nu_4)$. Their variation along the series is linear (fig. 10), pointing to a monotonically increasing interaction strength with the increase in electronic density on the R(III) ions. Similar observations are made for both the nitrates, alone or in presence of DMSO, and the triflates.

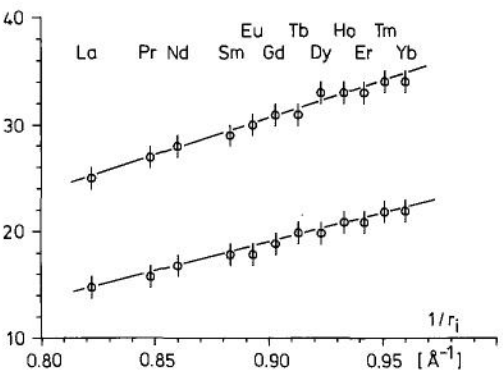

Fig. 10. Hypsochromic shift of the ν_2 (top) and $\nu_3 + \nu_4$ (bottom) vibrations of bonded acetonitrile molecules in $R(ClO_4)_3$ solutions 0.05 M in anhydrous acetonitrile (Bünzli and Kasparek 1991).

6.2. *Dimethylsulfoxide (DMSO)*

DMSO is a strong donor which dissolves the lanthanide salts readily, and adducts have been isolated with numerous counteranions, including hexafluorophosphate, triflate,

perchlorate, nitrate, chloride, bromide, and iodide (Davies 1981). In anhydrous DMSO, the absorption spectrum of neodymium perchlorate is characterized by only one band, the maximum of which coincides with the position of the absorption maximum in the spectrum of the crystalline $[Nd(DMSO)_8](ClO_4)_3$ species (Lugina et al. 1973). This suggests that the coordination around the Nd(III) is similar both in solution and in the solid state. The presence of two bands in the spectra of the mixed aqueous solutions indicates the simultaneous presence of two different solvates, possibly with coordination numbers 8 and 9. The spectroscopic properties of lanthanide solutions in DMSO have been thoroughly investigated, especially in view of their possible use as liquid lasers (e.g., Chrysochoos and Evers 1973a,b, Chrysochoos 1974, Kandpal et al. 1979, Legendziewicz et al. 1982, Stephens et al. 1986). We do not describe this work here.

The interaction between DMSO and lanthanide ions in organic solvents has been studied in anhydrous nitromethane and acetonitrile, essentially by vibrational spectroscopy.

6.2.1. *Nitromethane*

The complexation of hydrated Pr, Nd, Er and Lu perchlorates with DMSO in nitromethane was investigated by Lugina and Davidenko (1980). On the basis of conductimetric, infrared, and electronic absorption data, they conclude that all the DMSO is coordinated to the R(III) ions up to a ratio $[DMSO]_t/[R(III)]_t = R_{DMSO} = 8$. Upon addition of more DMSO, higher solvates form, which are believed to be of mixed composition, some of the DMSO molecules being bound in the outer coordination sphere. The latter analysis is based on the observation of several bands in the spectral range 980–1080 cm^{-1} assigned to bonded DMSO molecules. It overlooks, however, the fact that DMSO has two vibrations in this spectral range, ν_7(SO), comprised of two components, and $\nu_{20}(CH_3)$, and should be considered with some caution. In fact, recent FT-IR and Raman data obtained by Milicic-Tang and Bünzli (1992) in acetonitrile point to the formation of inner-sphere complexes only (*vide infra*).

6.2.2. *Acetonitrile*

When DMSO is added to solutions of lanthanide nitrates in anhydrous AN it quantitatively displaces the CH_3CN molecules out of the inner coordination sphere, and absorptions from bonded DMSO appear in the spectra (Bünzli et al. 1990). Several among the 24 vibrational modes of DMSO are affected by the complexation with the R(III) ions. The largest shift occurs for the S–O stretching, the ν_7 vibration, and the observed bathochromic effect is characteristic of a coordination through the oxygen atom. Absorptions of free DMSO appear when $R_{DMSO} > 3$ for the lighter lanthanides and $R_{DMSO} > 2.5$ for the heavier ions. Simultaneously, the absorptions of coordinated CH_3CN molecules disappear when $R_{DMSO} > 4$ and $R_{DMSO} > 3$, respectively. This points to the presence of equilibria involving species with different coordination numbers. Nitrate dissociation occurs only when $R_{DMSO} > 9$.

Similar results are observed for solutions of $[R(DMSO)_n](ClO_4)_3$ ($n = 7$–8) in AN (Milicic-Tang and Bünzli 1992, Bünzli 1993). When solid adducts $[R(DMSO)_n](ClO_4)_3$

Table 11
Average coordination number CN[a] (±0.3) for 0.05 M solutions of $R(NO_3)_3$ in acetonitrile-containing DMSO[b]

R	$R_{DMSO}=3$[c]	$R_{DMSO}=4$[c]	$R_{DMSO}=6$[c]
La	9.3[d]	9.4	10.2
Ce	9.3[d]	9.1	9.7
Pr	9.2[d]	9.2	9.9
Sm	9.2[d]	9.2	9.6
Gd	8.7	8.8	9.0
Dy	8.6	8.8	9.0
Ho	8.4	8.5	9.0
Tm	8.2	8.3	8.8
Yb	8.4	8.3	8.3
Lu	8.2	8.3	8.4

[a] CN = 6 + average number of coordinated DMSO molecules per R(III) ion.
[b] Bünzli et al. (1990).
[c] $R_{DMSO} = [DMSO]_t/[R]_t$.
[d] The inner coordination sphere contains, on average, 0.3 or 0.2 CH_3CN molecule.

are dissolved in acetonitrile, absorption bands of both bonded and free DMSO appear in the spectra. However, the main vibration of free DMSO (ν_7, 1060 cm^{-1}) gives rise to a fairly weak band, the intensity of which increases upon addition of increasing amounts of DMSO.

The ν_7(coordinated) − ν_7(free) shift ($\Delta\nu_7$) reflects the magnitude of the R(III)–DMSO interaction, and for a constant composition of the solution increases with Z, reflecting the increase in electrostatic interaction throughout the series: $\Delta\nu_7$ varies from −48 (La) to −58 (Lu) cm^{-1} in the perchlorate series and from −47 (La) to −51 (Lu) cm^{-1} in the nitrate series ($R_{DMSO}=6$). The decrease of this shift with increasing DMSO concentration is interpreted as arising from steric effect when more DMSO molecules are coordinated to the R(III) ion.

The average coordination numbers of the R(III) ions in solutions of lanthanide nitrates and perchlorates in anhydrous acetonitrile containing various amounts of DMSO were determined. In both cases, the quantitative analysis was performed using the ν_7(SO) vibration. For the nitrate solutions, the solvated species are $[R(NO_3)_3(DMSO)_n]$ with the three nitrate ions bonded in a bidentate fashion, and $CN = 6 + n$. As no interaction between R(III) and perchlorate ions or acetonitrile molecules was detected in the investigated perchlorate solutions ($R_{DMSO} > 7$), the average coordination number (CN) of the lanthanide ions is equal to the average number of bonded DMSO molecules, n_{DMSO}. Coordination numbers for three different compositions of the nitrate and perchlorate solutions are reported in tables 11 and 12 and graphically represented in figs. 11 and 12. These data represent the first consistent average coordination numbers determined in organic solution for the entire lanthanide series. They unambiguously point to a change in the average coordination number along the lanthanide series.

Table 12
Average coordination number CN (±0.4) for 0.05 M solutions of $R(ClO_4)_3$ in acetonitrile-containing DMSO (Milicic-Tang and Bünzli 1992)

R	$R_{DMSO} = 8$ [a]	$R_{DMSO} = 12$ [a]	$R_{DMSO} = 15$ [a]
La[b]	7.8	8.7	9.7
Ce	7.4	8.4	–
Pr	7.4	8.7	9.9
		9.0[c]	9.7[c]
Nd	7.7	8.7	9.5
	7.9[d]	8.9[c,d]	9.3[c]
Sm	7.4	8.6	9.3
Eu	7.5	8.8	8.5
	7.3[d]	8.9[d]	
Gd	7.2	7.7	8.5
Tb	7.2	7.6	8.5
	7.5[d]	8.8[d]	
Dy	7.0	7.8	8.3
Ho	7.2	7.9	8.6
Er	6.9	8.2	7.8
		8.2[c]	
		8.1[d]	8.1[2]
Tm	6.8	7.5	7.8
Yb	6.5	7.4	8.2
Lu	6.6	7.4	8.0

[a] $R_{DMSO} = [DMSO]_t/[R]_t$.
[b] Values recalculated for a 0.05 M concentration.
[c] In nitromethane (Lugina and Davidenko 1980).
[d] Mabillard (1983).

For the nitrate solutions, in the presence of a relatively low concentration of DMSO ($R_{DMSO} = 3$), this change occurs approximately in the middle of the series (Eu). In the first part of the series, the 9-coordinate species is predominant while the 8-coordinate species is the main solvate for heavier R(III) ions. Higher average coordination numbers can be obtained for most ions (La–Tm) if the DMSO concentration is increased ($R_{DMSO} = 6$). In this case, two groups of ions give rise to predominantly one solvate, La–Sm (CN = 10) and Eu–Tm (CN = 9), while Yb and Lu are intermediate with average CN's between 9 and 8. This study demonstrates that DMSO forms 6-, 7-, 8-, 9-, and 10-coordinated inner-sphere complexes with lanthanide ions. The average coordination number of a given ion increases when more donor molecules are introduced into the solution. The variation can amount up to the 2 units for the lighter lanthanides. As expected, the coordination number decreases regularly with increasing Z, but when a significant excess of DMSO is added ($R_{DMSO} > 8$), marked differences appear at some points in the series. A "break" of ca. 1 unit is observed around the middle of the series and other significant, although smaller variations appear around Nd and Er (ca. 0.5 unit).

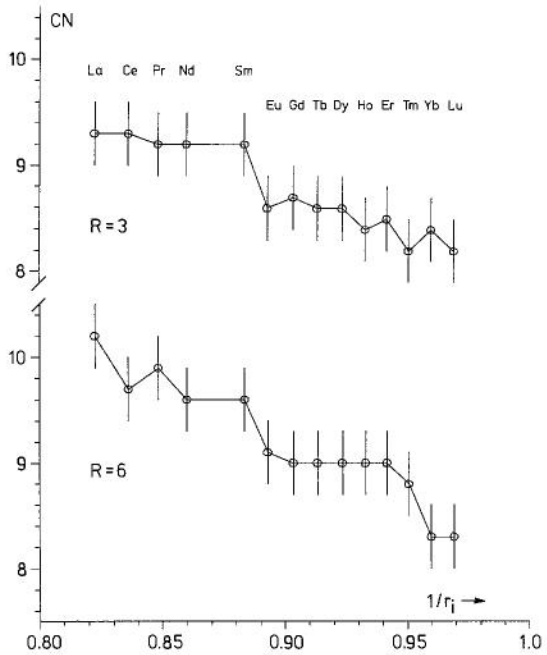

Fig. 11. Average coordination numbers of R(III) ions in 0.05 M $R(NO_3)_3$ solutions in acetonitrile containing DMSO vs. reciprocal ionic radii (for CN = 9); $R_{DMSO} = [DMSO]_t / [R(III)]_t$ (Bünzli et al. 1990).

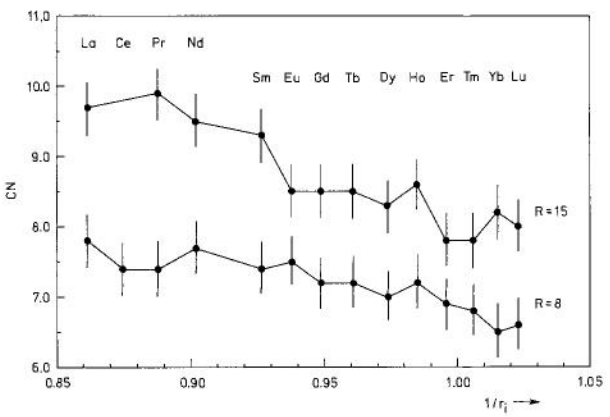

Fig. 12. Average coordination numbers of the R(III) ions in solutions of $R(ClO_4)_3 \cdot n$DMSO 0.05 M in anhydrous acetonitrile vs. the reciprocal ionic radii for CN = 8; $R_{DMSO} = [DMSO]_t / [R(III)]_t$ (Milicic-Tang and Bünzli 1992).

For perchlorates and $R_{DMSO} = 8$, the coordination numbers decrease regularly throughout the series. This situation reflects a gradual shift in the equilibria between 8-, 7- and 6-coordinate solvates. The 8-coordinate species is favoured for the lighter R(III) ions, while the 7- and 6-coordinate species predominate for heavier lanthanides. For $R_{DMSO} = 12$, the pattern is quite different: CN values are almost constant from La to Eu, pointing to an equilibrium between 8- and 9-coordinate solvates. A discontinuity occurs between Eu and

Table 13
Apparent equilibrium constants $\log K_x$ for $R(ClO_4)_3$ and $R(NO_3)_3$ solutions 0.05 M in anhydrous acetonitrile-containing DMSO

R	Perchlorates[a]			Nitrates[b]	
	$\log K_8$	$\log K_9$	$\log K_{10}$	$\log K_9$	$\log K_{10}$
La	2.2	1.0	0.9	–	2.2
Ce	1.3	0.7	0.4	–	1.7
Pr	1.4	1.0	0.6	–	1.0
Nd	2.0	0.9	0.6	–	–
Sm	1.5	0.8	0.3	–	0.9
Eu	1.6	0.9	–	–	–
Gd	1.0	0.5	–	1.8	–
Tb	0.9	0.5	–	–	–
Dy	0.9	0.4	–	1.7	–
Ho	0.9	0.4	–	1.3	–
Er	1.0	0.5	–	–	–
Tm	0.7	0.3	–	1.1	–
Yb	0.6	0.4		1.0	–
Lu	0.6	0.4	–	1.0	–

[a] $[R(DMSO)_{x-1}]^{3+} + DMSO \rightleftarrows [R(DMSO)_x]^{3+}$ (Milicic-Tang and Bünzli 1992).
[b] $[R(NO_3)_3(DMSO)_{n-1}] + DMSO \rightleftarrows [R(NO_3)_3(DMSO)_n]$, $x = 6 + n$ (Bünzli et al. 1990).

Gd, where CN drops by one unit and then remains practically constant down to Lu, with, however, a slight tendency to decrease after Er. With respect to the data for $R_{DMSO} = 8$, the average CN's are larger by 1.1 unit for the first half of the series and by 0.7 unit for the second. In the presence of a larger excess of DMSO ($R_{DMSO} = 15$), the CN values become even larger. For La–Sm, 10-coordinate species are present in the solutions, while 8-coordinate solvates prevail for Er–Lu. It is noteworthy that the average CN decreases by almost 2 units between La and Lu. For a given ion, the increase in CN upon increasing the DMSO concentration is usually monotonous. The largest variation is observed for the lighter lanthanides (La–Sm, change = 2 between $R_{DMSO} = 7$ and 15). For Eu–Lu, the difference is close to 1–1.2 units.

The average coordination numbers in the nitrate solutions are somewhat larger. This may be explained by the occurrence of smaller steric effects due to the small size of nitrate. Vibrational data do not evidence large inequivalences between the coordinated DMSO molecules, so that the variations in coordination numbers may be interpreted as follows. When excess DMSO is added, the inner coordination sphere of the R(III) ions expands to accept an additional donor molecule, resulting in a slightly weaker R(III)–DMSO interaction. The thermodynamic stabilities of the species $[R(DMSO)_x]^{3+}$ and $[R(DMSO)_{x+1}]^{3+}$ are close, as demonstrated by the small values calculated for $\log K_{x+1}$ (table 13). The electronic density on the trivalent ions increases with Z, therefore there are situations in which the expansion of the inner coordination sphere leads to species

with too small a free energy to be stable enough and for which the equilibrium involving two differently coordinated species is substantially shifted to favour the species with the smallest CN. Therefore, the observed breaks in CN along the series are second-order effects resulting from a subtle interplay between electronic and steric effects. A similar situation seems to prevail for aquo-ions, for which it has been demonstrated that the difference in free energy between 9-and 8-coordinate hydrates is rather small (Miyakawa et al. 1988).

6.3. *Dimethylformamide (DMF)*

Lanthanide solvates with DMF and other amides have been known for more than twenty-five years. Krishnamurthy and Soundararajan (1966) have isolated neutral adducts, $[Ln(DMF)_4(NO_3)_3]$ (Ln = La, Pr, Sm, Y), which dissociate in DMF solution to give 1:1 electrolytes. Lanthanide perchlorates form 8-coordinate solvates with DMF and 6-coordinate complexes with diphenylamide (Krishnamurthy and Soundararajan 1969). A calorimetric study of the reaction between lanthanide-hydrated triflates and DMF in ethanol has been carried out by Zinner et al. (1991). As in the case of DMSO, numerous spectroscopic studies (absorption, luminescence) have been conducted on lanthanide ions in DMF solutions (cf. Legendziewicz et al. 1985, Jezowska-Trzebiatowska et al. 1984, Lugina et al. 1973). These are not reviewed here.

It has been shown by luminescence measurements on Eu solutions that perchlorate does not interact with Eu(III) in DMF solutions and that the Eu solvate is probably 8-coordinate. The formation of DMF solvates with Pr, Nd and Er hydrated perchlorates has been investigated in nitromethane by Lugina et al. (1974) using vibrational spectroscopy. The change in intensity of the carbonyl stretching vibration was used to calculate the mean number of DMF molecules bonded to R(III). Fractional numbers were obtained, pointing to the presence of equilibria between species with different CN, namely 8 and 9.

The equilibrium between 8- and 9-coordinate solvates in pure DMF,

$$[R(DMF)_8]^{3+} + DMF \rightleftarrows [R(DMF)_9]^{3+}, \tag{45}$$

was studied by absorption and multinuclear NMR spectroscopy at variable pressure and temperature (cf. sect. 5.3.3, Pisaniello et al. 1983, Cossy and Merbach 1988). At room temperature the major species is $[R(DMF)_8]^{3+}$ when R = Ce–Nd, and this becomes the only stable species when R = Tb–Lu. Characteristic ^{17}O-, ^{13}C-, and ^{1}H-NMR shifts for $[R(DMF)_8]^{3+}$ are also reported.

6.4. *Complexation of La(III) in anhydrous acetonitrile*

Information concerning complex formation by the La(III) ion can be gained with the help of ^{139}La-NMR spectroscopy, namely by observing the variations in both the chemical shifts and the linewidths when a ligand is added to an anhydrous solution of lanthanum perchlorate. Evans and Missen (1982) have compared the effect of

several anions and several neutral donors in acetonitrile, including DMSO, DMF, trimethylphosphoramide and ethylenediamine. However, no quantitative data are reported. Recently, thermodynamic data for R(III) (R = La–Lu) complexation with ethylenediamine in DMSO have been reported by Cassol et al. (1992).

7. Interaction in aqueous and mixed organic solvents

Numerous publications deal with rare-earth complexation in aqueous and mixed organic solvents. Most articles describe work in aqueous alcohols, acetonitrile, acetone, DMSO, and DMF. The main studies are listed in table 14, and short comments are given below.

7.1. *Alcohols*

In water, no interaction is detected between perchlorate and Er(III) or Nd(III), but the addition of methanol causes complexation with Er(III) (Silber and Strozier 1987). The presence of water restricts chloride complexation to the monochloro complexes and the stability of this species diminishes regularly with increasing water content (Hamze et al. 1986). However, the electronic spectra of the Nd(III) solvates are nearly independent of water content (0–10%). Similar results are reported for the complex formation between Pr, Nd, Sm, Ho, Er and bromide in water and in 50% and 90% methanol (Kozachenko et al. 1973). The stability of the bromo complexes increases as the dielectric constant of the medium is reduced. In either water or aqueous methanol, bromo complexes are less stable than chloride complexes.

7.2. *Acetonitrile*

The solvation of lanthanide ions in acetonitrile–water solutions was investigated by several experimental techniques. ^{1}H-NMR data for $Eu(ClO_4)_3$ solutions show that the Eu ion is preferentially solvated by water in these mixtures (Haas and Navon 1972). Varying the perchlorate concentration did not affect the NMR spectra. Therefore, any inner-sphere interaction with perchlorate was disregarded in this interpretation, which is not completely rational, especially in solutions with low water content. Assuming a constant coordination number of 9 for Eu and the existence of three equatorial and six axial coordination sites, Haas and Navon (1972) suggest that the equatorial sites have a higher affinity for water. On the other hand, Batyaev et al. (1985) interpreted infra-red and electronic absorption spectra as reflecting the existence of mixed solvates $[Eu(H_2O)_y(CH_3CN)_{n-y}]^{3+}$ in aqueous acetonitrile solutions. In anhydrous acetonitrile, n was determined to be 8.3 ± 0.5. Finally, from the breaks observed in Stern–Völmer plots featuring the relative lifetimes of $^5D_4$(Tb) in $Tb(NO_3)_3$ solutions vs. DMSO or water concentration, Bünzli and Vuckovic (1983) concluded that the average coordination number of Tb is 9 in presence of DMSO, but somewhat lower in presence of water, with larger outer-sphere effects. This may be due to steric hindrance since water molecules form clusters through hydrogen bonding.

Table 14
Rare earth solvation studies in aqueous organic solvents

Solvent	R(III) ions	Counterions	Technique(s)	Ref.
MeOH	Sc, Y, La	Cl^-	Ultrasonic absorption	Silber and Mioduski (1984)
MeOH	La, Gd, Yb	Cl^-	Calorimetry	Blandamer et al. (1982)
MeOH	La, Eu, Er, Lu	Cl^-	Spectrophotometry	Mironov et al. (1983)
MeOH	Pr, Nd, Sm, Eu, Gd, Tb, Dy, Ho, Er, Yb	Cl^-	Spectrophotometry	Kozachenko and Batyaev (1971a)
MeOH	Pr, Nd, Sm	Cl^-	Spectrophotometry	Hamze et al. (1986)
MeOH	Pr, Nd, Sm, Ho, Er	Br^-	Spectrophotometry	Kozachenko et al. (1973)
MeOH	Nd, Gd, Er	Cl^-	Ultrasonic absorption	Silber et al. (1978)
MeOH	Nd	Cl^-, ClO_4^-	Spectrophotometry, Conductimetry	Zholdakov et al. (1971)
MeOH	Nd, Eu, Er	ClO_4^-, BrO_3^-, Br^-	Spectrophotometry	Davidenko et al. (1972)
MeOH	Nd, Er	ClO_4^-, NO_3^-	Spectrophotometry	Silber and Strozier (1987)
MeOH	Nd, Gd, Er	ClO_4^-	Ultrasonic absorption	Silber and Pezzica (1976)
MeOH	Nd	NO_3^-	Ultrasonic absorption	Silber and Fowler (1976)
MeOH	Eu	Cl^-	Luminescence	Tanaka et al. (1988)
MeOH	Eu	Cl^-	Spectrophotometry, Luminescence	Sayre et al. (1957)
MeOH	Eu	ClO_4^-, NO_3^-	Spectrophotometry	Silber and Strozier (1987)
MeOH	Eu	NO_3^-	Ultrasonic absorption	Silber and Campbell (1989)
MeOH	Tb	ClO_4^-	Spectrophotometry, Luminescence	Batyaev et al. (1975)
MeOH	Er	ClO_4^-	Ultrasonic absorption	Silber (1974)
MeOH	Er	Cl^-	Ultrasonic absorption	Reidler and Silber (1974b)
MeOH	Er	Cl^-	Ultrasonic absorption	Silber and Zhang Yue (1987)
MeOH	Er	Cl^-	Ultrasonic absorption	Silber (1980)
MeOH	Er	Cl^-, NO_3^-	Ultrasonic absorption	Reidler and Silber (1973)
MeOH	Er	Cl^-, Br^-, I^-	Ultrasonic absorption	Silber and Bordano (1978)
MeOH	Er	Br^-, I^-	Ultrasonic absorption	Silber and Bordano (1979)
MeOH	Er	NO_3^-	Ultrasonic absorption	Reidler and Silber (1974a)
MeOH	Er	NO_3^-	^{15}N-NMR	Fratiello et al. (1991)
EtOH	La, Gd, Yb	Cl^-	Calorimetry	Blandamer et al. (1982)
EtOH	Pr, Nd, Sm, Ho, Er	Cl^-	Spectrophotometry	Kozachenko and Batyaev (1971b)
EtOH	Pr, Nd, Sm, Eu, Tb, Dy, Ho, Er, Tm	NO_3^-	Spectrophotometry	Abrahamer and Marcus (1968)
EtOH	Eu	Cl^-	Spectrophotometry, Luminescence	Sayre et al. (1957)
n-PrOH	Pr, Nd, Ho, Er	Cl^-, Br^-, NO_3^-	Spectrophotometry	Krutous and Batyaev (1974)

continued on next page

Table 14, *continued*

Solvent	R(III) ions	Counterions	Technique(s)	Ref.
n-PrOH	Tb	ClO_4^-	Spectrophotometry, Luminescence	Batyaev et al. (1975)
t-ButOH	La, Gd, Yb	Cl^-	Calorimetry	Blandamer et al. (1982)
CH_3CN	Nd, Eu	ClO_4^-	Luminescence	Batyaev and Shilov (1983)
CH_3CN	Eu	ClO_4^-	Luminescence	Haas and Stein (1971a,b)
CH_3CN	Eu	ClO_4^-	Luminescence	Tanaka et al. (1988)
CH_3CN	Eu	ClO_4^-	Vibrational spectroscopy, Spectrophotometry	Batyaev et al. (1985)
CH_3CN	Eu	ClO_4^-	^{1}H-NMR	Haas and Navon (1972)
CH_3CN	Tb	ClO_4^-	Spectrophotometry, Luminescence	Batyaev et al. (1975)
CH_3CN	Tb	ClO_4^-, NO_3^-	Luminescence	Bünzli and Vuckovic (1983)
DMSO	La	Cl^-	Conductimetry	Campbell and Kartzmark (1984)
DMSO	La, Gd, Yb	Cl^-	Calorimetry	Blandamer et al. (1982)
DMSO	Pr	Cl^-	Spectrophotometry	Borina (1988)
DMSO	Nd	ClO_4^-	Spectrophotometry	Lugina et al. (1973)
DMSO	Nd	ClO_4^-, NO_3^-	Luminescence	Bünzli and Vuckovic (1984)
DMSO	Eu	Cl^-, NO_3^-, CH_3COO^-	Luminescence	Chrysochoos and Evers (1973a)
DMSO	Eu	Cl^-	Luminescence	Tanaka et al. (1988)
DMSO	Tb	ClO_4^-, NO_3^-	Luminescence	Bünzli and Vuckovic (1983)
DMSO	Tb	Cl^-	Luminescence	Chrysochoos and Evers (1973b)
DMSO	Er	Cl^-	Ultrasonic absorption	Silber (1978)
DMSO	Er	Cl^-	Ultrasonic absorption	Silber (1980)
DMSO	Er	NO_3^-	Ultrasonic absorption	Silber and Kromer (1980)
DMF	La	ClO_4^-, Cl^-, NO_3^-	^{139}La-NMR	Tarasov et al. (1986)
DMF	Pr, Nd, Sm, Eu, Tb, Dy, Ho, Er, Tm	NO_3^-	Spectrophotometry	Abrahamer and Marcus (1968)
DMF	Nd	ClO_4^-	Spectrophotometry	Lugina et al. (1973)
DMF	Nd	ClO_4^-, NO_3^-	Luminescence	Bünzli and Vuckovic (1984)
DMF	Eu	Cl^-	Luminescence, Spectrophotometry	Tanaka et al. (1988)
DMF	Tb	ClO_4^-, NO_3^-	Luminescence	Bünzli and Vuckovic (1983)
DMF	Tb	ClO_4^-	Luminescence	Batyaev et al. (1975)
DMF	Er	Cl^-	Ultrasonic absorption	Silber and Riddle (1982)
DMF	Er	Cl^-, NO_3^-	Ultrasonic absorption	Silber et al. (1983)
Acetone	Nd	ClO_4^-, NO_3^-	Luminescence	Bünzli and Vuckovic (1984)

continued on next page

Table 14, *continued*

Solvent	R(III) ions	Counterions	Technique(s)	Ref.
Acetone	Eu	ClO_4^-	Luminescence	Tanaka et al. (1988)
Acetone	Eu	NO_3^-	Luminescence	Gruzdev and Ermolaev (1975)
Acetone	Lu, Er, Yb	ClO_4^-, NO_3^-	^{1}H-NMR	Fratiello et al. (1973)
Acetone	La	ClO_4^-, NO_3^-	^{1}H-, ^{35}Cl-, ^{139}La-NMR	Fratiello et al. (1989b)
Acetone	Er	NO_3^-	^{15}N-NMR	Fratiello et al. (1991)
Acetone	Y	SCN^-	^{15}N-, ^{89}Y-NMR	Fratiello et al. (1994)
Acetone	Tb	ClO_4^-, NO_3^-	Luminescence	Bünzli and Vuckovic (1983)
Acetone	Yb, Tm	NO_3^-	Vibrational spectroscopy	Kavun et al. (1981)
Dioxane	Pr, Nd, Sm, Eu, Tb, Dy, Ho, Er, Tm	NO_3^-	Spectrophotometry	Abrahamer and Marcus (1968)
Dioxane	Eu	Cl^-	Luminescence	Tanaka et al. (1988)
TBP	Pr, Nd, Sm,Eu, Tb, Dy, Ho, Er, Tm	NO_3^-	Spectrophotometry	Abrahamer and Marcus (1968)
TBP	Nd	NO_3^-	Luminescence	Zinina and Shablya (1975)
Pyridine	Tb	ClO_4^-	Luminescence	Batyaev et al. (1975)

7.3. *Acetone*

The stability constants of the Eu aquo-complexes in acetone have been determined by adding water to anhydrous solutions of $Eu(NO_3)_3$ and measuring the lifetimes of the $^5D_0$ state (Gruzdev and Ermolaev 1975). The method of corresponding solutions yielded the following values for the first four hydrates $[Eu(NO_3)_3(H_2O)_x]$: $\log\beta_x = 3.1\pm0.2$, 4.7 ± 0.4, 5.6 ± 0.6, and 5.7 ± 0.8.

In water–acetone mixtures, ^{15}N-NMR signals at low nitrate to Er mole ratio are observed for the mono- and dinitrato complexes, but only the latter complex is present at higher anion concentrations (Fratiello et al. 1991). No spectral evidence for the trinitrato complex was seen at any nitrate concentration. In water–methanol–acetone mixtures, signals for the mono- and dinitrato complexes persist even at higher nitrate concentrations, indicating a reduced tendency to ion-pair with increasing dielectric constant. The coordination affinity of Lu(III) for nitrate and perchlorate has been studied in aqueous mixtures of acetone-d6 and freon-12 by ^{1}H-, ^{15}N- and ^{35}Cl-NMR spectroscopy (Fratiello et al. 1990). At temperatures lower than −90°C, proton and ligand exchange are slow enough to enable the direct observation of coordinated and free water molecules. In perchlorate solution, in the absence of inner-sphere ion pairing, Lu(III) exhibits a maximum hydration number of six. The absence of contact ion-pairing with perchlorate was confirmed by ^{35}Cl-NMR chemical shift and linewidth measurements. Extensive ion-pairing was observed in the nitrate solutions by ^{15}N-NMR, and a lower mean hydration number was found, pointing to the presence of $[Lu(NO_3)(H_2O)_4]^{2+}$ and

$[Lu(NO_3)_2(H_2O)_2]^+$ species. The presence of mono- and dinitrato complexes in these solutions is entirely analogous to the results obtained by ^1H- and ^{89}Y-NMR spectroscopy for yttrium solutions (Fratiello et al. 1989a, 1994).

7.4. *Dimethylsulfoxide*

Eu(III) is preferentially solvated by DMSO in water–DMSO mixtures over the whole range of solvent composition, as demonstrated by luminescence lifetime measurements (Tanaka et al. 1988). Similarly, solutions of europium chloride, nitrate and acetate in DMSO exhibit a considerable luminescence enhancement (Chrysochoos and Evers 1973a). Addition of large amounts of water has no effect at all, while adding very small quantities of DMSO to aqueous solutions of Eu(III) induces drastic changes in the transition probabilities. This clearly demonstrates the stronger coordination properties of DMSO as compared to water.

7.5. *Dimethylformamide*

Aqueous DMF solutions of lanthanum nitrate, chloride, and perchlorate have been investigated by ^{139}La-NMR spectroscopy as a function of the mole fraction x_s of the organic solvent (Tarasov et al. 1986). Both the perchlorate and chloride anions remain in the outer coordination sphere and the cation is preferentially solvated by DMF molecules. In the range $0.14 < x_s < 1$, nitrate ions are located both in the outer and inner coordination sphere, forming $[La(DMF)_x(NO_3)_y]^{(3-y)+}$ complexes. In solutions with a high content of DMF ($1 > x_s > 0.7$) the composition of the coordination sphere of La is constant and the predominant complex is $[La(DMF)_5(NO_3)_2]^+$.

8. Kinetic investigations

The rate of water exchange between the inner coordination sphere of rare earth ions and bulk water has been extensively studied by ultrasonic absorption and NMR spectroscopy. It is very fast and ranges between 10^7 and $10^9\ s^{-1}$ (Cossy and Merbach 1988, Rizkalla and Choppin 1991). Ligand substitution processes and the kinetics of lanthanide complexation in water, especially with polyaminocarboxylates, have also been the subject of several studies (Lincoln 1986, Nash and Sullivan 1991). As for the determination of solvation numbers, investigations in anhydrous organic solvents are more sporadic.

Using ultrasonic absorption, Silber and his group studied the complexation reactions between lanthanides and various anions (ClO_4^-, Cl^-, Br^-, I^-, NO_3^-) in aqueous organic solvents such as methanol, DMSO and DMF. All the kinetic measurements are consistent with the Eigen multi-step mechanism (cf. eq. 1). As the rate constants for the inner-sphere formation are similar in water and aqueous methanol, Silber and co-workers suggested that the slow step in the exchange is the cation–ligand bond formation rather than the removal of a solvent molecule. On the other hand, the low rates of exchange observed

Table 15
Kinetic parameters for DMF exchange on $[R(DMF)_8]^{3+}$ solvates in anhydrous DMF[a]

R	k^{200} (10^{-5} s^{-1})	k^{298} (10^{-5} s^{-1})	$\Delta H^{\ddagger}$ (kJ mol^{-1})	$\Delta S^{\ddagger}$ (JK^{-1} mol^{-1})	$\Delta V^{\ddagger}$ (cm^3 mol^{-1})
Tb	7.2±0.2	190±10	14.1±0.4	−58±2	+5.2±0.2
Dy	2.8±0.1	63±3	13.8±0.4	−69±2	+6.1±0.2
Ho	1.16±0.02	36±6	15.3±0.8	−68±4	+5.2±0.5
Er	0.80±0.03	130±40	23.6±1.8	−30±9	+5.4±0.3
Tm	0.29±0.01	310±30	33.2±0.5	+10±2	+0.4±0.3
Yb	0.28±0.01	990±90	39.3±0.6	+40±3	+11.8±0.4

[a] Cossy and Merbach (1988).

in aqueous DMSO were attributed to a structural reorganization. In some instances, ultrasonic absorption data clearly indicate a change in the solvation number upon inner-sphere complexation: for Er in aqueous methanol, such a change, attributed to steric crowding within the inner solvation shell, occurs for Br^-, I^- (Silber and Bordano 1979), NO_3^- (Reidler and Silber 1974a, Silber and Kromer 1980) and ClO_4^- (Silber 1974), but not for Cl^- (Silber 1980).

The only system studied in anhydrous solution is the exchange of DMF on $[R(DMF)_8]^{3+}$ (R = Tb–Yb), for which kinetic parameters have been determined by variable temperature and pressure ^{1}H-NMR in DMF (table 15). The observed systematic variation in activation parameters from Tb to Yb are interpreted in terms of a mechanistic cross-over at Er. Kinetic rate law determinations in CD_3NO_2 diluent indicate that an interchange mechanism operates for Tb whereas a dissociative mechanism is operative for Yb.

In summary, nonaqueous systems are less labile compared to aqueous systems, which facilitates the determination of their coordination numbers, and solvent and ligand exchange rate laws.

9. Conclusions

Recent data clearly indicate that in organic solvents, most anions, particularly perchlorate and triflate, interact in the inner coordination sphere of the rare-earths ions.

A large number of rare-earth adducts have been synthesized and characterized (see Gmelin Handbook of Inorganic Chemistry, Part D4, 1986 for a general review or Cunha et al. (1992) for a review on europium trigonal complexes). However, the molecular structure of only a few compounds has been established by means of single-crystal X-ray diffraction. In table 16, we compare the coordination numbers in the solid state and in solution for the solvates for which extensive data are at hand, that is, adducts with DMSO. Solid solvates $R(NO_3)_3 \cdot n$DMSO display a CN change from 10 to 9 between Eu and Tb. X-ray diffraction data for 1 M solutions of $Er(NO_3)_3$ in DMSO yield the same coordination number (CN = 9) and similar distances as in the crystalline phase (Johansson et al. 1991).

Table 16
Comparison of coordination numbers determined in the solid state and in solution

Complex	Site symmetry	CN (solid state)	CN (solution)	Ref.
$R(NO_3)_3 \cdot nDMSO$[a]				
$La(NO_3)_3 \cdot 4DMSO$	C_{2v}	10	9.4[b]10.2[c]	1,10
$Pr(NO_3)_3 \cdot 4DMSO$	C_{2v}	10	9.2[b]	2,10
			9.9[c]	
$Nd(NO_3)_3 \cdot 4DMSO$	C_{2v}	10	9.5[b]	3,10
			9.6[c]	
$Sm(NO_3)_3 \cdot 4DMSO$	C_{2v}	10	9.2[b]	4,10
			9.6[c]	
$Eu(NO_3)_3 \cdot 4DMSO$	C_{2v}	10	8.9[b]	5,10
			9.0[c]	
$Tb(NO_3)_3 \cdot 3DMSO$	D_{3h}	9	8.9[b]	4,10
			9.0[c]	
$Er(NO_3)_3 \cdot 3DMSO$	D_{3h}	9	8.9[b]	6,10
			9.0[c]	
			9.0[d]	
$Tm(NO_3)_3 \cdot 3DMSO$	D_{3h}	9	8.3[b]	4,10
			8.8[c]	
$Yb(NO_3)_3 \cdot 3DMSO$	D_{3h}	9	8.3[b]	8,10
			8.3[c]	
$Lu(NO_3)_3 \cdot 3DMSO$	D_{3h}	9	8.3[b]	9,10
			8.4[c]	
$R(ClO_4)_3 \cdot nDMSO$[e]				
$R(ClO_4)_3 \cdot 8DMSO$		8	7.8–7.2[f]	11,12
(R = La–Gd)			8.7–7.7[g]	
$R(ClO_4)_3 \cdot 7DMSO$		7	7.2–6.6[f]	11,12
(R = Tb–Lu)			7.6–7.4[g]	
$Sm(CH_3CN)_9] \cdot (AlCl_4)_3 \cdot CH_3CN$			9	13

[a] Data from single-crystal X-ray diffraction.
[b] Data for $R_{DMSO} = [DMSO]_t/[R(III)]_t = 4$.
[c] Data for $R_{DMSO} = [DMSO]_t/[R(III)]_t = 6$
[d] Data from X-ray diffraction measurements; 1 M solutions of $Er(NO_3)_3$ in DMSO.
[e] Data from IR and powder X-ray diffraction measurements.
[f] $R_{DMSO} = 8$.
[g] $R_{DMSO} = 12$.

References

(1) Bhandary and Manohar (1973)
(2) Lin Yonghua et al. (1984)
(3) Aslanov et al. (1972b)
(4) Bhandary et al. (1975a)
(5) Lin et al. (1981)
(6) Aslanov et al. (1972a)
(7) Johansson et al. (1991)
(8) Bhandary et al. (1975b)
(9) Aslanov et al. (1973)
(10) Bünzli et al. (1990);
data from FT-IR spectroscopy; 0.05 M solutions in anhydrous acetonitrile (La: 0.012 M)
(11) Krishnamurthy and Soundararajan (1967)
(12) Milicic-Tang and Bünzli (1992);
data from FT-IR spectroscopy; 0.05 M solutions in anhydrous acetonitrile
(13) Shen Qi et al. (1990);
monoclinic, space group $P2_1$

For dilute solutions of lanthanide nitrates in anhydrous acetonitrile, the coordination numbers determined by FT-IR spectroscopy for $R_{DMSO} = [DMSO]_t/[R(III)]_t = 4$ are smaller than those in the solid state, but higher coordination numbers can be obtained in presence of an excess of ligand ($R_{DMSO} = 6$). Similar results are observed for DMSO adducts and acetonitrile solutions of lanthanide perchlorates. Generally speaking, the solution data reflect a more gradual change along the lanthanide series, pointing to the presence of several species with different CN.

Coordination numbers vary wildly with both the nature of the ligands bonded in the inner coordination sphere and the composition of the solutions, although CN = 9 is often found (cf. the acetonitrile solvates). This establishes that the inner coordination sphere of the lanthanide ions is easily adjustable to the environment in which these ions are exposed. Henceforth, the versatility and adaptability of these elements which are found in many compounds, including organometallic molecules, and which are used as spectroscopic probes in complex biological or environmental systems.

References

Abrahamer, I., and Y. Marcus, 1968, J. Inorg. Nucl. Chem. **30**, 1563.

Airoldi, C., P.L.O. Volpe and A.P. Chagas, 1982, Polyhedron **1**, 49.

Aslanov, L.A., L.I. Soleva and M.A. Porai-Koshits, 1972a, Russ. J. Struct. Chem. (Engl. Transl.) **13**, 1021.

Aslanov, L.A., L.I. Soleva, M.A. Porai-Koshits and S.S. Goukhberg, 1972b, Russ. J. Struct. Chem. (Engl. Transl.) **13**, 610.

Aslanov, L.A., L.I. Soleva and M.A. Porai-Koshits, 1973, Russ. J. Struct. Chem. (Engl. Transl.) **14**, 998–1000.

Batyaev, I.M., and S.M. Shilov, 1983, Russ. J. Phys. Chem. (Engl. Transl.) **57**, 599.

Batyaev, I.M., N.N. Loginova and T.A. Privalova, 1975, Russ. J. Inorg. Chem. (Engl. Transl.) **20**, 1307.

Batyaev, I.M., S.M. Shilov and V.B. Zakharova, 1985, Russ. J. Inorg. Chem. (Engl. Transl.) **30**, 43–45.

Beck, M.T., and I. Nagypal, 1990, Chemistry of Complex Equilibria, 2nd Ed. (Ellis Horwood, Chichester).

Bertha, S.L., and G.R. Choppin, 1969, Inorg. Chem. **8**, 613–617.

Bhandary, K.K., and H. Manohar, 1973, Acta Crystallogr. B **29**, 1093.

Bhandary, K.K., H. Manohar and K. Venkatesan, 1975a, J. Chem. Soc., Dalton Trans., pp. 288–291.

Bhandary, K.K., H. Manohar and K. Venkatesan, 1975b, J. Inorg. Nucl. Chem. **37**, 1997.

Bjerrum, N., 1920, Z. Anorg. Allg. Chem. **119**, 179–201.

Blandamer, M.J., J. Burgess and J. Kijowski, 1982, Inorg. Chim. Acta **58**, 155.

Borina, A.F., 1988, Russ. J. Inorg. Chem. (Engl. Transl.) **33**, 964–967.

Brucher, E., J. Glaser, I. Grenthe and I. Puigdomenech, 1985, Inorg. Chim. Acta **109**, 111.

Bünzli, J.-C.G., 1989, Luminescent probes, in: Lanthanide Probes in Life, Chemical and Earth Sciences, eds J.-C.G. Bünzli and G.R. Choppin (Elsevier, Amsterdam) p. 219–293.

Bünzli, J.-C.G., 1993, J. Alloys & Compounds **192**, 266–270.

Bünzli, J.-C.G., and G.R. Choppin, eds, 1989, Lanthanide Probes in Life, Chemical and Earth Sciences (Elsevier, Amsterdam) 432pp.

Bünzli, J.-C.G., and V. Kasparek, 1991, Inorg. Chim. Acta **182**, 101–107.

Bünzli, J.-C.G., and C. Mabillard, 1986a, Inorg. Chem. **25**, 2750–2754.

Bünzli, J.-C.G., and C. Mabillard, 1986b, J. Less-Common Met. **126**, 379–388.

Bünzli, J.-C.G., and M.M. Vuckovic, 1983, Inorg. Chim. Acta **73**, 53–61.

Bünzli, J.-C.G., and M.M. Vuckovic, 1984, Inorg. Chim. Acta **95**, 105–112.

Bünzli, J.-C.G., and J.-R. Yersin, 1979, Inorg. Chem. **18**, 605–608.

Bünzli, J.-C.G., and J.-R. Yersin, 1982, Helv. Chim. Acta **65**, 2498–2506.

Bünzli, J.-C.G., and J.-R. Yersin, 1984, Inorg. Chim. Acta **94**, 301.

Bünzli, J.-C.G., E. Moret and J.-R. Yersin, 1978, Helv. Chim. Acta **61**, 762–771.

Bünzli, J.-C.G., C. Mabillard and J.-R. Yersin, 1982a, Inorg. Chem. **21**, 4214–4218.

Bünzli, J.-C.G., J.-R. Yersin and C. Mabillard, 1982b, Inorg. Chem. **21**, 1471–1476.

Bünzli, J.-C.G., A.E. Merbach and R.M. Nielson, 1987, Inorg. Chim. Acta **139**, 151–152.

Bünzli, J.-C.G., J.-P. Metabanzoulou, P. Froidevaux and L.P. Jin, 1990, Inorg. Chem. **29**, 3875–3881.

Bünzli, J.-C.G., A. Milicic-Tang and C. Mabillard, 1993, Helv. Chim. Acta **76**, 1292–1304.

Burgess, J., and J. Kijowski, 1981, J. Inorg. Nucl. Chem. **43**, 2289.

Buslaev, Yu.A., G.A. Kirakosyan and V.P. Tarasov, 1980, Sov. J. Coord. Chem. (Engl. Transl.) **6**, 172–180.

Campbell, A.N., and E.M. Kartzmark, 1984, J. Chem. Eng. Data **29**, 168.

Carnall, W.T., P.R. Fields and B.G. Wybourne, 1965, J. Chem. Phys. **42**, 3797.

Carvalho, R.G., and G.R. Choppin, 1967, J. Inorg. Nucl. Chem. **29**, 737.

Cassol, A., P. Di Bernardo, R. Portanova, M. Tolazzi, G. Tomat and P. Zanonato, 1992, J. Chem. Soc., Dalton Trans., pp. 469–474.

Chen, Zhigang, and C. Detellier, 1992, J. Solution Chem. **21**, 941–952.

Choppin, G.R., 1971, Pure Appl. Chem. **27**, 23.

Choppin, G.R., 1984, J. Less-Common Met. **100**, 141.

Choppin, G.R., and S.L. Bertha, 1973, J. Inorg. Nucl. Chem. **35**, 1309–1312.

Choppin, G.R., and A.J. Graffeo, 1965, Inorg. Chem. **4**, 1254–1257.

Choppin, G.R., and W.F. Strazik, 1965, Inorg. Chem. **4**, 1250.

Chrysochoos, J., 1974, J. Lumin. **9**, 79–93.

Chrysochoos, J., and A. Evers, 1973a, Chem. Phys. Lett. **18**, 115–119.

Chrysochoos, J., and A. Evers, 1973b, Spectrosc. Lett. **6**, 203.

Cossy, C., and A.E. Merbach, 1988, Pure & Appl. Chem. **60**, 1785–1796.

Cunha, M.C.F., H.F. Brito, L.B. Zinner, G. Vicentini and A.B. Nascimento, 1992, Coord. Chem. Rev. **1191–28**.

Davidenko, N.K., L.N. Lugina and K.B. Yatsimirskii, 1972, Russ. J. Inorg. Chem. (Engl. Transl.) **17**, 54.

Davies, J.A., 1981, Adv. Inorg. Chem. Radiochem. **24**, 115.

De Paoli, G., P. Ganis and P.L. Zanonato, 1993a, Polyhedron **12**, 671–676.

De Paoli, G., P. Ganis, P.L. Zanonato and G. Valle, 1993b, Polyhedron **12**, 1933–1938.

Di Bernardo, P., G.R. Choppin, R. Portanova and P.L. Zanonato, 1993, Inorg. Chim. Acta **207**, 85.

Dyer, R.B., D.H. Metcalf, R.G. Ghirardelli, R.A. Palmer and E.M. Holt, 1986, J. Am. Chem. Soc. **108**, 3621–3629.

Egorov, V.N., and I.E. Kuzinets, 1977, Russ. J. Inorg. Chem. (Engl. Transl.) **22**, 681.

Enderby, J.E., and G.W. Neilson, 1981, Rep. Prog. Phys. **44**, 593–653.

Evans, D.F., and P.H. Missen, 1982, J. Chem. Soc., Dalton Trans., pp. 1929–1932.

Favier, F., 1992, Ph.D. Thesis (Université de Montpellier).

Favier, F., and J.-L. Pascal, 1991, C.R. Acad. Sci. Paris. Ser. II **313**, 619–624.

Favier, F., and J.-L. Pascal, 1992, J. Chem. Soc., Dalton Trans., pp. 1997–2002.

Foster, D.R., and F.S. Richardson, 1983, Inorg. Chem. **22**, 3996.

Fratiello, A., V. Kubo and G.A. Vidulich, 1973, Inorg. Chem. **12**, 2066.

Fratiello, A., V. Kubo-Anderson, T. Bolinger, C. Cordero, B. DeMerit, T. Flores, D. Matejka and R. Perrigan, 1989a, J. Magn. Reson. **83**, 358–370.

Fratiello, A., V. Kubo-Anderson, T. Bolinger, C. Cordero, B. DeMerit, T. Flores and R.D. Perrigan, 1989b, J. Solution Chem. **18**, 313–330.

Fratiello, A., V. Kubo-Anderson, S. Azimi, T. Flores, E. Marinez, D. Matejka, R. Perrigan and M. Vigil, 1990, J. Solution Chem. **19**, 811–829.

Fratiello, A., V. Kubo-Anderson, S. Azimi, E. Marinez, D. Matejka, R. Perrigan and B. Yao, 1991, J. Solution Chem. **20**, 893–903.

Fratiello, A., S. Azimi, F. Laghaei, R.D. Perrigan and F. Reyes, 1992a, J. Solution Chem. **21**, 1015–1033.

Fratiello, A., V. Kubo-Anderson, E. Marinez, D. Matejka, R. Perrigan and B. Yao, 1992b, J. Solution Chem. **21**, 651–666.

Fratiello, A., V. Kubo-Anderson, S. Azimi, O. Chavez, F. Laghaei and R.D. Perrigan, 1993, J. Solution Chem. **22**, 519–538.

Fratiello, A., V. Kubo-Anderson, E.L. Bolanos, D. Haigh, F. Laghaei and R.D. Perrigan, 1994, J. Magn. Reson. A **107**, 56–66.

Glover, D.P., D.H. Metcalf and F.S. Richardson, 1992, J. Alloys & Compounds **180**, 83–92.

Görller-Walrand, C., and J. Godemont, 1977, J. Chem. Phys. **676**, 3655–3658.

Görller-Walrand, C., N. De Moitie-Neyt, Y. Beyens and J.-C.G. Bünzli, 1982, J. Chem. Phys. **77**, 2261.

Gruzdev, V.P., and V.L. Ermolaev, 1975, Russ. J. Inorg. Chem. (Engl. Transl.) **20**, 1467.

Haas, Y., and G. Navon, 1972, J. Phys. Chem. **76**, 1449.

Haas, Y., and G. Stein, 1971a, J. Phys. Chem. **75**, 3668.

Haas, Y., and G. Stein, 1971b, J. Phys. Chem. **75**, 3677.

Hamidi, M.E.M., 1992, Ph.D. Thesis (Université de Montpellier).

Hamze, M., J. Meullemeestre, M.-J. Schwing-Weill and F. Vierling, 1986, J. Less-Common Met. **118**, 153.

Hamze, M., J. Meullemeestre and F. Vierling, 1989, J. Less-Common Met. **146**, 75–87.

Helm, L., and A.E. Merbach, 1991, Eur. J. Solid State Inorg. Chem. **28**, 245–250.

Henrie, D.E., R.L. Fellows and G.R. Choppin, 1976, Coord. Chem. Rev. **18**, 199.

Hu, Jingyu, Shen Qi and Jin Zhongsheng, 1990, Kexue Tongbao (Chinese Sci. Bull.) **35**, 1090–1092.

Ishiguro, S., and R. Takahashi, 1991, Inorg. Chem. **30**, 1854–1858.

Janakiraman, R., and L. Kevan, 1981, J. Chem. Phys. **75**, 1658–1660.

Jezowska-Trzebiatowska, B., S. Ernst, J. Legendziewicz and G. Oczko, 1978, Bull. Pol. Acad. Sci. Ser. Chem. **26**, 805.

Jezowska-Trzebiatowska, B., J. Legendziewicz and W. Strek, 1984, Inorg. Chim. Acta **95**, 157.

Jin, Zhongsheng, Wang Shenglong, Wang Fusong, Shen Cheng, Yang Guangdi and Fan Yuguo, 1985, Gaodeng Xuexiao Huaxue Xuebao (Chem. J. Chin. Univ.) **6**, 735.

Johansson, G., H. Yokoyama and H. Ohtaki, 1991, J. Solution Chem. **20**.

Johansson, L., 1971, Acta Chem. Scand. **25**, 3569.

Jørgensen, C.K., 1979, in: Handbook on the Physics and Chemistry of Rare Earths, Vol. 3, eds K.A. Gschneidner Jr. and L. Eyring (North-Holland, Amsterdam) ch. 23.

Jørgensen, C.K., and R. Reisfeld, 1982, Struct. & Bonding **100**, 127.

Kandpal, H.C., A.K. Agarwal and H.B. Tripathi, 1979, J. Lumin. **20**, 207.

Kanno, H., and J. Hiraishi, 1984, J. Phys. Chem. **88**, 2787.

Kavun, V.Ya., B.N. Chernyshev, V.I. Kostin and V.I. Sergienko, 1981, Russ. J. Inorg. Chem. (Engl. Transl.) **26**, 1278.

Keller, B., K. Bukietynska and B. Jezowska-Trzebiatowska, 1982, Chem. Phys. Lett. **92**, 541.

Knoeck, J., 1969, Anal. Chem. **41**, 2069.

Kozachenko, N.N., and I.M. Batyaev, 1971a, Russ. J. Inorg. Chem. (Engl. Transl.) **16**, 66.

Kozachenko, N.N., and I.M. Batyaev, 1971b, Russ. J. Inorg. Chem. (Engl. Transl.) **16**, 978–979.

Kozachenko, N.N., I.M. Batyaev and V.E. Mironov, 1970, Russ. J. Inorg. Chem. (Engl. Transl.) **15**, 452–453.

Kozachenko, N.N., N.A. Panteleeva, V.S. Netsvetaeva and I.M. Batyaev, 1973, Russ. J. Inorg. Chem. (Engl. Transl.) **18**, 938–940.

Krestov, G.A., 1991, Thermodynamics of Solvation (Ellis Horwood, Chichester).

Krishnamurthy, S.S., and S. Soundararajan, 1966, J. Inorg. Nucl. Chem. **28**, 1689.

Krishnamurthy, S.S., and S. Soundararajan, 1969, Can. J. Chem. **47**, 995.

Krishnamurthy, V.N., and S. Soundararajan, 1967, J. Inorg. Nucl. Chem. **29**, 517.

Krutous, A.I., and I.M. Batyaev, 1973, Russ. J. Inorg. Chem. (Engl. Transl.) **18**, 1451.

Krutous, A.I., and I.M. Batyaev, 1974, Russ. J. Inorg. Chem. (Engl. Transl.) **19**, 671–674.

Legendziewicz, J., B. Keller and W. Strek, 1982, Chem. Phys. Lett. **92**, 205.

Legendziewicz, J., G. Oczko, B. Keller, W. Strek and B. Jezowska-Trzebiatowska, 1984, J. Mol. Struct. **115**, 421.

Legendziewicz, J., P. Deren, B. Jezowska-Trzebiatowska and W. Strek, 1985, J. Less-Common Met. **112**, 271–274.

Legendziewicz, J., G. Oczko and B. Keller, 1986, Bull. Pol. Acad. Sci. Ser. Chem. **34**, 257–265.

Legendziewicz, J., H. Maghrawy, B. Jezowska-Trzebiatowska and W. Strek, 1988, J. Mol. Struct. **174**, 473–476.

Lin, Y., N. Hu, S. Liu, Q. Zhou, S. Wu, M. Wang and E. Shi, 1981, Wuli Xuebao (Acta Phys. Sin.) **30**, 1586.

Lincoln, S.F., 1971, Coord. Chem. Rev. **6**, 309–329.

Lincoln, S.F., 1986, Adv. Inorg. Bioinorg. Mechanisms **4**, 217–287.

Lin, Yonghua, Hu Ninghai, Zhou Quinglian, Liu Shuzhen, Wu Shixue, Shi Endong and Wang Mingyi, 1984, Huaxue Xuebao (Acta Chim. Sin.) **42**, 372–376.

Lugina, L.N., and N.K. Davidenko, 1980, Russ. J. Inorg. Chem. (Engl. Transl.) **25**, 1322.

Lugina, L.N., N.K. Davidenko and K.B. Yatsimirskii, 1973, Russ. J. Inorg. Chem. (Engl. Transl.) **18**, 1453.

Lugina, L.N., N.K. Davidenko, L.N. Zabotina and K.B. Yatsimirskii, 1974, Russ. J. Inorg. Chem. (Engl. Transl.) **19**, 1456–1459.

Mabillard, C., 1983, Ph.D. Thesis No. 505 (Ecole Polytechnique Fédérale, Lausanne, Switzerland).

Marcantonatos, M.D., M. Deschaux and J.-J. Vuilleumier, 1981, Chem. Phys. Lett. **82**, 36.

Marcantonatos, M.D., M. Deschaux and J.-J. Vuilleumier, 1982, Chem. Phys. Lett. **91**, 149.

Meier, W., Ph. Bopp, M.M. Probst, E. Spohr and J.-I. Lin, 1990, J. Phys. Chem. **94**, 4672–4682.

Milicic-Tang, A., and J.-C.G. Bünzli, 1992, Inorg. Chim. Acta **192**, 201–209.

Mims, W.B., and J.L. Davis, 1976, J. Chem. Phys. **65**, 3266.

Mironov, V.E., N.I. Awramenko, A.A. Kopyrin and V.V. Bloshin, 1983, Izv. Vyss. Uch. Zav. Khim. Khim. Tekh. **26**, 158.

Miyakawa, K., Y. Kaizu and H. Kobayashi, 1988, J. Chem. Soc., Faraday Trans. 1 **84**, 1517–1529.

Nash, K.L., and J.C. Sullivan, 1991, Kinetics of complexation and redox reactions of the lanthanides in aqueous solutions, in: Handbook on the Physics and Chemistry of Rare Earths, Vol. 15, eds K.A. Gschneidner Jr. and L. Eyring (Elsevier, Amsterdam) p. 347–391.

Pilloud, F., and J.-C.G. Bünzli, 1987, Inorg. Chim. Acta **139**, 153–154.

Pisaniello, D.L., and A.E. Merbach, 1982, Helv. Chim. Acta **65**, 573.

Pisaniello, D.L., P.J. Nichols, P.Y. Ducommun and A.E. Merbach, 1982, Helv. Chim. Acta **65**, 1025.

Pisaniello, D.L., L. Helm, P. Meier and A.E. Merbach, 1983, J. Am. Chem. Soc. **105**, 4528.

Quill, L., P.W. Selwood and B.S. Hopkins, 1928, J. Am. Chem. Soc. **50**, 2929–2936.

Rard, J.A., and F.H. Spedding, 1982, J. Chem. Eng. Data **27**, 454.

Raymond, K.N., 1983, Chem. Eng. News **61**, 4.

Reidler, J., and H.B. Silber, 1973, J. Chem. Soc., Chem. Commun. 354–355.

Reidler, J., and H.B. Silber, 1974a, J. Inorg. Nucl. Chem. **36**, 175.

Reidler, J., and H.B. Silber, 1974b, J. Phys. Chem. **78**, 424–428.

Richardson, F.S., and H.G. Brittain, 1981, J. Am. Chem. Soc. **103**, 18–24.

Rizkalla, E.N., and G.R. Choppin, 1991, Hydration and hydrolysis of lanthanides, in: Handbook on the Physics and Chemistry of Rare Earths, Vol. 15, eds K.A. Gschneidner Jr. and L. Eyring (Elsevier, Amsterdam) p. 393–442.

Sayre, E.V., D.G. Miller and S. Freed, 1957, J. Chem. Phys. **26**, 109.

Shen, Qi, Hu Jingyu and Jin Zhongsheng, 1990, Zhongguo Xitu Xuebao (J. Chin. Rare Earth Soc.) **8**, 359–361.

Silber, H.B., 1974, J. Phys. Chem. **78**, 1940.

Silber, H.B., 1978, Rare Earths in Mod. Sci. & Technol. **1**, 149–154.

Silber, H.B., 1980, Rare Earths in Mod. Sci. & Technol. **2**, 93–98.

Silber, H.B., and G. Bordano, 1978, Rare Earths in Mod. Sci. & Technol. **1**, 129–134.

Silber, H.B., and G. Bordano, 1979, J. Inorg. Nucl. Chem. **41**, 1169.

Silber, H.B., and R.L. Campbell, 1989, J. Less-Common Met. **149**, 265–269.

Silber, H.B., and J. Fowler, 1976, J. Phys. Chem. **80**, 1451.

Silber, H.B., and L.U. Kromer, 1980, J. Inorg. Nucl. Chem. **42**, 103.

Silber, H.B., and T.J. Mioduski, 1984, Inorg. Chem. **23**, 1577.

Silber, H.B., and A. Pezzica, 1976, J. Inorg. Nucl. Chem. **38**, 2053.

Silber, H.B., and R. Riddle, 1982, Rare Earths in Mod. Sci. & Technol. **3**, 99.

Silber, H.B., and M.S. Strozier, 1987, Inorg. Chim. Acta **128**, 267–271.

Silber, H.B., and Zhang Yue, 1987, Inorg. Chim. Acta **139**, 107–109.

Silber, H.B., D. Bouler and T. White, 1978, J. Phys. Chem. **82**, 775.

Silber, H.B., D.M. Gilbert and M.R. Riddle, 1983, J. Less-Common Met. **94**, 319.

Silber, H.B., R. Bakhshandehfar, L.A. Contreras, F. Gaizer, M. Gonsalves and S. Ismail, 1990, Inorg. Chem. **29**, 4473–4475.

Smith Jr, L.S., D.C. McCain and D.L. Wertz, 1976, J. Am. Chem. Soc. **98**, 5125.

Spedding, F.H., L.E. Shiers, M.A. Brown, J.L. Derer, D.L. Swanson and A. Habenschuss, 1975, J. Chem. Eng. Data **20**, 81–88.

Spedding, F.H., M.A. Mohs, J.L. Derer and A. Habenschuss, 1977a, J. Chem. Eng. Data **22**, 142–153.

Spedding, F.H., J.A. Rard and A. Habenschuss, 1977b, J. Phys. Chem. **81**, 1069–1074.

Spedding, F.H., J.L. Baker and J.P. Walters, 1979, J. Chem. Eng. Data **24**, 298.

Steel, M.L., and D.L. Wertz, 1977, Inorg. Chem. **16**, 1225.

Stephens, E.M., 1989, Gadolinium as an EPR probe, in: Lanthanides in Life, Chemical and Earth Sciences, eds J.-C.G. Bünzli and G.R. Choppin (Elsevier, Amsterdam) p. 181–217.

Stephens, E.M., D.R. Foster and F.S. Richardson, 1986, J. Less-Common Met. **126**, 389–394.

Sudnick, D.R., and W. deW. Horrocks Jr, 1979, Biochim. Biophys. Acta **578**, 135–144.

Svetashev, A.G., and M.P. Tsvirko, 1991, Teor. & Eksp. Khim. (Engl. Transl.), pp. 108–113.

Takahashi, R., and S. Ishiguro, 1991, J. Chem. Soc., Faraday Trans. **87**, 3379–3383.

Takahashi, R., and S. Ishiguro, 1992, J. Chem. Soc., Faraday Trans. **88**, 3165–3170.

Tanaka, F., Y. Kawasaki and S. Yamashita, 1988, J. Chem. Soc., Faraday Trans. I **84**, 1083–1090.

Tarasov, V.P., G.A. Kirakosyan, Yu.A. Buslaev, S.V. Trots and V.T. Panyushkin, 1986, Sov. J. Coord. Chem. (Engl. Transl.) **11**, 514.

Thomas, R.R., V. Chebolu and A. Sen, 1986, J. Am. Chem. Soc. **108**, 4096–4103.

Troxler, L., and G. Wipff, 1994, J. Am. Chem. Soc. **116**, 1468–1480.

Volpe, P.L.O., A.P. Chagas and C. Airoldi, 1980, J. Inorg. Nucl. Chem. **42**, 1321.

Vuilleumier, J.-J., M. Deschaux and M.D. Marcantonatos, 1982, Chem. Phys. Lett. **86**, 242.

Wertz, D.L., and S.T. Finch, 1979, Inorg. Chem. **18**, 1590–1593.

Yamaguchi, T., H. Nomura, H. Wakita and H. Ohtaki, 1988, J. Chem. Phys. **89**, 5153–5159.

Yamaguchi, T., S. Tanaka, H. Wakita, M. Misawa, I. Okada, A.K. Soper and W.S. Howells, 1991, Z. Naturforsch. A **46**, 84–88.

Zholdakov, A.A., L.N. Lugina and N.K. Davidenko, 1971, Russ. J. Inorg. Chem. (Engl. Transl.) **16**, 1265–1268.

Zinina, E.M., and A.V. Shablya, 1975, Opt. Spectrosc. (Engl. Transl.) **39**, 386.

Zinner, L.B., G. Vicentini, D.M.A. Melo and O.A. Oliveira, 1991, Thermochim. Acta **180**, 341–344.

Handbook on the Physics and Chemistry of Rare Earths
Vol. 21
edited by K.A. Gschneidner, Jr. and L. Eyring

Chapter 146

TRACE DETERMINATION OF LANTHANIDES IN HIGH-PURITY RARE-EARTH OXIDES

V. BHAGAVATHY, T. PRASADA RAO and A.D. DAMODARAN
Regional Research Laboratory (CSIR), Trivandrum 695 019, India

Contents

List of abbreviations

AAS	Atomic absorption spectrometry	HPLC	High performance liquid chromatography
ES	Emission spectrometry	NAA	Neutron activation analysis
EDXRF	Energy dispersive X-ray fluorescence spectrometry	XRF	X-ray fluorescence spectrometry
DCP-ES	Direct current plasma emission spectrometry		

1. Introduction

High-purity individual rare-earth oxides are increasingly used as major components in lasers (Y_2O_3), phosphors (YVO_3, Eu_2O_3), magnetic bubble memory films (Gd_2O_3) and refractive-index lenses and fibre optics (La_2O_3) (see Murthy and Gupta 1980 and DeKalb and Fassel 1979). The electrical and magnetic properties of these materials are influenced by the levels of contaminating foreign trace elements. It is therefore important that such contaminants at trace levels be identified and quantified. The non-rare-earth analytes in rare-earth oxides can be determined by any of the analytical techniques either directly or by prior preconcentrative separation by ion exchange or solvent extraction. On the other hand, the determination of traces of lanthanides in high-purity rare-earth oxides is a more important and difficult task. This requires judicious selection of an analytical technique

for the specified determination of traces of lanthanides in high-purity rare-earth oxides. Various analytical procedures have been developed for this purpose over the years. These procedures are summarized in table 1.

2. Analytical techniques

2.1. *Spectrophotometry*

All lanthanides have similar absorption spectra when they are reacted with a chromogenic agent. Hence it is very difficult to determine traces of lanthanides in high-purity rare-earth oxides. However, two procedures have been described for the determination of neodymium, one in Y_2O_3 (Poluektov et al. 1973) and the other one in yttrium aluminum garnet (Meliman et al. 1983). Prasada Rao and Sukumar (1986) have described a higher-order derivative procedure for the simultaneous determination of lanthanum and europium. This method is based on the utilization of the third-order derivative for the determination of lanthanum and the second-order derivative for europium after reaction with bromopyrogallol red as the chromogenic reagent. Prasada Rao et al. (1988a) have developed a third-order derivative spectrophotometric procedure for the determination of praseodymium in the presence of samarium, europium, terbium, holmium, dysprosium and lutetium oxides. A third-order derivative spectrophotometric procedure was developed for the determination of traces of samarium in the presence of middle and heavy rare-earth oxides (Prasada Rao et al. 1988b). A fourth-order derivative spectrophotometric procedure was developed for the determination of ytterbium and dysprosium in a mixture of rare-earth metal oxides in 1 M $HClO_4$ medium (Yan and Ren 1990).

2.2. *Spectrofluorimetry*

A few fluorimetric procedures have been described for the trace determination of lanthanides in high-purity rare-earth oxides. These include the determination of (i) europium in La_2O_3 (Lyle and Maghzian 1975) and in La_2O_3 and Y_2O_3 (Beltyukova and Kravchenko 1982) and rare-earth oxides (Mischenko et al. 1978), (ii) terbium in La_2O_3 (Tischenko et al. 1978b) and in the oxides of lanthanum, gadolinium and yttrium (Poluektov et al. 1975) and (iii) cerium in rare-earth ores and R_2O_3 concentrates. Ozawa and Hersh (1976) described another procedure for the determination of lanthanides in yttria with terbium as an internal standard.

2.3. *Atomic absorption spectrometry (AAS)*

Flame atomic absorption spectrometry permits the determination of traces of lanthanides present in high-purity rare-earth oxides but is not that sensitive. Luo and Hu (1981) determined traces of holmium and erbium present in Y_2O_3 by employing a N_2O–C_2H_2 flame. Electrothermal atomic absorption spectrometry was successfully used for the

Table 1
Summary of analytical procedures

Sl.#	Method	Analyte element	Matrix	Reaction conditions	Sensitivity/ Limit of detection	Reference
1	Flame emission	Eu, Gd, Tb, Dy, Ho, Er, Tm, Yb, Lu	Y_2O_3	Pre-mixed air–acetylene burner, methanol	0.001, 0.3, 0.3, 0.02, 0.03, 0.2, 0.01 and 0.2 ppm, respectively	Matsuda and Hanamura (1977)
2	X-ray fluorescence	Eu, Gd and Yb	Y_2O_3	W-target, LiF analysing crystal	15 ppm (Eu, Gd), 68 ppm (Yb)	Dixit and Deshpande (1977a)
3	DC arc spectrography	Lanthanides	Y_2O_3	Ar–O (4:1) atmosphere separation with naphthenic–HCl system	0.013 ppb (Yb), 0.15 ppm (Ce)	Peng et al. (1979)
4	NAA	Lanthanides		Extraction chromatographic separation with *bis* (2-ethylhexyl) phosphate on Kieselguhr	–	Teixeira da Silva and Atalla (1979)
5	HPLC	Lanthanides	Monazite sand, high purity oxides of La, Ce, Sm, Y	Li-chromosorb cation exchanger, 2-hydroxy isobutyric acid	–	Hwang et al. (1981)
6	Fluorescence	Lanthanides	Yttria	Tb as internal standard	10 ppm	Ozawa and Hersh (1976)
7	XRF	Eu, Gd, Tb, Yb, Dy, Ho, Er	Y_2O_3	W-target tube, flow proportional counter	0.005%	Dixit and Deshpande (1975)
8	Luminescence	Gd, Eu, Dy, Sm or Tb	Y_2O_3	Excitation by condensed spark	0.008 ppm (Dy), 0.006 ppm (Tb), 0.01 ppm (Gd), 0.02 ppm (Eu), 0.05 ppm (Sm)	Antonov et al. (1973a)
9	Spectrophotometry	Nd	Y_2O_3	Gallein-CYAB, Tiron	1–4% Nd_2O_3 in Y_2O_3	Poluektov et al. (1973)
10	Neutron activation	Eu	Y_2O_3	Ge–Li detector, 1024 channel pulse height analyser	–	Ujihira et al. (1973)
11	Luminescence	Tn, Dy, Ho	La_2O_3	–	0.06 to 1 ppm	Efryushina et al. (1973a)
12	Cathode ray excited emission spectrometry	Pr, Tb, Eu, Dy	Y_2O_3	Conversion to oxysulphide	–	Larach and Shrader (1973)
13	X-ray excited optical luminescence	Ce to Yb	Y_2O_3	YPO_4 or YVO_4 as the host	0.001 ppm (Tb), 0.5 ppm (Ho, Yb)	De Silva and Fassel (1972)

continued on next page

Table 1, *continued*

Sl.#	Method	Analyte element	Matrix	Reaction conditions	Sensitivity/ Limit of detection	Reference
14	Emission spectroscopy	Y-subgroup elements	Y_2O_3	Extraction chromatographic separation with TBP–NH_4SCN	–	Zhang (1983)
15	DC arc spectrography	Trace rare earths	Sm_2O_3	Extraction chromatographic separation with 2-ethylhexyl(2-ethylhexyl)phosphonate–HCl	0.005–0.1 ppm	Yu and Miao (1983)
16	Emission spectrography	Lanthanides	R_2O_3	R-graphite (1:9) buffer is best	0.01–0.5 ppm	Yu et al. (1983)
17	NAA	La	Pr_6O_{11}	–	7 ppb	Dybczynski and Sterlinski (1972)
18	Spectrography	La	Y_2O_3	Special C-electrode in a stream of Ar–O	0.5 ppm	Dittrich et al. (1972)
19	DRF	Y, Ce, Pr, Nd, Eu, Gd	Sm_2O_3	W-target tube, LiF crystal	0.002–0.009%	Dixit and Deshpande (1978)
20	AC arc emission spectrometry	Eu, Sm, Gd, Y	Y_2O_3, Sm_2O_3, Gd_2O_3	3-prism spectrograph with 0.02 nm slit width and Ar–O atmosphere	2–14 ppm	Dittrich et al. (1978)
21	Spectrofluorimetry	Tb	Y_2O_3	1:1:3 terbium–diantipyrinyl–methan slaicylate complex	0.2 ppm (TB)	Tischenko et al. (1978a)
22	DC arc emission spectrography	Ce, Pr, Nd, Tb	La_2O_3	air/Ar–O–N	25–40 ppm	Dittrich and Niebergall (1978)
23	XRF	Ce, Pr, Sm, Eu, Gd	Nd_2O_3	W-target tube, LiF crystal	50–100 ppm	Chandola and Mohile (1977a)
24	Pulse polarography	Eu	R_2O_3	–0.7 VSCE	60 nm Eu^{3+}	Steeman et al. (1977)
25	HPLC	Sm, Nd, Ce, Pr	U	–	–	Larsen and Pedersen (1978)
26	NAA	Pr, Ce, Tb	Y_2O_3	–	0.1–1.0 ppm	Polkowska (1982)
27	ICP-ES	R	Y_2O_3	Ar as coolant and plasma gas	0.2–3.0 ppm	Tanaka et al. (1982)
28	XRF	Dy, Ho, Tm, Yb, Lu, Tb, Y	Er_2O_3	W-target tube, LiF crystal	50 ppm	Chandola et al. (1981)
29	Luminescence	Nd, Dy	Gd oxyfluoride	–	2.0 ppm	Efryushina et al. (1982)
30	Spectrofluorimetry	Tb	Gd_2O_3	EDTA–Tiron automated procedure	–	Lyle and Zatar (1983)
31	Luminescence	Dy	Tm_2O_3	–	10–250 ppm	Efryushina et al. (1984)
32	XRF	Nd	YAG	–	80 ppm	Shevtsov et al. (1983)
33	XRF	Gd, Tb, Dy, Er, Tm, Yb	Ho_2O_3	–	–	Dixit and Kapoor (1979)
34	AAS	Ho, Er	Y_2O_3	Nitrous oxide–acetylene flame	–	Luo and Hu (1981)

continued on next page

Table 1, *continued*

Sl.#	Method	Analyte element	Matrix	Reaction conditions	Sensitivity/ Limit of detection	Reference
35	Laser exited fluorescence	Eu, Pr, Nd, Sm, Tm, Tb, Dy, Ho, Er	–	–	0.4 to 450 pg/ml	Gustafson and Wright (1979)
36	Luminescence	Sm, Eu	Gd_2O_3	–	–	Smirdova et al. (1980)
37	XRF	Y, Eu, Gd, Tb, Ho, Er	Dy_2O_3	W-target tube, proportional counter, LiF crystal	2.6 to 15 ppm	Dixit and Deshpande (1980)
38	Luminescence	Eu	La, Gd, Tb, Y oxides	2-propionylindan 1, 3-dione forms 1:3 Eu–R complex in 90% acetone	0.1 ppm	Beltyukova et al. (1980)
39	X-ray/UV excited luminescence	Tb	Gd_2O_3	–	0.01 ppm (Laser) 0.4 ppm (UV)	A.K. Novikova et al. (1980)
40	Luminescence	Tb	Gd_2O_3	Gadolinium fluoride oxide phosphor	0.3 ppb	G.K. Novikova et al. (1981)
41	Spectrophotometry	Ce	La_2O_3	N-4-chlorophenyl-2-furohydroxamic acid	2 ppm	Abbasi (1980)
42	AC arc spectrography	Eu	Gd_2O_3	459.4 nm line is used	–	Nelder et al. (1980)
43	XRF	La, Ce, Nd, Sm	Pr_6O_{11}	W-target tube, LiF crystal	21–36 ppm	Chandola and Mohile (1977b)
44	Luminescence	Eu	Tb_4O_7	By formation of crystalline phosphor $Cs_2NaTb_{1-x}Eu_xCl_6$	0.5–50 ppm	Efryushina et al. (1977)
45	NAA	Gd	Eu_2O_3	–	–	Kubota (1976)
46	XRF	Sm, Eu, Tb, Dy, Ho, Yb	Gd_2O_3	W-target tube, LiF crystal	10–80 ppm	Dixit and Deshpande (1977b)
47	DC arc emission spectrography	Yb, Eu, Tm, Sm	Lanthanides	–	10–80 ppm	Dittrich and Borzyn (1977)
48	Fluorimetry	Sm	Nd_2O_3, Gd_2O_3	–	–	Jayawant et al. (1976)
49	XRF	Ce, Pr, Sm, Eu, Gd	Nd_2O_3	W-target tube, LiF	0.005–0.01%	Chandola and Mohile (1978)
50	Fluorescence	Tb	La_2O_3	Complex with N (2-hydroxy-phenyl) iminodiacetic acid	5–50 ppm	Tischenko et al. (1978b)
51	DC arc spectrography	Y, Pr, Sm, Eu, Gd, Dy	La_2O_3	–	–	Freidman et al. (1978)
52	Fluorescence	Eu	La_2O_3, Nd_2O_3, Gd_2O_3, Y_2O_3	EDTA, 1, 10-phenanthroline	0.014 ppm	Mischenko et al. (1978)

continued on next page

Table 1, *continued*

Sl.#	Method	Analyte element	Matrix	Reaction conditions	Sensitivity/ Limit of detection	Reference
53	Luminescence	Sm	Tb_4O_7	Sm drifted terbium phosphate phosphor	1 ppm	Gava et al. (1979)
54	Spectrography	Eu	Lanthanides	–	0.01%	Polyanskii et al. (1979)
55	Spectrophotometry	Nd	Y	Sulphoranzo III	0.19 ppm	Maltseva and Kharzeeva (1979)
56	NAA, PAA	Lanthanides	Y, Al garnets	Cyclotron accelerated protons	1 ppb (NAA), 0.1 ppm (PAA)	Muminov et al. (1979)
57	DC arc spectrography	La, Ce, Pr, Sm, Sm	Nd_2O_3	–	2.5 ppm	Peng et al. (1981)
58	X-ray spectrography	La, Ce, Nd, Sm, Eu, Gd	–	–	–	Agapova et al. (1981)
59	NAA	Lanthanides	CeO_2	Ge(Li) detector	0.3–25 ppm	Pung et al. (1980)
60	Luminescence	Pr	Gd_2O_3	Crystalline phosphor, Gd fluoride/oxide	10 ppb	Zhikareva et al. (1981)
61	NAA	Pr	La compounds	–	2.4 ppm	Kueppers and Erdtmann (1981)
62	Luminescence	Pr	La_2O_3	–	0.05 ppm	Smirdova et al. (1970)
63	Kinetic spectrophotometry	Pr, Yb	Pr, Yb	pH 4.8	Yatsimirskii et al. (1970)	
64	Cathode ray excited ES	Tb	Y_2O_3	–	0.001 ppm	Ross (1969)
65	ES	Tb, Gd, Dy, La, Yb	Y_2O_3	N_2O–C_2H_2 flame	–	Kniseley et al. (1969)
66	Photon activation analysis	Y	Lanthanides	NaI(Tl) detector	1 μg	Lutz and Lafleur (1969)
67	DC arc spectrography	La, Ce, Pr, Nd	Y, heavy lanthanides	–	–	Vakulenko et al. (1973)
68	Spectrography	Lanthanides	Eu_2O_3	–	0.1–10 ppm	Stroganova et al. (1973)
69	DC arc ES	Pr, Eu, Sm	Nd_2O_3	–	2 to 9 ppm	Osumi and Hiyake (1972)
70	Luminescence	Nd, Sm, Eu	La_2O_3	–	0.1 ppm	Poluektov et al. (1970)
71	Luminescence	Tb, Dy, Ho	La_2O_3	–	0.06 ppm	Efryushina et al. (1973a)
72	Luminescence	Eu	La, Gd, Lu, Y oxides	Dibenzoyl methane and diethylamine	0.03 ppm	Tischenko et al. (1973a)
73	Luminescence	Sm, Eu, Dy	Gd_2O_3	–	–	Poluektov and Gava (1969)
74	Luminescence/ spectrography	Lanthanides	Y_2O_3	–	–	Shmanenkova et al. (1969)
75	ICP-ES	Lanthanides	Gd_2O_3	Extr. with P-125	–	Li et al. (1987a)
76	XRF	Y, Er, Tm, Yb	Lu_2O_3	Philips PW-1220 with LiF crystal	0.002–1%	Chandola and Khanna (1987)

continued on next page

Table 1, *continued*

Sl.#	Method	Analyte element	Matrix	Reaction conditions	Sensitivity/ Limit of detection	Reference
77	Luminescence	Eu	Y_2O_3	–	–	F. Wang et al. (1986)
78	DCP-ES	Ce,Eu & Tb	Rare-earth matrices	–	1–30 mg/l	Jyrkas and Leskela (1986)
79	ICP-ES	Lanthanides	La, Ce, Pr, Nd, Sm, Y oxides		0.29–5.95 ppm	J. Ma et al. (1986)
80	ICP-ES	Lanthanides	CeO_2	Matrix of CeO_2 was separated by extraction with P-538	3.7 ppm	Guo and Fec (1986)
81	XRF	Sm, Dy, Eu, Tb	Y_2O_3	Cathode ray excitation source	0.4 to 1.0 ppm	Luo and Piao (1987)
82	AC arc spectrography	Lanthanides	Gd_2O_3	Solution–dry residue technique	–	Song et al. (1986)
83	AC arc spectrography	Lanthanides	Eu_2O_3	–	0–8 ppm	Song et al. (1987)
84	Magnetic resonance	Nd_2O_3	YAG–Nd_2O_3 laser crystal	Magnetic susceptibility was measured	–	Su and Wang (1985)
85	XRF	Lanthanides	Er_2O_3	W-target tube, LiF crystal	–	Chandola and Khanna (1985a)
86	Luminescence	Ho, Er	Y_2O_3	Based on formation of crystallophosphor yttrium fluoride oxide	50 ppb	Lebedeva and Karyakin (1985)
87	Electrothermal AAS	Yb	Y_2O_3	–	1–18 ppm	Chen et al. (1986)
88	Γ-activation	Nd, Y	La_2O_3, Tb_4O_7	–	–	Klinov and Ladeishchikov (1986)
89	XRF	Ho, Er, Y, Tm, Lu	Yb_2O_3	W-target tube, LiF	5–10 000 ppm	Chandola and Khanna (1985b)
90	AC arc spectrography	Lanthanides	Tb_4O_7	–	–	Song and Jin (1984)
91	DC arc spectrography	Lanthanides	Er_2O_3	–	1.5 to 60 ppm	Yu and Fu (1984)
92	Luminescence	Tb, Dy	Lanthanide oxide	Measured at 545/570 nm	10 ppb (Tb), 200 ppb (Dy)	Beltyukova et al. (1984)
93	Secondary ion mass spectrography	Lanthanides	YF_3 or LaF_3	Based on peaks due to double charged ions	39–560 ppm	Uwamino et al. (1984)
94	Laser fluorimetry	Tb, Dy, Sm	–	–	4 ppb (Tb), 20 ppb (Dy), 160 ppb (Sm)	Xu and Qui (1984)
95	Electrothermal AAS	Eu	R oxides	–	–	Yao and Zeng (1984)

continued on next page

Table 1, *continued*

Sl.#	Method	Analyte element	Matrix	Reaction conditions	Sensitivity/ Limit of detection	Reference
96	Luminescence	Tb, Eu, Sm	Gd_2O_3, Tb_4O_7	–	0.1 ppm (Tb), 0.5–500 ppm (Eu), 42–700 ppm (Sm)	Efryushina and Novikova (1984)
97	Stripping voltammetry	Ce	R oxides	Electrolysis for 20 min at 1.4 V, V, SCE. max. current occurs at 0.6 V in reverse scan	–	Iikova et al. (1983)
98	ICP-ES	Trace R	Y_2O_3	–	3–130 ppb	Ru et al. (1983)
99	Luminescence	Dy	Yb_2O_3	By formation of crystalline phosphor $GdYbF_2O_2$	0.01 ppm	G.K. Novikova et al. (1983)
100	Polarography	La	$[(LaGd)_2O_2S]$–		0.5 to 5 µm	Gao et al. (1983)
101	ICP-ES	R	La_2O_3	–	1–10 ppm	Ishii and Satoh (1983)
102	Spectrophotometry	Nd	YAG	Line at 588.3 µm	5 ppm	Meliman et al. (1983)
103	DCP-ES	Nd	Y_2O_3	–	–	Buehring and Buban (1981)
104	Luminescence	Tb	YbFO, GdFO	–	0.1–800 ppm	G.K. Novikova et al. (1981)
105	Luminescence	Gd, Tb, Dy	Y_2O_3, Sc_2O_3	–	0.5 ppm (Gd), 0.05 ppm (Tb), 0.1 ppm (Dy)	Gava et al. (1976)
106	XRF	R	CeO_2	–	50–100 ppm	Chandola et al. (1976)
107	XRF	R	Tb_4O_7	W-target tube, LiF (200) crystal	–	Chandola et al. (1976)
108	Fluorimetry	Tb	La, Gd, Y oxides	–	30–300 ppm	Poluektov et al. (1975)
109	Fluorimetry	Eu	La_2O_3	–	100 ppm	Lyle and Maghzian (1975)
110	Spectrography	R	CeO_2	–	–	Boitsov and Zilbershtein (1974)
111	NAA	R	Lu_2O_3	–	–	Kubota (1974)
112	NAA	Eu, Ho, Tb	Tm_2O_3	–	0.05 ppm (Eu), 2 ppm (Ho or Tb)	Antonov et al. (1973b)
113	Luminescence	Pr, Gd	Nd_2O_3	Proton beam excitation	10–200 ppm (Pr), 0.001 ppm (Gd)	Shulgin et al. (1973)
114	AC arc spectrography	R	R metal mixtures	–	–	Grampurohit and Sethumadhavan (1974)
115	Fluorimetry	Eu	R oxides	By formation of 1:1:1 Eu–TTA–2-hydroxy ethyl EDTA complex	–	Tischenko et al. (1973b)

continued on next page

Table 1, *continued*

Sl.#	Method	Analyte element	Matrix	Reaction conditions	Sensitivity/ Limit of detection	Reference
116	Fluorimetry	Tb	La_2O_3	By formation of 1:1:1 Tb–Tiron–iminodiacetic acid complex	23 ppb (Tb)	Tischenko et al. (1974)
117	Cathode ray excited emission spectrography	R	Y_2O_3	By conversion to oxysulphide	–	Larach and Shrader (1973)
118	Luminescence	R	La_2O_3, Y_2O_3	By formation of crystalline phosphors	–	Poluektov et al. (1972)
119	Luminescence	Eu, Tm, Yb	La_2O_3	–	–	Efryushina et al. (1973b)
120	AC arc emission spectrometry	R	Ho_2O_3	–	–	Song et al. (1989)
121	ICP-ES	R	Yb_2O_3	–	–	Piao et al. (1989)
122	Secondary ion mass spectrometry	R	Y_2O_3	–	16–10 000 µg/g	Morikawa et al. (1990)
123	Fluorimetry	Ce	Re ores and Re concentrates	Measured at 354 nm with excitation at 256 nm	–	Li (1988)
124	ICP-ES	R	Y_2O_3	–	0.4 ppm (Eu, Dy, Yb), 1 ppm (Er), 4 ppm (La, Pr, Gd, Tb, Ho, Tm, Lu), and 8 ppm (Ce, Nd, Sm)	Xi et al. (1988)
125	Spectrography	R	Y_2O_3	–	1.9–50 µg/ml	Jiang et al. (1988)
126	Spectrography	R	Y_2O_3	3.4 m plane grating spectrograph equipped with a 14-A DC arc	0.05–3.2% (La, Ho, Dy, Er), and 0.02–1.28% (Gd, Tm, Yb, Lu)	Qi et al. (1988)
127	Spectrography	R	Gd_2O_3	After extraction, chromatographic separation with P 507	–	You and Ma (1988)
128	ICP-ES	R	Lu_2O_3	After extraction, chromatographic separation with P 215	Coeff. of variation is 0.5–2.1%	Li et al. (1987b)
129	Spectrography	R	Nd_2O_3	After extraction, chromatographic separation with P 507 resin	6 ppm	You and Zhuang (1988)
130	ICP-ES	Eu, Gd, Dy, Ho, and Y	Tb_4O_7	–	70 ppm	Yuau et al. (1988)

continued on next page

Table 1, *continued*

Sl.#	Method	Analyte element	Matrix	Reaction conditions	Sensitivity/ Limit of detection	Reference
131	ICP-ES	R	Lu_2O_3	–	–	Piao et al. (1988)
132	ICP-ES	R	Pr_6O_{11}	–	–	Zhang (1990)
133	XRF	R	Eu_2O_3	Adsorption on P 507 resin	–	Lu et al. (1989)
134	ICP-ES	Sm, Eu, Tb, Dy and Y	Gd_2O_3	–	–	Yuau et al. (1990)
135	ICP-ES	R	Y_2O_3, La_2O_3, Gd_2O_3 and Yb_2O_3	–	–	Nakamura et al. (1990)
136	ICP-ES	R	Tb_4O_7	–	0.01–0.4 ppm	Chen et al. (1990a)
137	ICP-ES	Y, Sm, Eu, Gd, Dy, Ho, Er	Tb_4O_7	–	1.2–12 ng/ml	Biswas et al. (1991a)
138	Spectrography	R	Pr_6O_{11}	Extraction chromatographic separation with CLP-507 resin	9 ppm	D. Wang et al. (1986)
139	Luminescence	Tb	Tm_2O_3	–	20–250 pm	G.K. Novikova et al. (1981)
140	Fluorescence	Eu	La_2O_3, Y_2O_3	By reaction with ethanolic 1, 1, 1-trifluoro-5, 5 dimethyl hexane-2, 4-dione	2 pg/ml	Beltyukova and Kravchenko (1982)
141	Spectrography	R	Ho_2O_3	–	0.01–0.0001%	Li and Zhou (1991a)
142	XRF	R	R_2O_3	–	–	Le (1991)
143	Spectrography	R	Dy_2O_3	Ebert spectrograph with controlled Ar–O atmosphere DC arc excitation	5–100 ppm	Li and Zhou (1991b)
144	Derivative spectrophotometry	Yb, Dy	R_2O_3	Fourth-order derivative in 1 M $HClO_4$ solution	–	Yan and Ren (1990)
145	ICP-ES	Ce, Pr, Nd, Sm	La_2O_3	–	0.01–0.2 ppm	Biswas et al. (1991b)
146	ICP-ES	R	Y_2O_3, CeO_2	–	0.1–1 ppm	Dasklova et al. (1991)
147	ICP-ES	R	Tb_4O_7	–	–	Nakamura et al. (1991)
148	ICP-ES	R	Y_2O_3	–	0.48–5.0 ppm	Zhang (1991)
149	ICP-ES	R	R_2O_3	–	–	Liu (1991)
150	ICP-ES	R	R_2O_3	–	0.4–6.9 ppb	Chen et al. (1990b)
151	ICP-MS	R	Y_2O_3	–	0.03–0.2 µg/g	Prasada Rao and Damodaran (1991)
152	ICP-MS	R	R_2O_3	–	10 pf–10 µg/ml	Kawabata et al. (1991)
153	GD-MS	R	La, Pr, Nd, Gd and Tb metals	–	Low ppb range	Hirose et al. (1991)

continued on next page

Table 1, *continued*

Sl.#	Method	Analyte element	Matrix	Reaction conditions	Sensitivity/ Limit of detection	Reference
154	Derivative spectrophotometry	La, Eu	Eu_2O_3 and La_2O_3	pH 6.5, 15 min of heating using bromopyrogallol red as reagent	100 ppb (La^{3+}), 10 ppb (Eu^{3+})	Prasada Rao and Sukumar (1986)
155	Derivative spectrophotometry	Pr	Sm, Eu, Tm, Tb, Ho, Dy and Lu oxides	pH 7.0, 15 min. of heating	10 ppb (Pr^{3+})	Prasada Rao et al. (1988a)
156	Derivative spectrophotometry	Sm	Gd, Dy, Tb, Ho, Tm and Lu oxides	Methyl thymol blue–CTAB, pH 7.0	30 ppb (Sm^{3+})	Prasada Rao et al. (1988b)
157	EDXRF	R	Y_2O_3	Preconcentration in presence of Fe(III) hydroxide	10 ppb R	Prasada Rao et al. (1989)
158	EDXRF	R	Y_2O_3	Preconcentration on activated carbon in presence of quinoline-8-ol	10 ppb (R)	Prasada Rao et al. (1991)

determination of 1–18 ppm of ytterbium in Y_2O_3 (Chen et al. 1986) and europium in rare-earth oxides (Yao and Zeng 1984).

2.4. *Spectrography*

Both DC and AC arc spectrographic techniques were used for the determination of traces of lanthanides in high-purity rare-earth oxides. In a few cases spectrographic determinations were used in combination with various separation techniques. These include (i) separation of lanthanides in Y_2O_3 by extraction with naphthenic acid (Peng et al. 1979) and (ii) extraction chromatographic separation of traces of lanthanides in Nd_2O_3 (You and Zhuang 1988), Pr_6O_{11} (D. Wang et al. 1986) using 2-ethylhexyl(2-ethylhexyl)phosphonate–HCl medium. Other procedures involved the direct determination of lanthanides in high-purity rare-earth oxides (Yu et al. 1983), Ho_2O_3 (Li and Zhou 1991a), Y_2O_3 (Dittrich et al. 1972, Jiang et al. 1988, Qi et al. 1988), Sm_2O_3 and Gd_2O_3 (Nelder et al. 1980), La_2O_3 (Freidman et al. 1978), Pr_6O_{11} (Z. Ma et al. 1986), Gd_2O_3 (Song et al. 1986), Eu_2O_3 (Song et al. 1987), Dy_2O_3 (Li and Zhou 1991b), Tb_4O_7 (Song and Jin 1984), Er_2O_3 (Yu and Fu 1984), CeO_2 (Boitsov and Zilbershtein 1974) and rare-earth metal mixtures (Grampurohit and Sethumadhavan 1974).

2.5. *X-ray fluorescence (XRF)*

Wavelength-dispersive X-ray fluorescence, with a tungsten target and LiF analyzing crystal, is widely used for the determination of traces of lanthanides in high-purity

rare-earth oxides. Determinations include europium or gadolinium in Sm_2O_3 (Dixit and Deshpande 1978); cerium, praseodymium, samarium, europium and gadolinium in Nd_2O_3 (Chandola and Mohile 1977a); dysprosium, holmium, thulium, ytterbium, lutetium, terbium and yttrium in Er_2O_3 (Chandola et al. 1981); neodymium in YAG (Shevtsov et al. 1983); gadolinium, terbium, dysprosium thulium and ytterbium in Ho_2O_3 (Dixit and Kapoor 1979); yttrium, europium, gadolinium, terbium, holmium and erbium in Dy_2O_3 (Dixit and Deshpande 1980); lanthanum, cerium, neodymium and samarium in Pr_6O_{11} (Chandola and Mohile 1977b); samarium, europium, terbium, dysprosium, holmium and ytterbium in Gd_2O_3 (Chandola and Khanna 1987); samarium, dysprosium, europium and terbium in Y_2O_3 (Luo and Piao 1987); holmium, erbium, yttrium, thulium (Chandola et al. 1976), and 14 trace rare-earth elements in Eu_2O_3 (Lu et al. 1989) and in R_2O_3 (Le 1991). The utilization of chemometric approaches in energy-dispersive XRF procedures led to the determination of traces of lanthanides in Y_2O_3 (Prasada Rao et al. 1989, 1991).

2.6. *Emission spectrometry*

Of the various emission spectrometric techniques, the inductively coupled plasma emission spectrometric technique (ICPES) has been widely used for the determination of lanthanides in high-purity rare-earth oxides. Traces of lanthanides were determined by ICPES in high-purity La_2O_3 (Biswas et al. 1991b, Piao et al. 1989); in Yb_2O_3 (Piao et al. 1989); in Gd_2O_3 (Yuau et al. 1990, Li et al. 1987a); in Y_2O_3 (Xi et al. 1988, Zhang 1991); in Lu_2O_3 (Piao et al. 1988); in CeO_2 (Guo and Fec 1986); in Y_2O_3 and CeO_2 (Dasklova et al. 1991); in Tb_4O_7 (Nakamura et al. 1991, Yuau et al. 1988, Chen et al. 1990a, Biswas et al. 1991a); in Pr_6O_{11} (Zhang 1990); in matrices of Y, La, Gd, and Yb (Nakamura et al. 1990); and in high-purity rare-earth oxides (Liu 1991). An ICPES procedure was also developed in conjunction with a prior extraction procedure viz. extraction of 14 trace rare earths in Lu_2O_3 with P215–HNO_3 system (Li et al. 1987b).

2.7. *Luminescence spectrometry*

This technique is based on the formation of crystalline phosphors and measuring the resulting luminescence intensity. These procedures facilitate the determination of gadolinium, europium, dysprosium, samarium and terbium in Y_2O_3 (Antonov et al. 1973a); terbium, dysprosium and holmium in La_2O_3 (Efryushina et al. 1973a); neodymium and dysprosium in gadolinium oxyfluoride (Efryushina et al. 1973b); terbium (G.K. Novikova et al. 1981) and dysprosium (Efryushina et al. 1984) in Tm_2O_3; samarium and europium in Gd_2O_3 (Smirdova et al. 1980); europium in oxides of La, Gd, Tb and Y (Beltyukova et al. 1980); terbium in Gd_2O_3 (Zhikareva et al. 1981) and in La_2O_3 (Poluektov et al. 1973); terbium, dysprosium and holmium in La_2O_3 (Efryushina et al. 1973a); samarium, europium and dysprosium in Gd_2O_3 (Poluektov and Gava 1969); europium in Y_2O_3 (F. Wang et al. 1986); holmium and erbium in Y_2O_3 (Lebedeva and Karyakin 1985); terbium, europium and samarium in Gd_2O_3 and Tb_4O_7 (Efryushina and Novikova 1984); dysprosium in Yb_2O_3 (G.K. Novikova et al. 1983); terbium in YbOF

and GdOF (G.K. Novikova et al. 1981); gadolinium, terbium and dysprosium in Y_2O_3 (Gava et al. 1976); praseodymium in Nd_2O_3 (Shulgin et al. 1973); and europium, thulium and ytterbium in La_2O_3 (Efryushina et al. 1973b).

2.8. *Neutron activation analysis (NAA)*

Neutron activation analysis finds application in the determination of lanthanum in Pr_6O_{11} (Dybczynski and Sterlinski 1972); praseodymium, cerium and terbium in Y_2O_3 (Polkowska 1982); gadolinium in Eu_2O_3 (Kubota 1976); europium, holmium and terbium in Tm_2O_3 (Antonov et al. 1973b); and lanthanides in YAG (Muminov et al. 1979), in CeO_2 (Pung et al. 1980) and in Lu_2O_3 (Kubota 1974). Further, a procedure was developed for the determination of traces of yttrium in various rare-earth oxides after extraction chromatographic separation using bis-(2-ethyl hexyl)phosphate on Kieselguhr as support (Teixeira da Silva and Atalla 1979).

2.9. *Miscellaneous techniques*

A polarographic procedure was suggested for the determination of traces of lanthanum in lanthanum–gadolinium oxysulphide (Gao et al. 1983). Steeman et al. (1977) described pulse polarographic determination of traces of europium in rare-earth oxides. Cerium in rare-earth oxides was determined by stripping voltammetry (Iikova et al. 1983). Klinov and Ladeishchikov (1986) have developed a γ-activation procedure for the determination of traces of neodymium and yttrium in La_2O_3 and Tb_4O_7. Uwamino et al. (1984) and

Table 2
Results of the analysis of high-purity yttrium oxide samples

Element	Based on Y_2O_3 (μg/g)		
	Sample 1[a]	Sample 2[b]	Detection limit
La	0.22	0.07	0.03
Ce	0.45	0.08	0.02
Pr	0.13	<0.01	0.01
Nd	0.25	<0.1	0.10
Sm	1.20	<0.1	0.10
Eu	0.75	0.5	0.06
Gd	1.20	<0.19	0.19
Dy	6.20	<0.07	0.07
Ho	4.00	<0.03	0.03
Er	7.20	<0.12	0.12
Tm	0.89	<0.05	0.05
Yb	3.80	<0.16	0.16

[a] Supplied by M/s Indian Rare Earths Limited, India.
[b] Imported sample.

Morikawa et al. (1990) have described a secondary ion mass spectrometric procedure for the determination of rare earths in YF_3, LaF_3 and Y_2O_3. X-ray excited optical luminescence procedures were developed for the determination of traces of lanthanides in Y_2O_3 (De Silva and Fassel 1972) and terbium in Gd_2O_3 (A.K. Novikova et al. 1980). Prasada Rao and Damodaran (1991) have developed an ICP-mass spectrometric (ICPMS) procedure for the determination of traces of lanthanides in high-purity yttrium oxide. The results obtained are shown in table 2. Kawabata et al. (1991) developed an ICPMS procedure in combination with ion chromatography for the determination of traces of lanthanides in high purity rare earth oxides. A glow discharge mass spectrometric procedure (Hirose et al. 1991) was developed for the determination of traces of rare earths in high-purity lanthanum, praseodymium, neodymium, gadolinium and terbium metals. The detection limits were in the sub-ppb range for certain rare-earth elements.

3. Conclusions

The determination of traces of lanthanides in high-purity rare-earth oxides is a challenging task for analytical chemists in view of the similar properties of rare earths, arising from the lanthanide contraction. Spectrophotometry is not suitable for this analysis as it does not distinguish between various rare-earth species. Derivative spectrophotometry was employed recently to determine traces of lanthanides in high-purity rare-earth oxides. Spectrofluorimetry, like spectrophotometry, cannot distinguish between various rare-earth species and only a few procedures have been developed. Atomic absorption spectrometry, though applicable for the determination of traces of lanthanides in high-purity rare-earth oxides, is not that sensitive. Hence, this technique has attracted very little interest over the years.

Spectrography, X-ray fluorescence and luminescence spectrometry were widely used in the 1970s and early 1980s for the trace determination of lanthanides in high-purity rare-earth oxides. But these techniques require elaborate and cumbersome sample preparation procedures and are not found to be that popular in the 1990s. In view of this, ICP-ES is the most often sought analytical technique for the trace determination of lanthanides in high-purity rare-earth oxides. ICP-MS and GD-MS which are presently used for the reliable determination of rare earths in geological samples will be the techniques that find wide application in the determination of lanthanides in high-purity rare-earth oxides in the coming years.

In summary, the determination of lanthanides in high-purity rare-earth oxides depends on the ultimate use of rare-earth oxides in commercial devices. Derivative spectrophotometry and EDXRF (which are less costly) can be reliably used for monitoring lanthanides in 90% to 3 N purity rare-earth oxides. The determination of traces of lanthanides in high-purity rare-earth oxides (4 N to 6 N) invariably requires costlier ICP-MS or GD-MS techniques for liquid and solid samples.

References

Abbasi, S.A., 1980, Sep. Sci. Technol. **15**, 1789.

Agapova, L.V., A.V. Antanov, N.V. Tenova and N.V. Bagaev, 1981, Zavod Lab. **47**, 45.

Antonov, A.V., Sh.G. Melamed and L.V. Kulevskii, 1973a, Zh. Khim. **19GD**, 19.

Antonov, A.V., V.F. Vozhozhov, Yu.S. Kim and V.E. Moiseev, 1973b, Ref. Zh. Khim. **19GD**, Abstr. No. 20 G 106.

Beltyukova, S.V., and T.B. Kravchenko, 1982, Zavod. Lab. **48**, 13.

Beltyukova, S.V., N.S. Poluektov, T.B. Kravchenko and L.I. Kononenka, 1980, Zh. Anal. Khim. **35**, 1103.

Beltyukova, S.V., N.S. Poluektov, T.L. Gritsai and T.B. Kravchenko, 1984, Zavod. Lab. **50**, 25.

Biswas, S.S., A. Sethumadhavan and P.S. Murthy, 1991a, Microchim. Acta I, 71.

Biswas, S.S., R. Kaimal, A. Sethumadhavan and P.S. Murthy, 1991b, Anal. Lett. **24**, 1885.

Boitsov, A.A., and Kh.I. Zilbershtein, 1974, Ref. Zh. Khim. **19GD**, Abstr. No. 22 G 114.

Buehring, M., and H.P. Buban, 1981, Lab. Praxis **5**, 34.

Chandola, L.C., and P.P. Khanna, 1985a, J. Radioanal. Nucl. Chem. **91**, 157.

Chandola, L.C., and P.P. Khanna, 1985b, Microchim. Acta **111**, 191.

Chandola, L.C., and P.P. Khanna, 1987, Indian J. Pure Appl. Phys. **25**, 157.

Chandola, L.C., and A.N. Mohile, 1977a, India A.E.C. BARC **886**, 6.

Chandola, L.C., and A.N. Mohile, 1977b, Curr. Sci. **46**, 299.

Chandola, L.C., and A.N. Mohile, 1978, Indian J. Pure Appl. Phys. **16**, 851.

Chandola, L.C., I.J. Machado and A.N. Mohile, 1976, J. Radioanal. Chem. **34**, 389.

Chandola, L.C., P.P. Khanna and A. Thomas, 1981, India, Report BARC 1088 (India Atomic Energy Commission) p. 17.

Chen, D., Y. Zhong and S. Liang, 1986, Guangpuue, Yu. Guangpu Fenxi **6**, 53.

Chen, H., Z. Jiang, Z. Liao and Z. Lai, 1990a, Lihua Jianya Fence **26**, 268.

Chen, H., Z. Ziang and S. Shang, 1990b, Lihua Jianyau, Zuaxue Fence **26**, 207.

Dasklova, N., N. Krasnobaeva, S. Velichkov, B. Pavlovic, M. Pavlovic and M. Marinkovic, 1991, J. Serb. Chem. Soc. **56**, 205.

De Silva, A.P., and V.A. Fassel, 1972, Anal. Chem. **45**, 542.

DeKalb, E.L., and V.A. Fassel, 1979, in: Handbook on the Physics and Chemistry of Rare Earths, Vol. 4, eds K.A. Gschneidner Jr and L. Eyring (North-Holland, Amsterdam) ch. 37D.

Dittrich, K., and K. Borzyn, 1977, Anal. Chim. Acta. **94**, 83.

Dittrich, K., and K. Niebergall, 1978, Chem. Anal. (Warsaw) **23**, 51.

Dittrich, K., W. Thuemmler and K. Niebergall, 1972, Wiss. Karl Marx Univ. **21**, 31.

Dittrich, K., M. Gajek and P. Luan, 1978, Chem. Anal. (Warsaw) **23**, 41.

Dixit, R.M., and S.S. Deshpande, 1975, Report BARC 806 (India Atomic Energy Commission) p. 13.

Dixit, R.M., and S.S. Deshpande, 1977a, Fresenius Z. Anal. Chem. **287**, 132.

Dixit, R.M., and S.S. Deshpande, 1977b, Fresenius Z. Anal. Chem. **288**, 180.

Dixit, R.M., and S.S. Deshpande, 1978, Fresenius Z. Anal. Chem. **292**, 375.

Dixit, R.M., and S.S. Deshpande, 1980, Fresenius Z. Anal. Chem. **303**, 111.

Dixit, R.M., and S.K. Kapoor, 1979, Fresenius Z. Anal. Chem. **296**, 394.

Dybczynski, R., and S. Sterlinski, 1972, Chem. Anal. (Warsaw) **17**, 1275.

Efryushina, N.P., and G.K. Novikova, 1984, Zh. Anal. Khim. **39**, 295.

Efryushina, N.P., N.S. Poluektov, N.I. Smirdova and V.A. Kudryashov, 1973a, Zh. Anal. Khim. **28**, 1213.

Efryushina, N.P., N.I. Smirdova, N.S. Poluektov and V.A. Kudryashov, 1973b, Zavod. Lab. **39**, 129.

Efryushina, N.P., G.K. Novikova and N.S. Poluektov, 1977, Zh. Anal. Khim. **32**, 1731.

Efryushina, N.P., G.K. Novikova, E.A. Zhikareva and V.P. Dotsenko, 1982, Zh. Anal. Khim. **37**, 244.

Efryushina, N.P., G.K. Novikova and S.V. Ernakova, 1984, Zavod. Lab. **50**, 38.

Freidman, R., A.R. Lordello and A. Abrao, 1978, Publ. IEA No. 505, p. 26.

Gao, X., K. Jiao and S. Wu, 1983, Fenxi Huaxue **11**, 107.

Gava, S.A., E.A. Zhikareva, N.P. Efryushina and N.S. Poluektov, 1976, Zh. Anal. Khim. **31**, 2129.

Gava, S.A., G.K. Novikova and N.P. Efryushina, 1979, Zh. Anal. Khim. **34**, 117.

Grampurohit, S.V., and A. Sethumadhavan, 1974, Z. Anal. Chem. **272**, 25.
Guo, Y., and S. Fec, 1986, Fenxishiyanshi **5**, 27.
Gustafson, F.J., and J.C. Wright, 1979, Anal. Chem. **51**, 1762.
Hirose, F., S. Itoh and H. Okochi, 1991, Tetsu To Hagane **77**, 598.
Hwang, J., J. Shih, Y. Yeh and S. Wu, 1981, The Analyst **106**, 869.
Iikova, S.B., E.A. Zazimko and A.V. Antonov, 1983, Zavod. Lab. **49**, 85.
Ishii, H., and K. Satoh, 1983, Talanta **30**, 111.
Jayawant, D.V., N.S. Iyer and T.K.S. Murthy, 1976, Indian J. Technol. **14**, 151.
Jiang, Z., H. Chen, L. Xu, Z. Liao and S. Zhang, 1988, Fenxi Shiyanshi **7**, 31.
Jyrkas, K., and M. Leskela, 1986, J. Less-Common Met. **126**, 291.
Kawabata, K., Y. Kishi, O. Kawaguchi, Y. Watanabe and Y. Inoue, 1991, Anal. Chem. **63**, 2137.
Klinov, F.M., and A.V. Ladeishchikov, 1986, Ref. Zh. Khim. **19GD** Abstr. No. G 215.
Kniseley, R.N., C.C. Butler and V.A. Fassel, 1969, Anal. Chem. **41**, 1494.
Kubota, M., 1974, J. Nucl. Sci. Technol. **11**, 334.
Kubota, M., 1976, J. Nucl. Sci. Technol. **13**, 449.
Kueppers, G., and G. Erdtmann, 1981, Fresenius Z. Anal. Chem. **307**, 369.
Larach, S., and R.E. Shrader, 1973, Anal. Chim. Acta **63**, 459.
Larsen, N.R., and W.B. Pedersen, 1978, J. Radioanal. Chem. **45**, 135.
Le, Q., 1991, Huaxue Fence **27**, 207.
Lebedeva, N.A., and A.V. Karyakin, 1985, Zh. Anal. Khim. **40**, 1249.
Li, L., J. Ma and G. Jin, 1987a, Xiyou Jinshu **6**, 284.
Li, L., J. Ma and G. Jin, 1987b, Huaxue Shiji **9**, 324.
Li, Q., and C. Zhou, 1991a, Fenxi Shiyanshi **10**, 48.
Li, Q., and C. Zhou, 1991b, Fenxi Shiyanshi **10**, 35.
Li, X., 1988, Linua Jianyan **24**, 180.
Liu, W., 1991, Hauxue Fence **27**, 88.
Lu, S., Z. Wang, S. Li, J. Li and X. Wu, 1989, Zhongguo Xitu Xuebao **7**, 68.
Luo, J., and S. Piao, 1987, Xioyu, Jinshu **6**, 153.
Luo, S., and Q. Hu, 1981, Fenxi Huaxue **9**, 284.
Lutz, G.J., and P.D. Lafleur, 1969, Talanta **16**, 1457.
Lyle, S.J., and R. Maghzian, 1975, Anal. Chim. Acta **80**, 125.
Lyle, S.J., and N. Zatar, 1983, Anal. Proc. **20**, 616.
Ma, J., X. Chen and J. Tan, 1986, Guangpuxue Yu Guangpu. Fensci **6**, 44.
Ma, Z., Y. Xia and Y. Zhang, 1986, Fenxi Shiyanshi **5**, 24.
Maltseva, V.S., and S.E. Kharzeeva, 1979, Zavod. Lab. **45**, 198.
Matsuda, S., and S. Hanamura, 1977, Bunseki Kagaku **26**, 662.
Meliman, M.A., A.I. Kolomitsev, I.S. Volodina, A.G. Smagni, Kh.S. Bagdasarov and A.M. Keborkov, 1983, Zh. Prikl. Spektrosk. **38**, 755.
Mischenko, V.T., V.D. Kovtun, N.N. Alexandrova and N.S. Poluektov, 1978, Koord. Khim. **4**, 1658.
Morikawa, H., Y. Uwamino and J. Ishizuka, 1990, Z. Anal. Chem. **336**, 210.
Muminov, V.A., R.A. Khaidarov and J. Kharmarkulov, 1979, Zh. Anal. Khim. **34**, 703.
Murthy, T.K.S., and C.K. Gupta, 1980, Science and Technology of Rare Earth Materials (Academic Press, New York).
Nakamura, Y., K. Takahashi, O. Kujirai and H. Okochi, 1990, J. Anal. At. Spectromet. **5**, 501.
Nakamura, Y., Y. Murai, D. Ni and Y. Liu, 1991, Bunseki Kagaku **40**, 1125.
Nelder, V.V., A.A. Shtenke and A.A. Pupyshev, 1980, Zh. Anal. Khim. **35**, 2080.
Novikova, A.K., E.A. Zhikareva, S.A. Gava, N.P. Efryushina and N.S. Poluektov, 1980, Zh. Anal. Khim. **35**, 1288.
Novikova, G.K., N.P. Efryushina, E.A. Zhikhareva and V.P. Dotsenko, 1981, Zh. Anal. Khim. **36**, 663.
Novikova, G.K., E.A. Zhikareva, N.N. Zoltnikova and N.P. Efryushina, 1983, Zh. Anal. Khim. **38**, 60.
Osumi, Y., and Y. Hiyake, 1972, Z. Anal. Chem. **260**, 97.
Ozawa, L., and H.N. Hersh, 1976, Spec. Publ. Natl. Bur. Stand. US., No. 422, p. 1103.
Peng, C., A. Pei, S. Wu, Y. Ji, B. Yan, X. Sui and C. Liu, 1979, Hua Hsueh Hsueh Pao **34**, 267.
Peng, C., Y. Ji, C. Liu, S. Chunlan, H. Xiyun and A. Lu, 1981, Fen Hsi Hua Hsueh **99**, 278.
Piao, Z., A. Pei and B. Huang, 1988, Fenxi Juaxue **16**, 864.
Piao, Z., A. Pei, Z. Liu, X. Chen and B. Huang, 1989, Fenxi Huaxue **17**, 424.
Polkowska, H.M., 1982, Radiochem. Radioanal. Lett. **52**, 273.
Poluektov, N.S., and S.A. Gava, 1969, Zavod. Lab. **35**, 1458.
Poluektov, N.S., N.I. Smirdova and N.P. Efryushina, 1970, Zh. Anal. Khim. **25**, 715.
Poluektov, N.S., N.P. Efryushina, N.I. Smirdova and S.A. Gava, 1972, Zh. Anal. Khim. **27**, 282.

Poluektov, N.S., R.S. Lauer and L.A. Ovchar, 1973, Zh. Anal. Khim. **28**, 1490.
Poluektov, N.S., M.A. Tischenko and G.I. Gerasimenko, 1975, Zh. Anal. Khim. **30**, 1325.
Polyanskii, V.A., Yu.I. Turkin and N.M. Yakimba, 1979, Zh. Anal. Khim. **34**, 282.
Prasada Rao, T., and A.D. Damodaran, 1991, RRL(T) Report.
Prasada Rao, T., and R. Sukumar, 1986, Anal. Lett. **19**, 1731.
Prasada Rao, T., R. Sukumar and A.D. Damodaran, 1988a, The Analyst **113**, 1061.
Prasada Rao, T., V. Bhagavathy and A.D. Damodaran, 1988b, Anal. Lett. **21**, 901.
Prasada Rao, T., V. Bhagavathy, P.S.T. Sai and A.D. Damodaran, 1989, Anal. Lett. **22**, 197.
Prasada Rao, T., V. Bhagavathy, M.L.P. Reddy, P.S.T. Sai and A.D. Damodaran, 1991, Anal. Chim. Acta. **242**, 215.
Pung, T., H.T. Sai and S.C. Wu, 1980, Ho Tzu K'o Hsueh **17**, 190.
Qi, W., F. Yuan and R. Peng, 1988, Fenxi Huaxue **16**, 286.
Ross, E.S., 1969, Anal. Chim. Acta. **45**, 227.
Ru, N., W. Chang, Z. Jiang and Y. Zeng, 1983, Spectrochim. Acta. **38**, 175.
Shevtsov, N.I., A.B. Blank and I.T. Mirenskaya, 1983, Zh. Anal. Khim. **38**, 2259.
Shmanenkova, G.I., M.G. Zemskova, Sh.G. Melamed, G.P. Pleshakova and G.V. Sukhov, 1969, Zavod. Lab. **35**, 897.
Shulgin, B.V., A.V. Antonov, F.F. Gobrilov, F.G. Iveshev and A.A. Pwzanov, 1973, Ref. Zh. Khim. **19GD**, Abstr. No. 20 G 104.
Smirdova, N.I., N.P. Efryushina and N.S. Poluektov, 1970, Zavod. Lab. **36**, 1183.
Smirdova, N.I., G.K. Novikova and N.P. Efryushina, 1980, Zh. Anal. Khim. **35**, 471.
Song, W., and Y. Jin, 1984, Fenxi Huaxue **12**, 852.
Song, W., Y. Jing, S. Mong and S. Zhang, 1986, Fenxi Shiyanshi **5**, 21.
Song, W., J. Yuan and S. Meng, 1987, Guangpuxue, Yu Guangpu Fenxi **7**, 28.
Song, W., S. Meng and Y. Yang, 1989, Fenxi Huaxue **17**, 343.
Steeman, E., E. Temmerman and F. Verbeck, 1977, Bull. Soc. Chim. Belg. **86**, 491.
Stroganova, N.S., V.Ya. Ryabbukhim, I.P. Galkina and A.N. Ermakov, 1973, Zh. Anal. Khim. **28**, 1313.
Su, Q., and H. Wang, 1985, Fenxi Huaxue **13**, 354.
Tanaka, T., T. Yamada, T. Johnokuchi, J. Yamada, K. Kumamoto and K. Hattori, 1982, Bunseki Kagaku **31**, 385.
Teixeira da Silva, D.I., and L.T. Atalla, 1979, Inf. IEA No. 532, p. 10.
Tischenko, M.A., I.I. Zheltvai, I.V. Bakshun and N.S. Poluektov, 1973a, Zh. Anal. Khim. **28**, 1954.
Tischenko, M.A., I.I. Zheltvai, N.S. Poluektov and I.V. Bakshun, 1973b, Zavod. Lab. **39**, 671.
Tischenko, M.A., G.I. Gerasimenko and N.S. Poluektov, 1974, Zavod. Lab. **40**, 935.
Tischenko, M.A., G.I. Gerasimenko and N.S. Poluektov, 1978a, Zh. Anal. Khim. **33**, 77.
Tischenko, M.A., N.S. Poluektov, G.F. Yaroshenko, R.P. Lastovski, G.I. Gerasimenko, I.I. Zeltvai and L.M. Timakova, 1978b, Zh. Anal. Khim. **33**, 2368.
Ujihira, Y., Y. Suzuki and S. Yokono, 1973, Jpn. Analyst **22**, 1610.
Uwamino, Y., T. Ishizuka, A. Tsuge and H. Yamatera, 1984, Shitsuryo Bunseki **32**, 277.
Vakulenko, L.I., B.Ya. Kaplan, Yu.I. Merisov, A.I. Mikhalichenko and G.S. Stripkin, 1973, Zavod. Lab. **39**, 1342.
Wang, D., Z. Ma, L. Hao, Y. Xia and Y. Zhang, 1986, Fenxi Shiyanshi **5**, 4.
Wang, F., C. Jiang and X. He, 1986, Fenxi Shiyanshi **5**, 7.
Xi, W., F. Yuan and S. Guan, 1988, Xiyou Jinshu **7**, 59.
Xu, Y., and S. Qui, 1984, Fenxi Huaxue **12**, 703.
Yan, Y., and Y. Ren, 1990, Fenxi Huaxue **18**, 897.
Yao, J., and J. Zeng, 1984, Fenxi Huaxue **12**, 343.
Yatsimirskii, K.B., L.I. Budarin and A.G. Kachatryan, 1970, Dokl. Akad. Nauk. USSR **195**, 898.
You, W., and Z. Ma, 1988, Fenxi Shiyanshi **7**, 63.
You, W., and Y. Zhuang, 1988, Fenxi Shiyanshi **7**, 21.
Yu, S., and X. Fu, 1984, Fenxi Huaxue **12**, 1081.
Yu, S., and J. Miao, 1983, Huaxue Shiji **5**, 136.
Yu, S., J. Lin, Y. Weng and Z. Liu, 1983, Fenxi Huaxue **11**, 273.
Yuau, F., W. Qi and A. Pei, 1988, Fenxi Huaxue **16**, 837.
Yuau, F., W. Qi and X. Chen, 1990, Guangpuxue Yu Guangpu Fenxi **10**, 44.
Zhang, C., 1990, Guangpuxue Yu Guangpu Fenxi **10**, 54.
Zhang, C., 1991, Fenxi Shiyanshi **10**, 26.
Zhang, T., 1983, Talanta **30**, 864.
Zhikareva, E.A., G.K. Novikova and N.P. Efryushina, 1981, Zh. Anal. Khim. **36**, 1079.

SUBJECT INDEX

AUTHOR INDEX